TECHNISCHE UNIVERSITÄT MÜNCHEN
Lehrstuhl für Anorganische Chemie mit Schwerpunkt Neue Materialien

Synthesis, Characterization and Reactivity of Lithium-Containing Silicides, Germanides and Borosilicides

Michael Hermann Zeilinger

Vollständiger Abdruck der von der Fakultät für Chemie der Technischen Universität München zur Erlangung des akademischen Grades eines

Doktors der Naturwissenschaften (Dr. rer. nat.)

genehmigten Dissertation.

Vorsitzender:		Univ.-Prof. Dr. Tom Nilges
Prüfer der Dissertation:		
	1.	Univ.-Prof. Dr. Thomas F. Fässler
	2.	Univ.-Prof. Hubert Gasteiger, Ph.D.
	3.	Univ.-Prof. Dr. Wolfgang Scherer

Die Dissertation wurde am 13.02.2014 bei der Technischen Universität München eingereicht und durch die Fakultät für Chemie am 06.05.2014 angenommen.

I'd put my money on the sun and solar energy. What a source of power! I hope we don't have to wait until oil and coal run out before we tackle that.

Thomas Edison, 1931

Danken möchte ich

ganz besonders meinem Doktorvater

Prof. Dr. Thomas F. Fässler

für die überaus interessante Themenstellung, die sehr umfangreiche Unterstützung, Vertrauen, Wohlwollen und wissenschaftliche Freiheiten.

Prof. Dr. Ulrich Häussermann für die jährliche Organisation und den reibungslosen Ablauf der Forschungsaufenthalte an der ARIZONA STATE UNIVERSITY, der äußerst angenehmen und fruchtbaren Zusammenarbeit im Rahmen des Projektes „MATERIALS WORLD NETWORK“ sowie die stete Diskussions- und Hilfsbereitschaft.

dem *Fonds der Chemischen Industrie* für die Gewährung eines Promotionsstipendiums und die großzügige Unterstützung meiner Forschungsaufenthalte an der ARIZONA STATE UNIVERSITY.

meinen Büro- und Laborkollegen *Thomas Henneberger*, *Andrea Hoffmann*, *Dr. Tobias Köchner*, *Ulla Madan-Singh*, *Maria Müller*, *Lavinia Scherf* und *Patrick Woidy* für die positive Arbeitsatmosphäre und ihre Hilfe in vielen Bereichen. *Manuela Donaubauer* für ihre Hilfe hinsichtlich organisatorischer Angelegenheiten.

Priv. Doz. Dr. Florian Kraus für sehr viele gute Ratschläge, seine stete Diskussions- und Hilfsbereitschaft und die Bereitstellung von ^{6}Li. *Dr. Alexander Pöthig* für die Messerlaubnis an den Einkristalldiffraktometern der Gruppe Prof. Kühn und wertvolle kristallographische Tipps. *Prof. Dr. Tom Nilges*, *Dr. Viktor Hlukhyy*, *Dr. Wilhelm Klein* und *Dr. Bernhard Wahl* für Ihre Hilfe bei kristallographischen Angelegenheiten.

allen Koautoren für die Mitarbeit an unseren Publikationen.

den Gruppen *Fässler*, *Häussermann*, *Kraus* und *Nilges.*

meiner Forschungspraktikantin und Masterandin *Lavinia Scherf* sowie meinen Forschungspraktikanten *Alexander Hufnagel* und *Philipp Rheinländer* für das rege Interesse, eine hervorragende Zusammenarbeit und die Unterstützung meiner Arbeit durch ihre Beiträge.

allen weiteren Beteiligten des Projektes „MATERIALS WORLD NETWORK“, *Prof. Dr. Wolfgang Scherer*, *Prof. Dr. Otto Sankey*, *Prof. Dr. John Shumway*, *Volodymyr Baran*, *Dr. Daryn Benson*, *Daniel Eklöf*, *Andreas Fischer*, *Dr. Antti J. Karttunen*, *Sumit Konar* und *Dr. Yang Wu* für das Einbringen in viele Diskussionsrunden und sehr hilfreiche Beiträge. Insbesondere *Andreas Fischer*, für die sehr angenehme und bestens organisierte Arbeits- und Wohngemeinschaft während unserer USA-Aufenthalte sowie seine Hilfsbereitschaft. *Sumit Konar* und *Dr. Kati Puhakainen* für ihre Mithilfe bei der Organisation der Forschungsaufenthalte. *Dr. Kurt Leinenweber* und *Craig Naseyowma* für ihre Unterstützung bei Hochdruckexperimenten und das reibungslose Arbeiten im Hochdrucklabor der ARIZONA STATE UNIVERSITY. *ASU Associate Prof. Dr. Don Seo* für die Bereitstellung diverser Laborgeräte und *Dr. Thomas Groy* für die Benutzung der Pulver- und Einkristalldiffraktometer an der ARIZONA STATE UNIVERSITY.

Prof. Leo van Wüllen für NMR-Messungen, *Andrea Hoffmann* für SQUID-Messungen, *Katia Rodewald* und *Ingrid Werner* für diverse EDX-Messungen und REM-Aufnahmen.

meinen Kollegen *Dr. Sebastian Baer*, *Dr. Christian Benda*, *Manuel Bentlohner*, *Dr. M. Bele Boeddinghaus*, *Dr. Daniel Bräunling*, *Carina Dressel*, *Dr. Zoreh Fard*, *Haiyan He*, *Alexander Henze*, *Laura-Alice Jantke*, *Dr. Florian J. Kiefer*, *Dr. Aslihan Kircali*, *Iryna M. Kurylyshyn*, *Dr. Prashanth W. Menezes*, *Thomas Müller*, *Stefan Rudel*, *Dr. Annette Schier*, *Herta Slavik*, *Dr. Sheng Ping Guo*, *Dr. Lisa Siggelkow, Dr. Saskia Stegmaier*, *Lorenzo Toffoletti*, *Dr. Markus Waibel*, *Dr. Lei Zhang* für ihre Hilfsbereitschaft, die gute Zusammenarbeit, diverse Unternehmungen und eine schöne gemeinsame Zeit.

allen Mitarbeitern der Fakultät für Chemie der Technischen Universität München, die zum Gelingen dieser Arbeit beigetragen haben.

meinen *Freunden.*
meiner Freundin *Jennifer Ludwig*.
meiner *Familie* für Rückhalt und ihre jahrelange Unterstützung.

Zusammenfassung

Seit einigen Jahren wird der Einsatz von Silicium als Anodenmaterial für Lithium-Ionen-Akkumulatoren diskutiert, um den steigenden Leistungsanforderungen durch Erhöhung der Kapazität gerecht zu werden. Im Vergleich zu herkömmlichen, mit Graphit als Anode betriebenen Akkus kann ein massiver Kapazitätsgewinn durch Bildung der lithiumreichen Phase $Li_{15}Si_4$ erreicht werden, wobei in einigen Fällen auch die Bildung von $Li_{22}Si_5$ oder $Li_{21}Si_5$ postuliert wird. Ungeachtet der Bedeutung des damit eng in Verbindung stehenden Phasensystems Li–Si, insbesondere des lithiumreichen Teils, waren bislang grundlegende Charakteristika nur unzureichend untersucht.

Im Rahmen der vorliegenden Arbeit wurde das Li–Si-Phasendiagramm im Bereich > 76 at.% Li mittels dynamischer Differenzkalorimetrie neu bestimmt und deutlich verbessert. Voraussetzung hierfür war die Identifizierung und zweifelsfreie strukturelle Charakterisierung aller zugehörigen (lithiumreichen) Phasen. Im Einzelnen wurden durch röntgenographische Untersuchungen an Einkristallen $Li_{13}Si_4$ und $Li_{15}Si_4$, das fehlgeordnete Hochtemperatursilicid $Li_{16.4}Si_4$ sowie die lithiumreichste Phase des Systems $Li_{17}Si_4$ charakterisiert. Letztere löst das bislang als lithiumreichstes Silicid beschriebene $Li_{21}Si_5$ ($Li_{16.8}Si_4$) ab. Die Struktur von $Li_{13}Si_4$ wurde auf Grund von Diskrepanzen zwischen berechneten (auf Basis vorheriger Einkristalldaten) und experimentellen Röntgenpulverdiffraktogrammen von $Li_{13}Si_4$ neu bestimmt und deutlich verbessert. Geeignete Einkristalle, insbesondere im Falle der ersten Einkristalle zur metastabilen Phase $Li_{15}Si_4$, wurden größtenteils durch Züchtung mittels Metallbadtechnik (Li-Überschuss bzw. „Li-Flux“) erhalten. Entscheidender Bedeutung zur Revision des Li–Si-Phasendiagramms wird der Entdeckung der neuen Phase $Li_{16.4}Si_4$ beigemessen. Das thermische Zersetzungsverhalten der oberhalb von 170 °C nicht mehr stabilen Phase $Li_{15}Si_4$ wurde zudem eingehend untersucht. Dabei spiegelte die Phasenzusammensetzung der Zersetzungsprodukte ab 400 °C den Verlauf des neu etablierten Li–Si-Phasendiagrams exakt wider. Zwischen 170 °C und 300 °C zersetzt sich $Li_{15}Si_4$ in $Li_{17}Si_4$ und eine teilamorphe, nicht identifizierte Phase. Die Dotierung von $Li_{15}Si_4$ mit geringen Mengen Al im Sinne von $Li_{15-x}Al_xSi_4$ ($0.4 < x < 0.8$) führt jedoch zu thermodynamisch stabilen Produkten, die sich in einem reversiblen Prozess ab ca. 700 °C zersetzen. Die Ausweitung der Untersuchungen auf das System Li–Ge führten zur Charakterisierung der schwereren Homologen $Li_{17}Ge_4$ und $Li_{16.4}Ge_4$ sowie

zur Neubestimmung des Phasendiagramms im Bereich > 79 at.% Li. Im Zuge dessen wurde auch die Mischbarkeit der isotypen Phasen $Li_{17}Si_4$ und $Li_{17}Ge_4$ untersucht. Hier wurde die Gültigkeit der Vegard'schen Regel für die festen Lösungen $Li_{17}Si_{4-x}Ge_x$ [x = 2.30(2), 3.08(4), 3.53(3)] gezeigt.

Ein weiterer Fokus dieser Arbeit liegt auf der Synthese neuer Phasen im System Li–B–Si sowie der Elementmodifikation *allo*-Si, von denen angenommen wird, dass sie interessante Charakteristika hinsichtlich ihres Einsatzes als alternative Elektrodenmaterialien besitzen. Die Reproduktion der Synthese des Si-Polymorphs *allo*-Si durch Oxidation der Phase Li_3NaSi_6 führte zu *a*morphen Produkten (*a*-*allo*-Si). Starke Ähnlichkeiten der Pulverröntgenbeugungsdaten von *allo*-Si aus früheren Arbeiten und $NbSi_2$ deuten auf eine irrtümliche Phasenzuordnung auf Grund einer $NbSi_2$-Verunreinigung hin. $NbSi_2$ kann aus der Reaktion des Ampullenmaterials Nb mit α-Si bei der Synthese der Vorstufe Li_3NaSi_6 hervorgehen. Eine Analyse der Phasenumwandlungstemperaturen (amorph-zu-kristallin) verschiedener *a*-*allo*-Si Proben zeigte eine starke Schwankung in einem Temperaturbereich von 487–565 °C auf. Im Gegensatz dazu wandelt sich herkömmliches, vollständig *a*morphes Si (*a*-Si), hergestellt aus $Li_{15}Si_4$ durch Li-Extraktion mittels flüssigem Ammoniak, bei höheren Temperaturen um (~660 °C). Jedoch lässt sich dieser Unterschied auf einen hohen Anteil von α-Si Kristalliten und damit Kristallisationskeimen in *a*-*allo*-Si Proben zurückführen. Nach eingehenden Untersuchungen war keine eindeutige Differenzierung zwischen *a*-*allo*-Si und *a*-Si möglich, so dass die Existenz des Si Polymorphs *allo*-Si gemäß dem in der Literatur beschriebenen Syntheseverfahren nicht bestätigt werden konnte. Im Zuge der Untersuchungen von festen Lösungen $Li_3Na(Si_{1-x}Ge_x)_6$ als Vorstufe für *allo*-$Si_{1-x}Ge_x$ wurde des Weiteren die neue Zintl-Phase $Li_{18}Na_2Ge_{17}$ röntgenographisch am Einkristall charakterisiert. $Li_{18}Na_2Ge_{17}$ ist eines der wenigen Beispiele von Zintl-Phasen, welches drei verschiedene Anionensorten in seiner Struktur vereint (Ge^{4-}, $[Ge_4]^{4-}$, $[Ge_{12}]^{12-}$).

Bei systematischen Untersuchungen des Systems Li–B–Si wurde in einer Reihe von Hochdruck- und Hochtemperaturexperimenten die Zintl-Phase $LiBSi_2$ synthetisiert. $LiBSi_2$ besitzt ein einzigartiges, geordnetes B–Si Netzwerk bestehend aus zueinander senkrecht stehenden, mit Li gefüllten Kanälen. Auf Grund der noch nicht beschriebenen Topologie wurde das Netz mit „**tum**“ bezeichnet. Die Einbettung von Li Atomen in die kanalartige Gerüststruktur lassen weiterführende elektrochemische Untersuchungen an $LiBSi_2$ attraktiv erscheinen.

Abstract

In the last years silicon was particularly discussed as new anode material for lithium-ion batteries since it potentially could cope with the increasing demand for enhanced battery capacities. Compared to graphite being universally used in commercially available lithium-ion batteries, a massive capacity extension based on the formation of the lithium-rich phase $Li_{15}Si_4$ can be achieved. In some cases $Li_{22}Si_5$ or $Li_{21}Si_5$ were postulated instead of $Li_{15}Si_4$. Despite the great significance of the closely related Li–Si phase system, fundamental characteristics of the Li–Si phase diagram have not been elucidated adequately prior to this work.

In the course of the present thesis, the Li–Si phase diagram (> 76 at.% Li) was redetermined comprehensively and revised considerably by differential scanning calorimetry. This requested for the identification and unambiguous structural characterization of all phases in the respective lithium-rich section. In detail, the phases $Li_{13}Si_4$, $Li_{15}Si_4$, the disordered high-temperature silicide $Li_{16.4}Si_4$, as well as the lithium-richest representative of the Li–Si system $Li_{17}Si_4$ were characterized by single crystal X-ray diffraction. The latter replaces the previously reported lithium-richest silicide $Li_{21}Si_5$ ($Li_{16.8}Si_4$). Because of discrepancies between calculated (on the basis of previous single crystal data) and experimental powder X-ray diffraction data of $Li_{13}Si_4$, its structure was redetermined and improved markedly. Suitable single crystals, in particular the first crystals of the metastable phase $Li_{15}Si_4$, were mainly obtained from melt equilibration experiments (Li excess melts, “Li-flux”). Concerning the revision of the Li–Si phase diagram, the discovery of the phase $Li_{16.4}Si_4$ is ascribed a key role. Moreover, the thermal behavior of $Li_{15}Si_4$ which is not stable above 170 °C was investigated intensively. Thereby, the phase compositions of decomposition products exactly follow the newly established Li–Si phase diagram at temperatures higher than 400 °C. Between 170 and 300 °C, $Li_{15}Si_4$ decomposes into $Li_{17}Si_4$ and an unknown, weakly crystalline phase. However, replacing small amounts of Li with Al corresponding to $Li_{15-x}Al_xSi_4$ ($0.4 < x < 0.8$) led to thermodynamically stable phases which possess thermal stability of up to 700 °C. The decomposition process has proven to be reversible. Extending the studies to the Li–Ge system, the heavier homologues $Li_{17}Ge_4$ and $Li_{16.4}Ge_4$ could be characterized. This led to a rigorous redetermination of the respective section of the Li–Ge phase diagram (> 79 at.% Li), too. In this regard, the miscibility of the isotypic phases $Li_{17}Si_4$ and $Li_{17}Ge_4$ was investigated. Accordingly, the solid solutions $Li_{17}Si_{4-x}Ge_x$ [x = 2.30(2), 3.08(4), 3.53(3)] obey Vegard’s law.

Moreover, this work focuses on the synthesis of new phases in the Li–B–Si system as well as the synthesis of the Si polymorph *allo*-Si since these might serve as interesting anode materials. Attempts to reproduce the synthesis of the Si allotrope *allo*-Si through oxidation of the ternary phase Li_3NaSi_6 solely yielded *a*morphous products which were correspondingly denoted as *a-allo*-Si. Moreover, the powder X-ray diffraction data reported for *allo*-Si bear striking resemblance with $NbSi_2$ and thus indicate an erroneous phase assignment due to an $NbSi_2$ impurity. $NbSi_2$ may originate from a reaction of the ampule material Nb with α-Si during the synthesis of the Li_3NaSi_6 precursor. An analysis of the amorphous-to-crystalline phase transition temperatures of *a-allo*-Si revealed a strong fluctuation between 487 and 565 °C. In contrast, conventional *a*morphous Si (*a*-Si), which was obtained by Li extraction from $Li_{15}Si_4$ using liquid ammonia as solvent for Li, is transformed into α-Si at around 660 °C. However, the difference between *a*-Si and *a-allo*-Si can be attributed to large concentrations of α-Si crystallites and thus crystallization nuclei in *a-allo*-Si samples. Since comprehensive investigations did not reveal an unambiguous differentiation between *a-allo*-Si and *a*-Si, the existence of the Si polymorph *allo*-Si according to the reported synthesis could not be confirmed. In the course of investigations on the solid solution behavior of $Li_3Na(Si_{1-x}Ge_x)_6$ conceived as precursor for *allo*-$Si_{1-x}Ge_x$, the new Zintl phase $Li_{18}Na_2Ge_{17}$ could be identified and characterized crystallographically. $Li_{18}Na_2Ge_{17}$ is one of few Zintl phases whose structure comprises of three different Zintl anions (Ge^{4-}, $[Ge_4]^{4-}$, $[Ge_{12}]^{12-}$).

Explorative investigations in the Li–B–Si system using a high-pressure high-temperature synthesis technique led to the discovery of the novel Zintl phase $LiBSi_2$. It possesses a unique and strictly ordered B–Si open tetrahedral framework comprising mutually orthogonal channels hosting Li atoms inside. Since its network represents a not yet described topology it was named "**tum**". Owing to the fact that Li atoms are embedded in the channel-like framework structure of $LiBSi_2$, consecutive electrochemical investigations on $LiBSi_2$ seem to be very attractive.

List of Abbreviations

2b	two-bonded
3b	three-bonded
4b	four-bonded
4c	four-connected
A	alkaline metal
a-allo-Si	*a*morphous *allo*-Si
a-Si	*a*morphous silicon
AAS	atomic absorption spectroscopy
Ae	alkaline earth metal
ATR	attenuated total reflectance
bcc	body centered cubic
c-Si	crystalline silicon
calc.	calculated
CCD	charge coupled device
ccp	cubic close packed
cF	face-centered cubic
CIF	crystallographic information file
CN	coordination number
DFT	density functional theory
DSC	differential scanning calorimetry
DTA	differential thermal analysis
DOS	density of states
E	p-block (semi)metal
EC	ethylene carbonate
EDX	energy dispersive X-ray spectroscopy
E_F	Fermi energy
exp.	experimental
FE-SEM	field emission scanning electron microscopy
FT-IR	Fourier transform infrared spectroscopy
hcp	hexagonal close packed

hP	primitive hexagonal
ICSD	inorganic crystal structure database
ID	inner diameter
IPDS	imaging plate diffraction system
IR	infrared
L	length
LIB(s)	lithium-ion battery (batteries)
(L)PSD	(linear) position-sensitive detector
M	(semi)metal
MAS	magic angle spinning
nc-Si	nanocrystalline silicon
NMR	nuclear magnetic resonance
occ.	occupancy
OCV	open-circuit voltage
OD	outer diameter
OTF	open tetrahedral framework
PC	propylene carbonate
PL	photoluminescence
PP	polypropylene
(P)XRD	(powder) X-ray diffraction
Re	rare earth metal
ref.	reference(s)
SAED	selected area electron diffraction
SEI	solid electrolyte interphase
SEM	scanning electron microscopy
s.o.f.	site occupancy factor
SSM	solid state metathesis
SQUID	superconducting quantum interference device
SVP	sp-valence + polarization
TEM	transmission electron microscopy
tI	body-centered tetragonal
Tr	group 13 (triel) element
Tt	group 14 (tetrel) element
TTD	TOPOS topological database
VEC	valence electron concentration

Table of Contents

1 Introduction 1

1.1 Lithium-Ion Batteries 1

1.2 Lithium-Rich Intermetallics 5

1.3 Zintl Phases and Open Tetrahedral Frameworks 7

1.4 Scope and Outline 9

1.5 References 11

2 Experimental Section 15

2.1 Sample Handling and Preparation 15

2.2 Synthesis 15

2.2.1 Starting Materials 15

2.2.2 Reaction Containers and Sample Storage 16

2.2.3 Furnaces 17

2.2.4 Melt Equilibration Experiments and Isothermal Melt-Centrifugation 17

2.2.5 Ball-Milling 18

2.2.6 High-Pressure High-Temperature Synthesis 18

2.2.7 Li-Extraction Using Liquid Ammonia 19

2.2.8 Experimental Contributions from Coauthors 21

2.3 Characterization 22

2.3.1 Powder X-ray Diffraction (PXRD) 22

2.3.2 Single Crystal X-ray Diffraction, Structure Solution and Refinement 22

2.3.3 Differential Scanning Calorimetry (DSC) and Differential Thermal Analysis (DTA) 23

2.3.4 Scanning Electron Microscopy (SEM) and Energy Dispersive X-ray Spectroscopy (EDX) 24

2.3.5 Nuclear Magnetic Resonance (NMR) Spectroscopy 24

2.3.6 Transmission Electron Microscopy (TEM) 24

2.3.7 Infrared (IR) and Raman Spectroscopy 25

2.3.8 Photoluminescence (PL) Spectroscopy 25
2.3.9 Elemental Analysis 25
2.4 Computational Methods 26
2.5 References 26

3 Results and Discussion 29
3.1 Revision of the Li–*Tt* (*Tt* = Si, Ge) Phase Diagrams and New Lithium-Rich Tetrelides 29
3.1.1 Review of Relevant Literature 29
3.1.2 Revision of the Li–Si Phase Diagram: Thermodynamic Relation of $Li_{17}Si_4$, $Li_{16.42}Si_4$, $Li_{15}Si_4$ and $Li_{13}Si_4$ 34
3.1.3 Thermodynamic Stability of $Li_{14.37}Al_{0.63}Si_4$ — an Al-doped Variant of $Li_{15}Si_4$ 44
3.1.4 Revision of the Li–Ge Phase Diagram: Thermodynamic Relation of $Li_{17}Ge_4$, $Li_{16.38}Ge_4$, and $Li_{15}Ge_4$ 45
3.1.5 Solid Solutions $Li_{17}Si_{4-x}Ge_x$ [x = 2.30(2), 3.08(4), 3.53(3)] 47
3.1.6 References 48
3.2 Open Tetrahedral Frameworks (OTFs) 53
3.2.1 Review of Relevant Literature 53
3.2.2 OTF from Silicon: On the Existence of the Si Polymorph *allo*-Si 56
3.2.3 $Li_3Na(Si_{1-x}Ge_x)_6$ as Precursors for *allo*-$Si_{1-x}Ge_x$ and the Discovery of the Zintl Phase $Li_{18}Na_2Ge_{17}$ 59
3.2.4 $LiBSi_2$: A Novel Zintl Phase OTF Hosting Li Atoms Inside Channels 60
3.2.5 References 63

4 Summary and Conclusion 65

5 Publications and Manuscripts 69
5.1 Single Crystal Growth and Thermodynamic Stability of $Li_{17}Si_4$ 70
5.2 Revision of the Li–Si Phase Diagram: Discovery and Single Crystal X-ray Structure Determination of the High-Temperature Phase $Li_{4.11}Si$ 71
5.3 Revision of the $Li_{13}Si_4$ Structure 73

5.4 Stabilizing the Phase $Li_{15}Si_4$ through Lithium–Aluminum Substitution in $Li_{15-x}Al_xSi_4$ ($0.4 < x < 0.8$) — Single Crystal X-ray Structure Determination of $Li_{15}Si_4$ and $Li_{14.37}Al_{0.63}Si_4$ 75

5.5 Structural and Thermodynamic Similarities of Phases in the Li–*Tt* (*Tt* = Si, Ge) Systems: Redetermination of the Lithium-Rich Side of the Li–Ge Phase Diagram and Crystal Structures of $Li_{17}Si_{4.0-x}Ge_x$ for x = 2.3, 3.1, 3.5, and 4 as well as $Li_{4.1}Ge$ 77

5.6 Allotropism of Silicon: An Experimental Approach toward Amorphous Si and *a-allo*-Si Based on $Li_{15}Si_4$ and Li_3NaSi_6 as well as Theoretical Models for *allo*-Si 79

5.7 $Li_{18}Na_2Ge_{17}$ — a Compound Demonstrating Cation Effects on Cluster Shapes and Crystal Packing in Ternary Zintl Phases 127

5.8 $LiBSi_2$: A Tetrahedral Semiconductor Framework from Boron and Silicon Atoms Bearing Lithium Atoms in the Channels 129

Declaration

This dissertation is written as a publication-based thesis. The bibliographic data of articles published in peer-reviewed journals is compiled in Chapter 5. In case of unpublished work, corresponding manuscripts prepared for publication are included. The relevance of this work for science and research as well as the scope and outline are presented as introductory part in Chapter 1. The experimental section in Chapter 2 gives details on the synthesis and characterization of materials as well as computational methods. Contributions from coauthors (name and university affiliation) are explicitly stated therein. The results and discussion are presented in Chapter 3. The two subsections 3.1 and 3.2 are structured as follows: i) review of relevant literature, ii) results (summary of articles; in case of joint publications contributions are stated) and discussion across the respective topics, iii) references. An overall summary and conclusion is given in Chapter 4.

Chapter 1
Introduction

1.1 Lithium-Ion Batteries

“Sustainable development is development that meets the needs of the present without compromising the ability of future generations to meet their own needs”.[1] This quotation, taken from the report of the World Commission on Environment and Development (“Our Common future”, 1987), may certainly be seen as a well-founded definition of “sustainable development”. Nowadays, we are confronted with a massively increasing demand for energy which concomitantly causes severe environmental problems since fossil fuels are still the major source of energy. Therefore, the citation may better be perceived as an insistent calling for renewable energy sources, an environmentally compatible production of energy and, in particular, efficient energy storage. The latter aspect is certainly accommodated by the recent concept of “electromobility”, which has been intensively funded over the last years. Therein, research on novel energy storage materials and systems plays a decisive role.

In this field, a main focus is the development of efficient high-capacity lithium-ion batteries (LIBs). Analyzing the electrical energy that can be stored in different battery systems, i.e. the gravimetric and volumetric energy densities as functions of cell potential and capacity, it is clear that LIBs receive significant attention (see Figure 1.1). Going back in history of Li batteries, primary Li cells (non-rechargeable) were already developed more than 50 years ago in 1962.[2,3] One decade later, the first primary lithium-ion battery (Li metal anode, MnO_2 cathode, liquid electrolytes) became commercially available by SANYO INC. in 1972.[2,3]

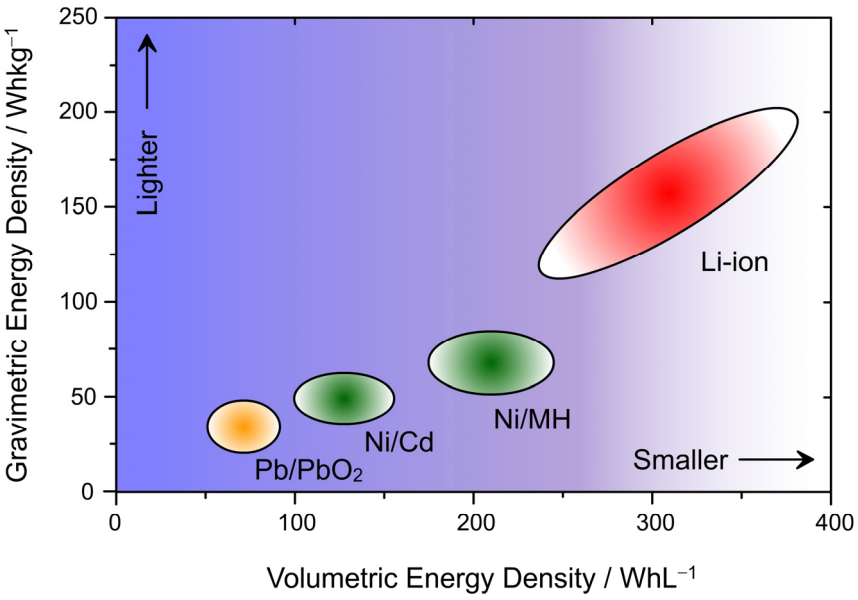

Figure 1.1. Volumetric and gravimetric energy densities of various battery systems. The figure was modified on the basis of ref. 2.

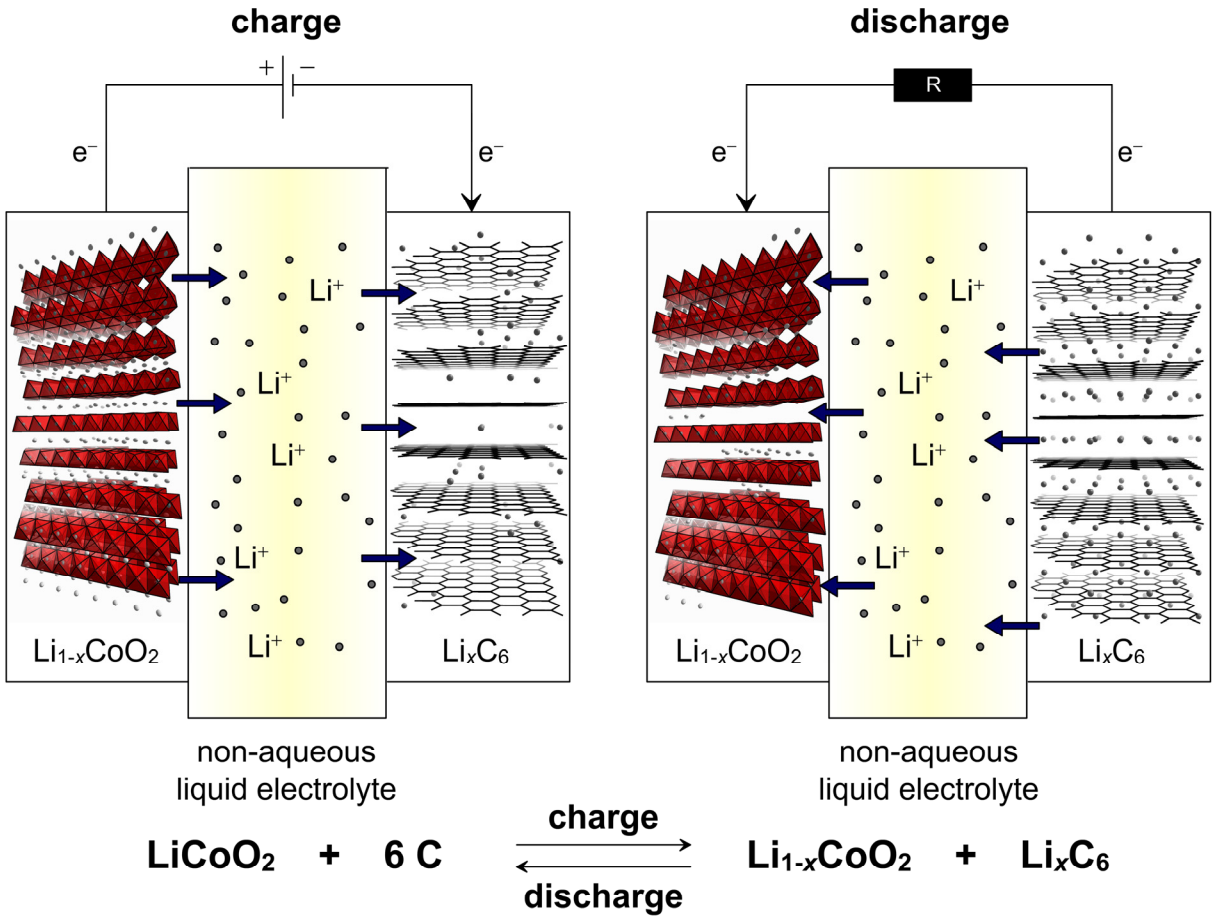

Figure 1.2. Functionality of a lithium-ion battery operating with a $LiCoO_2$ cathode, a graphite anode and a non-aqueous liquid electrolyte (typical lithium-ion secondary battery as introduced by SONY CORP. in 1991).

In case of rechargeable Li metal based lithium-ion batteries, the limits were soon encountered. The combination of Li metal/liquid electrolytes led to an irregular/uneven growth of Li on the Li metal anode surface after each charge-discharge cycle. The resulting growth of dendrites and their extension through several charging/discharging processes caused short circuits leading to cell overheating and battery explosions. The severe safety issues consequently fueled numerous work in the following years. Finally, this problem could be overcome using graphite as the new anode material of choice since on the one hand Li can be reversibly intercalated into the graphite layers at a low potential versus Li/Li^+ (0.25 V) and on the other hand, the formation of dendrites was circumvented.[4] Furthermore, the increase in potential when employing a graphite anode instead of Li metal was compensated by high-voltage cathode materials ($LiMO_2$ with M = Cr, Co, Ni; $LiMn_2O_4$).[5] In 1991, SONY CORP. commercialized the first lithium-ion secondary batteries (graphite anode, $LiCoO_2$ cathode, porous polypropylene (PP) separator foil, non-aqueous liquid electrolytes, e.g. ethylene carbonate (EC) and propylene carbonate (PC) as solvent and $LiPF_6$ as conducting salt).[2,6] The functionality of such a battery is depicted in Figure 1.2. Because of the rocking intercalation and deintercalation processes, LIBs are commonly known as "shuttle-cock" or "rocking-chair" batteries.[2,3] Examples of different types of commercially available LIBs are shown in Figure 1.3.

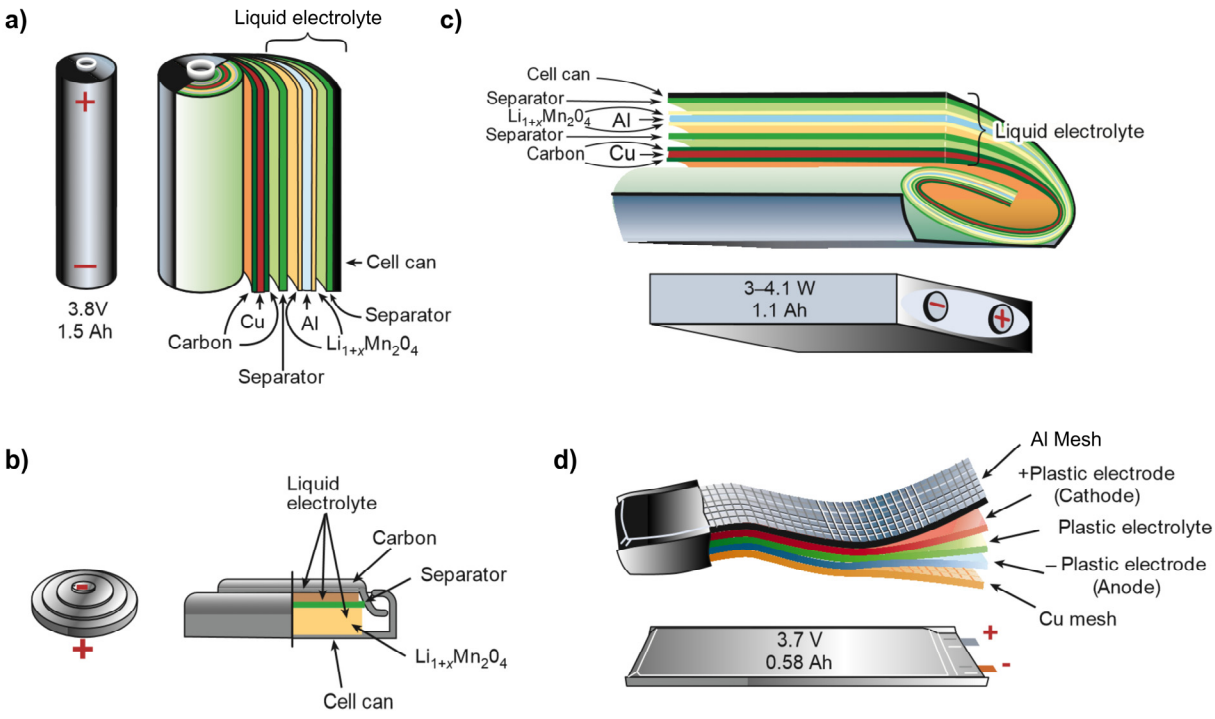

Figure 1.3. Schematic drawings of different lithium-ion battery geometries: a) cylindrical, b) coin, c) prismatic, and d) thin/flat. The figure was adopted from ref. 7.

Regarding the improvements of the lithium-ion battery technology, three main fields have to be considered inevitably: i) electrolytes, ii) cathode and iii) anode materials. In principal, desirable cathode and anode materials are those which possess high and low potentials versus Li metal (i.e. high and low open-circuit voltages (OCVs) when cycled against Li) at high rate capabilities and high specific capacities (volumetric and gravimetric, see Figure 1.1). Furthermore, Li insertion and extraction should be reversible (cycle life). Concomitantly, it has to be ascertained that electrolytes are stable within the operating voltage range to prevent their oxidation or reduction. Safety and toxicity aspects are of further importance. In the following, developments and viable improvements of anode materials are addressed.

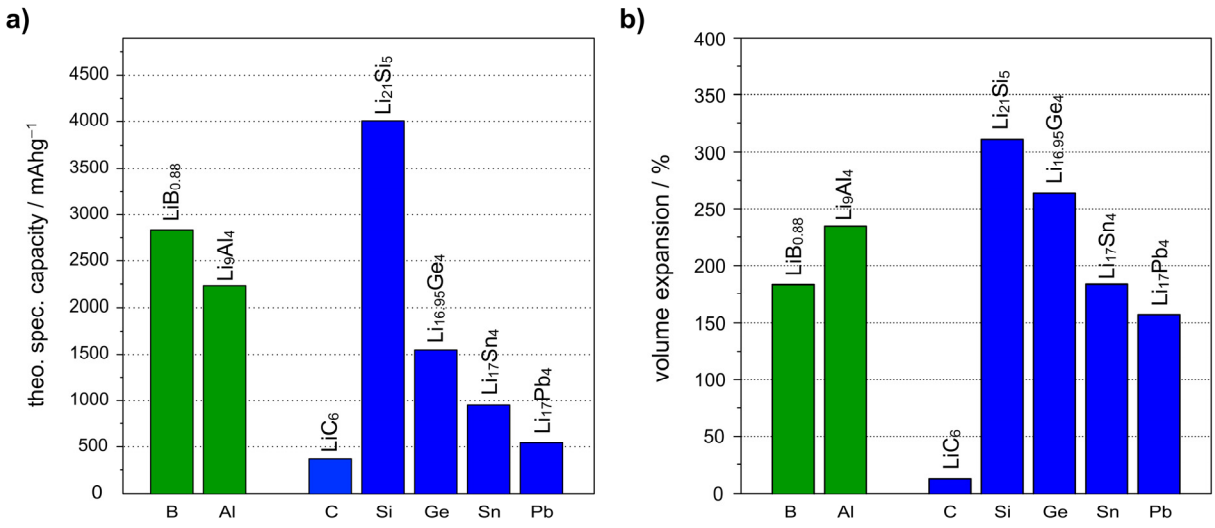

Figure 1.4. a) Theoretical specific (gravimetric) capacities and b) according volume changes of selected group 13 (*Tr*) and group 14 (*Tt*) elements based on the formation of the respective phases ($LiB_{0.88}$,[8] Li_9Al_4,[9,10] LiC_6,[11] $Li_{21}Si_5$,[12] $Li_{16.95}Ge_4$,[13] $Li_{17}Sn_4$,[14] $Li_{17}Pb_4$[13]; calculated according to $C_{theo} = \frac{x \cdot F}{M(Tr/Tt)} \cdot \frac{10}{36}$ in $mAhg^{-1}$ and $\Delta V = \frac{n(LiTr/LiTt)}{n(Tr/Tt)} \cdot \frac{M(LiTr/LiTt)}{M(Tr/Tt)} \cdot \frac{\rho(Tr/Tt)}{\rho(LiTr/LiTt)} - 1$, F = FARADAY constant, $x = \frac{n(Li)}{n(Tr/Tt)}$ for Li*Tr*/Li*Tt*, M = molecular mass, ρ = density, n = amount of substance).

As can be seen in Figure 1.4a, the theoretical gravimetric capacities of diverse group 13 (triel = *Tr*) and 14 (tetrel = *Tt*) elements based on the formation of the lithium-richest representatives in the Li–*Tr* and Li–*Tt* system (prior to this work), respectively, impressively exceed the one of graphite (372 $mAhg^{-1}$). Just recently, Sony commercialized enhanced LIBs operating with Sn-based anodes (NEXELION™ cells).[15] Most notably, B and especially Si are outstanding candidates owing to their low weight. Because of its natural abundance, the use of Si would additionally be advantageous. However, large volume changes during charging and discharging processes as indicated in Figure 1.4b cause severe problems, especially in case of a Si anode. The charge-discharge induced “breathing” of such active materials leads to a

contact loss of metal electrodes, a pulverization of active material and finally massive capacity fading during the first cycles.[16] These problems were countered by several suggestions, e.g. reducing the voltage range over which the cell is cycled,[17,18] employing Si–C composites to compensate for the large volume changes,[19,20] and the use of nanostructured Si anodes.[21,22]

Besides, a fundamental understanding of processes in Si-based lithium-ion batteries during charging and discharging is crucial. Limthongkul et al.[23,24] have shown that a previously crystalline Si anode undergoes complete amorphization when cycled against Li. None of the known thermodynamically stable Li–Si phases, that were $Li_{21}Si_5$,[12] $Li_{13}Si_4$,[25] Li_7Si_3,[26] $Li_{12}Si_7$,[27,28] and LiSi[29] by then, were formed directly by alloying Li and Si electrochemically. In 2004, Obrovac and Hatchard investigated structural changes in silicon anodes and discovered the new metastable phase $Li_{15}Si_4$ using ex-situ and in-situ X-ray diffraction methods, respectively.[18,30] Depending on the applied discharge voltage, $Li_{15}Si_4$ crystallizes from amorphous $Li_{3.75}Si$ corresponding to a specific capacity of 3579 $mAhg^{-1}$. Remarkably, the use of nanostructured Si anodes completely suppressed its crystallization.[30] Moreover, Kwon et al.[31] demonstrated that the maximum capacity due to the formation of $Li_{21}Si_5$ can be extended to 4008 $mAhg^{-1}$ at elevated temperatures ($T > 100$ °C).

Generally, when structural changes in Si anodes during Li insertion/extraction are studied, conventional methods such as X-ray diffraction due to the electrochemically driven amorphization deliver sparse information. Therefore, alternative techniques had to be employed. To this end, structural changes in Si anodes upon lithiation were monitored using in-situ/ex-situ solid state NMR techniques.[32,33] It was shown that the local structure of amorphous phases resembles that of crystalline ones ($Li_{12}Si_7$, Li_7Si_3, $Li_{13}Si_4$, $Li_{15}Si_4$). For that purpose and because of the complexity of the (de)lithiation processes, an unambiguous structural characterization of Li–Si phases and their assignment in the Li–Si phase diagram is essential.

1.2 Lithium-Rich Intermetallics

As highlighted in the previous chapter, phases of the binary system Li–Si and heavier homologues are of significant importance when novel anode materials for LIBs are discussed. In general, these phases belong to the family of “intermetallics” or “intermetallic phases” comprising of two or more (semi)metallic elements in a homogenous compound possessing either a certain composition (line phases) or a homogeneity range. Their crystal structures differ from those of the constituting elements. Consequentially, a slew of different structures may be obtained from literally endless possible element combinations. Note that more than 80% of naturally occurring elements in the earth crust are either metals or semimetals and thus the

term “intermetallics” is rather wide-ranging than specific. Except for Zintl phases (see Chapter 1.3), there are no universally valid rules to explain structures and compositions which in most cases do not correspond to the valences of the involved elements. Some phases can be classified according to their valence electron concentration (VEC = sum of valence electrons/number of atoms) or composition, i.e. Hume-Rothery- and Laves-phases, respectively. Lithium-rich phases of the Li–*Tt* (*Tt* = Si, Ge, Sn, Pb) systems can be classified more specifically as polar intermetallics. In general, this class of compounds comprises electropositive metals and electronegative (semi)metals. Again, structures and compositions cannot be deduced from simple electron counting rules and are frequently rather complex (exception: Zintl phases).

Regarding their use as high-capacity anode materials in LIBs, considerable importance is ascribed to lithium-rich polar intermetallics providing high specific capacities. In this regard, the aforementioned representatives of the binary systems Li–*Tt* (*Tt* = Si, Ge, Sn, Pb) are very promising, in particular, lithium-rich phases of the Li–Si system (see Figure 1.4). The Li–Ge system receives less attention since it is greatly outperformed by the Li–Si system. In terms of crystal structures, Li silicides and germanides provide an intriguing variety of different structure motifs. For instance, 3-bonded Si atoms forming a defect diamond structure in LiSi[29] (high-pressure phase, isotypic with LiGe[34,35] which is obtainable at ambient pressure), planar Si 4-stars and 5-rings in $Li_{12}Si_7$ ($Li_{12}Ge_7$),[27,28] 2-, 3-, and 4-bonded Ge atoms in polyanionic layers $^{2}_{\infty}[Ge_{12}]^{7-}$ of Li_7Ge_{12},[36-38] or Si–Si dumbbells in Li_7Si_3 (Li_7Ge_3).[26,38] With respect to anode materials, the lithium-richest candidates, $Li_{15}Tt_4$[18,39,40] and $Li_{21}Tt_5$ (*Tt* = Si, Ge),[12,41] are most important, though. Their structures exclusively bear isolated *Tt* atoms embedded in Li matrices. Going from *Tt*-rich to Li-rich Li–*Tt* phases, the anionic *Tt* substructures are closely related to Li–*Tt* ratios and compositions, respectively. Li uptake directly translates to successive bond-breaking and therefore it is clear that highly Li-containing phases solely comprise isolated *Tt* atoms in their structures.

Remarkably, despite their significance for recent LIB research, properties of lithium-rich Li–*Tt* (*Tt* = Si, Ge) phases at both fundamental and applied levels are not yet conclusively characterized. Recent examples in literature are surprisingly rare. In particular, the compositions of the lithium-richest representatives are controversially discussed, e.g. $Li_{22}Tt_5$ ($Li_{17.6}Tt_4$),[42,43] $Li_{21}Tt_5$ ($Li_{16.8}Tt_4$),[12,41] $Li_{20}Tt_5$ ($Li_{16}Tt_4$),[38,44] or $Li_{16.95}Ge_4$.[13] Additionally, thermodynamic properties are sparsely investigated, the decomposition characteristics of metastable $Li_{15}Si_4$ are barely studied, older structure reports need to be subject to review, and other phases even seem to have disappeared. Relating to these aspects, both the Li–Si and Li–Ge phase diagram, at least at the lithium-rich end, are unreliable and need a fundamental clarification.

1.3 Zintl Phases and Open-Tetrahedral Frameworks

Another important class of compounds are Zintl phases.[45-47] These are formed by electropositive alkaline, alkaline earth or rare earth metals (*A*/*Ae*/*Re*) and p-block (semi)metals (*E*). Assuming a full electron transfer from *A*/*Ae*/*Re* to *E*, the structures of the "salt-like" compounds can be explained as follows: i) the number of bonded neighboring atoms in the anionic substructure *E* follows the 8–*N* rule (two-center, two-electron bonds), ii) the structures of *E* correspond to those of elements with the same valence configuration (pseudoelement concept). In case of cluster compounds, cluster shapes and the electron count can be explained applying Wade's rules.[48] Thus, various anionic substructures may be realized by Zintl phases, e.g. isolated atoms (Ca_2Si:[49] Si^{4-}), Cl_2-like dumbbells ($BaMg_2Si_2$:[50] $[Si_2]^{6-}$), deltahedral clusters ($K_{12}Ge_{17}$:[51] $[Ge_4]^{4-}$, $[Ge_9]^{4-}$), large cages (Li_7RbGe_8:[52] $[Ge_4]^{4-}$, $[Ge_{12}]^{12-}$), polyanionic layers (Li_7Ge_{12}:[36,37] $^{2}_{\infty}[Ge_{12}]^{7-}$, Li_3NaSi_6:[53] $^{2}_{\infty}[Si_6]^{4-}$), or three-dimensional networks (LiSi:[29] Si^{-}). Relating to the Li–Si system, LiSi is the only representative whose structure is in unambiguous agreement with the Zintl concept. For others, a Zintl-conform description is difficult or even impossible.[41] Regarding the properties of Zintl phases, they are semiconductors with small band gaps and represent stoichiometric compounds.

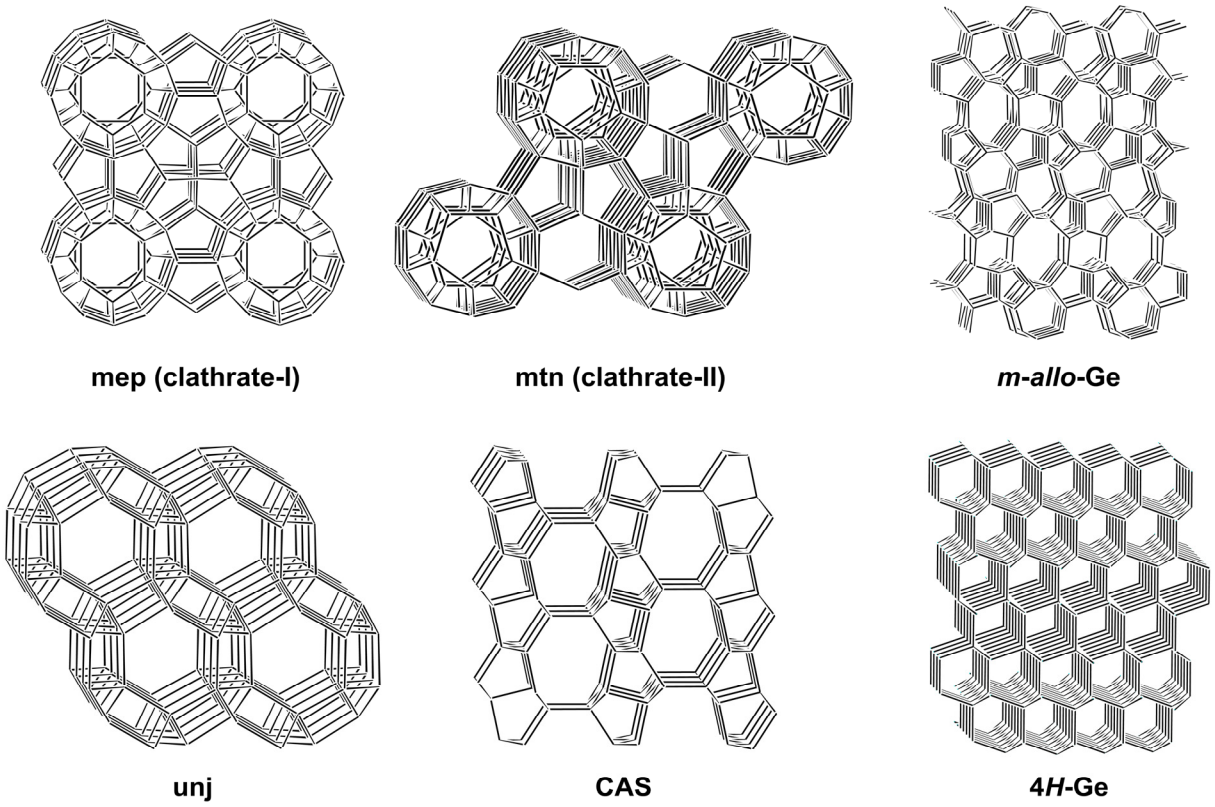

Figure 1.5. Examples of open tetrahedral frameworks realized from Zintl phases and group 14 elements emphasizing cages and channels. Symbols for nets follow either the zeolite code or the RCSR identifiers.[54] The figure was modified on the basis of ref. 55.

Moreover, *E* atoms in Zintl phases may also realize open tetrahedral frameworks (Zintl phase OTFs), an intriguing structure family which has received great attention for thermoelectric and superconducting properties of its representatives.[56-58] Generally, OTFs possess large and separated cages (clathratic frameworks) or channels (zeolitic frameworks). Zintl phase OTFs are composed of tetravalent group 14 elements (*Tt* = Si, Ge, Sn and mixtures thereof) and trivalent group 13 elements (*Tr*) representing tetrahedral nodes (host structure). The electron deficiency of the latter is balanced by electrons being completely transferred from electropositive metals (*M*) which are located in the cavities (guest atoms). Consequently, OTFs can formally be considered as $(4b\text{-}Tt)_n = (M^+)_m(4b\text{-}Tt)_{n-m}(4b\text{-}Tr)_m$ (4b = four-bonded).

The most prominent OTF representatives are clathrate-I (**mep**[54]) and clathrate-II (**mtn**) structures such as $K_7B_7Si_{39}$,[59] $K_8Zn_4Sn_{42}$[60] and $A_8Na_{16}Si_{136}$ (*A* = Rb, Cs, Ba),[61,62] Na_xSi_{136},[63] respectively (Figure 1.5). Others are zeolitic frameworks as realized by *hP*-Na_2ZnSn_5 (**unj**),[64] *tI*-Na_2ZnSn_5 (**unj**),[64] and $Eu_4Ga_8Ge_{16}$ (**CAS**).[65] Remarkably, except $K_7B_7Si_{39}$, OTFs involving B and C atoms are not known. Additionally, OTFs enclosing Li atoms at guest positions have not been described yet since suitably small cages may only be realized by host structures comprising the aforementioned light second row elements.[66] Such phases, however, might possess interesting physical and chemical properties.[67,68] Notably, it was shown just recently that the clathrate-II compound Na_xSi_{136} ($x \rightarrow 0$) can be lithiated electrochemically.[69]

Beside Zintl phase OTFs, OTFs of group 14 allotropes have always received significant attention. In particular, the variety of physical and chemical properties of a single element arising from different element modifications, e.g. the carbon allotropes diamond, graphite, and fullerenes, fueled a slew of experimental and theoretical studies. For instance, the porous structure Ge-*cF*136 (clathrate-II structure) was synthesized via polymerization and oxidation of $[Ge_9]^{4-}$ Zintl anions (Na_4Ge_9) in ionic liquids.[70] Additionally, various mesoporous Ge-based materials like cubic gyroidal MSU-Ge-1,[71] hexagonal MSU-Ge-2[72] and NU-Ge-1[73] were accessible by either a metathesis reaction of the Zintl anions Ge^{4-} (Mg_2Ge)/deltahedral cluster units $[Ge_9]^{4-}$ (K_4Ge_9) with $GeCl_4$ as linking agent or an oxidative polymerization of $[Ge_9]^{4-}$ (K_4Ge_9) without $GeCl_4$. These reactions were carried out in the presence of structure-directing cationic surfactants. Hexagonal nanoporous Ge could be prepared from an oxidative coupling of linear polymer chains ${}^1_\infty[Ge_9]^{2-}$ (K_2Ge_9) with ferrocenium hexafluorophosphate in a surfactant/ethylenediamine solution.[74] Moreover, the Ge allotrope *m-allo*-Ge (Figure 1.5) was obtained from a mild oxidation of Li_7Ge_{12}, a phase that possesses two-dimensional polyanionic slabs ${}^2_\infty[Ge_{12}]^{7-}$ which are separated by Li atoms.[36,37,75] Interstitial Li is deintercalated by treatment of Li_7Ge_{12} with protic solvents retaining the topology of these layers under interlayer Ge–Ge bond formation. At temperatures between 150 and 300 °C *m-allo*-Ge transforms into another

allotrope, 4*H*-Ge (Figure 1.5).[36,76] Similar to Ge, an allotropic form of Si named *allo*-Si originates from an analogous oxidation of the phase Li_3NaSi_6 consisting of polyanionic layers $^2_\infty[Si_6]^{6-}$ separated by Li and Na atoms.[53] However, the reaction yields poorly crystalline products not allowing a comprehensive structure determination by X-ray diffraction methods. To date, its structure has remained unknown and some structure models for *allo*-Si were proposed by quantum chemical calculations.[77]

1.4 Scope and Outline

The significance of binary lithium-rich tetrelides (Li_xTt_y phases, $x >> y$), open tetrahedral frameworks (OTFs) involving light elements in the second row of the periodic table, i.e. Li, B and C, as well as the chemistry of allotropic forms of group 14 elements was highlighted in Chapters 1.1–1.3. These topics, both on fundamental and applied levels, are part of recent research on cutting-edge materials which are ascribed a high potential for future applications such as next-generation lithium-ion batteries or thermoelectrics. Despite that fact, essential questions and issues as briefly commented afore have not been addressed prior to this work and some intriguing fields are not or rather sparsely investigated.

In this regard, this thesis makes an important contribution and opens further perspectives toward new materials in these fields of research. In detail, despite the great significance of the Li–Si system for LIB research, in particular of the lithium-richest representatives such as $Li_{15}Si_4$ and $Li_{21}Si_5$, fundamental questions are still unanswered and a comprehensive characterization of the lithium-rich section of the Li–Si phase diagram (mole fraction Li > 76 at.%) is more than overdue. Open issues are the composition of the lithium-richest phase, the sparsely studied decomposition behavior of metastable $Li_{15}Si_4$ and the influence of dopants, the (non)existence of a previously proposed phase Li_4Si (Zintl phase), a critical review of structures, and the thermodynamic relation of all involved phases. In this regard, the compositions, structures and the thermodynamic relation of representatives of the Li–Ge system also need a fundamental and comprehensive clarification. Therefore, a rigorous redetermination of the Li–Si and Li–Ge phase diagram was carried out with differential scanning calorimetry investigations employing samples with systematically different compositions. Large single crystals of lithium-rich phases for X-ray diffraction studies were grown from equilibrated melts (Li concentrations > 85 at.%, “flux method”) and separated by isothermally centrifuging off excess melt at various temperatures. Powder samples of metastable $Li_{15}Si_4$ were synthesized by ball-milling and investigated intensively with regard to the thermal behavior of $Li_{15}Si_4$. The combination of DSC investigations, melt equilibration experiments, structural

characterization by single crystal X-ray diffraction and long-term annealing of various samples at different temperatures (phase composition analysis by powder X-ray diffraction) allowed a fundamental revision of the Li–Si (mole fraction Li > 76 at.%) and Li–Ge (mole fraction Li > 79 at.%) phase diagrams (Chapters 3.1.2 and 3.1.4). The aforementioned methods combined with energy dispersive X-ray and NMR spectroscopy were applied for the characterization of Al-doped variants of $Li_{15}Si_4$ ($Li_{15-x}Al_xSi_4$) and studies on the solid solution behavior of the lithium-richest representatives of the Li–*Tt* (*Tt* = Si, Ge) systems (Chapters 3.1.3 and 3.1.5).

Another focus is set on OTFs realized by Zintl phases and group 14 elements. In detail, Zintl phase OTFs involving light second row elements and allotropic forms of Si are of particular interest since they might serve as potential electrode materials in LIBs. Therefore, the Li–B–Si system was studied and the synthesis of the Si polymorph *allo*-Si which was first reported in the 1980's came under scrutiny in the course of the present thesis. Another motivation for the reinvestigation of the formation of *allo*-Si is the fact that a structure has not been determined from X-ray diffraction experiments as yet. Hence, the oxidation of Li_3NaSi_6 to *allo*-Si was performed under inert gas atmosphere at various conditions (e.g. slow or fast oxidation, different morphologies of the Li_3NaSi_6 precursor). In comparison, the extraction of Li from $Li_{15}Si_4$ using liquid ammonia as solvent for Li was also investigated. Products from both oxidation reactions were characterized comprehensively by powder X-ray diffraction, differential thermal analysis as well as various spectroscopic and microscopic methods. This allowed a careful analysis of differences between the products obtained from each reaction and thus a clear statement on the existence of the Si polymorph *allo*-Si. According results are presented in Chapter 3.2.2. Moreover, the miscibility of Ge and Si in Li_3NaSi_6 corresponding to $Li_3Na(Si_{1-x}Ge_x)_6$ was investigated since such phases were conceived as precursors for *allo*-$Si_{1-x}Ge_x$ which might be interesting materials in terms of band gap tuning (Chapter 3.2.3). Respective products were analyzed by powder and single crystal X-ray diffraction.

Turning to the Li–B–Si system, the boron-rich phase $Li_2B_{12}Si_2$ was the only representative prior to this work. Thus, investigations using standard solid state synthesis techniques (ambient pressure, high temperature) targeted the discovery of new, and in particular, lithium-richer phases. However, the accessibility to novel materials turned out to be very limited and thus, high-pressure high-temperature experiments were performed at the high-pressure facility of the ARIZONA STATE UNIVERSITY (Tempe, AZ, USA) in a series of research stays. These investigations yielded a second representative of the ternary system Li–B–Si. The novel phase was structurally characterized by powder X-ray diffraction, solid state NMR and Raman spectroscopy (Chapter 3.2.4).

1.5 References

(1) *World Commission on Environment and Development, Our Common Future*; Oxford University Press, 1987; p 43.

(2) Nazri, G.-A.; Pistoia, G. *Lithium Batteries - Science and Technology* 6ed.; Kluwer Academic Publishers: USA, 2004.

(3) Ozawa, K. *Lithium Ion Rechargeable Batteries*; 6 ed.; Wiley VCH: Germany, 2009.

(4) Owen, J. R. *Chem. Soc. Rev.* **1997**, *26*, 259.

(5) Whittingham, M. S. *Chem. Rev.* **2004**, *104*, 4271.

(6) Nagaura, T.; Tozawa, K. *Prog. Batteries Solar Cells* **1990**, *9*, 209.

(7) Tarascon, J. M.; Armand, M. *Nature* **2001**, *414*, 359.

(8) Wörle, M.; Nesper, R. *Angew. Chem. Int. Edit.* **2000**, *39*, 2349.

(9) Hansen, D. A.; Smith, J. F. *Acta Crystallogr. B* **1968**, *24*, 913.

(10) Puhakainen, K.; Boström, M.; Groy, T. L.; Häussermann, U. *J. Solid State Chem.* **2010**, *183*, 2528.

(11) Juza, R.; Wehle, V. *Naturwissenschaften* **1965**, *52*, 560.

(12) Nesper, R.; von Schnering, H. G. *J. Solid State Chem.* **1987**, *70*, 48.

(13) Goward, G. R.; Taylor, N. J.; Souza, D. C. S.; Nazar, L. F. *J. Alloys Compd.* **2001**, *329*, 82.

(14) Lupu, C.; Mao, J. G.; Rabalais, J. W.; Guloy, A. M.; Richardson, J. W. *Inorg. Chem.* **2003**, *42*, 3765.

(15) Sony Corp., *Sony's New Nexelion Hybrid Lithium Ion Batteries To Have Thirty-Percent More Capacity Than Conventional Offering*, http://www.sony.net/SonyInfo/News/Press/200502/05-006E/ (accessed February 10, 2014)

(16) Zhang, W. J. *J. Power Sources* **2011**, *196*, 13.

(17) Obrovac, M. N.; Krause, L. J. *J. Electrochem. Soc.* **2007**, *154*, A103.

(18) Obrovac, M. N.; Christensen, L. *Electrochem. Solid-State Lett.* **2004**, *7*, A93.

(19) Cahen, S.; Janot, R.; Laffont-Dantras, L.; Tarascon, J. M. *J. Electrochem. Soc.* **2008**, *155*, A512.

(20) Cakan, R. D.; Titirici, M. M.; Antonietti, M.; Cui, G. L.; Maier, J.; Hu, Y. S. *Chem. Commun.* **2008**, 3759.

(21) Chan, C. K.; Peng, H.; Liu, G.; McIlwrath, K.; Zhang, X. F.; Huggins, R. A.; Cui, Y. *Nat. Nanotechnol.* **2008**, *3*, 31.

(22) Cui, L.-F.; Ruffo, R.; Chan, C. K.; Peng, H.; Cui, Y. *Nano Lett.* **2009**, *9*, 491.

(23) Limthongkul, P.; Jang, Y. I.; Dudney, N. J.; Chiang, Y. M. *Acta Mater.* **2003**, *51*, 1103.

(24) Limthongkul, P.; Jang, Y. I.; Dudney, N. J.; Chiang, Y. M. *J. Power Sources* **2003**, *119-121*, 604.

(25) Frank, U.; Müller, W.; Schäfer, H. *Z. Naturforsch. B* **1975**, *30*, 10.

(26) von Schnering, H. G.; Nesper, R.; Tebbe, K. F.; Curda, J. *Z. Metallkd.* **1980**, *71*, 357.

(27) von Schnering, H. G.; Nesper, R.; Curda, J.; Tebbe, K. F. *Angew. Chem.* **1980**, *92*, 1070.

(28) Nesper, R.; von Schnering, H. G.; Curda, J. *Chem. Ber.* **1986**, *119*, 3576.

(29) Evers, J.; Oehlinger, G.; Sextl, G. *Angew. Chem. Int. Ed.* **1993**, *32*, 1442.

(30) Hatchard, T. D.; Dahn, J. R. *J. Electrochem. Soc.* **2004**, *151*, A838.

(31) Kwon, J. Y.; Ryu, J. H.; Oh, S. M. *Electrochim. Acta* **2010**, *55*, 8051.

(32) Key, B.; Bhattacharyya, R.; Morcrette, M.; Seznec, V.; Tarascon, J. M.; Grey, C. P. *J. Am. Chem. Soc.* **2009**, *131*, 9239.

(33) Key, B.; Morcrette, M.; Tarascon, J. M.; Grey, C. P. *J. Am. Chem. Soc.* **2011**, *133*, 503.

(34) Oleksiv, G. I. *Probl. Rozvitku Prirodn. i. Tochn. Nauk, Sb.* **1964**, 76.

(35) Menges, E.; Hopf, V.; Schäfer, H.; Weiss, A. *Z. Naturforsch. B* **1969**, *21*, 1351.

(36) Grüttner, A.; Nesper, R.; von Schnering, H. G. *Angew. Chem. Int. Ed.* **1982**, *21*, 912.

(37) Kiefer, F.; Fässler, T. F. *Solid State Sci.* **2011**, *13*, 636.

(38) Grüttner, A.; Nesper, R.; von Schnering, H. G. *Acta Cryst.* **1981**, *A37*, C161.

(39) Johnson, Q.; Smith, G. S.; Wood, D. *Acta Cryst.* **1965**, *18*, 131.

(40) Gladyshevskii, E. I.; Kripyakevich, P. I. *Kristallografiya* **1960**, *5*, 574.

(41) Nesper, R. *Prog. Solid State Chem.* **1990**, *20*, 1.

(42) Gladyshevskii, E. I.; Oleksiv, G. I.; Kripyakevich, P. I. *Kristallografiya* **1964**, *9*, 338.

(43) Axel, H.; Schäfer, H.; Weiss, A. *Z. Naturforsch. B* **1966**, *21*, 115.

(44) Grüttner, A. *Dissertation*, Universität Stuttgart: Stuttgart, Germany, 1982.

(45) Zintl, E. *Angew. Chem.* **1939**, *52*, 1.

(46) Klemm, W. *Proc. Chem. Soc.* **1958**, *329*.

(47) Klemm, W.; Busmann, E. *Z. Anorg. Allg. Chem.* **1963**, *319*, 297.

(48) Wade, K. *Adv. Inorg. Chem. Radiochem.* **1976**, *18*, 1.

(49) Eckerlin, P.; Wölfel, E. *Z. Anorg. Allg. Chem.* **1955**, *280*, 321.

(50) Eisenman.B; Schäfer, H. *Z. Anorg. Allg. Chem.* **1974**, *403*, 163.

(51) von Schnering, H. G.; Baitinger, M.; Bolle, U.; Carrillo-Cabrera, W.; Curda, J.; Grin, Y.; Heinemann, F.; Llanos, J.; Peters, K.; Schmeding, A.; Somer, M. *Z. Anorg. Allg. Chem.* **1997**, *623*, 1037.

(52) Bobev, S.; Sevov, S. C. *Angew. Chem. Int. Ed.* **2001**, *40*, 1507.

(53) von Schnering, H. G.; Schwarz, M.; Nesper, R. *J. Less-Common Met.* **1988**, *137*, 297.

(54) Symbols for nets follow either the zeolite code according to ref. 54a or the RCSR identifiers according to ref. 54b; a) Baerlocher, C.; Meier, W. M.; Olson, D. H. *Atlas of Zeolite Framework Types*, 6th rev. ed., Elsevier, Amsterdam, **2007**. Data available online at http://www.iza-structure.org/databases/; (b) O'Keeffe, M.; Peskov, M. A.; Ramsden, S. J.; Yaghi, O. M. *Acc. Chem. Res.* **2008**, *41*, 1782.

(55) Zeilinger, M.; van Wüllen, L.; Benson, D.; Kranak, V. F.; Konar, S.; Fässler, T. F.; Häussermann, U. *Angew. Chem. Int. Ed.* **2013**, *52*, 5978.

(56) Beekman, M.; Nolas, G. S. *J. Mater. Chem.* **2008**, *18*, 842.

(57) Nolas, G. S.; Cohn, J. L.; Slack, G. A.; Schujman, S. B. *Appl. Phys. Lett.* **1998**, *73*, 178.

(58) Yamanaka, S. *Dalton Trans.* **2010**, *39*, 1901.

(59) Jung, W.; Lorincz, J.; Ramlau, R.; Borrmann, H.; Prots, Y.; Haarmann, F.; Schnelle, W.; Burkhardt, U.; Baitinger, M.; Grin, Y. *Angew. Chem. Int. Ed.* **2007**, *46*, 6725.

(60) Baran, V.; Fischer, A.; Scherer, W.; Fässler, T. F. *Z. Anorg. Allg. Chem.* **2013**, *639*, 2125.

(61) Bobev, S.; Sevov, S. C. *J. Solid State Chem.* **2000**, *153*, 92.

(62) Rachi, T.; Tanigaki, K.; Kumashiro, R.; Winter, J.; Kuzmany, H. *Chem. Phys. Lett.* **2005**, *409*, 48.

(63) Ammar, A.; Cros, C.; Pouchard, M.; Jaussaud, N.; Bassat, J. M.; Villeneuve, G.; Duttine, M.; Menetrier, M.; Reny, E. *Solid State Sci.* **2004**, *6*, 393.

(64) Stegmaier, S.; Kim, S. J.; Henze, A.; Fässler, T. F. *J. Am. Chem. Soc.* **2013**, *135*, 10654.

(65) Bryan, J. D.; Stucky, G. D. *Chem. Mater.* **2001**, *13*, 253.

(66) Liang, Y.; Böhme, B.; Ormeci, A.; Borrmann, H.; Pecher, O.; Haarmann, F.; Schnelle, W.; Baitinger, M.; Grin, Y. *Chem. Eur. J.* **2012**, *18*, 9818.

(67) Ker, A.; Todorov, E.; Rousseau, R.; Uehara, K.; Lannuzel, F. X.; Tse, J. S. *Chem. Eur. J.* **2002**, *8*, 2787.

(68) Rey, N.; Munoz, A.; Rodriguez-Hernandez, P.; San Miguel, A. *J. Phys.-Condens. Mat.* **2008**, *20*.

(69) Langer, T.; Dupke, S.; Trill, H.; Passerini, S.; Eckert, H.; Pöttgen, R.; Winter, M. *J. Electrochem. Soc.* **2012**, *159*, A1318.

(70) Guloy, A. M.; Ramlau, R.; Tang, Z.; Schnelle, W.; Baitinger, M.; Grin, Y. *Nature* **2006**, *443*, 320.

(71) Armatas, G. S.; Kanatzidis, M. G. *Nature* **2006**, *441*, 1122.

(72) Armatas, G. S.; Kanatzidis, M. G. *Science* **2006**, *313*, 817.

(73) Armatas, G. S.; Kanatzidis, M. G. *Adv. Mater.* **2008**, *20*, 546.

(74) Sun, D.; Riley, A. E.; Cadby, A. J.; Richman, E. K.; Korlann, S. D.; Tolbert, S. H. *Nature* **2006**, *441*, 1126.

(75) Kiefer, F.; Karttunen, A. J.; Döblinger, M.; Fässler, T. F. *Chem. Mater.* **2011**, *23*, 4578.

(76) Kiefer, F.; Hlukhyy, V.; Karttunen, A. J.; Fässler, T. F.; Gold, C.; Scheidt, E. W.; Scherer, W.; Nylen, J.; Häussermann, U. *J. Mater. Chem.* **2010**, *20*, 1780.

(77) Conesa, J. C. *J. Phys. Chem. B* **2002**, *106*, 3402.

Chapter 2

Experimental Section

2.1 Sample Handling and Preparation

Handling air- and moisture sensitive samples and preparations for solid state reactions were carried out in a glove box (MBRAUN, Ar atmosphere, H_2O and O_2 levels < 0.1 ppm). A high-vacuum all-glass Schlenk line supplied with purified Ar (dried over P_2O_5, molecular sieve, and heated (T = 750 °C) titanium sponge) was additionally used for handling air- and moisture sensitive materials, oxidation reactions in Schlenk tubes under Ar atmosphere or heating metal ampules and elements under dynamic vacuum ($p < 1 \cdot 10^{-3}$ mbar).

2.2 Synthesis

2.2.1 Starting Materials

Shapes and purities of starting materials are listed in Table 2.1. All elements were stored inside an Ar-filled glove box. Residual oxides or nitrides on the surface of Li and Na rods were removed by cutting. Prior to use, Si, Ge and B were heated to 800 °C (Si, Ge) and 1100 °C (B) under dynamic vacuum ($p < 1 \cdot 10^{-3}$ mbar) for several hours and transferred to the glove box subsequently. Liquid ammonia was dried over Na using a custom-built high-vacuum all-glass Schlenk line supplied with purified argon (see Chapters 2.1 and 2.2.7).

Table 2.1. Specifications of starting materials.

Element	Shape	Supplier	Purity
Li	rods	Rockwood Lithium	99%
Li	rods	Sigma-Aldrich (USA)	99.9%
Li	foil (0.5 mm thickness)	Rockwood Lithium	99.8%
Na	rods	Merck	99%
B	chunks	Chempur	99.95%
Al	granules	Chempur	99.99%
Si	powder	Alfa Aesar/Sigma-Aldrich	99.999%
Ge	chunks	Chempur	99.999%
NH_3	gas	Westfalen AG	99.98% (dried over Na)
Ethanol	liquid	-	technical grade (dried over Na)

2.2.2 Reaction Containers and Sample Storage

Depending on the batch size of the experiment, Ta (purity > 99.99%) ampules with *OD* = 10 mm, *ID* = 9 mm, *L* = 5–6 cm or *OD* = 12.7 mm, *ID* = 11.7 mm, *L* = 8–10 cm served as reaction containers. Prior to use, according Ta tubes and custom-built Ta lids were successively cleaned in ethanol, acetic acid, and acetone under ultrasonification and pre-dried in a drying oven at 120 °C. Subsequently, tubes and lids were transferred to a silica Schlenk tube and heated at 1000 °C under dynamic vacuum ($p < 1 \cdot 10^{-3}$ mbar) for several hours. Inside an Ar-filled glove box, lids were pressed onto the tubes and arc-welded (water-cooled arc furnace, MAM-1, JOHANNA OTTO GmbH). After the accordingly prepared ampules were loaded with samples or reaction mixtures, they were roughly closed either by crimping the open end or pressing a lid on top of them. Thereafter, ampules were sealed by arc-welding under cooling and an Ar-pressure of approximately 400–600 mbar. To prevent oxidation of Ta reaction containers during annealing in furnaces, ampules were encapsulated in silica jackets under vacuum using a high-vacuum all-glass Schlenk line (see Chapter 2.1).

Due to their extreme sensitivity toward air and moisture, synthesized samples were stored either in stainless steel (*OD* = 12.7 mm, *ID* = 11.7 mm) or glass ampules (*OD* = 10 mm, *ID* = 7 mm). The latter were self-made and prepared for plugging and sealing at a high-vacuum all-glass Schlenk line supplied with purified Ar (see Chapter 2.1) to guarantee complete exclusion of air and moisture. The sealed ends of glass ampules were additionally coated with apiezon wax (APIEZON-WAX W).

2.2.3 Furnaces

Reaction mixtures or samples as prepared for annealing according to Chapter 2.2.2 and 2.2.4 were vertically placed into muffle furnaces ($T_{max.}$ = 1100 °C, P330 controller, NABERTHERM GmbH). The monitored temperatures were additionally verified by an external Typ S thermocouple.

2.2.4 Melt Equilibration Experiments and Isothermal Melt-Centrifugation

Melt equilibration experiments (Li–*Tt* (*Tt* = Si, Ge) melts with Li concentrations > 85 at.%) were carried out in specially prepared ampules (*OD* = 12.7 mm, *ID* = 11.7 mm) either fabricated from Ta (purity > 99.99%) or stainless steel (Figure 2.1a). The procedure for cleaning Ta parts follows the methodology already described in Chapter 2.2.2. Pieces made from stainless steel were successively cleaned in ethanol and acetone under ultrasonification, pre-dried in a drying oven at 120 °C, and finally heated at 800 °C inside a silica Schlenk tube under dynamic vacuum ($p < 1 \cdot 10^{-3}$ mbar) for several hours.

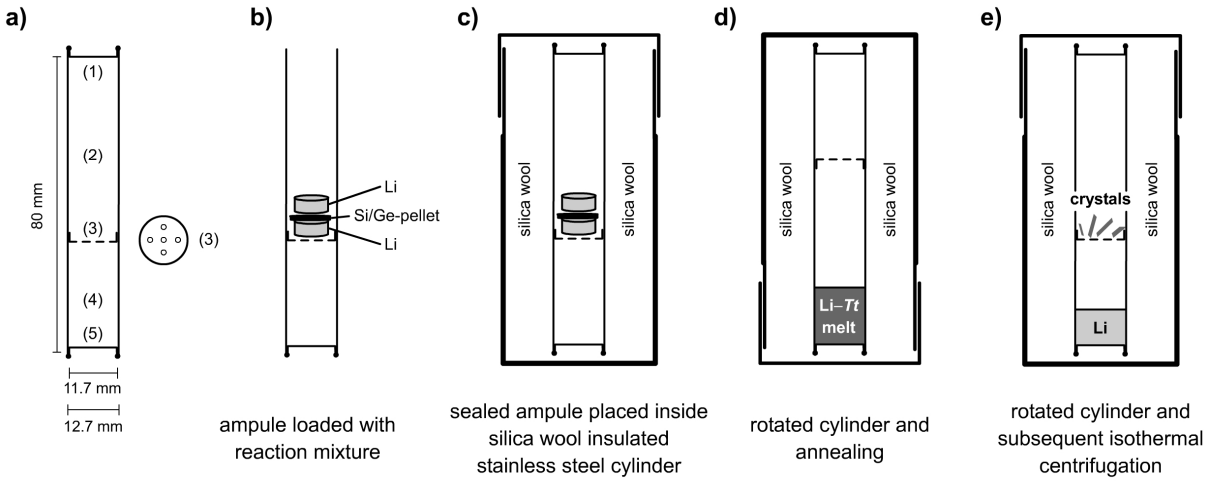

Figure 2.1. a) Specially prepared ampule for melt equilibration experiments according to ref. 1 (1 = top lid, 2 = sample space, 3 = filter lid with 0.5 mm holes, 4 = centrifugation space, 5 = bottom lid) and b–e) steps of synthesis.

The procedure of a typically performed melt equilibration experiment is depicted in Figure 2.1. If Ta ampules were employed, these had to be encapsulated inside silica jackets to prevent oxidation. Contrary, stainless steel ampules can be used up to 800 °C without

additional protection. The experiments were finally terminated by isothermally centrifuging off excess melt at various temperatures (centrifugation at 3000 rpm for 3 min, model HERAEUS MEGAFUGE 1.0; see Figure 2.1e).

2.2.5 Ball-Milling

Ball-milling experiments were carried out with a RETSCH PM 100 planetary ball mill. The reaction mixtures were loaded into a stainless steel jar (V = 50 mL, ball charge: 3 pieces with a diameter of 15 mm) inside an Ar-filled glove box. Subsequently, the jar was hermetically sealed using a safety closure device and transferred to the ball mill outside the glove box. Typical ball-milling parameters were 12–24 h duration with intervals of 10 min at 250 rpm followed by a 2–4 min break and direction reversal. Thereafter, products were recovered inside the glove box and obtained as fine powders.

2.2.6 High-Pressure High-Temperature Synthesis

High-pressure high-temperature experiments were performed at the high-pressure facility at the ARIZONA STATE UNIVERSITY (Tempe, AZ, USA) in a 6–8 Walker-type multi-anvil high-pressure device using an 18/12 assembly developed by Stoyanov et al.[2] A NaCl capsule served as reaction container (ID = 4 mm, OD = 6 mm, L = 8 mm; prepared from NaCl; dried under vacuum at 250–300 °C). It was loaded with the reaction mixture inside a glove box (MBRAUN, Ar atmosphere, H_2O and O_2 levels < 0.1 ppm) and sealed by pressing salt on top of the open end. Subsequently, the NaCl sample capsules were inserted in the high-pressure cell assembly. 25 mm tungsten carbide cubes truncated to 12 mm edge length were used to pressurize the samples at rate of about 0.5 GPa·h^{-1}. After reaching the target pressure (deviations are +/− 0.3 GPa) specified temperature programs were applied. The temperature was measured close to the sample using a thermocouple type C (W5%Re – W26%Re wire) in an Al_2O_3 sleeve. Usually, the reactions were terminated by quenching the samples through turning off the power to the furnace (quenching rate ~50 °C·min^{-1} at approximately constant pressure). Thereafter, the pressure was released slowly at a rate of ~0.5 GPa·h^{-1} and the samples were recovered inside the glove box. The different steps of preparing an 18/12 assembly for a typical high-pressure high-temperature experiment are depicted in Figure 2.2.

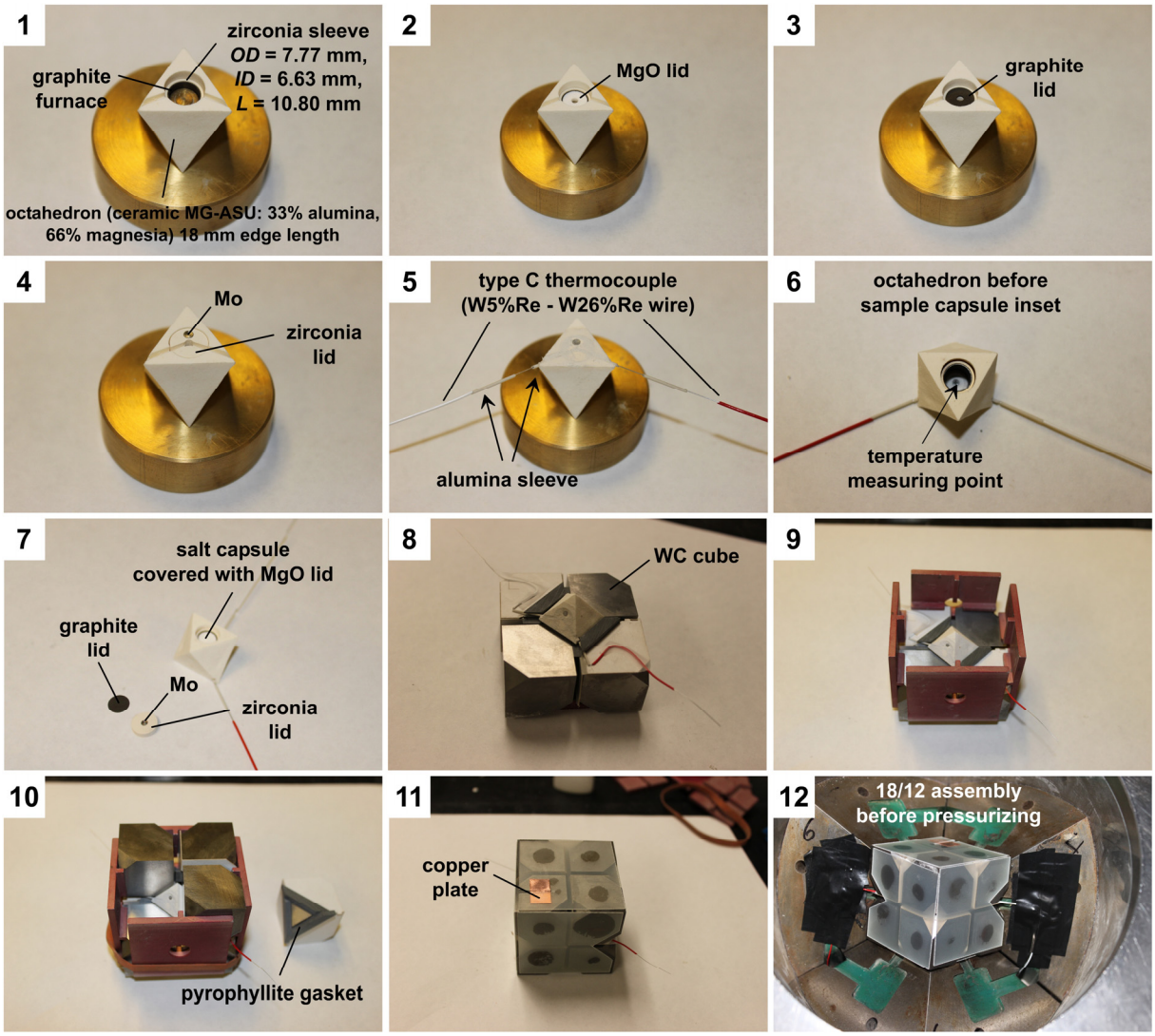

Figure 2.2. Steps of preparing an 18/12 assembly for a high-pressure high-temperature experiment in a 6–8 Walker-type multi-anvil high-pressure device.

2.2.7 Li-Extraction Using Liquid Ammonia

Liquid ammonia (dried over Na, see Chapter 2.2.1) was used for extracting Li from solids. This was carried out with a custom-built apparatus shown in Figure 2.4a. Prior to extraction cycles, the solid was filled onto the frit of the extractor inside an Ar-filled glove boxed. Subsequently, the closed device was connected to a custom-built high-vacuum all-glass Schlenk line supplied with purified argon (see Chapter 2.1) and liquid ammonia (Figure 2.3). For condensing ammonia onto the sample, the respective part is cooled with a mixture of isopropanol and dry ice (–78 °C). When closing valve (1) and cooling the reservoir (see Figure 2.4b), liquid ammonia

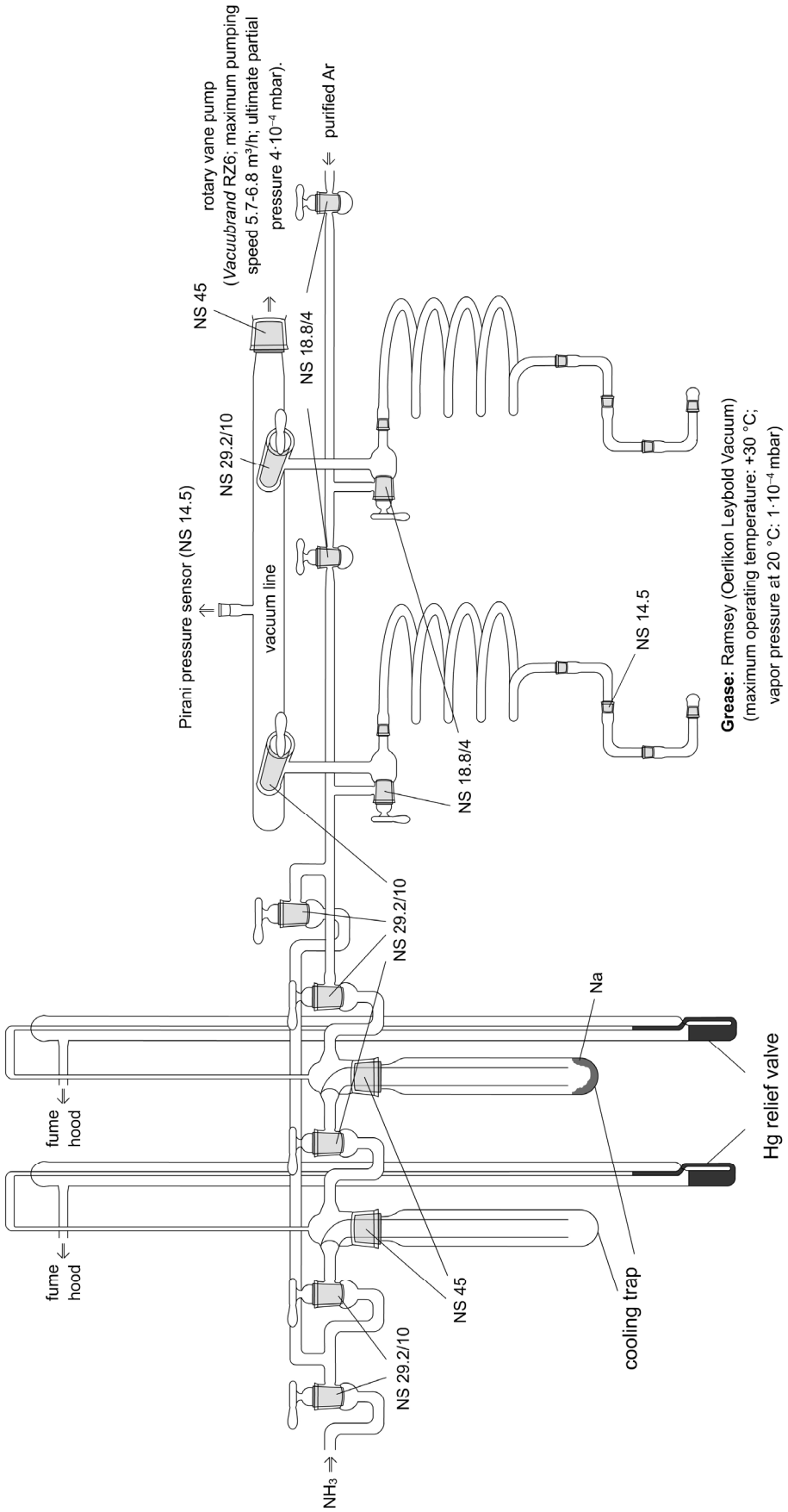

Figure 2.3. High-vacuum all-glass Schlenk line (borosilicate glass) supplied with purified argon. Ammonia is dried over sodium by condensing it into the sodium-filled cooling-trap. Adopted from ref. 3.

flows into the reservoir. If valve (1) is opened and the sample space is cooled again, the procedure can be repeated (see Figure 2.4c). At the end of the extraction procedure, liquid ammonia is evaporated from the reservoir and the product is recovered inside the glove box.

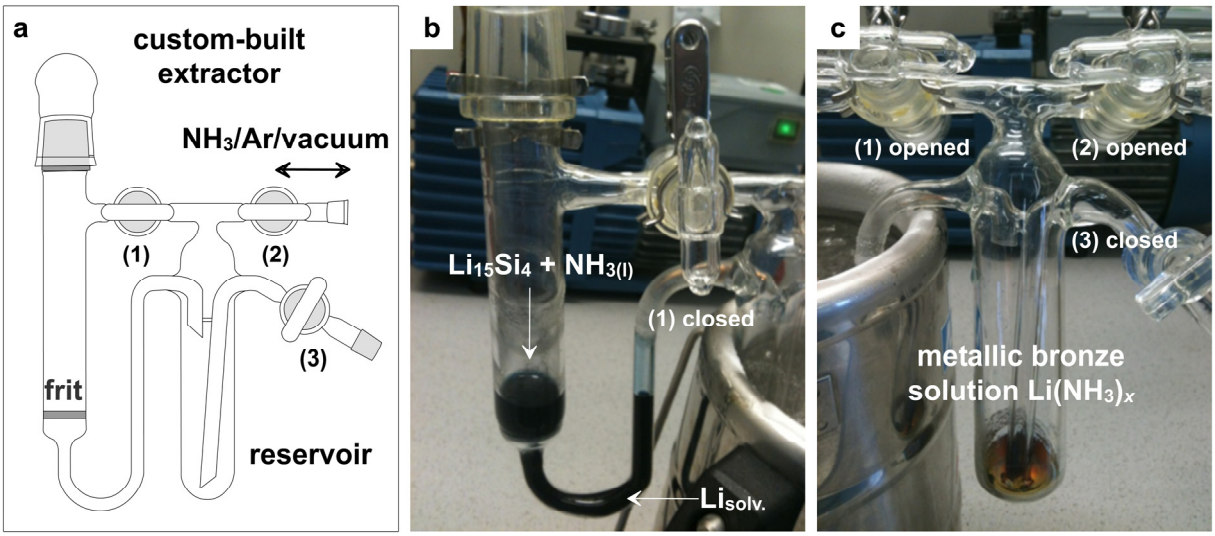

Figure 2.4. a) Custom-built apparatus for extracting Li from solids using liquid ammonia. An example of an extraction process is shown in (b) and (c): A deep blue color is observed as soon as ammonia is condensed onto $Li_{15}Si_4$ (b), extracted Li (concentrated metallic bronze solution of Li in NH_3) and $LiNH_2$ remains in the reservoir (c). The figure was adopted from Chapter 5.6.

2.2.8 Experimental Contributions from Coauthors

Table 2.2. Experimental contributions from coauthors to respective publications.

Publication	Author	Contributions
Chapters 5.1, 5.2, 5.3, 5.5	–	–
Chapter 5.4	Volodymyr Baran	synthesis of various $Li_{15-x}Al_xSi_4$ phases, single crystal X-ray diffraction of $Li_{14.37}Al_{0.63}Si_4$
Chapter 5.6	Lavinia M. Scherf	investigations on the solid solution behavior of $Li_3Na(Si_{1-x}Ge_x)_6$ and $Li_7(Ge_{1-y}Si_y)_{12}$ as precursors for *allo*-$Si_{1-x}Ge_x$ and *allo*-$Ge_{1-y}Si_y$, respectively.[4]
	Florian J. Kiefer	investigations on the synthesis of *allo*-Si, see also ref. 5
Chapter 5.7	Lavinia M. Scherf (first author)	investigations on the solid solution behavior of $Li_3Na(Si_{1-x}Ge_x)_6$, synthesis and characterization of $Li_{18}Na_2Ge_{17}$
Chapter 5.8	Sumit Konar	Raman spectra of $LiBSi_2$, support during high-pressure high-temperature experiments

2.3 Characterization

2.3.1 Powder X-ray Diffraction (PXRD)

PXRD patterns were recorded on a STOE STADI P diffractometer (Ge(111) monochromator for Cu$K_{\alpha1}$ radiation, λ = 1.54056 Å) equipped with a DECTRIS MYTHEN DCS 1K solid state detector. All samples were ground in agate mortars and sealed inside glass capillaries (*OD* = 0.3, 0.5, 0.7, HILGENBERG GmbH). Measurements (Debye-Scherer geometry) were performed in a 2θ-range of 5–90° (PSD steps: 0.06–1.50°; time/step: 10–40 s).

Raw data were handled with the STOE WinXPOW software package.[6] PXRD patterns were visualized with the ORIGIN 8.0 software.[7] For the phase identification, the SEARCH/MATCH module as implemented in the WinXPOW software,[6] the ICSD (FINDIT),[8] and the PEARSON'S CRYSTAL DATA[9] crystallographic databases were used. Rietveld refinements were performed with the BRUKER software TOPAS 4.0.[10] Ab initio structure determination from X-ray powder diffraction data was done using the parallel tempering algorithm implemented in the software FOX.[11-13] Structure solutions are approached by starting with reasonable "structural building blocks". Solutions are finalized by Rietveld refinement applying the final structure model obtained from FOX.

2.3.2 Single Crystal X-ray Diffraction, Structure Solution and Refinement

Using a microscope installed at an Ar-filled glove box, all single crystals were selected and cut in perfluoropolyalkylether or grease on a glass slide. The best specimens were placed inside glass capillaries with glass fibers. Subsequently, the funnels of the capillaries were filled with grease to guarantee exclusion of air and moisture during flame-sealing outside the glove box. Finally, the accordingly prepared capillaries were glued to copper pins suitable for mounting on the goniometer.

Single crystal X-ray diffraction experiments were performed at X-ray diffractometers from STOE (IPDS 2T), BRUKER and OXFORD DIFFRACTION using the X-AREA,[14] APEX2,[15] and CRYSALISRED software packages,[16] respectively. The BRUKER devices are equipped with CCD detectors (APEX II, κ-CCD) and either a fine-focused sealed tube with MoK_α radiation (λ = 0.71073 Å) and a graphite monochromator or a NONIUS FR591 rotating anode (MoK_α radiation) with a Montel mirror. The STOE IPDS 2T is operated with a rotating anode (λ = 0.71073 Å, MoK_α radiation) and a Montel mirror. The OXFORD XCALIBUR3 diffractometer is equipped with a Sapphire3 CCD detector and a graphite monochromated MoK_α radition

(λ = 0.71073 Å). Integration, data reduction and absorption correction was done with X-AREA, X-RED, X-SHAPE (STOE),[14,17,18] SAINT, SADABS (BRUKER),[19,20] and CRYSALISRED (OXFORD DIFFRACTION).[16] The space groups were assigned on the basis of the systematic absences and the statistical analysis of the intensity distributions. The structures were solved with direct methods (SHELXS[21]) and refined with full-matrix least squares on F^2 (SHELXL[22]). Difference Fourier maps F_o–F_c were calculated with JANA 2006.[23] Crystallographic information files (CIF) were generated with enCIFer[24] and publCIF[25] using the IUCr-CIF template. CIFs were finally checked with the CHECKCIF routine.[26] Structures were visualized with the DIAMOND 3.2d software.[27]

2.3.3 Differential Scanning Calorimetry (DSC) and Differential Thermal Analysis (DTA)

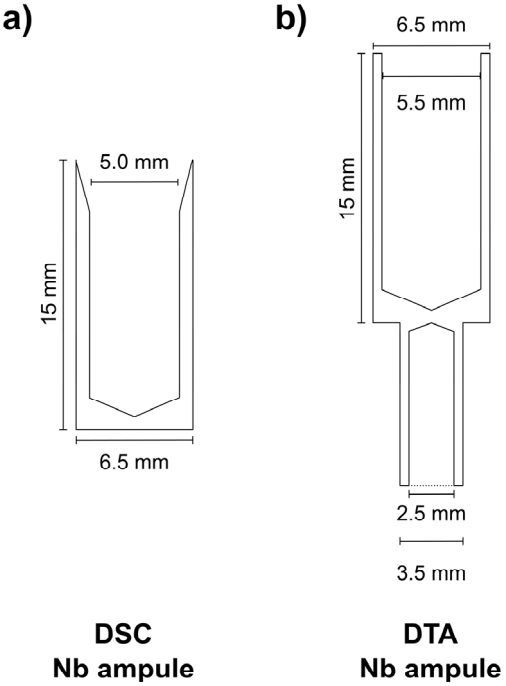

Figure 2.5. Drawings of cylindrical Nb crucibles used for a) DSC and b) DTA measurements.

Differential scanning calorimetry and differential thermal analysis investigations were performed with a NETZSCH DSC 404 Pegasus apparatus equipped with either a DSC or DTA carrier system. Niobium crucibles for DSC and DTA measurements (Figure 2.5) were thoroughly cleaned (analogously to Chapter 2.2.2), heated to 1000 °C under dynamic vacuum ($p < 1 \cdot 10^{-3}$ mbar) for 2 h and transferred to an Ar-filled glove box. Crucibles were loaded with 30–50 mg of sample. The open end was crimped and then sealed by arc-welding inside the glove box under cooling (see also Chapter 2.2.2). A sealed crucible without sample served as reference. All measurements were performed under an Ar-flow of 60–70 mL·min^{-1} and a heating/cooling rate of 10 K·min^{-1}. Samples were recovered after the measurement by opening the niobium crucibles inside an Ar-filled glove box. Data handling was done with the program PROTEUS THERMAL ANALYSIS.[28]

The device was calibrated for temperature by determining the melting and crystallization points of reference materials (In, Sn, Zn, Al, Ag). Note that in most cases the obtained onsets

of effects assigned to melting and recrystallization were almost identical. Otherwise, differences were marginal (±1 K) and according values were merged for the calibration curve.

2.3.4 Scanning Electron Microscopy (SEM) and Energy Dispersive X-ray Spectroscopy (EDX)

A JEOL-JSM 7500F scanning electron microscope (FE-SEM) equipped with an OXFORD X-MAX EDX analyzer with Mn as internal standard was used to determine elements with atomic numbers larger than four. Samples were handled inside an Ar-filled glove box or outside if not air sensitive and fixed on a graphite platelet which was attached to an aluminum stub. Measurements were performed by *Dipl. Min. Katia Rodewald* at the INSTITUT FÜR SILICIUMCHEMIE der TECHNISCHEN UNIVERSITÄT MÜNCHEN (Germany).

2.3.5 Nuclear Magnetic Resonance (NMR) Spectroscopy

Solid state NMR-spectroscopy was carried out by *Prof. Dr. Leo van Wüllen* (UNIVERSITY OF AUGSBURG, Germany). ^{7}Li- and ^{11}B-MAS (magic angle spinning) NMR spectra were collected on a VARIAN VNMRs 500, and ^{27}Al NMR data were acquired on a BRUKER AVANCE III spectrometer. For details, refer to according publications in Chapter 5.4 and 5.8, respectively.

2.3.6 Transmission Electron Microscopy (TEM)

Transmission electron microscopy and selected area electron diffraction (SAED) were performed by *Prof. Dr. Lorenz Kienle* (UNIVERSITY OF KIEL, Germany) with a PHILIPS CM30 ST microscope (LaB_6 cathode, 300 kV acceleration voltage, C_s = 1.15 mm) equipped with a GATAN multiscan CCD camera. EDX analysis as part of TEM examinations were carried out with a NORAN VOYAGER EDX system. For details, refer to the respective manuscript in Chapter 5.6.

2.3.7 Infrared (IR) and Raman Spectroscopy

A VARIAN 670-IR FT-IR spectrometer equipped with a PIKE GladiATR ATR stage was employed for the acquisition of ATR-FT-IR spectra. The VARIAN RESOLUTION PRO software was used for data handling.[29]

Raman spectra data were recorded at the spectroscopy facility of the UNIVERSITY of STOCKHOLM (Stockholm, Sweden; *M. Sc. Sumit Konar*) using a LABRAM HR 800 spectrometer equipped with an 800 mm focal length spectrograph and a back thinned CCD detector. For sample excitation, an air cooled double frequency Nd:YAG laser (532 nm, 5.6 mW) and an air cooled intra cavity regulated laser diode with point source (785 nm, 0.88 mW) were used. The laser was focused using a 50X super long working distance (20.5 mm) Mitutoyo objective with a numerical aperture of 0.42 and depth of focus of 1.6 mm. More specific experimental details are described in Chapters 5.6 and 5.8.

2.3.8 Photoluminescence (PL) Spectroscopy

PL-spectroscopy was carried out at the ARIZONA STATE UNIVERSITY (Tempe, AZ, USA; *Dr. Christian Poweleit*) using a 532 nm CW doubled Nd:YAG laser for photoexcitation. The collected energy was energy dispersed through a 0.5 m ACTON spectrometer with and a back-thinned liquid nitrogen cooled PRINCETON INSTRUMENTS CCD camera. Further details are described in Chapter 5.6.

2.3.9 Elemental Analysis

Elemental analysis was provided as service of the micro-analytical laboratory of the TECHNISCHEN UNIVERSITÄT MÜNCHEN (Germany). The lithium content in samples was determined by atomic absorption spectroscopy using a VARIAN AA280FS device. C,H, and N contents were obtained from a HEKATECH EURO EA CHNSO-Analyzer.

2.4 Computational Methods

Quantum chemical calculations were exclusively performed by coauthors. Relevant publications (investigated compounds referenced with Chapters), according coauthor names and employed programs are listed below.

a) $LiBSi_2$ (see Chapter 5.8), *Dr. Daryn Benson* (ARIZONA STATE UNIVERSITY, Tempe, AZ, USA): VIENNA AB INITIO SIMULATION PACKAGE (VASP),[30,31] *Prof. Dr. Leo van Wüllen* (UNIVERSITY OF AUGSBURG, Germany): WIEN2k[32]
b) *allo*-Si (see Chapter 5.6), *M.Sc. Laura A. Jantke* (TECHNISCHE UNIVERSITÄT MÜNCHEN, Germany), *Dr. Antti Karttunen* (UNIVERSITY OF JYVÄSKYLÄ, Finland): CRYSTAL09 software package[33]
c) $Li_{15}Si_4$, "$Li_{16}Si_4$" and "$Li_{16.5}Si_4$" (structure models for $Li_{16.42}Si_4$), $Li_{17}Si_4$ (see Chapter 5.1 and 5.2), *Dr. Daryn Benson* (ARIZONA STATE UNIVERSITY, Tempe, AZ, USA): VIENNA AB INITIO SIMULATION PACKAGE (VASP),[30,31] *M. Sc. Iryna M. Kurylyshyn* (TECHNISCHE UNIVERSITÄT MÜNCHEN, Germany): WIEN2k[32]

Specific details on the theoretical calculations may be obtained from the publications and manuscripts as cited above.

2.5 References

(1) Puhakainen, K.; Boström, M.; Groy, T. L.; Häussermann, U. *J. Solid State Chem.* **2010**, *183*, 2528.
(2) Stoyanov, E.; Häussermann, U.; Leinenweber, K. *High Pressure Res.* **2010**, *30*, 175.
(3) Zeilinger, M. *Master's Thesis*, Technische Universität München: München, Germany, 2010.
(4) Scherf, L. M. *Master's Thesis*, Technische Universität München: München, Germany, 2013.
(5) Kiefer, F. *Dissertation*, Technische Universität München: München, Germany, 2010.
(6) *WinXPOW*, Version 2.08a; STOE & Cie GmbH: Darmstadt, Germany, **2003**.
(7) *Origin Pro 8*, Version 8.0724; Origin Lab Corp.: Northampton, MA, USA, **2007**.
(8) *FindIt, Inorganic Crystal Structure Database (ICSD)*, Version 1.9.2, ICSD-Database Version 2013-1; Fachinformationszentrum Karlsruhe (FIZ): Karlsruhe, Germany, **2013**.

(9) Villars, P.; Cenzual, K. *Pearson's Crystal Data: Crystal Structure Base for Inorganic Compounds*, Version 1 (Release 2007/8), ASM International: Materilas Park, Ohio, USA, **2003**.

(10) *TOPAS - Rietveld Software*, Version 4.0; Bruker AXS Inc.: Madison, WI, USA, **2009**.

(11) Favre-Nicolin, V.; Cerny, R. *J. Appl. Crystallogr.* **2002**, *35*, 734.

(12) Cerny, R.; Favre-Nicolin, V. *Powder Diffr.* **2005**, *20*, 359.

(13) *FOX program*, F.O.X., Free Objects for Crystallography V 1.9.7.0, http://objcryst.sourceforge.net., **2011**.

(14) *X-Area*, Version 1.26 - Single Crystal Diffraction Software. Stoe & Cie.: Darmstadt (Germany), **2004**.

(15) *APEX suite of crystallographic software*, APEX 2 Version 2008.4; Bruker AXS Inc.: Madison, WI, USA, **2008**.

(16) *CrysalisRED*, Version 1.171.33.34d; Oxford Diffraction: UK, **2009**.

(17) *X-Red*, Version 1.26 - Data Reduction Program. Stoe & Cie.: Darmstadt (Germany), **2004**.

(18) *X-Shape*, Version 2.05 - Crystal Optimization for Numerical Absorption Correction. Stoe & Cie.: Darmstadt (Germany), **2004**.

(19) *SAINT*, Version 7.56a; Bruker AXS Inc.: Madison, WI, USA, **2008**.

(20) *SADABS*, Version 2008/1; Bruker AXS Inc.: Madison, WI, USA, **2008**.

(21) Sheldrick, G. M. *Shelxs-97 - Program for the Determination of Crystal Structures*, University of Göttingen: Göttingen, Germany, **1997**.

(22) Sheldrick, G. M. *Shelxl-97 - Program for Crystal Structure Refinement*, University of Göttingen: Göttingen, Germany, **1997**.

(23) Petricek, V.; Dusek, M.; Palatinus, L. *Jana 2006: The Crystallographic Computing System*, Version 03/15/2013; Institute of Physics: Praha, Czech Rupublic, **2006**.

(24) Allen, F. H.; Johnson, O.; Shields, G. P.; Smith, B. R.; Towler, M. *J. Appl. Cryst.* **2004**, *37*, 335.

(25) Westrip, S. P. *J. Appl. Cryst.* **2010**, *43*, 920.

(26) http://checkcif.iucr.org/

(27) Brandenburg, K. *Diamond*, Version 3.2d, Crystal Impact GbR: Bonn, Germany, **2012**.

(28) *Netzsch Proteus Thermal Analysis*, Version 4.8.2; Netzsch-Gerätebau GmbH: Selb, Germany, **2006**.

(29) *Resolution Pro*, Version 5.1.0.822; Varian Inc.: Santa Clara, CA, USA, **2009**.

(30) Kresse, G.; Hafner, J. *Phys. Rev. B* **1993**, *48*, 13115.

(31) Kresse, G.; Furthmüller, J. *Comp. Mater. Sci.* **1996**, *6*, 15.

(32) Blaha, P.; Schwarz, K.; Madsen, G. K. H.; Kvasnicka, D.; Luitz, J. *WIEN2k: An Augmented Plane Wave and Local Orbitals Program for Calculating Crystal Properties*, Version 12.0; Technische Universität Wien: Vienna, Austria, **2001**.

(33) Dovesi, R.; Orlando, R.; Civalleri, B.; Roetti, C.; Saunders, V. R.; Zicovich-Wilson, C. M. *Z. Kristallogr.* **2005**, *220*, 571.

Chapter 3

Results and Discussion

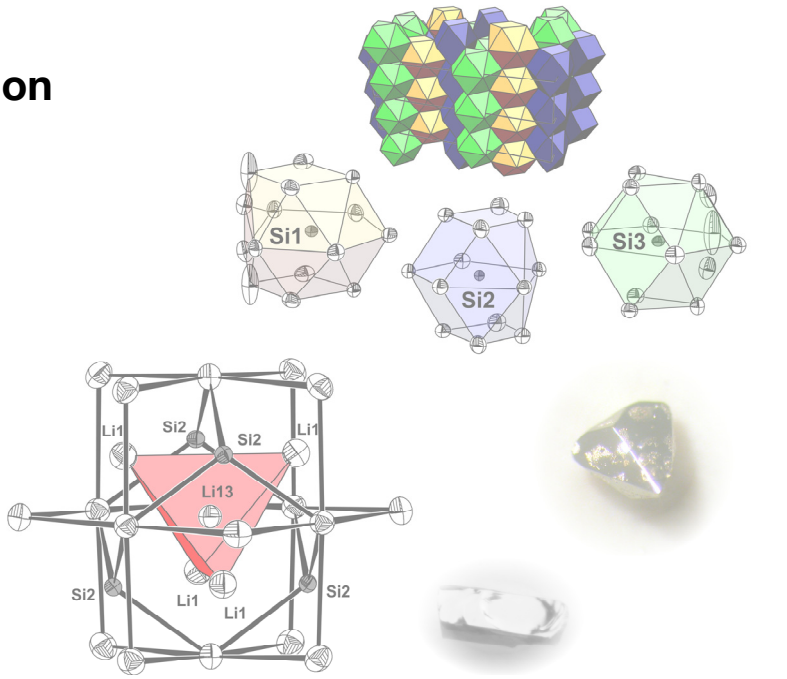

composed from ref. 64–67

3.1 Revision of the Li–*Tt* (*Tt* = Si, Ge) Phase Diagrams and New Lithium-Rich Tetrelides

3.1.1 Review of Relevant Literature

Discussing new materials for high-capacity lithium-ion batteries, a main focus has always been set on Li–Si phases because theoretical capacities being almost ten times higher than for the universally used graphite anodes can be achieved. The severe problems that occur during charging and discharging processes when Si is employed as electrode material, suggestions to overcome them and the role of the metastable phase $Li_{15}Si_4$ have already been addressed in Chapter 1. Furthermore, the possibility of monitoring structural changes in working LIBs by in-situ/ex-situ solid state NMR spectroscopy and total scattering methods are described in literature.[1,2] These investigations were followed by a detailed structural characterization of $Li_{15}Si_4$, $Li_{13}Si_4$, Li_7Si_3, $Li_{12}Si_7$, and $Li_{12}Ge_7$ applying NMR techniques.[3-5] Due to the general importance of the Li–Si phase diagram for LIB research it is evident that a comprehensive characterization of the lithium-rich section, i.e. the unambiguous determination of compositions, structures, and thermodynamic relations of relevant phases is essential. Also the related section of the Li–Ge phase diagram is overdue and has to be revised fundamentally. In the following, the chronicles of Li–Si and Li–Ge phases are briefly highlighted,

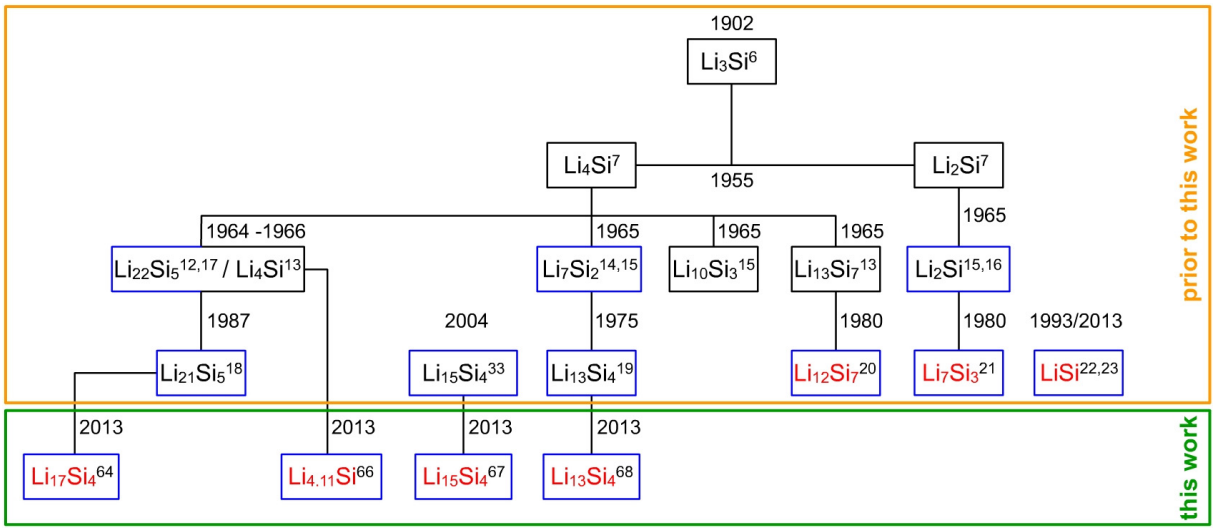

Figure 3.1. Chronicle of Li–Si phases (highlighted with a blue frame = structurally characterized, shown in red = ascertained structures). The figure was modified on the basis of ref. 66.

associated recent developments are presented and aspects that were of particular importance for this thesis are elucidated.

The first investigations on phases in the Li–Si system can be assigned to Moissan. In 1902, he reported on the phase Li_3Si[6] (Figure 3.1). Decades later, however, Klemm and Struck[7] postulated the phases Li_2Si and Li_4Si instead which were confirmed by Pell,[8] Böhm,[9] Obinata et al.,[10] and Federov and Ioffe[11] later on. The 1960's can be considered as the "era of the Li–Si system", mainly due to the work of Schäfer and Weiss. Several phases were characterized in this period (Figure 3.1).[12-16] In particular, the lithium-richest representative, $Li_{22}Si_5$, was identified as a new example of the $Li_{22}Pb_5$ structure type by Gladyshevskii et al.[17] using powder X-ray diffraction methods. Axel et al.[12] confirmed its existence by a single crystal X-ray diffraction study shortly after. In the following years, almost all of the phases reported in the 1960's were revised (Figure 3.1).[18-23] In this regard, the composition of the lithium-richest representative was discussed controversially ranging from reports on $Li_{20}Si_5$[24,25] to $Li_{21}Si_5$[18] and $Li_{22}Si_5$.[12,17] Still today, there are plenty of examples in literature referring to either $Li_{22}Si_5$ or its revision $Li_{21}Si_5$. Judging from the crystallographic data of $Li_{10}Si_3$,[15] this unconfirmed phase might have been $Li_{22}Si_5$ although its composition is rather different. More interestingly, the phase Li_4Si crystallizing with an orthorhombic base face-centered cell was reported in the 1960's. Yet, it was neither characterized structurally nor confirmed by subsequent investigations.[13] As a consequence, it was excluded from compilations of the Li–Si phase diagram (Figure 3.2a).[26-29] Although there are some reports on the possible existence of a phase with a composition Li_4Si or close to it,[30-32] Li_4Si became obscure most likely since other lithium-rich

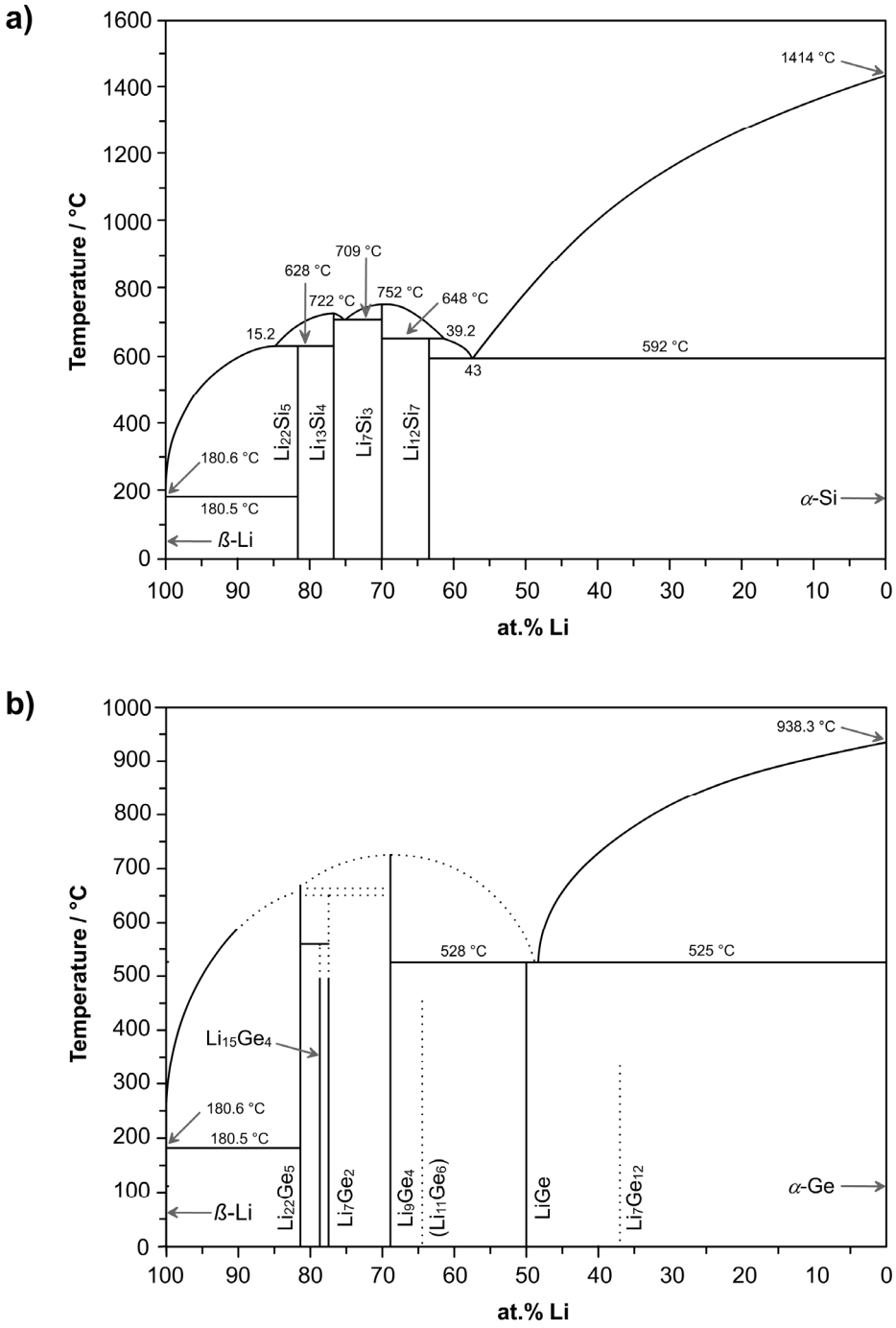

Figure 3.2. Phase diagram compilation for a) the Li–Si and b) the Li–Ge system according to ref. 27 (phase diagram assessment and calculation of liquidus boundaries) and 33 (phase diagram evaluation), respectively.

phases with a similar composition were established. Moreover, two further representatives of the Li–Si system were identified later on, $Li_{15}Si_4$[34] and LiSi.[22,23] The latter was synthesized at high pressure and metastable $Li_{15}Si_4$ was obtained electrochemically. Interestingly, $Li_{15}Si_4$ was first obtained from ball-milling the pure elements some years before it could be identified

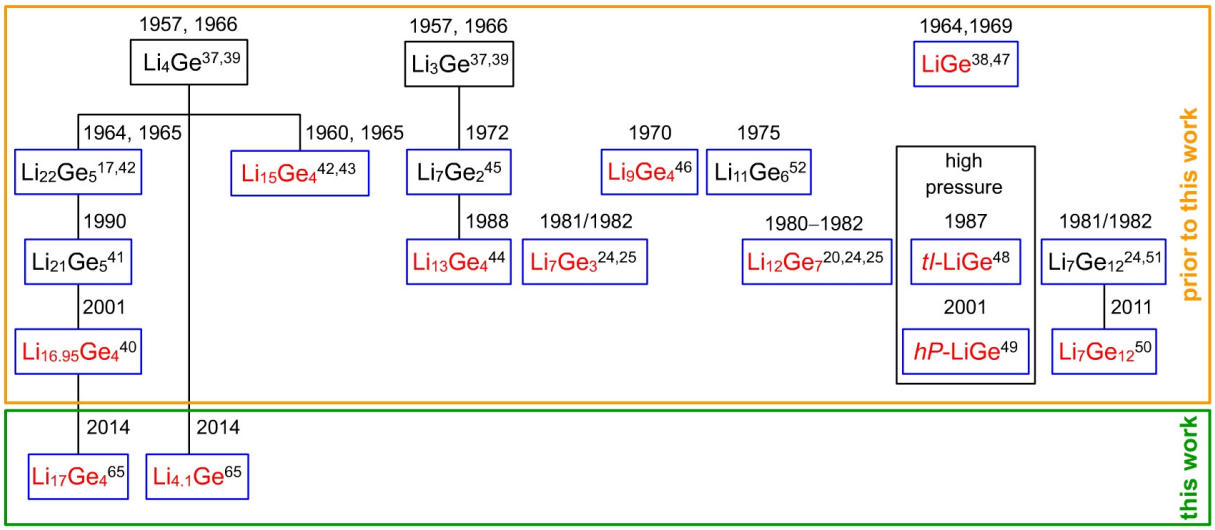

Figure 3.3. Chronicle of Li–Ge phases (highlighted with a blue frame = structurally characterized, shown in red = ascertained structures).

during electrochemical investigations. However, the authors denoted it as "metastable $Li_{4.4}Si$" ("metastable $Li_{22}Si_5$") and it somehow remained unrecognized.[35,36]

Turning to the Li–Ge system, the first binary compounds were reported in the 1950's and 60's (Figure 3.3). These were Li_3Ge, Li_4Ge and LiGe.[37-39] A first phase diagram determination was reported by Federov and Molochka in 1966.[39] Similar to the Li–Si system, several phases were proposed and revised later on. To date, the ascertained Li–Ge phases include $Li_{\sim 17}Ge_4$[40] (= $Li_{21+3/16}Ge_5$ revised from $Li_{21}Ge_5$[41] which was formerly reported as $Li_{22}Ge_5$[17,42]), $Li_{15}Ge_4$,[42,43] $Li_{13}Ge_4$[44] (formerly reported as Li_7Ge_2[45]), $Li_{14}Ge_6$,[24,25] Li_9Ge_4,[46] $Li_{12}Ge_7$,[20,24,25] LiGe (space group $I4_1/a$),[38,47] the hexagonal and tetragonal high-pressure forms of LiGe (space groups $P6_3/mmc$ and $I4_1/amd$, respectively),[48,49] and Li_7Ge_{12} (Figure 3.3).[24,50,51] In the course of an experimental redetermination of the Li–Ge phase diagram by Grüttner,[25] a previously determined phase $Li_{11}Ge_6$[52] could not be confirmed. It was suspected that it might have been identical with ternary Li_8MgGe_6 due to "striking similarities" to Li_8MgSi_6.[53] A recent compilation of the Li–Ge phase diagram is given by Sangster and Pelton (Figure 3.2b).[33] However, Grüttner's work is not included and therefore significant information is missing.

The Li–Si and Li–Ge phase systems were continuously developed over many years and plenty of phases have been established. In the last decade, contributions focusing on a fundamental understanding have been rare, for instance, structural investigations applying solid state NMR techniques,[1-5,54] further spectroscopic[54,55] and thermodynamic studies,[56-58] quantum chemical calculations,[59-62] and the determination of heat capacities and entropies of Li–Si phases.[63] However, the Li–Ge system has received significantly less attention, most likely because the demand for high-capacity LIBs particularly enforced investigations on

Li–Si phases which offer much higher theoretical specific capacities and because of the great abundance of Si. Despite the importance of both the Li–Si and Li–Ge system, their characterization is still unsatisfying and recent phase diagrams are outdated. In detail, all phases in the lithium-rich sections of these phase diagrams need to be identified, characterized structurally and investigated with regard to their thermodynamic properties. In particular, the controversy regarding the lithium-richest representatives of both systems and the potential existence of the Zintl phases Li_4Tt (*Tt* = Si, Ge) request for unambiguous clarification. Moreover, despite its important role in LIB research, little to nothing was known about the decomposition behavior of metastable $Li_{15}Si_4$ and the influence of dopants prior to this work.

In the following, the fundamental revision of the lithium-rich sections of the Li–*Tt* (*Tt* = Si, Ge) phase diagrams as well as the synthesis and characterization of $Li_{17}Tt_4$,[64,65] $Li_{4.1}Tt$[65,66] ($Li_{16.4}Tt_4$), $Li_{15}Si_4$,[67] $Li_{13}Si_4$,[68] $Li_{15-x}Al_xSi_4$[67] ($0.4 < x < 0.8$), and $Li_{17}Si_{4-x}Ge_x$ [x = 2.30(2), 3.08(4), 3.53(3)][65] are presented (see also Figure 3.1 and 3.3).

3.1.2 Revision of the Li–Si Phase Diagram: Thermodynamic Relation of $Li_{17}Si_4$, $Li_{16.42}Si_4$, $Li_{15}Si_4$ and $Li_{13}Si_4$

see Chapter 5.1	Zeilinger, M.; Benson, D.; Häussermann, U.; Fässler, T. F. *Chem. Mater.* **2013**, *25*, 1960.
see Chapter 5.2	Zeilinger, M.; Kurylyshyn, I. M.; Häussermann, U.; Fässler, T. F. *Chem. Mater.* **2013**, *25*, 4623.
see Chapter 5.3	Zeilinger, M.; Fässler, T. F. *Acta Cryst.* **2013**, *E69*, i81.
see Chapter 5.4	Zeilinger, M.; Baran, V.; Häussermann, U.; Fässler, T. F. *Chem. Mater.* **2013**, *25*, 4113.

Figure 3.4a illustrates the lithium-rich section (> 76 at.% Li) of the Li–Si phase diagram as reported prior to this work. In the course of the present thesis, this portion of the Li–Si system was comprehensively reinvestigated and revised fundamentally. The newly established Li–Si phase diagram section is depicted in Figure 3.4b.

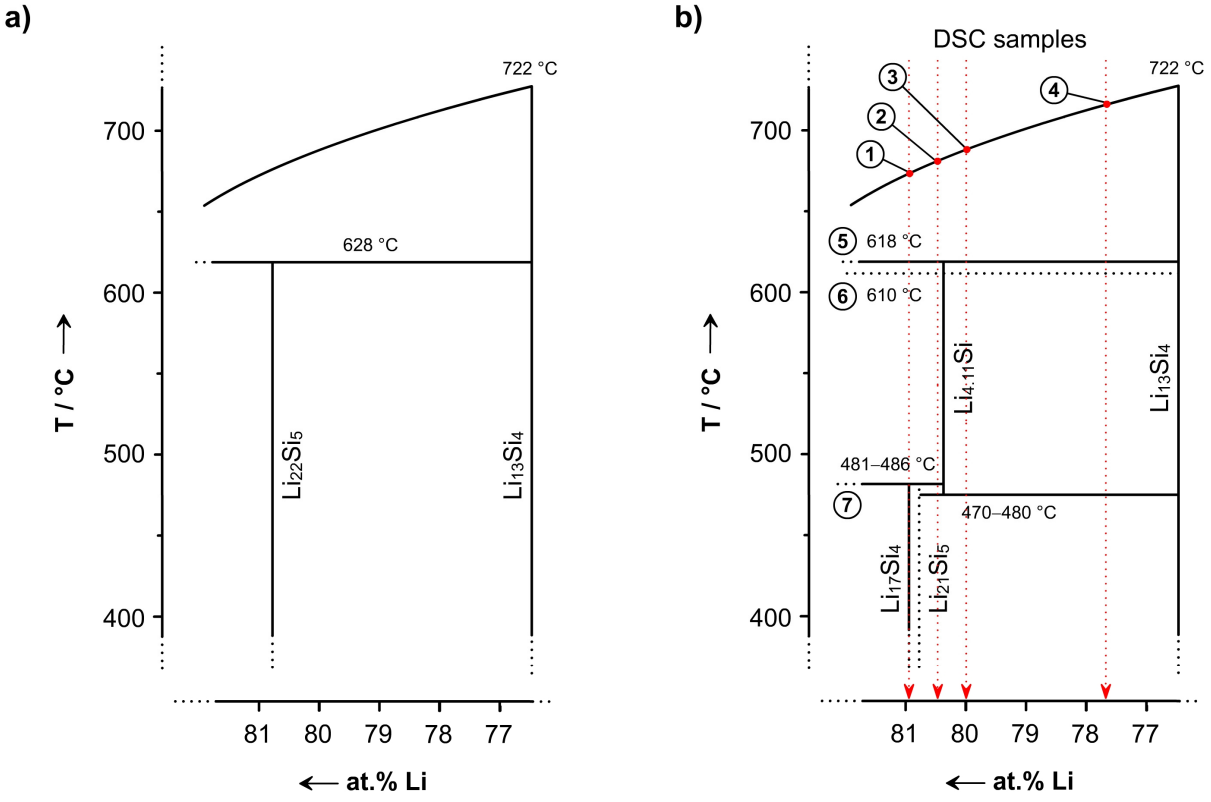

Figure 3.4. a) Li–Si phase diagram for Li concentrations > 76 at.% Li as reported by Okamoto[27,29] and Braga[28] and b) its revision based on results from DSC investigations (corresponding cooling traces and thermal effects are presented in Figure 3.5) and long term annealing experiments of "$Li_{16}Si_4$" samples.[64,66]

The phase diagram redetermination was achieved by differential scanning calorimetry investigations and melt equilibration experiments (Li_xSi_{100-x}, x > 85) at specific temperatures

where excess melt is removed by isothermal centrifugation. Various melts Li_xSi_{100-x} ($x > 85$) that were equilibrated below 500 °C yielded large crystals of $Li_{17}Si_4$, whereas crystals of the silicide $Li_{4.11}Si$ ($Li_{16.42}Si_4$) were isolated from excess melt above 500 °C (cf. Figure 3.4b). Consequentially, bulk samples of $Li_{17}Si_4$ and nominal compositions "$Li_{16.5}Si_4$", "$Li_{16}Si_4$", and "$Li_{14}Si_4$" were investigated by DSC. A careful analysis of cooling traces and powder X-ray diffraction patterns of these samples as well as results from melt equilibration experiments finally led to the revised version of the Li–Si phase diagram as depicted in Figure 3.4b.

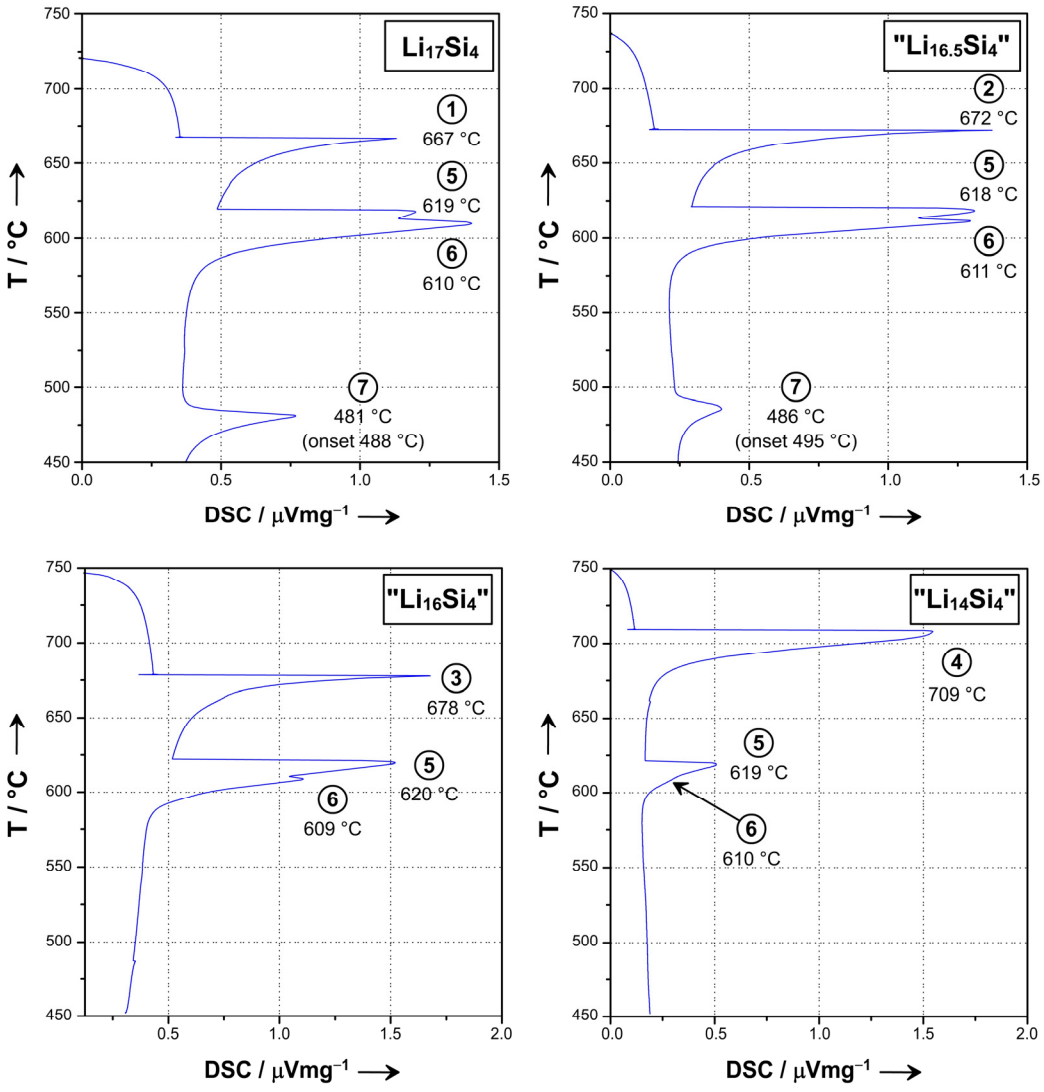

Figure 3.5. DSC cooling traces (recorded from 750 °C) for $Li_{17}Si_4$ and nominal compositions "$Li_{16.5}Si_4$", "$Li_{16}Si_4$" and "$Li_{14}Si_4$" (according to ref. 64). Thermal events are labeled and assigned in the updated Li–Si phase diagram in Figure 3.4. The figure was modified on the basis of ref. 66.

Remarkably, the isotherm at 470–480 °C could not be traced by DSC means due to the sluggish peritectoid decomposition of $Li_{16.42}Si_4$ into $Li_{17}Si_4$ and $Li_{13}Si_4$. However, long term annealing experiments of "$Li_{16}Si_4$" samples manifested $Li_{16.42}Si_4$ as high-temperature phase. Turning

to $Li_{15}Si_4$, it is not included in the phase diagram due to its metastability. Thus far, its decomposition behavior has been studied sparsely and is widely unknown.[1,69-71] Yet, the redetermination of the Li–Si phase diagram allowed a rigorous investigation of the decomposition behavior of $Li_{15}Si_4$ by DSC/DTA and annealing experiments. Above 170 °C $Li_{15}Si_4$ decomposes into $Li_{17}Si_4$ and an unidentified weakly crystalline phase (Figure 3.6a). The latter might be considered as "$Li_{13}Si_4$ pre-phase" since, according to the recent Li–Si phase diagram, $Li_{13}Si_4$ would have been expected instead. Above 300 °C, the decomposition products are in line with the Li–Si phase diagram (Figure 3.6b–d).

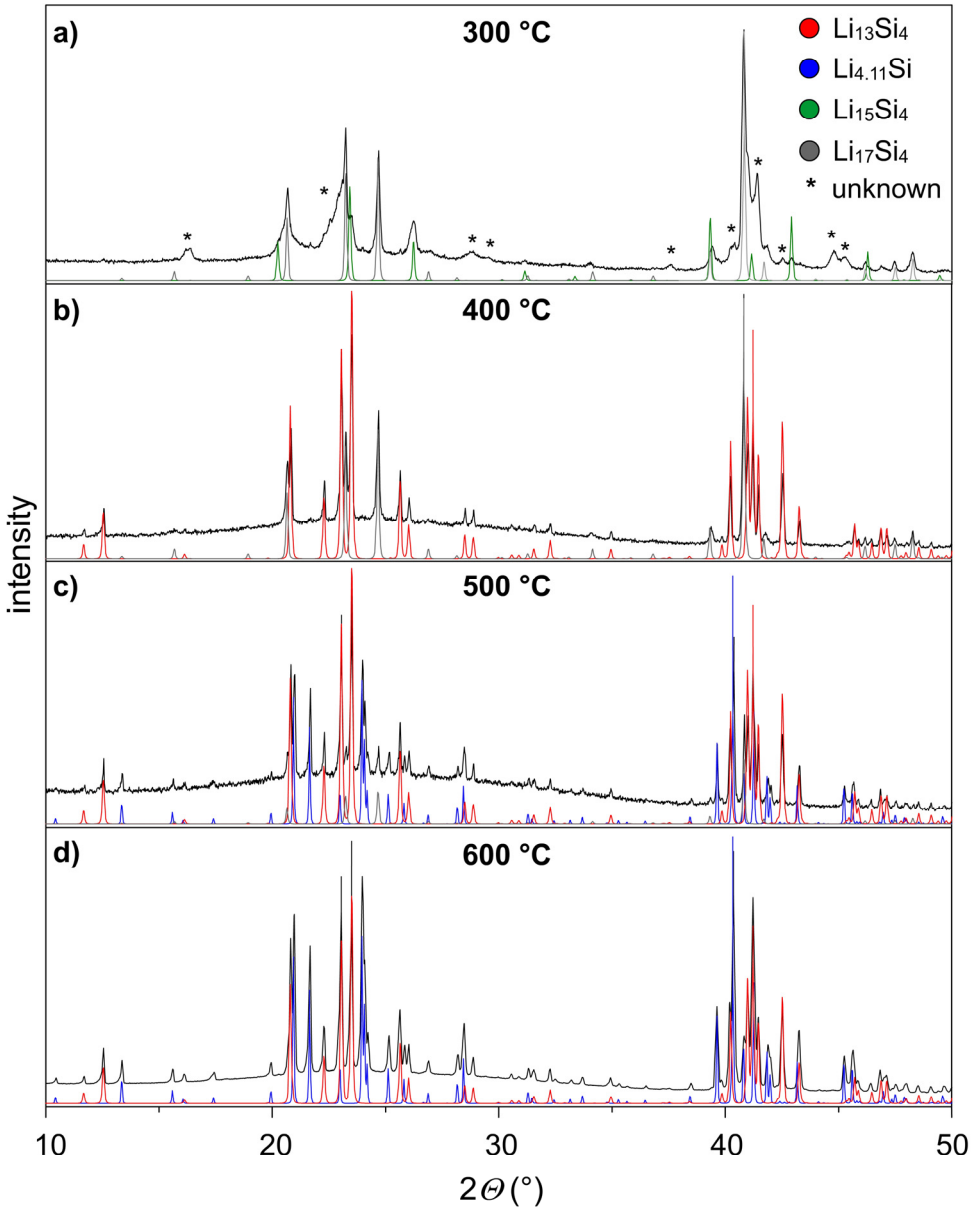

Figure 3.6. Evolution of the thermal decomposition of $Li_{15}Si_4$: powder X-ray diffraction patterns of bulk samples after annealing at 300 °C (a), 400 °C (b), 500 °C (c) and 600 °C (d) for three days (exp. = black; $Li_{13}Si_4$ calc. = red; $Li_{15}Si_4$ calc. = green; $Li_{4.11}Si$ calc. = blue; $Li_{17}Si_4$ calc. = gray; unknown reflections are marked with *). Figure and figure caption were adopted from ref. 67.

Of considerable importance for the phase diagram redetermination and the assignment of phases in powder X-ray diffraction patterns was the identification and unambiguous structural characterization of all relevant phases by single crystal X-ray diffraction. In the following, the structure determination and description of the newly established phases $Li_{17}Si_4$,[64] $Li_{4.11}Si$ ($Li_{16.42}Si_4$)[66] as well as the first single crystal X-ray diffraction study of $Li_{15}Si_4$[67] and the structure revision of $Li_{13}Si_4$[68] are addressed.

a) $Li_{17}Si_4$

The structure of the lithium-richest representative of the Li–Si phase diagram $Li_{17}Si_4$ was solved and refined with excellent reliability factors of R_1 = 0.028 and wR_2 = 0.037 for all data (θ-range = 1.89–47.62°). $Li_{17}Si_4$ crystallizes in the cubic space group $F\bar{4}3m$ with a = 18.6563(2) Å (Z = 20, T = −150 °C). The asymmetric unit contains four Si and 13 Li positions. All atoms are located on special positions which are fully occupied. Accordingly, the unit cell of $Li_{17}Si_4$ contains 80 Si and 340 Li atoms in total (*cF*420). $Li_{17}Si_4$ is isotypic with $Li_{17}Sn_4$.[72] The previously reported phase $Li_{21}Si_5$[18] (revised from $Li_{22}Si_5$[12,17]) is closely related to $Li_{17}Si_4$ and only differs in the occupation of one fourfold special position. In detail, the space group $F\bar{4}3m$ possesses four fourfold special positions 4*a*–*d* which are all unoccupied in $Li_{21}Si_5$ corresponding to 80 Si and 336 Li atoms per unit cell. In case of $Li_{17}Si_4$, the 4*a* site is fully occupied by Li which translates to 340 Li atoms in the unit cell.

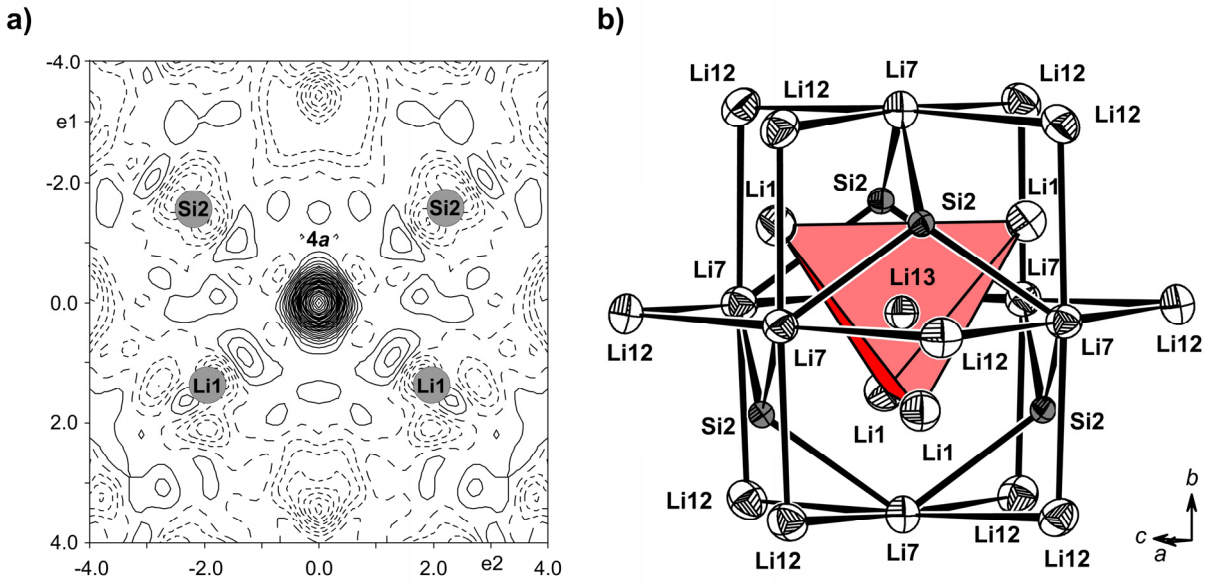

Figure 3.7. a) Difference Fourier map (F_o–F_c, contour lines ±0.075 e·Å^{-3}) for the plane defined by two Si2 and two Li1 atoms containing the site 4*a* and b) the coordination environment of Li13 on 4*a* in $Li_{17}Si_4$ (Si = gray; Li = white; thermal ellipsoids at a 90% probability level; single crystal data at −150 °C). Figures were adopted from ref. 64.

In order to demonstrate the fully occupied 4*a* site, the respective Li atom (Li13) was removed from the final refinement and a difference Fourier map F_o–F_c based on the newly refined data was generated (Figure 3.7a). Evidence for a phase with the composition $Li_{22}Si_5$, corresponding to a full occupancy of all fourfold positions 4*a*–*d*,[12,17] could not be found. The coordination environment of Li13 located on the 4*a* site is illustrated in Figure 3.7b. It centers a $(Li1)_4$ tetrahedron resulting in short but reasonable Li–Li distances. Further coordination shells are generated by a $(Si2)_4$ tetrahedron, a $(Li7)_6$ octahedron, and a $(Li12)_{12}$ cuboctahedron. Such 26 atom clusters M_{26} (*M* = Li + Si) are also centered at void sites 4*b*–*d*. Emphasizing the corresponding Si polyhedra, i.e. $(Si1)_4$ at 4*c*, $(Si2)_4$ at 4*a*, $(Si3)_6$ at 4*b*, and $(Si4)_6$ at 4*d*, the crystal structure of $Li_{17}Si_4$ can be considered as two interpenetrating ZnS-type lattices as described in Figure 3.8 (for more details see ref. 64).

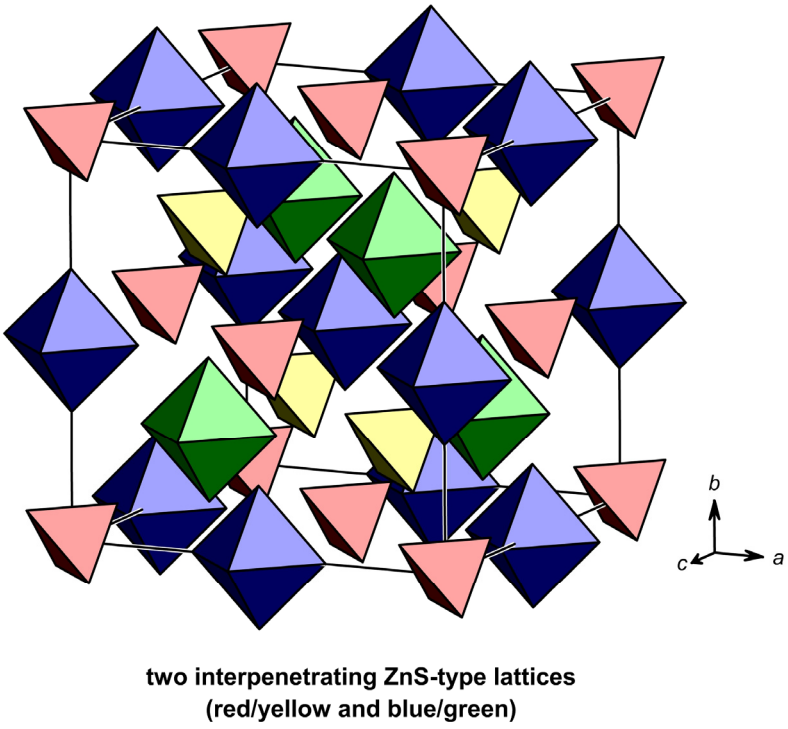

Figure 3.8. Crystal structure of $Li_{17}Si_4$: arrangement of Si polyhedra (no Si–Si bonds) which are part of crystallographically independent M_{26} (*M* = Li + Si) atom clusters around the sites 4*a*–*d* in the unit cell of $Li_{17}Si_4$.The figure was modified on the basis of ref. 64.

In order to further analyze the differences between $Li_{21}Si_5$ and $Li_{17}Si_4$, their structures were computationally relaxed and their equilibrium volume structure parameters determined. Whereas the experimentally established structure of $Li_{17}Si_4$ was reproduced, the relaxed structure of $Li_{21}Si_5$ reveals discrepancies to the experimental one regarding the coordination of position 4*a*. Furthermore, based on the calculated reaction energy (referring to zero Kelvin) for $Li_{84}Si_{20}$ + Li (bcc) = $Li_{85}Si_{20}$, Li uptake in $Li_{21}Si_5$ yielding $Li_{17}Si_4$ is slightly exothermic

(–0.04 eV). Thus, computational and experimental results cast doubts on the existence of $Li_{21}Si_5$ and firmly established $Li_{17}Si_4$ as lithium-richest representative in the Li–Si system. However, the existence of a small homogeneity range $Li_{17-x}Si_4$ ($0 < x < 0.2$) could not be ruled out by single crystal X-ray diffraction studies or DSC investigations.

b) $Li_{15}Si_4$

Melt equilibration experiments targeting the single crystal growth of $Li_{17}Si_4$ also yielded few needle-shaped crystals of metastable $Li_{15}Si_4$ as a side product (Figure 3.9a). This is a surprising result since samples of $Li_{15}Si_4$ are commonly obtained from either ball-milling the pure elements[1,35,36] (Figure 3.9b,c) or alloying Si with Li electrochemically.[34,73] Thus far, its crystal structure has been determined from powder data applying a Rietveld fit of the $Cu_{15}Si_4$ structure model (see also Figure 3.9b).[34,73] As part of this work, the structure of $Li_{15}Si_4$ could be readily solved and refined from single crystal X-ray diffraction data. $Li_{15}Si_4$ crystallizes in the cubic space group $I\bar{4}3d$ with a = 10.6322(9) Å (V = 1201.9(2) Å^3, Z = 4, T = –150 °C). The asymmetric unit contains Si on 16*c* (x, x, x), Li1 on 48*e* (x, y, z), and Li2 on 12*b* (½, ¼, ⅛), corresponding to an overall unit cell content of 16 Si and 60 Li atoms (*cI*76). Accordingly, the validity of the previously assigned $Cu_{15}Si_4$ structure model was confirmed resolutely.

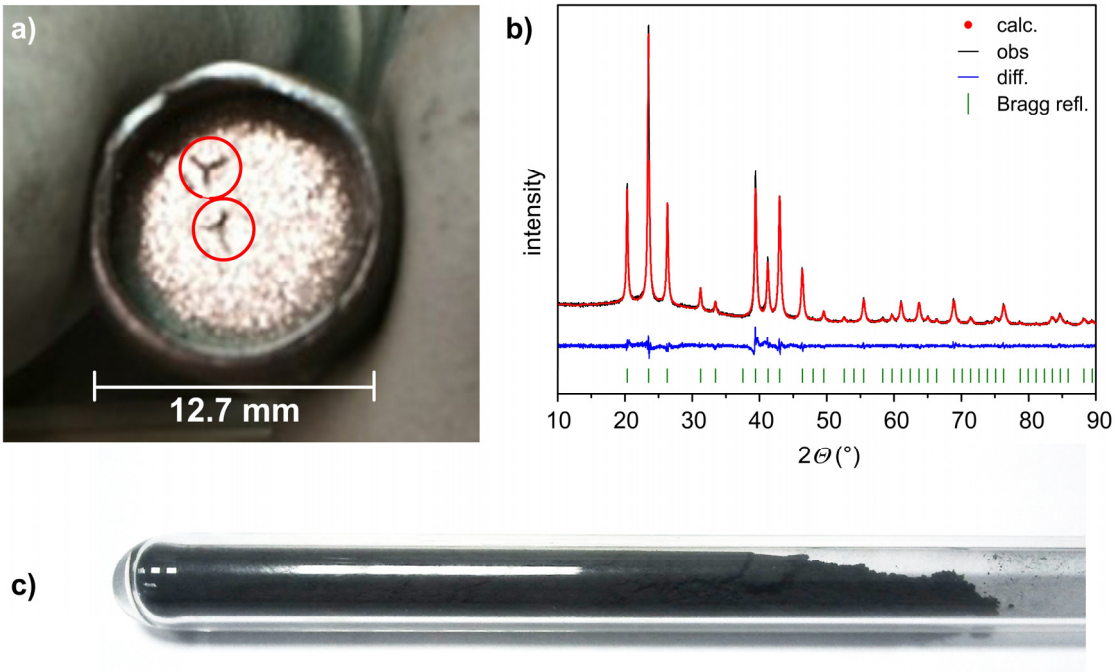

Figure 3.9. a) Needle-shaped crystals of $Li_{15}Si_4$ (encircled) grown at the bottom lid of a stainless steel ampule, b) Rietveld fit of the $Cu_{15}Si_4$ structure model to the powder X-ray diffraction pattern of a $Li_{15}Si_4$ bulk sample ($I\bar{4}3d$, a = 10.7163(1) Å, V = 1230.66(5) Å^3), c) photograph of $Li_{15}Si_4$ bulk sample obtained from ball-milling (sealed inside a glass ampule). Figures were adopted from ref. 67.

Regarding the structure of $Li_{15}Si_4$, the central motif is the quasi-anticuboctahedral coordination of Si atoms (Figure 3.10a,b). [Si@Li_{12}] pseudo-anticuboctahedra are condensed into strands by sharing opposite triangular faces $(Li1)_3$. These strands proceed along the threefold axes of the cubic unit cell as indicated by different colors in Figure 3.10a. Note that the blue strand is exactly located on the body diagonal. Each [Si@Li_{12}] pseudo-anticuboctahedron is coordinated by eleven further units sharing common faces and edges (Figure 3.10c). A more detailed analysis of the complex coordination environment of [Si@Li_{12}] units is illustrated in Figure 3.10d.

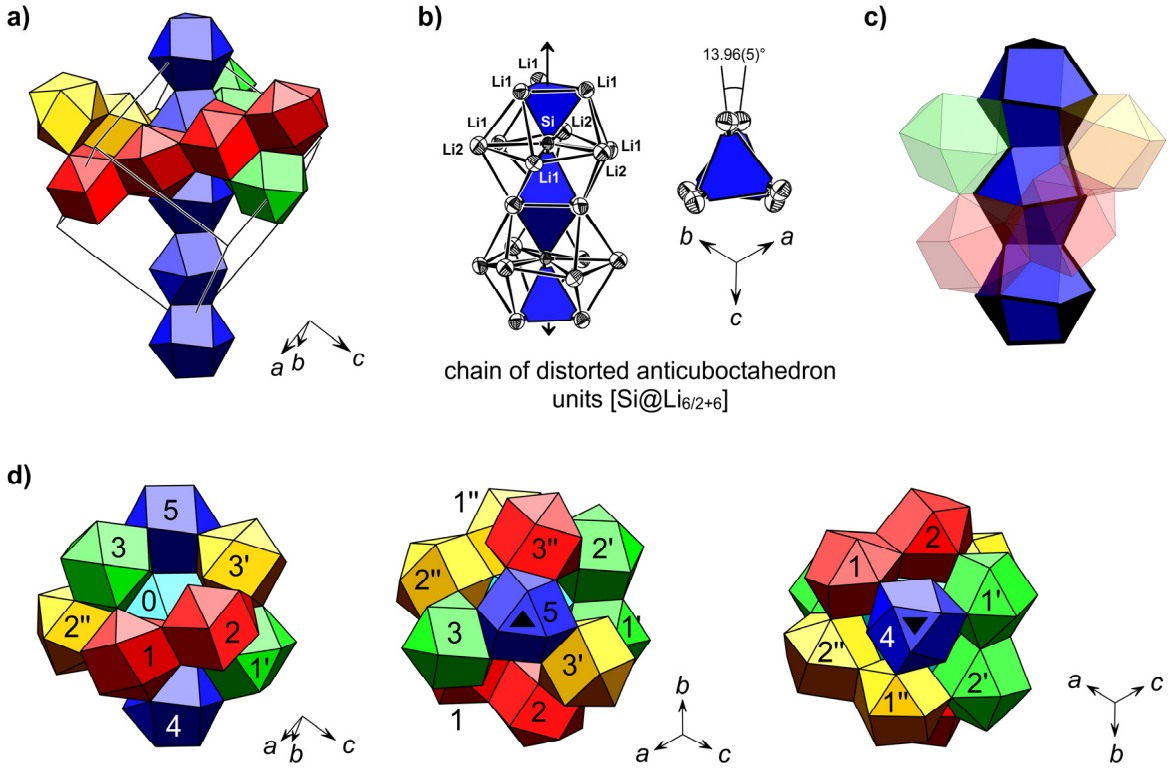

Figure 3.10. Structural motifs of $Li_{15}Si_4$ and $Li_{15-x}Al_xSi_4$ ($Cu_{15}Si_4$-type): a) strands of condensed [Si@Li_{12}] units proceeding in different directions of the unit cell as indicated by different colors, b) stacking of pseudo-anticuboctahedron units [Si@Li_{12}] emphasizing the skeleton formed by trigonal bipyramids, c) the connectivity of distorted anticuboctahedron units (shared faces/edges are marked in black), and d) the coordination of a pseudo-anticuboctahedron (light blue) by eleven neighboring [Si@Li_{12}] units (the position of the three-fold axis is indicated by its symbol). The figure was modified on the basis of ref. 67.

c) $Li_{4.11}Si$ ($Li_{16.42}Si_4$)

Millimeter-sized crystals of the high-temperature phase $Li_{16.42(1)}Si_4$ were obtained from a melt "$Li_{85}Si_{15}$" equilibrated at 510 °C in a Ta ampule. $Li_{4.106(2)}Si$ (referring to Z = 16) crystallizes in the orthorhombic space group *Cmcm* with a = 4.5246(2) Å, b = 21.944(1) Å, c = 13.2001(6) Å (V = 1310.6(1) Å^3). For a better comparability to $Li_{17}Si_4$, $Li_{15}Si_4$, and $Li_{13}Si_4$, $Li_{4.106(2)}Si$/$Li_{16.42(1)}Si_4$

is referred to as $Li_{16.42}Si_4$. Its structure was solved and refined with excellent reliability factors of R_1 = 0.017 and wR_2 = 0.029 for all data (θ-range = 1.86–45.29°). The unit cell contains three Si and 10 Li positions. All Si and eight Li sites are fully occupied, two Li positions are affected by occupational disorder. In detail, the sum of occupancies factors for Li4A on 4*c* (½, *y*, ¼) and Li4B on 8*g* (*x*, *y*, ¼) are constrained to one (0.575(3) and 0.425(3), respectively) to prohibit unreasonably short Li–Li distances (Figure 3.11). The corresponding disordered Li strand proceeding along the crystallographic *a*-axis is unique amongst Li–Si phases. The difference Fourier map (F_o–F_c) in Figure 3.11a emphasizes its strand-like shape. Additionally, a split position was introduced for Li5 [occupancy ratio 0.848(7)/0.152(7)]. The geometric situation around the disordered Li strand and an idealized structure model are illustrated in Figures 3.11b and c. Note that a simultaneous occupation of Li4B and Li5B is excluded as this would give rise to unreasonably short Li–Li distances.

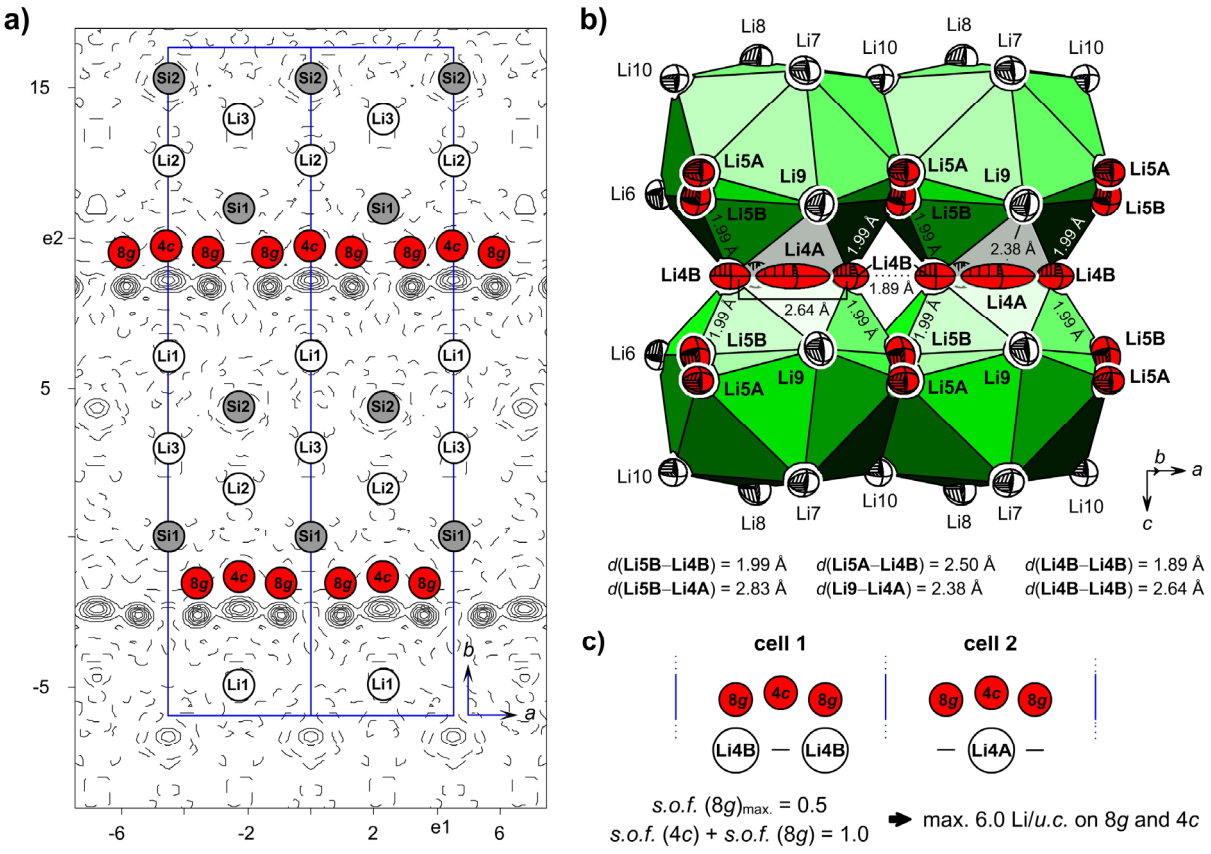

Figure 3.11. a) Difference Fourier map (F_o–F_c, contour lines ±0.6 e·Å^{-3}) shown for the *ab*-plane containing Si1, Si2, and Li1–3 (cell edges are shown in blue; calculated from single crystal data at –173 °C), b) the disordered Li-strand with view onto the *ac*-plane emphasizing its structural environment (perpendicular to the *ab*-plane of the difference Fourier map in Figure 3.11a) and c) schematic description of an idealized disorder model for Li4; thermal ellipsoids are shown at a 90% probability level. The figure was adopted from ref. 66.

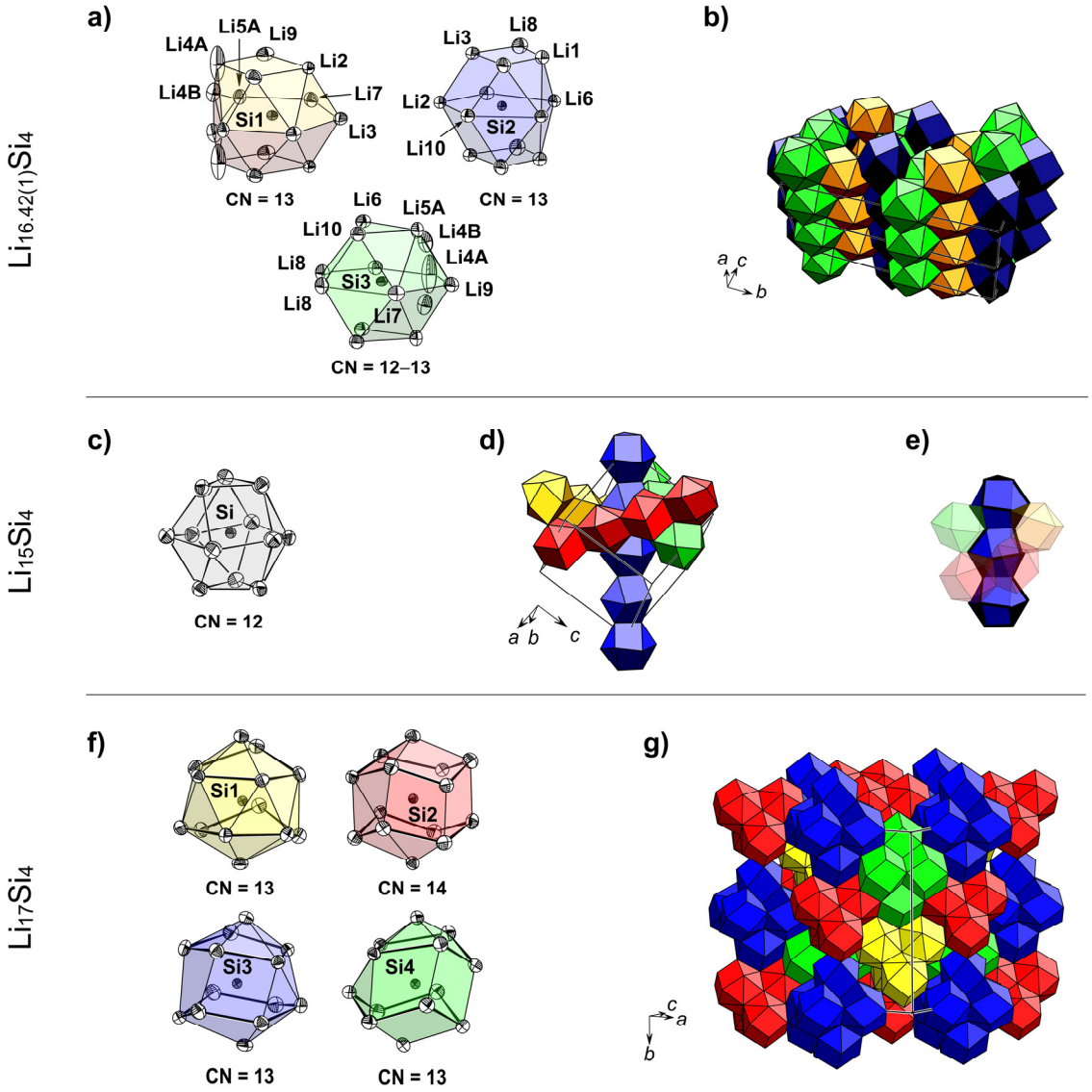

Figure 3.12. $SiLi_n$ coordination polyhedra and their arrangement in the unit cell of $Li_{16.42}Si_4$ (a, b), $Li_{15}Si_4$ (c–e), and $Li_{17}Si_4$ (f, g). In the structure of $Li_{16.42}Si_4$, $SiLi_n$ polyhedra (a) of the same kind are condensed into strands which share common faces, edges and vertices with parallel ones (b); pseudo-anticub-octahedron units $[Si@Li_{12}]$ in $Li_{15}Si_4$ (c) are condensed to strands and proceed along the 3-fold axes of the cubic unit cell (d; different directions are indicated by different colors); the relative arrangement of $[Si@Li_{12}]$ units is depicted in (e) (shared edges and faces in black); in case of $Li_{17}Si_4$, $SiLi_n$ coordination polyhedra (f) form supratetrahedra (yellow, red) and supraoctahedra (blue, green) as shown in (g); all thermal ellipsoids are shown at a 90% probability level. The figure was modified on the basis of ref. 66.

The complex structure of $Li_{16.42}Si_4$ may be visualized by $SiLi_n$ polyhedra since, similar to $Li_{17}Si_4$ and $Li_{15}Si_4$, all Si atoms are isolated. The $SiLi_n$ coordination polyhedra for Si1–3 are depicted in Figure 3.12a. Whereas Si1 and Si2 are permanently 13-coordinated, due to the disorder Si3 may attain a coordination of either 12 or 13 depending on whether the Li4A or Li4B position is occupied. $SiLi_n$ polyhedra of the same kind are condensed into strands by

sharing opposite faces as shown in Figure 3.12b. As mentioned before, the structures of the neighboring phases $Li_{15}Si_4$ and $Li_{17}Si_4$ comprise isolated Si atoms as well. Hence, their structures may also be represented utilizing $SiLi_n$ coordination polyhedra (Figure 3.11c–g). Remarkably, the series $Li_{15}Si_4$ (CN = 12), $Li_{16.42}Si_4$ (CN = 12–13), and $Li_{17}Si_4$ (CN = 13 and 14) demonstrates the enlargement of $SiLi_n$ coordination polyhedra with increasing Li content.

In addition, the density of states and band structures for $Li_{17}Si_4$, $Li_{16.42}Si_4$ and $Li_{15}Si_4$ were calculated. For that purpose, the disorder in $Li_{16.42}Si_4$ was resolved by constructing two structure models with compositions $Li_{16}Si_4$ (hypothetical Zintl phase, 16 Li^+, 4 Si^{4-}) and $Li_{16.5}Si_4$ (for details see Chapter 5.2). As a result, the density of states and band structures of $Li_{17}Si_4$, $Li_{16.5}Si_4$, $Li_{16}Si_4$, and $Li_{15}Si_4$ revealed a metallic character. In case of $Li_{15}Si_4$, a pseudo-gap is located above the Fermi level (see also Chapter 3.1.3).

d) $Li_{13}Si_4$

In the course of the reinvestigation of the Li–Si phase diagram[64,66] the crystal structure of $Li_{13}Si_4$ was redetermined by single crystal X-ray diffraction since experimental and calculated (on the basis of available structural data)[19,62] powder X-ray diffraction patterns of $Li_{13}Si_4$ did not match. Compared to the first single crystal structure determination,[19] the improvements of the new model are i) the introduction of a split position for one Li site, ii) the anisotropic refinement of atomic displacement parameters for all atoms, and iii) a significantly more precise determination of atom positions and thus unit cell parameters. As a result, experimental and calculated Bragg reflection positions and intensities of $Li_{13}Si_4$ match very well, allowing

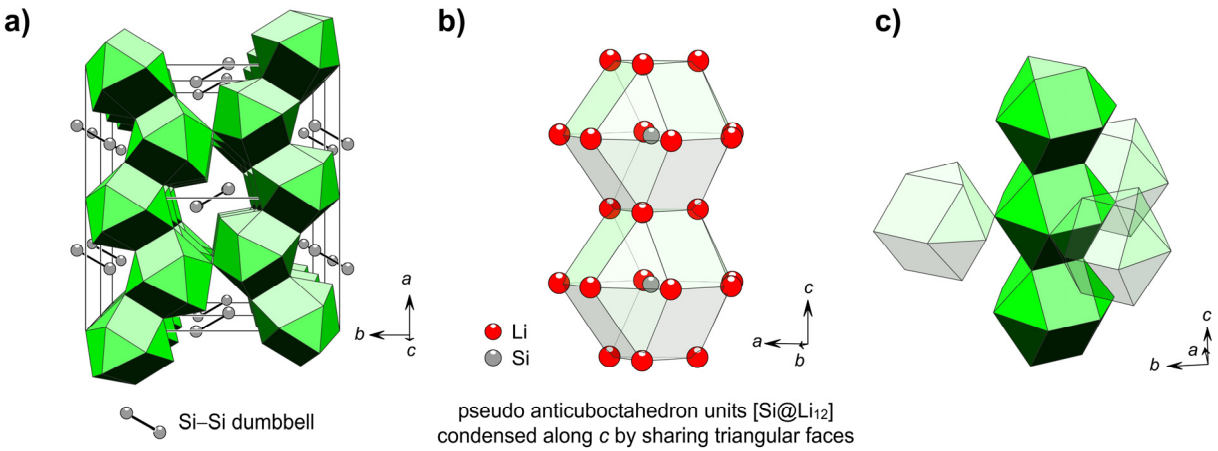

Figure 3.13. a) 2×1×2 super cell of orthorhombic $Li_{13}Si_4$ emphasizing the parallel stacking of Si–Si dumbbells which are embedded in channels formed by b) parallel strands of condensed pseudo-anticuboctahedron units [Si@Li_{12}] proceeding along the crystallographic *c*-axis. These parallel strands are connected by sharing common vertices and edges of neighboring ones (c).

an accurate assignment of phases in powder X-ray diffraction patterns of $Li_{13}Si_4$-containing samples. Regarding the structure of $Li_{13}Si_4$, it consists of isolated Si atoms coordinated by 12 Li atoms in a pseudo-anticuboctahedral fashion (Figure 3.13b). These [Si@Li_{12}] units are condensed along the *c*-direction of the unit cell forming parallel mutually connected strands which enclose Si-Si dumbbells in the resulting channel-like voids (Figure 3.13a,c).

3.1.3 Thermodynamic Stability of $Li_{14.37}Al_{0.63}Si_4$ — an Al-doped Variant of $Li_{15}Si_4$

see Chapter 5.4

Zeilinger, M.; Baran, V.; Häussermann, U.; Fässler, T. F. *Chem. Mater.* **2013**, *25*, 4113.

As mentioned in Chapter 3.1.2, the band structure of $Li_{15}Si_4$ reveals a pseudo-gap situated above the Fermi level (Figure 3.14a). Accordingly, an increase of the electron concentration could shift the Fermi level to the pseudo-gap in the electronic density of states. Thus, regarding $Li_{15}Si_4$ as an electron deficient Zintl phase (15 Li^+, 4 Si^{4-}), Al-doping corresponding to $Li_{15-x}Al_xSi_4$ could result in the formation of the Zintl phase $Li_{14.5}Al_{0.5}Si_4$ (x = 0.5; 14.5 Li^+, 0.5 Al^{3+}, 4 Si^{4-}). Since melt equilibration experiments are an expedient method for growing large single crystals of lithium-rich phases, $Li_{83}Al_{13}Si_4$ melts were equilibrated at 450 °C. These experiments almost exclusively yielded large single crystals of $Li_{14.37(1)}Al_{0.63(1)}Si_4$, an Al-doped variant of $Li_{15}Si_4$ (Figure 3.14b). In contrast, Li_xSi_{100-x} (x > 85) melts afforded crystals of $Li_{17}Si_4$ as the main product and only few needle-shaped crystals of $Li_{15}Si_4$.

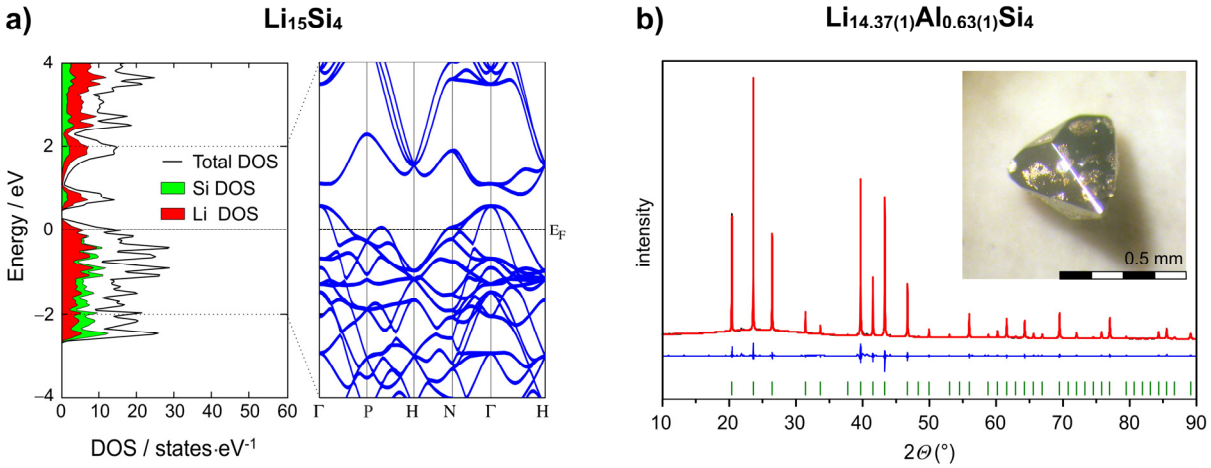

Figure 3.14. a) Total and partial DOS together with the band structure representation for $Li_{15}Si_4$ and b) Rietveld fit of the $Cu_{15}Si_4$ structure model to the powder X-ray diffraction pattern of ground single crystals of $Li_{14.37(1)}Al_{0.63(1)}Si_4$ ($I\bar{4}3d$, a = 10.66095(3) Å, V = 1211.68(1) Å^3). Figures were modified on the basis of ref. 66 and 67.

The powder X-ray diffraction pattern of ground single crystals of $Li_{14.37(1)}Al_{0.63(1)}Si_4$ was fitted well using the $Cu_{15}Si_4$ structure model (Figure 3.14b). Comparing the unit cell parameters of $Li_{15}Si_4$ and $Li_{14.37(1)}Al_{0.63(1)}Si_4$ determined from powder X-ray diffraction data (Rietveld refinements), the unit cell of $Li_{14.37(1)}Al_{0.63(1)}Si_4$ is slightly contracted (a = 10.7163(1) Å vs. a = 10.66095(3) Å). According to single crystal X-ray diffraction experiments, the two crystallographically independent Li positions in the structure of $Li_{15}Si_4$ are partially substituted by Al (3.95(7)% and 5.31(9)%). The incorporation of Al was further validated by ^{27}Al-MAS-NMR spectroscopy and supported by results from X-ray diffraction experiments and EDX investigations. The homogeneity range of $Li_{15-x}Al_xSi_4$ could be assessed as $x_{min.} \approx 0.4$ and $x_{max.} \approx 0.8$. Remarkably, the Zintl phase $Li_{14.5}Al_{0.5}Si_4$ exactly falls in this range and samples corresponding to $Li_{15-x}Al_xSi_4$ ($0.4 < x < 0.8$) feature diamagnetic behavior which is expected for Zintl phases.

Surprisingly, thermal investigations (DSC) of $Li_{15-x}Al_xSi_4$ ($0.4 < x < 0.8$) revealed thermodynamic stability of up to 700 °C whereas metastable $Li_{15}Si_4$ already decomposes in an exothermal irreversible process at around 170 °C.

3.1.4 Revision of the Li–Ge Phase Diagram: Thermodynamic Relation of $Li_{17}Ge_4$, $Li_{16.38}Ge_4$, and $Li_{15}Ge_4$

see Chapter 5.5

Zeilinger, M.; Fässler, T. F. *Dalton Trans.* **2014**, DOI:10.1039/C4DT00743C.

The lithium-rich section of the Li–Si phase diagram (> 76 at.% Li) was comprehensively and unambiguously characterized and a slight modification of $Li_{15}Si_4$ by Al doping led to thermodynamically stable phases $Li_{15-x}Al_xSi_4$ ($0.4 < x < 0.8$). Extending the phase diagram work to the Li–Ge system, $Li_{17}Ge_4$[65] (space group $F\bar{4}3m$) and $Li_{16.38}Ge_4$[65] (space group *Cmcm*) were identified as new phases which are isotypic with their Si counterparts $Li_{17}Si_4$ and $Li_{16.42}Si_4$. As demonstrated in the difference Fourier map in Figure 3.15, the disordered Li-strands apparent in $Li_{16.42(1)}Si_4$ and $Li_{16.38(2)}Ge_4$ are very similar. Within standard deviations (3σ), the occupancy ratios of the respective Wyckoff positions 4*c* and 8*g* are identical. $Li_{17}Ge_4$ replaces the closely related disordered $Li_{16.95}Ge_4$[40] as lithium-richest phase of the Li–Ge system. The latter can be regarded as a representative of a small homogeneity range $Li_{17-x}Ge_4$ ($0 < x < 0.2$) where x = 0.05. This may be enabled by the structural flexibility of the M_{26}-cluster unit (M = Li + Ge) around the 4*a* site as already proposed for $Li_{17-x}Si_4$ ($0 < x < 0.2$).[64]

Since the structure descriptions of $Li_{16.38}Ge_4$ and $Li_{17}Ge_4$ exactly follows those given for their isotypic silicides it is referred to Chapters 3.1.2 and 5.5.[66] Regarding the determination of the Li–Ge phase diagram for Li concentrations > 79 at.% Li, the same methodology was

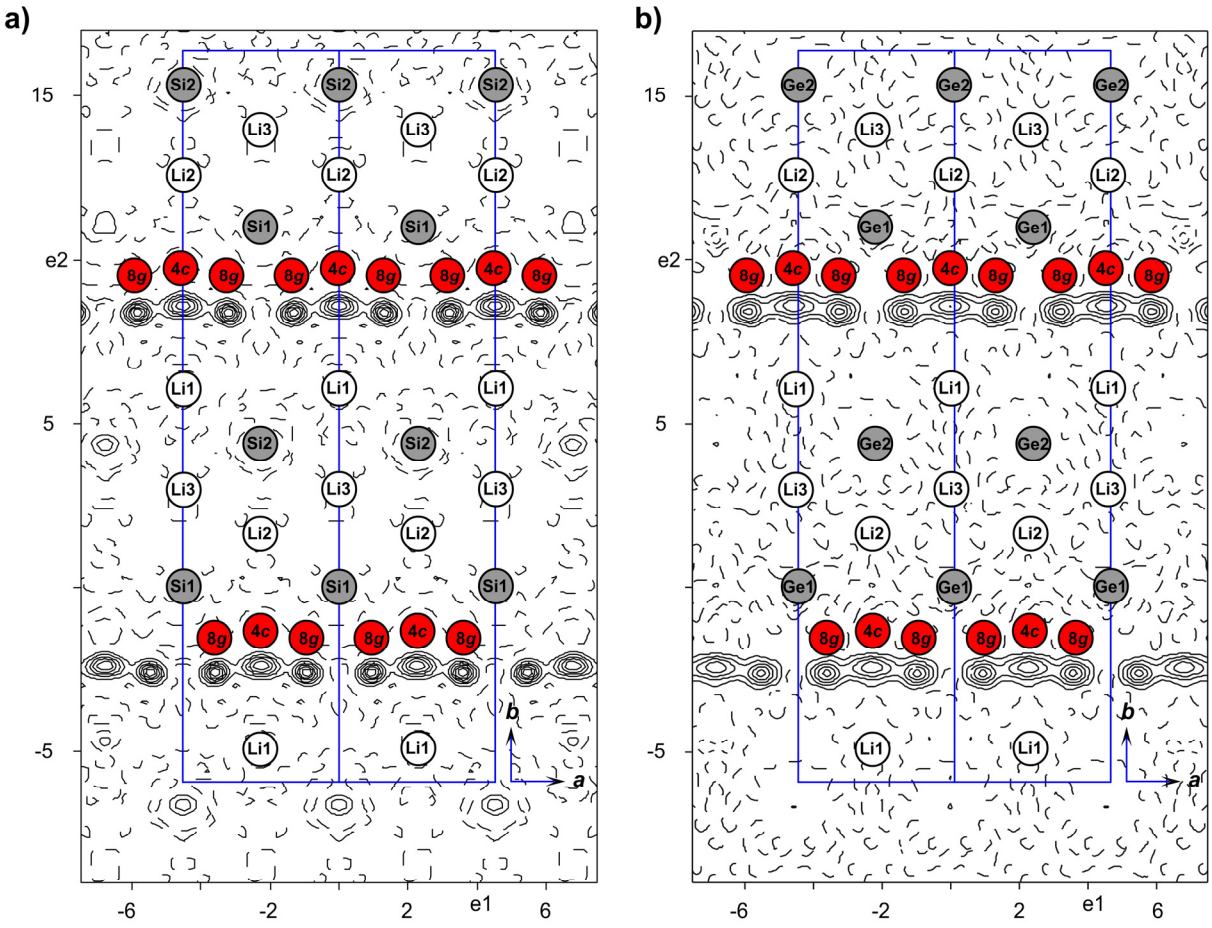

Figure 3.15. Difference Fourier map (F_o–F_c) shown for the layer defined by *Tt*1, *Tt*2 and Li2 in a) $Li_{16.42}Si_4$ and b) $Li_{16.38}Ge_4$ (parallel to *ab*-plane, calculated from single crystal data at −173 °C and −150 °C for $Li_{16.42}Si_4$ (contour lines ±0.6 e·Å^{-3}) and $Li_{16.38}Ge_4$ (contour lines ±0.5 e·Å^{-3}), respectively; cell edges are shown in blue). Figure and figure caption were adopted from ref. 65.

used as successfully applied for the Li–Si system.[64,66] Previously unrecognized work by Grüttner[25] was also considered for these investigations (Figure 3.16a). As a result, the Li–Ge phase diagram was revised according to Figure 3.16b. Thermal effects that were observed in the thermograms of $Li_{17}Ge_4$ and samples with nominal compositions "$Li_{16.5}Ge_4$" and "$Li_{16}Ge_4$" were assigned therein. Starting from different Li–Ge melts, effects (1–3) correspond to crossing the liquidus boundary and effects (4) and (5) are attributed to the peritectic decomposition of $Li_{17}Ge_4$ (into melt and $Li_{16.38}Ge_4$) and $Li_{16.38}Ge_4$ (into melt and $Li_{15}Ge_4$), respectively. The very sluggish peritectoid decomposition of $Li_{16.38}Ge_4$ into $Li_{17}Ge_4$ and $Li_{15}Ge_4$ at around 400 °C could be elucidated by long-term annealing experiments of "$Li_{16}Ge_4$" samples. A concluding comparison of the Li–Ge phase diagram with the Li–Si system (Figure 3.16c) reveals resemblance regarding the thermodynamic stability of $Li_{17}Tt_4$ and $Li_{16.4}Tt_4$. In contrast to $Li_{15}Ge_4$, which is a thermodynamically stable phase melting congruently at 720 °C,[25] isotypic $Li_{15}Si_4$ is metastable and therefore missing in the Li–Si phase diagram compilation.

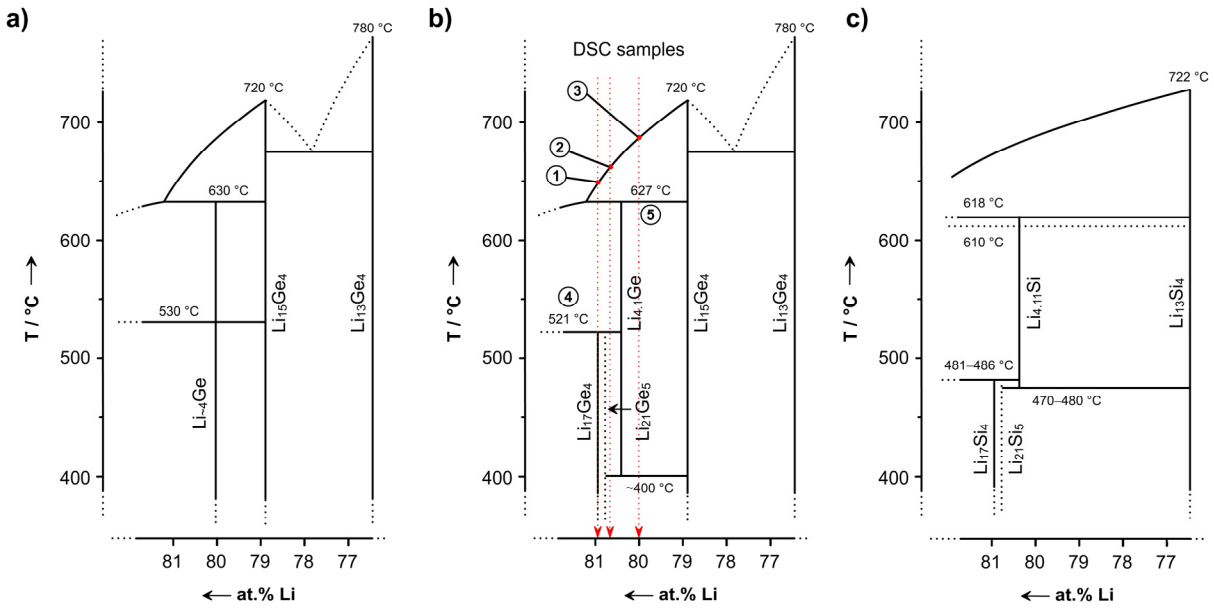

Figure 3.16. a) Excerpt of the Li–Ge phase diagram as reported by Grüttner[25] (the composition of the eutectic between $Li_{15}Ge_4$ and $Li_{13}Ge_4$ was not determined), b) its revision based on DSC investigations and annealing experiments of "$Li_{16}Ge_4$" samples reported herein, and c) the most recent Li–Si phase diagram for Li concentrations > 76%.[66] Figure and figure caption were adopted from ref. 65.

3.1.5 Solid Solutions $Li_{17}Si_{4-x}Ge_x$ [x = 2.30(2), 3.08(4), 3.53(3)]

see Chapter 5.5

Zeilinger, M.; Fässler, T. F. *Dalton Trans.* **2014**, DOI:10.1039/C4DT00743C.

As reported in the previous Chapter, the isotypic phases $Li_{17}Si_4$ and $Li_{17}Ge_4$ were manifested as the lithium-richest candidates of the Li–Si and Li–Ge system. According to Vegard's law,[74] they should form solid solutions corresponding to $Li_{17}Si_{4-x}Ge_x$ ($0 < x < 4$). Employing melt equilibration experiments, crystals of $Li_{17}Si_{4-x}Ge_x$ [x = 2.30(2), 3.08(4), 3.53(3)][65] were grown and subsequently characterized by single crystal and powder X-ray diffraction. Compositions obtained from single crystal X-ray diffraction studies were supported by EDX investigations. As demonstrated in Figure 3.17a, cell volumes of respective solid solutions linearly increase with increasing concentrations of Ge in $Li_{17}Si_{4-x}Ge_x$ as expected from Vegard's law.[74]

Evaluating the distribution of Si and Ge among the four crystallographically different tetrel positions *Tt*1–4 (*Tt* = Si, Ge) in $Li_{17}Si_{4-x}Ge_x$, the general trend can be observed that *Tt*2 is slightly preferred by Si (Figure 3.17b). Such a preferential site occupation is also known as the "coloring problem" and in some cases this phenomenon cannot be explained by simple chemical reasoning.[75] For $Li_{17}Si_{4-x}Ge_x$, albeit differences are quite small, future quantum

chemical calculations might elucidate the reasons for the different distribution of Si and Ge among the four crystallographically independent atom positions *Tt*1–4.

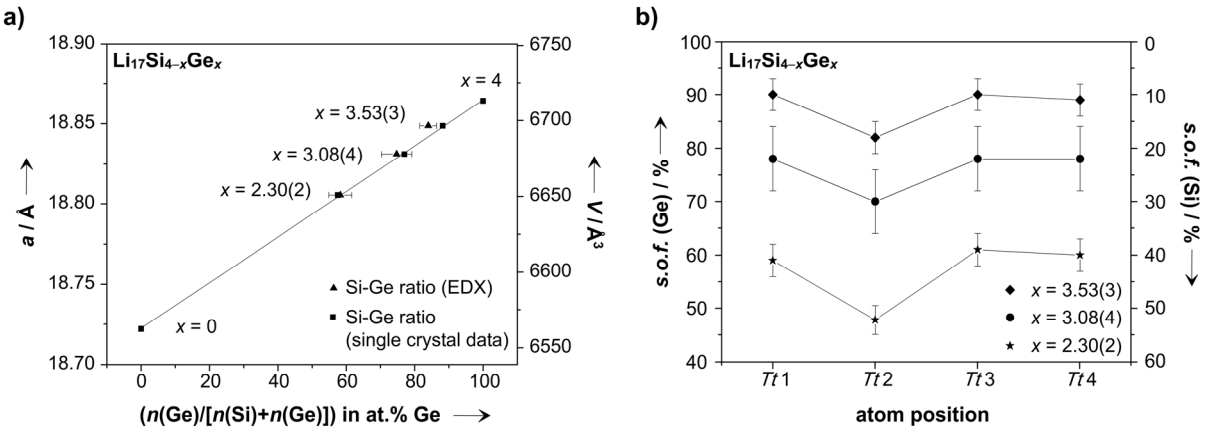

Figure 3.17. a) Trend of cell volumes *vs.* Ge contents in $Li_{17}Si_{4-x}Ge_x$ (x = 0, 2.30(2), 3.08(4), 3.53(3), 4); cell parameters were determined from powder X-ray diffraction patterns recorded for ground single crystals (Rietveld refinements), Ge contents were obtained from single crystal X-ray diffraction data (error bars are smaller than data point icons) and EDX. b) Distribution of Si and Ge among the four crystallographically different tetrel positions *Tt*1–4 (*Tt* = Si, Ge) in $Li_{17}Si_{4-x}Ge_x$ according to single crystal X-ray diffraction data (error bars = $\pm 3\sigma$). Figure 3.17a was adopted from ref. 65.

3.1.6 References

(1) Key, B.; Bhattacharyya, R.; Morcrette, M.; Seznec, V.; Tarascon, J. M.; Grey, C. P. *J. Am. Chem. Soc.* **2009**, *131*, 9239.

(2) Key, B.; Morcrette, M.; Tarascon, J. M.; Grey, C. P. *J. Am. Chem. Soc.* **2011**, *133*, 503.

(3) Kuhn, A.; Sreeraj, P.; Pöttgen, R.; Wiemhöfer, H. D.; Wilkening, M.; Heitjans, P. *J. Am. Chem. Soc.* **2011**, *133*, 11018.

(4) Dupke, S.; Langer, T.; Pöttgen, R.; Winter, M.; Passerini, S.; Eckert, H. *Phys. Chem. Chem. Phys.* **2012**, *14*, 6496.

(5) Dupke, S.; Langer, T.; Pöttgen, R.; Winter, M.; Eckert, H. *Solid State Nucl. Magn. Reson.* **2012**, *42*, 17.

(6) Moissan, H. *C. R. Hebd. Séances Acad. Sci.* **1902**, *134*, 1083.

(7) Klemm, W.; Struck, M. *Z. Anorg. Allg. Chem.* **1955**, *278*, 117.

(8) Pell, E. M. *Phys. Chem. Solids* **1957**, *3*, 77.

(9) Böhm, H. *Z. Metallkd.* **1959**, *50*, 44.

(10) Obinata, I.; Takeuchi, Y.; Kurihara, K.; Watanabe, M. *J. Jpn. Inst. Met.* **1964**, *28*, 568.

(11) Federov, P. I.; Ioffe, A. A. *Izv. Vyssh. Uchebn. Zaved., Tsvetn. Metall.* **1962**, *1*, 127.

(12) Axel, H.; Schäfer, H.; Weiss, A. *Z. Naturforsch. B* **1966**, *21*, 115.

(13) Schäfer, H.; Axel, H.; Weiss, A. *Z. Naturforsch. B* **1965**, *20*, 1302.

(14) Schäfer, H.; Axel, H.; Weiss, A. *Z. Naturforsch. B* **1965**, *20*, 1010.

(15) Schäfer, H.; Axel, H.; Menges, E.; Weiss, A. *Z. Naturforsch. B* **1965**, *20*, 394.

(16) Axel, H.; Schäfer, H.; Weiss, A. *Angew. Chem. Int. Ed.* **1965**, *4*, 358.

(17) Gladyshevskii, E. I.; Oleksiv, G. I.; Kripyakevich, P. I. *Kristallografiya* **1964**, *9*, 338.

(18) Nesper, R.; von Schnering, H. G. *J. Solid State Chem.* **1987**, *70*, 48.

(19) Frank, U.; Müller, W.; Schäfer, H. *Z. Naturforsch. B* **1975**, *30*, 10.

(20) von Schnering, H. G.; Nesper, R.; Curda, J.; Tebbe, K. F. *Angew. Chem.* **1980**, *92*, 1070.

(21) von Schnering, H. G.; Nesper, R.; Tebbe, K. F.; Curda, J. *Z. Metallkd.* **1980**, *71*, 357.

(22) Evers, J.; Oehlinger, G.; Sextl, G. *Angew. Chem. Int. Ed.* **1993**, *32*, 1442.

(23) Tang, W. S.; Chotard, J.-N.; Janotz, R. *J. Electrochem. Soc.* **2013**, *160*, A1232.

(24) Grüttner, A.; Nesper, R.; von Schnering, H. G. *Acta Cryst.* **1981**, *A37*, C161. The authors claimed that "$Li_{20}Si_5$ replaces $Li_{22}Si_5$" and that "four special positions of the "$Li_{22}Si_5$" structure are not occupied". These four special positions should be 4*a–d*. However, if these are unoccupied, the correct composition is $Li_{21}Si_5$. Thus, the formula $Li_{20}Si_5$ might be attributed to an erroneous calculation of the sum formula.

(25) Grüttner, A. *Dissertation*, Universität Stuttgart: Stuttgart, Germany, 1982.

(26) Demidov, A. I.; Morachevskii, A. G.; Nikolaev, V. P.; Berenda, N. V. *J. Appl. Chem. (USSR)* **1988**, *61*, 1254.

(27) Okamoto, H. *Bull. Alloy Phase Diagrams* **1990**, *11*, 306.

(28) Braga, M. H.; Malheiros, L. F.; Ansara, I. *J. Phase Equilib.* **1995**, *16*, 324.

(29) Okamoto, H. *J. Phase Equilib. Diff.* **2009**, *30*, 118.

(30) Sharma, R. A.; Seefurth, R. N. *J. Electrochem. Soc.* **1976**, *123*, 1763.

(31) Lai, S. C. *J. Electrochem. Soc.* **1976**, *123*, 1196.

(32) Nikolaev, V. P.; Morachevskii, A. G.; Demidov, A. I.; Bairachnyi, E. V. *J. Appl. Chem. (USSR)* **1980**, *53*, 1549.

(33) Sangster, J.; Pelton, A. D. *J. Phase Equilib.* **1997**, *18*, 289.

(34) Obrovac, M. N.; Christensen, L. *Electrochem. Solid-State Lett.* **2004**, *7*, A93.

(35) Tamori, R.; Machida, N.; Shigematsu, T. *J. Jpn. Soc. Powder Powder Metall.* **2001**, *48*, 267.

(36) Hashimoto, Y.; Machida, N.; Shigematsu, T. *Solid State Ionics* **2004**, *175*, 177.

(37) Pell, E. M. *J. Phys. Chem. Solids* **1957**, *3*, 74.

(38) Oleksiv, G. I. *Probl. Rozvitku Prirodn. i Tochn. Nauk, Sb.* **1964**, 76.

(39) Federov, P. I.; Molochka, V. A. *Izv. Akad. Nauk. SSSR, Neorg. Mater.* **1966**, *2*, 1870.

(40) Goward, G. R.; Taylor, N. J.; Souza, D. C. S.; Nazar, L. F. *J. Alloys Compd.* **2001**, *329*, 82.

(41) Nesper, R. *Prog. Solid State Chem.* **1990**, *20*, 1.

(42) Johnson, Q.; Smith, G. S.; Wood, D. *Acta Cryst.* **1965**, *18*, 131.

(43) Gladyshevskii, E. I.; Kripyakevich, P. I. *Kristallografiya* **1960**, *5*, 574.

(44) Nesper, R. *Habilitation*, Universität Stuttgart: Stuttgart, Germany, 1988.

(45) Hopf, V.; Müller, W.; Schäfer, H. *Z. Naturforsch. B* **1972**, *27*, 1157.

(46) Hopf, V.; Schäfer, H.; Weiss, A. *Z. Naturforsch. B* **1970**, *25*, 653.

(47) Menges, E.; Hopf, V.; Schäfer, H.; Weiss, A. *Z. Naturforsch. B* **1969**, *21*, 1351. According to ref. 25, the structures of LiGe reported in ref. 38 and 47 are identical (only two different cell settings).

(48) Evers, J.; Oehlinger, G.; Sextl, G.; Becker, H. O. *Angew. Chem. Int. Ed.* **1987**, *26*, 76.

(49) Evers, J.; Oehlinger, G. *Angew. Chem. Int. Ed.* **2001**, *40*, 1050.

(50) Kiefer, F.; Fässler, T. F. *Solid State Sci.* **2011**, *13*, 636.

(51) Grüttner, A.; Nesper, R.; von Schnering, H. G. *Angew. Chem. Int. Ed.* **1982**, *21*, 912.

(52) Frank, U.; Müller, W. *Z. Naturforsch. B* **1975**, *30*, 313.

(53) Nesper, R.; Curda, J.; von Schnering, H. G. *J. Solid State Chem.* **1986**, *62*, 199.

(54) Stearns, L. A.; Gryko, J.; Diefenbacher, J.; Ramachandran, G. K.; McMillan, P. F. *J. Solid State Chem.* **2003**, *173*, 251.

(55) Gruber, T.; Thomas, D.; Roder, C.; Mertens, F.; Kortus, J. *J. Raman Spectrosc.* **2013**, *44*, 934.

(56) Debski, A.; Gasior, W.; Goral, A. *Intermetallics* **2012**, *26*, 157.

(57) Wang, P.; Kozlov, A.; Thomas, D.; Mertens, F.; Schmid-Fetzer, R. *Intermetallics* **2013**, *42*, 137.

(58) Debski, A.; Zakulski, W.; Major, L.; Goral, A.; Gasior, W. *Thermochim. Acta* **2013**, *551*, 53.

(59) Xu, Y. H.; Yin, G. P.; Zuo, P. J. *Electrochim. Acta* **2008**, *54*, 341.

(60) Kubota, Y.; Escano, M. C. S.; Nakanishi, H.; Kasai, H. *J. Appl. Phys.* **2007**, *102*, 053704.

(61) Kubota, Y.; Escano, M. C. S.; Nakanishi, H.; Kasai, H. *J. Alloys Compd.* **2008**, *458*, 151.

(62) Chevrier, V. L.; Zwanziger, J. W.; Dahn, J. R. *J. Alloy Compd.* **2010**, *496*, 25.

(63) Thomas, D.; Abdel-Hafiez, M.; Gruber, T.; Huttl, R.; Seidel, J.; Wolter, A. U. B.; Buchner, B.; Kortus, J.; Mertens, F. *J. Chem. Thermodyn.* **2013**, *64*, 205.

(64) Zeilinger, M.; Benson, D.; Häussermann, U.; Fässler, T. F. *Chem. Mater.* **2013**, *25*, 1960.

(65) Zeilinger, M.; Fässler, T. F. *Dalton Trans.* **2014**, DOI:10.1039/C4DT00743C.

(66) Zeilinger, M.; Kurylyshyn, I. M.; Häussermann, U.; Fässler, T. F. *Chem. Mater.* **2013**, *25*, 4623.

(67) Zeilinger, M.; Baran, V.; van Wüllen, L.; Häussermann, U.; Fässler, T. F. *Chem. Mater.* **2013**, *25*, 4113.

(68) Zeilinger, M.; Fässler, T. F. *Acta Cryst.* **2013**, *E69*, i81.

(69) Wang, Y. D.; Dahn, J. *J. Electrochem. Soc.* **2006**, *153*, A2314.

(70) Chevrier, V. L.; Dahn, H. M.; Dahn, J. R. *J. Electrochem. Soc.* **2011**, *158*, A1207.

(71) Profatilova, I. A.; Langer, T.; Badillo, J. P.; Schmitz, A.; Orthner, H.; Wiggers, H.; Passerini, S.; Winter, M. *J. Electrochem. Soc.* **2012**, *159*, A657.

(72) Lupu, C.; Mao, J. G.; Rabalais, J. W.; Guloy, A. M.; Richardson, J. W. *Inorg. Chem.* **2003**, *42*, 3765.

(73) Hatchard, T. D.; Dahn, J. R. *J. Electrochem. Soc.* **2004**, *151*, A838.

(74) Vegard, L. *Z. Phys.* **1921**, *5*, 17.

(75) Miller, G. J. *Eur. J. Inorg. Chem.* **1998**, 523.

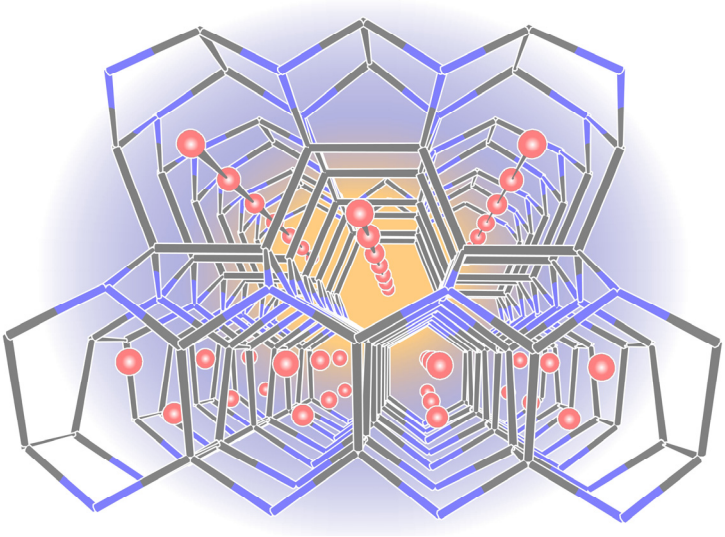

3.2 Open Tetrahedral Frameworks (OTFs)

3.2.1 Review of Relevant Literature

Lithium-rich tetrelides such as $Li_{17}Tt_4$, $Li_{16.4}Tt_4$ or $Li_{15}Tt_4$ (*Tt* = Si, Ge) solely comprise isolated, highly negatively charged tetrel atoms which are embedded in Li matrices. A sound description of their complex structures is achieved by visualizing the arrangement of $TtLi_n$ coordination polyhedra. Gradually going to *Tt*-rich phases, these, for example, contain *Tt*–*Tt* dumbbells (Li_7Tt_3), clusters such as $[Tt_4]^{4-}$ and $[Tt_9]^{4-}$ ($K_{12}Tt_{17}$[1,2]), two-dimensional layers like $^2_\infty[Ge_{12}]^{7-}$ (Li_7Ge_{12}[3,4], see also Figure 3.19a) or extended network structures. The latter, in particular Zintl phases realizing open tetrahedral framework (OTF) structures, have been a focus of the Fässler group for many years. Recent examples are *hP*-Na_2ZnSn_5 and *tI*-Na_2ZnSn_5 possessing zeolitic Zn–Sn-frameworks,[5] the clathrate-I type $Na_8Zn_4Ge_{42}$[6] and $K_8Zn_4Sn_{42}$,[7] or Li_2ZnGe_3 revealing a hexagonal diamond (2*H* polytype[8]) like Zn–Ge network (Figure 3.18a–c).[9] In terms of electrode materials for LIBs, light-weight Zintl phase OTFs involving elements of the second row (Li, B, C) are most interesting. Yet, the synthesis of such phases has long been unsuccessful. Prior to this work, $K_7B_7Si_{39}$[10] (Si is partially replaced by B) and $K_8Li_xGe_{44-x/4}\square_{2-3x/4}$[11] have been the only representatives (Figure 3.18d). Notably, Li replaces small amounts of Ge in the Ge host structure of the latter and does not occupy framework cavities. Additionally, an electrochemical lithiation of the clathrate-II compound Na_xSi_{136} ($x \rightarrow 0$) was reported.[12] In the Li–B–C system, the completely intercalated heterographite LiBC (a variant of the **AlB**$_2$ structure, i.e. **LiBC**) is the lithium-richest phase (Figure 3.18e).[13] However, it was shown that its performance as a cathode or anode material is very poor.[14] The

boron-rich phases $Li_2B_{12}C_2$,[15] $Li_2B_{13}C_2$,[15] $Li_{1.68}B_{38.76}C_6$,[16] and $Li_{1.43}B_{38.82}C_6$[16] bearing B_{12}-icosahedral units in their structures are less attractive. In case of the Li–B–Si system, $Li_2B_{12}Si_2$ was the only known phase prior to this work (Figure 3.18f).[17] The synthesis, crystal and electronic structure of the second representative $LiBSi_2$ is addressed in Chapter 3.2.4. $LiBSi_2$ consists of a strictly ordered tetrahedral B–Si network, to which the symbol **tum** was assigned in the TOPOS topological database (TTD).[18] The Zintl phase OTF hosts Li atoms inside mutually orthogonal channels and may therefore be considered as an interesting electrode material.

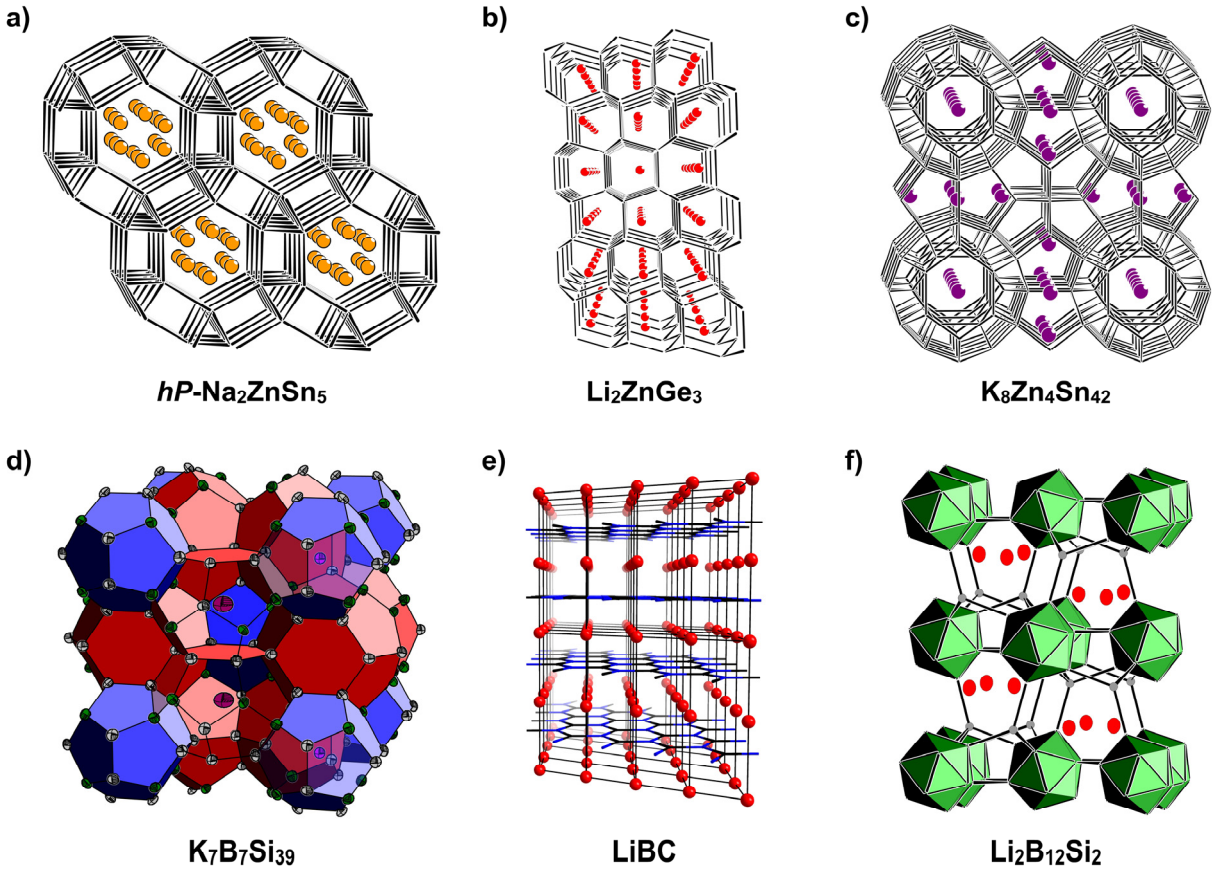

Figure 3.18. Examples of Zintl phase OTFs revealing Zn–Sn or Zn–Ge networks: a) *hP*-Na_2ZnSn_5 (Na atoms exhibit occupational disorder), b) Li_2ZnGe_3, and c) $K_8Zn_4Sn_{42}$. Clathrate-I type $K_7B_7Si_{39}$ (mixed Si/B sites are shown in green) as an example of a Zintl phase OTF involving a second row element (d), the fully Li-intercalated heterographite LiBC (e), and, prior to this work, the only representative of the Li–B–Si system bearing B_{12}-icosahedral units (f). Li, Na, and K atoms are shown in yellow, red, and violet, respectively. The methodology for drawing Figure (a–c) follows ref. 18.

In terms of open tetrahedral frameworks, another focus of the Fässler group are group 14 allotropes. These may possess interesting properties regarding their application as electrode or semiconducting materials. For instance, the Ge polymorphs *allo*-Ge and 4*H*-Ge were characterized comprehensively during the last years (Figure 3.19c,d). The synthesis of *allo*-Ge and

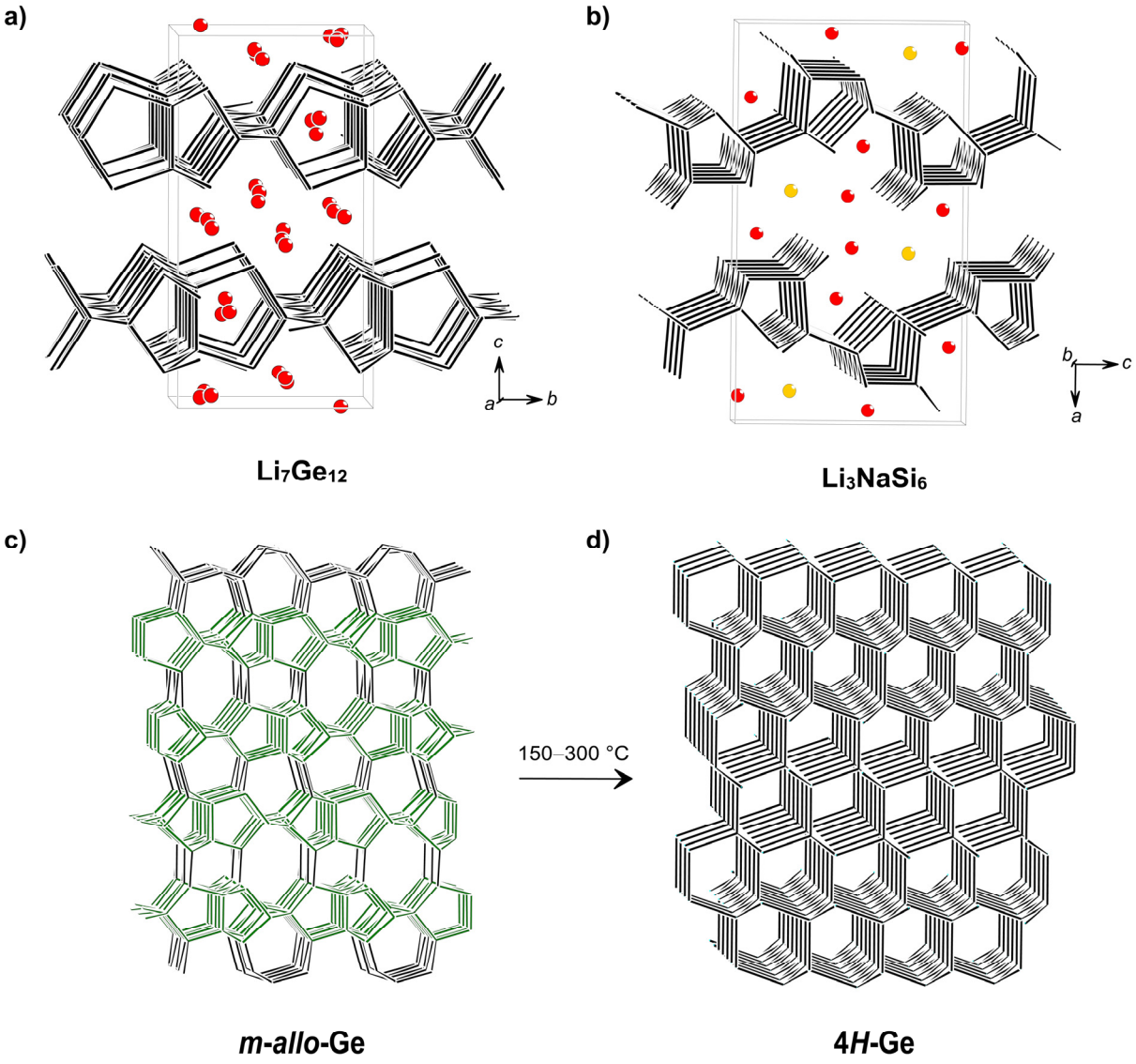

Figure 3.19. Crystal structures of a) Li_7Ge_{12} and b) Li_3NaSi_6 revealing polyanionic layers ${}^2_\infty[Ge_{12}]^{7-}$ and ${}^2_\infty[Si_6]^{4-}$, respectively, separated by Li (red) and Na (yellow) atoms. A mild oxidation of Li_7Ge_{12}, i.e. a Li deintercalation and concomitant interlayer bond formation (corresponding layers are shown in green), leads to the formation of *m-allo*-Ge (c) which transforms into the further allotrope 4*H*-Ge (d). Figure 3.19c was modified on the basis of ref. 18.

its transformation to 4*H*-Ge (isotypic to the 4*H* polytype of SiC) was first described in the 1980's.[3,19] Accordingly, *allo*-Ge was obtained through a mild oxidation of Li_7Ge_{12}, a phase that possesses polyanionic slabs ${}^2_\infty[Ge_{12}]^{7-}$ which are separated from each other by Li atoms (Figure 3.19a). By treatment of Li_7Ge_{12} with protic solvents, interstitial Li is removed. Thereby, the topology of the ${}^2_\infty[Ge_{12}]^{7-}$ layers is retained under interlayer Ge–Ge bond formation (topochemical reaction, Scheme 3.1a). However, the oxidation reaction afforded microcrystalline products which did not allow a comprehensive structure determination. Consequently, the structure model for *allo*-Ge remained unsatisfying until lately. Applying a combination of selected

area electron diffraction, powder X-ray diffraction, quantum chemical calculations and simulated powder X-ray diffraction patterns, the structure model for *m-allo*-Ge (*m*icrocrystalline *allo*-Ge) was improved considerably by Fässler and coworkers.[20] Between 150 and 300 °C *m-allo*-Ge transforms into 4*H*-Ge (Figure 3.19d).[3,21] Similar to the synthesis of *allo*-Ge, *allo*-Si was obtained from an oxidation of Li_3NaSi_6 as yet another group 14 polymorph (Scheme 3.1b). Li_3NaSi_6 comprises of polyanionic layers $^2_\infty[Si_6]^{4-}$ that are separated by Li and Na atoms (Figure 3.19b).[22,23] The treatment of this phase with protic solvents leads to a topochemical oxidation reaction where Li and Na atoms are deintercalated under formation of a three-dimensional four-connected (4c) Si-network through interlayer bond formation.[22,23] However, this reaction only afforded poorly crystalline products which did not allow a conclusive structure determination. As yet, the structure of *allo*-Si is only sketchily described and sparse successive work is found in literature. Employing quantum chemical calculations, hypothetical structures for *allo*-Si[24] and other Si allotropes were predicted.[25–31]

a) $Li_7Ge_{12} + 7\ R\text{OH} \longrightarrow 12\ \textit{allo}\text{-Ge} + 3.5\ H_2 + 7\ \text{LiO}R$

b) $Li_3NaSi_6 + 4\ R\text{OH} \longrightarrow 6\ \textit{allo}\text{-Si} + 2\ H_2 + 3\ \text{LiO}R + \text{NaO}R$

Scheme 3.1. Oxidation reactions of Li_7Ge_{12}/Li_3NaSi_6 yielding *allo*-Ge and *allo*-Si.

In the course of this thesis, the synthesis of the Si polymorph *allo*-Si came under scrutiny and comprehensive investigations could not confirm its existence. According results are presented in Chapter 3.2.2. As part of these studies, the incorporation of Ge into the structure of Li_3NaSi_6 (note that Li_3NaGe_6 is not known) was studied additionally since $Li_3Na(Si_{1-x}Ge_x)_6$ phases might serve as a precursors for *allo*-$Si_{1-x}Ge_x$. This led to the discovery of the novel Zintl phase $Li_{18}Na_2Ge_{17}$[32] which contains the three Zintl anions Ge^{4-}, $[Ge_4]^{4-}$, and $[Ge_{12}]^{12-}$ in a 1:1:1 ratio (see Chapter 3.2.3).

3.2.2 OTF from Silicon: On the Existence of the Si Polymorph *allo*-Si

see Chapter 5.6 — Zeilinger, M.; Jantke, L. A.; Scherf, L. M.; Kiefer, F. J.; Konar, S.; Kienle, L.; Karttunen, A. J.; Häussermann, U; Fässler, T. F., *manuscript for publication*.

As briefly addressed in the introduction, the structure of the Ge polymorph *m-allo*-Ge (*allo*-Ge) was elucidated just recently.[20] Thereby, quantum chemical calculations on differently modeled structures played an important role. Since the structure of *allo*-Ge is directly related to the polyanionic $^2_\infty[Ge_{12}]^{7-}$ slabs in Li_7Ge_{12}, these models were constructed by connecting

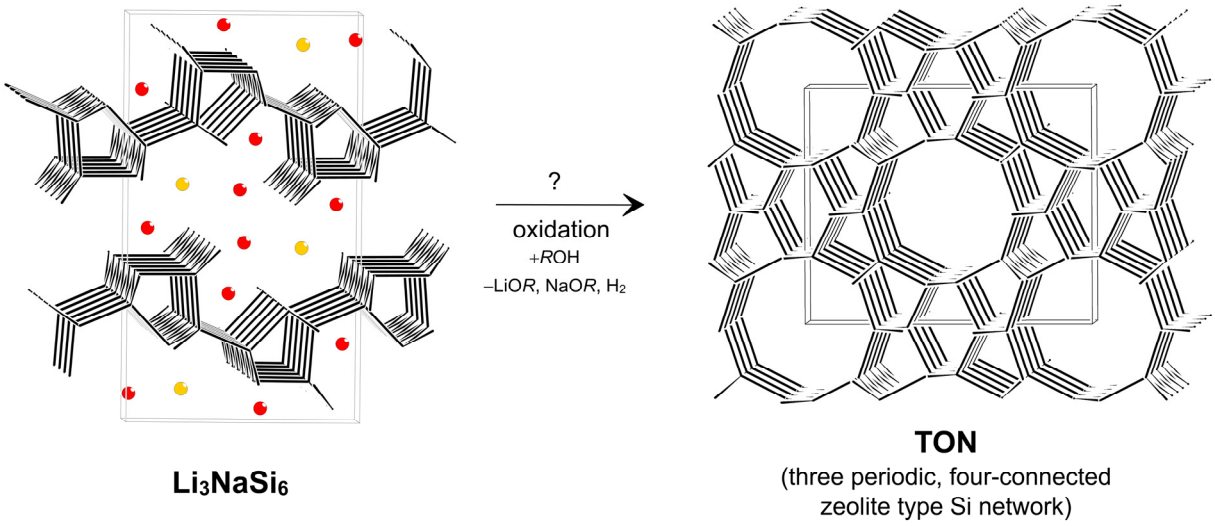

Figure 3.20. Hypothetical oxidation of Li_3NaSi_6 with alcohols *R*OH (*R* = $–CH_3$, $–CH_2CH_3$) yielding a zeolite-type Si open tetrahedral framework (**TON**, ZSM-22). In the present work, the **TON** structure was obtained after a full structural relaxation starting from the Si substructure of Li_3NaSi_6. Li and Na atoms are shown in red and yellow, respectively. Figures were adopted from Chapter 5.6.

$^2_\infty[Ge_{12}]^{7-}$ slab units differently.[20] Turning to *allo*-Si, an analogous approach would be reasonable. However, a phase Li_7Si_{12} has not been described thus far. Considering Li_3NaSi_6 with its $^2_\infty[Si_6]^{4-}$ layers as a precursor for *allo*-Si, a full structural relaxation of its Si substructure concluded with the zeolite-type structure **TON** (Figure 3.20). This strongly fuels the prospect of obtaining crystalline samples of *allo*-Si which could facilitate a conclusive structure determination of the Si polymorph first described in the 1980's.

As part of this thesis, diverse reactions targeting the synthesis of *allo*-Si only yielded amorphous products which were correspondingly denoted as *a-allo*-Si. Attempts to reproduce reports from literature failed. Previously reported reflections for *allo*-Si (ICSD 41-1111) were not traced in any of the powder X-ray diffraction patterns recorded for samples that were synthesized according to Scheme 3.1b. However, it could be shown that the published diffraction pattern of *allo*-Si bears a striking resemblance to $NbSi_2$. Since the authors employed Nb ampules for the synthesis of the precursor Li_3NaSi_6 at relatively high reaction temperatures,[22,23] the reflections of *allo*-Si most likely originated from an $NbSi_2$ impurity. The corresponding reflections may dominate the powder X-ray diffraction pattern after Li_3NaSi_6 was fully converted into an amorphous phase. Thus, it seems that the oxidation of Li_3NaSi_6 with protic solvents is merely a further method to produce amorphous Si. However, Schwarz et al.[22,23] reported on a phase transition of *allo*-Si yielding α-Si at 527 °C which is drastically lower than the amorphous-to-crystalline phase transition of ordinary amorphous Si. This was additionally supported by temperature-dependent powder X-ray diffraction experiments and

claimed as a “good proof that *allo*-Si is in fact a new silicon modification”.[23] In order to clarify this issue, amorphous Si (*a*-Si) was produced by an extraction of Li from the lithium-rich silicide $Li_{15}Si_4$ using liquid ammonia as a solvent for Li (Scheme 3.2).

$$Li_{15}Si_4 \xrightarrow{NH_3} 15\,(1-x)\,Li_{NH3} + 4\,a\text{-Si} + 15\,x\,LiNH_2 + 7.5\,x\,H_2$$

Scheme 3.2. Synthesis of *a*morphous Si (*a*-Si) starting from $Li_{15}Si_4$ and NH_3 as solvent for Li.

Since this reaction produces a mixture of *a*-Si and $LiNH_2$, the extraction process was followed by an aqueous treatment of the *a*-Si/$LiNH_2$ intermediate to remove $LiNH_2$. Subsequently, the corresponding products were rigorously characterized by powder X-ray diffraction, diverse spectroscopic and microscopic methods which provided evidence for a completely amorphous character, a slight surface oxidation of nano- and micrometer-sized particles, and virtually no residual Li.

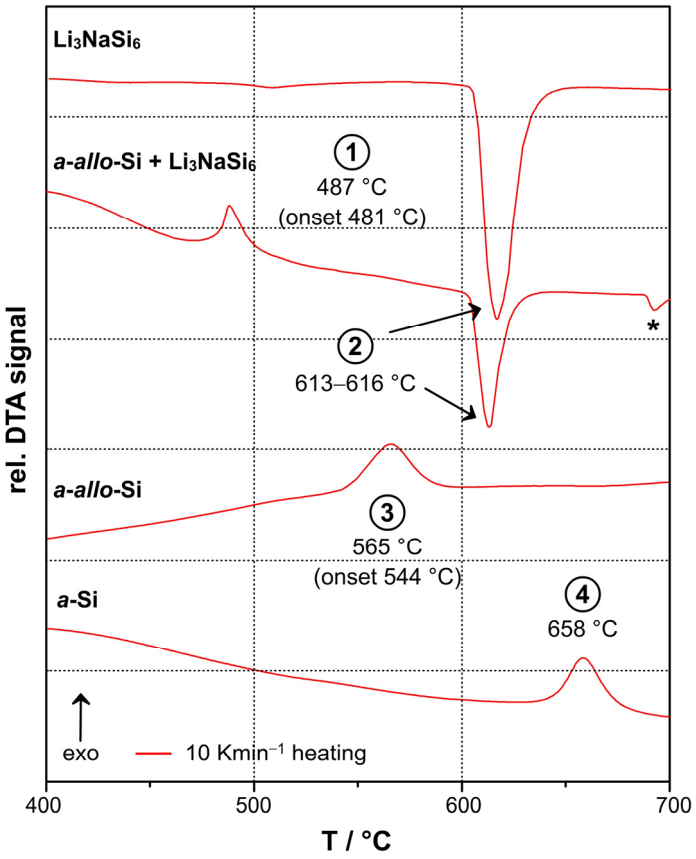

Figure 3.21. First DTA heating traces of thermograms recorded for Li_3NaSi_6, partially oxidized Li_3NaSi_6 (Li_3NaSi_6/*a-allo*-Si mixture), *a-allo*-Si, and *a*-Si obtained from $Li_{15}Si_4$ ($T_{max.}$ = 750 °C, ±10 K·min^{-1} heating/cooling rate, heat effects marked with * could not be assigned). Figure and figure caption were adopted from Chapter 5.6.

As can be recognized from DTA heating traces in Figure 3.21, fully and partially oxidized samples of Li_3NaSi_6 corresponding to *a-allo*-Si and a mixture *a-allo*-Si/Li_3NaSi_6, respectively,

undergo an amorphous-to-crystalline phase transition at 487 and 565 °C (effect 1 and 3), embracing the reported phase transition temperature of *allo*-Si (527 °C).[22,23] Effect (2) is attributed to the decomposition of Li_3NaSi_6. In case of *a*-Si, the phase transition is observed at 658 °C (effect 4) which is markedly higher than found for *a-allo*-Si. These findings support previous results on the thermal behavior of *allo*-Si. However, Raman spectroscopy studies and powder X-ray diffraction of *a*-Si and *a-allo*-Si samples indicate that, in contrast to *a*-Si, *a-allo*-Si contains large concentrations of α-Si crystallites which act as crystallization nuclei. Note that the formation of α-Si crystallites was also mentioned in previous work.[23] Thus, the different phase transition temperatures in the series Li_3NaSi_6/*a-allo*-Si, *a-allo*-Si, and *a*-Si can be explained. Therefore, it is concluded that the oxidation of Li_3NaSi_6 with protic solvents according to previous work[23] solely leads to the formation of amorphous Si. The difficulties to synthesize crystalline samples of *allo*-Si were also explained by quantum chemical calculations since structures derived from the substructure of hypothetical Li_7Si_{12} are distinctly favored over those composed of $^2_\infty[Si_6]^{4-}$ layers apparent in Li_3NaSi_6. Interestingly, some Zintl phase OTFs (**mep**, **mtn**, **CAS**, **unj**, **tum**) were shown to be suitable for Si since these possess more favorable energies relative to α-Si. This nicely demonstrates that new polymorphs of Si might be obtainable by employing other precursors or new routes.

3.2.3 $Li_3Na(Si_{1-x}Ge_x)_6$ as Precursor for *allo*-$Si_{1-x}Ge_x$ and the Discovery of the Zintl Phase $Li_{18}Na_2Ge_{17}$

see Chapter 5.7

Scherf, L. M.; Zeilinger, M.; Fässler, T. F.
Inorg. Chem. **2014**, *53*, 2096.

The oxidation of the ternary lithium sodium silicide Li_3NaSi_6 solely led to the formation of amorphous Si. In contrast, Li_7Ge_{12} is transformed into microcrystalline *allo*-Ge by an oxidative deintercalation.[3,20] For both cases the homologues Li_3NaGe_6 and Li_7Si_{12} are not known. However, a limited solubility of the respective tetrel element corresponding to $Li_7(Si_{1-x}Ge_x)_{12}$ and $Li_3Na(Si_{1-x}Ge_x)_6$ may be possible. These phases could then serve as precursors for crystalline *allo*-$Si_{1-x}Ge_x$ which might be interesting in terms of band gap tuning. However, the solid solution behavior is very limited and other phases are formed instead.[33] Within investigations on $Li_3Na(Si_{1-x}Ge_x)_6$, the novel Zintl phase $Li_{18}Na_2Ge_{17}$ could be identified and subsequently synthesized from a stoichiometric mixture of the pure elements. As part of the corresponding joint publication, $Li_{18}Na_2Ge_{17}$ was characterized by single crystal X-ray diffraction. $Li_{18}Na_2Ge_{17}$ crystallizes in the trigonal space group *P*31*m* with a = 17.0905(4) Å, c = 8.0783(2) Å and Z = 3.

The non-centrosymmetric structure was readily solved and refined with reliability factors of R_1 = 0.0212 and wR_2 = 0.0420 for all data and a flack parameter of 0.01(2). The asymmetric unit contains 13 Li, three Na, and 12 Ge positions which are all fully occupied. This corresponds to a total unit cell content of 54 Li, six Na, and 51 Ge atoms (*hP*111). Atomic displacement parameters were refined anisotropically for all atoms.

$Li_{18}Na_2Ge_{17}$ is one of few examples comprising three different Zintl anions in its unit cell (Figure 3.22a). These are $[Ge_{12}]^{12-}$ centering a Li atom ($[Li@Li_4Ge_{12}]^{11-}$), $[Ge_4]^{4-}$, and Ge^{4-} in a 1:1:1 ratio (Figure 3.22b,c).

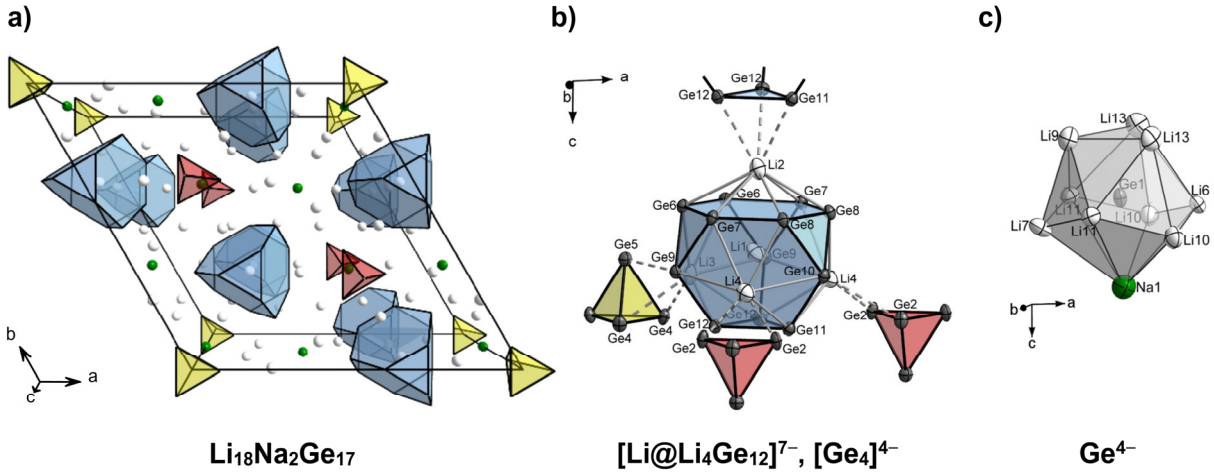

Figure 3.22. a) Unit cell of $Li_{18}Na_2Ge_{17}$ with view along the crystallographic *c*-axis emphasizing the Friauf polyhedra $[Li@Li_4Ge_{12}]^{11-}$ (light blue) and the two crystallographically independent tetrahedra $[Ge_4]^{4-}$ (red and yellow). The coordination environments of $[Li@ Li_4Ge_{12}]^{11-}$ units and isolated Ge^{4-} atoms are depicted in (b) and (c), respectively. Thermal ellipsoids in (b) and (c) are shown at a 90% probability level (Li = white, Na = green, Ge = dark gray). Figures were adopted from ref. 32.

3.2.4 $LiBSi_2$: A Novel Zintl Phase OTF Hosting Li Atoms Inside Channels

see Chapter 5.8

Zeilinger, M.; van Wüllen, L.; Benson, D.; Kranak, V. F.; Konar, S.; Fässler, T. F.; Häussermann, U.
Angew. Chem. Int. Ed. **2013**, *52*, 5978.

Turning to OTFs that are realized by Zintl phases, a high-pressure high-temperature experiment employing a 1:1 mixture of LiB and α-Si encapsulated in a salt cylinder yielded the novel Zintl phase $LiBSi_2$. The thoroughly mixed reactants were pressurized at a maximum pressure of 10 GPa and subsequently reacted at 900 °C for one hour. The powder X-ray diffraction pattern of the product corresponded to $LiBSi_2$ and reflections originating from an unknown

phase. Serendipitously, the latter is air and moisture sensitive and could be removed by washing. In contrast, $LiBSi_2$ is stable in air and toward strong acids. The structure of $LiBSi_2$ could then be solved from powder X-ray diffraction data using a parallel tempering algorithm.[34–36]

A rigorous investigation of the formation conditions of $LiBSi_2$ proved that $LiBSi_2$ can be directly synthesized from a 1:2 mixture of LiB and α-Si. However, an appreciable conversion is only observed if the educts are reacted at least 90 hours at 900 °C and 10 GPa (Figure 3.23).

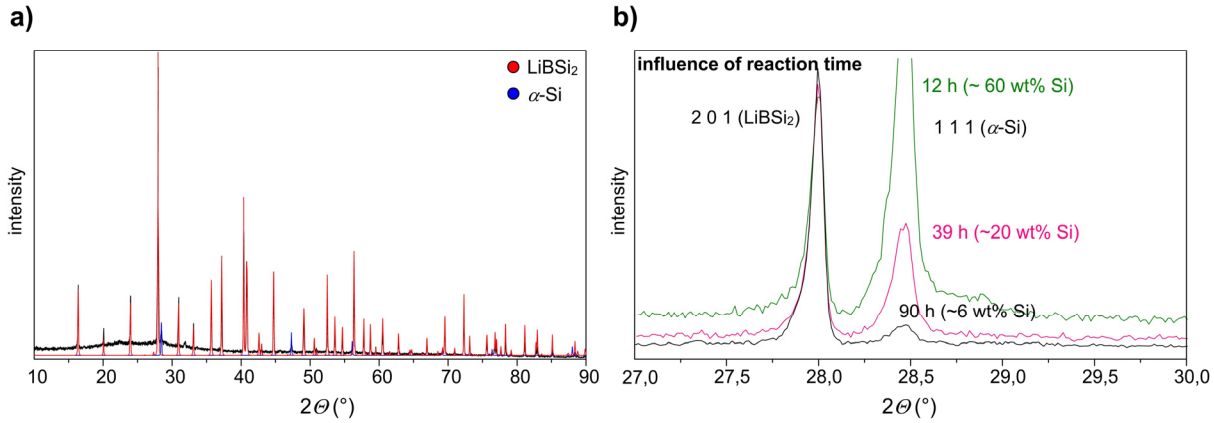

Figure 3.23. a) Powder X-ray diffraction pattern of a $LiBSi_2$ sample obtained after reacting a 1:2 mixture of LiB and α-Si at 900 °C for 90 h at a pressure of 10 GPa. Reducing the dwell time at 900 °C, the corresponding powder X-ray diffraction patterns (b) reveal drastically higher portions of α-Si (α-Si contents were determined by Rietveld refinement; calculated patterns for $LiBSi_2$ and α-Si are shown in red and blue, respectively, experimental ones in black, pink, and green).

$LiBSi_2$ crystallizes in the tetragonal space group $P4_2/nmc$ with a = 6.83225(3) Å, c = 8.83924(6) Å, V = 412.612(5) Å^3, and eight formula units in the unit cell (*tP*32). The asymmetric unit contains four crystallographically independent atom positions. Si1 and Si2, being located on different 8*g* (¼, *y*, *z*) positions, and B on 8*f* (*x*, *y* ,¼) form a strictly ordered open tetrahedral framework (OTF) that encloses Li atoms (on 8*g*) inside mutually orthogonal channels (Figure 3.24a). B atoms are exclusively bonded to Si atoms. Remarkably, $LiBSi_2$ is the first example that reveals such a strictly ordered B–Si framework. It comprises five-, six-, and seven-membered rings. The bonding situation can be easily explained with the Zintl concept: $(Li^+)(4b\text{-}B^-)(4b\text{-}Si^0)$ where B^- is isoelectronic with C and thus four-bonded (4b).

The central motifs in the structure of $LiBSi_2$ are $[B_4Si2_4]$ realgar-like units and Si1–Si1 dumbbells in a 1:2 ratio forming two-dimensional slabs that embed elongated Li_4-tetrahedra (edge lengths: 3.36 and 3.85 Å) as illustrated in Figure 3.24b. These slabs are connected along the crystallographic *c*-axis (Figure 3.24a). Since they are related by the *n* glide perpendicular

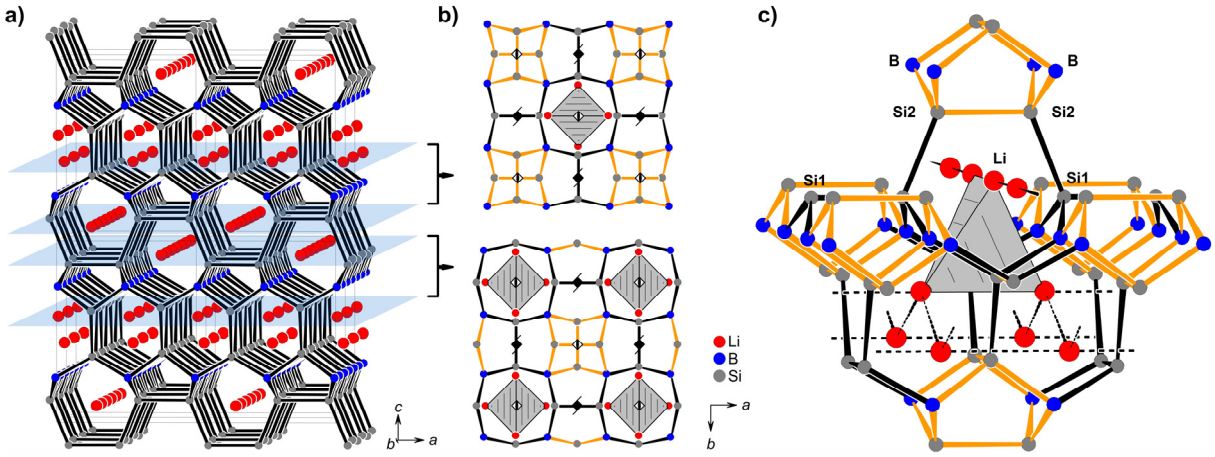

Figure 3.24. Crystal structure of $LiBSi_2$. a) 2×2×2 supercell with view along the *b*-axis (Li, B, and Si atoms are shown in red, blue, and dark gray; isotropic atomic displacement at a 90 % probability level); b) *ab*-projection of two consecutive slab building units whose boundaries are indicated by blue planes in Figure (a). Slab building units comprise realgar-like units that are emphasized by yellow bonds. Elongated Li_4-tetrahedra (shown in gray) are embedded in each slab. Symmetry elements (4_2 and $\bar{4}$ axes) are indicated by their respective symbols; c) excerpt of a structural building block that results from connecting three consecutive slab building units. Li atoms are hosted inside six- and seven-membered orthogonal channels which are recognizable as linear chains and zig-zag chains, respectively (dotted lines between Li atoms do note indicated interactions). Figures were adopted from ref. 18.

to *c* (Figure 3.24b), realgar units and Li_4-tetrahedra are alternatingly stacked whereas Si1–Si1 dumbbells are situated on top of each other by a 90° rotation. As a result of stacking the two-dimensional slab building units, Li atoms are hosted inside mutually perpendicular channels. Interestingly, the arrangement of Li atoms may be described as linear chains and zig-zag chains when viewing along channels formed from seven-membered and six-membered rings, respectively (Figure 3.24a,c). These chains run along the *a*- and *b*-direction. It is noteworthy that if parallel channels formed by the seven-membered rings (hosting linear Li chains at different heights), for example recognized in the *b*-direction, are viewed from the (perpendicular) *a*-direction, their side view corresponds to parallel channels formed by six-membered rings (hosting Li zig zag chains).

The fascinating structure of $LiBSi_2$ which represents a new three periodic, four connected net (it was assigned the symbol **tum** in the TOPOS topological database) was also confirmed by Raman and NMR spectroscopy. Additionally, quantum chemical calculations revealed a band gap of 1.1 eV.

3.2.5 References

(1) von Schnering, H. G.; Baitinger, M.; U. Bolle, U.; Carrillo-Cabrera, W.; Curda, J.; Grin, Y.; Heinemann, F.; Llanos, J.; Peters, K.; Schmeding, A.; Somer, M. *Z. Anorg. Allg. Chem.* **1997**, *623*, 1037.

(2) Hoch, C.; Wendorff, M.; Röhr, C. *J. Alloys Compd.* **2003**, *361*, 206.

(3) Grüttner, A.; Nesper, R.; von Schnering, H. G. *Angew. Chem. Int. Ed.* **1982**, *21*, 912.

(4) Kiefer, F.; Fässler, T. F. *Solid State Sci.* **2011**, *13*, 636.

(5) Stegmaier, S.; Kim, S. J.; Henze, A.; Fässler, T. F. *J. Am. Chem. Soc.* **2013**, *135*, 10654.

(6) Stegmaier, S. *Dissertation*, Technische Universität München: München, Germany, 2012.

(7) Baran, V.; Fischer, A.; Scherer, W.; Fässler, T. F. *Z. Anorg. Allg. Chem.* **2013**, *639*, 2125.

(8) Ramsdell, L. S. *Am. Mineral.* **1947**, *32*, 64.

(9) Stegmaier, S.; Fässler, T. F. *Inorg. Chem.* **2013**, *52*, 2809.

(10) Jung, W.; Lorincz, J.; Ramlau, R.; Borrmann, H.; Prots, Y.; Haarmann, F.; Schnelle, W.; Burkhardt, U.; Baitinger, M.; Grin, Y. *Angew. Chem. Int. Ed.* **2007**, *46*, 6725.

(11) Liang, Y.; Böhme, B.; Ormeci, A.; Borrmann, H.; Pecher, O.; Haarmann, F.; Schnelle, W.; Baitinger, M.; Grin, Y. *Chem. Eur. J.* **2012**, *18*, 9818.

(12) Langer, T.; Dupke, S.; Trill, H.; Passerini, S.; Eckert, H.; Pöttgen, R.; Winter, M. *J. Electrochem. Soc.* **2012**, *159*, A1318.

(13) Wörle, M.; Nesper, R.; Mair, G.; Schwarz, M.; von Schnering, H. G. *Z. Anorg. Allg. Chem.* **1995**, *621*, 1153.

(14) Langer, T.; Dupke, S.; Dippel, C.; Winter, M.; Eekert, H.; Pöttgen, R. *Z. Naturforsch. B* **2012**, *67*, 1212.

(15) Vojteer, N.; Hillebrecht, H. *Angew. Chem. Int. Ed.* **2006**, *45*, 165.

(16) Vojteer, N. *Dissertation*, Universität Freiburg/Breisgau: Freiburg, Germany, 2008.

(17) Vojteer, N.; Schroeder, M.; Röhr, C.; Hillebrecht, H. *Chem. Eur. J.* **2008**, *14*, 7331.

(18) Zeilinger, M.; van Wüllen, L.; Benson, D.; Kranak, V. F.; Konar, S.; Fässler, T. F.; Häussermann, U. *Angew. Chem. Int. Ed.* **2013**, *52*, 5978.

(19) Grüttner, A.; Nesper, R.; von Schnering, H. G. *Acta Cryst.* **1981**, *A37*, C161.

(20) Kiefer, F.; Karttunen, A. J.; Döblinger, M.; Fässler, T. F. *Chem. Mater.* **2011**, *23*, 4578.

(21) Kiefer, F.; Hlukhyy, V.; Karttunen, A. J.; Fässler, T. F.; Gold, C.; Scheidt, E. W.; Scherer, W.; Nylen, J.; Häussermann, U. *J. Mater. Chem.* **2010**, *20*, 1780.

(22) Schwarz, M. *Dissertation*, Universität Stuttgart: Stuttgart, Germany, 1988.

(23) von Schnering, H. G.; Schwarz, M.; Nesper, R. *J. Less-Common Met.* **1988**, *137*, 297.

(24) Conesa, J. C. *J. Phys. Chem. B* **2002**, *106*, 3402.

(25) Zwijnenburg, M. A.; Jelfs, K. E.; Bromley, S. T. *Phys. Chem. Chem. Phys.* **2010**, *12*, 8505.

(26) Pickard, C. J.; Needs, R. J. *Phys. Rev. B* **2010**, *81*.

(27) Karttunen, A. J.; Fässler, T. F.; Linnolahti, M.; Pakkanen, T. A. *Inorg. Chem.* **2011**, *50*, 1733.

(28) Wu, F.; Jun, D.; Kan, E.; Li, Z. *Solid State Commun.* **2011**, *151*, 1228.

(29) Zhao, Z.; Tian, F.; Dong, X.; Li, Q.; Wang, Q.; Wang, H.; Zhong, X.; Xu, B.; Yu, D.; He, J.; Wang, H. T.; Ma, Y.; Tian, Y. *J. Am. Chem. Soc.* **2012**, *134*, 12362.

(30) Botti, S.; Flores-Livas, J. A.; Amsler, M.; Goedecker, S.; Marques, M. A. L. *Phys. Rev. B* **2012**, *86*.

(31) Zhao, H.-Y.; Wang, J.; Ma, Q.-M.; Liu, Y. *Phys. Chem. Chem. Phys.* **2013**, *15*, 17619.

(32) Scherf, L. M.; Zeilinger, M.; Fässler, T. F. *Inorg. Chem.* **2014**, *53*, 2096.

(33) Scherf, L. M. *Master's Thesis*, Technische Universität München: München, Germany, 2013.

(34) *FOX program*, F.O.X., Free Objects for Crystallography V 1.9.7.0, http://objcryst.sourceforge.net., 2011.

(35) Favre-Nicolin, V.; Cerny, R. *J. Appl. Crystallogr.* **2002**, *35*, 734.

(36) Cerny, R.; Favre-Nicolin, V. *Powder Diffr.* **2005**, *20*, 359.

Chapter 4
Summary and Conclusion

Efficient and at the same time affordable energy storage has become one of the most important aspects of the present and future generation. This particularly emerged from an increasing demand for portable electronics and electric vehicles. In this regard, the lithium-ion battery (LIB) technology is the system of choice since it offers high energy densities at light weight in combination with a plethora of different battery designs. Enhancing the well-established LIB technology in order to meet current requirements is directly associated with the question of how single components of the system can be viably improved. To this end, a deep understanding of respective part systems is crucial and inevitable.

In the course of the present thesis, the binary phase diagram Li–Si came under scrutiny since Si has been regarded as a promising anode material for future LIBs. Theoretically, a Si anode would offer a specific capacity being almost ten times higher than that of graphite, which is commercially used as anode material in most LIBs. However, the use of Si is confronted with a massive swelling/contraction of active material during lithiation/delithiation processes, contact loss of electrodes and poor cyclability. While various solutions were proposed to compensate these problems, a fundamental characterization of the Li–Si system, in particular, the lithium-rich portion, has not been addressed prior to this work. In detail, it was shown that $Li_{17}Si_4$ is the lithium-richest representative of the Li–Si system replacing the previously reported phase $Li_{21}Si_5$ ($Li_{16.8}Si_4$). The structures of $Li_{17}Si_4$ and $Li_{21}Si_5$ are closely related and solely differ in the occupation of one fourfold special position (Figure 4.1a). The existence of a phase with a composition $Li_{22}Si_5$ ($Li_{17.6}Si_4$) was ruled out and thus the controversy in literature regarding the composition of the lithium-richest Li–Si phase could be clarified. Remarkably, these investigations led to the discovery of a new compound. $Li_{16.42}Si_4$ was established as a high-temperature phase in the Li–Si system and exhibits a structural disorder which is unique amongst Li–Si phases. Despite their resembling compositions, the structures of $Li_{17}Si_4$ and $Li_{16.42}Si_4$ are very different (Figure 4.1a,b). The discovery of $Li_{16.42}Si_4$ is ascribed a key role since this allowed a conclusive revision of the lithium-rich section of the Li–Si system (> 76 at.% Li). Analogous investigations of the Li–Ge phase system revealed the existence of the heavier homologues $Li_{17}Ge_4$ and $Li_{16.38}Ge_4$. Consequentially, the lithium-rich section of the Li–Ge system (> 79 at.% Li) could be redetermined accordingly. Interestingly, the Li–Ge phase

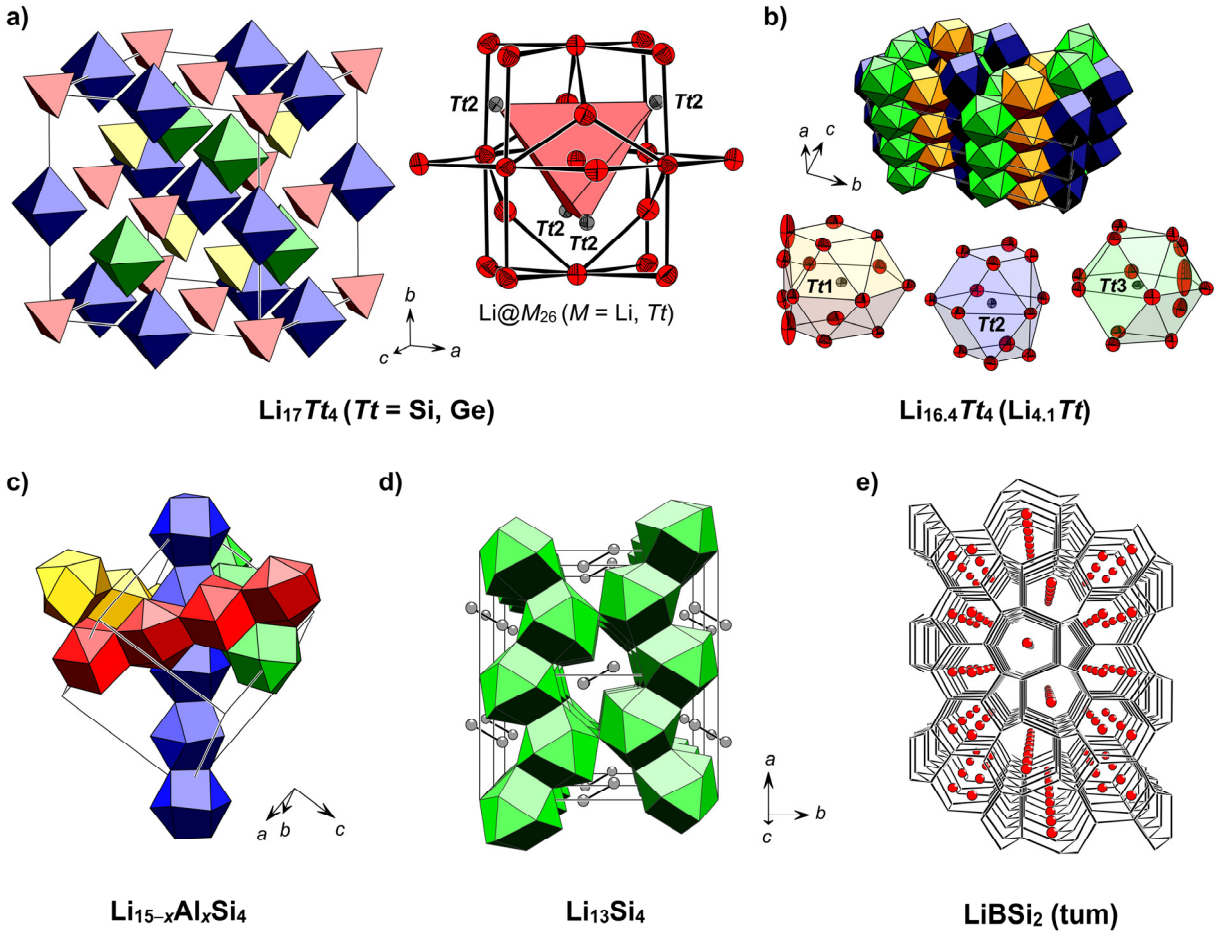

Figure 4.1. Crystal structures of phases which were characterized in the course of the present thesis. a) cubic unit cell of $Li_{17}Tt_4$ emphasizing the NaTl-type arrangement of *Tt*-tetrahedra (red, yellow) and octahedra (blue, green) which correspond to M_{26} clusters (*M* = Li + *Tt*) being centered at Wyckoff positions 4*a*, 4*c* and 4*b*, 4*d*, respectively. The 4*a* position is occupied by Li which centers a M_{26}-cluster; b) $TtLi_n$ coordination polyhedra and their strand-like arrangement in the orthorhombic unit cell (2×1×1) of $Li_{16.4}Tt_4$ ($Li_{4.1}Tt$); c) strands of condensed pseudo-anticuboctahedral units [Si@Li_{12}] proceeding along the three-fold axes of the cubic unit cell of $Li_{15-x}Al_xSi_4$. Different directions of $^1_\infty$[Si@Li_{12}] strands are indicated by different colors; d) 2×1×2 super cell of the orthorhombic phase $Li_{13}Si_4$ emphasizing Si–Si dumbbells and interconnected parallel strands of condensed $^1_\infty$[Si@Li_{12}] units (green); e) the Zintl phase OTF of $LiBSi_2$ hosting Li atoms inside mutually orthogonal channels which are formed by six- and seven-membered rings. The novel, strictly ordered B–Si framework was assigned the symbol **tum** in the TOPOS topological database; Li and *Tt* (*Tt* = Si, Ge) atoms in Figures 4.1a,b,d,e are shown in red and dark gray, respectively.

diagram bears strong resemblance with the Li–Si system regarding the thermodynamic stabilities of $Li_{17}Tt_4$ and $Li_{16.4}Tt_4$. Moreover, melt equilibration experiments employing Li–Si melts with Li concentrations > 85 at.% surprisingly yielded few single crystals of the metastable phase $Li_{15}Si_4$. Hitherto, its structural parameters were merely determined from Rietveld fits of

the $Cu_{15}Si_4$ structure model to respective powder X-ray diffraction patterns. As part of this work, the first single crystal diffraction study on $Li_{15}Si_4$ validated the assignment of the $Cu_{15}Si_4$ structure type. Again, the structure of $Li_{15}Si_4$ is very different from $Li_{17}Si_4$ and $Li_{16.42}Si_4$ (Figure 4.1a–c). Besides, the crystal structure of $Li_{13}Si_4$ (Figure 4.1d) was redetermined by single crystal X-ray diffraction and improved distinctly in comparison to previous work. The unambiguous structural and thermodynamic characterization of all aforementioned phases finally allowed the elucidation of the decomposition behavior of $Li_{15}Si_4$.

Looking at the series $Li_{13}Si_4$, $Li_{15}Si_4$, $Li_{16.42}Si_4$, and $Li_{17}Si_4$, it is interesting to note that none of these meet the criteria for a Zintl phase, albeit $Li_{16.42}Si_4$ is very close to it. Hence, the question of how a Zintl phase may be formed arises. In this regard, the analysis of the band structure of $Li_{15}Si_4$ reveals a peculiarity since a pseudo-gap is located above the Fermi level. Consequently, it can be speculated that an increase of the electron concentration by replacing small amounts of Li by a suitable dopant could shift the Fermi level toward the pseudo-gap resulting in the formation of an electron-precise (semiconducting) Zintl phase. Remarkably, it was shown that substituting small concentrations of Li in $Li_{15}Si_4$ by Al leads to the formation of $Li_{15-x}Al_xSi_4$ ($0.4 < x < 0.8$) which also include the Zintl phase $Li_{14.5}Al_{0.5}Si_4$ (14.5 Li^+, 0.5 Al^{3+}, 4 Si^{4-}). In contrast to $Li_{15}Si_4$, these phases are thermodynamically stable up to ~700 °C ($Li_{15}Si_4$ irreversibly decomposes at ~170 °C) and reveal a diamagnetic behavior.

Another focus of this thesis was set on open tetrahedral framework (OTF) structures realized by Zintl phases and group 14 elements. These materials might serve as alternative electrode materials or could be interesting with respect to semiconducting properties. Regarding OTFs realized from elements, the synthesis of the Si polymorph *allo*-Si was studied comprehensively. Similar to the Ge allotrope *allo*-Ge, *allo*-Si can be obtained from an oxidation of the layer-like phase Li_3NaSi_6. It bears polyanionic layers ${}^2_\infty[Si_6]^{4-}$ that are separated by alkaline metal atoms (*allo*-Ge: Li_7Ge_{12}, ${}^2_\infty[Ge_{12}]^{7-}$). The oxidative deintercalation of Li_3NaSi_6 with protic solvents goes along with a concomitant interlayer bond formation leading to a four-connected network. Contrary to *allo*-Ge, authors reported on the formation of poorly crystalline *allo*-Si samples that did not allow a conclusive structural characterization. As part of this work, only *a*morphous samples of *allo*-Si were afforded and denoted as *a*-*allo*-Si. Furthermore, previous results from powder X-ray diffraction experiments were shown to be ambiguous since the reported *allo*-Si Bragg reflections most likely originated from an impurity. It could be proven by thermal investigations that the amorphous-to-crystalline phase transition temperature of *a*-*allo*-Si (into α-Si, 487–565 °C) is markedly lower than the one of ordinary *a*morphous Si (*a*-Si, ~660 °C). For these studies, *a*-Si was obtained from a new route employing liquid ammonia as a solvent for Li to extract it from $Li_{15}Si_4$. However, the different phase transition temperatures of *a*-Si and *a*-*allo*-Si are attributed to large concentrations of α-Si

crystallites (crystallization nuclei) in *a-allo*-Si samples. A reliable and unambiguous differentiation between *a-allo*-Si and *a*-Si was not possible and, therefore, evidence for the existence of *allo*-Si was not found. The difficulties for obtaining crystalline *allo*-Si samples could also be elucidated by quantum chemical calculations. Remarkably, these calculations also traced a potential capability of Si to form certain Zintl phase OTFs and thus strengthened the prospect of obtaining new Si polymorphs. Furthermore, the solid solutions $Li_3Na(Si_{1-x}Ge_x)_6$ were conceived as precursors for *allo*-$Si_{1-x}Ge_x$ in the course of extensive studies on the synthesis of *allo*-Si. However, the incorporation of Ge into the structure of Li_3NaSi_6 is very limited. Instead, the novel Zintl phase $Li_{18}Na_2Ge_{17}$ could be identified and characterized by single crystal X-ray diffraction. It is one of few phases containing three different Zintl anions (Ge^{4-}, $[Ge_4]^{4-}$, $[Ge_{12}]^{12-}$) in its structure and only the second example of the largest known Ge cluster unit $[Ge_{12}]^{12-}$.

In terms of Zintl phase OTFs, the novel Zintl phase $LiBSi_2$ was synthesized in a high-pressure high-temperature experiment. The structure of $LiBSi_2$ reveals a strictly ordered B–Si network where B atoms are exclusively involved in heteronuclear contacts. Central structure motifs are realgar-like units $[B_4Si_4]^{4-}$ interconnected by Si–Si dumbbells. Mutually orthogonal channels formed from six- and seven-membered rings host Li atoms inside (Figure 4.1e). The novel three periodic, four-connected framework was assigned the symbol **tum** in the TOPOS topological database.

In conclusion, the binary phase diagrams Li–Si and Li–Ge were extensively investigated, revised and established resolutely. The results impressively illustrate that despite the recent interest in these systems essential characteristics have not been recognized to date. The new insights may possibly lead to a reconsideration of previous work and certainly account for a better understanding of these systems on a fundamental level. Moreover, the experimental and theoretical work on the Si polymorph *allo*-Si brought up interesting aspects for future investigations on *allo*-Si or Si allotropes in general. Also the serendipitous discovery of the Zintl phase $Li_{18}Na_2Ge_{17}$ is an important result since it could contribute to further work regarding the influence of cations on cluster shapes and crystal packing in Zintl phases as well as the different behavior of Si and Ge toward their accessibility to certain Zintl phases. In addition, the discovery of $LiBSi_2$ demonstrates that the high-pressure high-temperature technique can be an expedient and powerful method to obtain novel materials in solid state chemistry. The intriguing crystal structure of $LiBSi_2$ hosting Li atoms in a channel-like fashion and the thermodynamically stable phases $Li_{15-x}Al_xSi_4$ will certainly fuel further work, particularly with regard to their potential use as electrode materials.

Chapter 5

Publications and Manuscripts

5.1 Single Crystal Growth and Thermodynamic Stability of $Li_{17}Si_4$

CHEMISTRY OF MATERIALS

Article

pubs.acs.org/cm

Single Crystal Growth and Thermodynamic Stability of $Li_{17}Si_4$

Michael Zeilinger,[†] Daryn Benson,[‡] Ulrich Häussermann,[§] and Thomas F. Fässler*[,†]

[†]Department Chemie, Technische Universität München, Lichtenbergstraße 4, 85747 Garching b. München, Germany

[‡]Department of Physics, Arizona State University, Tempe, Arizona 85287-1504, United States

[§]Department of Materials and Environmental Chemistry, Stockholm University, SE-10691 Stockholm, Sweden

Supporting Information

ABSTRACT: Single crystals of $Li_{17}Si_4$ were synthesized from melts Li_xSi_{100-x} ($x > 85$) at various temperatures and isolated by isothermal centrifugation. $Li_{17}Si_4$ crystallizes in the space group $F\bar{4}3m$ (a = 18.7259(1) Å, Z = 20). The highly air and moisture sensitive compound is isotypic with $Li_{17}Sn_4$. $Li_{17}Si_4$ represents a new compound and thus the lithium-richest phase in the binary system Li−Si superseding known $Li_{21}Si_5$ ($Li_{16.8}Si_4$). As previously shown $Li_{22}Si_5$ ($Li_{17.6}Si_4$) has been determined incorrectly. The findings are supported by theoretical calculations of the electronic structure, total energies, and structural optimizations using first-principles methods. Results from melt equilibration experiments and differential scanning calorimetry investigations suggest that $Li_{17}Si_4$ decomposes peritectically at 481 ± 2 °C to "Li_4Si" and melt. In addition a detailed investigation of the Li−Si phase system at the Li-rich side by thermal analysis using differential scanning calorimetry is given.

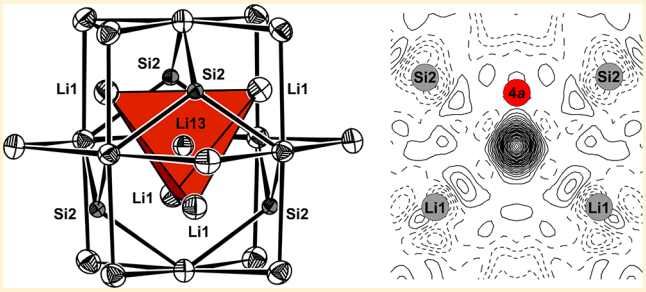

KEYWORDS: *$Li_{17}Si_4$, lithium ion battery, lithium silicides, lithium−silicon system, Li−Si system, lithium−silicon phase diagram, Li−Si phase diagram, isothermal melt centrifugation, crystal growth*

1. INTRODUCTION

Silicon has attracted considerable interest as an anode material for high-energy lithium ion batteries. The theoretical specific capacity is an order of magnitude larger than for graphite. Yet, the use of silicon as anode material is problematic because of the drastic volume changes of up to 300% during charging and discharging, resulting in a contact loss of electrodes.[1] The lithiation and delithiation mechanism of silicon is much more complex compared to graphite and far from being understood. Lithiated silicon provides a specific theoretical capacity of 3579 mAh g^{-1} based on the formation of $Li_{15}Si_4$.[2,3] Recently, Kwon et al.[4] presented a capacity extension to 4008 mAh g^{-1} by observing the formation of $Li_{21}Si_5$ ($Li_{16.8}Si_4$) at lithiation temperatures above 100 °C. However, it was reported that the formation of $Li_{21}Si_5$ is kinetically slow and can only be observed at extended short-circuit times higher than 24 h.

The lithiation/delithiation process of Si is obscured by crystalline-to-amorphous phase transitions and the manifold of existing Li−Si phases. A large amount of ex situ, in situ, and in operando studies have been performed.[2,3,5−10] Interesting are the results from ^{7}Li- and ^{29}Si NMR experiments by Gray et al. identifying Si cluster units as intermediates in the lithiation/delithiation process.[11,12] These investigations indicate that thermodynamic relations between phases in the binary Li−Si system may be more complex as earlier thought.

We put the focus on reinvestigation of structure and phase relations in the Li rich part of the binary Li−Si system, which yielded surprising results. The lithium-richest silicide in the binary system Li−Si has been reported 50 years ago as $Li_{22}Si_5$ ($Li_{4.4}Si$),[13,14] which has been corrected 25 years ago to $Li_{21}Si_5$.[15] Here we report on the stoichiometric phase $Li_{17}Si_4$ ($Li_{4.25}Si$) which supersedes $Li_{21}Si_5$[15] ($Li_{4.2}Si$) as the most Li-rich phase in the binary system. The latter most likely does not exist as a stable phase. On the other hand the $Li_{17}T_4$ structure is known for T = Ge, Sn,[16,17] and the discovery of $Li_{17}Si_4$ demonstrates that the Li-rich portion of the phase diagram of the three systems is actually very similar.

2. EXPERIMENTAL SECTION

Synthesis. Single crystals were grown in melts Li−Si. Starting materials were rods of Li (99.9%, Sigma-Aldrich) and silicon powder (99.999%, Sigma-Aldrich). All steps of synthesis and sample preparation were carried out in a glovebox (MBraun, Ar-atmosphere, H_2O and O_2 levels < 0.1 ppm). Reactions targeting the equilibrium between melt and the Li-richest phase at a certain temperature were performed in tantalum ampules with dimensions L = 80.0 mm, OD = 12.7 mm, and ID = 11.7 mm. Prior to use, these ampules were thoroughly cleaned and heated to 1000 °C under dynamic vacuum ($p < 1 \times 10^{-3}$ mbar) for at least 2 h. Subsequently a filter was inserted and reactions were prepared according to ref 18. Mixtures with compositions of 85−95 atom % Li and a total mass of 300 mg were loaded and sealed in such ampules which were then encapsulated in silica jackets. Finally, silica jackets were placed in a silica wool insulated

Received: February 21, 2013
Revised: March 26, 2013
Published: March 28, 2013

reaction container made of stainless steel. Reaction mixtures were heated in a box furnace to 700 °C at a rate of 5 °C min^{-1}, kept at this temperature for 1 h, and subsequently cooled down with a rate of 5 °C h^{-1} to various temperatures. After a dwell time of 48 h, reactions were terminated by isothermally centrifuging off the melt. Figure 1

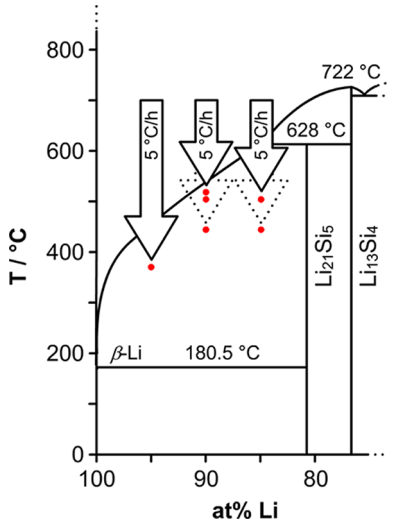

Figure 1. Lithium-rich section of the Li−Si phase diagram as published by Okamoto[42] and applied synthesis scheme: Melts with nominal compositions $Li_{95}Si_5$, $Li_{90}Si_{10}$, and $Li_{85}Si_{15}$ were heated to 700 °C and equilibrated at the dwell temperatures indicated by red circles, followed by isothermal centrifugation of crystalline products.

shows the employed Li−Si atomic ratios as well as the target temperatures before centrifugation. Obtained crystalline products are highly air and moisture sensitive. The crystal diameters varied from 0.2 mm to over 1 cm.

Structure Determination. Crystals of $Li_{17}Si_4$ were selected in an Ar-filled glovebox and sealed in 0.3 mm glass capillaries. Intensity data was collected at room temperature and −150 °C. For the latter a Bruker X-ray diffractometer equipped with a CCD detector (APEX II, κ-CCD), a fine-focused sealed tube with Mo Kα radiation (λ = 0.71073 Å), and a graphite monochromator were employed (for details on the room temperature experiments see Supporting Information, Tables S1 and S2). Data collection was controlled with the Bruker APEX Software Suite.[19] Integration, data reduction, and absorption correction were performed with the packages SAINT[20] and SADABS.[21] Space group symmetry was assigned on the basis of the systematic absences and the statistical analysis of the intensity distributions. In all cases Friedel pairs were not merged as the assigned space group is noncentrosymmetric. The structures were solved with direct methods (SHELXS-97[22]) and refined with full-matrix least-squares on F^2 (SHELXL-97[23]). Difference Fourier maps $F_o - F_c$ were calculated with JANA2006.[24] Details of the single crystal data collections and refinements are listed in Table 1. Atom position parameters and selected interatomic distances are given in Tables 2 and 3. Further details of the crystal structure investigations may be obtained as Supporting Information and from Fachinformationszentrum Karlsruhe, D-76344 Eggenstein-Leopoldshafen, Germany (fax (+49)7247−808−666; e-mail crysdata@fiz-karlsruhe.de) on quoting the depository numbers CSD-425779 ($Li_{17}Si_4$-123K) and CSD-425780 ($Li_{17}Si_4$-298K).

Powder X-ray Diffraction (PXRD). PXRD patterns were recorded on a Stoe STADI P diffractometer (Ge(111) monochromator for Cu Kα radiation, λ = 1.54056 Å) equipped with a Detectris MYTHEN DCS 1K solid state detector. Single crystals of $Li_{17}Si_4$ and DSC bulk samples were ground in an agate mortar and filled in 0.3 mm glass capillaries which were sealed. All samples were measured within a 2θ range of 5−90° (PSD steps: 0.06−1.50°; time/step: 15−40 s). TOPAS 4.0 was used for Rietveld refinements.[25]

Table 1. Crystallographic Data and Structure Refinement for $Li_{17}Si_4$

empirical formula	$Li_{17}Si_4$
T (K)	123(2)
formula weight (g·mol^{-1})	230.34
crystal size (mm^3)	0.30 × 0.30 × 0.30
crystal color	metallic silver
crystal shape	block
space group	$F\bar{4}3m$
unit cell dimension (Å)	a = 18.6563(2)
Z	20
V (Å^3)	6493.5(1)
ρ (calc.) (g·cm^{-3})	1.178
μ (mm^{-1})	0.394
F(000)	2140
θ range (deg)	1.89−47.62
index range hkl	$-38 < h < 37$, $-38 < k < 28$, $-35 < l < 26$
reflections collected	32178
independent reflections	2971 (R_{int} = 0.036)
reflections with $I > 2\sigma(I)$	2620 (R_σ = 0.021)
absorption correction	multiscan
data/restraints/parameter	2971/0/67
goodness-of-fit on F^2	1.061
final R indices $[I > 2\sigma(I)]^{a,b}$	R_1 = 0.021, wR_2 = 0.035
R indices (all data)^{a,b}	R_1 = 0.028, wR_2 = 0.037
flack	0.49(7)
largest diff. peak and hole (e·Å^{-3})	0.20 and −0.41

$^aR_1 = \sum||F_o| - |F_c||/\sum|F_o|$. $^bwR_2 = [\sum w(F_o^2 - F_c^2)^2/\sum w(F_o^2)^2]^{1/2}$.

Table 2. Fractional Atomic Coordinates and Isotropic Equivalent Atomic Displacement Parameters for $Li_{17}Si_4$ ($F\bar{4}3m$, Z = 20, T = 123 K, Estimated Standard Deviations in Parentheses)

atom	Wyckoff position	x	y	z	U_{eq} (Å^2·10^3)
Si1	16e	0.15976(1)	0.15976(1)	0.15976(1)	6.89(4)
Si2	16e	0.91660(1)	0.91660(1)	0.91660(1)	6.26(4)
Si3	24f	0.32133(1)	0	0	7.01(4)
Si4	24g	0.57031(1)	1/4	1/4	6.81(4)
Li1	16e	0.07410(6)	0.07410(6)	0.07410(6)	14.9(3)
Li2	16e	0.30284(5)	0.30284(5)	0.30284(5)	12.5(3)
Li3	16e	0.41794(7)	0.41794(7)	0.41794(7)	12.7(3)
Li4	16e	0.55713(5)	0.55713(5)	0.55713(5)	12.5(3)
Li5	16e	0.68687(5)	0.68687(5)	0.68687(5)	12.3(3)
Li6	16e	0.83168(6)	0.83168(6)	0.83168(6)	13.5(3)
Li7	24f	0.16807(8)	0	0	11.8(3)
Li8	24g	0.07492(9)	1/4	1/4	13.9(3)
Li9	48h	0.09068(4)	0.09068(4)	0.26186(6)	15.7(3)
Li10	48h	0.09013(5)	0.09013(5)	0.76176(6)	16.0(2)
Li11	48h	0.15503(4)	0.15503(4)	0.51978(6)	16.1(2)
Li12	48h	0.16327(4)	0.16327(4)	0.00286(7)	14.3(3)
Li13	4a	0	0	0	10.5(6)

Differential Scanning Calorimetry (DSC). DSC measurements were performed with a NETZSCH DSC 404 Pegasus instrument. Cylindrical niobium crucibles (L = 15.0 mm, OD = 6.5 mm, ID = 5.0 mm) were thoroughly cleaned and heated to 1000 °C under dynamic vacuum ($p < 1 \times 10^{-3}$ mbar) for 2 h and then transferred to an Ar-

dx.doi.org/10.1021/cm400612k | Chem. Mater. 2013, 25, 1960−1967

Table 3. Relevant Interatomic Distances in $Li_{17}Si_4$ ($F\bar{4}3m$, Z = 20, T = 123 K, Estimated Standard Deviations in Parentheses)

atom pair			d (Å)	atom pair			d(Å)
Si1	Li9	×3	2.636(1)	Si3	Li7		2.859(1)
	Li1		2.768(2)		Li11	×3	2.9489(6)
	Li2	×3	2.8459(5)	Si4	Li11	×2	2.664(1)
	Li8	×3	2.8589(9)		Li12	×2	2.6771(9)
	Li12	×2	2.929(1)		Li8		2.710(2)
Si2	Li12	×3	2.652(1)		Li5	×2	2.7392(2)
	Li13		2.6949(3)		Li6	×2	2.8263(5)
	Li7	×3	2.7087(8)		Li10	×3	3.0135(8)
	Li6		2.744(2)	Li6	Li10	×3	2.441(2)
	Li10	×3	2.894(1)		Li5	×3	2.746(2)
	Li1		2.949(1)		Si4	×3	2.8263(5)
Si3	Li9	×2	2.637(1)		Li12	×2	3.196(2)
	Li4	×2	2.7228(2)	Li13	Li1	×4	2.395(2)
	Li3	×2	2.8171(5)		Si2	×4	2.6949(3)
	Li10	×2	2.839(1)		Li7	×6	3.136(1)

filled glovebox. Crucibles were loaded with 30−50 mg of sample and subsequently sealed by arc-welding inside the glovebox under cooling. An empty sealed crucible served as reference. All measurements were done under an Ar flow of 60−70 mL/min and applying a heating/cooling rate of 10 °C min^{-1}. Samples were recovered after the measurement and analyzed by PXRD. Handling of the DSC data was done with the program Proteus Thermal Analysis.[26] Samples for DSC investigations consisted of (i) ground single crystals $Li_{17}Si_4$ obtained according to the synthesis description above and (ii) bulk samples with a nominal composition $Li_{17}Si_4$, $Li_{16.5}Si_4$, $Li_{16}Si_4$ (Li_4Si), and $Li_{14}Si_4$. The latter were synthesized from the elements in tantalum ampules as batches with a total mass of 2.5 g. This batch size was deemed appropriate to keep weighing errors minimal for achieving targeted compositions with sufficient precision. The ampules were sealed by arc-welding inside the glovebox, enclosed in silica jackets under vacuum and annealed at 750 °C for at least 0.5 h. The products were ground in an agate mortar and characterized by X-ray powder diffraction prior use. The patterns are shown in the Supporting Information section.

Computational Details. The theoretical calculations of the electronic structure, total energies, and structural optimizations were performed using the first-principles all-electron projector augmented waves (PAW[27,28]) method within VASP[29,30] (Vienna ab initio Simulation Package). Exchange-correlation effects were treated within the generalized gradient approximation (GGA) via the PBE[31,32] (Perdew−Burke−Ernzerhof) parametrization. The structures were relaxed with respect to volume, lattice parameters, and atomic positions with forces being converged to better than 1×10^{-3} eV/Å. The equilibrium volume and equation of states parameters were determined using the third-order Birch−Murnaghan[33] equation. The electronic integration over the Brillouin zone was performed on a Monkhorst−Pack[34] grid of special k-points of size 3 × 3 × 3. To determine the plane waves, a kinetic energy cutoff of 350 eV was used.

3. RESULTS AND DISCUSSION

Structure Analysis of $Li_{17}Si_4$. Equilibrating reaction mixtures Li_xSi_{100-x} (x > 85) at temperatures below 500 °C and subsequent isothermal centrifugation afforded irregularly shaped, silvery shiny crystals with sizes up to 3 mm. When equilibrating at 510 °C crystals were found to be larger and of a different appearance. A selection of crystal specimens is shown in Figure 2. PXRD patterns from ground crystals synthesized below 500 °C were readily indexed with a F-centered cubic cell and the cell parameter refined to be a = 18.7259(1) Å. Importantly, the parameter did not vary significantly across

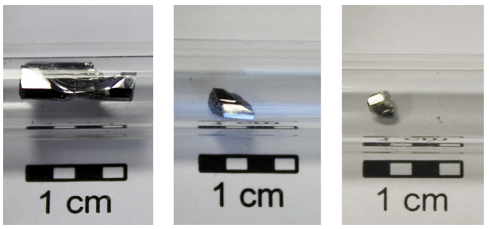

Figure 2. Examples of crystalline specimens separated from equilibrated melts $Li_{90}Si_{10}$ at 510 °C (left, middle) and 450 °C (right).

samples obtained at different temperatures. PXRD patterns could be fitted very well to the known $Li_{21}Si_5$ structure with the space group $F\bar{4}3m$ and Z = 16 (cf. Figure S1 in the Supporting Information), although the cell parameter of this phase has been reported slightly—but significantly—smaller, a = 18.710(2) Å.[15]

The subsequent analysis by single crystal XRD confirmed the space group $F\bar{4}3m$. Refinements yielded reliability factors around 0.02, reflecting an excellent crystal quality (see Table 1 and Supporting Information Table S1). $F\bar{4}3m$ is a non-centrosymmetric space group, and merohedral twinning of the two enantiomorphic species is frequently observed. Hence, twinning had to be considered for the structure refinement. Importantly, Li positions could be refined anisotropically and with very good accuracy (Tables 2 and 3). Further, refinement of their site occupancy factor indicated no significant deviation from full occupancy. As the final result a structure with 340 lithium and 80 silicon atoms in the unit cell was obtained which corresponds to a formula $Li_{17}Si_4$ (Z = 20). The structure of $Li_{17}Si_4$ is analogous to $Li_{17}Sn_4$[16] and actually also $Li_{17}Ge_4$.[17]

The conspicuous difference between the $Li_{17}Si_4$ and $Li_{21}Si_5$ ($Li_{16.8}Si_4$) structures is the occupation of the site 4a by Li (Li13, Table 2) in the former. In space group $F\bar{4}3m$ there are four 4-fold positions (4a−d) which are all unoccupied for $Li_{21}Si_5$. Thus its unit cell contains 80 silicon and 336 instead of 340 lithium atoms. (The atomic position parameters for the $Li_{21}Si_5$ structure are compiled in Supporting Information Table S4 for comparison; note that the originally reported unit cell has been transformed to the standard setting. The here to referred position 4a corresponds to 4d in ref 15.)

To explicitly demonstrate the fully occupied 4a site, the lithium atom situated at this position (Li13) was removed and a difference Fourier map $F_o - F_c$ was generated. The residual electron density map shown in Figure 3 clearly confirms the occupation of the 4a site by Li13. The interatomic distances are reasonable: Li13 centers a tetrahedron formed by Li1 atoms which in turn has all faces capped by Si2 atoms. This arrangement is frequently called "tetrahedral star" and has been recognized as the central building block of a manifold of main group intermetallics.[35] Obviously, the shortest Li−Li distance in $Li_{17}Si_4$ occurs between Li13 and Li1 atoms. This distance is 2.40 Å which is similar to the shortest Li−Li distances found in other silicides, e.g., $Li_{12}Si_7$.[36] The structural fragment around the site 4a (a 26 atom "cluster") is shown in Figure 4. It is noteworthy that the edges of the tetrahedra spanned by Li1 and Si2 atoms measure 3.910(2) Å and 4.4009(2) Å, respectively, while the edges in the corresponding motifs in $Li_{21}Si_5$ are significantly shorter, 3.76(5) Å and 4.366(5) Å. Thus occupying position 4a by additional Li in the structure of $Li_{21}Si_5$ would result in unreasonably short Li−Li distances. Finally, it may be suspected that site 4a in $Li_{17}Si_4$ is partially occupied by C, N, or O (X) impurities, instead of Li. However, Li−X distances are

dx.doi.org/10.1021/cm400612k | Chem. Mater. 2013, 25, 1960−1967

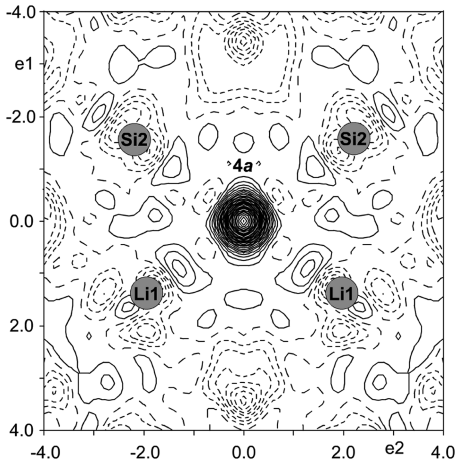

Figure 3. Difference Fourier map ($F_o - F_c$, contour lines ±0.075 e/Å^3) for the plane through two Si2 and two Li1 atoms containing the site 4*a* (cf. Figure 4; single crystal data at 123 K).

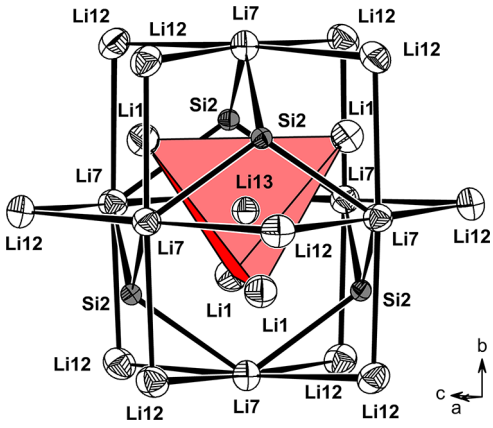

Figure 4. Coordination around the site 4*a* in $Li_{17}Si_4$ (Si = gray; Li = white; thermal ellipsoids at 90% probability, single crystal data at 123 K). Li1 and Si2 atoms form a tetrahedral star unit, Li7 atoms an octahedron, and Li12 atoms a cuboctahedron.

typically shorter (2−2.2 Å). Also, the incorporation of electronegative X is expected to reduce interatomic distances within the tetrahedral star unit $(Li1)_4(Si2)_4$ with respect to $Li_{21}Si_5$, rather than the observed expansion.

At this point it appears that $Li_{17}Si_4$ may not be considered as a mere structure revision of $Li_{21}Si_5$ but represents a different phase with a slightly but distinctly different structure. These structural differences may be traced to a (geometrically) flexible $(Li1)_4(Si2)_4$ tetrahedral star unit around the site 4*a*, allowing the incorporation of additional Li. Before we return to this issue, we conclude the structure description of $Li_{17}Si_4$ which will essentially follow the one given by Nesper and von Schnering[15] for $Li_{21}Si_5$.

The cubic F-centered structure of $Li_{21}Si_5$ can be considered as a 6 × 6 × 6 superstructure of the body centered cubic (bcc) structure ($6^3 \times 2 = 432$ atoms), with a characteristic defect distribution corresponding to vacancies at the sites 4*a*−*d* (416 atoms, i.e., 336 Li and 80 Si). The (defect) sites 4*a*−*d* represent centers of 26 atom clusters (M_{26}), and the one around 4*a* has already been shown in Figure 4. The clusters are shown in Figure 5. Each cluster displays an analogue shell structure: the inner shell is represented by a Li_4 tetrahedron, capped by either four Si (4*a*, 4*c*) or four Li atoms (4*b*, 4*d*) (second shell). The resulting tetrahedral star unit is then surrounded by an octahedron of six Li (4*a*, 4*c*) or six Si atoms (4*b*, 4*d*). Finally, all clusters are concluded by a shell of 12 cuboctahedrally arranged Li atoms. We emphasize the arrangement of Si atoms which gives the advantage of a clearer presentation of the total structure. Importantly M_{26} clusters are crystallographically independent, and no atom is shared between them. The complete structure represents a NaTl-type arrangement of cluster units with the sites 4*a*, 4*c* (i.e., Si_4 tetrahedra) and the sites 4*b*, 4*d* (i.e., Si_6 octahedra) corresponding to Na and Tl atoms, respectively.

To investigate closer the relation between $Li_{17}Si_4$ and $Li_{21}Si_5$ their structures were computationally relaxed and their equilibrium volume structure parameters determined. Those parameters are listed in Tables S4 and S5 (Supporting Information) in comparison with the experimental ones. As a result, the $Li_{17}Si_4$ structure was reproduced splendidly (Table 4); maximum deviations in interatomic distances were at the order of only 1.5%. This is an excellent agreement and supports strongly the structure model for $Li_{17}Si_4$, thus ruling out the incorporation of impurities. Turning to $Li_{21}Si_5$, the overall agreement between experimental structure (according to ref 15) and the computationally relaxed one is also good, although not to the same degree as for $Li_{17}Si_4$ which may be partly due to the lower accuracy of the $Li_{21}Si_5$ refinement. One can notice a singularly large deviation associated with the atomic position parameter of Li1 (x = 0.071(2) vs 0.0553, Table S4 in the Supporting Information). As a matter of fact, the experimental value is actually rather close to the value for $Li_{17}Si_4$ (x = 0.07410(6)) which indicates that without Li13 occupying the site 4*a* the $(Li1)_4$ tetrahedron should be considerably smaller. The edge length in the computationally relaxed structure is 2.902 Å which is drastically shorter than the experimental value of 3.76(5) Å.

It is also interesting to compare the atomic position parameters of the Li atoms situated on the cuboctahedral sites 48*h*. Those atoms define the outer shell of M_{26} clusters. We note that the Li12 position representing the boundary of M_{26} around the site 4*a* is distinguished; its position parameters (x, y, z) are very closely corresponding to the situation in the ideal bcc structure (1/6, 1/6, 0). The other cuboctahedra (around 4*b*−*d*) appear considerably contracted with respect to ideal bcc (most pronounced with Li11 around the site 4*b*). This phenomenon is especially also observed in the computationally relaxed $Li_{21}Si_5$ structure where all sites 4*a*−*d* are unambiguously vacant (cf. Table S6 in the Supporting Information). Thus, site 4*a* is distinguished over the other 4-fold sites by being surrounded by the largest cuboctahedron. This ensures geometrical flexibility of the $(Li1)_4(Si2)_4$ tetrahedral star unit around the site 4*a*, which enables accommodation of the additional Li atom. However, whereas this Li incorporation may be plausible from a structural point of view the deviation between experimental and calculated $Li_{21}Si_5$ structure is clearly suspicious, indicating that the Li13 atom may have been overlooked in the earlier refinement. Furthermore when calculating the reaction energy (referring to zero Kelvin) for $Li_{84}Si_{20}$ + Li (bcc) = $Li_{85}Si_{20}$ a slightly exothermic (−0.04 eV) result is obtained. Therefore we conclude that whereas the computational investigation of $Li_{17}Si_4$ and $Li_{21}Si_5$ firmly confirms the structure of the former it casts doubts on the latter. A phase $Li_{21}Si_5$ may not be stable in the Li−Si system. In the following we describe thermal investigations to further elucidate on this issue.

dx.doi.org/10.1021/cm400612k | *Chem. Mater.* 2013, 25, 1960−1967

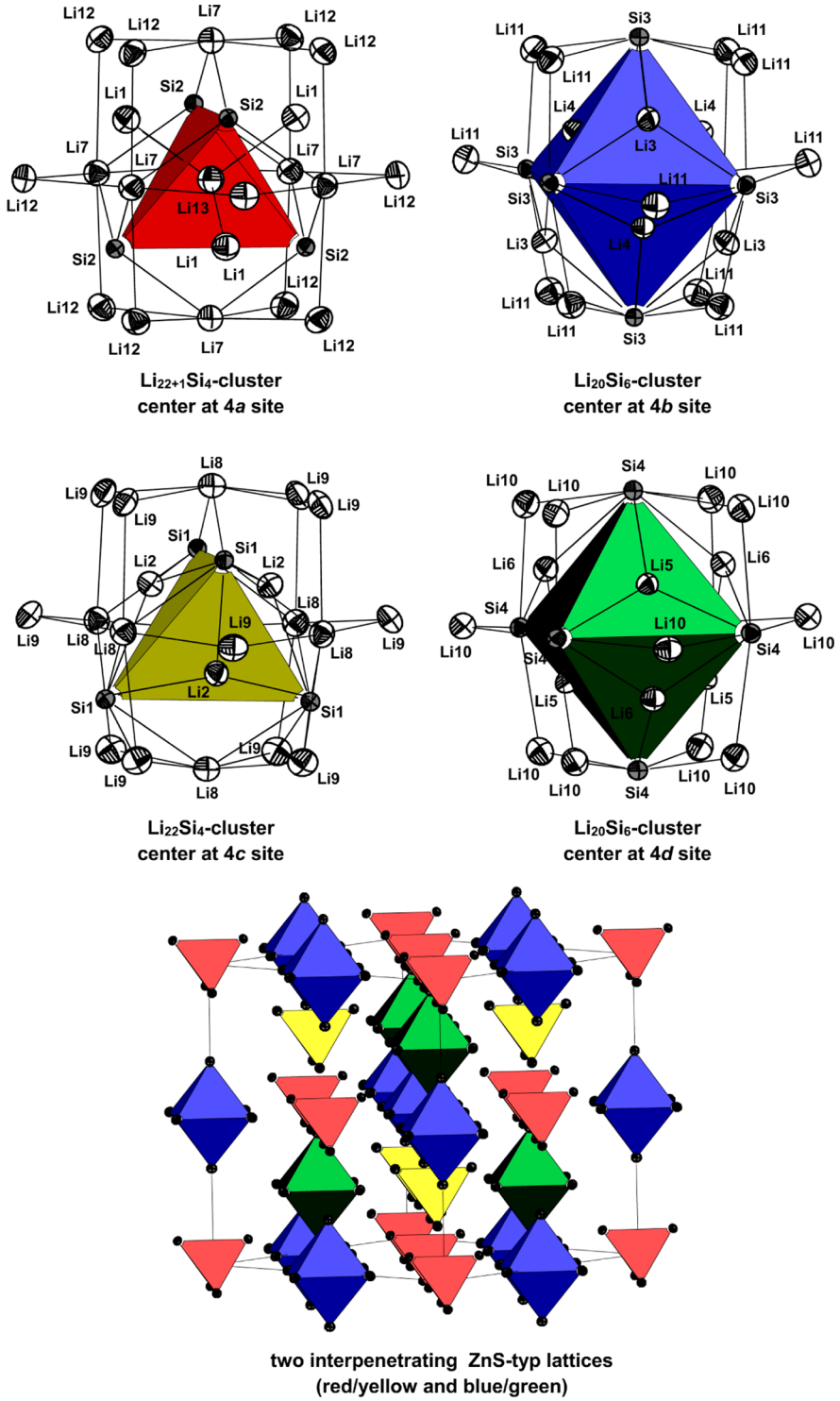

Figure 5. Crystallographically independent M_{26} atom clusters in the structure of $Li_{17}Si_4$ around the sites 4*a*–*d* (Si = gray; Li = white; thermal ellipsoids at 90% probability, single crystal data at 123 K). The Si atom arrangement is highlighted as colored polyhedra. The NaTl-type arrangement of clusters in the complete structure of $Li_{17}Si_4$ is shown in the bottom part (view along [110]).

Thermal Analysis of $Li_{17}Si_4$. $Li_{21}Si_5$ ($Li_{16.8}Si_4$; for reasons of clarity are all compositions normalized to Li_ySi_4) has been described as an incongruently melting phase which decomposes at 617 °C.[15] Additionally, there are several reports prior to ref 15 on phases "$Li_{22}Si_5$" ($Li_{17.6}Si_4$) and "Li_4Si" ($Li_{16}Si_4$).[13,14,37−41] The latter phase was found to possess a homogeneity range between 19.2 and 20.1 atom % Si and to occur in two polymorphic forms.[39] However, there are no consecutive reports supporting those findings. An excerpt of the lithium rich part of the Li−Si phase diagram according to Okamoto[42] is shown in Figure 1.

$Li_{17}Si_4$ and samples with compositions $Li_{16.5}Si_4$, $Li_{16}Si_4$, and $Li_{14}Si_4$ were investigated by thermal analysis using differential scanning calorimetry (DSC). Detected events were found reversible and appeared on cooling and heating. In heating curves events are shifted (by about 20 °C) toward higher

dx.doi.org/10.1021/cm400612k | *Chem. Mater.* 2013, 25, 1960−1967

Table 4. Comparison of Essential Structure Parameters for Experimental and Computational Relaxed $Li_{21}Si_5$ and $Li_{17}Si_4$

	$Li_{21}Si_5$		$Li_{17}Si_4$	
	exp. (ref 15[a])	calc.	exp. (this work[b])	calc.
a, Å	18.710(2)	18.5541	18.6563(2)	18.5732
d(Li1−Li1), Å	3.76(5)	2.902	3.910(2)	3.940
d(Si2−Si2), Å	4.366(5)	4.466	4.4009(2)	4.376
d(Si2−Li7), Å	2.77(2)	2.760	2.7087(9)	2.707
d(Li13−Li1), Å	-	-	2.395(2)	2.413
d(Li13−Si2), Å	-	-	2.6949(3)	2.680

[a]Experimental data refer to room temperature measurement, see Table S4 in Supporting Information. [b]Experimental data refer to the 123 K measurement, see also Table S5 in Supporting Information.

temperatures (cf. Supporting Information, Figure S2 and S3). For $Li_{17}Si_4$, crystal and bulk samples were employed, showing identical results. Cooling traces of bulk samples are compiled in Figure 6.

Upon cooling a melt $Li_{17}Si_4$ from 750 °C the solidus is reached at 667 °C, and congruently melting $Li_{13}Si_4$ crystallizes. This event, marked as (1) in Figure 6, is unambiguously identified. The solidus shifts to higher temperatures with increasing Si content of the melt; 672, 678, and 709 °C for $Li_{16.5}Si_4$, $Li_{16}Si_4$, and $Li_{14}Si_4$, respectively, which is in agreement with the reported phase diagram. On further cooling $Li_{17}Si_4$ shows two, just resolved, events at 610 and 618 °C (marked as (2) and (3) in Figure 6), and finally a fourth event (4) at low temperature (481 °C). The appearance of three thermal events for melts $Li_{17}Si_4$ after passing the liquidus is surprising. One event should account for the peritectic formation of the phase $Li_{17}Si_4$ and a second may be associated with a phase $Li_{21}Si_5$ ($Li_{16.8}Si_4$). A third peak could then either mean the presence of an unknown phase with a composition richer in Li than $Li_{13}Si_4$ or temperature polymorphism of $Li_{17}Si_4/Li_{21}Si_5$. Melts with a composition $Li_{16.5}Si_4$ also show three events, at similar temperatures as $Li_{17}Si_4$ after having passed the solidus. Since this composition is more Si rich than $Li_{21}Si_5$ it can be ruled out that event (4) at 481 ± 2 °C corresponds to a peritectic formation reaction of $Li_{17}Si_4$ (from $Li_{21}Si_5$). It is however clear from our synthesis of $Li_{17}Si_4$ crystals from, e.g., equilibrated melts $Li_{90}Si_{10}$ that $Li_{17}Si_4$ is stable and the most Li-rich phase at temperatures below 481 ± 2 °C.

Event (4) at low temperatures is absent when cooling melts with compositions $Li_{16}Si_4$ and $Li_{14}Si_4$. The powder pattern of solidified $Li_{16}Si_4$ (shown as Supporting Information, Figure S6) reveals a new phase in the Li−Si system. The composition of this phase is $Li_{4.11}Si$ ($Li_{16.42(1)}Si_4$).[a] The characterization of its highly complex structure and detailed thermodynamic properties will be presented in a forthcoming article. In the following we refer to this phase as "Li_4Si". With the presence of "Li_4Si", event (4) upon cooling corresponds to the peritectic formation of $Li_{17}Si_4$ (from "Li_4Si"). This is in agreement with $Li_{90}Si_{10}$ equilibration experiments that yielded crystals of "Li_4Si" at temperatures above 500 °C (cf. Figure 2). The thermal events at 619 ± 2 °C (2) and 610 ± 2 °C (3) which are seen for all four investigated melt compositions are attributed to "Li_4Si". The first event represents the peritectic formation (from $Li_{13}Si_4$ upon cooling) of its high temperature form, the latter the transition into the low temperature form.

Thermal analysis of melts with composition $Li_{17}Si_4$, $Li_{16.5}Si_4$, $Li_{16}Si_4$, and $Li_{14}Si_4$, and the investigation of crystalline products

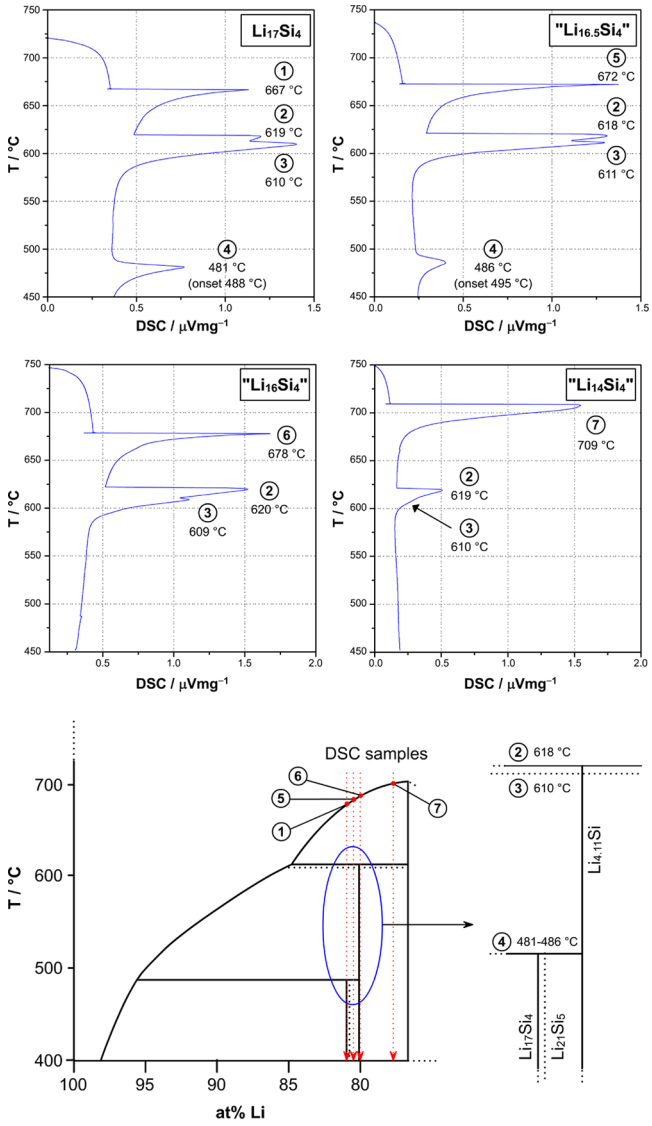

Figure 6. DSC thermograms recorded in cooling mode (from 750 °C) for $Li_{17}Si_4$ and for the nominal compositions "$Li_{16.5}Si_4$", "$Li_{16}Si_4$", and "$Li_{14}Si_4$"(top). Revised sketch of the Li−Si phase diagram with events from the DSC thermograms indicated (bottom).

from equilibrated melts Li_xSi_{100-x} ($x < 85$) at different temperatures established $Li_{17}Si_4$ as the most Li rich phase in the Li−Si system. In addition a phase "Li_4Si" ($Li_{16.42(1)}Si_4$) was detected. "Li_4Si" is not included in current Li−Si phase diagrams but its potential existence has been mentioned in the literature from the 1950s and 1960s.[37−41] Its thermodynamic relation to $Li_{17}Si_4$ and $Li_{13}Si_4$ is just sketched in this work which focuses on $Li_{17}Si_4$. Our investigations provide no evidence that $Li_{21}Si_5$ ($Li_{16.8}Si_4$), which hitherto has been considered as the most Li rich phase, is a stable phase in the Li−Si system. Especially, computational analysis of the crystal structures for $Li_{21}Si_5$ and $Li_{17}Si_4$, which were relaxed with respect to volume, lattice parameters, and atomic position parameters, thus simulating the ideal arrangement of atoms within each composition, finds a decisive discrepancy for $Li_{21}Si_5$.The occupation of the 4*a* position by additional Li may have been overlooked in the earlier work.[15] This is especially likely if there is a homogeneity range $Li_{17-x}Si_4$ ($0 \le x \le 0.2$) associated with the occupation of this position, and the site 4*a* in the crystal of

dx.doi.org/10.1021/cm400612k | Chem. Mater. 2013, 25, 1960−1967

ref 15 was only partially occupied. Again, we have no evidence for such a solid solution behavior, but we cannot rule it out.

4. CONCLUSION

The reinvestigation of the binary system Li−Si yielded $Li_{17}Si_4$ as the most Li-rich phase and casts doubts on the existence of $Li_{21}Si_5$ ($Li_{16.8}Si_4$). $Li_{17}Si_4$ is isostructural to $Li_{17}Sn_4$[16] and also $Li_{17}Ge_4$,[17] which are the Li-richest phases in their respective systems. $Li_{17}Si_4$ decomposes peritectically into a phase "Li_4Si" and melt at 481 ± 2 °C. "Li_4Si" represents either a new or rediscovered phase in the Li−Si system and details about its actual composition and complex crystal structure will be presented separately. "Li_4Si" decomposes peritectically into $Li_{13}Si_4$ and melt at temperatures around 618 °C. The discovery of $Li_{17}Si_4$ and "Li_4Si" shows that elementary relations between phases and structures in the Li−Si systems are still not completely understood. However, a sound understanding of the Li−Si phase diagram is of tremendous significance for research with high-energy lithium ion batteries when considering silicon as anode material.

■ ASSOCIATED CONTENT

Supporting Information

Details on X-ray single crystal data collection at room temperature (Table S1), refinement results (Table S2), equation of states parameters for the computationally relaxed structures of $Li_{21}Si_5$ and $Li_{17}Si_4$ (Table S3), their comparison with experimental data (Tables S4 and S5), idealized atomic position parameters for $Li_{21}Si_5$ corresponding to the body centered cubic structure (Table S6), Rietveld fit to the powder X-ray diffraction data of $Li_{17}Si_4$ employing the $Li_{21}Si_5$ structure model (Figure S1), DSC thermograms recorded for $Li_{17}Si_4$ and $Li_{16.5}Si_4$ showing the heating and cooling trace (Figures S2 and S3), powder X-ray diffraction patterns of DSC bulk samples $Li_{17}Si_4$, "$Li_{16.5}Si_4$", "$Li_{16}Si_4$", and "$Li_{14}Si_4$" (Figures S4−S7), and crystallographic information (CIF format).This material is available free of charge via the Internet at http://pubs.acs.org.

■ AUTHOR INFORMATION

Notes

The authors declare no competing financial interest.

■ ACKNOWLEDGMENTS

This work has been funded by Fonds der chemischen Industrie, TUM Graduate School, Swedish Research Council under contract number 2010-4827, and the Deutsche Forschungsgemeinschaft Project No. FA 198/11-1 as well as the National Science Foundation through grant DMR-1007557.

■ ADDITIONAL NOTE

[a]$Li_{4.106(2)}Si$ crystallizes with a = 4.5246(2) Å, b = 21.944(1) Å, c = 13.2001(6) Å (space group $Cmcm$, Z = 16, T = 100 K); quote depository numbers CSD-425864 ($Li_{4.11}Si$-100K) and CSD-425865 ($Li_{4.11}Si$-298K).

■ REFERENCES

(1) Zhang, W. J. *J. Power Sources* **2011**, *196* (1), 13−24.
(2) Obrovac, M. N.; Christensen, L. *Electrochem. Solid-State Lett.* **2004**, *7* (5), A93−A96.
(3) Hatchard, T. D.; Dahn, J. R. *J. Electrochem. Soc.* **2004**, *151* (6), A838−A842.
(4) Kwon, J. Y.; Ryu, J. H.; Oh, S. M. *Electrochim. Acta* **2010**, *55* (27), 8051−8055.
(5) Li, J.; Dahn, J. R. *J. Electrochem. Soc.* **2007**, *154* (3), A156−A161.
(6) Misra, S.; Liu, N.; Nelson, J.; Hong, S. S.; Cui, Y.; Toney, M. F. *ACS Nano* **2012**, *6* (6), 5465−5473.
(7) Wang, C. M.; Li, X. L.; Wang, Z. G.; Xu, W.; Liu, J.; Gao, F.; Kovarik, L.; Zhang, J. G.; Howe, J.; Burton, D. J.; Liu, Z. Y.; Xiao, X. C.; Thevuthasan, S.; Baer, D. R. *Nano Lett.* **2012**, *12* (3), 1624−1632.
(8) Dupke, S.; Langer, T.; Pöttgen, R.; Winter, M.; Passerini, S.; Eckert, H. *Phys. Chem. Chem. Phys.* **2012**, *14* (18), 6496−6508.
(9) Dupke, S.; Langer, T.; Pöttgen, R.; Winter, M.; Eckert, H. *Solid State Nucl. Magn. Reson.* **2012**, *42*, 17−25.
(10) Langer, T.; Dupke, S.; Trill, H.; Passerini, S.; Eckert, H.; Pöttgen, R.; Winter, M. *J. Electrochem. Soc.* **2012**, *159* (8), A1318−A1322.
(11) Key, B.; Bhattacharyya, R.; Morcrette, M.; Seznéc, V.; Tarascon, J.; Grey, C. P. *J. Am. Chem. Soc.* **2009**, *131*, 9239−9249.
(12) Key, B.; Morcrette, M.; Tarascon, J. M.; Grey, C. P. *J. Am. Chem. Soc.* **2011**, *133* (3), 503−512.
(13) Gladyshevskii, E. I.; Oleksiv, G. I.; Kripyakevich, P. I. *Kristallografiya* **1964**, *9* (3), 338−341.
(14) Axel, H.; Schäfer, H.; Weiss, A. *Z. Naturforsch.* **1966**, *21b* (2), 115−117.
(15) Nesper, R.; von Schnering, H. G. *J. Solid State Chem.* **1987**, *70* (1), 48−57.
(16) Lupu, C.; Mao, J. G.; Rabalais, J. W.; Guloy, A. M.; Richardson, J. W. *Inorg. Chem.* **2003**, *42* (12), 3765−3771.
(17) Zeilinger, M.; Fässler, T. F. Unpublished results. A reinvestigation of the Li-Ge system revealed that $Li_{17}Ge_4$ also crystallizes with the $Li_{17}Sn_4$ structure, contrary to previous reports claiming Li disorder: Goward, G. R.; Taylor, N. J.; Souza, D. C. S.; Nazar, L. F. *J. Alloys Compd.* **2001**, *329* (1−2), 82−91.
(18) Puhakainen, K.; Boström, M.; Groy, T. L.; Häussermann, U. *J. Solid State Chem.* **2010**, *183* (11), 2528−2533.
(19) *APEX Suite of Crystallographic Software*, APEX 2 Version 2008.4; Bruker AXS Inc.: Madison, WI, U.S.A., 2008.
(20) *SAINT*, Version 7.56a; Bruker AXS Inc.: Madison, WI, U.S.A., 2008.
(21) *SADABS*, Version 2008/1; Bruker AXS Inc.: Madison, WI, U.S.A., 2008.
(22) Sheldrick, G. M. *Shelxs-97 - Program for the Determination of Crystal Structures*; University of Göttingen: Göttingen, Germany, 1997.
(23) Sheldrick, G. M. *Shelxl-97 - Program for Crystal Structure Refinement*; University of Göttingen: Göttingen, Germany, 1997.
(24) Petricek, V.; Dusek, M.; Palatinus, L. *The Crystallographic Computing System*; Institute of Physics: Praha, Czech Rupublic, 2006.
(25) *TOPAS 4.0 - Rietveld Software*; Bruker AXS: Madison, WI, U.S.A., 2009.
(26) *Netzsch Proteus Thermal Analysis V4.8.2*, Netzsch-Gerätebau GmbH: Selb, Germany, 2006.
(27) Blöchl, P. E. *Phys. Rev. B* **1994**, *50* (24), 17953−17979.
(28) Kresse, G.; Joubert, D. *Phys. Rev. B* **1999**, *59* (3), 1758−1775.
(29) Kresse, G.; Hafner, J. *Phys. Rev. B* **1993**, *48* (17), 13115−13118.
(30) Kresse, G.; Furthmüller, J. *Comput. Mater. Sci.* **1996**, *6* (1), 15−50.
(31) Wang, Y.; Perdew, J. P. *Phys. Rev. B* **1991**, *44* (24), 13298−13307.
(32) Perdew, J. P.; Chevary, J. A.; Vosko, S. H.; Jackson, K. A.; Pederson, M. R.; Singh, D. J.; Fiolhais, C. *Phys. Rev. B* **1992**, *46* (11), 6671−6687.
(33) Birch, F. *Phys. Rev.* **1947**, *71* (11), 809−824.
(34) Monkhorst, H. J.; Pack, J. D. *Phys. Rev. B* **1976**, *13* (12), 5188−5192.
(35) Häussermann, U.; Svensson, C.; Lidin, S. *J. Am. Chem. Soc.* **1998**, *120* (16), 3867−3880.
(36) von Schnering, H. G.; Nesper, R.; Curda, J.; Tebbe, K. F. *Angew. Chem.* **1980**, *92*, 1070.
(37) Klemm, W.; Struck, M. *Z. Anorg. Allg. Chem.* **1955**, *278* (3−4), 117−121.
(38) Böhm, H. *Z. Metallkd.* **1959**, *50* (1), 44−46.

(39) Federov, P. I.; Ioffe, A. A. *Izv. Vyssh. Uchebn. Zaved., Tsvetn. Metall.* **1962**, *1*, 127−131.
(40) Obinata, I.; Takeuchi, Y.; Kurihara, K.; Watanabe, M. *J. Jpn. Inst. Met.* **1964**, *28*, 568−576.
(41) Schäfer, H.; Axel, H.; Weiss, A. *Z. Naturforsch.* **1965**, *20b*, 1302.
(42) Okamoto, H. *Bull. Alloy Phase Diagrams* **1990**, *11*, 306−312 and references therein.

SUPPORTING INFORMATION

Single crystal growth and thermodynamic stability of $Li_{17}Si_4$

Michael Zeilinger[†], Daryn Benson[‡], Ulrich Häussermann[‡‡], Thomas F. Fässler[†]

[†]Department Chemie, Technische Universität München, Lichtenbergstraße 4, 85747 Garching b. München, Germany

[‡]Department of Physics, Arizona State University, Tempe, Arizona 85287-1504, United States

[‡‡]Department of Materials and Environmental Chemistry, Stockholm University, SE-10691 Stockholm, Sweden

Details on single crystal X-ray data collection for $Li_{17}Si_4$ at room temperature.

Single crystal diffraction of $Li_{17}Si_4$ was performed on a Stoe IPDS IIT diffractometer equipped with a rotating anode (Bruker AXS, FR591) with MoK_α radiation (λ = 0.71073 Å) and a Montel mirror.

Table S1. Crystallographic data and structure refinement for $Li_{17}Si_4$.

empirical formula	$Li_{17}Si_4$
T (K)	298(2)
formula weight ($g \cdot mol^{-1}$)	230.34
crystal size (mm^3)	0.30 x 0.30 x 0.30
crystal colour	metallic silver
crystal shape	block
space group	$F\bar{4}3m$
unit cell dimension (Å)	
single crystal data	a = 18.7353(3)
powder data	a = 18.7259(1)
Z	20
V ($Å^3$)	6576.3(2)
ρ (calc.) ($g \cdot cm^{-3}$)	1.163
μ (mm^{-1})	0.389
F (000)	2140
θ range (deg)	3.61-29.16
index range hkl	±25, ±25, ±25
reflections collected	46589
independent reflections	935 (R_{int} = 0.054)
reflections with $I > 2\sigma(I)$	930 (R_σ = 0.010)
absorption correction	-
data/restraints/parameter	935/0/67
goodness-of-fit on F^2	1.255
final R indices [$I > 2\sigma(I)$][a, b]	R_1 = 0.020
	wR_2= 0.055
R indices (all data)[a, b]	R_1 = 0.021
	wR_2= 0.055
flack	0.5(3)
largest diff. peak and	0.26 and −0.23

hole ($e \cdot Å^{-3}$)

[a] $(R_1) = \sum \big| |F_o| - |F_c| \big| / \sum |F_o|$;

[b] $wR_2 = [\sum w(F_o^2 - F_c^2)^2 / \sum w(F_o^2)^2]^{1/2}$

Table S2. Fractional atomic coordinates and isotropic equivalent atomic displacement parameters for $Li_{17}Si_4$ ($F\bar{4}3m$, Z = 20, T = 298 K, estimated standard deviations in parentheses).

Atom	Wyckoff position	*x*	*y*	*z*	U_{eq} ($Å^2 \cdot 10^3$)
Si1	16*e*	0.15980(3)	0.15980(3)	0.15980(3)	11.4(2)
Si2	16*e*	0.91674(3)	0.91674(3)	0.91674(3)	9.6(2)
Si3	24*f*	0.32106(4)	0	0	11.6(2)
Si4	24*g*	0.57004(4)	1/4	1/4	10.9(2)
Li1	16*e*	0.0733(2)	0.0733(2)	0.0733(2)	27(1)
Li2	16*e*	0.3031(2)	0.3031(2)	0.3031(2)	20(1)
Li3	16*e*	0.4177(2)	0.4177(2)	0.4177(2)	17(1)
Li4	16*e*	0.5573(2)	0.5573(2)	0.5573(2)	22(1)
Li5	16*e*	0.6876(2)	0.6876(2)	0.6876(2)	23(1)
Li6	16*e*	0.8313(2)	0.8313(2)	0.8313(2)	27(2)
Li7	24*f*	0.1685(3)	0	0	23(1)
Li8	24*g*	0.0749(3)	1/4	1/4	23(1)
Li9	48*h*	0.0914(2)	0.0914(2)	0.2614(2)	28(1)
Li10	48*h*	0.0900(2)	0.0900(2)	0.7614(2)	27.7(9)
Li11	48*h*	0.1544(1)	0.1544(1)	0.5199(2)	26.6(7)
Li12	48*h*	0.1635(1)	0.1635(1)	0.0016(3)	22(1)
Li13	4*a*	0	0	0	16(2)

Table S3. Equation of state parameters for the computationally relaxed structures of $Li_{21}Si_5$ and $Li_{17}Si_4$.

	$Li_{21}Si_5$	$Li_{17}Si_4$
Total energy E_0 (eV/primitive cell)	-293.9462	-291.6550
Volume V_0 ($Å^3$) of primitive cell.	1601.767	1596.835
Bulk modulus K_0 (GPa)	31.49	31.10
Derivative K_0'	3.76	3.67

Table S4. Comparison of experimental and computational relaxed fractional atomic coordinates for $Li_{21}Si_5$. Experimental data are taken from ref. 15 (a = 18.710(2) Å (T = 298 K), $a_{calc.}$ = 18.55411 Å, $F-43m$, Z = 16, estimated standard deviations in parentheses). Singularly most differing Li1 is marked in bold, calculated data in italic.

Atom	Wyckoff position	*x*	*y*	*z*
Si1	16*e*	0.1595(2)	0.1595(2)	0.1595(2)
		0.1605	*0.1605*	*0.1605*
Si2	16*e*	0.9175(2)	0.9175(2)	0.9175(2)
		0.9149	*0.9149*	*0.9149*
Si3	24*f*	0.3220(3)	0	0
		0.3219	*0*	*0*
Si4	24*g*	0.5691(3)	1/4	1/4
		0.5700	*1/4*	*1/4*
Li1	**16*e***	**0.071(2)**	**0.071(2)**	**0.071(2)**
		0.0553	***0.0553***	***0.0553***
Li2	16*e*	0.304(1)	0.304(2)	0.304(2)
		0.3027	*0.3027*	*0.3027*
Li3	16*e*	0.417(1)	0.417(1)	0.417(1)
		0.4189	*0.4189*	*0.4189*
Li4	16*e*	0.559(2)	0.559(2)	0.559(2)
		0.5572	*0.5572*	*0.5572*
Li5	16*e*	0.688(2)	0.688(2)	0.688(2)
		0.6862	*0.6862*	*0.6862*
Li6	16*e*	0.829(1)	0.829(1)	0.829(1)
		0.8301	*0.8301*	*0.8301*
Li7	24*f*	0.174(2)	0	0
		0.1725	*0*	*0*
Li8	24*g*	0.073(2)	1/4	1/4
		0.0747	*1/4*	*1/4*
Li9	48*h*	0.092(1)	0.092(1)	0.262(1)
		0.0910	*0.0910*	*0.2630*
Li10	48*h*	0.088(1)	0.088(1)	0.761(1
		0.0905	*0.0905*	*0.7616*
Li11	48*h*	0.153(1)	0.153(1)	0.521(1)
		0.1550	*0.1550*	*0.5203*
Li12	48*h*	0.164(1)	0.164(1)	0.000(1)
		0.1607	*0.1607*	*0.0068*

Table S5. Comparison of experimental and computational relaxed fractional atomic coordinates for $Li_{17}Si_4$. Experimental data are from this work ($a_{exp.}$ = 18.6563(2) Å (T = 123 K), $a_{calc.}$ = 18.57319 Å, $F\bar{4}3m$, Z = 20, estimated standard deviations in parentheses). Calculated data is marked in italic.

Atom	Wyckoff position	*x*	*y*	*z*
Si1	16*e*	0.15976(1)	0.15976 (1)	0.15976 (1)
		0.1600	*0.1600*	*0.1600*
Si2	16*e*	0.91660(1)	0.91660(1)	0.91660(1)
		0.9167	*0.9167*	*0.9167*
Si3	24*f*	0.32133(1)	0	0
		0.3215	*0*	*0*
Si4	24*g*	0.57031(1)	1/4	1/4
		0.5708	*1/4*	*1/4*
Li1	16*e*	0.07410(6)	0.07410(6)	0.07410(6)
		0.0750	*0.0750*	*0.0750*
Li2	16*e*	0.30284(5)	0.30284(5)	0.30284(5)
		0.3031	*0.3031*	*0.3031*
Li3	16*e*	0.41794(7)	0.41794(7)	0.41794(7)
		0.4180	*0.4180*	*0.4180*
Li4	16*e*	0.55713(5)	0.55713(5)	0.55713(5)
		0.5572	*0.5572*	*0.5572*
Li5	16*e*	0.68687(5)	0.68687(5)	0.68687(5)
		0.6867	*0.6867*	*0.6867*
Li6	16*e*	0.83168(6)	0.83168(6)	0.83168(6)
		0.8311	*0.8311*	*0.8311*
Li7	24*f*	0.16807(8)	0	0
		0.1691	*0*	*0*
Li8	24*g*	0.07492(9)	1/4	1/4
		0.0750	*1/4*	*1/4*
Li9	48*h*	0.09068(4)	0.09068(4)	0.26186(6)
		0.0907	*0.0907*	*0.2616*
Li10	48*h*	0.09013(5)	0.09013(5)	0.76176(6)
		0.0900	*0.0900*	*0.7604*
Li11	48*h*	0.15503(4)	0.15503(4)	0.51978(6)
		0.1551	*0.1551*	*0.5193*
Li12	48*h*	0.16327(4)	0.16327(4)	0.00286(7)
		0.1635	*0.1635*	*0.0029*
Li13	4*a*	0	0	0
		0	*0*	*0*

Table S6. Idealized atomic position parameters for $Li_{21}Si_5$ corresponding to the body centered cubic structure.

Atom	Wyckoff position	*x*	*y*	*z*
Si1	16*e*	1/6 (0.1666)	1/6 (0.1666)	1/6 (0.1666)
Si2	16*e*	11/12 (0.9166)	11/12 (0.9166)	11/12 (0.9166)
Si3	24*f*	1/3 (0.3223)	0	0
Si4	24*g*	7/12 (0.5833)	1/4	1/4
Li1	16*e*	1/12 (0.0833)	1/12 (0.0833)	1/12 (0.0833)
Li2	16*e*	1/3 (0.3333)	1/3 (0.3333)	1/3 (0.3333)
Li3	16*e*	5/12 (0.4166)	5/12 (0.4166)	5/12 (0.4166)
Li4	16*e*	7/12 (0.5833)	7/12 (0.5833)	7/12 (0.5833)
Li5	16*e*	2/3 (0.6666)	2/3 (0.6666)	2/3 (0.6666)
Li6	16*e*	5/6 (0.8333)	5/6 (0.8333)	5/6 (0.8333)
Li7	24*f*	1/6 (0.1666)	0	0
Li8	24*g*	1/12 (0.0833)	1/4	1/4
Li9	48*h*	1/12 (0.0833)	1/12 (0.0833)	¼
Li10	48*h*	1/12 (0.0833)	1/12 (0.0833)	¾
Li11	48*h*	1/6 (0.1666)	1/6 (0.1666)	½
Li12	48*h*	1/6 (0.1666)	1/6 (0.1666)	0

Figures S1 – S7

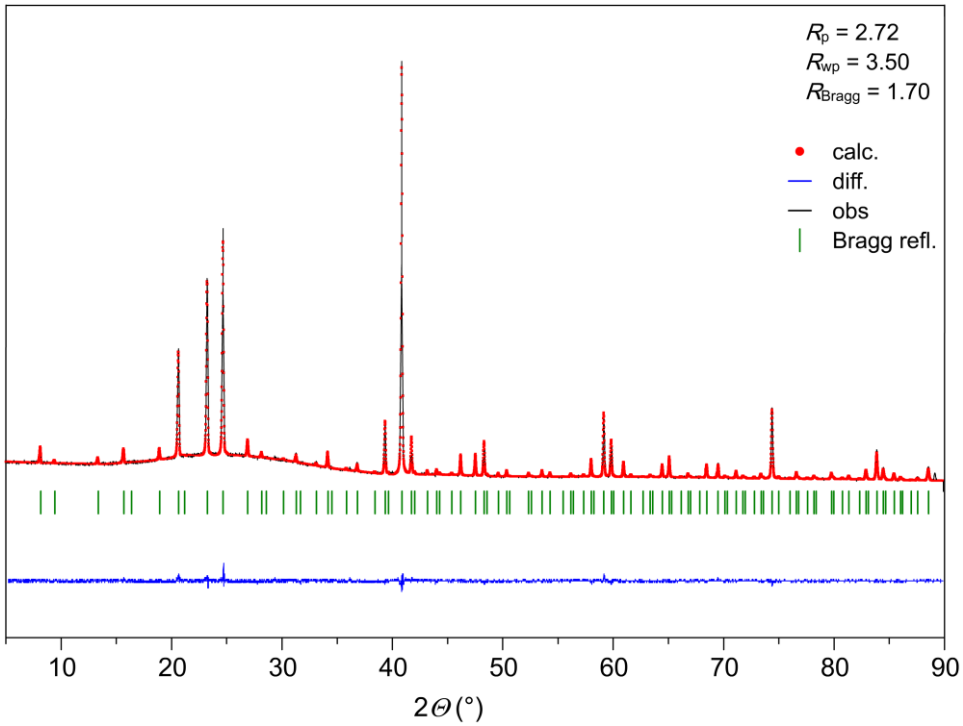

Figure S1 Rietveld fit to the powder X-Ray diffraction data of $Li_{17}Si_4$ employing the $Li_{21}Si_5$ structure model.

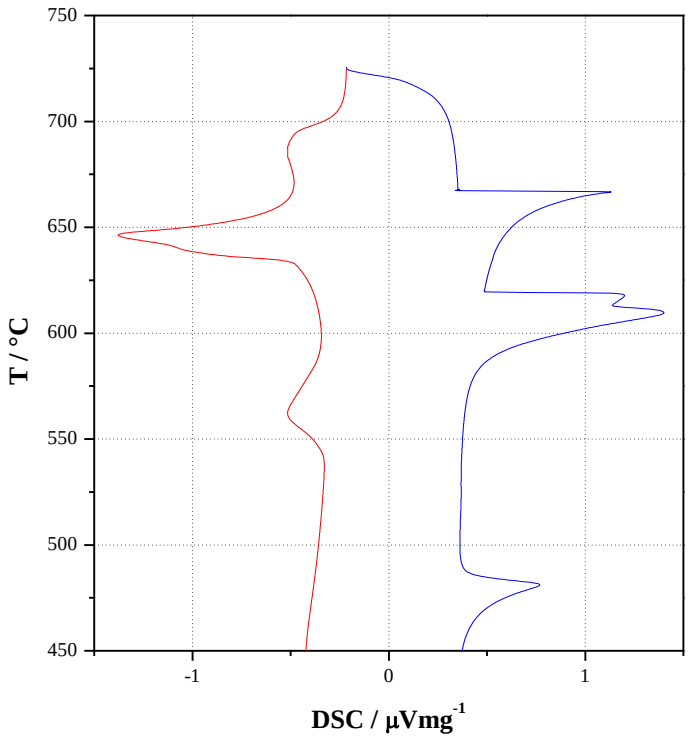

Figure S2. DSC thermogram recorded for $Li_{17}Si_4$ showing the heating (red) and cooling (blue) trace.

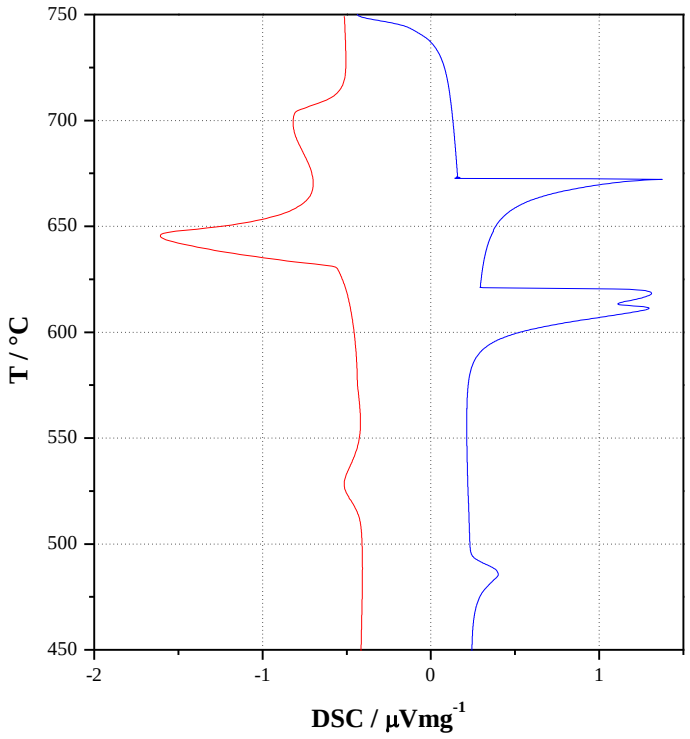

Figure S3. DSC thermogram recorded for $Li_{16.5}Si_4$ showing the heating (red) and cooling (blue) trace.

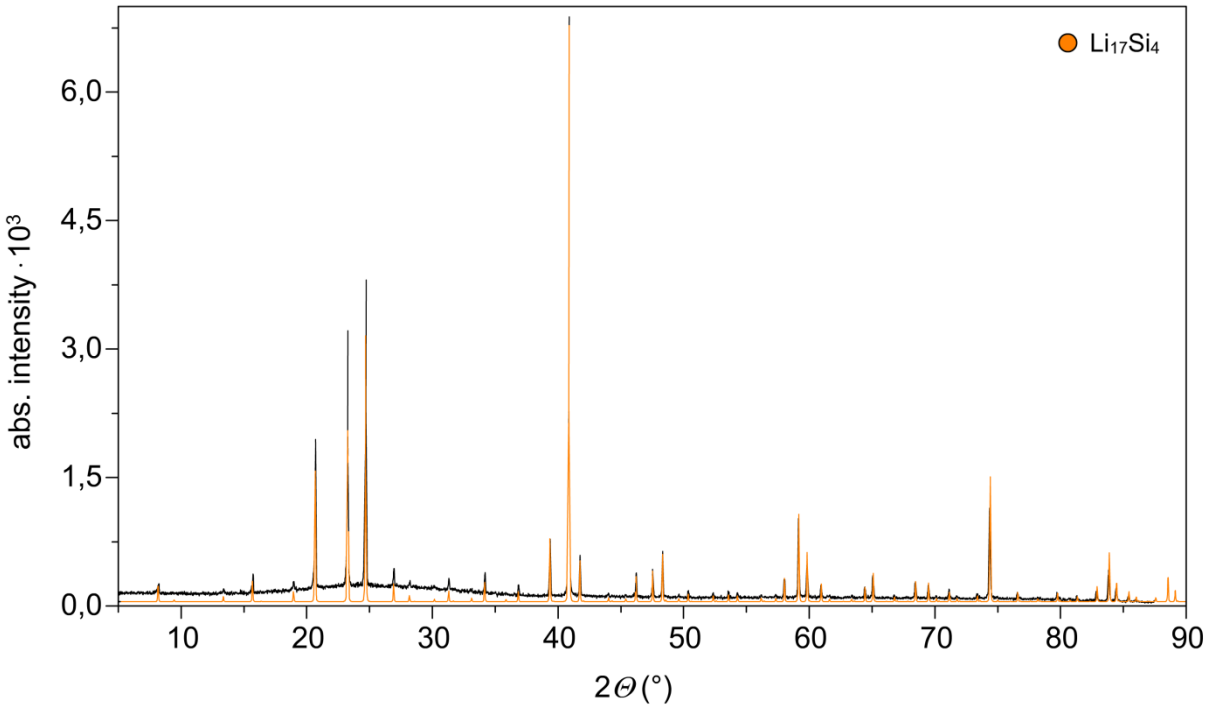

Figure S4. Powder X-ray diffraction pattern of the $Li_{17}Si_4$ bulk sample used for DSC investigations (pure $Li_{17}Si_4$; experimental = black; $Li_{17}Si_4$ calculated = yellow).

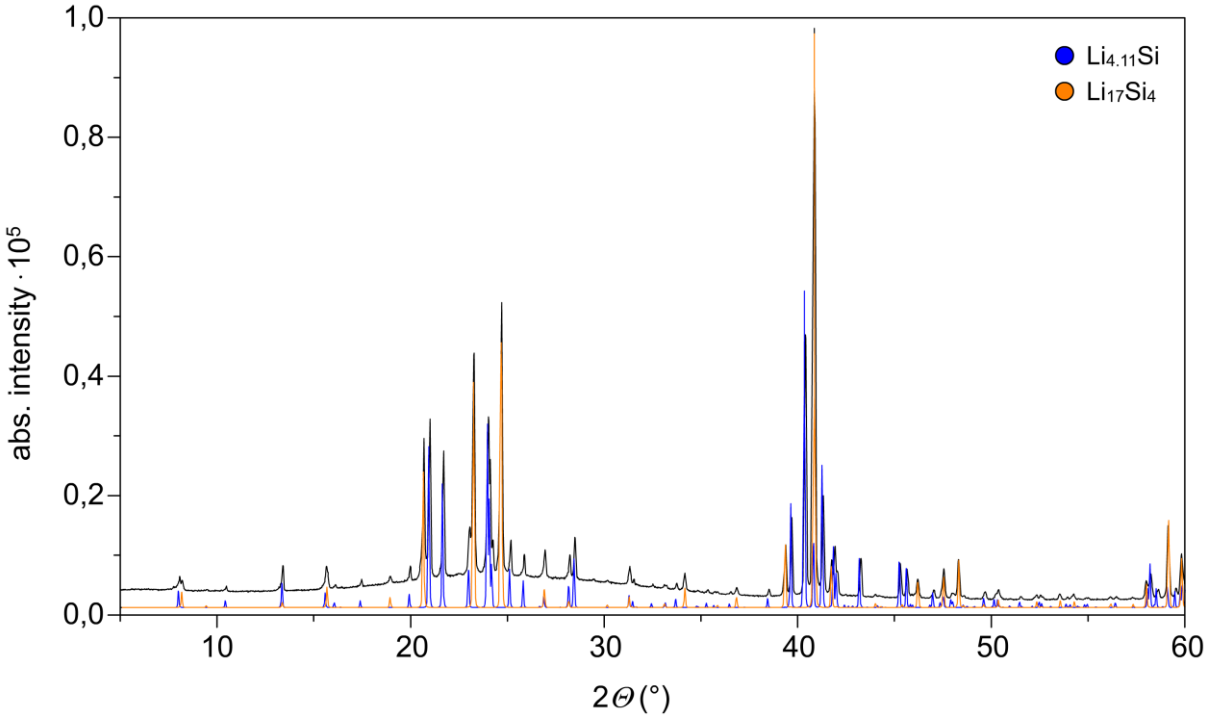

Figure S5. Powder X-ray diffraction pattern of the "$Li_{16.5}Si_4$" bulk sample used for DSC investigations (mixture of $Li_{17}Si_4$ and $Li_{4.11}Si$; experimental = black; $Li_{17}Si_4$ calculated = yellow; $Li_{4.11}Si$ calculated = blue).

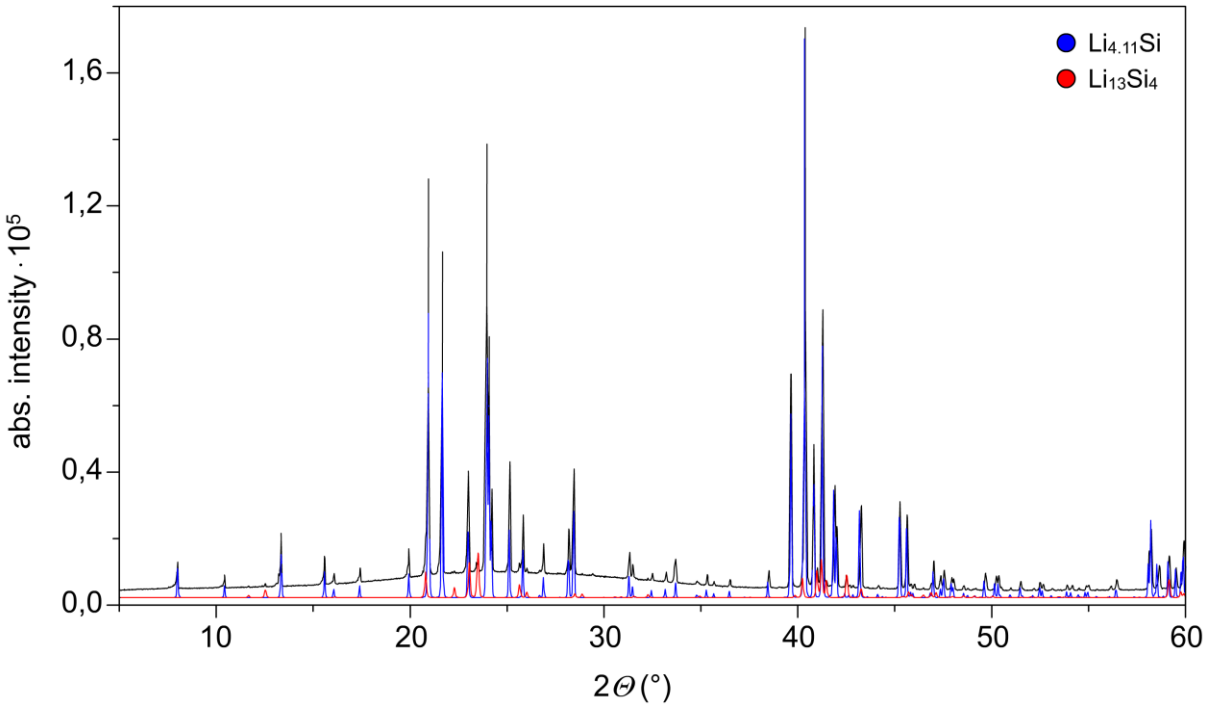

Figure S6. Powder X-ray diffraction pattern of the "Li_4Si" bulk sample used for DSC investigations ($Li_{4.11}Si$ and tiny amounts of $Li_{13}Si_4$; experimental = black; $Li_{4.11}Si$ calculated = blue; $Li_{13}Si_4$ calculated = red).

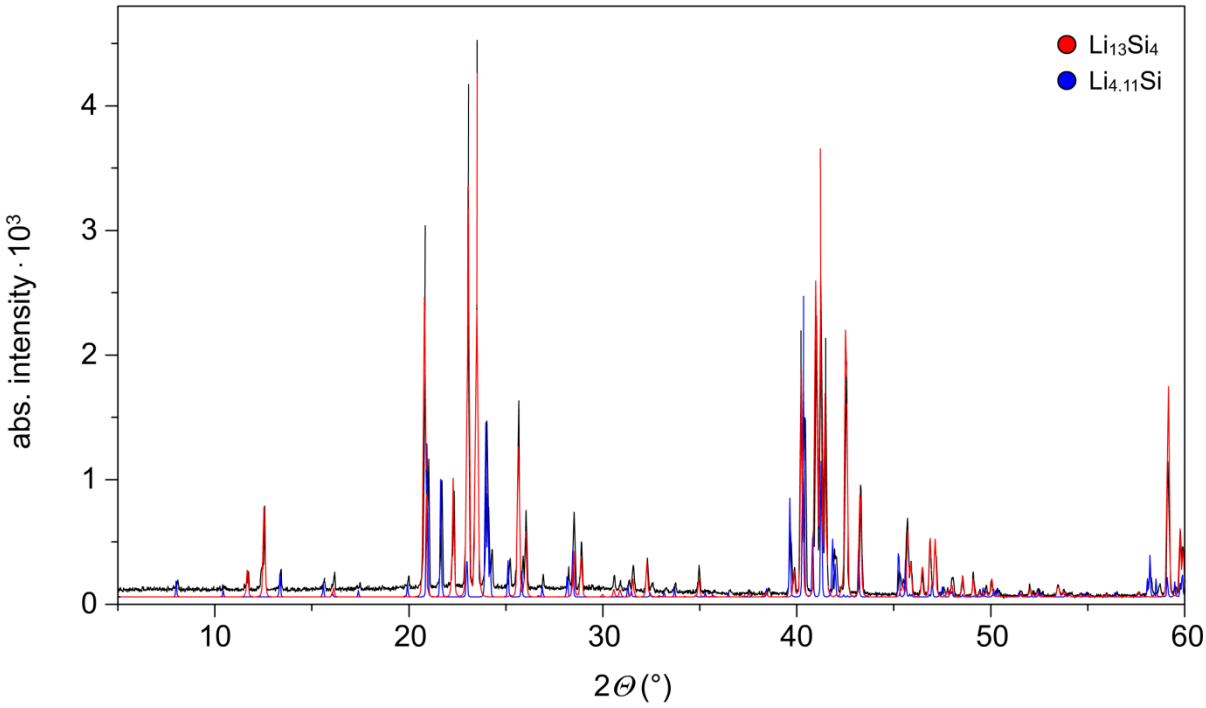

Figure S7. Powder X-ray diffraction pattern of the "$Li_{14}Si_4$" bulk sample used for DSC investigations (mixture of $Li_{13}Si_4$ and $Li_{4.11}Si$; experimental = black; $Li_{13}Si_4$ calculated = red; $Li_{4.11}Si$ calculated = blue).

5.2 Revision of the Li–Si Phase Diagram: Discovery and Single Crystal X-ray Structure Determination of the High-Temperature Phase $Li_{4.11}Si$

CHEMISTRY OF MATERIALS

Article

pubs.acs.org/cm

Revision of the Li–Si Phase Diagram: Discovery and Single-Crystal X-ray Structure Determination of the High-Temperature Phase $Li_{4.11}Si$

Michael Zeilinger,[†] Iryna M. Kurylyshyn,[†] Ulrich Häussermann,[‡] and Thomas F. Fässler*[,†]

[†]Department Chemie, Technische Universität München, Lichtenbergstraße 4, 85747 Garching b. München, Germany

[‡]Department of Materials and Environmental Chemistry, Stockholm University, 10691 Stockholm, Sweden

Supporting Information

ABSTRACT: Silicon has been regarded as a promising anode material for future lithium-ion batteries, and Li–Si phases play an important role. A detailed reinvestigation of the Li-rich part of the binary Li–Si phase diagram revealed the existence of a new phase, $Li_{4.106(2)}Si$ ($Li_{16.42}Si_4$). $Li_{16.42}Si_4$ forms through the peritectic decomposition of the Li-richest phase $Li_{17}Si_4$ at 481–486 °C and was characterized by single-crystal X-ray diffraction (a = 4.5246(2) Å, b = 21.944(1) Å, c = 13.2001(6) Å, space group $Cmcm$, Z = 16), differential scanning calorimetry, and theoretical calculations. $Li_{16.42}Si_4$ represents a high-temperature phase that is thermodynamically stable above ∼480 °C and decomposes peritectically at 618 ± 2 °C to $Li_{13}Si_4$ and a melt. $Li_{16.42}Si_4$ can be retained at room temperature. The structure consists of 3 and 10 different kinds of Si and Li atoms, respectively. Two Li positions show occupational disorder. Si atoms are well-separated from each other and have only Li atoms as nearest neighbors. This is similar to $Li_{17}Si_4$ and $Li_{15}Si_4$ compositionally embracing $Li_{16.42}Si_4$. The $SiLi_n$ coordination polyhedra in the series $Li_{15}Si_4$, $Li_{16.42}Si_4$, and $Li_{17}Si_4$ are compared. $Li_{15}Si_4$ exclusively features coordination numbers of 12, $Li_{16.42}Si_4$ of 12 and 13, and $Li_{17}Si_4$ reveals 13- and 14-coordinated Si atoms. The band structure and density of states of $Li_{16.42}Si_4$ were calculated on the basis of two ordered model structures with nominal compositions $Li_{16}Si_4$ (a hypothetical Zintl phase) and $Li_{16.5}Si_4$. Both reveal a metallic character that is analogous to $Li_{17}Si_4$. In contrast, the electronic structure of $Li_{15}Si_4$ is characteristic of a p-doped semiconductor.

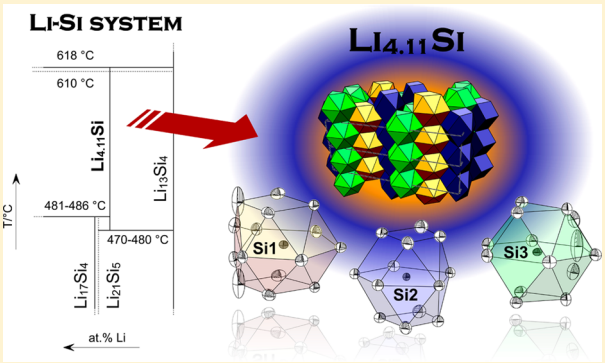

KEYWORDS: *Li_4Si, $Li_{4.11}Si$, $Li_{16.42}Si_4$, lithium silicide, thermodynamic stability of silicides, Li–Si phase diagram, Li–Si system, lithium–silicon system, lithium-ion batteries*

1. INTRODUCTION

The Li–Si system has been of great interest, particularly because silicon is regarded as promising anode material for future lithium-ion batteries (LIBs). Although silicon offers a high theoretical specific capacity, its use in such systems is accompanied with several difficulties, such as massive volume expansion during Li "insertion" combined with contact loss of electrodes and a huge capacity loss during the first cycles.[1] Many research groups have been focusing on characterizing the processes during charging and discharging of lithium. Naturally, it has been assumed that the known Li–Si phases will play an important role. Before 2004, those included $Li_{21}Si_5$,[2] $Li_{13}Si_4$,[3] Li_7Si_3,[4] $Li_{12}Si_7$,[5] and the high-pressure phase LiSi[6,7] (Figure 1). However, none of these phases were observed in a crystalline form during charging and discharging.[8,9] In 2004, Obrovac et al.[10] and Hatchard et al.[11] found a previously unknown silicide, $Li_{15}Si_4$, at discharge voltages below 50 mV by ex-situ/in situ X-ray diffraction experiments, and its structure was confirmed recently by a single-crystal structure determination.[12] The fact that intermediate phases between the fully charged and the discharged states occur predominately amorphous has fueled an increasing number of studies based on total scattering and/or NMR techniques.[13−17]

Although it appears that crystalline lithium silicides may play a minor role in the lithiation/delithiation process of Si anodes, a fundamental understanding of the Li–Si phase diagram and associated specific thermodynamic relations between lithium silicides is of considerable importance for future silicon-based LIBs. In this respect, only a few investigations have been performed. Exemplary work is given in refs 10, 11, and 18–25. Recently, we reported on the new lithium silicide $Li_{17}Si_4$, which was obtained by equilibration experiments of Li-rich melts (Li conc. > 85 at. %).[25] It is closely related to $Li_{21}Si_5$,[2] which, in turn, was formerly reported as $Li_{22}Si_5$.[26,27] Going further back in history, the first investigation of the Li–Si system can be assigned to Moissan, who, in 1902, claimed the existence of a

Received: September 5, 2013
Revised: October 10, 2013
Published: October 10, 2013

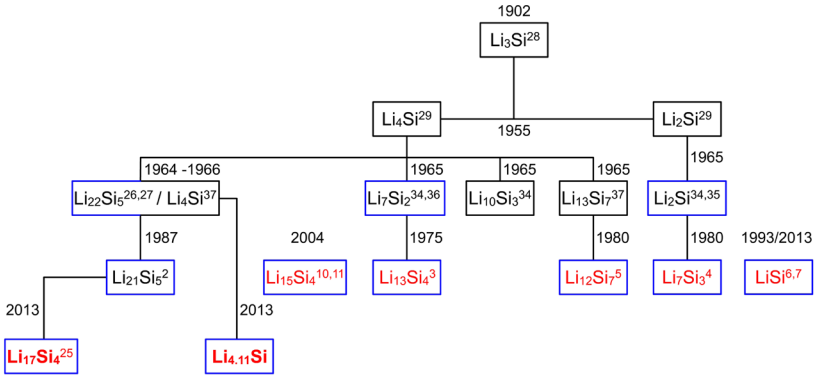

Figure 1. Chronicle of phases in the Li−Si phase system. Structurally characterized phases are marked with a blue frame, unambiguously ascertained ones are shown in red.

phase with the nominal composition Li_3Si.[28] In 1955, Klemm and Struck were not able to confirm Moissan's finding and instead postulated the phases Li_4Si and Li_2Si.[29] Those compounds were later confirmed by Pell,[30] Böhm,[31] Obinata et al.,[32] and Federov and Ioffe.[33] In the 1960s, Schäfer and Weiss recognized the complexity of the Li−Si system and identified several more phases (Figure 1).[27,34−37] In this time falls also the characterization of the phase $Li_{22}Si_5$ from powder X-ray powder diffraction by Gladyshevskii et al.[26] and single-crystal X-ray diffraction by Axel et al.[27] Later, compositions and structures of many of the phases proposed in the 1960s were revised.[2−5] However, the phase Li_4Si (Figure 1) has never been characterized structurally[37] or confirmed by later investigations and has thus disappeared from recent compilations of the Li−Si phase diagram,[38−40] despite reports on the possible existence of phases with the same composition or close to it.[41−43]

Herein, we report on a detailed analysis of the Li-rich part of the Li−Si phase diagram and the single-crystal X-ray structure determination as well as the thermodynamic stability of a not yet characterized silicide $Li_{4.11}Si$. For better comparability with phases of similar composition in this article, $Li_{4.11}Si$ will be referred to as $Li_{16.42}Si_4$. Its stability is limited to the range of 470−618 °C, and thus, $Li_{16.42}Si_4$ represents a high-temperature phase in the Li−Si phase diagram. Of particular interest are the Si coordination environments and how those change with respect to other Li-rich silicides. Furthermore, theoretical calculations for the disordered structure of $Li_{16.42}Si_4$ were approached by two idealized models and their electronic structures related to those of $Li_{15}Si_4$ and $Li_{17}Si_4$ with compositions embracing $Li_{16.42}Si_4$.

2. EXPERIMENTAL SECTION

Synthesis. Starting materials were lithium rods (99%, Rockwood-Lithium) and silicon powder (99.999%, Alfa Aesar). All steps of synthesis and sample preparation were carried out in a glovebox (MBraun, Ar atmosphere, H_2O and O_2 levels < 0.1 ppm). Tantalum ampules were thoroughly cleaned, heated to 1000 °C under dynamic vacuum ($p < 1 \times 10^{-3}$ mbar) for at least 2 h, and transferred to the glovebox. Heating and handling under inert conditions was done by using an all-glass Schlenk line supplied with Ar, which is dried over P_2O_5, a molecular sieve, and a heated titanium sponge (T = 750 °C).

Elemental mixtures with nominal compositions $Li_{17}Si_4$, "$Li_{16.5}Si_4$", "$Li_{16}Si_4$", and "$Li_{14}Si_4$" were loaded into tantalum ampules that were sealed by arc-welding inside the glove box. The total mass of samples amounted to 2.5 g. This batch size was deemed appropriate to keep weighing errors minimal for achieving targeted compositions with sufficient precision.[25] Subsequently, ampules were sealed in silica jackets under vacuum and annealed in a muffle furnace. The temperature was raised to 750 °C at a rate of 10 K·min^{-1} and held for 0.5 h, followed by cooling to 500 °C at a rate of 10 K·min^{-1}. After a dwell time of 1 h, ampules were quenched in liquid nitrogen and transferred back to the glove box. Obtained products were ground in an agate mortar and characterized by powder X-ray diffraction (cf. Figure S1 in the Supporting Information). Millimeter-sized crystals of $Li_{4.11}Si$ ($Li_{16.42}Si_4$) were obtained from equilibrating a melt with the composition "$Li_{85}Si_{15}$" at 510 °C in a tantalum ampule and subsequent isothermal melt-centrifugation.[25]

Differential Scanning Calorimetry (DSC). Differential scanning calorimetry was performed with a NETZSCH DSC 404 Pegasus apparatus. Cylindrical niobium crucibles (L = 15.0 mm, O.D. = 6.5 mm, I.D. = 5.0 mm) were thoroughly cleaned, heated to 1000 °C under dynamic vacuum ($p < 1 \times 10^{-3}$ mbar) for 2 h, and transferred to an Ar-filled glovebox. Crucibles were loaded with 30−50 mg of sample ($Li_{17}Si_4$, "$Li_{16.5}Si_4$", "$Li_{16}Si_4$", "$Li_{14}Si_4$"). The open end was roughly closed by squeezing and then sealed by arc-welding inside the glovebox under cooling. A sealed niobium crucible without a sample served as reference. All measurements were performed under an Ar-flow of 60−70 mL·min^{-1} and a heating/cooling rate of 10 K·min^{-1}. Samples were recovered after the measurement by opening the niobium crucibles inside an Ar-filled glove box. Data handling was done with the program Proteus Thermal Analysis.[44]

Annealing Experiments. To investigate the thermodynamic stability of $Li_{4.11}Si$ ($Li_{16.42}Si_4$), batches of 100−150 mg of bulk sample "$Li_{16}Si_4$" were sealed in tantalum ampules and annealed in a muffle furnace at 300, 400, 470, and 500 °C (10 K·min^{-1} heating rate) for 3 days. Thereafter, ampules were quenched in liquid nitrogen and transferred inside an argon-filled glovebox. Products were ground in an agate mortar and characterized by powder X-ray diffraction (cf. Figure S2 in the Supporting Information).

Single-Crystal X-ray Diffraction and Structure Determination. Crystals of $Li_{4.11}Si$ ($Li_{16.42}Si_4$) obtained from an equilibrated Li−Si melt according to ref 25 were handled in an Ar-filled glovebox, selected under a microscope, and sealed inside 0.5 mm glass capillaries. Intensity data were collected at 100 K on a Bruker X-ray diffractometer equipped with a CCD detector (APEX II, κ-CCD), a fine-focused sealed tube with Mo Kα radiation (λ = 0.71073 Å), and a graphite monochromator by using the Bruker APEX Software Suite.[45] Integration, data reduction, and absorption correction were done with SAINT and SADABS.[46,47] The space group *Cmcm* was assigned on the basis of the systematic absences and the statistical analysis of the intensity distributions. The structure was solved with direct methods (SHELXS-97[48]) and refined with full-matrix least-squares on F^2 (SHELXL-97[49]). Difference Fourier maps $F_o - F_c$ were calculated with JANA2006.[50] Extinction was refined to very small values and, therefore, set to zero. Atom positions were determined on the basis of successive analysis of difference Fourier maps. Two out of 10 Li positions display occupational disorder, which is described in more detail later on. Table 1 lists a summary of the refinement results. Results for room-temperature data are given in Tables S1 and S2 in the Supporting Information. Further data may be obtained from

dx.doi.org/10.1021/cm4029885 | *Chem. Mater.* 2013, 25, 4623−4632

Table 1. Crystallographic Data and Structure Refinement for $Li_{4.11}Si$

empirical formula	$Li_{4.106(2)}Si$
T/K	100(2)
formula weight/g·mol^{-1}	56.59
crystal size/mm^3	0.40 × 0.30 × 0.28
crystal color	metallic silver
crystal shape	block
space group	*Cmcm*
unit cell dimension/Å	a = 4.5246(2), b = 21.944(1), c = 13.2001(6)
V/Å^3	1310.6(1)
Z	16
ρ (calcd)/g·cm^{-3}	1.147
μ/mm^{-1}	0.390
F(000)	421
θ range/deg	1.86−45.29
index range *hkl*	±9, ±43, ±26
reflns collected	53 893
independent reflns	3052 (R_{int} = 0.020)
reflns with $I > 2\sigma(I)$	2596 (R_σ = 0.007)
data/restraints/param	3052/0/81
absorption correction	multiscan
goodness-of-fit on F^2	1.087
final R indices $[I > 2\sigma(I)]^{a,b}$	R_1 = 0.012
	wR_2 = 0.027
R indices (all data)^{a,b}	R_1 = 0.017
	wR_2 = 0.029
largest diff. peak and hole/e Å^{-3}	0.35 and −0.31

$^a R_1 = \sum||F_o| - |F_c||/\sum|F_o|$. $^b wR_2 = [\sum w(F_o^2 - F_c^2)^2/\sum w(F_o^2)^2]^{1/2}$.

Fachinformationszentrum Karlsruhe, D-76344 Eggenstein-Leopoldshafen, Germany (Fax: (+49)7247-808-666; E-mail: crysdata@fiz-karlsruhe.de) on quoting the depository numbers CSD-425864 ($Li_{4.11}Si$ ($Li_{16.42}Si_4$) 100 K) and CSD-425865 ($Li_{4.11}Si$ ($Li_{16.42}Si_4$) 298 K).

Powder X-ray Diffraction (PXRD). PXRD patterns were recorded on a Stoe STADI P diffractometer (Ge(111) monochromator for Cu Kα radiation, λ = 1.54056 Å) equipped with a Dectris MYTHEN DCS 1K solid-state detector. Ground samples were sealed inside 0.3 mm glass capillaries, and measurements were performed in a 2θ range of 5−90° (PSD steps: 0.06−1.00°; time/step: 20−40 s). Rietveld analysis of samples was performed with the TOPAS 4.0 software.[51]

Computational Details. Theoretical studies on $Li_{15}Si_4$, $Li_{16.42}Si_4$, and $Li_{17}Si_4$ were performed within density functional theory (DFT) using the full potential linearized augmented plane-wave (FP-LAPW) method as implemented in WIEN2k.[52] Exchange and correlation effects were treated by the generalized gradient approximation (GGA[53,54]) using the parametrization according to Perdew−Burke−Ernzerhof (PBE[55]). Valence configurations were $1s^2 2s^1$ and $3s^2 3p^2$ for Li and Si, respectively. R_{MT} was set equal to 2.0 au for all atoms; the value used for $R_{MT} \times K_{max}$ was 8. The disordered structure of $Li_{16.42}Si_4$ was approximated by two ordered models with nominal compositions $Li_{16}Si_4$ (Li_4Si) (model **A**) and $Li_{16.5}Si_4$ (model **B**). Their design followed symmetry considerations (cf. Figure S4 in the Supporting Information). The models are presented in the structure discussion part of $Li_{16.42}Si_4$ (Figure 6). Convergence during the SCF iteration was considered to be reached when the total energy of the system was stable within 10^{-4} Ry. The k-meshes used for the calculations were constructed according to the Monkhorst−Pack scheme[56] and corresponded to a 9 × 9 × 3 grid for model **A** ($Li_{16}Si_4$), a 5 × 3 × 4 grid mesh for model **B** ($Li_{16.5}Si_4$), and 3 × 3 × 3 grids for $Li_{15}Si_4$ and $Li_{17}Si_4$.

Geometry optimization was performed for models **A** and **B** by exploiting the quadratic approximation as implemented in the Optimize and Mini routines of WIEN2k. During the minimization procedure, forces on all atoms were fully relaxed until residual forces became smaller than 1 mRy·bohr^{-1} (≈0.026 eV·Å^{-1}). The volume and unit cell metrics of **A** and **B** corresponded to the experimental structure of $Li_{16.42}Si_4$. Electronic structure calculations were performed for the relaxed models **A** and **B** as well as for $Li_{15}Si_4$[12] and $Li_{17}Si_4$[25] using their experimental structure parameters. Fermi energy and weight of bands for the band structure calculations and corresponding DOS were computed using a modified tetrahedron method.[57] The XCrySDen code was used for data rendering and analysis.[58] Formation energies were assessed according to $\Delta E(Li_xSi) = E(Li_xSi) - x \cdot E(bcc\text{-}Li) - E(\alpha\text{-}Si)$, where $E(bcc\text{-}Li)$ and $E(\alpha\text{-}Si)$ represent the total energies of elemental structures of Li and Si per atom, and $E(Li_xSi)$ the total energy of the considered Li−Si phases per formula unit Li_xSi.

3. RESULTS AND DISCUSSION

Revision of the Li−Si Phase Diagram and Thermodynamic Stability of $Li_{16.42}Si_4$. First evidence of a not yet identified phase $Li_{16.42}Si_4$ was obtained from the equilibration of melts with compositions "$Li_{85}Si_{15}$" or "$Li_{90}Si_{10}$" at temperatures above 500 °C.[25] These experiments were targeting the crystal growth of $Li_{17}Si_4$, which was then established as the Li-richest phase in the Li−Si system. At temperatures around 510 °C, however, the product corresponded to a mixture of crystals of $Li_{17}Si_4$ and an unknown phase.

Figure 2 shows thermograms from bulk samples $Li_{17}Si_4$, "$Li_{16.5}Si_4$", "$Li_{16}Si_4$", and "$Li_{14}Si_4$" recorded in cooling mode. According to PXRD analysis (Figure S1 in the Supporting Information), these samples correspond to pure-phase $Li_{17}Si_4$, a mixture of phases $Li_{17}Si_4$ and $Li_{16.42}Si_4$, and mixtures of phases $Li_{16.42}Si_4$ and $Li_{13}Si_4$, respectively. When cooling melts with the considered compositions from 750 °C, the first thermal effect (labeled as (1), (2), (3), and (4) in Figure 2) is assigned to the crossing of the liquidus boundary. $Li_{17}Si_4$ forms peritectically at 481 ± 2 °C (event (7)) from a melt and $Li_{16.42}Si_4$.[25] The thermograms of all compositions persistently show thermal effects at 618 ± 2 °C (event (5)) and 610 ± 2 °C (event (6)). Signal (5) is tentatively assigned to the peritectic formation of $Li_{16.42}Si_4$. The origin of the second effect at 610 °C is not yet clear. It may be associated with a structural change of disordered $Li_{16.42}Si_4$. However, it may be as well that, between 610 and 618 °C, a phase with yet another composition (a high-temperature phase) exists, which forms peritectically at 618 °C and from which $Li_{16.42}Si_4$ forms at 610 °C. An unambiguous elucidation would only be possible by an in situ structural study (e.g., PXRD) covering this temperature range. Long-term annealing experiments of samples "$Li_{16}Si_4$" between 200 and 500 °C revealed that, at temperatures below 470 °C, the phase $Li_{16.42}Si_4$ decomposes into $Li_{17}Si_4$ and $Li_{13}Si_4$. The PXRD patterns of products of these annealing experiments are compiled in Figure S2 in the Supporting Information. We note that the peritectoid decomposition of $Li_{16.42}Si_4$ into $Li_{17}Si_4$ and $Li_{13}Si_4$ proceeds very slowly. A complete decomposition is not even achieved after 3 days of annealing at 400 °C. The long-term annealing experiments manifest $Li_{16.42}Si_4$ as a high-temperature phase, which, however, can be retained at room temperature.

As a consequence of our DSC and annealing experiments, a revision of the Li−Si phase diagram according to Figure 3 is suggested. We emphasize that this part (Li conc. > 76 at. %) still contains two uncertainties: first, it is not yet clear whether $Li_{17}Si_4$ possesses a homogeneity range;[25] and second is the assignment of the already discussed isotherms at 610 and 618 °C. As mentioned in the Introduction, the existence of a phase

dx.doi.org/10.1021/cm4029885 | *Chem. Mater.* 2013, 25, 4623−4632

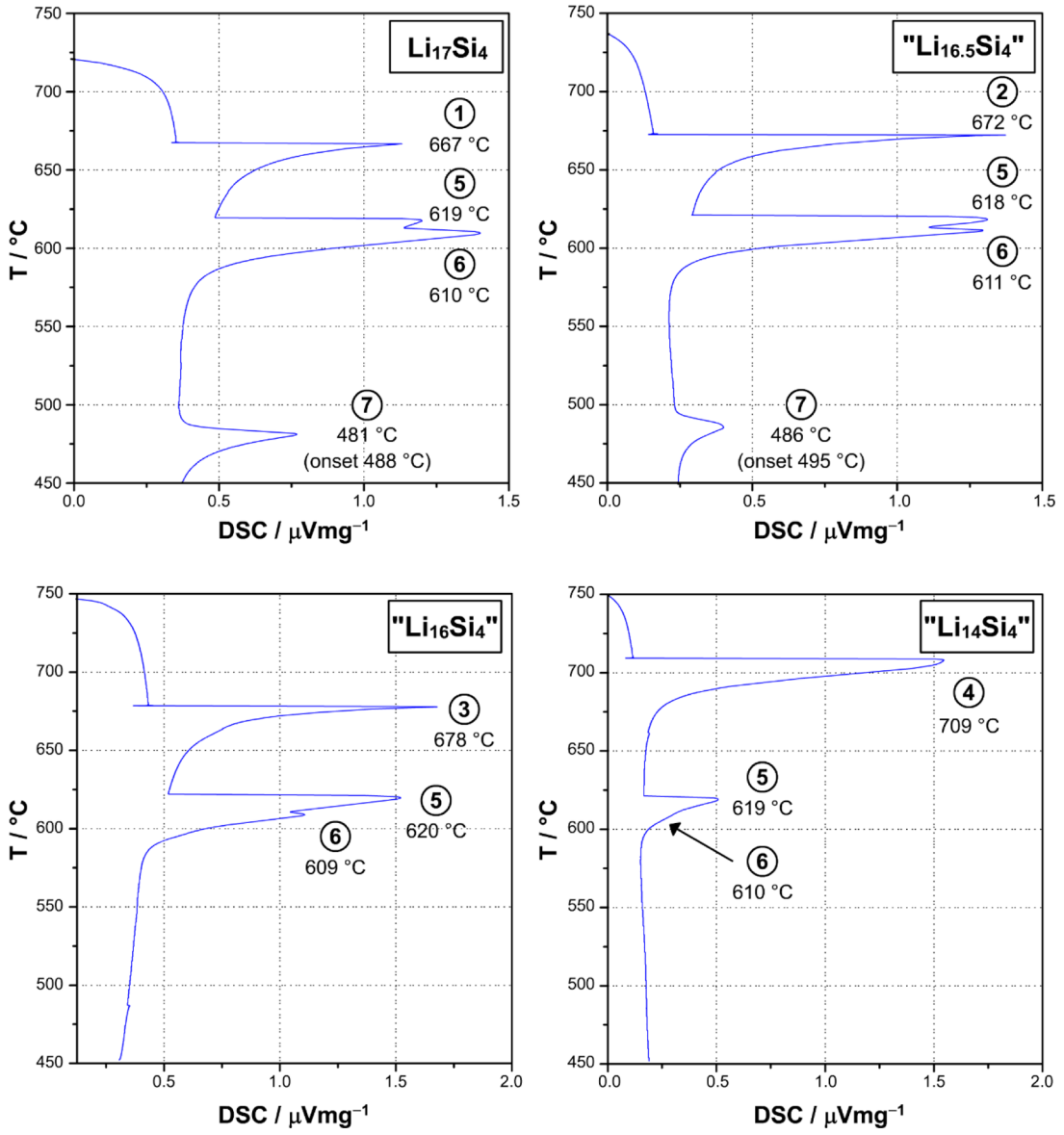

Figure 2. DSC thermograms recorded in cooling mode (from 750 °C) for $Li_{17}Si_4$ and nominal compositions "$Li_{16.5}Si_4$", "$Li_{16}Si_4$", and "$Li_{14}Si_4$" (according to ref 25). Thermal effects are assigned in an updated Li−Si phase diagram in Figure 3.

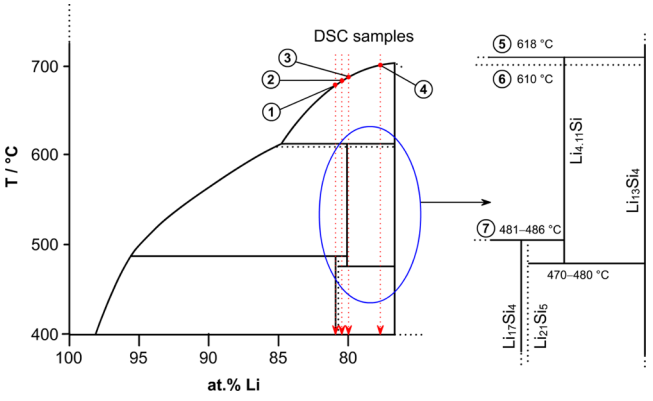

Figure 3. Revised Li−Si phase diagram (modified on the basis of ref 25) with thermal events from current DSC investigations and long-term annealing experiments of "$Li_{16}Si_4$" samples.

"Li_4Si" has been described in the earlier literature.[29−33,59] However, a conclusive characterization has never been performed and eventually "Li_4Si" became obscure, presumably because of the several Li−Si phases with a similar composition. We note in passing that our reinvestigation of the Li−Ge system revealed the existence of a phase $Li_{16.38(2)}Ge_4$ for this system as well.[60]

Determination and Description of the Structure of $Li_{16.42}Si_4$. $Li_{16.42(1)}Si_4$ crystallizes with the orthorhombic space group *Cmcm*, with a = 4.5246(2) Å, b = 21.944(1) Å, c = 13.2001(6) Å (V = 1310.6(1) Å^3), and Z = 16 (referring to $Li_{4.106(2)}Si$ as one formula unit). The unit cell contains 3 distinct Si atom positions (16 Si atoms in total) and 10 Li positions (Table 2). Two of the Li positions (Li4 and Li5) display occupational disorder. Whereas the split position of Li5 was easily extracted from difference Fourier maps, the assignment of Li4 was somewhat peculiar. Figure 4a shows that significant residual electron density is located along the a axis in a strandlike shape. The peak maxima correspond to the sites 4*c* (1/2, y, 1/4) and 8*g* (x, y, 1/4). Too small interatomic distances prohibit their simultaneous occupancy (Figure 4b).

dx.doi.org/10.1021/cm4029885 | *Chem. Mater.* 2013, 25, 4623−4632

Table 2. Fractional Atomic Coordinates and Isotropic Equivalent Atomic Displacement Parameters for $Li_{4.11}Si$ (*Cmcm*, *Z* = 16, *T* = 100 K, Estimated Standard Deviations in Parentheses)

atom	Wyckoff position	*x*	*y*	*z*	*s.o.f*	$U_{eq}/Å^2 \cdot 10^3$
Si1	4*c*	0	0.256155(4)	1/4	1	7.89(2)
Si2	4*c*	1/2	0.454324(4)	1/4	1	6.81(2)
Si3	8*f*	1/2	0.105366(3)	0.067645(5)	1	7.75(1)
Li1	4*c*	1/2	0.03270(3)	1/4	1	13.4(1)
Li2	4*c*	1/2	0.32951(3)	1/4	1	12.7(1)
Li3	4*c*	0	0.39263(3)	1/4	1	16.5(1)
Li4A	4*c*	1/2	0.14744(7)	1/4	0.575(3)	43.5(7)
Li4B	8*g*	0.2084(3)	0.13867(5)	1/4	0.425(3)	18.1(3)
Li5A	8*f*	0	0.17392(4)	0.0849(1)	0.848(7)	14.2(2)
Li5B	8*f*	0	0.1641(3)	0.1246(9)	0.152(7)	18(2)
Li6	8*f*	0	0.04654(2)	0.12217(4)	1	13.09(8)
Li7	8*f*	0	0.31629(3)	0.07895(4)	1	15.35(8)
Li8	8*f*	0	0.47119(3)	0.09071(4)	1	18.14(9)
Li9	8*f*	1/2	0.23121(3)	0.13577(4)	1	17.96(9)
Li10	8*f*	1/2	0.40459(2)	0.06398(4)	1	14.02(8)

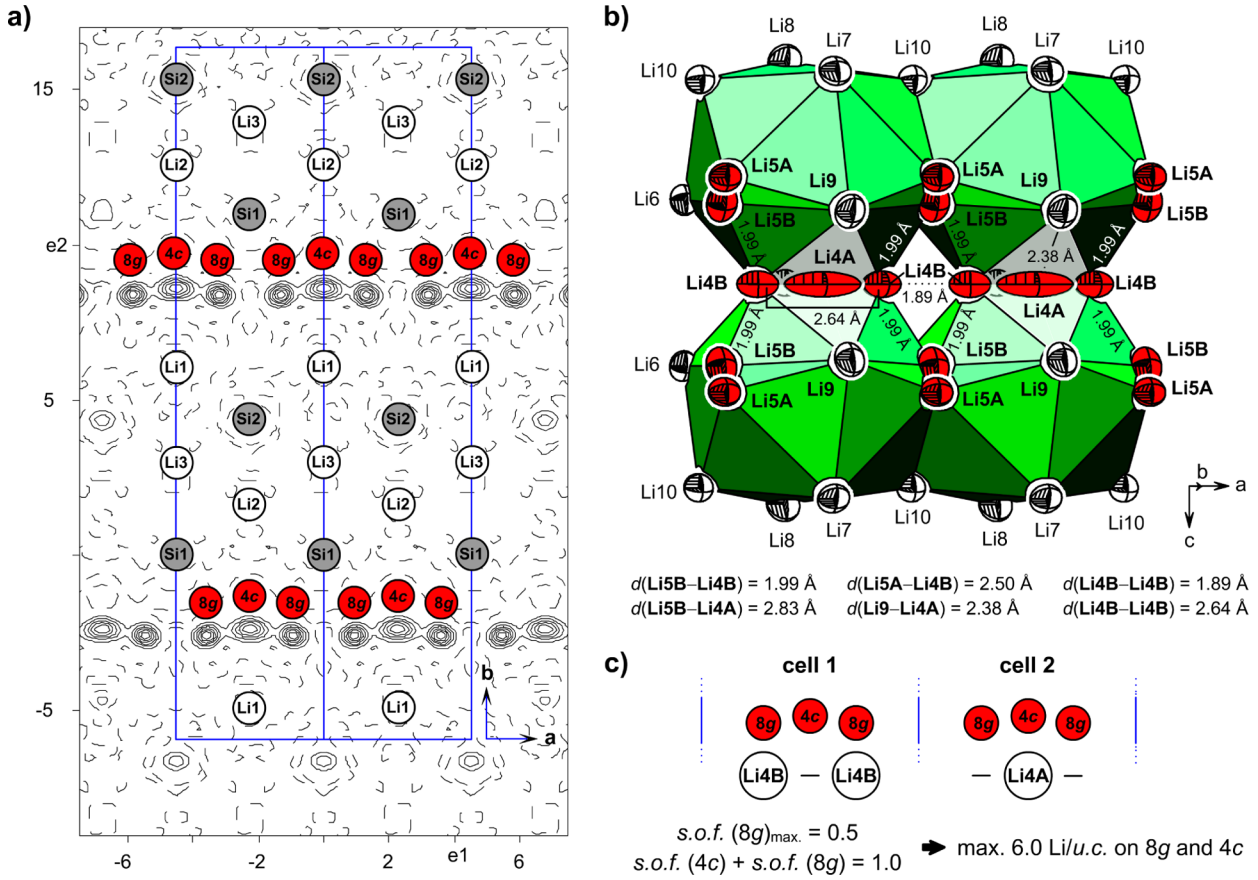

Figure 4. (a) Difference Fourier map ($F_o - F_c$, contour lines ± 0.6 e·Å^{-3}) shown for the layer defined by Si1, Si2, and Li2 (parallel to *ab* plane; cell edges are shown in blue; calculated from single-crystal data at 100 K). (b) The structural environment of the disordered Li-strand with view on the *ac* plane (perpendicular to the extracted plane for the difference Fourier map in (a). (c) Schematic description of an idealized disorder model for Li4; thermal ellipsoids are shown at a 90% probability level.

The sum of refined occupancies yielded a value very close to 1. Therefore, the sum of occupancy factors was constrained to 1, and the two sites were assigned Li4A and Li4B, respectively. The structure was then refined with excellent reliability factors of R_1 = 0.017 and wR_2 = 0.029 for all data (cf. Table 1). A meaningful anisotropic refinement of atomic displacement parameters was possible for all atoms. Because of the disorder, the unit cell contains 65.70(3) Li atoms, and the crystallographic density of $Li_{16.42(1)}Si_4$ is 1.147 g·cm^{-3}. In the following, we elaborate briefly on the disorder in $Li_{16.42}Si_4$; further details are described in the Supporting Information.

The refined proportions of Li4A (site 4*c*) and Li4B (site 8*g*) are 0.575(3) and 0.425(3), respectively. An occupancy of Li4B below 0.5 allows for an arrangement of Li atoms that excludes distances *d*(Li−Li) < 1.89 Å (Figure 4c). In this case, the Li4B site may be occupied in every other unit cell, whereas cells void

dx.doi.org/10.1021/cm4029885 | *Chem. Mater.* 2013, 25, 4623−4632

Table 3. Relevant Interatomic Distances in $Li_{4.11}Si$ (*Cmcm*, $Z = 16$, $T = 100$ K, Estimated Standard Deviations in Parentheses)

atom pair			d/Å	atom pair			d/Å	atom pair			d/Å
Si1	Li5B	2×	2.612(5)	Si3	Li7		2.5884(5)	Li4B	Li1		2.674(1)
	Li7	2×	2.6152(5)		Li8		2.6817(5)		Li6	2×	2.797(1)
	Li4B	2×	2.745(1)		Li6	2×	2.7023(3)		Li9	2×	2.853(1)
	Li9	4×	2.7733(3)		Li5B	2×	2.710(2)	Li5A	Li4B	2×	2.498(2)
	Li2	2×	2.7766(4)		Li5A	2×	2.7263(4)		Li10		2.613(2)
	Li5A	2×	2.830(1)		Li4B	2×	2.8406(7)		Li9	2×	2.6739(5)
	Li3		2.9948(7)		Li10	2×	2.8609(3)		Li6		2.838(1)
	Li4A	2×	3.288(1)		Li1		2.8873(4)		Li7		3.125(1)
Si2	Li6	2×	2.6348(5)		Li9		2.9042(7)		Li7	2×	3.137(1)
	Li3	2×	2.6364(4)		Li8		2.9600(7)	Li5B	Li6		2.579(6)
	Li10	2×	2.6870(5)	Li4A	Li9	2×	2.378(1)		Li9	2×	2.704(3)
	Li2		2.7388(7)		Li1		2.518(2)		Li4A	2×	2.827(7)
	Li1	2×	2.8419(4)		Li5B	4×	2.827(7)		Li10		2.910(8)
	Li8	4×	3.1106(4)	Li4B	Li5A	2×	2.498(2)				
Si3	Li4A		2.5781(6)		Li4B		2.639(3)				

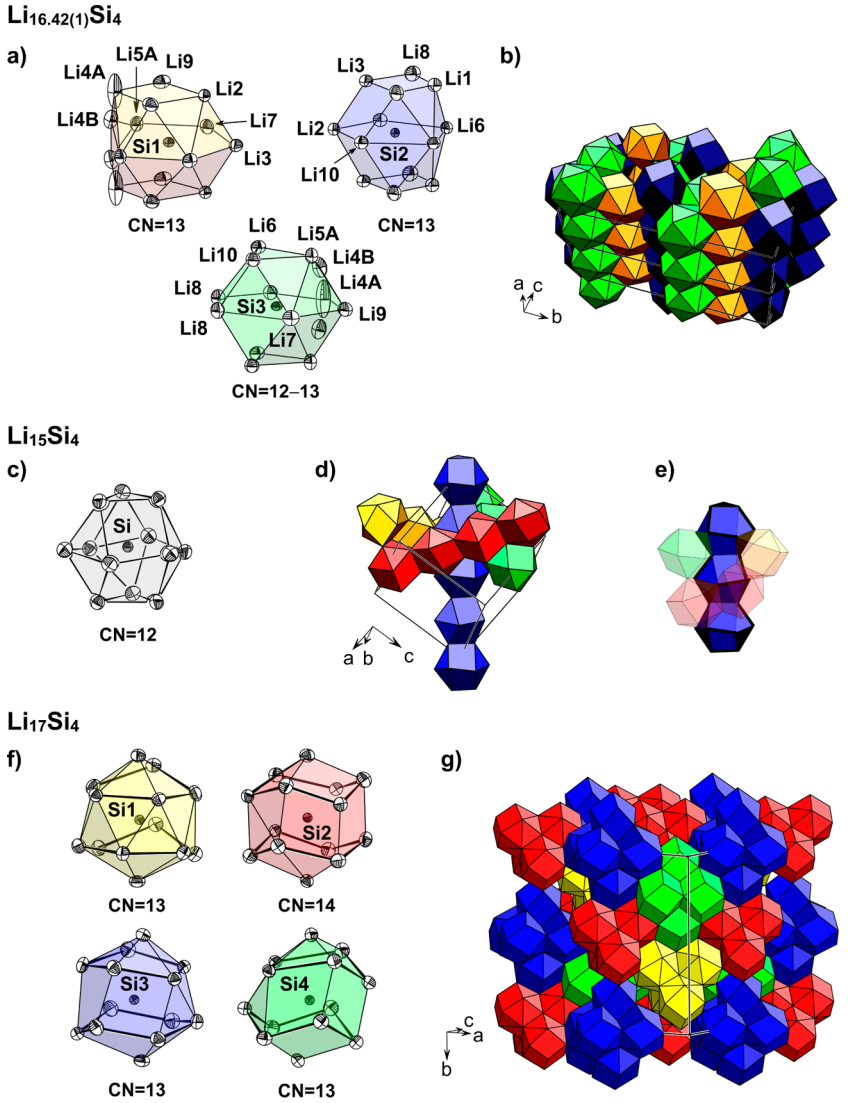

Figure 5. Structural details of $Li_{16.42}Si_4$ (a, b), $Li_{15}Si_4$ (c–e), and $Li_{17}Si_4$ (f, g). Parallel rods of face-sharing Si coordination polyhedra (a) and their relative arrangement in the unit cell of $Li_{16.42}Si_4$ (b). Chains of distorted anticuboctahedron units [Si@Li_{12}] (c) proceeding along the 3-fold axes of the cubic unit cell of $Li_{15}Si_4$ (d; different directions are indicated by different colors of the polyhedra) and (e) their relative arrangement (shared edges and faces in black). Clusters of Si centered polyhedra appear in $Li_{17}Si_4$ (f, g) that form supratetrahedra (yellow and red) and supraoctahedra (blue and green); thermal ellipsoids are shown at a 90% probability level.

dx.doi.org/10.1021/cm4029885 | *Chem. Mater.* 2013, 25, 4623–4632

of Li4B would contain Li4A. The scenario corresponds to 0.5 occupation of each Li4A and Li4B site (i.e., maximal 6 Li atoms per unit cell (u.c.) on 4*c* and 8*g*) and is in reasonable close agreement with the refinement result (5.70(3) Li atoms/u.c. on 4*c* and 8*g*). The disorder described by Li4A/Li4B has then consequences to the split position of Li5 (Li5A/0.848(7) and Li5B/0.152(7)). The presence of a Li5B atom excludes the simultaneous presence of Li4B in the same cell because distances Li4B−Li5B are unreasonably short (1.99 Å, cf. Figure 4b).

In the structure of $Li_{16.42}Si_4$, the Si atoms are exclusively coordinated by Li atoms. Nearest-neighbor distances range from 2.38 to 3.29 Å (Table 3) and are well-separated from next-nearest-neighbor ones starting off at 4.07 Å. The $SiLi_n$ coordination polyhedra for Si1−Si3 are shown in Figure 5a. Disorder affects the coordination of Si1 and Si3 atoms. Si1 and Si2 atoms are 13-coordinated, whereas Si3 atoms attain either a 12- or a 13-coordination, depending on whether Li4A or Li4B is occupied. SiL_n polyhedra are further condensed into strands running along the *a* direction by sharing opposite faces (Figure 5b). Strands of polyhedra are connected via sharing vertices, edges, and faces. Similar to $Li_{16.42}Si_4$, the structures of $Li_{15}Si_4$ and $Li_{17}Si_4$ can also be built from $SiLi_n$ coordination polyhedra. All three structures have in common that Si atoms are separated from each other by more than 4.4 Å. In the $Li_{15}Si_4$ structure, Si atoms are exclusively 12-coordinated in a distorted anti-cuboctahedral fashion (Figure 5c).

This coordination is closely related to that of atoms in an *hcp* packing.[12] Similar to $Li_{16.42}Si_4$, polyhedra are condensed into strands via sharing opposite (triangular) faces (Figure 5d). Strands run parallel to the body diagonals (3-fold axes) in the cubic unit cell and are connected by sharing common edges and faces (Figure 5e). The four directions of the cubic cell are indicated by different colors in Figure 5d. In the Li-richest phase $Li_{17}Si_4$, two different $SiLi_n$ coordinations occur, with n = 13 and n = 14 (Figure 5f). The $Li_{17}Si_4$ structure is closely related to a 6 × 6 × 6 superstructure of the *bcc* structure[25] in which the Si atoms occupy specific positions. Emphasizing the Si atom arrangement, Si_4 tetrahedra (Si1 and Si2) and Si_6 octahedra (Si3 and Si4) appear, which form together with their Li coordination spheres equal numbers of supratetrahedra (red and yellow) and supraoctahedra (green and blue). The $SiLi_n$ polyhedra share vertices, edges, and faces to give the arrangement shown in Figure 5g. One way to interpret the $Li_{17}Si_4$ structure is to consider the arrangement of supra-tetrahedra and supraoctahedra as two interpenetrating supra-diamond structures (corresponding to a hierarchical variant of the NaTl structure type) by sharing common edges. In conclusion, the series $Li_{15}Si_4$, $Li_{16.42}Si_4$, and $Li_{17}Si_4$ shows the gradual enlargement of SiL_n coordination polyhedra (n = 12−14) with increasing Li content.

The disorder of the Li4A and Li4B atoms in $Li_{16.42(1)}Si_4$ may be resolved in two alternative ordered models **A** and **B** (Figure 6). Structure model **A** excludes Li4B on 8*g* (*x*, *y*, 1/4) but includes fully occupied Li4A at 4*c* (1/2, *y*, 1/4) and Li5A positions. As a consequence, Si3 coordinates to 12 Li atoms and Si1 to 13 Li atoms. The composition of model **A** is $Li_{16}Si_4$ (Li_4Si). Ordered model **B** includes both sites Li4B on 8*g* (*x*, *y*, 1/4) and Li4a on 4*c* (1/2, *y*, 1/4), each with 50% occupancy. Model **B** cannot be realized in the actual space group *Cmcm*. Two crystallographically independent Li4B positions (i.e., Li4B and Li4B′, Figure 6) are achieved by a symmetry reduction and a larger unit cell (space group $P2_1/m$, a = 9.0492(4) Å, b = 13.2001(6) Å, c = 11.2027(5) Å, β = 101.650°, the Li5 position is presented by Li5A; for the Bärnighausen tree, see Figure S4 in the Supporting Information). In model **B**, Si3 alternately coordinates to 12 and 13 Li atoms, whereas the Si1 coordination polyhedron comprises exclusively 13 Li atoms as in model **A**. The composition of model **B** is $Li_{16.5}Si_4$ ($Li_{4.125}Si$) (Figure 6).

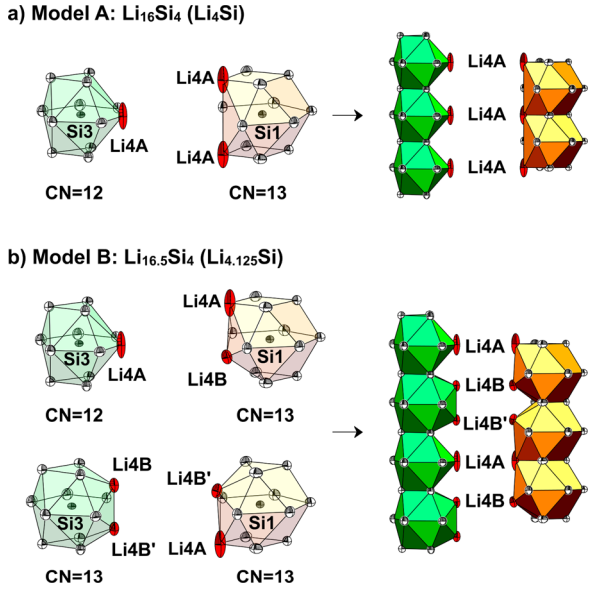

Figure 6. Two alternative models for $Li_{16.42}Si_4$ with an ordered distribution of Li atoms. (a) In model **A**, Li4A and Li5A are fully occupied and Li4B and Li5B are void (resulting composition: $Li_{16}Si_4$). (b) Model **B** includes a fully occupied Li5A position and half occupied positions Li4A and Li4B (resulting composition: $Li_{16.5}Si_4$). Si, Li (ordered), and Li (disordered) atoms are shown as gray, white, and red ellipsoids, respectively. All displacement ellipsoids are drawn at a 90% probability level.

Electronic Structure of $Li_{4.11}Si$. Theoretical studies on $Li_{16.42}Si_4$ were approached on the basis of the two ordered structure models **A** and **B**. Since these models represent an approximation to the real structure of $Li_{16.42}Si_4$, Hellmann−Feynman forces on specific atoms are expected. However, after geometry optimization, atom positions were found only marginally different from their starting values. The formation energies of the model structures are very different, −0.67 and −1.35 Ry for **A** and **B**, respectively, implying that model **B** is highly favored over **A**. Model **B** has a composition close to $Li_{16.42}Si_4$, and its structure probably also represents a good approximation to the experimental crystal structure. $Li_{17}Si_4$, the most rich Li−Si phase, attains a formation energy of −1.78 Ry and metastable $Li_{15}Si_4$ −0.68 Ry, which is very similar to model **A**.

The results of electronic structure calculations of the three Li silicides are compiled in Figure 7. We first note their similar overall electronic structure. The s-bands stemming from Si atoms are only weakly dispersed and confined in the energy range from −6.5 to −7.5 eV below the Fermi level. Because they are not significant to bonding properties, they have been excluded in Figure 7. Also, the shape and width of the Si-p bands starting off at around −3 eV and terminating at around the Fermi level are very similar for the four structures. Strong Li−Si bonding interactions are apparent from the significant mixing of Li states into these bands. Interesting are the differences around the Fermi level. The DOS of $Li_{15}Si_4$ actually

dx.doi.org/10.1021/cm4029885 | *Chem. Mater.* 2013, 25, 4623−4632

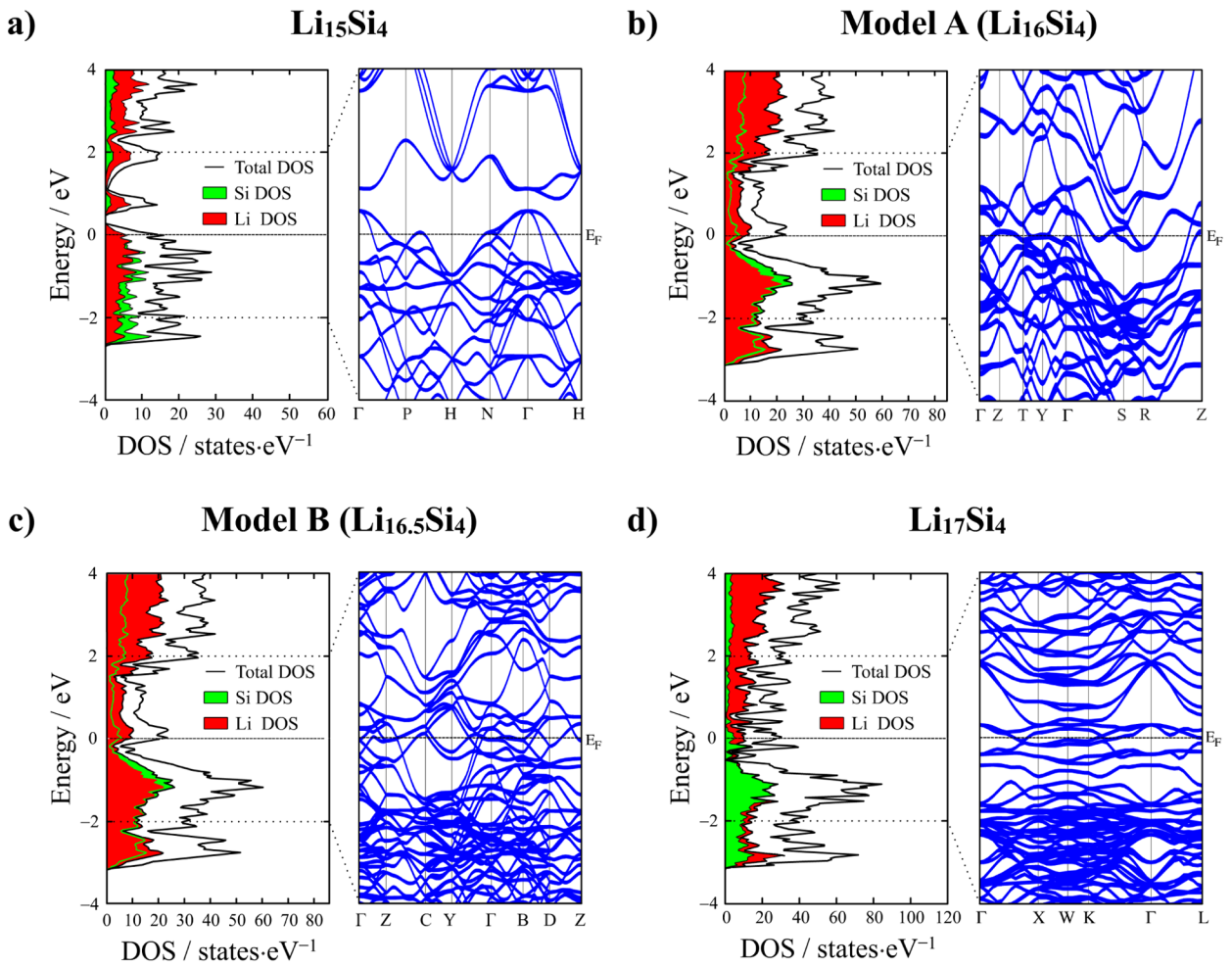

Figure 7. Total and partial DOS together with the band structure representation in the range from −4 to 4 eV for (a) $Li_{15}Si_4$, (b) structure model **A** ($Li_{16}Si_4$), (c) structure model **B** ($Li_{16.5}Si_4$), and (d) $Li_{17}Si_4$.

shows a small band gap (0.1 eV) just above the Fermi level, separating the Si-p bands from a peculiar narrow band centered approximately at 0.7 eV above the Fermi level. The band structure is in agreement with earlier reports[19] and suggests that $Li_{15}Si_4$ could reach a semiconducting state with one additional electron per formula unit (assuming a rigid band behavior). This would be in agreement with a Zintl phase description $(Si^{4-})_4$.[61] Therefore, $Li_{15}Si_4$ may be considered as a p-doped semiconductor. When turning to the model structures **A** and **B**, however, it is apparent that the Si-p band does not follow a rigid band behavior for states around the Fermi level. For model **A** with a composition $Li_{16}Si_4$ appropriate for a Zintl phase, the band gap present in $Li_{15}Si_4$ has closed and the system represents a metallic conductor. The "$Li_{15}Si_4$ gap" is also absent in the DOS and band structure for model **B** and for $Li_{17}Si_4$. Provided a rigid band behavior, for those systems, this gap should be situated below the Fermi level. Both systems clearly reveal a metallic character.

In conclusion, among the Li-rich silicides, only $Li_{15}Si_4$ displays an electronic structure that is characteristic of a Zintl phase, yet $Li_{15}Si_4$ is electron-deficient. Interestingly, it has been shown that a small concentration of Li can be exchanged for Al ($Li_{15-x}Al_xSi_4$, $x \approx 0.5$),[12] which increases the electron concentration of the system. When going from $Li_{15}Si_4$ to more Li-rich phases, the electronic structure changes decisively around the Fermi level. This is attributed to the altered Li−Si bonding interactions.

4. CONCLUSION

The binary lithium silicide $Li_{4.11}Si$ ($Li_{16.42}Si_4$) was synthesized, and its thermodynamic relation with $Li_{17}Si_4$ and $Li_{13}Si_4$ in the Li−Si phase system was firmly established. $Li_{16.42}Si_4$ forms from the peritectic decomposition of $Li_{17}Si_4$ and decomposes peritectically at 618 ± 2 °C. The crystal structure is rather complex and displays some occupational disorder affecting Li positions. The accumulation of Li-rich phases in the interval of 75−81 at. % Li is characteristic of Li-tetrel (Si, Ge, Sn) systems. It is a consequence of rather strong covalent Li-tetrel bonding interactions that, in turn, make the application of structure-bonding correlations according to the Zintl−Klemm concept difficult or even impossible.[62] Among the Li−Si phases, only the most Si-rich equimolar LiSi, which is metastable and accessible through high-pressure techniques or high-energy ball-milling,[6,7] displays a structure in unambiguous agreement with the Zintl−Klemm concept. It features a three-dimensional network of three-bonded Si atoms.[6] Reaching the area of the Li-rich side, now various lithium silicides are established in the phase diagram and structurally characterized even though crystalline lithium silicides are considered to play a minor role in the lithiation/delithiation process of Si anodes. The here reported $Li_{16.42}Si_4$ might not appear during charging/discharg-

dx.doi.org/10.1021/cm4029885 | Chem. Mater. 2013, 25, 4623−4632

ing processes since it represents a high-temperature phase. However, $Li_{16.42}Si_4$ reveals important structural information since it is in line with the description of the Li-rich structures presented here as $SiLi_n$ polyhedra with increasing n from 12 to 14 going from $Li_{15}Si_4$ to $Li_{17}Si_4$. Interestingly, although $Li_{17}Si_4$, $Li_{16.42}Si_4$, and $Li_{15}Si_4$ are metallic and have very similar compositions, they appear without significant phase width.

■ ASSOCIATED CONTENT

Supporting Information

Details on single-crystal X-ray data collection at room temperature of $Li_{16.42}Si_4$ (Table S1), fractional atomic coordinates and isotropic equivalent displacement parameters (Table S2), PXRD patterns of bulk samples $Li_{17}Si_4$, "$Li_{16.5}Si_4$", "$Li_{16}Si_4$", and "$Li_{14}Si_4$" (Figure S1), PXRD patterns of samples "$Li_{16}Si_4$" annealed at different temperatures for 3 days (Figure S2), Rietveld fit to the X-ray powder diffraction pattern of $Li_{16.42}Si_4$ (Figure S3), Bärnighausen tree for generating ordered structure models of $Li_{16.42}Si_4$ (Figure S4) (PDF), and crystallographic information (CIF format). This material is available free of charge via the Internet at http://pubs.acs.org.

■ AUTHOR INFORMATION

Corresponding Author

*E-mail: Thomas.Faessler@lrz.tum.de.

Notes

The authors declare no competing financial interest.

■ ACKNOWLEDGMENTS

This work has been funded by Fonds der Chemischen Industrie, the Deutsche Forschungsgemeinschaft project number FA 198/11-1, the Swedish Research Council (Project No. 2010-4827) and the National Science Foundation through grant DMR-1007557.

■ REFERENCES

(1) Zhang, W. J. *J. Power Sources* **2011**, *196*, 13.
(2) Nesper, R.; von Schnering, H. G. *J. Solid State Chem.* **1987**, *70*, 48.
(3) Frank, U.; Müller, W.; Schäfer, H. *Z. Naturforsch.* **1975**, *30b*, 10.
(4) von Schnering, H. G.; Nesper, R.; Tebbe, K. F.; Curda, J. *Z. Metallkd.* **1980**, *71*, 357.
(5) von Schnering, H. G.; Nesper, R.; Curda, J.; Tebbe, K. F. *Angew. Chem.* **1980**, *92*, 1070.
(6) Evers, J.; Oehlinger, G.; Sextl, G. *Angew. Chem., Int. Ed. Engl.* **1993**, *32*, 1442.
(7) Tang, W. S.; el Chotard, J.-N.; el Janotz, R. *J. Electrochem. Soc.* **2013**, *160*, A1232.
(8) Limthongkul, P.; Jang, Y. I.; Dudney, N. J.; Chiang, Y. M. *Acta Mater.* **2003**, *51*, 1103.
(9) Limthongkul, P.; Jang, Y. I.; Dudney, N. J.; Chiang, Y. M. *J. Power Sources* **2003**, *119–121*, 604.
(10) Obrovac, M. N.; Christensen, L. *Electrochem. Solid-State Lett.* **2004**, *7*, A93.
(11) Hatchard, T. D.; Dahn, J. R. *J. Electrochem. Soc.* **2004**, *151*, A838.
(12) Zeilinger, M.; Baran, V.; Häussermann, U.; Fässler, T. F. *Chem. Mater.* **2013**, *25*, 4113.
(13) Key, B.; Bhattacharyya, R.; Morcrette, M.; Seznec, V.; Tarascon, J. M.; Grey, C. P. *J. Am. Chem. Soc.* **2009**, *131*, 9239.
(14) Key, B.; Morcrette, M.; Tarascon, J. M.; Grey, C. P. *J. Am. Chem. Soc.* **2011**, *133*, 503.
(15) Kuhn, A.; Sreeraj, P.; Pöttgen, R.; Wiemhöfer, H. D.; Wilkening, M.; Heitjans, P. *J. Am. Chem. Soc.* **2011**, *133*, 11018.
(16) Dupke, S.; Langer, T.; Pöttgen, R.; Winter, M.; Passerini, S.; Eckert, H. *Phys. Chem. Chem. Phys.* **2012**, *14*, 6496.
(17) Dupke, S.; Langer, T.; Pöttgen, R.; Winter, M.; Eckert, H. *Solid State Nucl. Magn. Reson.* **2012**, *42*, 17.
(18) Stearns, L. A.; Gryko, J.; Diefenbacher, J.; Ramachandran, G. K.; McMillan, P. F. *J. Solid State Chem.* **2003**, *173*, 251.
(19) Xu, Y. H.; Yin, G. P.; Zuo, P. J. *Electrochim. Acta* **2008**, *54*, 341.
(20) Chevrier, V. L.; Zwanziger, J. W.; Dahn, J. R. *J. Alloys Compd.* **2010**, *496*, 25.
(21) Debski, A.; Gasior, W.; Goral, A. *Intermetallics* **2012**, *26*, 157.
(22) Gruber, T.; Thomas, D.; Roder, C.; Mertens, F.; Kortus, J. *J. Raman Spectrosc.* **2013**, *44*, 934.
(23) Wang, P.; Kozlov, A.; Thomas, D.; Mertens, F.; Schmid-Fetzer, R. *Intermetallics* **2013**, *42*, 137.
(24) Thomas, D.; Abdel-Hafiez, M.; Gruber, T.; Huttl, R.; Seidel, J.; Wolter, A. U. B.; Buchner, B.; Kortus, J.; Mertens, F. *J. Chem. Thermodyn.* **2013**, *64*, 205.
(25) Zeilinger, M.; Benson, D.; Häussermann, U.; Fässler, T. F. *Chem. Mater.* **2013**, *25*, 1960.
(26) Gladyshevskii, E. I.; Oleksiv, G. I.; Kripyakevich, P. I. *Kristallografiya* **1964**, *9*, 338.
(27) Axel, H.; Schäfer, H.; Weiss, A. *Z. Naturforsch.* **1966**, *21b*, 115.
(28) Moissan, H. *C. R. Hebd. Séances Acad. Sci.* **1902**, *134*, 1083.
(29) Klemm, W.; Struck, M. *Z. Anorg. Allg. Chem.* **1955**, *278*, 117.
(30) Pell, E. M. *Phys. Chem. Solids* **1957**, *3*, 77.
(31) Böhm, H. *Z. Metallkd.* **1959**, *50*, 44.
(32) Obinata, I.; Takeuchi, Y.; Kurihara, K.; Watanabe, M. *J. Jpn. Inst. Met.* **1964**, *28*, 568.
(33) Federov, P. I.; Ioffe, A. A. *Izv. Vyssh. Uchebn. Zaved., Tsvetn. Metall.* **1962**, *1*, 127.
(34) Schäfer, H.; Axel, H.; Menges, E.; Weiss, A. *Z. Naturforsch.* **1965**, *20b*, 394.
(35) Axel, H.; Schäfer, H.; Weiss, A. *Angew. Chem., Int. Ed. Engl.* **1965**, *4*, 358.
(36) Schäfer, H.; Axel, H.; Weiss, A. *Z. Naturforsch.* **1965**, *20b*, 1010.
(37) Schäfer, H.; Axel, H.; Weiss, A. *Z. Naturforsch.* **1965**, *20b*, 1302.
(38) Demidov, A. I.; Morachevskii, A. G.; Nikolaev, V. P.; Berenda, N. V. *J. Appl. Chem. (USSR)* **1988**, *61*, 1254.
(39) (a) Okamoto, H. *Bull. Alloy Phase Diagrams* **1990**, *11*, 306 and references therein. (b) Okamoto, H. *J. Phase Equilib. Diffus.* **2009**, *30*, 118.
(40) Braga, M. H.; Malheiros, L. F.; Ansara, I. *J. Phase Equilib.* **1995**, *16*, 324 and references therein.
(41) Sharma, R. A.; Seefurth, R. N. *J. Electrochem. Soc.* **1976**, *123*, 1763.
(42) Lai, S. C. *J. Electrochem. Soc.* **1976**, *123*, 1196.
(43) Nikolaev, V. P.; Morachevskii, A. G.; Demidov, A. I.; Bairachnyi, E. V. *J. Appl. Chem. (USSR)* **1980**, *53*, 1549.
(44) *Netzsch Proteus Thermal Analysis*, Version 4.8.2; Netzsch-Gerätebau GmbH: Selb, Germany, 2006.
(45) *APEX 2: APEX Suite of Crystallographic Software*, Version 2008.4; Bruker AXS Inc.: Madison, WI, 2008.
(46) *SAINT*, Version 7.56a; Bruker AXS Inc.: Madison, WI, 2008.
(47) *SADABS*, Version 2008/1; Bruker AXS Inc.: Madison, WI, 2008.
(48) Sheldrick, G. M. *Shelxs-97: Program for the Determination of Crystal Structures*; University of Göttingen: Göttingen, Germany, 1997.
(49) Sheldrick, G. M. *Shelxl-97: Program for Crystal Structure Refinement*; University of Göttingen: Göttingen, Germany, 1997.
(50) Petricek, V.; Dusek, M.; Palatinus, L. *Jana 2006: The Crystallographic Computing System*, Version 03/15/2013; Institute of Physics: Praha, Czech Rupublic, 2006.
(51) *TOPAS: Rietveld Software*, Version 4.0; Bruker AXS Inc.: Madison, WI, 2009.
(52) Blaha, P.; Schwarz, K.; Madsen, G. K. H.; Kvasnicka, D.; Luitz, J. *WIEN2k: An Augmented Plane Wave and Local Orbitals Program for Calculating Crystal Properties*, Version 12.0; Technische Universität Wien: Vienna, Austria, 2001.
(53) Wang, Y.; Perdew, J. P. *Phys. Rev. B* **1991**, *44*, 13298.
(54) Perdew, J. P.; Chevary, J. A.; Vosko, S. H.; Jackson, K. A.; Pederson, M. R.; Singh, D. J.; Fiolhais, C. *Phys. Rev. B* **1992**, *46*, 6671.

(55) Perdew, J. P.; Burke, K.; Ernzerhof, M. *Phys. Rev. Lett.* **1996**, *77*, 3865.
(56) Monkhorst, H. J.; Pack, J. D. *Phys. Rev. B* **1976**, *13*, 5188.
(57) Blöchl, P. E.; Jepsen, O.; Andersen, O. K. *Phys. Rev. B* **1994**, *49*, 16223.
(58) Kokalj, A.*Comput. Mater. Sci.* **2003**, *28*, 155. Code availabe from http://www.xcrysden.org.
(59) An orthorhombic base face-centered orthorhombic cell with a = 34.4 ± 0.1 Å, b = 25.0 ± 0.1 Å, c = 4.49 ± 0.01 Å was reported for the composition "Li_4Si" with the cell volume being approximately 3 times that of $Li_{4.11}Si$.[37] For two reported samples, the densities were 1.19 g·cm^{-3} (50 Si and 200 Li atoms/u.c.) and 1.18 g·cm^{-3} (48 Si and 200 Li atoms/u.c.).[37] These ratios are similar to $Li_{4.11}Si$ corresponding to 48 Si atoms (Z = 48) and 197.1(1) Li atoms/u.c.).
(60) $Li_{4.10}Ge$ is isotypic with $Li_{4.11}Si$ and crystallizes with a = 4.5511(2) Å, b = 22.0862(7) Å, c = 13.2751(4) Å, V = 1334.37(8) Å^3 (single-crystal data, space group *Cmcm*, Z = 16, T = 123 K).
(61) (a) Zintl, E. *Angew. Chem.* **1939**, *52*, 1. (b) Klemm, W. *Proc. Chem. Soc.* **1958**, 329. (c) Klemm, W.; Busmann, E. *Z. Anorg. Allg. Chem.* **1963**, *319*, 297.
(62) Nesper, R. *Prog. Solid State Chem.* **1990**, *20*, 1.

SUPPORTING INFORMATION

Revision of the Li–Si Phase Diagram: Discovery and Single Crystal X-ray Structure Determination of the High Temperature Phase $Li_{4.11}Si$

Michael Zeilinger, Iryna M. Kurylyshyn, Ulrich Häussermann, Thomas F. Fässler*

Details on the single crystal X-ray structure refinement of $Li_{4.11}Si$

As shown in the crystallographic section of this article, the disorder in the $Li_{4.11}Si$ structure affects Li5 on 8*f*, Li4A on 4*c* and Li4B on 8*g* (Table 2). If the occupancies for Li4A and Li4B are refined freely, the values converge to 0.577(5) and 0.425(3), respectively, with the sum being very close to one. Thus, the constrain *occ*(Li4A) + *occ*(Li4B) = 1, which excludes a simultaneous occupancy of both sites, is justified. The variables then converge to 0.575(3) and 0.425(3). Furthermore, it was demonstrated in the structure discussion part that the maximum occupancy of Li4B is 0.5, as higher values would give rise to unreasonably short Li–Li distances by neighboring Li4B–Li4B pairs (Figure 4). An interpretation of the example *occ*(Li4A) = *occ*(Li4B) = 0.5, which represents the maximum accumulation of Li on those sites (6 Li atoms/*u.c.*), is highlighted as well.

Furthermore, a careful analysis of residual electron densities during the structure refinement procedure elucidated further positional disorder for Li5 on 8*f*. The atom split reveals *occ*(Li5A) = 0.848(7) and *occ*(Li5B) = 0.152(7), respectively (Table 2). Again, a free refinement delivers equal results (*occ*(Li5A) = 0.851(8) and *occ*(Li5B) = 0.155(8)). It might be speculated that due to the weak scattering power of lithium introducing a split position with a small split fraction for Li5B is not meaningful. However, when deleting Li5B for the refinement, the occupancy of Li5 (former Li5A) refines to 0.950(5) and significant residual electron density is almost exactly located at the former Li5B position (+1.238 $e \cdot Å^{-3}$). The reliability factors for all data are $R_1 = 0.023$ and $wR_2 = 0.047$. Without ignoring the atom split, we obtain markedly lower *R*-values of $R_1 = 0.017$ and $wR_2 = 0.029$ for all data and very small (as well as balanced) residual electron densities (+0.35 $e \cdot Å^{-3}$ and −0.31 $e \cdot Å^{-3}$).

Details on the single crystal X-ray data collection for $Li_{4.11}Si$ at room temperature

Single crystal diffraction of $Li_{4.11}Si$ was performed on a Stoe IPDS IIT diffractometer equipped with a rotating anode (Bruker AXS, FR591) with MoK_α radiation (λ = 0.71073 Å) and a Montel mirror.

Table S1. Crystallographic data and structure refinement for $Li_{4.11}Si$ at 298 K.

empirical formula	$Li_{4.105(6)}Si$
T / K	298(2)
formula weight / g·mol^{-1}	56.59
crystal size / mm^3	0.40 × 0.30 × 0.28
crystal color	metallic silver
crystal shape	block
space group	*Cmcm*
unit cell dimension / Å	a = 4.5467(9), b = 22.065(4), c = 13.240(3)
V / Å^3	1328.3(5)
Z	16
ρ (calc.) / g·cm^{-3}	1.132
μ / mm^{-1}	0.385
F (000)	421
θ range / °	8.47–30.49
index range *hkl*	±6, ±31, ±18
reflections collected	15579
independent reflections	1120 (R_{int} = 0.047)
reflections with $I > 2\sigma(I)$	1049 (R_σ = 0.015)
data/restraints/parameter	1120/0/81
absorption correction	–
goodness-of-fit on F^2	1.206
Final R indices [$I > 2\sigma(I)$][a, b]	R_1 = 0.019
	wR_2 = 0.031
R indices (all data)[a, b]	R_1 = 0.021
	wR_2 = 0.032
Largest diff. peak and hole / e·Å^{-3}	0.15 and −0.14

[a] $R_1 = \sum \big| |F_o| - |F_c| \big| / \sum |F_o|$

[b] $wR_2 = [\sum w(F_o^2 - F_c^2)^2 / \sum w(F_o^2)^2]^{1/2}$

Table S2. Fractional atomic coordinates and isotropic equivalent atomic displacement parameters for $Li_{4.11}Si$ (*Cmcm*, $Z = 16$, $T = 298$ K, estimated standard deviations in parentheses).

Atom	Wyckoff position	*x*	*y*	*z*	*s.o.f*	U_{eq} / $Å^2 \cdot 10^3$
Si1	4*c*	0	0.25634(1)	¼	1	13.02(6)
Si2	4*c*	½	0.45423(1)	¼	1	12.38(6)
Si3	8*f*	½	0.105557(7)	0.06740(1)	1	12.62(5)
Li1	4*c*	½	0.03229(8)	¼	1	25.1(3)
Li2	4*c*	½	0.32954(7)	¼	1	21.7(3)
Li3	4*c*	0	0.39256(9)	¼	1	32.1(4)
Li4A	4*c*	½	0.1473(2)	¼	0.58(1)	64(3)
Li4B	8*g*	0.213(1)	0.1390(2)	¼	0.42(1)	43(2)
Li5A	8*f*	0	0.1736(2)	0.0858(6)	0.91(3)	25.5(9)
Li5B	8*f*	0	0.162(2)	0.128(5)	0.09(3)	22(9)
Li6	8*f*	0	0.04662(5)	0.12234(9)	1	22.5(2)
Li7	8*f*	0	0.31628(6)	0.07904(9)	1	27.6(2)
Li8	8*f*	0	0.47120(7)	0.0909(1)	1	35.5(3)
Li9	8*f*	½	0.23095(6)	0.1362(1)	1	27.8(2)
Li10	8*f*	½	0.40482(6)	0.06375(8)	1	25.4(2)

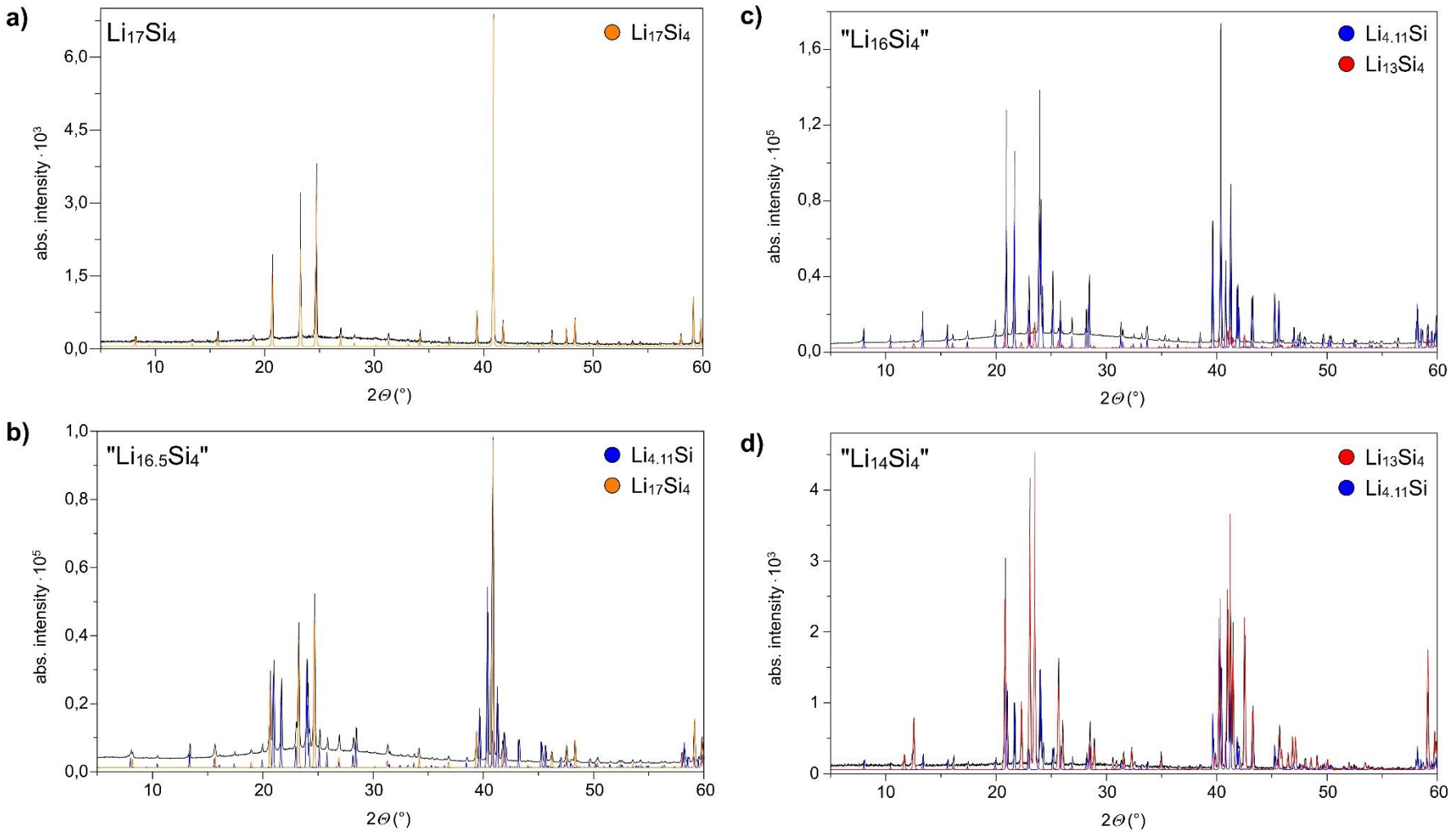

Figure S1. PXRD patterns of the bulk samples $Li_{17}Si_4$ (a), $Li_{16.5}Si_4$ (b), $Li_{16}Si_4$ (c) and $Li_{14}Si_4$ (d) (experimental = black, $Li_{17}Si_4$ (calc.) = yellow, $Li_{4.11}Si$ (calc.) = blue, $Li_{13}Si_4$ (calc.) = red).

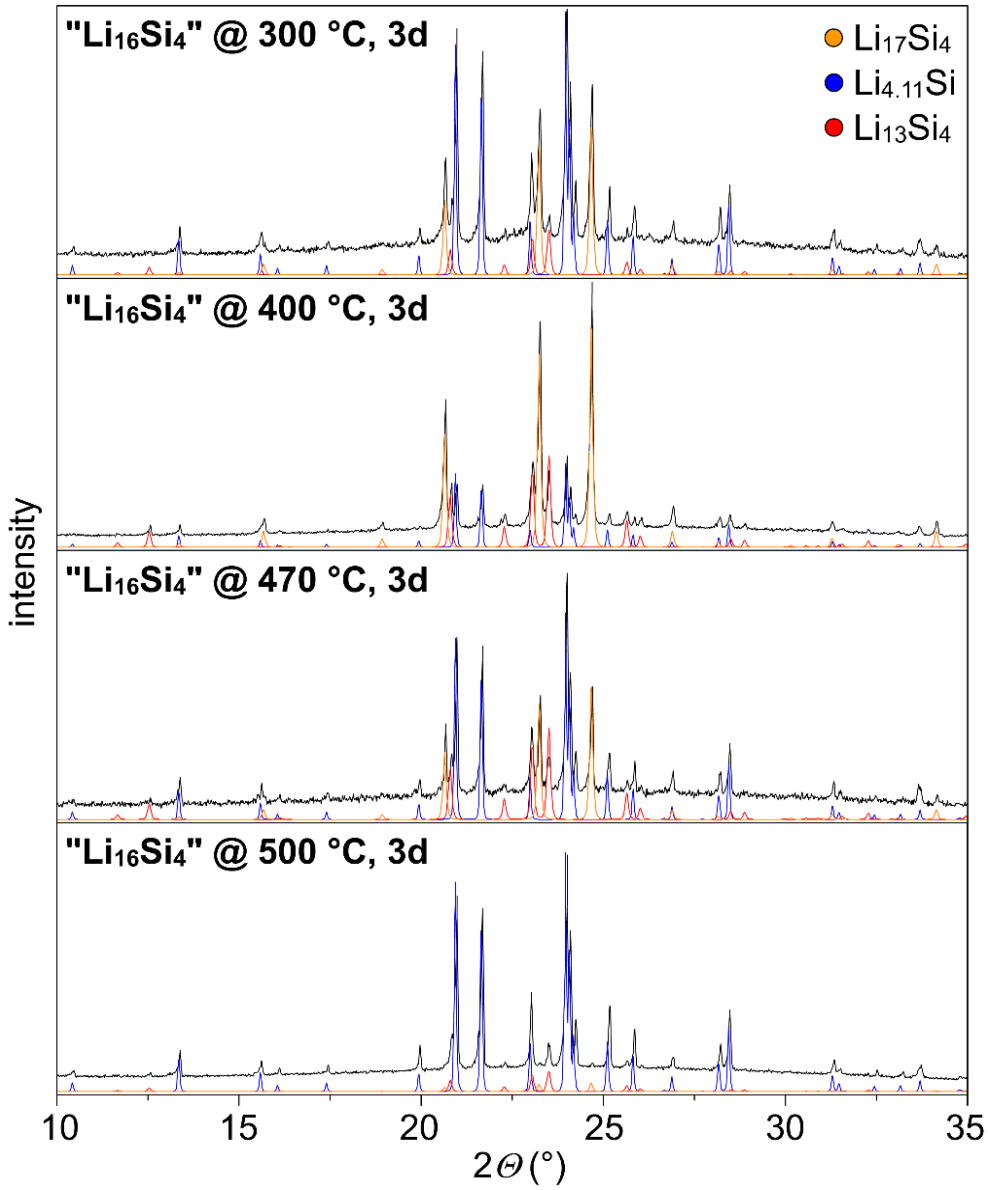

Figure S2. PXRD patterns of "$Li_{16}Si_4$" samples annealed at different temperatures for three days followed by quenching in liquid nitrogen (experimental = black; $Li_{17}Si_4$ calculated = orange; $Li_{4.11}Si$ calculated = blue; $Li_{13}Si_4$ calculated = red).

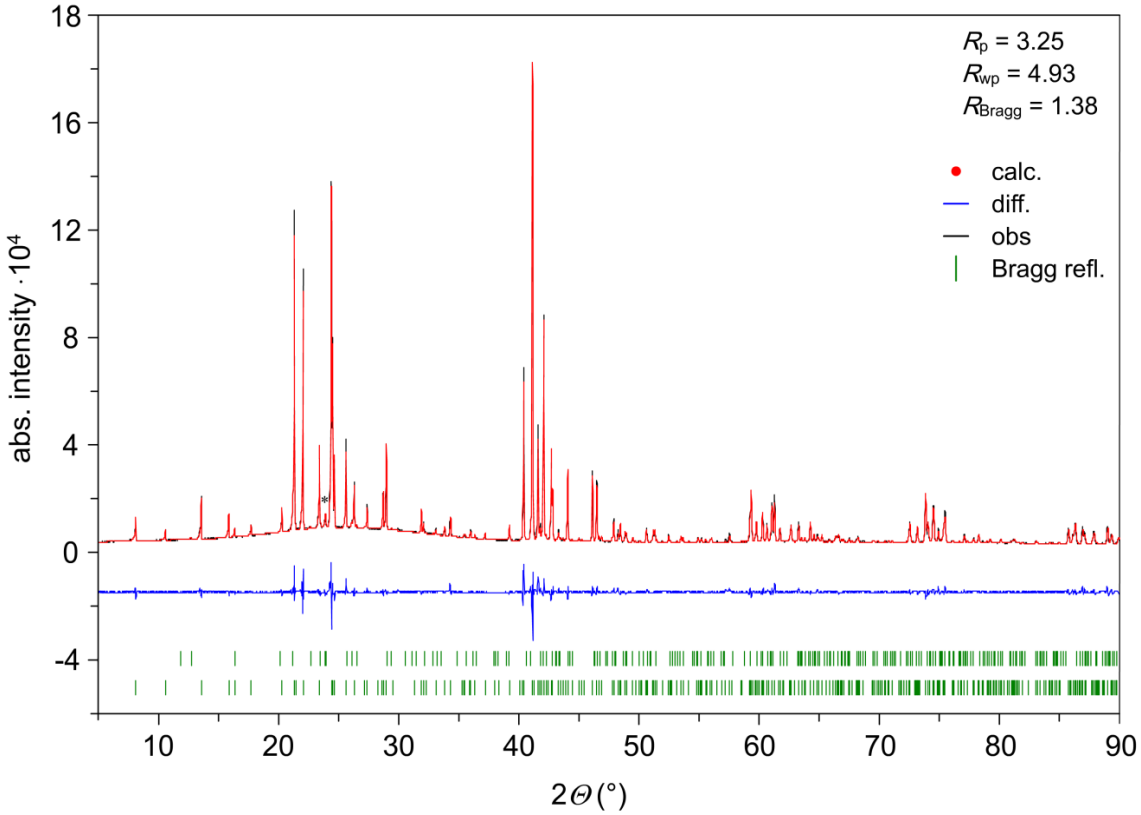

Figure S3. Experimental (black) X-ray powder diffraction pattern of $Li_{4.11}Si$ referenced with the theoretical powder pattern obtained from Rietveld refinement. The difference plot is shown in blue, Bragg positions in green (up: $Li_{13}Si_4$, down: $Li_{4.11}Si$). The strongest reflection of $Li_{13}Si_4$ (111) at ~23.5° is labeled with *.

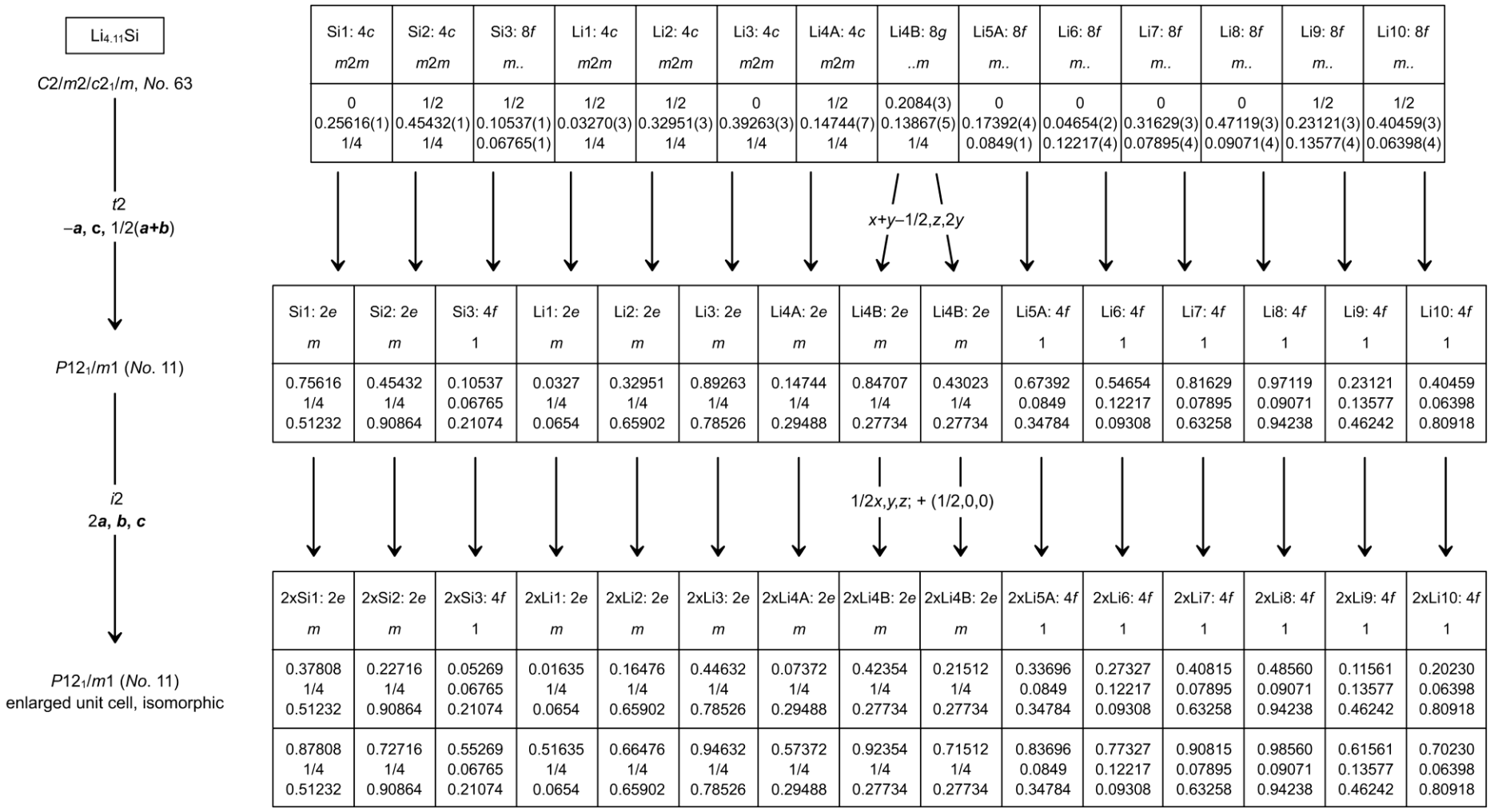

Si1: 4*c* m2m	Si2: 4*c* m2m	Si3: 8*f* m..	Li1: 4*c* m2m	Li2: 4*c* m2m	Li3: 4*c* m2m	Li4A: 4*c* m2m	Li4B: 8*g* ..m	Li5A: 8*f* m..	Li6: 8*f* m..	Li7: 8*f* m..	Li8: 8*f* m..	Li9: 8*f* m..	Li10: 8*f* m..
0 0.25616(1) 1/4	1/2 0.45432(1) 1/4	1/2 0.10537(1) 0.06765(1)	1/2 0.03270(3) 1/4	1/2 0.32951(3) 1/4	0 0.39263(3) 1/4	1/2 0.14744(7) 1/4	0.2084(3) 0.13867(5) 1/4	0 0.17392(4) 0.0849(1)	0 0.04654(2) 0.12217(4)	0 0.31629(3) 0.07895(4)	0 0.47119(3) 0.09071(4)	1/2 0.23121(3) 0.13577(4)	1/2 0.40459(3) 0.06398(4)

Si1: 2*e* m	Si2: 2*e* m	Si3: 4*f* 1	Li1: 2*e* m	Li2: 2*e* m	Li3: 2*e* m	Li4A: 2*e* m	Li4B: 2*e* m	Li4B: 2*e* m	Li5A: 4*f* 1	Li6: 4*f* 1	Li7: 4*f* 1	Li8: 4*f* 1	Li9: 4*f* 1	Li10: 4*f* 1
0.75616 1/4 0.51232	0.45432 1/4 0.90864	0.10537 0.06765 0.21074	0.0327 1/4 0.0654	0.32951 1/4 0.65902	0.89263 1/4 0.78526	0.14744 1/4 0.29488	0.84707 1/4 0.27734	0.43023 1/4 0.27734	0.67392 0.0849 0.34784	0.54654 0.12217 0.09308	0.81629 0.07895 0.63258	0.97119 0.09071 0.94238	0.23121 0.13577 0.46242	0.40459 0.06398 0.80918

2xSi1: 2*e* m	2xSi2: 2*e* m	2xSi3: 4*f* 1	2xLi1: 2*e* m	2xLi2: 2*e* m	2xLi3: 2*e* m	2xLi4A: 2*e* m	2xLi4B: 2*e* m	2xLi4B: 2*e* m	2xLi5A: 4*f* 1	2xLi6: 4*f* 1	2xLi7: 4*f* 1	2xLi8: 4*f* 1	2xLi9: 4*f* 1	2xLi10: 4*f* 1
0.37808 1/4 0.51232	0.22716 1/4 0.90864	0.05269 0.06765 0.21074	0.01635 1/4 0.0654	0.16476 1/4 0.65902	0.44632 1/4 0.78526	0.07372 1/4 0.29488	0.42354 1/4 0.27734	0.21512 1/4 0.27734	0.33696 0.0849 0.34784	0.27327 0.12217 0.09308	0.40815 0.07895 0.63258	0.48560 0.09071 0.94238	0.11561 0.13577 0.46242	0.20230 0.06398 0.80918
0.87808 1/4 0.51232	0.72716 1/4 0.90864	0.55269 0.06765 0.21074	0.51635 1/4 0.0654	0.66476 1/4 0.65902	0.94632 1/4 0.78526	0.57372 1/4 0.29488	0.92354 1/4 0.27734	0.71512 1/4 0.27734	0.83696 0.0849 0.34784	0.77327 0.12217 0.09308	0.90815 0.07895 0.63258	0.98560 0.09071 0.94238	0.61561 0.13577 0.46242	0.70230 0.06398 0.80918

Figure S4. Bärnighausen[1] tree for generating ordered structure models of $Li_{4.11}Si$.

(1) Bärnighausen, H. *MATCH, Commun. Math. Chem.* **1980**, *9*, 139.

5.3 Revision of the $Li_{13}Si_4$ structure

Zeilinger, M.; Fässler, T. F. *Acta Cryst.* **2013**, *E69*, i81. Reproduced with permission of the International Union of Crystallography (http://journals.iucr.org).

Acta Crystallographica Section E
Structure Reports Online
ISSN 1600-5368

Revision of the $Li_{13}Si_4$ structure

Michael Zeilinger and Thomas F. Fässler*

Department of Chemistry, Technische Universität München, Lichtenbergstrasse 4, 85747 Garching, Germany
Correspondence e-mail: thomas.faessler@lrz.tum.de

Received 14 October 2013; accepted 30 October 2013

Key indicators: single-crystal X-ray study; T = 100 K; mean σ(Si–Li) = 0.0007 Å; disorder in main residue; R factor = 0.015; wR factor = 0.044; data-to-parameter ratio = 40.5.

Besides $Li_{17}Si_4$, $Li_{16.42}Si_4$, and $Li_{15}Si_4$, another lithium-rich representative in the Li–Si system is the phase $Li_{13}Si_4$ (tridecalithium tetrasilicide), the structure of which has been determined previously [Frank *et al.* (1975). *Z. Naturforsch. Teil B*, **30**, 10–13]. A careful analysis of X-ray diffraction patterns of $Li_{13}Si_4$ revealed discrepancies between experimentally observed and calculated Bragg positions. Therefore, we redetermined the structure of $Li_{13}Si_4$ on the basis of single-crystal X-ray diffraction data. Compared to the previous structure report, decisive differences are (i) the introduction of a split position for one Li site [occupancy ratio 0.838 (7):0.162 (7)], (ii) the anisotropic refinement of atomic displacement parameters for all atoms, and (iii) a high accuracy of atom positions and unit-cell parameters. The asymmetric unit of $Li_{13}Si_4$ contains two Si and seven Li atoms. Except for one Li atom situated on a site with symmetry 2/m, all other atoms are on mirror planes. The structure consists of isolated Si atoms as well as Si–Si dumbbells surrounded by Li atoms. Each Si atom is either 12- or 13-coordinated. The isolated Si atoms are situated in the ab plane at z = 0 and are strictly separated from the Si–Si dumbbells at z = 0.5.

Related literature

For details of the structural description of $Li_{13}Si_4$, see: Frank *et al.* (1975). For structural data for $Li_{13}Si_4$ based on computational methods, see: Chevrier *et al.* (2010). For details of the synthesis, thermodynamic properties and crystal structures of $Li_{17}Si_4$, $Li_{16.42}Si_4$ and $Li_{15}Si_4$, see: Zeilinger & Benson *et al.* (2013); Zeilinger & Kurylyshyn *et al.* (2013); Zeilinger & Baran *et al.* (2013). For further thermodynamic investigations on the Li–Si system, see: Thomas *et al.* (2013); Wang *et al.* (2013). The behavior of silicon as anode material upon lithiation/delithiation is described by Limthongkul *et al.* (2003) and Obrovac & Christensen (2004). For *in-situ*/*ex-situ* solid state NMR investigations of structural changes in silicon electrodes for lithium-ion batteries, see: Key *et al.* (2009, 2011).

Experimental

Crystal data

$Li_{13}Si_4$
M_r = 202.58
Orthorhombic, *Pbam*
a = 7.9488 (4) Å
b = 15.1248 (8) Å
c = 4.4661 (2) Å
V = 536.93 (5) Å^3
Z = 2
Mo $K\alpha$ radiation
μ = 0.47 mm^{-1}
T = 100 K
0.2 × 0.2 × 0.2 mm

Data collection

Bruker APEXII CCD diffractometer
Absorption correction: multi-scan (*SADABS*; Bruker, 2008)
T_{min} = 0.781, T_{max} = 0.818
25938 measured reflections
2429 independent reflections
2333 reflections with $I > 2\sigma(I)$
R_{int} = 0.033

Refinement

$R[F^2 > 2\sigma(F^2)]$ = 0.015
$wR(F^2)$ = 0.044
S = 1.08
2429 reflections
60 parameters
$\Delta\rho_{max}$ = 0.68 e Å^{-3}
$\Delta\rho_{min}$ = −0.40 e Å^{-3}

Data collection: *APEX2* (Bruker, 2008); cell refinement: *SAINT* (Bruker, 2008); data reduction: *SAINT*; program(s) used to solve structure: *SHELXS97* (Sheldrick, 2008); program(s) used to refine structure: *SHELXL97* (Sheldrick, 2008); molecular graphics: *DIAMOND* (Brandenburg, 2012); software used to prepare material for publication: *publCIF* (Westrip, 2010).

This work has been funded by the Fonds der Chemischen Industrie and the SolTech (Solar Technologies go Hybrid) program of the State of Bavaria.

Supplementary data and figures for this paper are available from the IUCr electronic archives (Reference: WM2778).

References

Brandenburg, K. (2012). *DIAMOND*. Crystal Impact GbR, Bonn, Germany.
Bruker (2008). *APEX2*, *SAINT* and *SADABS*. Bruker AXS Inc., Madison, Wisconsin, USA.
Chevrier, V. L., Zwanziger, J. W. & Dahn, J. R. (2010). *J. Alloys Compd*, **496**, 25–36.
Frank, U., Müller, W. & Schäfer, H. (1975). *Z. Naturforsch. Teil B*, **30**, 10–13.
Key, B., Bhattacharyya, R., Morcrette, M., Seznec, V., Tarascon, J. M. & Grey, C. P. (2009). *J. Am. Chem. Soc.* **131**, 9239–9249.
Key, B., Morcrette, M., Tarascon, J. M. & Grey, C. P. (2011). *J. Am. Chem. Soc.* **133**, 503–512.
Limthongkul, P., Jang, Y. I., Dudney, N. J. & Chiang, Y. M. (2003). *Acta Mater.* **51**, 1103–1113.
Obrovac, M. N. & Christensen, L. (2004). *Electrochem. Solid State Lett.* **7**, A93–A96.
Sheldrick, G. M. (2008). *Acta Cryst.* A**64**, 112–122.
Thomas, D., Abdel-Hafiez, M., Gruber, T., Huttl, R., Seidel, J., Wolter, A. U. B., Buchner, B., Kortus, J. & Mertens, F. J. (2013). *J. Chem. Thermodyn.* **64**, 205–225.
Wang, P., Kozlov, A., Thomas, D., Mertens, F. & Schmid-Fetzer, R. (2013). *Intermetallics*, **42**, 137–145.
Westrip, S. P. (2010). *J. Appl. Cryst.* **43**, 920–925.
Zeilinger, M., Baran, V., Häussermann, U. & Fässler, T. F. (2013). *Chem. Mater.* **25**, 4113–4121.

Zeilinger, M., Benson, D., Häussermann, U. & Fässler, T. F. (2013). *Chem. Mater.* **25**, 1960–1967.

Zeilinger, M., Kurylyshyn, I. M., Häussermann, U. & Fässler, T. F. (2013). *Chem. Mater.* doi:10.1021/cm4029885.

supplementary materials

Acta Cryst. (2013). E**69**, i81–i82 [doi:10.1107/S1600536813029759]

Revision of the $Li_{13}Si_4$ structure

Michael Zeilinger and Thomas F. Fässler

1. Comment

In the last decade, the demand for high capacity lithium-ion batteries (LIBs) particularly fueled the research on the Li—Si phase system since as anode material, Si theoretically offers a specific capacity of 3579 mA h g^{-1} based on the formation of the metastable phase $Li_{15}Si_4$ (Obrovac & Christensen, 2004). It is well known that $Li_{15}Si_4$ is the only Li—Si phase that appears in crystalline form during charging and discharging processes in silicon based LIBs at room temperature (Limthongkul *et al.*, 2003; Obrovac & Christensen, 2004). However, in order to understand the lithiation/delithiation mechanism, X-ray diffraction methods only provide sparse information and therefore other techniques such as *in-situ* / *ex-situ* solid state NMR are frequently used (Key & Bhattacharyya *et al.*, 2009; Key & Morcrette *et al.*, 2011).

Furthermore, a fundamental understanding of the thermodynamic relation of Li—Si phases, especially in the lithium-rich section of the phase diagram, is of considerable importance. Exemplary work is given by Zeilinger & Baran *et al.* (2013), Zeilinger & Benson *et al.* (2013), Zeilinger & Kurylyshyn *et al.* (2013), Thomas *et al.* (2013) and Wang *et al.* (2013). For those studies as well as for NMR investigations it is crucial that all existing Li—Si phases are structurally well characterized since otherwise a phase identification of model compounds can be difficult (Key & Bhattacharyya *et al.*, 2009; Thomas *et al.*, 2013). In the course of our investigations on the thermodynamic properties of Li—Si phases, we identified two new phases, $Li_{17}Si_4$ (Zeilinger & Benson *et al.*, 2013) and $Li_{16.42}Si_4$ (Zeilinger & Kurylyshyn *et al.*, 2013). The latter is assigned a high temperature phase existing in a temperature range of 743–891 K, the former decomposes peritectically at 754–759 K. $Li_{16.42}Si_4$ is compositionally embraced by the lithium-richer phase $Li_{17}Si_4$ and the lithium-poorer phase $Li_{13}Si_4$. Since the determination of the Li—Si phase diagram in the aforementioned section is carried out by thermal investigations on various samples with different Li concentrations, the structures of the relevant phases have to be ascertained for an unambiguous assignment of phases in X-ray powder diffraction patterns of those samples. However, the calculated X-ray diffraction pattern of $Li_{13}Si_4$ based on structural data published by Frank *et al.* (1975) decisively differs from the experimentally observed pattern of a $Li_{13}Si_4$ sample (Fig. 1). More recent data based on theoretical calculations were reported by Chevrier *et al.* (2010). Yet, the accordingly calculated pattern is slightly but still distinctly different (Fig. 1).

Therefore, we redetermined the structure of $Li_{13}Si_4$ based on single crystal X-ray diffraction data. As can be seen in Fig. 1, the resulting calculated pattern is in very good agreement with the experimental one. Main differences to the previous single-crystal X-ray structure determination by Frank *et al.* (1975) are i) a significantly more precise determination of atomic positions and unit-cell parameters, respectively (a = 7.99 (2) Å, b = 15.21 (3) Å, c = 4.43 (1) Å compared with a = 7.9488 (4) Å, b = 15.1248 (8) Å, c = 4.4661 (2) Å), ii) an anisotropic refinement of atomic displacement parameters for all atoms and iii) the introduction of a split position for Li6 (occupancy ratio 0.838 (7):0.162 (7)).

Regarding the structure of $Li_{13}Si_4$ we briefly elaborate on the main structure motifs since this has already been described in detail by Frank *et al.* (1975). Contrary to the lithium-richer phases $Li_{17}Si_4$, $Li_{16.42}Si_4$ and $Li_{15}Si_4$ where all Si atoms are isolated, $Li_{13}Si_4$ contains Si—Si dumbbells beside isolated Si atoms (Fig. 2a). Li—Si distances range from 2.5173 (2) Å

to 3.2283 (7) Å and next nearest neighbor distances are clearly separated, starting off from 4.1899 (2) Å. The shortest Li—Li distance is 2.429 (7) Å and comparable to other Li—Si phases (Zeilinger & Benson *et al.*, 2013). The Si—Si distance within the Si—Si dumbbells is 2.3852 (2) Å, further Si atoms are separated by distances larger than 4.4661 (2) Å. Whereas Si1 is coordinated by 12 Li and one Si atom, Si2 is exclusively surrounded by 12 Li atoms. In addition, dumbbells and isolated Si atoms are strictly separated from each other in a layer like fashion as they are located in different *ab*-planes (Figs. 2 b and c).

2. Experimental

In our previous work we reported on thermal investigations by differential scanning calorimetry (DSC) means which were targeting the determination of the lithium-rich section of the Li—Si phase diagram (Zeilinger & Kurylyshyn *et al.* 2013). Various samples with different Li—Si compositions ($Li_{17}Si_4$, "$Li_{16.5}Si_4$", "$Li_{16}Si_4$" and "$Li_{14}Si_4$") were synthesized. Crystals of $Li_{13}Si_4$ could be obtained from a sample with a nominal composition "$Li_{14}Si_4$". For the synthesis of "$Li_{14}Si_4$" we refer to Zeilinger & Kurylyshyn *et al.* (2013). $Li_{13}Si_4$ crystals were handled inside an Ar-filled glove box, selected under a microscope and sealed inside 0.3 mm glass capillaries for X-ray diffraction experiments.

3. Refinement

For better comparison between the first structure refinement and the current redetermination, atomic coordinates and atom labels were taken from Frank *et al.* (1975). During the structure refinement procedure the positions of two Si and seven Li atoms were confirmed. If refined freely, the site occupation factors of all atoms converged to values very close to full occupancy for the respective sites and were therefore constrained for full occupancy. Extinction was refined to non-significant values and thus excluded from the refinement. Furthermore, an anisotropic refinement of atomic displacement parameters was possible for all atoms. This model resulted in *R*-values of $R_1 = 0.020$ and $wR_2 = 0.059$ for all data and residual electron densities of +1.223 e Å^{-3} and -0.740 e Å^{-3}. However, the atomic displacement parameters for Li6 on Wyckoff position 4*h* (0.0895 (2), 0.25508 (9), 1/2) indicated a large prolongation in the *x*-direction. Additionally, significant residual electron density (+1.22 e Å^{-3}) is located closely to Li6. To account for that, we introduced a split position for Li6. This resulted in markedly better *R*-values of $R_1 = 0.016$ and $wR_2 = 0.044$ for all data as well as acceptable residual electron densities of +0.68 e Å^{-3} and -0.40 e Å^{-3}. The refined fractions are 0.838 (7) for Li6A and 0.162 (7) for Li6B. An example for a similar introduction of an atom split in lithium-rich Li—Si phases is given by Zeilinger & Kurylyshyn *et al.* (2013).

Computing details

Data collection: *APEX2* (Bruker, 2008); cell refinement: *SAINT* (Bruker, 2008); data reduction: *SAINT* (Bruker, 2008); program(s) used to solve structure: *SHELXS97* (Sheldrick, 2008); program(s) used to refine structure: *SHELXL97* (Sheldrick, 2008); molecular graphics: *DIAMOND* (Brandenburg, 2012); software used to prepare material for publication: *publCIF* (Westrip, 2010).

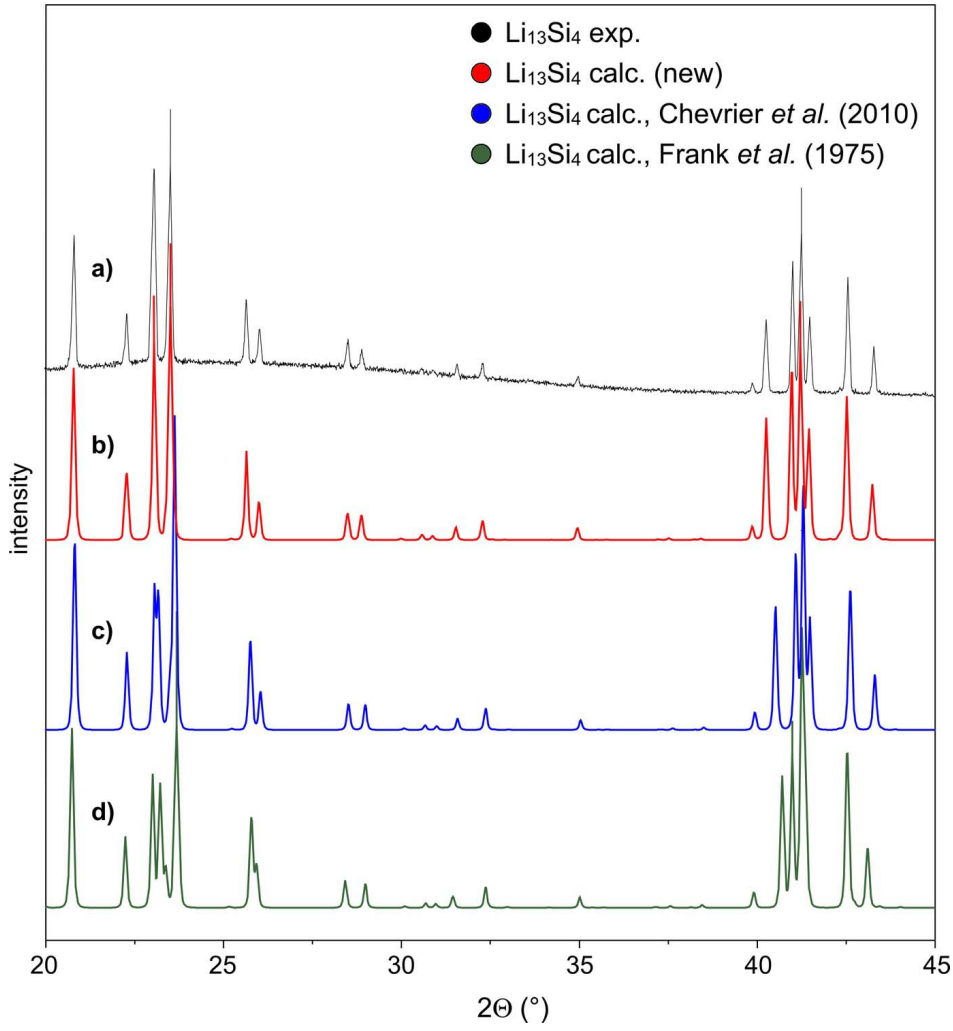

Figure 1

(*a*) Powder X-ray diffraction pattern of a $Li_{13}Si_4$ sample referenced with the theoretical patterns calculated from (*b*) single-crystal X-ray data presented herein, previous structural data published by (*c*) Chevrier *et al.* (2010) and (*d*) Frank *et al.* (1975).

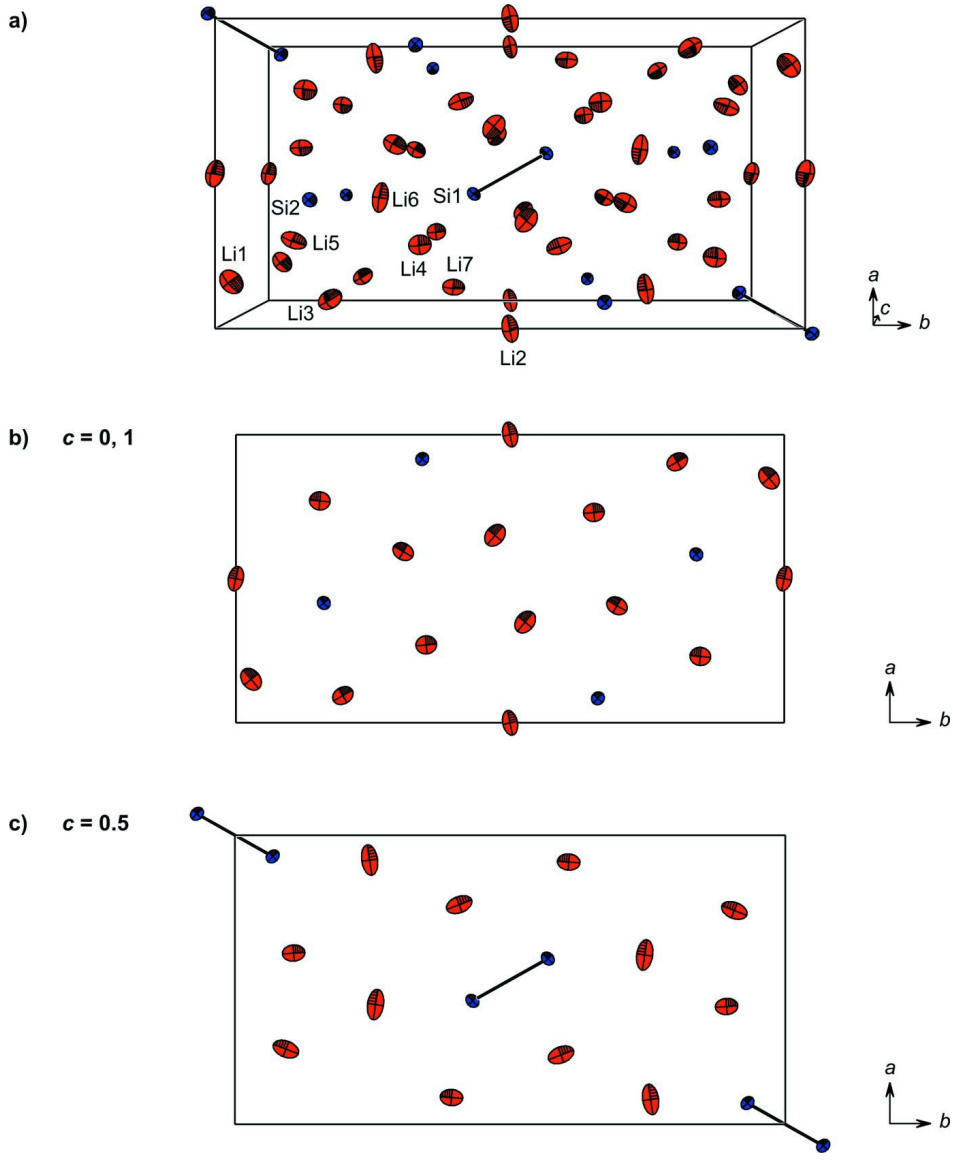

Figure 2

Structure motifs in $Li_{13}Si_4$: (*a*) perspective view along the crystallographic *c*-axis of the unit cell of $Li_{13}Si_4$ (atoms of the asymmetric unit are labeled), (*b*) isolated Si atoms, and (*c*) Si—Si dumbbells located in different *ab*-planes (*c* = 0, 1 and *c* = 1/2, respectively). Ellipsoids are drawn at a 80% probability level (Li = red, Si = blue; only the major component of Li6 is shown).

Tridecalithium tetrasilicide

Crystal data

$Li_{13}Si_4$
M_r = 202.58
Orthorhombic, *Pbam*
Hall symbol: -P 2 2ab
a = 7.9488 (4) Å
b = 15.1248 (8) Å
c = 4.4661 (2) Å
V = 536.93 (5) Å^3
Z = 2
F(000) = 190
D_x = 1.253 Mg m^{-3}
Melting point: 995 K
Mo *Kα* radiation, *λ* = 0.71073 Å
Cell parameters from 9823 reflections

θ = 2.9–57.3°
μ = 0.47 mm^{-1}
T = 100 K

Block, metallic silver
0.2 × 0.2 × 0.2 mm

Data collection

Bruker APEXII CCD diffractometer
Radiation source: rotating anode FR591
MONTEL optic monochromator
Detector resolution: 16 pixels mm^{-1}
φ– and ω–rotation scans
Absorption correction: multi-scan (*SADABS*; Bruker, 2008)
T_{min} = 0.781, T_{max} = 0.818

25938 measured reflections
2429 independent reflections
2333 reflections with $I > 2\sigma(I)$
R_{int} = 0.033
θ_{max} = 45.3°, θ_{min} = 2.7°
h = −13→15
k = −28→30
l = −8→8

Refinement

Refinement on F^2
Least-squares matrix: full
$R[F^2 > 2\sigma(F^2)]$ = 0.015
$wR(F^2)$ = 0.044
S = 1.08
2429 reflections
60 parameters
0 restraints

Primary atom site location: structure-invariant direct methods
Secondary atom site location: difference Fourier map
$w = 1/[\sigma^2(F_o^2) + (0.0204P)^2 + 0.0373P]$ where $P = (F_o^2 + 2F_c^2)/3$
$(\Delta/\sigma)_{max}$ = 0.002
$\Delta\rho_{max}$ = 0.68 e Å^{-3}
$\Delta\rho_{min}$ = −0.40 e Å^{-3}

Special details

Geometry. All e.s.d.'s (except the e.s.d. in the dihedral angle between two l.s. planes) are estimated using the full covariance matrix. The cell e.s.d.'s are taken into account individually in the estimation of e.s.d.'s in distances, angles and torsion angles; correlations between e.s.d.'s in cell parameters are only used when they are defined by crystal symmetry. An approximate (isotropic) treatment of cell e.s.d.'s is used for estimating e.s.d.'s involving l.s. planes.

Refinement. Refinement of F^2 against all reflections. The weighted R-factor wR and goodness of fit S are based on F^2, conventional R-factors R are based on F, with F set to zero for negative F^2. The threshold expression of $F^2 > \sigma(F^2)$ is used only for calculating R-factors(gt) *etc*. and is not relevant to the choice of reflections for refinement. R-factors based on F^2 are statistically about twice as large as those based on F, and R-factors based on all data will be even larger.

Fractional atomic coordinates and isotropic or equivalent isotropic displacement parameters (Å^2)

	x	y	z	U_{iso}*/U_{eq}	Occ. (<1)
Si1	0.426415 (11)	0.431285 (6)	0.5000	0.00704 (2)	
Si2	0.415184 (11)	0.160356 (6)	0.0000	0.00617 (2)	
Li1	0.15083 (11)	0.02778 (6)	0.0000	0.01635 (13)	
Li2	0.0000	0.5000	0.0000	0.01727 (19)	
Li3	0.09442 (12)	0.19506 (7)	0.0000	0.0242 (2)	
Li4	0.27005 (11)	0.34697 (6)	0.0000	0.01476 (13)	
Li5	0.25998 (11)	0.09271 (6)	0.5000	0.01663 (14)	
Li6A	0.4138 (3)	0.25535 (7)	0.5000	0.0195 (4)	0.838 (7)
Li6B	0.3327 (12)	0.2487 (4)	0.5000	0.0192 (15)	0.162 (7)
Li7	0.09281 (10)	0.39330 (6)	0.5000	0.01429 (13)	

Atomic displacement parameters (Å^2)

	U^{11}	U^{22}	U^{33}	U^{12}	U^{13}	U^{23}
Si1	0.00650 (4)	0.00658 (4)	0.00803 (4)	−0.00146 (2)	0.000	0.000

Si2	0.00659 (4)	0.00652 (4)	0.00541 (4)	−0.00044 (2)	0.000	0.000
Li1	0.0192 (3)	0.0173 (3)	0.0126 (3)	−0.0052 (3)	0.000	0.000
Li2	0.0249 (5)	0.0097 (4)	0.0172 (5)	−0.0035 (4)	0.000	0.000
Li3	0.0129 (3)	0.0169 (3)	0.0427 (6)	0.0034 (3)	0.000	0.000
Li4	0.0133 (3)	0.0173 (3)	0.0137 (3)	0.0004 (2)	0.000	0.000
Li5	0.0127 (3)	0.0262 (4)	0.0110 (3)	−0.0061 (3)	0.000	0.000
Li6A	0.0374 (11)	0.0107 (4)	0.0104 (4)	0.0041 (4)	0.000	0.000
Li6B	0.019 (4)	0.017 (2)	0.022 (3)	0.003 (2)	0.000	0.000
Li7	0.0105 (3)	0.0204 (3)	0.0119 (3)	−0.0008 (2)	0.000	0.000

Geometric parameters (Å, º)

Si1—Si1^{i}	2.3852 (2)	Li3—Li6A^{xii}	2.7585 (14)
Si1—Li6A	2.6628 (12)	Li3—Li6A^{xiii}	2.7585 (14)
Si1—Li5^{ii}	2.6762 (8)	Li3—Li5	3.0191 (9)
Si1—Li7	2.7133 (8)	Li3—Li5^{viii}	3.0191 (9)
Si1—Li1^{iii}	2.7374 (5)	Li3—Li6B	3.038 (7)
Si1—Li1^{iv}	2.7374 (5)	Li3—Li6B^{viii}	3.038 (7)
Si1—Li5^{iii}	2.8559 (9)	Li3—Li6B^{xii}	3.168 (7)
Si1—Li4^{v}	2.8561 (5)	Li4—Li3^{ii}	2.6556 (13)
Si1—Li4	2.8561 (5)	Li4—Li6B	2.728 (3)
Si1—Li6B	2.860 (7)	Li4—Li6B^{viii}	2.728 (3)
Si1—Li1^{vi}	2.9244 (6)	Li4—Li7	2.7317 (7)
Si1—Li1^{ii}	2.9244 (6)	Li4—Li7^{viii}	2.7318 (7)
Si2—Li2^{vii}	2.5174 (2)	Li4—Li1^{iv}	2.8060 (12)
Si2—Li3	2.6031 (9)	Li4—Si2^{xiii}	2.8229 (9)
Si2—Li3^{ii}	2.6099 (10)	Li4—Si1^{viii}	2.8562 (5)
Si2—Li6A	2.6554 (6)	Li4—Li6A^{viii}	2.8659 (11)
Si2—Li6A^{viii}	2.6554 (6)	Li4—Li6A	2.8659 (11)
Si2—Li6B^{viii}	2.684 (3)	Li5—Li6B	2.429 (7)
Si2—Li6B	2.684 (3)	Li5—Li1^{v}	2.5892 (6)
Si2—Li5	2.7487 (5)	Li5—Li7^{ii}	2.6540 (12)
Si2—Li5^{viii}	2.7487 (5)	Li5—Si1^{xiii}	2.6762 (8)
Si2—Li7^{ii}	2.7638 (5)	Li5—Li6A	2.7472 (18)
Si2—Li7^{ix}	2.7638 (5)	Li5—Si2^{v}	2.7487 (5)
Si2—Li4^{ii}	2.8229 (9)	Li5—Si1^{xi}	2.8559 (9)
Li1—Li1^{x}	2.5408 (17)	Li5—Li3^{v}	3.0191 (9)
Li1—Li3	2.5696 (13)	Li5—Li7^{xi}	3.2351 (14)
Li1—Li5^{viii}	2.5892 (6)	Li6A—Si2^{v}	2.6553 (6)
Li1—Li5	2.5892 (6)	Li6A—Li7^{ii}	2.6605 (16)
Li1—Si1^{vii}	2.7374 (5)	Li6A—Li3^{vi}	2.7585 (14)
Li1—Si1^{xi}	2.7374 (5)	Li6A—Li3^{ii}	2.7585 (14)
Li1—Li4^{vii}	2.8060 (12)	Li6A—Li4^{v}	2.8659 (11)
Li1—Li2^{vii}	2.8071 (9)	Li6A—Li7	3.296 (2)
Li1—Si1^{xii}	2.9244 (6)	Li6A—Li3^{v}	3.5021 (19)
Li1—Si1^{xiii}	2.9244 (6)	Li6B—Si2^{v}	2.684 (3)
Li2—Si2^{xiii}	2.5173 (2)	Li6B—Li4^{v}	2.728 (3)
Li2—Si2^{iv}	2.5174 (2)	Li6B—Li7	2.902 (7)
Li2—Li1^{xiii}	2.8071 (9)	Li6B—Li7^{ii}	2.981 (7)
Li2—Li1^{iv}	2.8071 (9)	Li6B—Li3^{v}	3.038 (7)

Li2—Li7^{viii}	2.8522 (6)	Li6B—Li3^{vi}	3.168 (7)
Li2—Li7^{xiv}	2.8522 (6)	Li6B—Li3^{ii}	3.168 (7)
Li2—Li7^{xv}	2.8522 (6)	Li7—Li5^{xiii}	2.6540 (12)
Li2—Li7	2.8522 (6)	Li7—Li6A^{xiii}	2.6605 (16)
Li2—Li4^{xv}	3.1567 (9)	Li7—Li4^{v}	2.7317 (7)
Li2—Li4	3.1567 (9)	Li7—Si2^{xiii}	2.7638 (5)
Li2—Li5^{iii}	3.2546 (7)	Li7—Si2^{xvi}	2.7638 (5)
Li2—Li5^{iv}	3.2546 (7)	Li7—Li2^{v}	2.8522 (6)
Li3—Si2^{xiii}	2.6099 (10)	Li7—Li6B^{xiii}	2.981 (7)
Li3—Li4^{xiii}	2.6556 (13)	Li7—Li5^{iii}	3.2351 (14)
Li3—Li4	2.6884 (13)		

Si1^{i}—Si1—Li6A	152.78 (5)	Li3^{ii}—Li4—Li7	124.20 (2)
Si1^{i}—Si1—Li5^{ii}	68.43 (2)	Li3—Li4—Li7	87.21 (3)
Li6A—Si1—Li5^{ii}	84.35 (5)	Li6B—Li4—Li7	64.21 (14)
Si1^{i}—Si1—Li7	131.60 (2)	Li6B^{viii}—Li4—Li7	154.5 (2)
Li6A—Si1—Li7	75.63 (5)	Li3^{ii}—Li4—Li7^{viii}	124.20 (2)
Li5^{ii}—Si1—Li7	159.98 (3)	Li3—Li4—Li7^{viii}	87.21 (3)
Si1^{i}—Si1—Li1^{iii}	69.231 (19)	Li6B—Li4—Li7^{viii}	154.5 (2)
Li6A—Si1—Li1^{iii}	121.62 (2)	Li6B^{viii}—Li4—Li7^{viii}	64.21 (14)
Li5^{ii}—Si1—Li1^{iii}	107.13 (2)	Li7—Li4—Li7^{viii}	109.66 (4)
Li7—Si1—Li1^{iii}	83.90 (2)	Li3^{ii}—Li4—Li1^{iv}	90.90 (4)
Si1^{i}—Si1—Li1^{iv}	69.231 (19)	Li3—Li4—Li1^{iv}	161.67 (4)
Li6A—Si1—Li1^{iv}	121.62 (2)	Li6B—Li4—Li1^{iv}	119.34 (14)
Li5^{ii}—Si1—Li1^{iv}	107.13 (2)	Li6B^{viii}—Li4—Li1^{iv}	119.34 (14)
Li7—Si1—Li1^{iv}	83.90 (2)	Li7—Li4—Li1^{iv}	82.28 (3)
Li1^{iii}—Si1—Li1^{iv}	109.32 (3)	Li7^{viii}—Li4—Li1^{iv}	82.28 (3)
Si1^{i}—Si1—Li5^{iii}	60.62 (2)	Li3^{ii}—Li4—Si2^{xiii}	163.90 (4)
Li6A—Si1—Li5^{iii}	146.60 (5)	Li3—Li4—Si2^{xiii}	56.47 (3)
Li5^{ii}—Si1—Li5^{iii}	129.047 (16)	Li6B—Li4—Si2^{xiii}	99.3 (2)
Li7—Si1—Li5^{iii}	70.97 (3)	Li6B^{viii}—Li4—Si2^{xiii}	99.3 (2)
Li1^{iii}—Si1—Li5^{iii}	55.100 (14)	Li7—Li4—Si2^{xiii}	59.65 (2)
Li1^{iv}—Si1—Li5^{iii}	55.100 (14)	Li7^{viii}—Li4—Si2^{xiii}	59.65 (2)
Si1^{i}—Si1—Li4^{v}	127.050 (14)	Li1^{iv}—Li4—Si2^{xiii}	105.20 (3)
Li6A—Si1—Li4^{v}	62.45 (3)	Li3^{ii}—Li4—Si1	71.60 (2)
Li5^{ii}—Si1—Li4^{v}	111.752 (19)	Li3—Li4—Si1	127.412 (15)
Li7—Si1—Li4^{v}	58.678 (17)	Li6B—Li4—Si1	61.57 (14)
Li1^{iii}—Si1—Li4^{v}	60.17 (2)	Li6B^{viii}—Li4—Si1	143.5 (2)
Li1^{iv}—Si1—Li4^{v}	141.10 (3)	Li7—Li4—Si1	58.048 (18)
Li5^{iii}—Si1—Li4^{v}	98.97 (2)	Li7^{viii}—Li4—Si1	138.51 (4)
Si1^{i}—Si1—Li4	127.051 (14)	Li1^{iv}—Li4—Si1	57.815 (16)
Li6A—Si1—Li4	62.45 (3)	Si2^{xiii}—Li4—Si1	116.896 (19)
Li5^{ii}—Si1—Li4	111.752 (19)	Li3^{ii}—Li4—Si1^{viii}	71.60 (2)
Li7—Si1—Li4	58.678 (17)	Li3—Li4—Si1^{viii}	127.413 (15)
Li1^{iii}—Si1—Li4	141.10 (3)	Li6B—Li4—Si1^{viii}	143.5 (2)
Li1^{iv}—Si1—Li4	60.17 (2)	Li6B^{viii}—Li4—Si1^{viii}	61.57 (14)
Li5^{iii}—Si1—Li4	98.97 (2)	Li7—Li4—Si1^{viii}	138.51 (4)
Li4^{v}—Si1—Li4	102.86 (3)	Li7^{viii}—Li4—Si1^{viii}	58.048 (18)
Si1^{i}—Si1—Li6B	165.72 (19)	Li1^{iv}—Li4—Si1^{viii}	57.814 (16)

Li6A—Si1—Li6B	12.94 (15)	Si2^{xiii}—Li4—Si1^{viii}	116.896 (19)
Li5^{ii}—Si1—Li6B	97.30 (19)	Si1—Li4—Si1^{viii}	102.86 (3)
Li7—Si1—Li6B	62.68 (19)	Li3^{ii}—Li4—Li6A^{viii}	59.80 (4)
Li1^{iii}—Si1—Li6B	117.15 (8)	Li3—Li4—Li6A^{viii}	78.11 (4)
Li1^{iv}—Si1—Li6B	117.15 (8)	Li6B—Li4—Li6A^{viii}	107.55 (12)
Li5^{iii}—Si1—Li6B	133.66 (19)	Li6B^{viii}—Li4—Li6A^{viii}	13.10 (18)
Li4^{v}—Si1—Li6B	57.02 (7)	Li7—Li4—Li6A^{viii}	165.17 (5)
Li4—Si1—Li6B	57.02 (7)	Li7^{viii}—Li4—Li6A^{viii}	72.11 (3)
Si1^{i}—Si1—Li1^{vi}	61.073 (16)	Li1^{iv}—Li4—Li6A^{viii}	112.45 (4)
Li6A—Si1—Li1^{vi}	103.56 (3)	Si2^{xiii}—Li4—Li6A^{viii}	112.31 (5)
Li5^{ii}—Si1—Li1^{vi}	54.856 (16)	Si1—Li4—Li6A^{viii}	130.66 (5)
Li7—Si1—Li1^{vi}	129.866 (14)	Si1^{viii}—Li4—Li6A^{viii}	55.47 (3)
Li1^{iii}—Si1—Li1^{vi}	53.20 (3)	Li3^{ii}—Li4—Li6A	59.80 (4)
Li1^{iv}—Si1—Li1^{vi}	130.304 (9)	Li3—Li4—Li6A	78.10 (4)
Li5^{iii}—Si1—Li1^{vi}	97.78 (2)	Li6B—Li4—Li6A	13.10 (18)
Li4^{v}—Si1—Li1^{vi}	76.29 (2)	Li6B^{viii}—Li4—Li6A	107.55 (12)
Li4—Si1—Li1^{vi}	163.14 (2)	Li7—Li4—Li6A	72.11 (3)
Li6B—Si1—Li1^{vi}	111.30 (11)	Li7^{viii}—Li4—Li6A	165.17 (5)
Si1^{i}—Si1—Li1^{ii}	61.073 (16)	Li1^{iv}—Li4—Li6A	112.45 (4)
Li6A—Si1—Li1^{ii}	103.56 (3)	Si2^{xiii}—Li4—Li6A	112.31 (5)
Li5^{ii}—Si1—Li1^{ii}	54.856 (16)	Si1—Li4—Li6A	55.47 (3)
Li7—Si1—Li1^{ii}	129.866 (14)	Si1^{viii}—Li4—Li6A	130.66 (5)
Li1^{iii}—Si1—Li1^{ii}	130.304 (9)	Li6A^{viii}—Li4—Li6A	102.37 (5)
Li1^{iv}—Si1—Li1^{ii}	53.20 (3)	Li6B—Li5—Li1	116.63 (6)
Li5^{iii}—Si1—Li1^{ii}	97.78 (2)	Li6B—Li5—Li1^{v}	116.63 (6)
Li4^{v}—Si1—Li1^{ii}	163.14 (2)	Li1—Li5—Li1^{v}	119.19 (5)
Li4—Si1—Li1^{ii}	76.29 (2)	Li6B—Li5—Li7^{ii}	71.7 (2)
Li6B—Si1—Li1^{ii}	111.30 (11)	Li1—Li5—Li7^{ii}	111.36 (3)
Li1^{vi}—Si1—Li1^{ii}	99.56 (3)	Li1^{v}—Li5—Li7^{ii}	111.36 (3)
Li2^{vii}—Si2—Li3	117.17 (2)	Li6B—Li5—Si1^{xiii}	111.6 (2)
Li2^{vii}—Si2—Li3^{ii}	131.38 (2)	Li1—Li5—Si1^{xiii}	67.45 (3)
Li3—Si2—Li3^{ii}	111.451 (16)	Li1^{v}—Li5—Si1^{xiii}	67.45 (3)
Li2^{vii}—Si2—Li6A	121.49 (2)	Li7^{ii}—Li5—Si1^{xiii}	176.78 (5)
Li3—Si2—Li6A	83.51 (5)	Li6B—Li5—Li6A	12.67 (19)
Li3^{ii}—Si2—Li6A	63.18 (4)	Li1—Li5—Li6A	119.26 (3)
Li2^{vii}—Si2—Li6A^{viii}	121.49 (2)	Li1^{v}—Li5—Li6A	119.26 (3)
Li3—Si2—Li6A^{viii}	83.51 (5)	Li7^{ii}—Li5—Li6A	58.99 (5)
Li3^{ii}—Si2—Li6A^{viii}	63.18 (4)	Si1^{xiii}—Li5—Li6A	124.23 (6)
Li6A—Si2—Li6A^{viii}	114.48 (4)	Li6B—Li5—Si2	62.07 (9)
Li2^{vii}—Si2—Li6B^{viii}	123.03 (10)	Li1—Li5—Si2	65.853 (16)
Li3—Si2—Li6B^{viii}	70.1 (2)	Li1^{v}—Li5—Si2	172.86 (4)
Li3^{ii}—Si2—Li6B^{viii}	73.51 (18)	Li7^{ii}—Li5—Si2	61.506 (17)
Li6A—Si2—Li6B^{viii}	115.43 (10)	Si1^{xiii}—Li5—Si2	119.680 (19)
Li6A^{viii}—Si2—Li6B^{viii}	14.03 (17)	Li6A—Li5—Si2	57.78 (2)
Li2^{vii}—Si2—Li6B	123.03 (10)	Li6B—Li5—Si2^{v}	62.07 (9)
Li3—Si2—Li6B	70.1 (2)	Li1—Li5—Si2^{v}	172.86 (4)
Li3^{ii}—Si2—Li6B	73.51 (18)	Li1^{v}—Li5—Si2^{v}	65.854 (16)
Li6A—Si2—Li6B	14.03 (17)	Li7^{ii}—Li5—Si2^{v}	61.506 (17)
Li6A^{viii}—Si2—Li6B	115.43 (10)	Si1^{xiii}—Li5—Si2^{v}	119.680 (19)

Li6B^{viii}—Si2—Li6B	112.6 (2)	Li6A—Li5—Si2^{v}	57.78 (2)
Li2^{vii}—Si2—Li5	76.21 (2)	Si2—Li5—Si2^{v}	108.66 (3)
Li3—Si2—Li5	68.62 (2)	Li6B—Li5—Si1^{xi}	162.5 (2)
Li3^{ii}—Si2—Li5	123.840 (16)	Li1—Li5—Si1^{xi}	60.12 (2)
Li6A—Si2—Li5	61.08 (4)	Li1^{v}—Li5—Si1^{xi}	60.12 (2)
Li6A^{viii}—Si2—Li5	151.98 (5)	Li7^{ii}—Li5—Si1^{xi}	125.82 (4)
Li6B^{viii}—Si2—Li5	138.7 (2)	Si1^{xiii}—Li5—Si1^{xi}	50.954 (16)
Li6B—Si2—Li5	53.11 (15)	Li6A—Li5—Si1^{xi}	175.18 (6)
Li2^{vii}—Si2—Li5^{viii}	76.21 (2)	Si2—Li5—Si1^{xi}	123.439 (18)
Li3—Si2—Li5^{viii}	68.62 (2)	Si2^{v}—Li5—Si1^{xi}	123.440 (18)
Li3^{ii}—Si2—Li5^{viii}	123.840 (16)	Li6B—Li5—Li3	66.78 (13)
Li6A—Si2—Li5^{viii}	151.98 (5)	Li1—Li5—Li3	53.88 (3)
Li6A^{viii}—Si2—Li5^{viii}	61.08 (4)	Li1^{v}—Li5—Li3	133.34 (4)
Li6B^{viii}—Si2—Li5^{viii}	53.11 (15)	Li7^{ii}—Li5—Li3	113.18 (3)
Li6B—Si2—Li5^{viii}	138.7 (2)	Si1^{xiii}—Li5—Li3	68.76 (2)
Li5—Si2—Li5^{viii}	108.66 (3)	Li6A—Li5—Li3	74.63 (4)
Li2^{vii}—Si2—Li7^{ii}	65.184 (19)	Si2—Li5—Li3	53.408 (19)
Li3—Si2—Li7^{ii}	124.026 (15)	Si2^{v}—Li5—Li3	127.28 (4)
Li3^{ii}—Si2—Li7^{ii}	88.12 (3)	Si1^{xi}—Li5—Li3	102.25 (3)
Li6A—Si2—Li7^{ii}	58.76 (3)	Li6B—Li5—Li3^{v}	66.78 (13)
Li6A^{viii}—Si2—Li7^{ii}	147.18 (5)	Li1—Li5—Li3^{v}	133.34 (4)
Li6B^{viii}—Si2—Li7^{ii}	160.6 (2)	Li1^{v}—Li5—Li3^{v}	53.88 (3)
Li6B—Si2—Li7^{ii}	66.34 (14)	Li7^{ii}—Li5—Li3^{v}	113.18 (3)
Li5—Si2—Li7^{ii}	57.56 (2)	Si1^{xiii}—Li5—Li3^{v}	68.76 (2)
Li5^{viii}—Si2—Li7^{ii}	140.93 (3)	Li6A—Li5—Li3^{v}	74.63 (4)
Li2^{vii}—Si2—Li7^{ix}	65.184 (18)	Si2—Li5—Li3^{v}	127.28 (4)
Li3—Si2—Li7^{ix}	124.026 (15)	Si2^{v}—Li5—Li3^{v}	53.408 (19)
Li3^{ii}—Si2—Li7^{ix}	88.12 (3)	Si1^{xi}—Li5—Li3^{v}	102.25 (3)
Li6A—Si2—Li7^{ix}	147.18 (5)	Li3—Li5—Li3^{v}	95.40 (4)
Li6A^{viii}—Si2—Li7^{ix}	58.77 (3)	Li6B—Li5—Li7^{xi}	145.0 (2)
Li6B^{viii}—Si2—Li7^{ix}	66.34 (14)	Li1—Li5—Li7^{xi}	76.56 (3)
Li6B—Si2—Li7^{ix}	160.6 (2)	Li1^{v}—Li5—Li7^{xi}	76.56 (3)
Li5—Si2—Li7^{ix}	140.93 (3)	Li7^{ii}—Li5—Li7^{xi}	73.37 (4)
Li5^{viii}—Si2—Li7^{ix}	57.56 (2)	Si1^{xiii}—Li5—Li7^{xi}	103.41 (3)
Li7^{ii}—Si2—Li7^{ix}	107.80 (3)	Li6A—Li5—Li7^{xi}	132.36 (5)
Li2^{vii}—Si2—Li4^{ii}	72.216 (17)	Si2—Li5—Li7^{xi}	100.64 (2)
Li3—Si2—Li4^{ii}	170.62 (3)	Si2^{v}—Li5—Li7^{xi}	100.64 (2)
Li3^{ii}—Si2—Li4^{ii}	59.16 (3)	Si1^{xi}—Li5—Li7^{xi}	52.46 (2)
Li6A—Si2—Li4^{ii}	91.45 (5)	Li3—Li5—Li7^{xi}	129.47 (2)
Li6A^{viii}—Si2—Li4^{ii}	91.45 (5)	Li3^{v}—Li5—Li7^{xi}	129.47 (2)
Li6B^{viii}—Si2—Li4^{ii}	105.3 (2)	Si2^{v}—Li6A—Si2	114.48 (4)
Li6B—Si2—Li4^{ii}	105.3 (2)	Si2^{v}—Li6A—Li7^{ii}	62.65 (2)
Li5—Si2—Li4^{ii}	115.713 (19)	Si2—Li6A—Li7^{ii}	62.65 (2)
Li5^{viii}—Si2—Li4^{ii}	115.713 (19)	Si2^{v}—Li6A—Si1	122.72 (2)
Li7^{ii}—Si2—Li4^{ii}	58.534 (15)	Si2—Li6A—Si1	122.72 (2)
Li7^{ix}—Si2—Li4^{ii}	58.534 (15)	Li7^{ii}—Li6A—Si1	145.53 (10)
Li1^{x}—Li1—Li3	99.26 (5)	Si2^{v}—Li6A—Li5	61.14 (3)
Li1^{x}—Li1—Li5^{viii}	116.21 (3)	Si2—Li6A—Li5	61.14 (3)
Li3—Li1—Li5^{viii}	71.64 (3)	Li7^{ii}—Li6A—Li5	58.76 (3)

Li1^{x}—Li1—Li5	116.21 (3)	Si1—Li6A—Li5	155.71 (9)
Li3—Li1—Li5	71.64 (3)	Si2^{v}—Li6A—Li3^{vi}	57.60 (2)
Li5^{viii}—Li1—Li5	119.19 (5)	Si2—Li6A—Li3^{vi}	145.67 (8)
Li1^{x}—Li1—Si1^{vii}	67.17 (2)	Li7^{ii}—Li6A—Li3^{vi}	87.22 (5)
Li3—Li1—Si1^{vii}	119.07 (2)	Si1—Li6A—Li3^{vi}	73.07 (4)
Li5^{viii}—Li1—Si1^{vii}	64.776 (18)	Li5—Li6A—Li3^{vi}	118.37 (3)
Li5—Li1—Si1^{vii}	168.80 (4)	Si2^{v}—Li6A—Li3^{ii}	145.67 (8)
Li1^{x}—Li1—Si1^{xi}	67.17 (2)	Si2—Li6A—Li3^{ii}	57.61 (2)
Li3—Li1—Si1^{xi}	119.07 (2)	Li7^{ii}—Li6A—Li3^{ii}	87.22 (5)
Li5^{viii}—Li1—Si1^{xi}	168.80 (4)	Si1—Li6A—Li3^{ii}	73.07 (4)
Li5—Li1—Si1^{xi}	64.776 (18)	Li5—Li6A—Li3^{ii}	118.37 (3)
Si1^{vii}—Li1—Si1^{xi}	109.32 (3)	Li3^{vi}—Li6A—Li3^{ii}	108.10 (8)
Li1^{x}—Li1—Li4^{vii}	83.64 (4)	Si2^{v}—Li6A—Li4	156.71 (9)
Li3—Li1—Li4^{vii}	177.10 (5)	Si2—Li6A—Li4	66.92 (2)
Li5^{viii}—Li1—Li4^{vii}	107.13 (3)	Li7^{ii}—Li6A—Li4	128.45 (2)
Li5—Li1—Li4^{vii}	107.13 (3)	Si1—Li6A—Li4	62.08 (3)
Si1^{vii}—Li1—Li4^{vii}	62.011 (17)	Li5—Li6A—Li4	104.80 (6)
Si1^{xi}—Li1—Li4^{vii}	62.012 (18)	Li3^{vi}—Li6A—Li4	134.98 (5)
Li1^{x}—Li1—Li2^{vii}	152.08 (6)	Li3^{ii}—Li6A—Li4	56.31 (3)
Li3—Li1—Li2^{vii}	108.66 (4)	Si2^{v}—Li6A—Li4^{v}	66.92 (2)
Li5^{viii}—Li1—Li2^{vii}	74.07 (3)	Si2—Li6A—Li4^{v}	156.71 (9)
Li5—Li1—Li2^{vii}	74.07 (3)	Li7^{ii}—Li6A—Li4^{v}	128.45 (2)
Si1^{vii}—Li1—Li2^{vii}	98.16 (2)	Si1—Li6A—Li4^{v}	62.08 (3)
Si1^{xi}—Li1—Li2^{vii}	98.16 (2)	Li5—Li6A—Li4^{v}	104.80 (6)
Li4^{vii}—Li1—Li2^{vii}	68.44 (3)	Li3^{vi}—Li6A—Li4^{v}	56.31 (3)
Li1^{x}—Li1—Si2	155.65 (6)	Li3^{ii}—Li6A—Li4^{v}	134.98 (5)
Li3—Li1—Si2	56.39 (3)	Li4—Li6A—Li4^{v}	102.37 (5)
Li5^{viii}—Li1—Si2	59.72 (2)	Si2^{v}—Li6A—Li7	110.22 (5)
Li5—Li1—Si2	59.72 (2)	Si2—Li6A—Li7	110.22 (5)
Si1^{vii}—Li1—Si2	122.029 (17)	Li7^{ii}—Li6A—Li7	161.59 (8)
Si1^{xi}—Li1—Si2	122.029 (17)	Si1—Li6A—Li7	52.88 (3)
Li4^{vii}—Li1—Si2	120.71 (4)	Li5—Li6A—Li7	102.83 (7)
Li2^{vii}—Li1—Si2	52.269 (16)	Li3^{vi}—Li6A—Li7	103.34 (4)
Li1^{x}—Li1—Si1^{xii}	59.63 (2)	Li3^{ii}—Li6A—Li7	103.34 (4)
Li3—Li1—Si1^{xii}	71.64 (2)	Li4—Li6A—Li7	52.06 (3)
Li5^{viii}—Li1—Si1^{xii}	57.691 (19)	Li4^{v}—Li6A—Li7	52.06 (3)
Li5—Li1—Si1^{xii}	141.50 (4)	Si2^{v}—Li6A—Li3	113.47 (6)
Si1^{vii}—Li1—Si1^{xii}	49.695 (9)	Si2—Li6A—Li3	47.61 (3)
Si1^{xi}—Li1—Si1^{xii}	126.80 (3)	Li7^{ii}—Li6A—Li3	99.65 (4)
Li4^{vii}—Li1—Si1^{xii}	110.06 (2)	Si1—Li6A—Li3	106.70 (5)
Li2^{vii}—Li1—Si1^{xii}	129.406 (14)	Li5—Li6A—Li3	56.23 (4)
Si2—Li1—Si1^{xii}	107.16 (2)	Li3^{vi}—Li6A—Li3	164.63 (7)
Li1^{x}—Li1—Si1^{xiii}	59.63 (2)	Li3^{ii}—Li6A—Li3	86.09 (2)
Li3—Li1—Si1^{xiii}	71.64 (2)	Li4—Li6A—Li3	48.69 (3)
Li5^{viii}—Li1—Si1^{xiii}	141.50 (4)	Li4^{v}—Li6A—Li3	109.49 (7)
Li5—Li1—Si1^{xiii}	57.691 (19)	Li7—Li6A—Li3	66.64 (4)
Si1^{vii}—Li1—Si1^{xiii}	126.80 (3)	Si2^{v}—Li6A—Li3^{v}	47.61 (3)
Si1^{xi}—Li1—Si1^{xiii}	49.695 (9)	Si2—Li6A—Li3^{v}	113.47 (6)
Li4^{vii}—Li1—Si1^{xiii}	110.06 (2)	Li7^{ii}—Li6A—Li3^{v}	99.65 (4)

Li2^{vii}—Li1—Si1^{xiii}	129.406 (14)	Si1—Li6A—Li3^{v}	106.70 (5)
Si2—Li1—Si1^{xiii}	107.16 (2)	Li5—Li6A—Li3^{v}	56.23 (4)
Si1^{xii}—Li1—Si1^{xiii}	99.56 (3)	Li3^{vi}—Li6A—Li3^{v}	86.09 (2)
Si2^{xiii}—Li2—Si2^{iv}	180.000 (4)	Li3^{ii}—Li6A—Li3^{v}	164.63 (7)
Si2^{xiii}—Li2—Li1^{xiii}	65.859 (17)	Li4—Li6A—Li3^{v}	109.48 (7)
Si2^{iv}—Li2—Li1^{xiii}	114.141 (17)	Li4^{v}—Li6A—Li3^{v}	48.69 (3)
Si2^{xiii}—Li2—Li1^{iv}	114.142 (17)	Li7—Li6A—Li3^{v}	66.64 (4)
Si2^{iv}—Li2—Li1^{iv}	65.859 (17)	Li3—Li6A—Li3^{v}	79.23 (5)
Li1^{xiii}—Li2—Li1^{iv}	180.0	Li5—Li6B—Si2^{v}	64.82 (11)
Si2^{xiii}—Li2—Li7^{viii}	61.584 (16)	Li5—Li6B—Si2	64.82 (11)
Si2^{iv}—Li2—Li7^{viii}	118.416 (16)	Si2^{v}—Li6B—Si2	112.6 (2)
Li1^{xiii}—Li2—Li7^{viii}	99.849 (19)	Li5—Li6B—Li4	119.1 (2)
Li1^{iv}—Li2—Li7^{viii}	80.151 (19)	Si2^{v}—Li6B—Li4	175.5 (4)
Si2^{xiii}—Li2—Li7^{xiv}	118.417 (16)	Si2—Li6B—Li4	68.579 (18)
Si2^{iv}—Li2—Li7^{xiv}	61.583 (16)	Li5—Li6B—Li4^{v}	119.1 (2)
Li1^{xiii}—Li2—Li7^{xiv}	80.151 (19)	Si2^{v}—Li6B—Li4^{v}	68.579 (19)
Li1^{iv}—Li2—Li7^{xiv}	99.849 (19)	Si2—Li6B—Li4^{v}	175.5 (4)
Li7^{viii}—Li2—Li7^{xiv}	180.0	Li4—Li6B—Li4^{v}	109.86 (19)
Si2^{xiii}—Li2—Li7^{xv}	118.417 (16)	Li5—Li6B—Si1	178.7 (4)
Si2^{iv}—Li2—Li7^{xv}	61.583 (16)	Si2^{v}—Li6B—Si1	114.7 (2)
Li1^{xiii}—Li2—Li7^{xv}	80.151 (19)	Si2—Li6B—Si1	114.7 (2)
Li1^{iv}—Li2—Li7^{xv}	99.849 (19)	Li4—Li6B—Si1	61.41 (11)
Li7^{viii}—Li2—Li7^{xv}	76.94 (3)	Li4^{v}—Li6B—Si1	61.41 (11)
Li7^{xiv}—Li2—Li7^{xv}	103.06 (3)	Li5—Li6B—Li7	125.1 (4)
Si2^{xiii}—Li2—Li7	61.584 (16)	Si2^{v}—Li6B—Li7	122.40 (15)
Si2^{iv}—Li2—Li7	118.417 (16)	Si2—Li6B—Li7	122.40 (15)
Li1^{xiii}—Li2—Li7	99.850 (19)	Li4—Li6B—Li7	57.95 (11)
Li1^{iv}—Li2—Li7	80.151 (19)	Li4^{v}—Li6B—Li7	57.95 (11)
Li7^{viii}—Li2—Li7	103.06 (3)	Si1—Li6B—Li7	56.18 (10)
Li7^{xiv}—Li2—Li7	76.94 (3)	Li5—Li6B—Li7^{ii}	57.68 (13)
Li7^{xv}—Li2—Li7	180.0	Si2^{v}—Li6B—Li7^{ii}	58.12 (12)
Si2^{xiii}—Li2—Li4^{xv}	121.622 (16)	Si2—Li6B—Li7^{ii}	58.12 (12)
Si2^{iv}—Li2—Li4^{xv}	58.378 (16)	Li4—Li6B—Li7^{ii}	121.27 (18)
Li1^{xiii}—Li2—Li4^{xv}	55.76 (2)	Li4^{v}—Li6B—Li7^{ii}	121.27 (18)
Li1^{iv}—Li2—Li4^{xv}	124.24 (2)	Si1—Li6B—Li7^{ii}	121.0 (3)
Li7^{viii}—Li2—Li4^{xv}	126.209 (14)	Li7—Li6B—Li7^{ii}	177.2 (4)
Li7^{xiv}—Li2—Li4^{xv}	53.791 (15)	Li5—Li6B—Li3	65.94 (17)
Li7^{xv}—Li2—Li4^{xv}	53.791 (15)	Si2^{v}—Li6B—Li3	129.1 (3)
Li7—Li2—Li4^{xv}	126.210 (14)	Si2—Li6B—Li3	53.69 (8)
Si2^{xiii}—Li2—Li4	58.378 (16)	Li4—Li6B—Li3	55.26 (9)
Si2^{iv}—Li2—Li4	121.622 (16)	Li4^{v}—Li6B—Li3	129.3 (3)
Li1^{xiii}—Li2—Li4	124.24 (2)	Si1—Li6B—Li3	114.84 (14)
Li1^{iv}—Li2—Li4	55.76 (2)	Li7—Li6B—Li3	77.97 (19)
Li7^{viii}—Li2—Li4	53.791 (14)	Li7^{ii}—Li6B—Li3	103.89 (14)
Li7^{xiv}—Li2—Li4	126.210 (14)	Li5—Li6B—Li3^{v}	65.94 (17)
Li7^{xv}—Li2—Li4	126.210 (14)	Si2^{v}—Li6B—Li3^{v}	53.69 (8)
Li7—Li2—Li4	53.790 (15)	Si2—Li6B—Li3^{v}	129.1 (3)
Li4^{xv}—Li2—Li4	180.0	Li4—Li6B—Li3^{v}	129.3 (3)
Si2^{xiii}—Li2—Li5^{iii}	124.896 (15)	Li4^{v}—Li6B—Li3^{v}	55.26 (9)

Si2^{iv}—Li2—Li5^{iii}	55.104 (15)	Si1—Li6B—Li3^{v}	114.84 (14)
Li1^{xiii}—Li2—Li5^{iii}	130.096 (14)	Li7—Li6B—Li3^{v}	77.97 (19)
Li1^{iv}—Li2—Li5^{iii}	49.904 (14)	Li7^{ii}—Li6B—Li3^{v}	103.89 (14)
Li7^{viii}—Li2—Li5^{iii}	129.00 (2)	Li3—Li6B—Li3^{v}	94.6 (3)
Li7^{xiv}—Li2—Li5^{iii}	51.00 (2)	Li5—Li6B—Li3^{vi}	114.65 (17)
Li7^{xv}—Li2—Li5^{iii}	116.42 (2)	Si2^{v}—Li6B—Li3^{vi}	52.18 (10)
Li7—Li2—Li5^{iii}	63.58 (2)	Si2—Li6B—Li3^{vi}	124.0 (3)
Li4^{xv}—Li2—Li5^{iii}	94.745 (17)	Li4—Li6B—Li3^{vi}	123.4 (3)
Li4—Li2—Li5^{iii}	85.255 (17)	Li4^{v}—Li6B—Li3^{vi}	52.90 (9)
Si2^{xiii}—Li2—Li5^{iv}	124.896 (15)	Si1—Li6B—Li3^{vi}	64.52 (16)
Si2^{iv}—Li2—Li5^{iv}	55.104 (15)	Li7—Li6B—Li3^{vi}	103.25 (14)
Li1^{xiii}—Li2—Li5^{iv}	130.096 (14)	Li7^{ii}—Li6B—Li3^{vi}	74.81 (18)
Li1^{iv}—Li2—Li5^{iv}	49.904 (14)	Li3—Li6B—Li3^{vi}	177.4 (3)
Li7^{viii}—Li2—Li5^{iv}	63.58 (2)	Li3^{v}—Li6B—Li3^{vi}	87.879 (16)
Li7^{xiv}—Li2—Li5^{iv}	116.42 (2)	Li5—Li6B—Li3^{ii}	114.65 (17)
Li7^{xv}—Li2—Li5^{iv}	51.00 (2)	Si2^{v}—Li6B—Li3^{ii}	124.0 (3)
Li7—Li2—Li5^{iv}	129.00 (2)	Si2—Li6B—Li3^{ii}	52.18 (10)
Li4^{xv}—Li2—Li5^{iv}	94.745 (17)	Li4—Li6B—Li3^{ii}	52.90 (9)
Li4—Li2—Li5^{iv}	85.255 (17)	Li4^{v}—Li6B—Li3^{ii}	123.4 (3)
Li5^{iii}—Li2—Li5^{iv}	86.65 (2)	Si1—Li6B—Li3^{ii}	64.52 (16)
Li1—Li3—Si2	68.32 (3)	Li7—Li6B—Li3^{ii}	103.25 (14)
Li1—Li3—Si2^{xiii}	156.96 (5)	Li7^{ii}—Li6B—Li3^{ii}	74.81 (18)
Si2—Li3—Si2^{xiii}	134.72 (4)	Li3—Li6B—Li3^{ii}	87.879 (16)
Li1—Li3—Li4^{xiii}	86.20 (4)	Li3^{v}—Li6B—Li3^{ii}	177.4 (3)
Si2—Li3—Li4^{xiii}	154.51 (5)	Li3^{vi}—Li6B—Li3^{ii}	89.6 (3)
Si2^{xiii}—Li3—Li4^{xiii}	70.77 (3)	Li5^{xiii}—Li7—Li6A^{xiii}	62.25 (5)
Li1—Li3—Li4	138.67 (5)	Li5^{xiii}—Li7—Si1	163.20 (4)
Si2—Li3—Li4	70.35 (3)	Li6A^{xiii}—Li7—Si1	134.55 (6)
Si2^{xiii}—Li3—Li4	64.37 (3)	Li5^{xiii}—Li7—Li4^{v}	122.31 (2)
Li4^{xiii}—Li3—Li4	135.14 (4)	Li6A^{xiii}—Li7—Li4^{v}	93.38 (4)
Li1—Li3—Li6A^{xii}	111.01 (3)	Si1—Li7—Li4^{v}	63.27 (2)
Si2—Li3—Li6A^{xii}	124.37 (4)	Li5^{xiii}—Li7—Li4	122.31 (2)
Si2^{xiii}—Li3—Li6A^{xii}	59.21 (3)	Li6A^{xiii}—Li7—Li4	93.38 (4)
Li4^{xiii}—Li3—Li6A^{xii}	63.89 (4)	Si1—Li7—Li4	63.27 (2)
Li4—Li3—Li6A^{xii}	92.17 (4)	Li4^{v}—Li7—Li4	109.66 (4)
Li1—Li3—Li6A^{xiii}	111.01 (3)	Li5^{xiii}—Li7—Si2^{xiii}	60.933 (17)
Si2—Li3—Li6A^{xiii}	124.37 (4)	Li6A^{xiii}—Li7—Si2^{xiii}	58.58 (2)
Si2^{xiii}—Li3—Li6A^{xiii}	59.21 (3)	Si1—Li7—Si2^{xiii}	124.156 (15)
Li4^{xiii}—Li3—Li6A^{xiii}	63.89 (4)	Li4^{v}—Li7—Si2^{xiii}	148.06 (4)
Li4—Li3—Li6A^{xiii}	92.17 (4)	Li4—Li7—Si2^{xiii}	61.815 (18)
Li6A^{xii}—Li3—Li6A^{xiii}	108.10 (8)	Li5^{xiii}—Li7—Si2^{xvi}	60.933 (17)
Li1—Li3—Li5	54.48 (2)	Li6A^{xiii}—Li7—Si2^{xvi}	58.58 (2)
Si2—Li3—Li5	57.97 (2)	Si1—Li7—Si2^{xvi}	124.156 (15)
Si2^{xiii}—Li3—Li5	131.88 (2)	Li4^{v}—Li7—Si2^{xvi}	61.815 (18)
Li4^{xiii}—Li3—Li5	107.49 (3)	Li4—Li7—Si2^{xvi}	148.06 (4)
Li4—Li3—Li5	102.23 (3)	Si2^{xiii}—Li7—Si2^{xvi}	107.79 (3)
Li6A^{xii}—Li3—Li5	164.79 (5)	Li5^{xiii}—Li7—Li2^{v}	72.37 (2)
Li6A^{xiii}—Li3—Li5	76.55 (4)	Li6A^{xiii}—Li7—Li2^{v}	109.87 (3)
Li1—Li3—Li5^{viii}	54.48 (2)	Si1—Li7—Li2^{v}	97.64 (2)

Si2—Li3—Li5^{viii}	57.97 (2)	Li4^{v}—Li7—Li2^{v}	68.809 (17)
Si2^{xiii}—Li3—Li5^{viii}	131.88 (2)	Li4—Li7—Li2^{v}	156.71 (4)
Li4^{xiii}—Li3—Li5^{viii}	107.48 (3)	Si2^{xiii}—Li7—Li2^{v}	131.80 (3)
Li4—Li3—Li5^{viii}	102.23 (3)	Si2^{xvi}—Li7—Li2^{v}	53.233 (8)
Li6A^{xii}—Li3—Li5^{viii}	76.55 (4)	Li5^{xiii}—Li7—Li2	72.37 (2)
Li6A^{xiii}—Li3—Li5^{viii}	164.79 (5)	Li6A^{xiii}—Li7—Li2	109.87 (3)
Li5—Li3—Li5^{viii}	95.40 (4)	Si1—Li7—Li2	97.64 (2)
Li1—Li3—Li6B	98.86 (11)	Li4^{v}—Li7—Li2	156.71 (4)
Si2—Li3—Li6B	56.17 (14)	Li4—Li7—Li2	68.810 (17)
Si2^{xiii}—Li3—Li6B	96.70 (11)	Si2^{xiii}—Li7—Li2	53.233 (8)
Li4^{xiii}—Li3—Li6B	132.00 (14)	Si2^{xvi}—Li7—Li2	131.80 (3)
Li4—Li3—Li6B	56.51 (11)	Li2^{v}—Li7—Li2	103.06 (3)
Li6A^{xii}—Li3—Li6B	147.86 (12)	Li5^{xiii}—Li7—Li6B	135.66 (19)
Li6A^{xiii}—Li3—Li6B	69.93 (11)	Li6A^{xiii}—Li7—Li6B	73.41 (15)
Li5—Li3—Li6B	47.28 (10)	Si1—Li7—Li6B	61.14 (18)
Li5^{viii}—Li3—Li6B	114.13 (14)	Li4^{v}—Li7—Li6B	57.84 (5)
Li1—Li3—Li6B^{viii}	98.86 (11)	Li4—Li7—Li6B	57.84 (5)
Si2—Li3—Li6B^{viii}	56.17 (14)	Si2^{xiii}—Li7—Li6B	96.57 (11)
Si2^{xiii}—Li3—Li6B^{viii}	96.70 (11)	Si2^{xvi}—Li7—Li6B	96.57 (11)
Li4^{xiii}—Li3—Li6B^{viii}	132.00 (14)	Li2^{v}—Li7—Li6B	126.62 (4)
Li4—Li3—Li6B^{viii}	56.51 (11)	Li2—Li7—Li6B	126.62 (4)
Li6A^{xii}—Li3—Li6B^{viii}	69.93 (11)	Li5^{xiii}—Li7—Li6B^{xiii}	50.66 (18)
Li6A^{xiii}—Li3—Li6B^{viii}	147.86 (12)	Li6A^{xiii}—Li7—Li6B^{xiii}	11.59 (14)
Li5—Li3—Li6B^{viii}	114.13 (14)	Si1—Li7—Li6B^{xiii}	146.14 (18)
Li5^{viii}—Li3—Li6B^{viii}	47.28 (10)	Li4^{v}—Li7—Li6B^{xiii}	99.96 (10)
Li6B—Li3—Li6B^{viii}	94.6 (3)	Li4—Li7—Li6B^{xiii}	99.96 (10)
Li1—Li3—Li6B^{xii}	112.27 (10)	Si2^{xiii}—Li7—Li6B^{xiii}	55.54 (4)
Si2—Li3—Li6B^{xii}	134.21 (13)	Si2^{xvi}—Li7—Li6B^{xiii}	55.54 (4)
Si2^{xiii}—Li3—Li6B^{xii}	54.31 (10)	Li2^{v}—Li7—Li6B^{xiii}	103.19 (11)
Li4^{xiii}—Li3—Li6B^{xii}	55.03 (13)	Li2—Li7—Li6B^{xiii}	103.19 (11)
Li4—Li3—Li6B^{xii}	96.40 (11)	Li6B—Li7—Li6B^{xiii}	85.00 (3)
Li6A^{xii}—Li3—Li6B^{xii}	9.86 (10)	Li5^{xiii}—Li7—Li5^{iii}	106.63 (4)
Li6A^{xiii}—Li3—Li6B^{xii}	98.97 (16)	Li6A^{xiii}—Li7—Li5^{iii}	168.88 (6)
Li5—Li3—Li6B^{xii}	160.95 (12)	Si1—Li7—Li5^{iii}	56.57 (2)
Li5^{viii}—Li3—Li6B^{xii}	84.41 (12)	Li4^{v}—Li7—Li5^{iii}	93.01 (3)
Li6B—Li3—Li6B^{xii}	148.83 (4)	Li4—Li7—Li5^{iii}	93.02 (3)
Li6B^{viii}—Li3—Li6B^{xii}	79.609 (14)	Si2^{xiii}—Li7—Li5^{iii}	117.29 (2)
Li3^{ii}—Li4—Li3	107.43 (3)	Si2^{xvi}—Li7—Li5^{iii}	117.29 (2)
Li3^{ii}—Li4—Li6B	72.1 (2)	Li2^{v}—Li7—Li5^{iii}	64.282 (19)
Li3—Li4—Li6B	68.24 (17)	Li2—Li7—Li5^{iii}	64.281 (19)
Li3^{ii}—Li4—Li6B^{viii}	72.1 (2)	Li6B—Li7—Li5^{iii}	117.71 (18)
Li3—Li4—Li6B^{viii}	68.24 (17)	Li6B^{xiii}—Li7—Li5^{iii}	157.29 (18)
Li6B—Li4—Li6B^{viii}	109.86 (19)		

Symmetry codes: (i) −*x*+1, −*y*+1, −*z*+1; (ii) *x*+1/2, −*y*+1/2, *z*; (iii) −*x*+1/2, *y*+1/2, −*z*+1; (iv) −*x*+1/2, *y*+1/2, −*z*; (v) *x*, *y*, *z*+1; (vi) *x*+1/2, −*y*+1/2, *z*+1; (vii) −*x*+1/2, *y*−1/2, −*z*; (viii) *x*, *y*, *z*−1; (ix) *x*+1/2, −*y*+1/2, *z*−1; (x) −*x*, −*y*, −*z*; (xi) −*x*+1/2, *y*−1/2, −*z*+1; (xii) *x*−1/2, −*y*+1/2, *z*−1; (xiii) *x*−1/2, −*y*+1/2, *z*; (xiv) −*x*, −*y*+1, −*z*+1; (xv) −*x*, −*y*+1, −*z*; (xvi) *x*−1/2, −*y*+1/2, *z*+1.

5.4 Stabilizing the Phase $Li_{15}Si_4$ through Lithium–Aluminum Substitution in $Li_{15-x}Al_xSi_4$ ($0.4 < x < 0.8$) — Single Crystal X-ray Structure Determination of $Li_{15}Si_4$ and $Li_{14.37}Al_{0.63}Si_4$

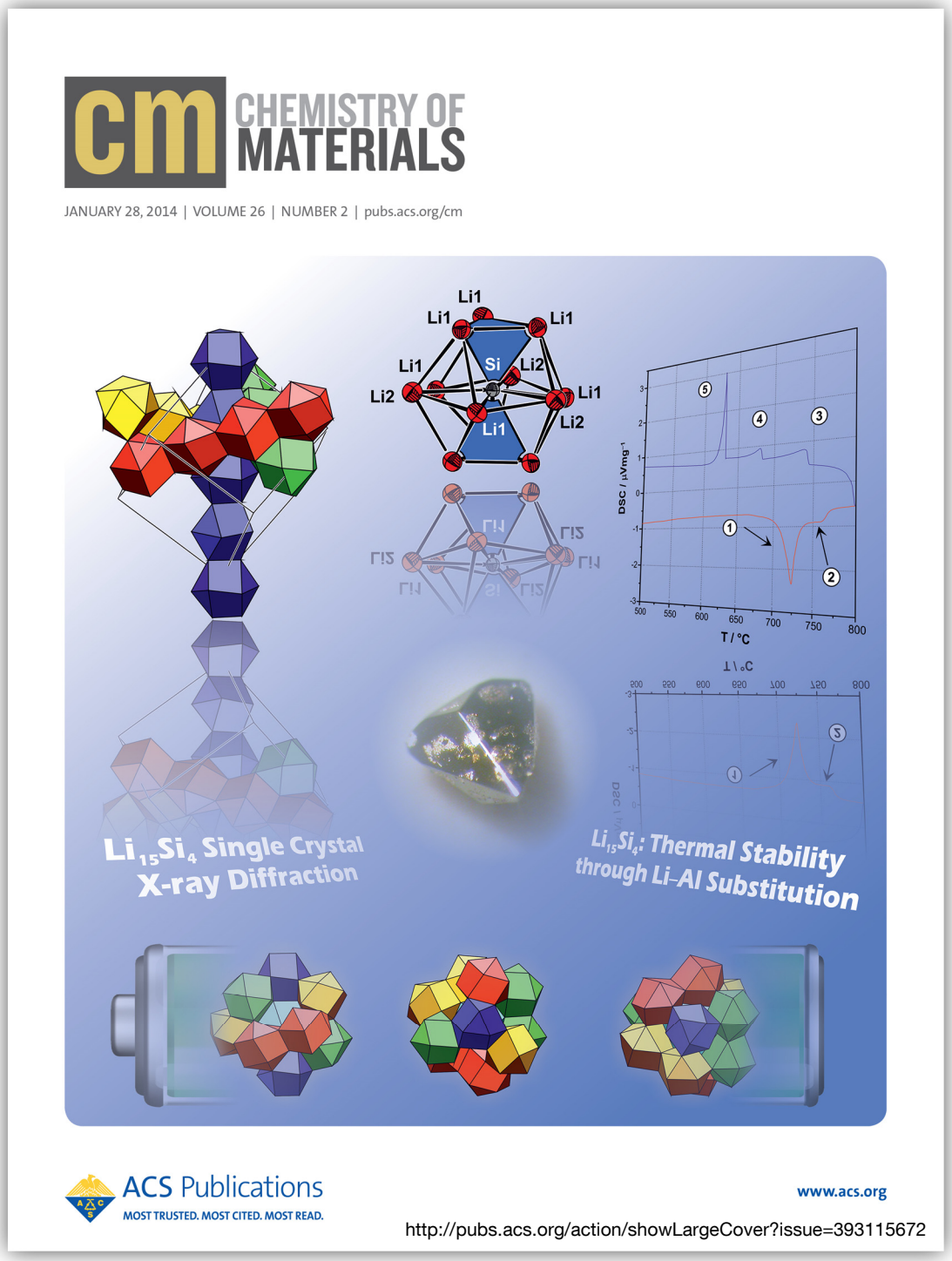

CHEMISTRY OF MATERIALS

Article

pubs.acs.org/cm

Stabilizing the Phase $Li_{15}Si_4$ through Lithium−Aluminum Substitution in $Li_{15-x}Al_xSi_4$ ($0.4 < x < 0.8$)—Single Crystal X-ray Structure Determination of $Li_{15}Si_4$ and $Li_{14.37}Al_{0.63}Si_4$

Michael Zeilinger,[†] Volodymyr Baran,[†] Leo van Wüllen,[‡] Ulrich Häussermann,[§] and Thomas F. Fässler*,[†]

[†]Department Chemie, Technische Universität München, Lichtenbergstraße 4, 85747 Garching b. München, Germany

[‡]Department of Physics, University of Augsburg, Universitätsstr. 1, 86159 Augsburg, Germany

[§]Department of Materials and Environmental Chemistry, Stockholm University, SE-10691 Stockholm, Sweden

Supporting Information

ABSTRACT: Single crystals of $Li_{15}Si_4$ and $Li_{15-x}Al_xSi_4$ ($x = 0.63(1)$) were obtained from equilibrated melts with compositions $Li_{100-x}Si_x$ ($x = 10$, 15) and $Li_{83}Al_{13}Si_4$, respectively, and isolated by isothermal centrifugation. $Li_{15}Si_4$ and $Li_{14.37(1)}Al_{0.63(1)}Si_4$ crystallize with the $Cu_{15}Si_4$ structure type ($I\bar{4}3d$, $a_{x=0} = 10.6322(9)$ Å, $a_{x=0.63(1)} = 10.6172(4)$ Å, $Z = 4$, $T = 123$ K). The incorporation of Al equally affects both crystallographically distinguished Li positions in the $Li_{15}Si_4$ structure. The replacement of about 4% of Li is firmly established by the refinement of single crystal diffraction data and NMR spectroscopy. The homogeneity range of $Li_{15-x}Al_xSi_4$ was assessed as $0.4 < x < 0.8$ from synthesis experiments using stoichiometric proportions of the elements. Differential scanning calorimetry studies confirm the metastable character of $Li_{15}Si_4$, decomposing exothermally at temperatures around 200 °C. However, the decomposition process of $Li_{15}Si_4$ is sluggish and appreciable rates are not observed before temperatures reach 400 °C. In contrast $Li_{15-x}Al_xSi_4$ is thermodynamically stable. The decomposition temperature is at about 700 °C. It is speculated that the thermodynamic stability of $Li_{15-x}Al_xSi_4$ is a consequence of the increased electron concentration, shifting the Fermi level to a pseudo-gap in the electronic density of states. Since metastable $Li_{15}Si_4$ plays an important role during electrochemical lithiation of a silicon anode, thermodynamically stable $Li_{15-x}Al_xSi_4$ may have interesting properties as anode material in lithium ion batteries.

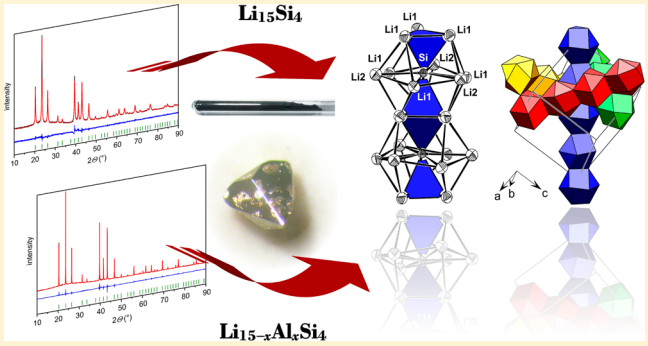

KEYWORDS: *$Li_{15}Si_4$, lithium silicides, Li−Si system, lithium−silicon system, Li−Al−Si system, lithium−aluminum−silicon system, thermodynamic stability of lithium silicides*

1. INTRODUCTION

Efforts on implementing silicon as anode material in future lithium ion batteries have fueled numerous investigations of the binary Li−Si system. The lithiation/delithiation process of Si is highly complex, involving crystalline-to-amorphous phase transitions and various amorphous phases.[1−6] It has been shown that the local structure of the amorphous Li_xSi materials resembles that of crystalline phases,[3,4] and the complexity of the (de)lithiation process of Si probably relates to the complexity of the Li−Si phase diagram showing three, or possibly four, stable phases in the narrow range 76.5−81 atom % Li.[7]

Of particular significance in the (de)lithiation process is the composition $Li_{3.75}Si$ (78.9 atom % Li) which is considered to be the fully lithiated state in a typical electrochemical reaction.[1,2] Depending on the applied discharge voltage and the design of the Si anode amorphous $Li_{3.75}Si$ can undergo a transition to a crystalline but metastable phase $Li_{15}Si_4$.[1,2,8] The conditions of formation of crystalline $Li_{15}Si_4$ and the lithiation mechanism in silicon electrodes are topics of extensive current research.[9−13]

Remarkably, despite its significance, a range of fundamental properties of $Li_{15}Si_4$ are still not conclusively characterized. Although metastable, the bulk synthesis of $Li_{15}Si_4$ can be achieved through electrochemical reactions or mechanical ball milling at room temperature.[1−3,14,15] On the basis of powder X-ray diffraction data and theoretical calculations $Li_{15}Si_4$ has been assigned the cubic $Cu_{15}Si_4$ structure type.[1,2,16−19] This structure model may be correct; however, our recent discovery of interstitial Li in $Li_{21}Si_5$[20] shows clearly the superiority of diffraction data from high quality single crystals for the unambiguous location and refinement of Li atom positions in lithium silicides.[7] Further, it was reported that upon annealing metastable $Li_{15}Si_4$ decomposes into "unknown",[3] "new but unidentified"[21] or "unexpected" known phases.[22,23] These widely varying results are confusing and need clarification. According to

Received: August 12, 2013
Revised: September 11, 2013
Published: September 16, 2013

   dx.doi.org/10.1021/cm402721n | *Chem. Mater.* 2013, 25, 4113−4121

Table 1. Crystallographic Data and Structure Refinement for $Li_{15}Si_4$ and $Li_{14.37(1)}Al_{0.63(1)}Si_4$

	empirical formula	
	$Li_{15}Si_4$	$Li_{14.367(9)}Al_{0.633(9)}Si_4$
T, K	123(2)	123(2)
formula weight, g·mol^{-1}	216.46	229.14
crystal size, mm^3	0.30 × 0.30 × 0.30	0.30 × 0.20 × 0.20
crystal color	metallic silver	metallic silver
crystal shape	block	block
space group	$I\bar{4}3d$	$I\bar{4}3d$
unit cell dimension, Å	a = 10.6322(9)	a = 10.6172(4)
V, Å^3	1201.9(2)	1196.82(8)
Z	4	4
ρ(calcd), g·cm^{-3}	1.196	1.272
μ, mm^{-1}	0.424	0.474
F(000)	404	429
θ range, deg	4.70−31.47	4.70−36.24
index range hkl	±15, ±15, ±15	±17, ±17, −15 < l < 17
reflections collected	6926	24153
independent reflections	335 (R_{int} = 0.019)	485 (R_{int} = 0.022)
reflections with $I > 2\sigma(I)$	335 (R_σ = 0.006)	480 (R_σ = 0.005)
absorption correction	multiscan	multiscan
data/restraints/parameter	335/0/15	485/0/17
goodness-of-fit on F^2	1.145	1.299
final R indices $[I > 2\sigma(I)]^{a,b}$	R_1 = 0.010	R_1 = 0.006
	wR_2 = 0.030	wR_2 = 0.017
R indices (all data)^{a,b}	R_1 = 0.010	R_1 = 0.007
	wR_2= 0.030	wR_2= 0.017
Flack parameter	−0.2(2)	0.07(7)
largest diff. peak and hole, e·Å^{-3}	0.19 and −0.08	0.06 and −0.05

$^a R_1 = \sum||F_o| - |F_c||/\sum|F_o|$. $^b wR_2 = [\sum w(F_o^2 - F_c^2)^2/\sum w(F_o^2)^2]^{1/2}$.

latest findings, the Li−Si system contains a previously overlooked phase, $Li_{4.11}Si$,[7,24] which may play an important role for understanding the decomposition behavior of $Li_{15}Si_4$.

Herein, we report on the structural characterization of $Li_{15}Si_4$ from single crystal X-ray diffraction data and a detailed analysis of its thermal decomposition behavior. Additionally, we show that the substitution of small concentrations of Li by Al (about 4%) in $Li_{15}Si_4$ leads to a thermodynamically stable system which decomposes at around 700 °C.

2. EXPERIMENTAL SECTION

Synthesis. All steps of synthesis and sample preparation were carried out in a glovebox (MBraun, Ar-atmosphere, H_2O and O_2 levels < 0.1 ppm). Starting materials were rods of Li (99%, Rockwood Lithium), aluminum granules (99.99%, Chempur), and silicon powder (99.999%, Sigma-Aldrich). $Li_{15}Si_4$ bulk material was synthesized by mechanical ball-milling of a stoichiometric mixture of lithium and silicon in a RETSCH PM 100 planetary ball mill. A total amount of 3.0 g of lithium pieces and silicon powder were loaded into a stainless steel jar (V = 50 mL, ball charge: 3 pieces with a diameter of 15 mm) inside an argon filled glovebox. Using a safety closure device the jar was hermetically sealed and transferred to the ball mill outside the glovebox. The mixture was ball milled for 12−16 h (intervals: 10 min at 250 rpm followed by a 4 min break and direction reversal). Afterward the jar was transferred back to the glovebox where the $Li_{15}Si_4$ product was recovered. For the preparation of $Li_{15-x}Al_xSi_4$ a fine powder "AlSi" was employed as precursor. A 1:1 molar mixture of Al and Si with a total amount of 0.7−1.0 g was arc-melted inside the glovebox, subsequently fragmented into smaller pieces, and finally ball milled for 2−4 h.

Single crystals of $Li_{15}Si_4$ were obtained as a byproduct from experiments aimed at the single crystal growth of $Li_{17}Si_4$ from equilibrated melts with compositions $Li_{90}Si_{10}$ and $Li_{85}Si_{15}$.[7] In contrast to ref 7 the experiments reported here were performed in stainless steel ampules with dimensions L = 80.0 mm, OD = 12.7 mm, and ID = 11.7 mm. Prior to use, ampules were thoroughly cleaned and heated to 750 °C under dynamic vacuum ($p < 1 \times 10^{-3}$ mbar) for at least 2 h. A filter was inserted and reactions prepared according to ref 25. Reaction mixtures of $Li_{90}Si_{10}$ and $Li_{85}Si_{15}$ with a total mass of 300 mg were loaded and sealed in such ampules which were then placed in silica wool insulated reaction containers made of stainless steel. The mixtures were heated in a box furnace to 700 °C at a rate of 5 K min^{-1}, kept at this temperature for 1 h, and subsequently cooled at a rate of 5 K h^{-1} to 450 °C. After a dwell time of 48 h reactions were terminated by isothermally centrifuging off the melt. For the synthesis of single crystals $Li_{14.37(1)}Al_{0.63(1)}Si_4$ a reaction mixture $Li_{83}Al_{13}Si_4$ (where "AlSi" powder and small Al pieces served as Al source) was employed. Additionally, bulk synthesis of $Li_{15-x}Al_xSi_4$ was attempted by reacting mixtures $Li_{15-x}Al_xSi_4$ with x = 0.25, 0.50, 0.75, and 1.00 (where "AlSi" powder served as Al source) in tantalum ampules at 700 °C for 1 h, followed by cooling to 450 °C at a rate of 10 K min^{-1}, dwelling for four days, and subsequent quenching in liquid nitrogen. Samples where then ground in an agate mortar, annealed for one day at 800 °C, and quenched.

Annealing experiments were performed with 150 mg batches of $Li_{15}Si_4$ powder (obtained by mechanical ball-milling of the elements) which were sealed in tantalum ampules by arc-welding inside the glovebox. Tantalum ampules were enclosed in silica jackets under vacuum, annealed at various temperatures, and quenched in liquid nitrogen after different dwell times.

Single Crystal X-ray Diffraction and Structure Determination. Crystals of $Li_{15}Si_4$ and $Li_{14.37(1)}Al_{0.63(1)}Si_4$ were selected and cut in an Ar-filled glovebox and sealed in glass capillaries. Intensity data was collected at room temperature and −150 °C. For the latter a Bruker X-ray diffractometer equipped with a CCD detector (APEX II, κ-CCD), a fine-focused sealed tube with Mo Kα radiation (λ = 0.71073 Å), and a graphite monochromator was employed (for details on the room temperature experiments see Supporting Information, Tables S1 and S2). Data collection was controlled with the Bruker APEX Software

dx.doi.org/10.1021/cm402721n | Chem. Mater. 2013, 25, 4113−4121

Suite.[26] Integration, data reduction, and absorption correction was performed with the programs SAINT and SADABS.[27,28] Space group symmetry was assigned on the basis of the systematic absences and the statistical analysis of the intensity distributions. Friedel pairs were not merged as the assigned space group ($I\bar{4}3d$) is noncentrosymmetric. Fractional atomic coordinates and atomic displacement parameters for Li/Al mixed sites were set equal. The structures were solved with direct methods (SHELXS-97) and refined with full-matrix least-squares on F^2 (SHELXL-97).[29,30] Details of the single crystal data collections and refinements are listed in Table 1. Further details of the crystal structure investigations are supplied as Supporting Information or can be obtained from Fachinformationszentrum Karlsruhe, D-76344 Eggenstein-Leopoldshafen, Germany (fax: (+49) 7247-808-666; e-mail: crysdata@fiz-karlsruhe.de) on quoting the depository numbers CSD-426034 ($Li_{15}Si_4$-123K), CSD-426035 ($Li_{15}Si_4$-298K), CSD-426037 ($Li_{14.37}Al_{0.63}Si_4$-123K), and CSD-426038 ($Li_{14.41}Al_{0.59}Si_4$-298K).

Powder X-ray Diffraction (PXRD). PXRD patterns were recorded on a Stoe STADI P diffractometer (Ge(111) monochromator for Cu Kα radiation, λ = 1.54056 Å) equipped with a Detectris MYTHEN DCS 1K solid state detector. PXRD patterns were recorded from $Li_{15}Si_4$ and $Li_{15-x}Al_xSi_4$ bulk samples, ground single crystals of $Li_{15-x}Al_xSi_4$, and the products of $Li_{15}Si_4$ annealing experiments, as well as from recovered samples of thermal analysis investigation runs (see below). Samples were ground in an agate mortar, sealed in glass capillaries, and measured within a 2θ range of 10−90° (PSD steps: 0.06−1.50°; time/step: 15−40 s). TOPAS 4.0 was used for Rietveld refinements.[31]

Differential Scanning Calorimetry (DSC). DSC measurements were performed with a NETZSCH DSC 404 Pegasus instrument. Cylindrical niobium crucibles (L = 15.0 mm, OD = 6.5 mm, ID = 5.0 mm) were thoroughly cleaned and heated to 1000 °C under dynamic vacuum ($p < 1 \times 10^{-3}$ mbar) for 2 h and then transferred to an Ar-filled glovebox. Crucibles were loaded with 30−50 mg of sample and subsequently sealed by arc-welding inside the glovebox under cooling. An empty sealed crucible served as reference. All measurements were done under an Ar flow of 60−70 mL min^{-1} and applying a heating/cooling rate of 10 K min^{-1}. Handling of the DSC data was done with the program Proteus Thermal Analysis.[32] Samples for DSC investigations consisted of (i) $Li_{15}Si_4$ bulk material, (ii) ground single crystals of $Li_{14.37(1)}Al_{0.63(1)}Si_4$, and (iii) $Li_{14.25}Al_{0.75}Si_4$ bulk material. The thermal behavior of $Li_{15}Si_4$ between 25 and 300 °C was additionally studied with a Shimadzu DTA-50 instrument. A total of 15−25 mg of sample were loaded in stainless steel pans which were sealed airtight. Measurements are performed analogously to the previous description.

Energy Dispersive X-ray Spectroscopy (EDX). A JEOL-JSM 7500F scanning electron microscope equipped with an Oxford X-Max EDX analyzer with Mn as internal standard was used for determining the Al−Si ratio in $Li_{14.37(1)}Al_{0.63(1)}Si_4$. Samples were handled inside an Ar-filled glovebox and fixed on a graphite platelet which was mounted on an aluminum stub.

Solid State Nuclear Magnetic Resonance (NMR) Spectroscopy. Solid State NMR experiments were performed on a Bruker Avance III spectrometer operating at 7 T at a resonance frequency of 78.5 MHz for ^{27}Al. MAS NMR experiments were performed employing a 4 mm Bruker MAS NMR probe and spinning frequencies of 12 kHz, using dry N_2-gas as the bearing/drive gas. The rotor was packed in an Ar glovebox. Spectra are referenced to the ^{27}Al resonance of a 1 M aqueous solution of $Al(NO_3)_3$ at 0 ppm. The repetition delay was set to 5−15 s; an increase of this delay did not alter the appearance of the spectrum.

3. RESULTS AND DISCUSSION

Synthesis, Structure, and Phase Analysis of $Li_{15-x}Al_xSi_4$. Bulk synthesis by mechanical ball milling of stoichiometric mixtures of lithium and silicon affords $Li_{15}Si_4$ as a fine, dark gray powder consisting of submicrometer sized particles (Figure 1a). High-energy ball milling has been previously applied for the synthesis of metastable $Li_{15}Si_4$, and our result is in accordance with earlier investigations.[3,14,15]

Surprisingly, needle shaped single crystals of $Li_{15}Si_4$ with dimensions 1.5 × 0.3 × 0.3 mm were obtained as a side product

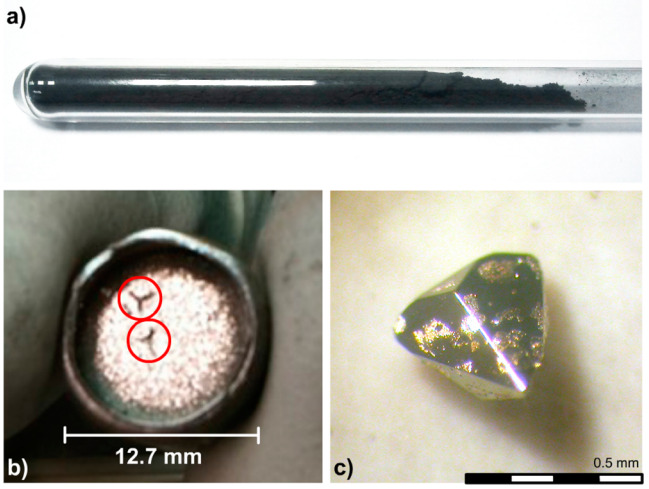

Figure 1. Photographs of obtained specimens. (a) Bulk sample of $Li_{15}Si_4$ obtained from high-energy mechanical ball milling. (b) Needle-shaped, intergrown crystals of $Li_{15}Si_4$ (encircled) grown at the bottom lid of a stainless steel ampule. (c) Representative single crystal of $Li_{14.37(1)}Al_{0.63(1)}Si_4$ separated from an equilibrated melt with the composition $Li_{83}Al_{13}Si_4$ at 450 °C.

when equilibrating melts with compositions $Li_{90}Si_{10}$ and $Li_{85}Si_{15}$ at 450 °C. Such melts targeted the crystal growth of $Li_{17}Si_4$[7] and were regularly accompanied by very few crystals of $Li_{15}Si_4$. These crystals grow at the surface of the bottom lid of the stainless steel ampule (Figure 1b) hosting the melt and stay attached to it during the centrifugation process separating $Li_{17}Si_4$ crystals from the melt. Their needle-like appearance is very different from the block-shaped $Li_{17}Si_4$ crystals. It is not clear why and at which stage of the melt equilibration $Li_{15}Si_4$ crystals are formed. However, it is apparent that their formation reflects non-equilibrium conditions either by virtue of the melt or the presence of the iron/iron-silicide surface. It is well-known that flux reactions can afford metastable materials through a kinetic control of reactions, although details often remain speculative.[33,34]

Interestingly, melts $Li_{83}Al_{13}Si_4$ equilibrated at 450 °C exclusively afford $Li_{15-x}Al_xSi_4$, with crystal diameters varying from 0.2 mm to 2.5 mm (Figure 1c). The presence of Al suppresses completely the formation of $Li_{17}Si_4$ otherwise obtained from binary Li-rich melts. Melts with the Al-poorer composition $Li_{87}Al_4Si_9$ also yield $Li_{15-x}Al_xSi_4$ although with a minor amount of byproduct (cf. Figure S1a, Supporting Information). The PXRD patterns of $Li_{15-x}Al_xSi_4$ obtained from both melts are virtually identical which indicates a very similar value of x despite the different composition of the melts.

Figure 2a,b show the PXRD pattern of $Li_{15}Si_4$ and ground single crystals of $Li_{15-x}Al_xSi_4$ from a melt $Li_{83}Al_{13}Si_4$. The high crystallinity of the latter in comparison with $Li_{15}Si_4$ from mechanical ball milling is clearly recognizable. The patterns can be fit to the $Cu_{15}Si_4$ structure model suggested in the literature with excellent reliability factors. The cell parameters are only slightly different, a = 10.7163(1) and a = 10.66095(3) Å for $Li_{15}Si_4$ and $Li_{15-x}Al_xSi_4$, respectively. Single crystal X-ray diffraction studies confirm unambiguously and resolutely the validity of $Cu_{15}Si_4$ structure (space group $I\bar{4}3d$, Z = 4) for both systems. The structure refinements concluded with excellent reliability factors (all data) of R_1 = 0.010 (wR_2 = 0.030) for $Li_{15}Si_4$ and R_1 = 0.007 (wR_2 = 0.017) for $Li_{15-x}Al_xSi_4$ and residual electron densities of virtually zero. Table 1 lists a summary of

dx.doi.org/10.1021/cm402721n | Chem. Mater. 2013, 25, 4113−4121

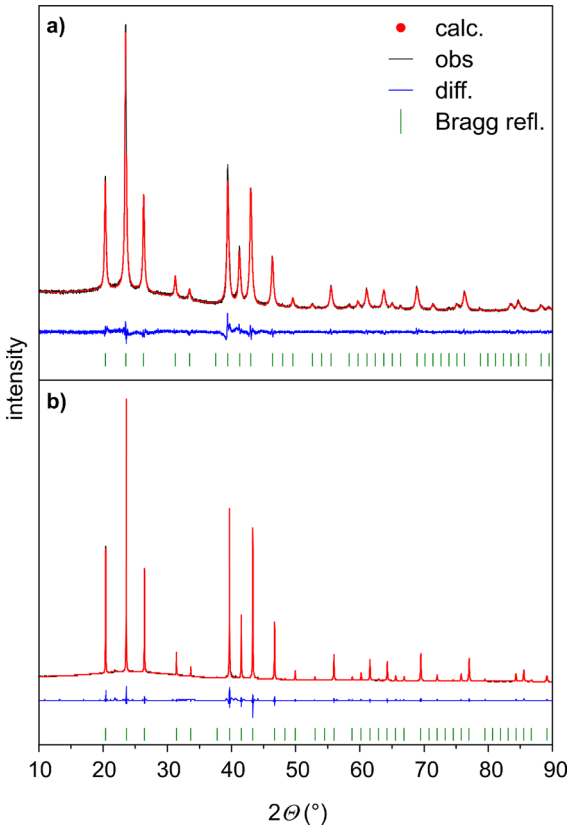

Figure 2. Rietveld fit of the $Cu_{15}Si_4$ structure model to the PXRD data of (a) $Li_{15}Si_4$ (bulk sample; R_p = 3.22, R_{wp} = 4.21, GOF = 1.37, space group $I\bar{4}3d$, a = 10.7163(1), V = 1230.66(5)), and (b) $Li_{14.37(1)}Al_{0.63(1)}Si_4$ (ground single crystals; R_p = 3.18, R_{wp} = 4.65, GOF = 3.49, space group $I\bar{4}3d$, a = 10.66095(3), V = 1211.68(1)).

refinement results of low temperature data and Table 2 atomic position parameters (for room temperature data see Table S1 and S2, Supporting Information).

The cubic $Cu_{15}Si_4$ structure (which is described in more detail in the next section) is composed of two crystallographically different metal atoms situated on sites 48*e* (*x*, *y*, *z*) and 12*b* (1/2, 1/4, 1/8) and one kind of Si atom on site 16*c* (*x*, *x*, *x*). The refinement of single crystal diffraction data for $Li_{15-x}Al_xSi_4$ shows that Al substitutes a small amount of Li atoms on both sites, 4% on 48*e* and 5.3% on 12*b*, indicating a slight preference for the higher symmetry position (Table 2). The average replacement is 4.2% which results in a total Al content of 3.3 atom % and the formula $Li_{14.37(1)}Al_{0.63(1)}Si_4$ (x = 0.63(1)). Rietveld refinement of (room temperature) PXRD data, which is less accurate, provides a slightly lower value of x = 0.49(1). The Al/(Al + Si) ratio obtained from EDX analysis is 11.8(7) atom %, which translates to x = 0.54(4) and agrees well with the crystallographically determined composition.

The incorporation of Al into $Li_{15}Si_4$, leading to a small contraction of the unit cell volume (by 1.6%), is clearly a consequence of Li substitution. In the ^{27}Al MAS NMR spectrum (Figure 3) two different ^{27}Al signals with peak positions of

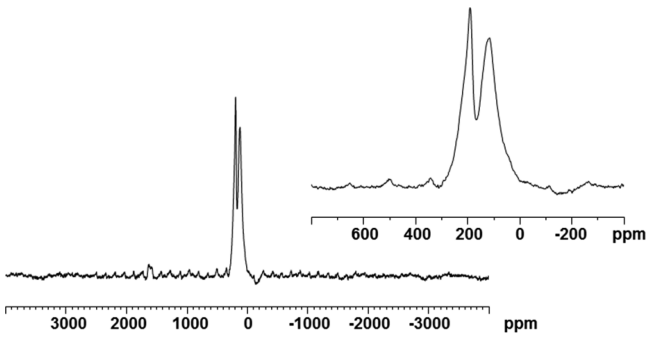

Figure 3. ^{27}Al MAS NMR spectrum of $Li_{14.37(1)}Al_{0.63(1)}Si_4$. Two signals are identified at 120 ppm and 193 ppm, respectively. The signal at approximately 1635 ppm indicates the presence of some residual metallic Al.[45]

193 ppm and 120 ppm are discerned. From additional experiments at a different B_0-field (11.7 T) and the observed field dependent peak positions[35] we estimate the isotropic chemical shift values to 150 ppm and 230 ppm for the downfield and high field signal, respectively. Due to the limited resolution and the ill-defined line shape of the signals no attempt was undertaken to exactly simulate the line shape; we can, however—using a set of two Gaussians for the downfield and a single Gaussian for the high field signal—approximate the relative amounts of the two signals as 3:7, respectively. Thus, the NMR results of the powdered sample reveal Al in two different environments in a ratio of 2.3:1 and are thus rather close to the findings from the single crystal X-ray analysis (3:1).

For assessing the homogeneity range of $Li_{15-x}Al_xSi_4$, bulk samples with x = 0.25, 0.50, 0.75, and 1.00 were prepared by heating and quenching stoichiometric mixtures of the elements. This procedure resulted in highly crystalline products, which for x = 0.50 and x = 0.75 corresponded to phase pure $Li_{15-x}Al_xSi_4$ according to PXRD. For x = 0.25 and x = 1.00 PXRD patterns revealed the presence of other phases next to $Li_{15-x}Al_xSi_4$, which could not be identified (cf. Figure S2, Supporting Information). It is therefore concluded that $Li_{15-x}Al_xSi_4$ has a small homogeneity range around x = 0.63, $x_{min} \sim 0.4$ and $x_{max} \sim 0.8$. The composition $x \approx 0.63$ of crystals grown in equilibrated Li-rich melts with different compositions is considered as the preferred, most stable, composition of $Li_{15-x}Al_xSi_4$. Earlier

Table 2. Fractional Atomic Coordinates and Isotropic Equivalent Atomic Displacement Parameters for $Li_{15}Si_4$ and $Li_{14.37(1)}Al_{0.63(1)}Si_4$[a]

atom	Wyckoff position	*x*	*y*	*z*	U_{eq}, Å^2·10^3	occ.
Si	16*c*	0.29247(1)	0.29247(1)	0.29247(1)	8.88(8)	1
		0.292808(5)	**0.292808(5)**	**0.292808(5)**	**11.00(3)**	**1**
Li1	48*e*	0.34994(8)	0.46209(9)	0.12524(8)	17.0(2)	1
Li1|Al1		**0.34839(3)**	**0.46277(3)**	**0.12354(3)**	**15.2(1)**	**0.9605(7)/0.0395(7)**
Li2	12*b*	1/2	1/4	1/8	18.7(3)	1
Li2|Al2		**1/2**	**1/4**	**1/8**	**13.3(2)**	**0.9469(9)/0.0531(9)**

[a] $I\bar{4}3d$, Z = 4, T = 123 K, estimated standard deviations in parentheses; values for $Li_{14.37(1)}Al_{0.63(1)}Si_4$ are marked bold.

dx.doi.org/10.1021/cm402721n | Chem. Mater. 2013, 25, 4113−4121

Table 3. Interatomic Distances in $Li_{15}Si_4$ and $Li_{14.37(1)}Al_{0.63(1)}Si_4$[a]

atom pair			d, Å	Atom pair			d, Å
Si	Li1	3×	2.605(1)	**Li1|Al1**	**Li2|Al2**		**2.7739(4)**
Si	**Li1|Al1**	**3×**	**2.6143(4)**	Li1	Li1		2.773(2)
	Li1	3×	2.7151(9)		**Li1|Al1**		**2.7993(5)**
	Li1|Al1	**3×**	**2.7173(4)**		Si		2.819(1)
	Li1	3×	2.819(1)		**Si**		**2.8056(3)**
	Li1|Al1	**3×**	**2.8056(3)**		Li1	2×	3.039(1)
	Li2	3×	2.8711(2)		**Li1|Al1**	**2×**	**3.0161(5)**
	Li2|Al2	**3×**	**2.8670(1)**		Li1	2×	3.2503(5)
Li1	Si		2.605(1)		**Li1|Al1**	**2×**	**3.2494(5)**
Li1|Al1	**Si**		**2.6143(4)**		Li1		3.407(1)
	Li1	2×	2.660(2)		**Li1|Al1**		**3.3536(5)**
	Li1|Al1	**2×**	**2.6500(6)**	Li2	Li1	4×	2.762(1)
	Si		2.7151(9)	**Li2|Al2**	**Li1|Al1**	**4×**	**2.7539(4)**
	Si		**2.7173(4)**		Li1	4×	2.7644(9)
	Li2		2.762(1)		**Li1|Al1**	**4×**	**2.7739(4)**
	Li2|Al2		**2.7539(4)**		Si	4×	2.8711(2)
	Li2		2.7644(9)		**Si**	**4×**	**2.8670(1)**

[a] $I\bar{4}3d$, $Z = 4$, $T = 123$ K, estimated standard deviations in parentheses; values for $Li_{14.37(1)}Al_{0.63(1)}Si_4$ are marked bold.

reports on the existence of $Li_{12}Al_3Si_4$ with the $Cu_{15}Si_4$ structure (that is $x = 3$) could not be confirmed.[36] Thus $Li_{15-x}Al_xSi_4$ presented herein is an additional representative of the Li−Al−Si phase system. Further structurally characterized ternary phases are LiAlSi, $Li_8Al_3Si_5$, $Li_7Al_3Si_4$, Li_5AlSi_2, Li_9AlSi_3, α-Li_5AlSi_2, and β-Li_5AlSi_2.[37]

Description of the Crystal Structure of $Li_{15-x}Al_xSi_4$. $Li_{15}Si_4$ and $Li_{15-x}Al_xSi_4$ ($0.4 < x < 0.8$) crystallize with the cubic $Cu_{15}Si_4$ structure[16] (space group $I\bar{4}3d$). This structure type is not very common among intermetallic compounds. Further representatives include $Li_{15}Ge_4$,[38,39] $Na_{15}Pb_4$,[40] $Na_{15}Sn_4$,[41] $Li_{15}Pd_4$,[42] and $Li_{15}Au_4$.[43] Table 3 lists the interatomic distances for $Li_{15}Si_4$ and $Li_{14.37(1)}Al_{0.63(1)}Si_4$, which are very similar. Si (on 16*c* (*x*, *x*, *x*)) is surrounded by 12 Li atoms at distances ranging from 2.61 Å to 2.87 Å. There is a clear separation between nearest and next nearest neighbor distances, the latter starting off above 4 Å. Li2 (on 12*b*) is 12-coordinated by 4 Si and 8 Li1 atoms, whereas Li1 (on 48*e*) is 13-coordinated by 3 Si, 8 Li1, and 2 Li2 atoms. The range of interatomic distances defining nearest neighbor coordination of Li atoms extends to 3.4 Å. The separation with respect to next nearest neighbors (above 3.9 Å) is much less pronounced than with Si.

The prominent feature of the $Cu_{15}Si_4$ structure is the quasi anticuboctahedral coordination of Si atoms. Anticuboctahedra are the basic structural motif of a hexagonal close packing. The $Cu_{15}Si_4$ structure has been interpreted earlier as a topological close packing of atoms of different size by Kripyakevich and Gladyshevskii.[44] The [Si@Li_{12}] anticuboctahedron in $Li_{15}Si_4$ is shown in Figure 4a,b. The polyhedra are slightly distorted; first there is a mutual rotation of $(Li1)_3$ triangles by about 14°, and second the six-membered ring situated between the $(Li1)_3$ triangle faces (formed by 3 Li1 and 3 Li2 atoms) is slightly puckered.

These polyhedra are condensed into strands by sharing opposite and parallel triangular faces formed by Li1 atoms (Figure 4a). In Figure 4c these strands are better visualized as a skeleton of $Si(Li1)_3$ corner-shared trigonal bipyramids $^1{}_\infty[Si_{2/2}(Li1)_3]$. Furthermore, Figure 4d shows all $^1{}_\infty[Si_{2/2}(Li1)_3]$-strands interpenetrating the unit cell with view along $[\bar{1}11]$. Thereby, segments of equal directions are represented with the same color. It can be seen easily that the blue strand is exactly situated at a body diagonal of the cubic unit cell whereas the green, red, and yellow segments are arranged in parallel to all residual body diagonals of directions $[\bar{1}11]$, $[1\bar{1}1,]$ and $[11\bar{1}]$. Finally, Figure 4e shows the connectivity of the [Si@Li_{12}] units. Each polyhedron of a strand having two neighboring polyhedra is further connected to nine from neighboring strands, three of which share faces and six of which share edges. This results in overall 11 neighboring anticuboctahedra. Figure 4f depicts the full environment of 11 polyhedra generated from two polyhedra (4 and 5) of the blue segment that are condensed via $(Li1)_3$ triangle faces above and below, three polyhedra (3, 3′, and 3″) and pairs of polyhedra (1 and 2, 1′ and 2′, and 1″ and 2″) that are fused via triangular sites. There are also 11 anticuboctahedra in an ideal *hcp* atom packing; however, they share edges and quadratic faces instead of edges and triangle faces (cf. Figure S3, Supporting Information).

One may speculate for possible reasons for the existence of $Li_{15-x}Al_xSi_4$. A plausible explanation could be that the exchange of Li by Al atoms leads to an increase of the electron concentration and a concomitant shift of Fermi level toward a pseudo gap in the electronic density of states. The electronic structure of $Li_{15}Si_4$ has been recently calculated by Xu et al.[18] It was found that the Fermi level of $Li_{15}Si_4$ with the $Cu_{15}Si_4$ structure is situated below a pseudo gap. Alternatively, in a simplified picture $Li_{15}Si_4$ may be classified as an electron-deficient Zintl phase $(Li^+)_{15}(Si^{4-})_4$. Within this picture and assuming Al as cation-like (Al^{3+}) in $Li_{15-x}Al_xSi_4$, the optimum concentration of Al would be $x = 0.5$, which falls in the range of the experimentally determined homogeneity range $x_{min} \sim 0.4$ and $x_{max} \sim 0.8$. Supportingly, magnetic measurements reveal diamagnetic behavior for a sample with x in this range.

Thermal Analysis of $Li_{15-x}Al_xSi_4$. $Li_{15}Si_4$ is a metastable compound. However, the nature of the decomposition process and products remains largely unknown. Key et al.[3] reported a decomposition into a mixture of unidentified phases at high temperatures. Wang and Dahn investigated phase changes in electrochemically lithiated silicon at temperatures of up to 450 °C.[22] Yet, their results are ambiguous, as the decomposition of electrochemically produced $Li_{15}Si_4$ yielded $Li_{13}Si_4$ and Li_7Si_3 at 450 °C whereas $Li_{17}Si_4$ and $Li_{13}Si_4$ would have been expected according to the Li−Si phase diagram. Similar observations have

dx.doi.org/10.1021/cm402721n | Chem. Mater. 2013, 25, 4113−4121

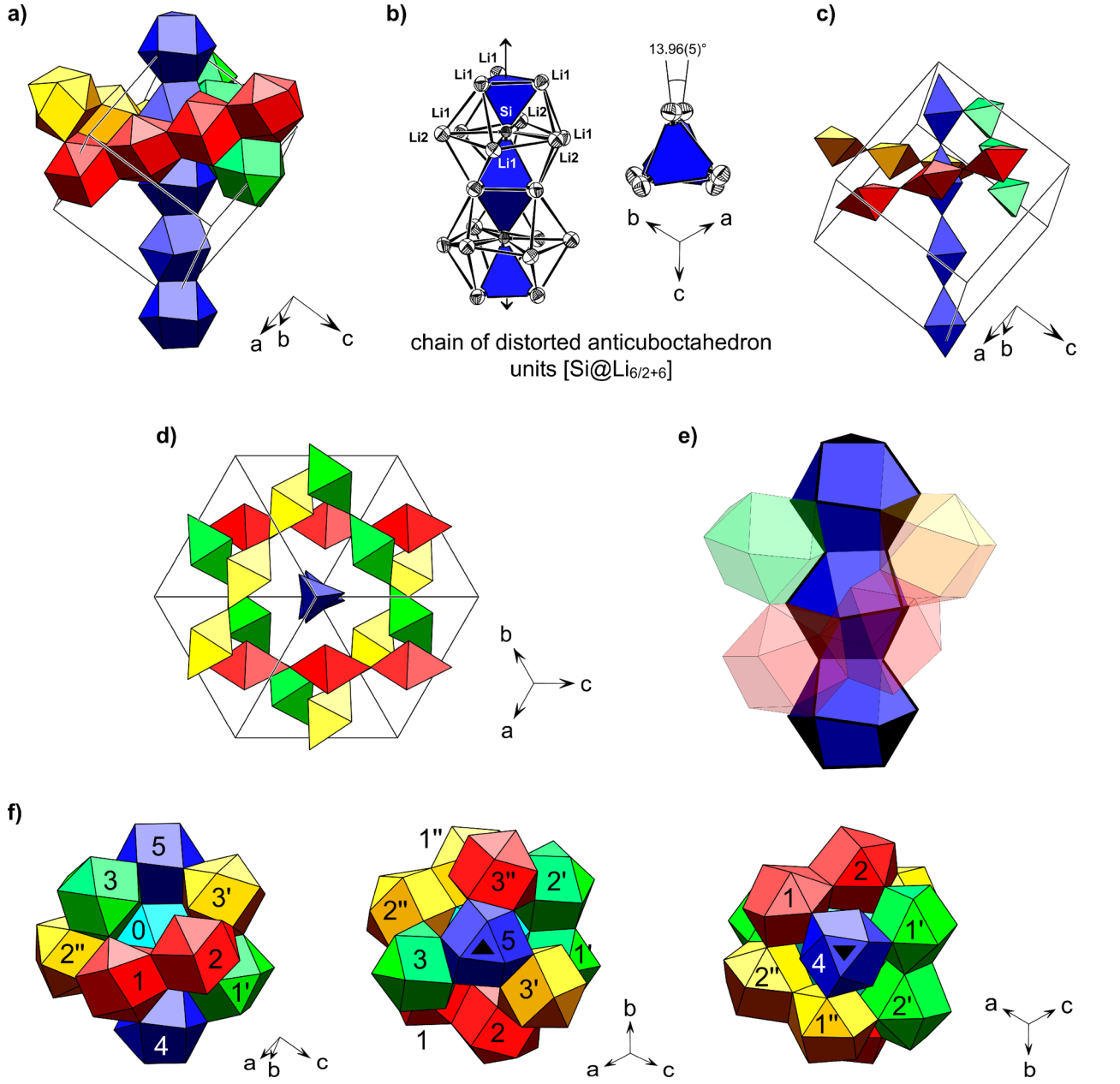

Figure 4. Crystal structure motifs of $Li_{15}Si_4$ and $Li_{15-x}Al_xSi_4$ ($Cu_{15}Si_4$ type). (a) $^1_\infty$[Si@Li_{12}]-strands running in different directions as indicated by different colors; (b) stacking of distorted anticuboctahedron units [Si@Li_{12}]. The skeleton formed by trigonal bipyramids is emphasized. (c) Arrangement of $^1_\infty$[Si@Li_{12}]-strands in (a) shown in the skeleton representation; (d) three-dimensional arrangement of strands of pseudo trigonal-bipyramids with view along $[\bar{1}11]$; (e) connectivity of distorted anticuboctahedron units (shared faces/edges are marked in black); (f) three orientations showing the eleven neighboring [Si@Li_{12}] cuboctahedra around a central one (light blue, denoted with 0).

been made by Chevrier et al.:[23] heating of electrochemically generated $Li_{15}Si_4$ to 500 °C only afforded $Li_{13}Si_4$. In both cases the observed lithium loss might be deduced from a reaction of residual amounts of SEI (Solid Electrolyte Interphase) components or binder during the heating.[22,23] Profatilova et al.[21] reported on the formation of a further but not identifiable phase when they quenched DSC measurements for electrochemically generated $Li_{15}Si_4$ at temperatures between 230 and 300 °C.

We attempted diligently to monitor the decomposition of $Li_{15}Si_4$ (synthesized through mechanical ball-milling) by performing thermal analysis (both DTA and DSC) experiments. Yet, results were inconclusive. At best, thermal decomposition was indicated by a very broad signal and only one experiment showed clear evidence of an exothermic event, occurring around 177 °C (Figure 5).

As a next step we performed ex situ investigations where $Li_{15}Si_4$ was annealed for three days (72 h) at various temperatures and subsequently quenched and analyzed. At 120 °C we found $Li_{15}Si_4$ unchanged whereas at 200 °C a partial decomposition occurred. The PXRD patterns after annealing at 200 and 300 °C were almost identical, and the one obtained for the product after annealing at 300 °C is shown in Figure 6a. This pattern contains sharp diffraction lines from $Li_{17}Si_4$ and still presents crystalline $Li_{15}Si_4$. Additionally, there is a range of broad peaks indicating a partially amorphous Li−Si phase. The presence of $Li_{17}Si_4$ requires the simultaneous formation of a Li poorer phase. According to the Li−Si phase diagram this should be $Li_{13}Si_4$. It

dx.doi.org/10.1021/cm402721n | Chem. Mater. 2013, 25, 4113−4121

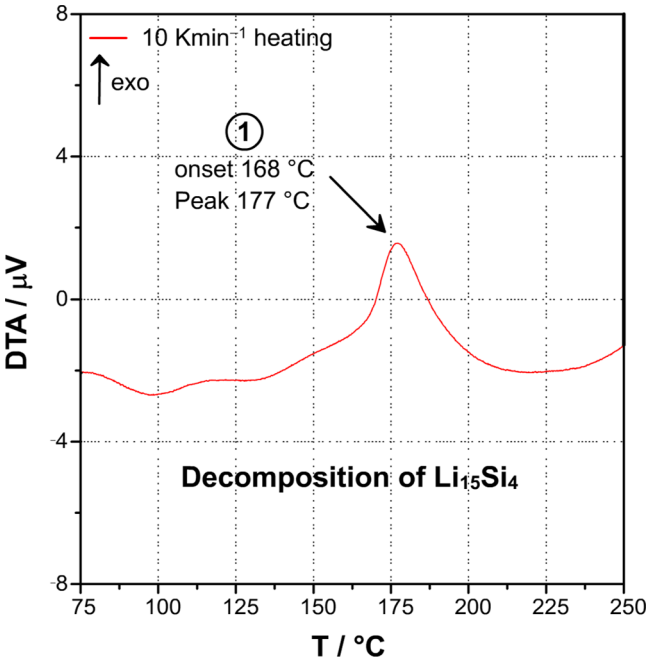

Figure 5. DTA thermogram for $Li_{15}Si_4$. The event (1) corresponds to exothermic decomposition.

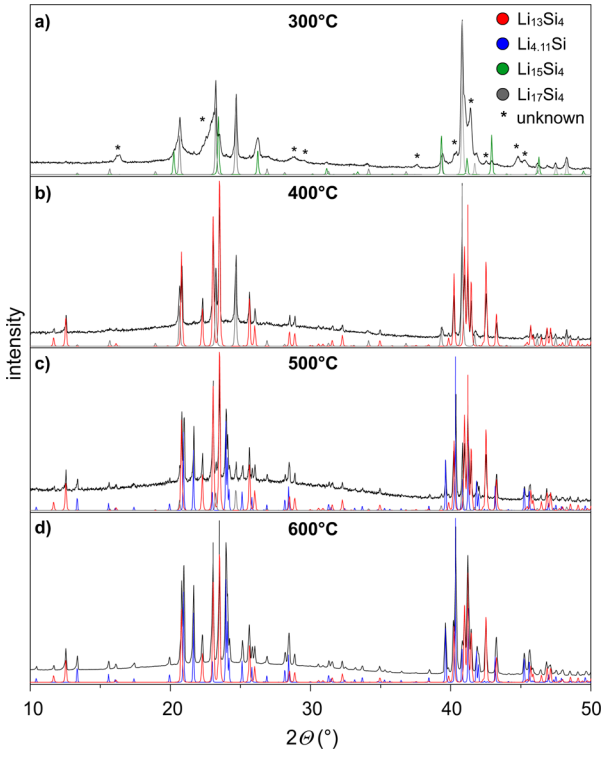

Figure 6. Evolution of the thermal decomposition of $Li_{15}Si_4$: PXRD patterns of bulk samples after annealing at 300 °C (a), 400 °C (b), 500 °C (c), and 600 °C (d) for three days (experimental = black; $Li_{13}Si_4$ calculated = red; $Li_{15}Si_4$ calculated = green; $Li_{4.11}Si$ calculated = blue; $Li_{17}Si_4$ calculated = gray; unknown reflections are marked with *).

may be suspected that the broad diffraction peaks associate to an amorphous "pre-phase" to $Li_{13}Si_4$. The ex situ experiments confirm a very slow kinetics of the decomposition of $Li_{15}Si_4$ which explains the difficulties of detecting this event in in situ thermal investigations.

The result from the annealing experiment at 400 °C is shown in Figure 6b. Now crystalline $Li_{13}Si_4$ is clearly recognizable in the PXRD pattern. The product corresponds to a mixture of $Li_{17}Si_4$ and $Li_{13}Si_4$. After annealing at 500 °C the product consists of three crystalline phases, $Li_{17}Si_4$, $Li_{4.11}Si$, and $Li_{13}Si_4$ (Figure 6c). The amount of $Li_{17}Si_4$ is considerably reduced. This is in accordance with the recently revised Li−Si phase diagram (Figure 7a): (i) the peritectic decomposition interval of $Li_{17}Si_4$ is 481−486 °C (i.e., the amount of $Li_{17}Si_4$ is decreased for $T >$ 486 °C)[7] and (ii) we recently could identify $Li_{4.11}Si$ as a high temperature phase in the Li−Si system which forms from a slow peritectoid reaction between $Li_{13}Si_4$ and $Li_{17}Si_4$ at 470−480 °C (i.e., no $Li_{4.11}Si$ phase is observed for $T <$ 470 °C).[24] As expected, after annealing at 600 °C the product represents a mixture of $Li_{4.11}Si$ and $Li_{13}Si_4$ (Figure 6d). In a control experiment a DSC thermogram was recorded for $Li_{15}Si_4$ after heating to 750 °C (cooling curve). This is shown in Figure 7b. The three thermal events correspond to crossing the liquidus boundary (1), the peritectic formation temperature of $Li_{4.11}Si$ (2), and a proposed high temperature phase transition of $Li_{4.11}Si$ (3) which is in agreement with the recent phase diagram.[24] The event for the peritectoid decomposition of $Li_{4.11}Si$ around 500 °C is not seen in the thermogram because of its slow kinetics.[24]

Lastly we performed thermal analysis (DSC) experiments with $Li_{15-x}Al_xSi_4$ ($x = 0.75$) and found a surprisingly different behavior compared to $Li_{15}Si_4$. The thermogram is shown in Figure 8. The first event upon heating is detected around 700 °C (1) followed by another one at approximately 760 °C (2). Those signals are tentatively assigned to the decomposition of $Li_{14.25}Al_{0.75}Si_4$ followed by a crossing of the liquidus boundary. The cooling trace reveals then two broad signals at 744 and 683 °C (3, 4) and a sharp one at 631 °C (5). A consecutive second heating−cooling cycle exactly reproduces events (1−5). Also the PXRD pattern of $Li_{14.25}Al_{0.75}Si_4$ after DSC investigations is unchanged (cf. Figure S4, Supporting Information), which confirms a complete reversibility of the thermal processes. Consequently, signals (3−5) are attributed to a stepwise formation of $Li_{14.25}Al_{0.75}Si_4$ from the melt. The substitution of about 2.7% of Li by Al ($x \approx$ 0.4) transforms metastable $Li_{15}Si_4$ into a stable phase which decomposes beyond 650 °C.

4. CONCLUSION

Metastable $Li_{15}Si_4$ is an important phase in the lithiation process of silicon. In this work we were able to obtain single crystals of $Li_{15}Si_4$ for the first time and to perform a rigorous structure characterization based on single crystal X-ray diffraction data which unambiguously confirmed the previously assigned $Cu_{15}Si_4$ structure type. We further showed that $Li_{15}Si_4$ thermally decomposes at temperatures above 200 °C. However, the decomposition process is sluggish and appreciable rates are not observed before temperatures approach 400 °C. At these temperatures the decomposition products are in accordance with the most recent Li−Si phase diagram (crystalline $Li_{13}Si_4$ and $Li_{17}Si_4/Li_{4.11}Si$).[24] At temperatures between 200 and 300 °C decomposition yields amorphous/weakly crystalline products. A surprising result is the discovery of the solid solution $Li_{15-x}Al_xSi_4$ ($0.4 < x < 0.8$), where small concentrations of Li in $Li_{15}Si_4$ are replaced by Al. Contrary to $Li_{15}Si_4$, $Li_{15-x}Al_xSi_4$ is thermodynamically stable until about 700 °C. It will be interesting to investigate its potential use as anode material in lithium ion batteries, especially if the $Li_{15-x}Al_xSi_4$ phases possess a higher inertness against reactions with electrolyte solution than $Li_{15}Si_4$. Preliminary investigations indeed indicate that $Li_{15-x}Al_xSi_4$

dx.doi.org/10.1021/cm402721n | Chem. Mater. 2013, 25, 4113−4121

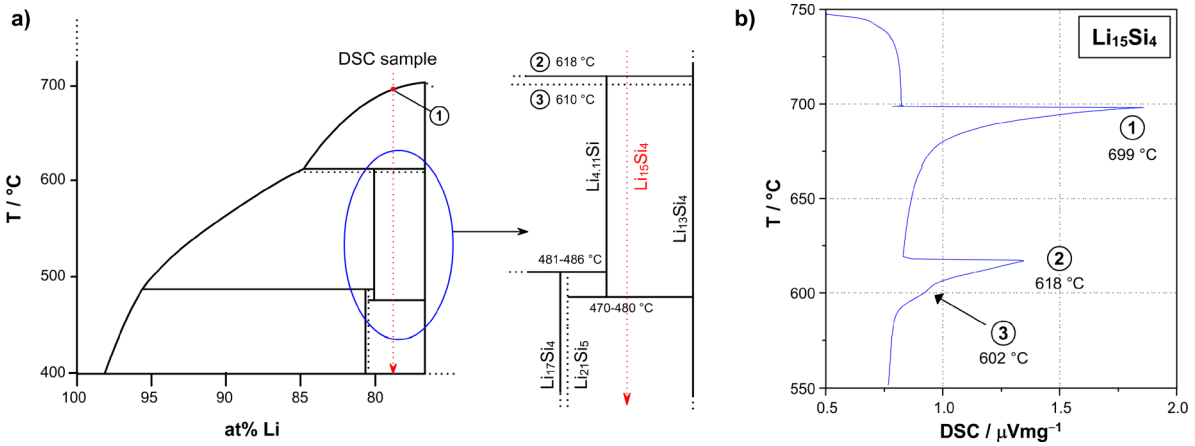

Figure 7. (a) Portion of the recently updated Li–Si phase diagram (according to refs 7 and 24). (b) DSC thermogram for $Li_{15}Si_4$ recorded in cooling mode (from 750 °C). Thermal events occur according to the Li–Si phase diagram shown in (a).

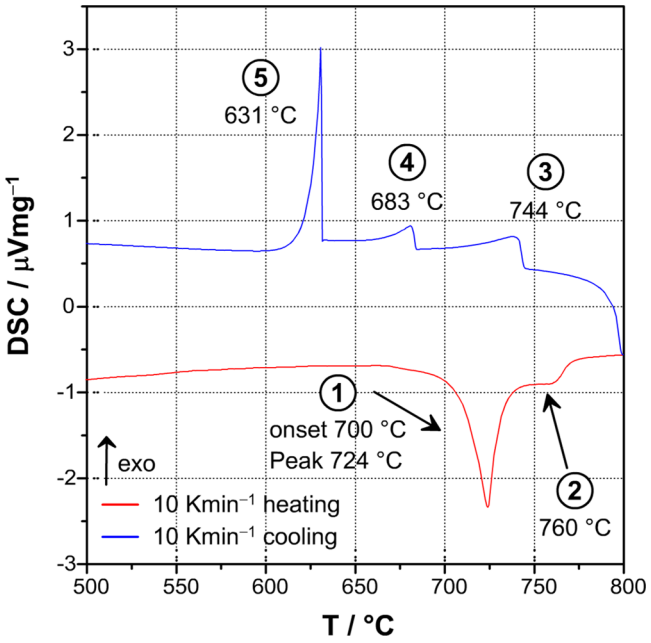

Figure 8. DSC thermogram for $Li_{14.25}Al_{0.75}Si_4$ (heating–cooling cycle). Thermal events (1) and (2) correspond to a decomposition followed by crossing the liquidus boundary, whereas (3–5) represent steps of formation of $Li_{14.25}Al_{0.75}Si_4$ from the melt.

exhibits a much lower sensitivity toward air and moisture than crystalline powders of Li-rich phases such as $Li_{17}Si_4$ and $Li_{4.11}Si$.

■ ASSOCIATED CONTENT

Supporting Information

Crystallographic data and structure refinement for $Li_{15}Si_4$ and $Li_{14.42(2)}Al_{0.58(2)}Si_4$ (T = 298 K; Table S1), fractional atomic coordinates and isotropic equivalent atomic displacement parameters for $Li_{15}Si_4$ and $Li_{14.42(2)}Al_{0.58(2)}Si_4$ (T = 298 K; Table S2), PXRD patterns of ground crystals $Li_{15-x}Al_xSi_4$ ($x \approx 0.63$) obtained from equilibrated melts with compositions $Li_{87}Al_4Si_9$ and $Li_{83}Al_{13}Si_4$ (Figure S1), PXRD patterns of bulk samples $Li_{15-x}Al_xSi_4$ with $x = 0.25$, $x = 0.50$, $x = 0.75$, and $x = 1.00$ (Figure S2), the relation of distorted anticuboctahedron units in $Li_{15}Si_4$ to an ideal *hcp* atom arrangement (Figure S3), and PXRD pattern of $Li_{14.25}Al_{0.75}Si_4$ before and after DSC investigation (Figure S4) and Crystallographic Information Files. This material is available free of charge via the Internet at http://pubs.acs.org.

■ AUTHOR INFORMATION

Corresponding Author

*E-mail: thomas.faessler@lrz.tum.de.

Notes

The authors declare no competing financial interest.

■ ACKNOWLEDGMENTS

This work has been funded by Fonds der Chemischen Industrie, TUM Graduate School, the Swedish Resarch Council (Project No. 2010-4827) and the Deutsche Forschungsgemeinschaft (Project No. FA 198/11-1) as well as the National Science Foundation through Grant DMR-1007557.

■ REFERENCES

(1) Obrovac, M. N.; Christensen, L. *Electrochem. Solid-State Lett.* **2004**, *7*, A93.
(2) Hatchard, T. D.; Dahn, J. R. *J. Electrochem. Soc.* **2004**, *151*, A838.
(3) Key, B.; Bhattacharyya, R.; Morcrette, M.; Seznec, V.; Tarascon, J. M.; Grey, C. P. *J. Am. Chem. Soc.* **2009**, *131*, 9239.
(4) Key, B.; Morcrette, M.; Tarascon, J. M.; Grey, C. P. *J. Am. Chem. Soc.* **2011**, *133*, 503.
(5) Limthongkul, P.; Jang, Y. I.; Dudney, N. J.; Chiang, Y. M. *Acta Mater.* **2003**, *51*, 1103.
(6) Limthongkul, P.; Jang, Y. I.; Dudney, N. J.; Chiang, Y. M. *J. Power Sources* **2003**, *119–121*, 604.
(7) Zeilinger, M.; Benson, D.; Häussermann, U.; Fässler, T. F. *Chem. Mater.* **2013**, *25*, 1960.
(8) Li, J.; Dahn, J. R. *J. Electrochem. Soc.* **2007**, *154*, A156.
(9) Wang, C. M.; Li, X. L.; Wang, Z. G.; Xu, W.; Liu, J.; Gao, F.; Kovarik, L.; Zhang, J. G.; Howe, J.; Burton, D. J.; Liu, Z. Y.; Xiao, X. C.; Thevuthasan, S.; Baer, D. R. *Nano Lett.* **2012**, *12*, 1624.
(10) Chan, M. K. Y.; Wolverton, C.; Greeley, J. P. *J. Am. Chem. Soc.* **2012**, *134*, 14362.
(11) Gu, M.; Wang, Z.; Connell, J. G.; Perea, D. E.; Lauhon, L. J.; Gao, F.; Wang, C. *ACS Nano* **2013**, *7*, 6303.
(12) Misra, S.; Liu, N.; Nelson, J.; Hong, S. S.; Cui, Y.; Toney, M. F. *ACS Nano* **2012**, *6*, 5465.
(13) Radvanyi, E.; De Vito, E.; Porcher, W.; Danet, J.; Desbois, P.; Colin, J. F.; Larbi, S. J. S. *J. Mater. Chem. A* **2013**, *1*, 4956.
(14) Hashimoto, Y.; Machida, N.; Shigematsu, T. *Solid State Ionics* **2004**, *175*, 177.
(15) Tamori, R.; Machida, N.; Shigematsu, T. *J. Jpn. Soc. Powder Powder Metall.* **2001**, *48*, 267.

(16) Morral, F. R.; Westgren, A. *Ark. Kem., Mineral. Geol. B* **1934**, *11*, 1.
(17) Kubota, Y.; Escano, M. C. S.; Nakanishi, H.; Kasai, H. *J. Appl. Phys.* **2007**, *102*, 053704.
(18) Xu, Y. H.; Yin, G. P.; Zuo, P. J. *Electrochim. Acta* **2008**, *54*, 341.
(19) Chevrier, V. L.; Zwanziger, J. W.; Dahn, J. R. *J. Alloys Compd.* **2010**, *496*, 25.
(20) Nesper, R.; von Schnering, H. G. *J. Solid State Chem.* **1987**, *70*, 48.
(21) Profatilova, I. A.; Langer, T.; Badillo, J. P.; Schmitz, A.; Orthner, H.; Wiggers, H.; Passerini, S.; Winter, M. *J. Electrochem. Soc.* **2012**, *159*, A657.
(22) Wang, Y. D.; Dahn, J. *J. Electrochem. Soc.* **2006**, *153*, A2314.
(23) Chevrier, V. L.; Dahn, H. M.; Dahn, J. R. *J. Electrochem. Soc.* **2011**, *158*, A1207.
(24) Zeilinger, M.; Kurylyshyn, I.; Häussermann, U.; Fässler, T. F. *Chem. Mater.* **2013**. submitted.
(25) Puhakainen, K.; Boström, M.; Groy, T. L.; Häussermann, U. *J. Solid State Chem.* **2010**, *183*, 2528.
(26) *APEX suite of crystallographic software, APEX 2*, Version 2008.4; Bruker AXS Inc.: Madison, WI, USA, 2008.
(27) *SAINT*, Version 7.56a; Bruker AXS Inc.: Madison, WI, USA, 2008.
(28) *SADABS*, Version 2008/1; Bruker AXS Inc.: Madison, WI, USA, 2008.
(29) Sheldrick, G. M. *Shelxs-97 – Program for the Determination of Crystal Structures*; University of Göttingen: Göttingen, Germany, 1997.
(30) Sheldrick, G. M. *Shelxl-97 – Program for Crystal Structure Refinement*; University of Göttingen: Göttingen, Germany, 1997.
(31) *TOPAS – Rietveld Software*, Version 4.0; Bruker AXS Inc.: Madison, WI, USA, 2009.
(32) *Netzsch Proteus Thermal Analysis*, Version 4.8.2; Netzsch-Gerätebau GmbH: Selb, Germany, 2006.
(33) Tenga, A.; Lidin, S.; Belieres, J. P.; Newman, N.; Wu, Y.; Häussermann, U. *J. Am. Chem. Soc.* **2008**, *130*, 15564.
(34) Kanatzidis, M. G.; Pöttgen, R.; Jeitschko, W. *Angew. Chem., Int. Ed.* **2005**, *44*, 6996.
(35) Müller, D.; Jahn, E.; Ladwig, G.; Haubenreisser, U. *Chem. Phys. Lett.* **1984**, *109*, 332.
(36) Pavlyuk, V. V.; Bodak, O. I. *Izv. Akad. Nauk. SSSR, Neorg. Mater.* **1992**, *28*, 988.
(37) (a) Kevorkov, D.; Grobner, J.; Schmid-Fetzer, R. *J. Solid State Chem.* **2001**, *156*, 500. (b) Spina, L.; Jia, Y. Z.; Ducourant, B.; Tillard, M.; Belin, C. *Z. Kristallogr.* **2003**, *218*, 740. (c) Spina, L.; Tillard, M.; Belin, C. *Acta Crystallogr. C* **2003**, *59*, I9. (d) Zürcher, S. Systematic Investigations on the Transition from Zintl Phases to Intermetallics. Dissertation; ETH Zürich: Zürich, Switzerland, 2001.
(38) Gladyshevskii, E. I.; Kripyakevich, P. I. *Kristallographiya* **1960**, *5*, 574.
(39) Johnson, Q.; Smith, G. S.; Wood, D. *Acta Crystallogr.* **1965**, *18*, 131.
(40) Zintl, E.; Harder, A. *Z. Phys. Chem., Abt. B* **1936**, *B38*, 238.
(41) Müller, W.; Volk, K. *Z. Naturforsch.* **1978**, *33B*, 275.
(42) van Vucht, J. H. N.; Buschow, K. H. J. *J. Less-Common Met.* **1976**, *48*, 345.
(43) Kienast, G.; Verma, J.; Klemm, W. *Z. Anorg. Allg. Chem.* **1961**, *310*, 143.
(44) Kripyakevich, P. I.; Gladyshevskii, E. I. *Zh. Strukt. Khim.* **1961**, *2*, 573.
(45) Lay, M. D. H.; Hill, A. J.; Saksida, P. G.; Gibson, M. A.; Bastow, T. J. *Acta Mater.* **2012**, *60*, 79.

SUPPORTING INFORMATION

Stabilizing the Phase $Li_{15}Si_4$ through Lithium-Aluminum Substitution in $Li_{15-x}Al_xSi_4$ ($0.4 < x < 0.8$) – Single Crystal X-ray Structure Determination of $Li_{15}Si_4$ and $Li_{14.37}Al_{0.63}Si_4$

Michael Zeilinger, Volodymyr Baran, Leo van Wüllen, Ulrich Häussermann, Thomas F. Fässler*

Details on the single crystal X-ray data collection for $Li_{15}Si_4$ and $Li_{15-x}Al_xSi_4$ at room temperature.

Single crystal diffraction measurement of $Li_{14.42(2)}Al_{0.58(2)}Si_4$ was performed on a Stoe IPDS IIT diffractometer equipped with a rotating anode (Bruker AXS, FR591) with MoK_α radiation ($\lambda = 0.71073$ Å) and a Montel mirror. Single crystal data for $Li_{15}Si_4$ was recorded on a Bruker X-ray diffractometer equipped with a CCD detector (APEX II, κ-CCD), a fine-focused sealed tube with MoK_α radiation ($\lambda = 0.71073$ Å) and a graphite monochromator.

Table S1. Crystallographic data and structure refinement for $Li_{15}Si_4$ and $Li_{14.42(2)}Al_{0.58(2)}Si_4$.

empirical formula	$Li_{15}Si_4$	$Li_{14.42(2)}Al_{0.58(2)}Si_4$
T / K	298(2)	298(2)
formula weight / g·mol^{-1}	216.46	228.13
crystal size / mm^3	0.20 × 0.20 × 0.20	0.20 × 0.20 × 0.15
crystal color	metallic silver	metallic silver
crystal shape	block	block
space group	$I\bar{4}3d$	$I\bar{4}3d$
unit cell dimension / Å	a = 10.687(7)	a = 10.664(1)
V / Å^3	1221(1)	1212.7(2)
Z	4	4
ρ (calc.) / g·cm^{-3}	1.178	1.250
μ / mm^{-1}	0.418	0.464
F (000)	404	427
θ range / °	4.67–31.44	4.68–29.18
index range hkl	±15, ±15, ±15	±14, ±14, ±14
reflections collected	9378	14445
independent reflections	343 (R_{int} = 0.029)	277 (R_{int} = 0.058)
reflections with $I > 2\sigma(I)$	338 (R_σ = 0.008)	276 (R_σ = 0.009)
absorption correction	multi-scan	multi-scan
data/restraints/parameter	343/0/15	277/0/17
goodness-of-fit on F^2	1.195	1.307
final R indices [$I > 2\sigma(I)$][a, b]	R_1 = 0.010	R_1 = 0.013
	wR_2 = 0.027	wR_2 = 0.031
R indices (all data)[a, b]	R_1 = 0.010	R_1 = 0.013
	wR_2 = 0.027	wR_2 = 0.032
Flack parameter	−0.2(2)	0.1(2)
largest diff. peak and hole / e·Å^{-3}	0.12 and −0.06	0.08 and −0.07

[a] $R_1 = \sum \big| |F_o| - |F_c| \big| / \sum |F_o|$;

[b] $wR_2 = [\sum w(F_o^2 - F_c^2)^2 / \sum w(F_o^2)^2]^{1/2}$

Table S2. Fractional atomic coordinates and isotropic equivalent atomic displacement parameters for $Li_{15}Si_4$ and $Li_{14.42(2)}Al_{0.58(2)}Si_4$ ($I\bar{4}3d$, $Z = 4$, $T = 298$ K, estimated standard deviations in parentheses; values for $Li_{14.42(2)}Al_{0.58(2)}Si_4$ are marked bold).

Atom	Wyckoff position	*x*	*y*	*z*	U_{eq} / $Å^2 \cdot 10^3$	occ.
Si	16*c*	0.29232(1)	0.29232(1)	0.29232(1)	15.29(7)	1
		0.29268(2)	**0.29268(2)**	**0.29268(2)**	**14.6(1)**	**1**
Li1	48*e*	0.35029(8)	0.4619(1)	0.12560(9)	26.9(2)	1
Li1 | Al1		**0.34860(9)**	**0.4630(1)**	**0.1243(1)**	**21.4(4)**	**0.961(2) / 0.039(2)**
Li2	12*b*	½	¼	⅛	29.8(4)	1
Li2 | Al2		**½**	**¼**	**⅛**	**19.4(8)**	**0.958(3) / 0.042(3)**

FIGURES

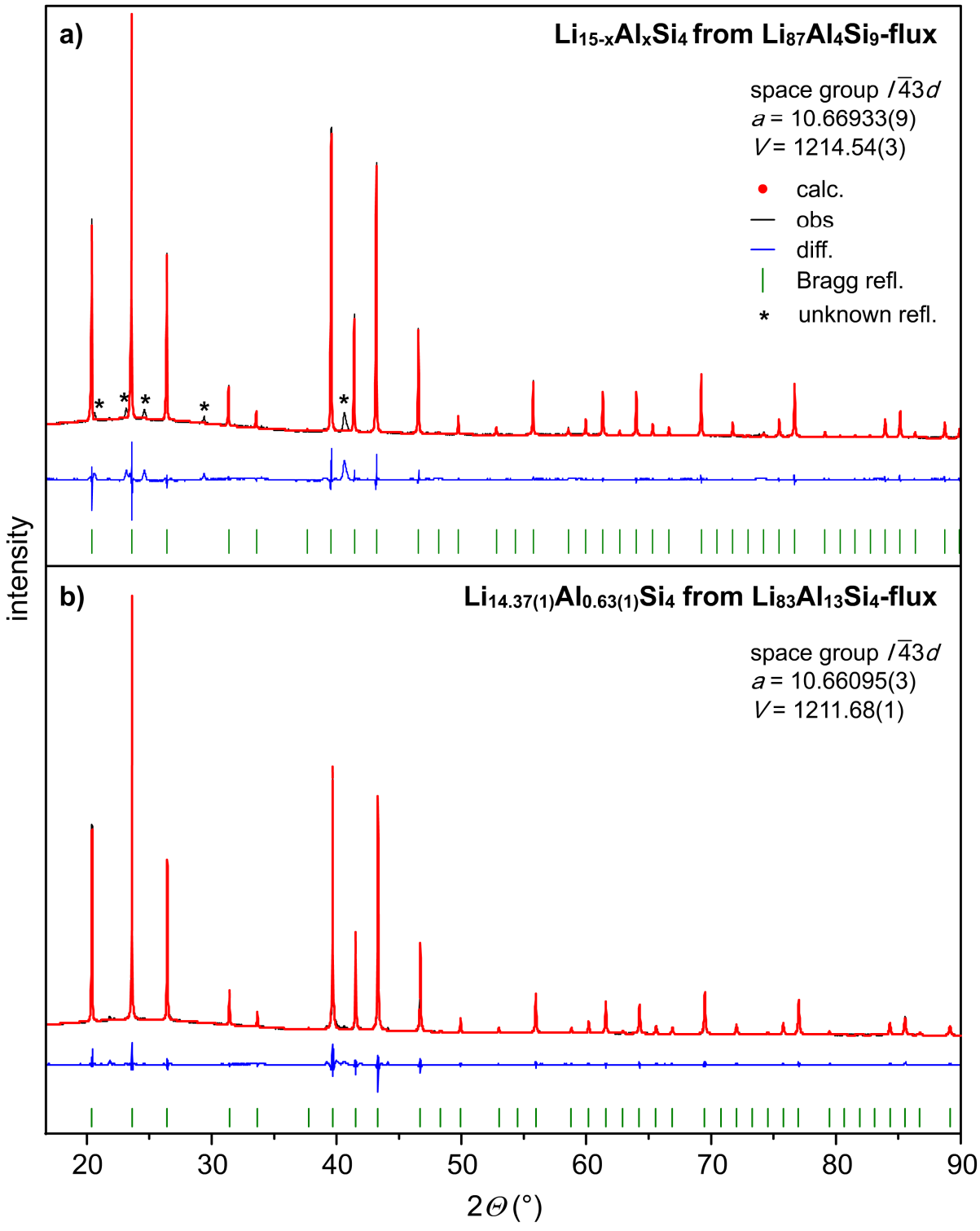

Figure S1. Rietveld fits of the $Cu_{15}Si_4$ model to PXRD patterns of ground crystals $Li_{15-x}Al_xSi_4$ ($x \approx 0.63$) obtained from equilibrated melts with compositions $Li_{87}Al_4Si_9$ (a) and $Li_{83}Al_{13}Si_4$ (b).

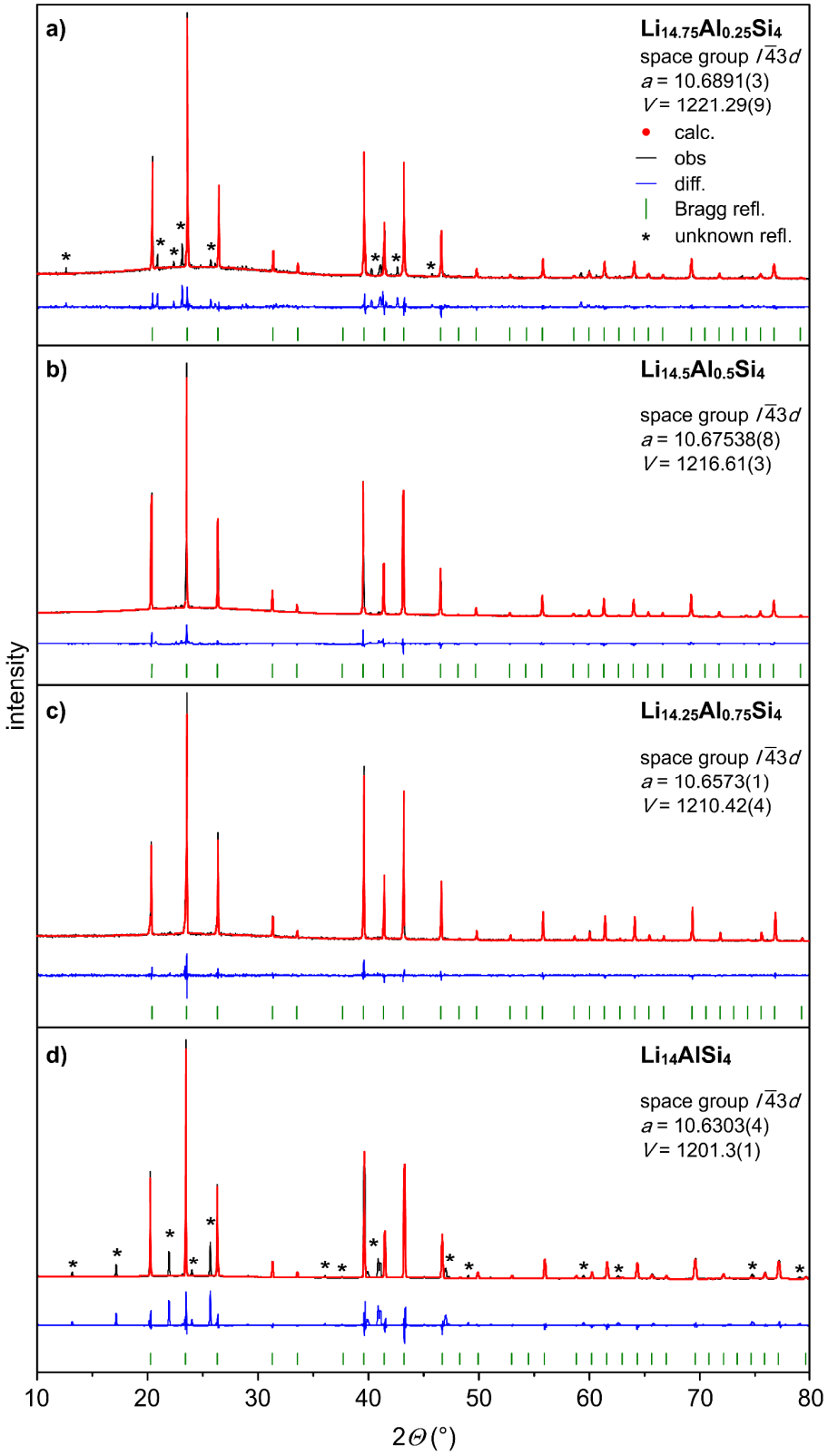

Figure S2. Rietveld fits of the $Cu_{15}Si_4$ model to PXRD patterns of bulk samples $Li_{15-x}Al_xSi_4$ with $x = 0.25$ (a), $x = 0.50$ (b), $x = 0.75$ (c) and $x = 1.00$ (d).

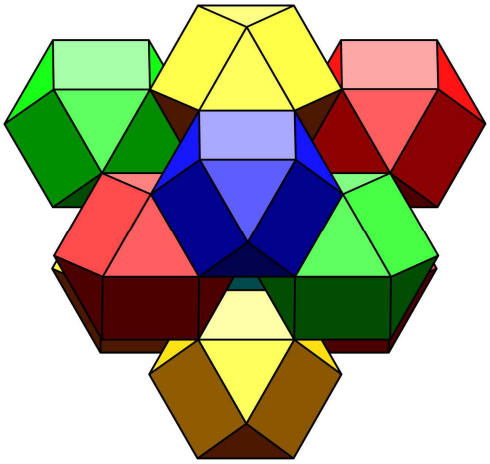

Figure S3. The full environment of eleven anticuboctahedra as they appear in an ideal *hcp* atom arrangement.

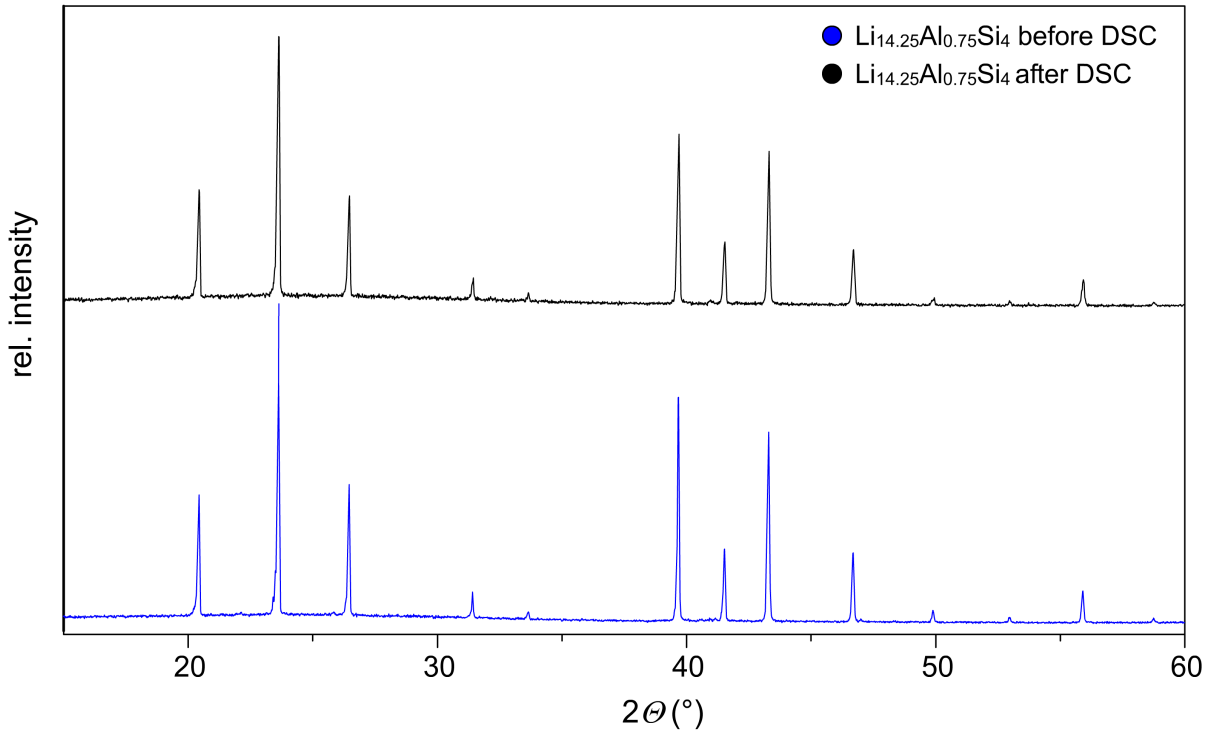

Figure S4. PXRD pattern of $Li_{14.25}Al_{0.75}Si_4$ before (blue) and after two DSC heating (800 °C) and cooling cycles (black).

5.5 Structural and Thermodynamic Similarities of Phases in the Li–*Tt* (*Tt* = Si, Ge) Systems: Redetermination of the Lithium-Rich Side of the Li–Ge Phase Diagram and Crystal Structures of $Li_{17}Si_{4.0-x}Ge_x$ for x = 2.3, 3.1, 3.5, and 4 as well as $Li_{4.1}Ge$

Dalton Transactions

PAPER

View Article Online
View Journal

Cite this: DOI: 10.1039/c4dt00743c

Structural and thermodynamic similarities of phases in the Li–Tt (Tt = Si, Ge) systems: redetermination of the lithium-rich side of the Li–Ge phase diagram and crystal structures of $Li_{17}Si_{4.0-x}Ge_x$ for x = 2.3, 3.1, 3.5, and 4 as well as $Li_{4.1}Ge$†

Michael Zeilinger and Thomas F. Fässler*

Received 12th March 2014,
Accepted 12th May 2014

DOI: 10.1039/c4dt00743c

www.rsc.org/dalton

A reinvestigation of the lithium-rich section of the Li–Ge phase diagram reveals the existence of two new phases, $Li_{17}Ge_4$ and $Li_{4.10}Ge$ ($Li_{16.38}Ge_4$). Their structures are determined by X-ray diffraction experiments of large single crystals obtained from equilibrated melts with compositions $Li_{95}Ge_5$ and $Li_{85}Ge_{15}$. Excess melt is subsequently removed through isothermal centrifugation at 400 °C and 530 °C, respectively. $Li_{17}Ge_4$ crystallizes in the space group $F\bar{4}3m$ (a = 18.8521(3) Å, V = 6700.1(2) Å^3, Z = 20, T = 298 K) and $Li_{4.10}Ge$ ($Li_{16.38}Ge_4$) in $Cmcm$ (a = 4.5511(2) Å, b = 22.0862(7) Å, c = 13.2751(4) Å, V = 1334.37(8) Å^3, Z = 16, T = 123 K). Both phases are isotypic with their Si counterparts and are further representative of the $Li_{17}Pb_4$ and $Li_{4.11}Si$ structure types. Additionally, the solid solutions $Li_{17}Si_{4-x}Ge_x$ follows Vegard's law. A comparison of the $GeLi_n$ coordination polyhedra shows that isolated Ge atoms are 13- and 14-coordinated in $Li_{17}Ge_4$, whereas in $Li_{16.38}Ge_4$ the Ge atoms possess coordination numbers 12 and 13. Regarding the thermodynamic stability, $Li_{16.38}Ge_4$ is assigned a high-temperature phase existing between ~400 °C and 627 °C, whereas $Li_{17}Ge_4$ decomposes peritectically at 520–522 °C. Additionally, the decomposition of $Li_{16.38}Ge_4$ below ~400 °C was found to be very sluggish. These findings are manifested by differential scanning calorimetry, long-term annealing experiments and the results from melt equilibration experiments. Interestingly, the thermodynamic properties of the lithium-rich tetrelides $Li_{17}Tt_4$ and $Li_{4.1}Tt$ ($Li_{16.4}Tt_4$) are very similar (Tt = Si, Ge). Besides $Li_{15}Tt_4$, $Li_{14}Tt_6$, $Li_{12}Tt_7$, and LiTt, the title compounds are further examples of isotypic tetrelides in the systems Li–Tt.

Introduction

In the last decade, the demand for high capacity lithium-ion batteries (LIBs) decisively influenced numerous fields of research; in particular, the chemistry of group 14 elements (tetrel = Tt) plays an important role in the development of more efficient anode materials. Since Si theoretically offers a specific capacity of 3579 mA h g^{-1} (based on the formation of $Li_{15}Si_4$) and thus massively exceeds the capacity of the commonly used graphite anode (372 mA h g^{-1}, LiC_6),[1,2] research on Li–Si materials has been in focus for many years. As the high capacity of Si is associated with several problems such as a large volume expansion of up to 300% upon lithiation accompanied by contact loss of electrodes and poor cycle life, a large number of these studies target these issues.[3] Further, Li–Si phases predominantly occur amorphously during charging and discharging, and only at low discharge voltages, crystalline $Li_{15}Si_4$ is observed.[1,2,4,5] However, the processes in working LIBs can be nicely monitored by *in situ*/*ex situ* NMR investigations.[6,7] Moreover, a fundamental understanding of thermodynamic properties and an unambiguous structural characterization of Li–Si phases are of considerable impor-

Department Chemie, Technische Universität München, Lichtenbergstraße 4, 85747 Garching b. München, Germany. E-mail: Thomas.Faessler@lrz.tum.de, michael.zeilinger@mytum.de; Tel: (+49) 89 289 13131

†Electronic supplementary information (ESI) available: Crystallographic data, refinement results, fractional atomic coordinates, and isotropic equivalent atomic displacement parameters for $Li_{17}Si_{4-x}Ge_x$ [x = 2.30(2), 3.08(4), 3.53(3)] (Table S1–4), comparison of experimental and computational relaxed fractional atomic coordinates for both $Li_{21}Si_5$ and $Li_{17}Si_4$ (Table S5), experimental fractional atomic coordinates for $Li_{17}Si_4$, $Li_{17}Ge_4$, $Li_{17-\varepsilon}Zn_\varepsilon Ge_4$, and $Li_{16.95}Ge_4$ (Table S6), comparison of experimental fractional atomic coordinates for $Li_{16.95}Ge_4$ and computational relaxed ones for $Li_{21}Si_5$ (Table S7), PXRD patterns of "$Li_{16}Ge_4$" samples annealed at various temperatures (Fig. S1), Rietveld refinement results for $Li_{17}Si_{4-x}Ge_x$ (x = 0, 2.30(2), 3.08(4), 3.53(3), 4) (Fig. S2). See DOI: 10.1039/c4dt00743c

tance. Just recently, we reported on detailed investigations on lithium-rich silicides, including the metastable phase $Li_{15}Si_4$,[8] $Li_{17}Si_4$[9] and the high-temperature phase $Li_{4.11}Si$ ($Li_{16.42}Si_4$).[10] Further examples are given in ref. 11–17.

The heavier tetrel element Ge has received less attention regarding its use as an anode material due to its low natural abundance connected with a lower theoretical specific capacity compared to silicon (1564 mA h g^{-1} *vs.* 4056 mA h g^{-1}, based on the formation of $Li_{16.95}Ge_4$[18] and $Li_{17}Si_4$,[9] respectively). However, the diffusivity of lithium in Ge is approximately 400 times larger than in Si at room temperature,[19,20] which intrinsically puts germanium to the foreground. Since some Si analogues are not known we put emphasis on the structural variety of lithium germanides and their thermodynamic relation.

Li–Ge phases were first postulated in the 1950s and 1960s (Li_3Ge, Li_4Ge, LiGe),[21–23] fueling numerous investigations in this field later on. Before 2001, the ascertained Li–Ge representatives included $Li_{21}Ge_5$[24] (formerly described as $Li_{20}Ge_5$[25,26] and $Li_{22}Ge_5$[27,28]), $Li_{15}Ge_4$,[28,29] $Li_{13}Ge_4$[30] (formerly reported as Li_7Ge_2[31]), $Li_{14}Ge_6$,[25,26] Li_9Ge_4,[32] $Li_{12}Ge_7$,[25,26,33] LiGe (space group $I4_1/a$, ambient pressure),[22,34] LiGe (space group $I4_1/amd$, high pressure),[35] and Li_7Ge_{12}.[26,36] A previously described phase $Li_{11}Ge_6$[37] could not be reproduced in the course of the redetermination of the Li–Ge phase diagram by Grüttner,[25] and due to the "striking similarity" to Li_8MgSi_6,[38] it might have been ternary Li_8MgGe_6. Until then, solely $Li_{21}Tt_5$, $Li_{14}Tt_6$, $Li_{12}Tt_7$, and LiTt (LiSi[39] is obtainable from high-pressure synthesis) were known for both Si and Ge. We note that $Li_{13}Si_4$ and $Li_{13}Ge_4$ are not isotypic and crystallize with their own structure types. In the following years new Li–Tt phases were found and others were revised, *e.g.* a hexagonal high-pressure form of LiGe (space group $P6_3/mmc$),[40] metastable $Li_{15}Si_4$[1,2] being isotypic with the congruently melting phase $Li_{15}Ge_4$[25] ($Li_{15}Tt_4$), $Li_{\sim 17}Ge_4$ ($Li_{21+3/16}Si_5$ = $Li_{16.95}Ge_4$)[18] revised from $Li_{21}Ge_5$, and the revision of the Li_7Ge_{12} structure.[41] The synthesis of solid solutions $Li_{15}Si_{4-x}Ge_x$ by mechanical ball-milling was also reported.[42] An experimental determination of the Li–Ge phase diagram involving most of the aforementioned phases is given by Grüttner in his dissertation.[25]

We recently reported on the single crystal structures and thermodynamic properties of $Li_{17}Si_4$,[9] the high-temperature phase $Li_{4.11}Si$ ($Li_{16.42}Si_4$),[10] and metastable $Li_{15}Si_4$.[8] The Li–Si phase diagram was revised accordingly. Consequently, we extended our studies on the Li–Ge system. Herein, we present the single crystal X-ray structure determination of $Li_{17}Ge_4$ and $Li_{4.10}Ge$ which crystallize isotypically with their Si counterparts. Earlier structure reports on $Li_{\sim 17}Ge_4$ ($Li_{21+3/16}Si_5$ = $Li_{16.95}Ge_4$)[18] involving partially occupied Li sites could not be confirmed. Solid solutions of the isotypic phases $Li_{17}Si_4$ and $Li_{17}Ge_4$ follow Vegard's law.[43] Due to clarity and a better comparability, the phase $Li_{4.10}Ge$ is referred to as $Li_{16.38}Ge_4$. Furthermore, the lithium-rich section of the Li–Ge phase diagram (Li concentrations >79 at%) is reinvestigated by differential scanning calorimetry and long-term annealing experiments, manifesting $Li_{16.38}Ge_4$ as a high-temperature phase which possesses a very sluggish decomposition behavior below ~400 °C. $Li_{17}Ge_4$ is peritectically formed at 520–522 °C from cooling an according melt.

Results and discussion

Single crystal X-ray structure determination of $Li_{17}Ge_4$ and $Li_{16.38}Ge_4$

Large single crystals of $Li_{17}Ge_4$ and $Li_{16.38}Ge_4$ were grown in Li–Ge melts $Li_{95}Ge_5$ and $Li_{85}Ge_{15}$ at 400 °C and 530 °C, respectively. For $Li_{16.38}Ge_4$, bar-shaped crystals with a size of up to 0.6 × 0.25 × 0.25 cm^3 could be obtained. A representative specimen is depicted in Fig. 1. Generally, crystals of $Li_{17}Ge_4$ grew much smaller in a block-like shape with diameters of 0.1 × 0.1 × 0.1 cm^3. Those crystals allowed acquisition of high quality single crystal X-ray diffraction data.

The phase $Li_{17}Ge_4$ crystallizes in the space group $F\bar{4}3m$ with a = 18.8521(3) Å (V = 6700.1(2) $Å^3$) and Z = 20. The asymmetric unit consists of 13 Li and four Ge atoms each being located on a special position (Table 1). As already reported for $Li_{17}Si_4$, $Li_{17}Sn_4$, and $Li_{17}Pb_4$,[9,18,44] the Wyckoff position 4*a* with symmetry $\bar{4}3m$ was found to be fully occupied. We note that the refinement of occupancy factors did not indicate significantly large deviations from full occupancy and thus they were regarded as being fully occupied. Accordingly, the cubic unit cell of $Li_{17}Ge_4$ contains 340 Li and 80 Ge atoms ($cF420$). Further, atomic displacement parameters were refined anisotropically with meaningful results for all atoms, revealing excellent reliability factors of R_1 = 0.022 and wR_2 = 0.038 (all data) for the final model (Table 6). The structure of $Li_{17}Ge_4$ is isotypic with $Li_{17}Si_4$, $Li_{17}Sn_4$, and $Li_{17}Pb_4$.[9,18,44]

$Li_{16.38(2)}Ge_4$ crystallizes in the space group $Cmcm$ with a = 4.5511(2) Å, b = 22.0862(7) Å, c = 13.2751(4) Å (V = 1334.37(8) $Å^3$) and Z = 16 referring to $Li_{4.096(4)}Ge$ as one formula unit. The

Fig. 1 Example of a bar-shaped single crystal of $Li_{16.38}Ge_4$ obtained from a melt $Li_{85}Ge_{15}$ at 530 °C.

Table 1 Fractional atomic coordinates and isotropic equivalent atomic displacement parameters for $Li_{17}Ge_4$ ($F\bar{4}3m$, Z = 20, T = 298 K, estimated standard deviations in parentheses)

Atom	Wyckoff position	x	y	z	U_{eq}/Å^2·10^3
Ge1	16*e*	0.159545(8)	*x*	*x*	13.03(4)
Ge2	16*e*	0.916568(8)	*x*	*x*	11.37(4)
Ge3	24*f*	0.32102(1)	0	0	13.27(5)
Ge4	24*g*	0.57015(1)	1/4	1/4	13.06(4)
Li1	16*e*	0.0734(2)	*x*	*x*	31(1)
Li2	16*e*	0.3031(2)	*x*	*x*	21.6(8)
Li3	16*e*	0.4175(2)	*x*	*x*	22.3(9)
Li4	16*e*	0.5575(2)	*x*	*x*	23(1)
Li5	16*e*	0.6877(2)	*x*	*x*	28(1)
Li6	16*e*	0.8314(2)	*x*	*x*	27(1)
Li7	24*f*	0.1677(3)	0	0	25(1)
Li8	24*g*	0.0743(3)	1/4	1/4	23.1(9)
Li9	48*h*	0.0913(2)	*x*	0.2624(2)	32.0(9)
Li10	48*h*	0.0896(2)	*x*	0.7612(2)	31.1(8)
Li11	48*h*	0.1547(1)	*x*	0.5205(2)	32.5(8)
Li12	48*h*	0.1637(1)	*x*	0.0027(2)	22.5(8)
Li13	4*a*	0	0	0	17(2)

unit cell contains 10 Li and three Ge atom positions (Table 2) where Li4 and Li5 are disordered. A careful analysis of difference Fourier maps after assigning all Ge and nine Li atom positions (Li1–Li3 and Li5–Li10) revealed occupational disorder along the crystallographic *a*-axis like that reported for $Li_{16.42}Si_4$.[10] As can be seen in Fig. 2a and 2b, the difference Fourier maps showing the strand-like residual electron density with peak-maxima at Wyckoff positions 4*c* and 8*g* are almost identical for $Li_{16.42(1)}Si_4$ and $Li_{16.38(2)}Ge_4$. Applying the disorder model as reported for $Li_{16.42(1)}Si_4$,[10] we subsequently obtained a very similar occupancy ratio of 0.616(8)/0.384(8) for Li4A on 4*c* (1/2, *y*, 1/4) and Li4B on 8*g* (*x*, *y*, 1/4), respectively, compared with 0.575(3)/0.425(3) found in $Li_{16.42(1)}Si_4$. Analogously to $Li_{16.42(1)}Si_4$,[10] a split position for Li5 on 8*f* (0, *x*, *y*) was introduced. The split fractions converged to 0.75(4) for Li5A and 0.25(4) for Li5B (0.848(7)/0.152(7) in $Li_{16.42(1)}Si_4$;[10] refinement details and the geometric relevance of the atom split are given in the ESI†). In case of atoms being uninvolved in disorder, site occupancy factors were refined to values close to full occupancy and therefore those positions were constrained to full occupancy. Thus, the unit cell contains 65.54(7) Li atoms as a consequence of the disorder (65.70(3) in $Li_{16.42(1)}Si_4$[10]) and 16 Ge atoms, resulting in a crystallographic density of 2.011 g cm^{-3}. The structure was finally solved with reliability factors of R_1 = 0.023 and wR_2 = 0.027 for all data (Table 6). $Li_{16.38(2)}Ge_4$ crystallizes isotypically with $Li_{16.42(1)}Si_4$.[10]

Table 2 Fractional atomic coordinates and isotropic equivalent atomic displacement parameters for $Li_{4.096(4)}Ge$ (*Cmcm*, Z = 16, T = 100 K, estimated standard deviations in parentheses)

Atom	Wyckoff position	x	y	z	s.o.f.	$U_{eq.}$/Å^2·10^3
Ge1	4*c*	0	0.256372(6)	1/4	1	7.83(3)
Ge2	4*c*	1/2	0.454314(5)	1/4	1	6.35(3)
Ge3	8*f*	1/2	0.105220(4)	0.067609(6)	1	6.83(2)
Li1	4*c*	1/2	0.0333(1)	1/4	1	14.4(4)
Li2	4*c*	1/2	0.3297(1)	1/4	1	13.5(4)
Li3	4*c*	0	0.3922(1)	1/4	1	17.5(5)
Li4A	4*c*	1/2	0.1476(2)	1/4	0.616(8)	52(3)
Li4B	8*g*	0.210(1)	0.1385(2)	1/4	0.384(8)	21(2)
Li5A	8*f*	0	0.1741(3)	0.0842(7)	0.75(4)	14(1)
Li5B	8*f*	0	0.164(1)	0.123(4)	0.25(4)	24(6)
Li6	8*f*	0	0.04650(7)	0.1225(1)	1	13.9(3)
Li7	8*f*	0	0.31636(9)	0.0788(1)	1	16.5(3)
Li8	8*f*	0	0.47089(9)	0.0908(1)	1	18.7(3)
Li9	8*f*	1/2	0.23155(8)	0.1356(1)	1	19.1(3)
Li10	8*f*	1/2	0.40425(8)	0.0639(1)	1	14.5(3)

Structure description of $Li_{17}Ge_4$ and $Li_{16.38}Ge_4$

In our previous work we reported on the structures of $Li_{17}Si_4$ and $Li_{16.42}Si_4$ in detail.[9,10] Both phases were comparatively highlighted on the basis of $SiLi_n$ coordination polyhedra and the disorder in $Li_{16.42}Si_4$ was illustrated with various structure models. Hence, we analogously elaborate on the structures of the isotypic phases $Li_{17}Ge_4$ and $Li_{16.38}Ge_4$ herein.

The structure of $Li_{17}Ge_4$ is closely related to the previously reported phase $Li_{21}Ge_5$[24] ($Li_{16.8}Ge_4$) only differing in the occupation of one fourfold special position. In detail, their common space group $F\bar{4}3m$ possesses four positions with site symmetry $\bar{4}3m$ (4*a*–*d*). Whereas Wyckoff positions 4*a*–*d* were claimed to be void in $Li_{21}Ge_5$, we found a fully occupied 4*a* site in $Li_{17}Ge_4$ with short but reasonable next nearest neighbor distances of 2.397(7) Å for Li1–Li13 (*cf.* Fig. 3 and Table 4). We note that since $Li_{22}Si_5$[27,45] (its composition corresponds to a full occupancy of sites 4*a*–*d*) was revised to $Li_{21}Si_5$,[46] heavier analogues such as $Li_{22}Ge_5$ were supposed to crystallize with the $Li_{21}Si_5$ structure type as well ($Li_{21}Ge_5$).[24] We have already shown by computational methods that the fully relaxed structures of $Li_{17}Si_4$ and $Li_{21}Si_5$ decisively differ regarding the coordination environment around the 4*a* site.[9] If this position is unoccupied, the first coordination shell, which is a $(Li1)_4$ tetrahedron (*cf.* Fig. 3), is markedly contracted, which was not observed in experimental data of $Li_{21}Si_5$ (Table S5 in the ESI†). Therefore it could be concluded that Li might have been overseen in the previous structure refinement (most likely a partial occupancy). Turning to $Li_{17}Ge_4$, the positional parameters are almost identical with $Li_{17}Si_4$ (Table S6 in the ESI†) and therefore an equal conclusion is reasonable.

In 2001, Goward *et al.*[18] have already reported on the revision of $Li_{22}M_5$ to $Li_{17}M_4$ (M = Ge, Sn, Pb). However, their model for "$Li_{17}Ge_4$" involved partially occupied Li sites (Table 3), namely Li1A on 16*e* (3/4 occ.), Li1B on 16*e* (1/4 occ.), and Li13 on 4*a* (3/4 occ.) resulting in the composition $Li_{16.95}Ge_4$ (note that for a better comparability the fractional atomic coordinates and labels were adapted to $Li_{17}Ge_4$). In the case of a void 4*a* site, the surrounding $(Li1A)_4$ tetrahedron (comparable with Li1 in Fig. 3) is slightly contracted to $(Li1B)_4$ whose vertices are markedly closer to the 4*a* center (2.52 Å *vs.* 1.91 Å).[18] Interestingly, this scenario is in close agreement with the computationally relaxed structure of $Li_{21}Si_5$[9] (Table S7 in the ESI†) where all fourfold positions are void. Consequently, a partial occupancy of the 4*a* position as reported for $Li_{16.95}Ge_4$ and hence the existence of a small homogeneity

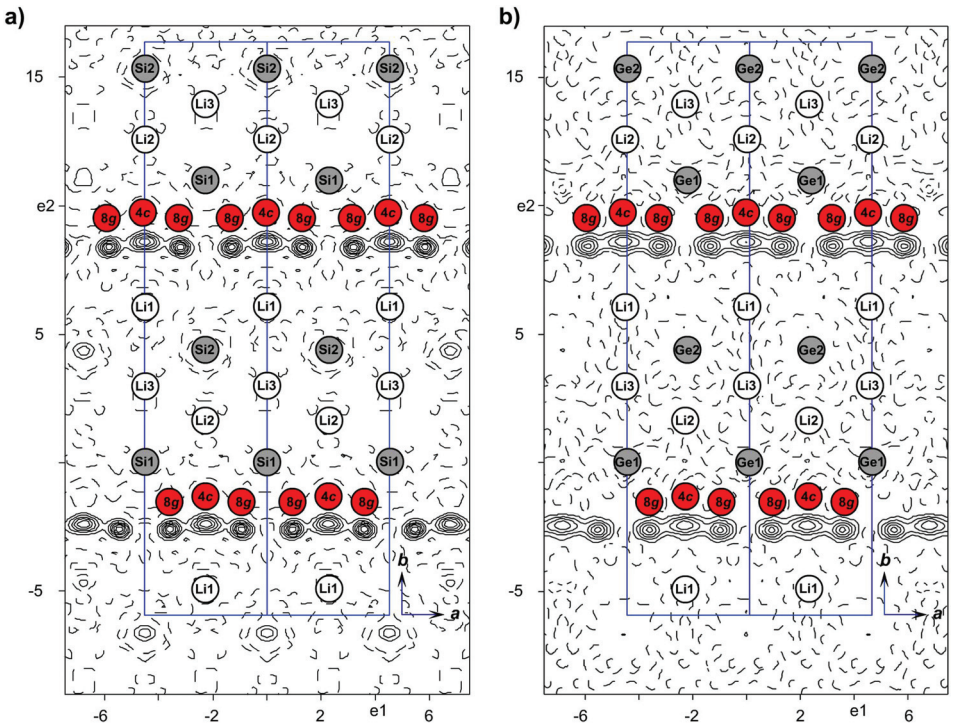

Fig. 2 Difference Fourier map ($F_o - F_c$) shown for the layer defined by Tt1, Tt2 and Li2 in (a) $Li_{16.42}Si_4$[10] and (b) $Li_{16.38}Ge_4$ (parallel to the *ab*-plane, calculated from single crystal data at 100 K and 123 K for $Li_{16.42}Si_4$ (contour lines ±0.6 e Å^{-3}) and $Li_{16.38}Ge_4$ (contour lines ±0.5 e Å^{-3}), respectively; cell edges are shown in blue).

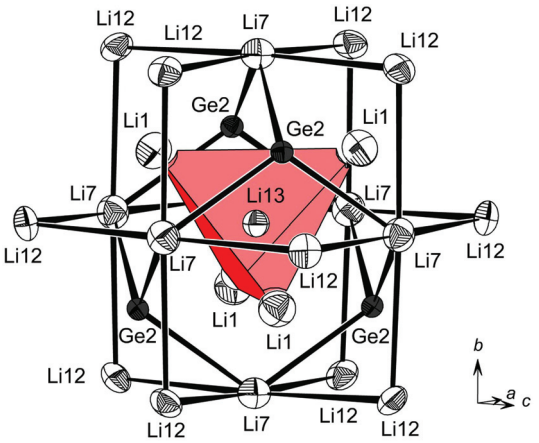

Fig. 3 Coordination environment of Li13 on the Wyckoff position 4*a* (Ge = black; Li = white; thermal ellipsoids at 70% probability, single crystal data at room temperature). The 1st, 2nd, 3rd, and 4th coordination shell is formed by a $(Li1)_4$ and $(Ge2)_4$ tetrahedron as well as a $(Li7)_6$ octahedron and a $(Li12)_{12}$ cuboctahedron.

region $Li_{17-x}Tt_4$ ($0 < x < 0.2$) are indeed meaningful. More recently, Lacroix-Orio *et al.*[47] presented a Zn-doped derivative of the $Li_{17}Ge_4$ compound. They could not find any evidence for partially occupied Li positions and instead found small concentrations of Zn being incorporated at the 4*a* position ($Li_{17-\varepsilon}Zn_\varepsilon Ge_4$, $\varepsilon = 0.005(1)$).

Concluding, the fractional atomic coordinates of all $Li_{17}Ge_4$ related phases listed in Table 3 are very similar and the scenario of an unoccupied 4*a* position in $Li_{16.95}Ge_4$ fits the calculated data of the corresponding $Li_{21}Si_5$ structure very well. This strengthens the existence of a homogeneity region $Li_{17-x}Tt_4$ ($0 < x < 0.2$) which is deduced from the flexibility of the $(Li1)_4(Tt_2)_4$ tetrahedral star around the Wyckoff position 4*a*.[9] Accordingly, the herein reported phase $Li_{17}Ge_4$ is regarded as the lithium-richest representative in the Li–Ge system.

The structure of $Li_{17}Ge_4$ is closely related to a 6 × 6 × 6 superstructure of the body centered cubic (bcc) structure.[46] As already shown by von Schnering and Nesper,[46] it can be easily interpreted by 26 atom clusters (M_{26} with M = Tt, Li) centered at the special positions 4*a*–*d* whereas Ge_4 tetrahedra and Ge_6 octahedra (note that Ge atoms are isolated by distances larger than 4.44 Å) are situated around 4*a*, 4*c* and 4*b*, 4*d*, respectively, corresponding to the arrangement of Na and Tl atoms in the NaTl structure.[46]

Yet another possible way of looking at the structure of $Li_{17}Ge_4$ is the comparison of $GeLi_n$ coordination polyhedra and their arrangement in the unit cell. This has proven to be a neat method for the comparison of lithium-rich Li–Si phases solely bearing isolated Si atoms in their structures ($Li_{17}Tt_4$, $Li_{16.4}Tt_4$ and $Li_{15}Tt_4$).[10] As shown in Fig. 4a, Ge1, Ge3 and Ge4 are 13-coordinated by Li atoms, whereas Ge2 attains a coordination number (CN) of 14. Corresponding to the first coordination shell of Ge atoms, Li–Ge distances range from 2.659(4) Å to 3.053(3) Å (Table 4). The second Li shell is clearly separated with distances larger than 4.2564(3) Å. Interestingly, the polyhedra around Wyckoff positions 4*a*, 4*c* and 4*b*, 4*d* either form

Table 3 Comparison of fractional atomic coordinates for $Li_{17}Ge_4$, $Li_{17-\varepsilon}Zn_\varepsilon Ge_4$, and $Li_{16.95}Ge_4$ (space group $F\bar{4}3$ m (for all phases), Z = 20, estimated standard deviations in parentheses). Listed are x values for the special positions 16*e* (x, x, x), 24*f* (x, 0, 0), 24*g* (x, 1/4, 1/4) and x, z pairs for 48*h* (x, x, z)

At.	Wyck. pos.	$Li_{17}Ge_4$	$Li_{17-\varepsilon}Zn_\varepsilon Ge_4$[47]	$Li_{16.95}Ge_4$[18]	At.	Wyck. pos.	$Li_{17}Ge_4$	$Li_{17-\varepsilon}Zn_\varepsilon Ge_4$[47]	$Li_{16.95}Ge_4$[18]
Ge1	16*e*	0.15955(1)	0.15958(2)	0.15952(5)	Li8	24*g*	0.0743(3)	0.0740(6)	0.075(1)
Ge2	16*e*	0.91657(1)	0.91667(3)	0.91684(5)	Li9	48*h*	0.0913(2)	0.0906(3)	0.0907(7)
Ge3	24*f*	0.32102(1)	0.32118(4)	0.32112(7)			0.2624(2)	0.2631(4)	0.2660(8)
Ge4	24*g*	0.57015(1)	0.57020(4)	0.56965(7)	Li10	48*h*	0.0896(2)	0.0904(4)	0.0914(7)
Li1A	16*e*	0.0734(2)	0.0747(6)	0.0775			0.7612(2)	0.7613(4)	0.7597(9)
Li1B	16*e*	—	—	0.0587	Li11	48*h*	0.1547(1)	0.1554(3)	0.1540(5)
Li2	16*e*	0.3031(2)	0.3033(3)	0.3032(6)			0.5205(2)	0.5216(4)	0.5216(9)
Li3	16*e*	0.4175(2)	0.4179(5)	0.4169(9)	Li12	48*h*	0.1637(1)	0.1632(3)	0.1625(5)
Li4	16*e*	0.5575(2)	0.5584(4)	0.5579(6)			0.0027(2)	0.0025(5)	0.005(1)
Li5	16*e*	0.6877(2)	0.6864(4)	0.6876(7)	Li13	4*a*	0	0	0
Li6	16*e*	0.8314(2)	0.8331(4)	0.8329(7)	Zn1	4*a*	—	0	—
Li7	24*f*	0.1677(3)	0.1678(6)	0.170(1)					

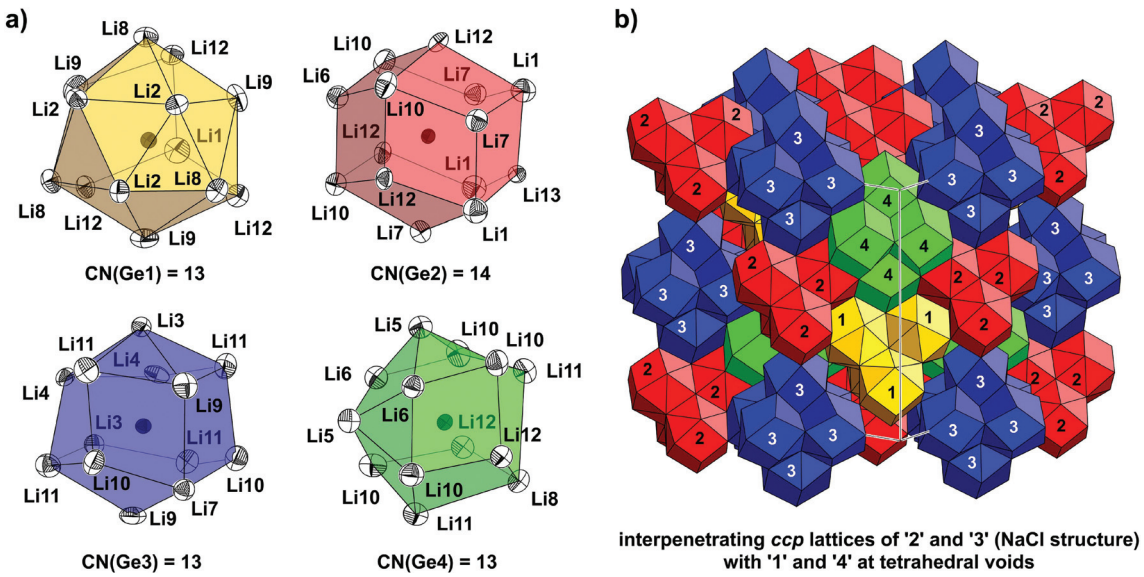

Fig. 4 (a) $GeLi_n$ coordination polyhedra (CN = coordination number) and (b) their relative arrangement in the cubic unit cell of $Li_{17}Ge_4$ (Ge = black; Li = white; thermal ellipsoids at 70% probability, single crystal data at room temperature). Supratetrahedra and supraoctahedra are formed from $Ge1Li_{13}$, $Ge2Li_{14}$ and $Ge3Li_{13}$, $Ge4Li_{13}$ coordination polyhedra (denoted as 1, 2, 3 and 4).

supratetrahedra ($[Ge1Li_{13}]_4$ and $[Ge2Li_{14}]_4$ denoted as (1) and (2)) or supraoctahedra ($[Ge3Li_{13}]_6$ and $[Ge4Li_{13}]_6$ denoted as (3) and (4)), respectively (Fig. 4b). Accordingly, the structure of $Li_{17}Ge_4$ can be considered as two interpenetrating *ccp* lattices of (2) and (3), *i.e.* the NaCl structure, where tetrahedral voids are filled with (1) and (4).

Besides $Li_{17}Ge_4$ and $Li_{15}Ge_4$, $Li_{16.38}Ge_4$ is yet another representative exclusively bearing isolated Ge atoms. It is isotypic with $Li_{16.42}Si_4$[10] which possesses a peculiar structure involving occupational and positional disorder along the crystallographic *a*-axes (*cf.* Fig. 2). A convenient way of illustrating the disordered structure of $Li_{16.38}Ge_4$ is the assumption of a simplified ordered model which has already been applied for the description and band structure calculations of $Li_{16.42}Si_4$.[10] In detail, the atom positions Li4A, Li4B and Li5A (*cf.* Table 2) affected by disorder corresponding to the Wyckoff positions 4*c*

Table 4 Selected interatomic distances in $Li_{17}Ge_4$ ($F\bar{4}3m$, Z = 20, T = 298 K, estimated standard deviations in parentheses)

Atom pair			*d*(Å)	Atom pair			*d*(Å)
Ge1	Li9	×3	2.659(4)	Ge3	Li10	×2	2.849(4)
	Li1		2.813(7)		Li3	×2	2.855(2)
	Li2	×3	2.884(1)		Li7		2.890(5)
	Li8	×3	2.898(3)		Li11	×4	2.977(2)
	Li12	×3	2.959(4)	Ge4	Li12	×2	2.680(3)
Ge2	Li12	×3	2.686(3)		Li11	×2	2.709(3)
	Li13		2.7244(3)		Li8		2.723(5)
	Li7	×3	2.734(3)		Li5	×2	2.769(4)
	Li6		2.780(6)		Li6	×2	2.856(2)
	Li10	×3	2.933(4)		Li10	×4	3.053(3)
	Li1	×3	2.969(4)	Li13	Li1	×4	2.397(7)
Ge3	Li9	×2	2.673(4)		Ge2	×4	2.7244(3)
	Li4	×2	2.760(3)		Li7	×6	3.162(5)

(0.616(8) occ.), 8*g* (0.384(8) occ.) and 8*f* (0.75(4) occ.), respectively, are either regarded as half (Li4A, Li4B) or fully occupied (Li5A) resulting in the composition $Li_{16.5}Ge_4$. An accordingly ordered model with fully occupied atom positions and crystallographically independent sites for Li4B′ and Li4B″ (translate to Li4B in *Cmcm*) can be achieved by symmetry reduction and a cell enlargement (space group $P2_1/m$, a = 9.1016(4) Å, b = 13.2751(4) Å, c = 11.2744(4) Å, β = 101.643(1)°; for crystallographic details, see ref. 10). The $GeLi_n$ polyhedra occurring in the respective model "$Li_{16.5}Ge_4$" are depicted in Fig. 5a.

Similar to $Li_{17}Ge_4$, the first shell of Li atoms surrounding each Ge atom is clearly separated from the second one with distances between 2.596(2) Å to 3.309(3) Å and distances above 4.103(4) Å (Table 5). Whereas Ge1 and Ge2 are permanently 13-coordinated ($Ge1Li_{13}$/$Ge1'Li_{13}$ and $Ge2Li_{13}$ denoted as (1)/(1′) and (2)), Ge3 attains coordination numbers of either 12 or 13 ($Ge3Li_{12}$ and $Ge3'Li_{13}$ denoted as (3) and (3′)). The different coordination of Ge3 is attributed to the varying occupation of atom positions Li4A, Li4B′ and Li4B″. The arrangement of $GeLi_n$ polyhedra in the unit cell of $Li_{16.38}Ge_4$ is achieved by stacking them into strands which proceed along the crystallographic *a*-axis (Fig. 5b). For the ordered model "$Li_{16.5}Ge_4$", the stacking sequence is indicated by numbers corresponding to various $GeLi_n$ polyhedra highlighted in Fig. 5a.

Comparing the $TtLi_n$ coordination polyhedra of all lithium-rich Li–Tt phases, which exclusively comprise isolated Tt atoms in their structures, the coordination numbers consistently increase from CN = 12 ($Li_{15}Tt_4$), over CN = 12–13 ($Li_{16.4}Tt_4$) to CN = 13–14 ($Li_{17}Ge_4$).

Solid solutions $Li_{17}Si_{4-x}Ge_x$ [x = 2.30(2), 3.08(4), 3.53(3)]

$Li_{17}Si_4$ and $Li_{17}Ge_4$ are isotypic phases that form solid solutions. Single crystalline samples of $Li_{17}Si_{4-x}Ge_x$ were obtained from melt equilibration experiments and analyzed by single crystal and powder X-ray diffraction as well as energy dispersive X-ray spectroscopy. The Si–Ge ratios for $Li_{17}Si_{4-x}Ge_x$ samples obtained from single crystal X-ray diffraction data were x = 2.30(2), 3.08(4), and 3.53(3). We note that these values deviate from the initial ones x = 1.0, 2.0, and 3.0 corresponding to the employed melts "$Li_{90}Si_{7.5}Ge_{2.5}$", "$Li_{90}Si_5Ge_5$" and "$Li_{90}Si_{2.5}Ge_{7.5}$" as the Si amount is reduced due to a partial reaction of Si with the stainless steel ampules; thus the Si–Ge ratios in the products are shifted toward higher Ge contents. As can be seen in Fig. 6, the cell axes and volumes (determined from PXRD patterns of the respective samples by Rietveld refinement, Fig. S2†) linearly increase with increasing Ge concentrations in $Li_{17}Si_{4-x}Ge_x$ revealing a perfect behavior obeying Vegard's law.[43] Additionally, results from EDX measurements agree well with the crystallographically determined Si–Ge ratios (impurities originating from the stainless steel ampule were not detected).

Analyzing the distribution of Si and Ge on atom positions Tt1–4, the Si–Ge ratios are very similar for Tt1, Tt3, and Tt4, whereas Tt2 on the Wyckoff position 16*e* (x, x, x) features a slight preference for Si (Table S1–4†). Comparing the coordination environment of Tt2 and Tt1, Tt3, Tt4, the former is

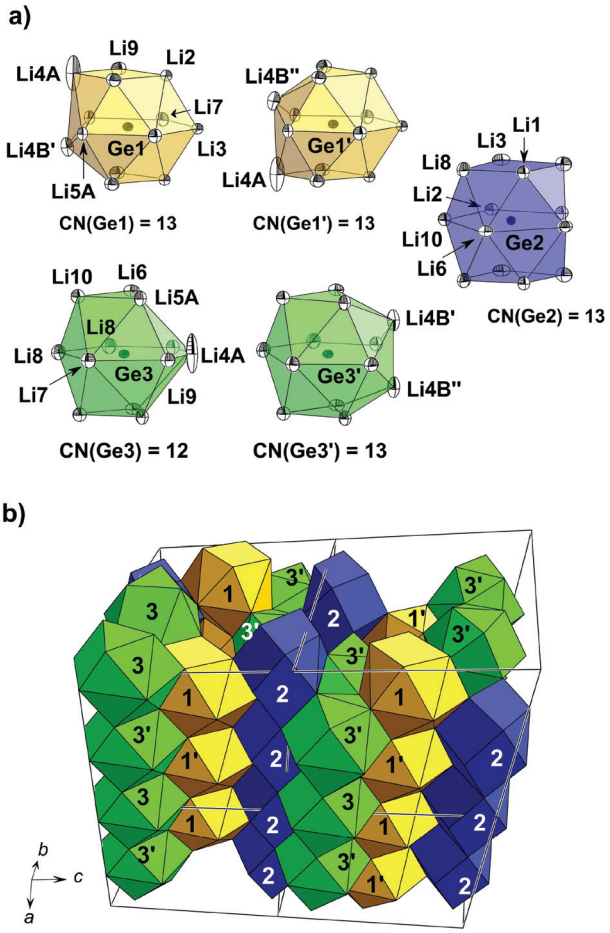

Fig. 5 (a) $GeLi_n$ coordination polyhedra occurring in an idealized model for $Li_{16.38}Ge_4$ with a composition of $Li_{16.5}Ge_4$ (space group $P2_1/m$, fully occupied and crystallographically independent atom positions Li4B′, Li4B″ (both correspond to Li4B in $Li_{16.38}Ge_4$), Li4A, and Li5A); (b) stacking of $GeLi_n$ polyhedra by sharing opposite faces resulting in parallel rods which run along the crystallographic *a*-axis (Ge = black, Li = white, thermal ellipsoids at 90% probability, single crystal data at 100 K). The polyhedra stacking in the structure model "$Li_{16.5}Ge_4$" is indicated by numbers *X* which correspond to the coordination polyhedra of atom Ge*X* in (a).

Table 5 Selected interatomic distances in $Li_{16.38}Ge_4$ (*Cmcm*, Z = 16, T = 123 K, estimated standard deviations in parentheses)

Atom pair			d(Å)	Atom pair			d(Å)
Ge1	Li7	×2	2.631(2)	Ge2	Li8	×4	3.127(1)
	Li5B	×2	2.64(2)	Ge3	Li4A		2.596(2)
	Li4B	×2	2.772(4)		Li7		2.603(2)
	Li9	×4	2.790(1)		Li8		2.693(2)
	Li2	×2	2.792(1)		Li6	×2	2.7188(9)
	Li5A	×2	2.854(8)		Li5B	×2	2.723(8)
	Li3		3.001(2)		Li5A	×2	2.747(3)
	Li4A	×2	3.309(3)		Li4B	×2	2.854(3)
Ge2	Li6	×2	2.647(2)		Li10	×2	2.875(1)
	Li3	×2	2.657(1)		Li1		2.896(1)
	Li10	×2	2.707(2)		Li9		2.932(2)
	Li2		2.753(2)		Li8		2.983(2)
	Li1	×2	2.867(2)				

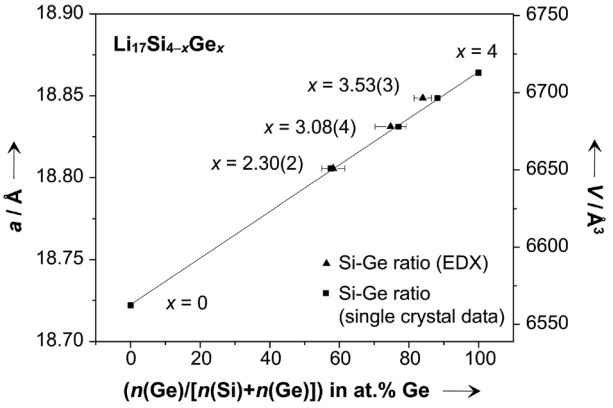

Fig. 6 Trend of cell volumes *vs.* Ge contents in $Li_{17}Si_{4-x}Ge_x$ (x = 0, 2.30(2), 3.08(4), 3.53(3), 4). Cell parameters were determined from respective PXRD patterns by Rietveld refinement (Fig. S2), and Ge contents were obtained from either single crystal X-ray diffraction data or EDX (error bars for a, V, and $x_{single\ crystal}$ (in at%) are smaller than data point icons).

14- and the latter are 13-coordinated by Li atoms with similar Ge–Li distances (2.68 Å–2.95 Å *vs.* 2.65–3.04 Å). The phenomenon that different crystallographic sites are substituted differently is also known as the "coloring problem".[48] In some cases the site preferences cannot be deduced on the basis of simple chemical reasoning (*e.g.* differences in electronegativities) and quantum chemical calculations may give a reasonable explanation.[49] Here, the focus is set on experimental work and we note that small differences in the distribution of Si and Ge on atom positions Tt2 and Tt1, Tt3, Tt4 were traced.

Thermodynamic stability of $Li_{17}Ge_4$ and $Li_{16.38}Ge_4$

The Li–Ge phase diagram was determined by Federov & Molochka[23] in 1966 and later revised by Grüttner[25] in his dissertation. However, a current compilation of the Li–Ge system[50] did not include Grüttner's results and, hence, significant information is missing. Therefore and due to the recent improvements of the Li–Si phase diagram (>76 at% Li),[8–10] a detailed redetermination of the respective portion of the Li–Ge system is essential.

The lithium-rich section of the Li–Ge phase diagram (>79 at % Li) was studied by DSC investigations of samples with systematically different compositions $Li_{17}Ge_4$, "$Li_{16.5}Ge_4$" and "$Li_{16}Ge_4$". Accordingly, PXRD patterns correspond to pure-phase $Li_{17}Ge_4$, a mixture of $Li_{17}Ge_4$ and $Li_{16.38}Ge_4$, and a mixture of $Li_{16.38}Ge_4$ and $Li_{15}Ge_4$, respectively (Fig. 7).

The thermograms of these samples are depicted in Fig. 7. The first thermal events in these cooling traces (signal 1–3) are assigned to the crossing of the liquidus boundary. Analogously to the Li–Si system,[10] signals (4) and (5) at 520–522 °C and 627 °C are attributed to the peritectic formation temperatures of $Li_{17}Ge_4$ (481–486 °C for $Li_{17}Si_4$) and $Li_{16.38}Ge_4$ (618 °C for $Li_{16.42}Si_4$), respectively. This is additionally strengthened by our results from melt equilibration experiments (see above) where crystals of $Li_{16.38}Ge_4$ are only afforded above temperatures of 520 °C. Note that signal (5) corresponding to the peritectic formation of $Li_{16.38}Ge_4$ from melt and $Li_{15}Ge_4$ is superimposed by signals (1) and (2) in the cooling traces of $Li_{17}Ge_4$ and "$Li_{16.5}Ge_4$" (Fig. 7), respectively, but clearly visible for the "$Li_{16}Ge_4$" sample. Instead, it can be recognized at around 630 °C in the respective heating trace, exemplarily shown for $Li_{17}Ge_4$ (effect 5′). Furthermore, long term annealing experiments of "$Li_{16}Ge_4$" samples (Fig. S1 in the ESI†) established $Li_{16.38}Ge_4$ as a high-temperature phase being stable above ~400 °C until 627 °C, just like $Li_{16.42}Si_4$ existing between 470 and 618 °C.[10] We note that the decomposition behavior of $Li_{16.38}Ge_4$ is very sluggish and even harder to trace than in the case of its Si counterpart.

Finally, the recent results from DSC investigations are compiled in an updated Li–Ge phase diagram (Fig. 8b) which was revised from Grüttner's previously determined one shown in Fig. 8a. A comparison with the Li–Si phase diagram (Fig. 8c) reveals similarities to the Li–Ge system. An interesting difference is the stability of $Li_{15}Tt_4$. Whereas $Li_{15}Si_4$ is metastable and decomposes above ~170 °C,[8] $Li_{15}Ge_4$ is thermodynamically stable and melts congruently at 720 °C.[25] Furthermore, uncertainties regarding the isotherms at 610 °C and 618 °C in the Li–Si phase diagram[10] could not be found for the Li–Ge system.

Conclusion

The germanides $Li_{17}Ge_4$ and $Li_{16.38}Ge_4$ were established as further representatives of the Li–Ge system. The latter is assigned a high-temperature phase which exists between ~400 and 627 °C, the former, the lithium-richest Li–Ge phase, decomposes peritectically at 521 °C into melt and $Li_{16.38}Ge_4$. $Li_{16.38}Ge_4$ can be retained at room temperature if according melts are cooled to the respective temperature region and subsequently quenched. Both germanides are isotypic to the silicides $Li_{17}Si_4$ and $Li_{16.42}Si_4$ extending the family of isotypic lithium tetrelides to $Li_{17}Tt_4$, $Li_{16.4}Tt_4$, $Li_{15}Tt_4$, $Li_{14}Tt_6$, $Li_{12}Tt_7$, and LiTt (Tt = Si, Ge). The previously reported $Li_{16.95}Ge_4$ can be regarded as representative of a homogeneity region $Li_{17-x}Tt_4$ ($0 < x < 0.2$) with $Li_{17}Ge_4$ and $Li_{16.8}Ge_4$ ($Li_{21}Ge_5$) as border phases only differing in the occupation of the Wyckoff position 4*a*. Moreover, the validity of Vegard's law for the solid solutions $Li_{17}Si_{4-x}Ge_x$ was confirmed and small differences in the distribution of Si and Ge to the four crystallographically independent atom positions were observed. Regarding the thermodynamic properties, the regions of stability for $Li_{17}Tt_4$ and $Li_{16.42}Tt_4$ are very similar. Interesting are also the thermodynamic and structural differences of lithium silicides and germanides. For instance, whereas $Li_{15}Si_4$ is a metastable phase, $Li_{15}Ge_4$ melts congruently at 720 °C. Further, the phases Li_9Ge_4 and Li_7Ge_{12} are not known in the Li–Si system. In particular, the synthesis of a hypothetical phase Li_7Si_{12} would be an intriguing field of research since it may serve as a precursor for a new allotrope of Si, just as was reported for Li_7Ge_{12} and its mild oxidation to *allo*-Ge.[36,51]

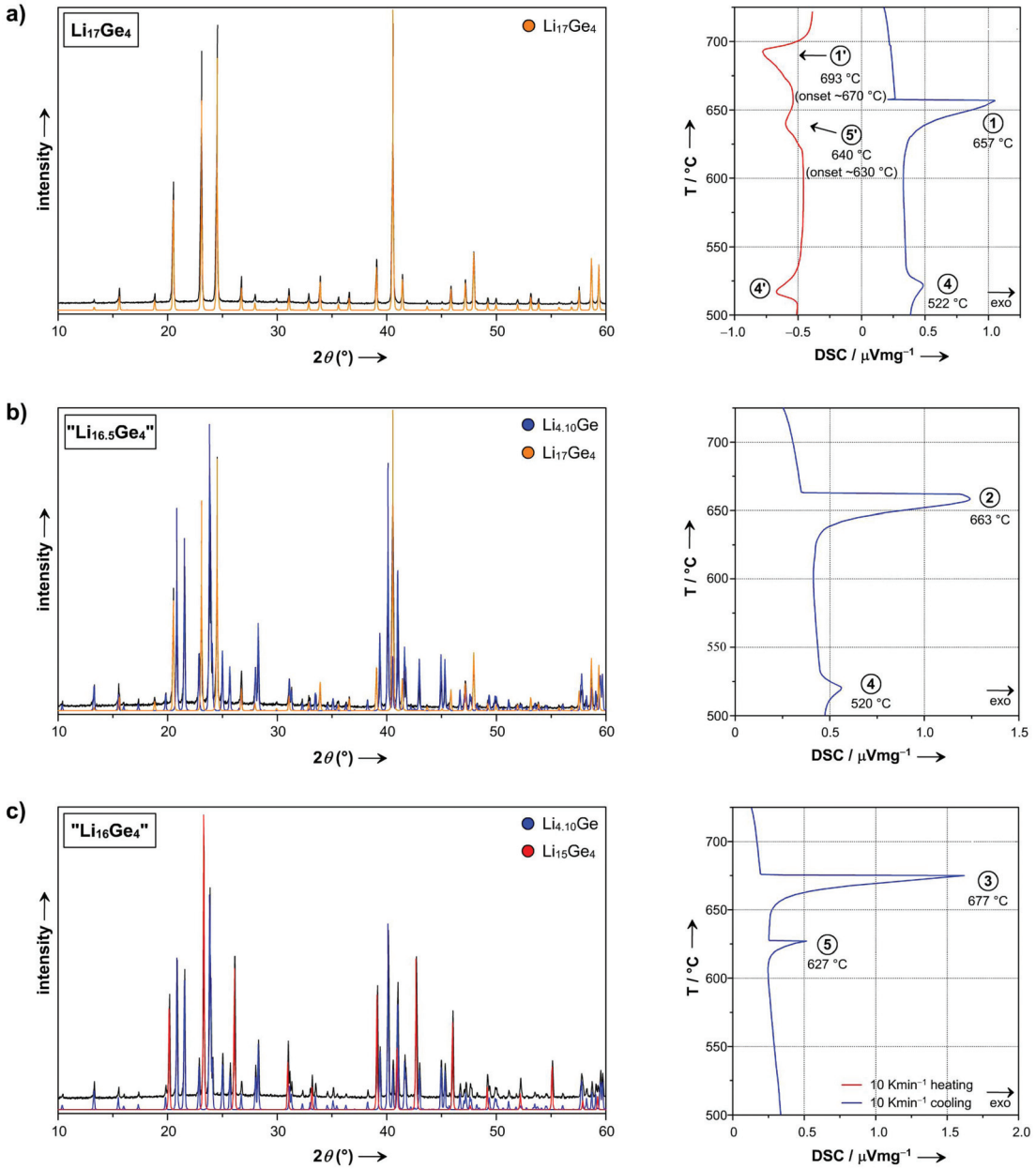

Fig. 7 PXRD patterns and corresponding DSC thermograms of bulk samples (a) $Li_{17}Ge_4$, (b) $Li_{16.5}Ge_4$, and (c) $Li_{16}Ge_4$ (PXRD patterns: experimental = black, $Li_{17}Ge_4$ (calc.) = yellow, $Li_{4.10}Ge$ (calc.) = blue, $Li_{15}Ge_4$ (calc.) = red; DSC thermograms: heating and cooling traces are shown in red and blue, respectively, a signal assignment is given in the Li–Ge phase diagram in Fig. 8b).

Experimental section

Synthesis

Starting materials were Li rods (99%, Rockwood-Lithium), Si powder (99.999%, Alfa Aesar) and Ge pieces (99.999%, Chempur). All steps of synthesis and sample preparation were carried out in a glove box (MBraun, Ar atmosphere, H_2O and O_2 levels <0.1 ppm). Ta and stainless steel ampules were thoroughly cleaned, heated to 1000 °C (Ta) or 800 °C (stainless steel) under dynamic vacuum ($p < 1 \times 10^{-3}$ mbar) for at least 2 h and transferred to the glove box. An all-glass Schlenk line supplied with Ar, which is dried over P_2O_5, molecular sieve and heated titanium sponge (T = 750 °C), was used for heating and handling under inert conditions.

Large single crystals of $Li_{17}Ge_4$ and $Li_{4.10}Ge$ ($Li_{16.38}Ge_4$) (*cf.* Fig. 1) were obtained from equilibrating melts with compositions "$Li_{95}Ge_5$" and "$Li_{85}Ge_{15}$" at temperatures of 400 and 530 °C in Ta ampules (slow cooling from 700 °C at a rate of 5 K h^{-1} followed by 48 hours dwelling at specified temperatures) and subsequent isothermal melt-centrifugation. Details of this procedure have already been described in ref. 9 and 52. Crystals of $Li_{17}Si_{4-x}Ge_x$ [x = 0, 2.30(2), 3.08(4), 3.53(3)] were

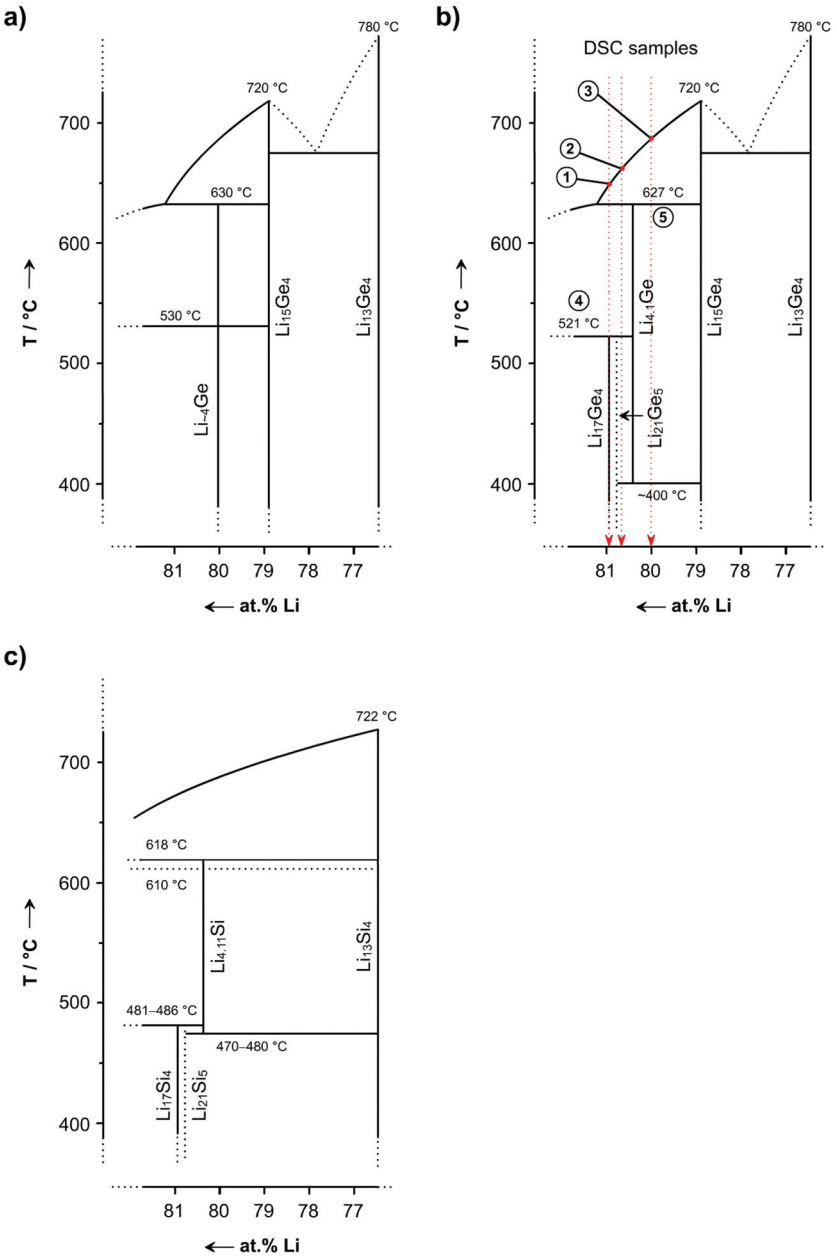

Fig. 8 (a) Excerpt of the Li–Ge phase diagram as reported from Grüttner[25] (the composition of the eutectic between $Li_{15}Ge_4$ and $Li_{13}Ge_4$ was not determined), (b) its revision based on DSC investigations and annealing experiments of "$Li_{16}Ge_4$" samples reported herein, and (c) the most recent Li–Si phase diagram for Li concentrations >76%.[10]

grown analogously in stainless steel ampules from melts with compositions "$Li_{90}Si_{10}$", "$Li_{90}Si_{7.5}Ge_{2.5}$", "$Li_{90}Si_5Ge_5$" and "$Li_{90}Si_{2.5}Ge_{7.5}$" equilibrated at 450 °C.

Furthermore, elemental mixtures with compositions $Li_{17}Ge_4$, "$Li_{16.5}Ge_4$" and "$Li_{16}Ge_4$" with a total amount of 2.5 g each were loaded into Ta ampules which were sealed by arc welding inside the glove box. For achieving targeted compositions with sufficient precision, a batch size of 2.5 g was deemed appropriate to keep weighing errors minimal.[9,10] Subsequently, ampules were sealed in silica jackets under vacuum and annealed in a muffle furnace. The temperature was raised to 750 °C at a rate of 10 K min^{-1} and held for 0.5 h followed by cooling to 500–550 °C at a rate of 10 K min^{-1}. After a dwell time of one hour, ampules were quenched in water and transferred back to the glove box. Obtained products were ground in agate mortars and characterized by powder X-ray diffraction (*cf.* Fig. 7).

Differential scanning calorimetry (DSC)

Differential scanning calorimetry was carried out with a Netzsch DSC 404 Pegasus apparatus. Cylindrical Nb crucibles (L = 15.0 mm, OD = 6.5 mm, ID = 5.0 mm) were thoroughly

cleaned, heated to 1000 °C under dynamic vacuum ($p < 1 \times 10^{-3}$ mbar) for 2 h and transferred to an Ar-filled glove box. Crucibles were loaded with 30–50 mg of the sample ($Li_{17}Ge_4$, "$Li_{16.5}Ge_4$" and "$Li_{16}Ge_4$"). Subsequently, the open end was roughly closed by crimping and then sealed by arc-welding inside the glove box under cooling. A sealed Nb crucible without the sample served as a reference. For all measurements an Ar-flow of 60–70 mL min^{-1} and a heating/cooling rate of 10 K min^{-1} were used. Samples were recovered after the measurement inside an Ar-filled glove box. Data were handled with the program Proteus Thermal Analysis.[53]

Annealing experiments

In order to further investigate the thermodynamic stability of $Li_{4.10}Ge$ ($Li_{16.38}Ge_4$), batches of 100–150 mg of "$Li_{16}Ge_4$" bulk material were sealed in Ta ampules and annealed in a muffle furnace at 200, 400 and 510 °C (10 K min^{-1} heating rate) for three days. Thereafter, ampules were quenched in water and transferred inside an Ar-filled glove box. Products were ground in agate mortars and subsequently characterized by powder X-ray diffraction (Fig. S1†).

Single crystal X-ray diffraction and structure determination

Crystals of $Li_{17}Ge_4$ and $Li_{4.096(4)}Ge$ ($Li_{16.38(2)}Ge_4$) were handled in an Ar-filled glove box, selected under a microscope and sealed inside glass capillaries. For the best specimen, intensity data were collected at room temperature ($Li_{17}Ge_4$) and 123 K ($Li_{16.38(2)}Ge_4$) on a Bruker X-ray diffractometer equipped with a CCD detector (Apex II, κ-CCD), a fine-focused sealed tube with MoK_α radiation (λ = 0.71073 Å) and a graphite monochromator using the Bruker Apex2 software.[54] Integration, data reduction and absorption correction were done using SAINT and SADABS.[55,56] The space groups $F\bar{4}3m$ ($Li_{17}Ge_4$) and $Cmcm$ ($Li_{16.38(2)}Ge_4$) were assigned on the basis of the systematic absence and the statistical analysis of the intensity distributions. For $Li_{17}Ge_4$, Friedel pairs were not merged since the assigned space group is non-centrosymmetric. The Flack[57] parameter was determined as 0.50(3). The structures were solved by direct methods (Shelxs-97[58]) and refined with full-matrix least squares on F^2 (Shelxl-97[59]). Difference Fourier maps $F_o - F_c$ were calculated with Jana2006.[60] All refinement results are compiled in Table 6.

Details of the single crystal X-ray structure determination, refinement data, fractional atomic coordinates and isotropic equivalent atomic displacement parameters for $Li_{17}Si_{4-x}Ge_x$ [(x = 2.30(2), 3.08(4), 3.53(3)] are given in Table S1–4 in the ESI.† Further data may be obtained from Fachinformationszentrum Karlsruhe, D-76344 Eggenstein-Leopoldshafen, Germany (fax: (+49)7247-808-666; e-mail: crysdata@fiz-karlsruhe.de) on quoting the depository numbers CSD-427231 ($Li_{4.10}Ge$ ($Li_{16.38}Ge_4$)), CSD-427232 ($Li_{17}Ge_4$), CSD-427233 ($Li_{17}Si_{0.47}Ge_{3.53}$), CSD-427234 ($Li_{17}Si_{0.92}Ge_{3.08}$), and CSD-427235 ($Li_{17}Si_{1.70}Ge_{2.30}$).

Powder X-ray diffraction (PXRD)

PXRD patterns were recorded on a Stoe Stadi P diffractometer (Ge(111) monochromator for Cu$K_{\alpha1}$ radiation, λ = 1.54056 Å) equipped with a Dectris Mythen DCS 1 K solid state detector. Investigated samples were (i) single crystals of $Li_{17}Si_{4-x}Ge_x$ (x = 0, 2.30(2), 3.08(4), 3.53(3), 4), (ii) bulk samples of $Li_{17}Ge_4$, "$Li_{16.5}Ge_4$" and "$Li_{16}Ge_4$", and (iii) samples of "$Li_{16}Ge_4$" annealed at different temperatures. These were thoroughly ground in agate mortars, sealed inside 0.3 mm glass capillaries and measured in a 2θ-range of 5–90° (PSD steps: 0.06–1.00°; time per step: 20–40 s).

Table 6 Crystallographic data and structure refinement for $Li_{17}Ge_4$ and $Li_{4.096(4)}Ge$

Empirical formula	$Li_{17}Ge_4$	$Li_{4.096(4)}Ge$
T/K	298(2)	123(2)
Formula weight/g·mol^{-1}	408.34	101.01
Crystal size/mm^3	0.40 × 0.40 × 0.35	0.37 × 0.24 × 0.23
Crystal color	Metallic silver	Metallic silver
Crystal shape	Block	Bar
Space group	$F\bar{4}3m$	$Cmcm$
Structure type	$Li_{17}Pb_4$	$Li_{4.11}Si$
Unit cell dimension/Å	a = 18.8521(3)	a = 4.5511(2)
		b = 22.0862(7)
		c = 13.2751(4)
V/Å^3	6700.1(2)	1334.37(8)
Z	20	16
ρ (calc.)/g cm^{-3}	2.024	2.011
μ/mm^{-1}	8.832	8.860
F (000)	3580	709
θ Range/°	1.87–45.26	1.84–40.25
Index range hkl	$-37 \le h \le +23$	$-6 \le h \le +8$
	$-37 \le k \le +30$	$-32 \le k \le +40$
	$-37 \le l \le +37$	$-24 \le l \le +19$
Reflections collected	67 542	15 241
Independent reflections	2757 (R_{int} = 0.047)	2369 (R_{int} = 0.023)
Reflections with $I > 2\sigma(I)$	2547 (R_σ = 0.017)	1920 (R_σ = 0.017)
Data/restraints/parameter	2757/0/68	2369/0/82
Absorption correction	Multi-scan	Multi-scan
Goodness-of-fit on F^2	1.106	1.042
Final R indices $[I > 2\sigma(I)]^{a,b}$	R_1 = 0.018	R_1 = 0.015
	wR_2 = 0.037	wR_2 = 0.026
R indices (all data)^{a,b}	R_1 = 0.022	R_1 = 0.023
	wR_2 = 0.038	wR_2 = 0.027
Extinction coefficient	1.59(9) × 10^{-4}	1.52(7) × 10^{-3}
Flack parameter	0.50(3)	—
Largest diff. peak and hole/e Å^{-3}	0.46 and −0.69	0.69 and −0.52

$^a R_1 = \sum||F_o|-|F_c||/\sum|F_o|$. ^{b} w$R_2 = [\sum w(F_o^2 - F_c^2)^2/\sum w(F_o^2)^2]^{1/2}$.

Energy dispersive X-ray spectroscopy (EDX)

A Jeol-JSM 7500F scanning electron microscope equipped with an Oxford X-Max EDX analyzer with Mn as an internal standard was used for determining the Si–Ge ratios in $Li_{17}Si_{4-x}Ge_x$ [x = 2.30(2), 3.08(4), 3.53(3)]. Samples were handled inside an Ar-filled glove box and fixed on a graphite platelet which was mounted on an aluminum stub.

Acknowledgements

M.Z. thanks the Fonds der Chemischen Industrie for his fellowship, the authors thank K. Rodewald for EDX measurements.

References

1 M. N. Obrovac and L. Christensen, *Electrochem. Solid-State Lett.*, 2004, **7**, A93–A96.
2 T. D. Hatchard and J. R. Dahn, *J. Electrochem. Soc.*, 2004, **151**, A838–A842.
3 W. J. Zhang, *J. Power Sources*, 2011, **196**, 13–24.
4 P. Limthongkul, Y. I. Jang, N. J. Dudney and Y. M. Chiang, *Acta Mater.*, 2003, **51**, 1103–1113.
5 P. Limthongkul, Y. I. Jang, N. J. Dudney and Y. M. Chiang, *J. Power Sources*, 2003, **119–121**, 604–609.
6 B. Key, M. Morcrette, J. M. Tarascon and C. P. Grey, *J. Am. Chem. Soc.*, 2011, **133**, 503–512.
7 B. Key, R. Bhattacharyya, M. Morcrette, V. Seznec, J. M. Tarascon and C. P. Grey, *J. Am. Chem. Soc.*, 2009, **131**, 9239–9249.
8 M. Zeilinger, V. Baran, L. van Wüllen, U. Häussermann and T. F. Fässler, *Chem. Mater.*, 2013, **25**, 4113–4121.
9 M. Zeilinger, D. Benson, U. Häussermann and T. F. Fässler, *Chem. Mater.*, 2013, **25**, 1960–1967.
10 M. Zeilinger, I. M. Kurylyshyn, U. Häussermann and T. F. Fässler, *Chem. Mater.*, 2013, **25**, 4623–4632.
11 M. Zeilinger and T. F. Fässler, *Acta Crystallogr., Sect. E: Struct. Rep. Online*, 2013, **69**, i81–i82.
12 D. Thomas, M. Abdel-Hafiez, T. Gruber, R. Hüttl, J. Seidel, A. U. B. Wolter, B. Büchner, J. Kortus and F. Mertens, *J. Chem. Thermodyn.*, 2013, **64**, 205–225.
13 P. Wang, A. Kozlov, D. Thomas, F. Mertens and R. Schmid-Fetzer, *Intermetallics*, 2013, **42**, 137–145.
14 A. Debski, W. Gasior and A. Goral, *Intermetallics*, 2012, **26**, 157–161.
15 S. Dupke, T. Langer, R. Pöttgen, M. Winter, S. Passerini and H. Eckert, *Phys. Chem. Chem. Phys.*, 2012, **14**, 6496–6508.
16 S. Dupke, T. Langer, R. Pöttgen, M. Winter and H. Eckert, *Solid State Nucl. Magn. Reson.*, 2012, **42**, 17–25.
17 A. Kuhn, P. Sreeraj, R. Pöttgen, H. D. Wiemhöfer, M. Wilkening and P. Heitjans, *J. Am. Chem. Soc.*, 2011, **133**, 11018–11021.
18 G. R. Goward, N. J. Taylor, D. C. S. Souza and L. F. Nazar, *J. Alloys Compd.*, 2001, **329**, 82–91.
19 C. S. Fuller and J. C. Severiens, *Phys. Rev.*, 1954, **96**, 21–24.
20 J. Graetz, C. C. Ahn, R. Yazami and B. Fultz, *J. Electrochem. Soc.*, 2004, **151**, A698–A702.
21 E. M. Pell, *J. Phys. Chem. Solids*, 1957, **3**, 74–76.
22 G. I. Oleksiv, *Probl. Rozvitku Prirodn. i Tochn. Nauk, Sb.*, 1964, 76–77.
23 P. I. Federov and V. A. Molochka, *Izv. Akad. Nauk. SSSR, Neorg. Mater.*, 1966, **2**, 1870–1871.
24 R. Nesper, *Prog. Solid State Chem.*, 1990, **20**, 1–45.
25 A. Grüttner, PhD thesis, University of Stuttgart, 1982.
26 A. Grüttner, R. Nesper and H. G. von Schnering, *Acta Crystallogr., Sect. A: Cryst. Phys., Diffr., Theor. Gen. Cryst.*, 1981, **37**, C161.
27 E. I. Gladyshevskii, G. I. Oleksiv and P. I. Kripyakevich, *Kristallografiya*, 1964, **9**, 338–341.
28 Q. Johnson, G. S. Smith and D. Wood, *Acta Crystallogr.*, 1965, **18**, 131–132.
29 E. I. Gladyshevskii and P. I. Kripyakevich, *Kristallografiya*, 1960, **5**, 574–576.
30 R. Nesper, *Habilitation*, University of Stuttgart, 1988.
31 V. Hopf, W. Müller and H. Schäfer, *Z. Naturforsch., B: Anorg. Chem. Org. Chem.*, 1972, **27**, 1157–1160.
32 V. Hopf, H. Schäfer and A. Weiss, *Z. Naturforsch., B: Anorg. Chem. Org. Chem.*, 1970, **25**, 653.
33 H. G. von Schnering, R. Nesper, J. Curda and K. F. Tebbe, *Angew. Chem.*, 1980, **92**, 1070.
34 E. Menges, V. Hopf, H. Schäfer and A. Weiss, *Z. Naturforsch., B: Anorg. Chem. Org. Chem.*, 1969, **21**, 1351–1352. According to ref. 25, the structures of LiGe reported in ref. 22 and 34 are identical (only two different cell settings).
35 J. Evers, G. Oehlinger, G. Sextl and H. O. Becker, *Angew. Chem., Int. Ed. Engl.*, 1987, **26**, 76–78.
36 A. Grüttner, R. Nesper and H. G. von Schnering, *Angew. Chem., Int. Ed. Engl.*, 1982, **21**, 912–913.
37 U. Frank and W. Müller, *Z. Naturforsch., B: Anorg. Chem. Org. Chem.*, 1975, **30**, 313–315.
38 R. Nesper, J. Curda and H. G. von Schnering, *J. Solid State Chem.*, 1986, **62**, 199–206.
39 J. Evers, G. Oehlinger and G. Sextl, *Angew. Chem., Int. Ed. Engl.*, 1993, **32**, 1442–1444.
40 J. Evers and G. Oehlinger, *Angew. Chem., Int. Ed.*, 2001, **40**, 1050–1053.
41 F. Kiefer and T. F. Fässler, *Solid State Sci.*, 2011, **13**, 636–640.
42 Y. Hashimoto, N. Machida and T. Shigematsu, *Solid State Ionics*, 2004, **175**, 177–180.
43 L. Vegard, *Z. Phys.*, 1921, **5**, 17–26.
44 C. Lupu, J. G. Mao, J. W. Rabalais, A. M. Guloy and J. W. Richardson, *Inorg. Chem.*, 2003, **42**, 3765–3771.
45 H. Axel, H. Schäfer and A. Weiss, *Z. Naturforsch., B: Anorg. Chem. Org. Chem.*, 1966, **21**, 115–117.
46 R. Nesper and H. G. von Schnering, *J. Solid State Chem.*, 1987, **70**, 48–57.
47 L. Lacroix-Orio, M. Tillard and C. Belin, *J. Alloys Compd.*, 2008, **465**, 47–50.
48 G. J. Miller, *Eur. J. Inorg. Chem.*, 1998, 523–536.
49 N. Kazem, W. Xie, S. Ohno, A. Zevalkink, G. J. Miller, G. J. Snyder and S. M. Kauzlarich, *Chem. Mater.*, 2014, **26**, 1393–1403.
50 J. Sangster and A. D. Pelton, *J. Phase Equilib.*, 1997, **18**, 289–294 and references therein.
51 F. Kiefer, A. J. Karttunen, M. Döblinger and T. F. Fässler, *Chem. Mater.*, 2011, **23**, 4578–4586.
52 K. Puhakainen, M. Boström, T. L. Groy and U. Häussermann, *J. Solid State Chem.*, 2010, **183**, 2528–2533.
53 Netzsch Proteus Thermal Analysis, *Version 4.8.2*, Netzsch-Gerätebau GmbH, Selb, Germany, 2006.
54 APEX suite of crystallographic software, *APEX 2 Version 2008.4*, Bruker AXS Inc., Madison, WI, USA, 2008.
55 SAINT, *Version 7.56a*, Bruker AXS Inc., Madison, WI, USA, 2008.

56 SADABS, *Version 2008/1*, Bruker AXS Inc., Madison, WI, USA, 2008.
57 H. D. Flack, *Acta Crystallogr., Sect. A: Fundam. Crystallogr.*, 1983, **39**, 876.
58 G. M. Sheldrick, *Shelxs-97 – Program for the Determination of Crystal Structures*, University of Göttingen, Göttingen, Germany, 1997.
59 G. M. Sheldrick, *Shelxl-97 – Program for Crystal Structure Refinement*, University of Göttingen, Göttingen, Germany, 1997.
60 V. Petricek, M. Dusek and L. Palatinus, *Jana 2006: The Crystallographic Computing System, Version 03/15/2013*, Institute of Physics, Praha, Czech Rupublic, 2006.

SUPPORTING INFORMATION

Structural and Thermodynamic Similarities of Phases in the Li–*Tt* (*Tt* = Si, Ge) Systems: Redetermination of the Lithium-Rich Side of the Li–Ge Phase Diagram and Crystal Structures of $Li_{17}Si_{4.0-x}Ge_x$ for x = 2.3, 3.1, 3.5, and 4 as well as $Li_{4.1}Ge$

Michael Zeilinger and Thomas F. Fässler*

Department Chemie, Technische Universität München, Lichtenbergstraße 4, 85747 Garching b. München, Germany

Details on the structure refinement of $Li_{4.096(4)}Ge$

The structure of $Li_{16.38(2)}Ge_4$ is isotypic with $Li_{4.11}Si$ ($Li_{16.42(1)}Si_4$) and the disorder model highlighted in this article corresponds to the one reported for $Li_{16.42(1)}Si_4$. Atom positions Li4A on 4*c* (½, *y*, ¼), Li4B on 8*g* (*x*, *y*, ¼), and Li5 on 8*f* (0, *x*, *y*) are affected by disorder (cf. Table 2). A free refinement of occupancy factors for Li4A and Li4B delivers values of 0.669(15) und 0.390(8). Within standard deviations (3σ), those values are in agreement with refinement results using the constraint *occ*(Li4A) + *occ*(Li4B) = 1 (0.616(8) and 0.384(8)) which excludes their simultaneous occupancy since otherwise meaningless Li–Li distances are observed.

For Li5 on 8*f* (0, *x*, *y*), a split position was introduced. The split fractions converged to 0.25(4) and 0.75(4) which is identical with results obtained from a free refinement of occupancy factors for these positions (0.74(4) and 0.25(4)). The *R*-values of the final model are R_1 = 0.023 and wR_2 = 0.027 for all data and residual electron densities are +0.69 e·Å^{-3} and −0.52 e·Å^{-3}. Ignoring the atom split, the reliability factors for all data are slightly higher (R_1 = 0.024 and wR_2 = 0.030) but significant residual electron density is almost exactly located at the former Li5B position (+1.134 e·Å^{-3}).

Regarding the relevance of the atom split for Li5, it demonstrates structural flexibility which comes along with the disorder of Li4A and Li4B. In detail, if position Li4B is occupied, a simultaneous occupancy of Li5B is excluded due to unreasonably short Li–Li distances (2.02(4) Å). In case of an occupied Li4A site, either Li5A or Li5B can be occupied (2.86(3) Å (Li4A–Li5B), 3.220(7) Å (Li4A–Li5B)).

$Li_{17}Si_{4-x}Ge_x$ [x = 2.30(2), 3.08(4), 3.53(3)]: Single Crystal X-ray diffraction and crystallographic details

The preparation of crystals from $Li_{17}Si_{4-x}Ge_x$ [x = 2.30(2), 3.08(4), 3.53(3)] exactly follows the procedure described in the main article. For $Li_{17}Si_{4-x}Ge_x$ [x = 2.30(2), 3.08(4)], single crystal diffraction data were collected at 123 K on an OXFORD XCALIBUR3 diffractometer (SAPPHIRE3 CCD detector) equipped with a graphite monochromated MoK_α radition (λ = 0.71073 Å) using the Oxford CrysAlisRED software.[1] Empirical absorption correction was carried out with the SCALE3 ABSPACK scaling algorithm as implemented in CRYSALISRED. For $Li_{17}Si_{0.47(3)}Ge_{3.53(3)}$, intensity data were collected at 123 K on a BRUKER X-ray diffractometer equipped with a CCD detector (APEX II, κ-CCD), a rotating anode (NONIUS, FR591) with MoK_α radiation (λ = 0.71073 Å) and a Montel mirror using the BRUKER APEX Software Suite.[2] Integration, data reduction and absorption correction was done with SAINT and SADABS.[3, 4]

In case of $Li_{17}Si_{0.92(4)}Ge_{3.08(4)}$, penetration twinning along [1 1 1] was detected (twin fraction 0.45). Only single reflections of the main domain were used, composite reflections from both domains were omitted. For all compounds, the space group $F\bar{4}3m$ was assigned on the basis of the systematic absences and the statistical analysis of the intensity distributions. Since $F\bar{4}3m$ is non-centrosymmetric, only identical indices were merged. Fractional atomic coordinates and atomic displacement parameters for Si/Ge mixed sites were set equal. The structures were solved with direct methods (SHELXS-97) and refined with full-matrix least squares on F^2 (SHELXL-97).[5, 6] Table S1–S4 list refinement results, fractional atomic coordinates, and isotropic equivalent atomic displacement parameters for $Li_{17}Si_{4-x}Ge_x$ [x = 2.30(2), 3.08(4), 3.53(3)].

Table S1. Crystallographic data and structure refinement for $Li_{17}Si_{4-x}Ge_x$ [x = 2.30(2), 3.08(4), 3.53(3)].

empirical formula	$Li_{17}Si_{1.70(2)}Ge_{2.30(2)}$	$Li_{17}Si_{0.92(4)}Ge_{3.08(4)}$	$Li_{17}Si_{0.47(3)}Ge_{3.53(3)}$
T / K	123(2)	123(2)	123(2)
diffractometer	Oxford Xcalibur	Oxford Xcalibur	Bruker APEX II
formula weight / g·mol^{-1}	332.69	367.44	387.34
crystal size / mm^3	0.20 × 0.20 × 0.10	0.10 × 0.10 × 0.10	0.20 × 0.20 × 0.15
crystal color	metallic silver	metallic silver	metallic silver
crystal shape	block	block	block
space group	$F\bar{4}3m$	$F\bar{4}3m$	$F\bar{4}3m$
structure type	$Li_{17}Pb_4$	$Li_{17}Pb_4$	$Li_{17}Pb_4$
unit cell dimension / Å	a = 18.7125(1)	a = 18.7515(2)	a = 18.7721(5)
V / Å^3	6552.33(6)	6593.4(1)	6615.1(3)
Z	20	20	20
ρ (calc.) / (g·cm^{-3})	1.686	1.851	1.945
μ / mm^{-1}	5.354	6.995	7.928
F (000)	2968	3249	3410
θ - range / °	3.61–30.45	3.07–30.00	2.17–30.03
index range hkl	$-26 \le h \le +14$, $-26 \le k \le +26$, $-26 \le l \le +26$	$-26 \le h \le +25$, $-26 \le k \le +26$, $-26 \le l \le +26$	$-26 \le h \le +18$, $-26 \le k \le +19$, $-24 \le l \le +22$
reflections collected	31663	26446	19618
independent reflections	1035 (R_{int} = 0.032)	952 (R_{int} = 0.061)	1019 (R_{int} = 0.041)
reflections with $I > 2\sigma(I)$	991 (R_σ = 0.010)	880 (R_σ = 0.021)	1016 (R_σ = 0.015)
data/restraints/parameter	1035/0/72	952/0/72	1019/0/72
absorption correction	multi-scan	multi-scan	multi-scan
goodness-of-fit on F^2	1.260	1.000	1.202
Final R indices [$I > 2\sigma(I)$][a, b]	R_1 = 0.016	R_1 = 0.022	R_1 = 0.014
	wR_2 = 0.036	wR_2 = 0.047	wR_2 = 0.036
R indices (all data)[a, b]	R_1 = 0.017	R_1 = 0.025	R_1 = 0.014
	wR_2 = 0.036	wR_2 = 0.048	wR_2 = 0.037
extinction coefficient	4.4(3)×10^{-4}	2.4(3)×10^{-4}	0.9(1)×10^{-4}
Flack parameter	0.42(3)	0.54(5)	0.54(3)
Largest diff. peak and hole / e·Å^{-3}	0.45 and −0.28	0.32 and −0.26	0.28 and −0.37

[a] $R_1 = \sum \big| |F_o| - |F_c| \big| / \sum |F_o|$

[b] $wR_2 = [\sum w(F_o^2 - F_c^2)^2 / \sum w(F_o^2)^2]^{1/2}$

Table S2. Fractional atomic coordinates and isotropic equivalent atomic displacement parameters for $Li_{17}Si_{1.70(2)}Ge_{2.30(2)}$ ($F\bar{4}3m$, $Z = 20$, $T = 123$ K, estimated standard deviations in parentheses).

Atom	Wyckoff position	*x*	*y*	*z*	U_{eq} / ($Å^2 \cdot 10^{-3}$)	*s.o.f.*
Si/Ge1	16*e*	0.15972(2)	*x*	*x*	7.2(2)	0.41(1) / 0.59(1)
Si/Ge2	16*e*	0.91675(2)	*x*	*x*	6.6(2)	0.522(9) / 0.478(9)
Si/Ge3	24*f*	0.32154(3)	0	0	7.6(2)	0.39(1) / 0.61(1)
Si/Ge4	24*g*	0.57001(3)	¼	¼	7.8(1)	0.40(1) / 0.60(1)
Li1	16*e*	0.0743(3)	*x*	*x*	16(2)	1
Li2	16*e*	0.3027(2)	*x*	*x*	11(1)	1
Li3	16*e*	0.4187(3)	*x*	*x*	12(1)	1
Li4	16*e*	0.5573(2)	*x*	*x*	12(1)	1
Li5	16*e*	0.6882(2)	*x*	*x*	15(1)	1
Li6	16*e*	0.8325(2)	*x*	*x*	19(2)	1
Li7	24*f*	0.1686(4)	0	0	19(2)	1
Li8	24*g*	0.0746(3)	¼	¼	10(2)	1
Li9	48*h*	0.0909(2)	*x*	0.2625(3)	19(1)	1
Li10	48*h*	0.0907(2)	*x*	0.7609(3)	21(1)	1
Li11	48*h*	0.1550(2)	*x*	0.5211(2)	21(1)	1
Li12	48*h*	0.1632(2)	*x*	0.0026(3)	12(1)	1
Li13	4*a*	0	0	0	13(3)	1

Table S3. Fractional atomic coordinates and isotropic equivalent atomic displacement parameters for $Li_{17}Si_{0.92(4)}Ge_{3.08(4)}$ ($F\bar{4}3m$, $Z = 20$, $T = 123$ K, estimated standard deviations in parentheses).

Atom	Wyckoff position	*x*	*y*	*z*	U_{eq} / ($Å^2 \cdot 10^{-3}$)	*s.o.f.*
Si/Ge1	16*e*	0.15999(3)	*x*	*x*	9.5(2)	0.22(2) / 0.78(2)
Si/Ge2	16*e*	0.91708(3)	*x*	*x*	8.6(2)	0.30(2) / 0.70(2)
Si/Ge3	24*f*	0.32192(4)	0	0	9.6(2)	0.22(2) / 0.78(2)
Si/Ge4	24*g*	0.56959(4)	¼	¼	10.8(2)	0.21(2) / 0.79(2)
Li1	16*e*	0.0732(5)	*x*	*x*	29(4)	1
Li2	16*e*	0.3019(3)	*x*	*x*	17(2)	1
Li3	16*e*	0.4186(5)	*x*	*x*	20(3)	1
Li4	16*e*	0.5578(3)	*x*	*x*	16(2)	1
Li5	16*e*	0.6893(4)	*x*	*x*	20(3)	1
Li6	16*e*	0.8329(5)	*x*	*x*	45(5)	1
Li7	24*f*	0.1694(7)	0	0	27(5)	1
Li8	24*g*	0.0755(6)	¼	¼	12(4)	1
Li9	48*h*	0.0910(4)	*x*	0.2622(4)	22(2)	1
Li10	48*h*	0.0919(5)	*x*	0.7631(6)	41(3)	1
Li11	48*h*	0.1553(3	*x*	0.5218(4)	23(2)	1
Li12	48*h*	0.1636(3)	*x*	0.0031(5)	15(2)	1
Li13	4*a*	0	0	0	17(6)	1

Table S4. Fractional atomic coordinates and isotropic equivalent atomic displacement parameters for $Li_{17}Si_{0.47(3)}Ge_{3.53(3)}$ ($F\bar{4}3m$, $Z = 20$, $T = 123$ K, estimated standard deviations in parentheses).

Atom	Wyckoff position	*x*	*y*	*z*	U_{eq} / ($Å^2 \cdot 10^{-3}$)	*s.o.f.*
Si/Ge1	16*e*	0.15962(1)	*x*	*x*	7.5(1)	0.10(1) / 0.90(1)
Si/Ge2	16*e*	0.91657(1)	*x*	*x*	6.2(1)	0.18(1) / 0.82(1)
Si/Ge3	24*f*	0.32124(2)	0	0	7.3(1)	0.10(1) / 0.90(1)
Si/Ge4	24*g*	0.57034(2)	¼	¼	7.3(1)	0.11(1) / 0.89(1)
Li1	16*e*	0.0740(3)	*x*	*x*	20(2)	1
Li2	16*e*	0.3028(2)	*x*	*x*	14(1)	1
Li3	16*e*	0.4179(3)	*x*	*x*	14(2)	1
Li4	16*e*	0.5573(2)	*x*	*x*	14(1)	1
Li5	16*e*	0.6872(2)	*x*	*x*	15(1)	1
Li6	16*e*	0.8317(2)	*x*	*x*	18(2)	1
Li7	24*f*	0.1672(4)	0	0	19(2)	1
Li8	24*g*	0.0747(3)	¼	¼	12(2)	1
Li9	48*h*	0.0908(2)	*x*	0.2622(3)	22(1)	1
Li10	48*h*	0.0900(2)	*x*	0.7614(3)	18(1)	1
Li11	48*h*	0.1553(2)	*x*	0.5197(2)	17.1(9)	1
Li12	48*h*	0.1633(2)	*x*	0.0018(3)	14(1)	1
Li13	4*a*	0	0	0	8(3)	1

Table S5.[8] Comparison of experimental and computational relaxed fractional atomic coordinates for $Li_{21}Si_5$[7, 8] ($a_{exp.}$ = 18.710(2) Å (T = 298 K), $a_{calc.}$ = 18.55411 Å, $F\bar{4}3m$, Z = 16) and $Li_{17}Si_4$[8] ($a_{exp.}$ = 18.6563(2) Å (T = 123 K) and $a_{calc..}$ = 18.57319 Å, $F\bar{4}3m$, Z = 20). Estimated standard deviations are given in parentheses; most differing Li1 is marked in bold.

Atom	Wyck. pos.	x ($Li_{21}Si_5$)	x ($Li_{21}Si_5$ calc.)	z ($Li_{21}Si_5$)	z ($Li_{21}Si_5$ calc.)	x ($Li_{17}Si_4$)	x ($Li_{17}Si_4$ calc.)	z ($Li_{17}Si_4$)	z ($Li_{17}Si_4$ calc.)
*Tt*1	16*e*	0.1595(2)	0.1605	*x*	*x*	0.15976(1)	0.1600	*x*	*x*
*Tt*2	16*e*	0.9175(2)	0.9149	*x*	*x*	0.91660(1)	0.9167	*x*	*x*
*Tt*3	24*f*	0.3220(3)	0.3219	0	0	0.32133(1)	0.3215	0	0
*Tt*4	24*g*	0.5691(3)	0.5700	¼	¼	0.57031(1)	0.5708	¼	¼
Li1	16*e*	**0.071(2)**	**0.0553**	*x*	*x*	**0.07410(6)**	**0.0750**	*x*	*x*
Li2	16*e*	0.304(1)	0.3027	*x*	*x*	0.30284(5)	0.3031	*x*	*x*
Li3	16*e*	0.417(1)	0.4189	*x*	*x*	0.41794(7)	0.4180	*x*	*x*
Li4	16*e*	0.559(2)	0.5572	*x*	*x*	0.55713(5)	0.5572	*x*	*x*
Li5	16*e*	0.688(2)	0.6862	*x*	*x*	0.68687(5)	0.6867	*x*	*x*
Li6	16*e*	0.829(1)	0.8301	*x*	*x*	0.83168(6)	0.8311	*x*	*x*
Li7	24*f*	0.174(2)	0.1725	0	0	0.16807(8)	0.1691	0	0
Li8	24*g*	0.073(2)	0.0747	¼	¼	0.07492(9)	0.0750	¼	¼
Li9	48*h*	0.092(1)	0.0910	0.262(1)	0.2630	0.09068(4)	0.0907	0.26186(6)	0.2616
Li10	48*h*	0.088(1)	0.0905	0.761(1)	0.7616	0.09013(5)	0.0900	0.76176(6)	0.7604
Li11	48*h*	0.153(1)	0.1550	0.521(1)	0.5203	0.15503(4)	0.1551	0.51978(6)	0.5193
Li12	48*h*	0.164(1)	0.1607	0.000(1)	0.0068	0.16327(4)	0.1635	0.00286(7)	0.0029
Li13	4*a*	-	-	-	-	0	0	0	0

Table S6. Comparison of experimental fractional atomic coordinates for $Li_{17}Si_4$[8] (a = 18.6563(2) Å, T = 123 K), $Li_{17}Ge_4$ (a = 18.8521(3) Å, T = 298 K), $Li_{17-\varepsilon}Zn_\varepsilon Ge_4$[9] ($a$ = 18.842(1) Å, T = 173 K), and $Li_{16.95}Ge_4$[10] (a = 18.756(2) Å, T = 160 K; space group $F\bar{4}3m$, Z = 20). Estimated standard deviations are given in parentheses.

Atom	Wyck. pos.	x ($Li_{17}Si_4$)	x ($Li_{17}Ge_4$)	x ($Li_{17-\varepsilon}Zn_\varepsilon Ge_4$)	x ($Li_{16.95}Ge_4$)	z ($Li_{17}Si_4$)	z ($Li_{17}Ge_4$)	z ($Li_{17-\varepsilon}Zn_\varepsilon Ge_4$)	z ($Li_{16.95}Ge_4$)
*Tt*1	16*e*	0.15976(1)	0.15955(1)	0.15958(2)	0.15952(5)	*x*	*x*	*x*	*x*
*Tt*2	16*e*	0.91660(1)	0.91657(1)	0.91667(3)	0.91684(5)	*x*	*x*	*x*	*x*
*Tt*3	24*f*	0.32133(1)	0.32102(1)	0.32118(4)	0.32112(7)	0	0	0	0
*Tt*4	24*g*	0.57031(1)	0.57015(1)	0.57020(4)	0.56965(7)	¼	¼	¼	¼
Li1A	16*e*	0.07410(6)	0.0734(2)	0.0747(6)	0.0775	*x*	*x*	*x*	*x*
Li1B	16*e*	-	-	-	0.0587	-	-	-	*x*
Li2	16*e*	0.30284(5)	0.3031(2)	0.3033(3)	0.3032(6)	*x*	*x*	*x*	*x*
Li3	16*e*	0.41794(7)	0.4175(2)	0.4179(5)	0.4169(9)	*x*	*x*	*x*	*x*
Li4	16*e*	0.55713(5)	0.5575(2)	0.5584(4)	0.5579(6)	*x*	*x*	*x*	*x*
Li5	16*e*	0.68687(5)	0.6877(2)	0.6864(4)	0.6876(7)	*x*	*x*	*x*	*x*
Li6	16*e*	0.83168(6)	0.8314(2)	0.8331(4)	0.8329(7)	*x*	*x*	*x*	*x*
Li7	24*f*	0.16807(8)	0.1677(3)	0.1678(6)	0.170(1)	0	0	0	0
Li8	24*g*	0.07492(9)	0.0743(3)	0.0740(6)	0.075(1)	¼	¼	¼	¼
Li9	48*h*	0.09068(4)	0.0913(2)	0.0906(3)	0.0907(7)	0.26186(6)	0.2624(2)	0.2631(4)	0.2660(8)
Li10	48*h*	0.09013(5)	0.0896(2)	0.0904(4)	0.0914(7)	0.76176(6)	0.7612(2)	0.7613(4)	0.7597(9)
Li11	48*h*	0.15503(4)	0.1547(1)	0.1554(3)	0.1540(5)	0.51978(6)	0.5205(2)	0.5216(4)	0.5216(9)
Li12	48*h*	0.16327(4)	0.1637(1)	0.1632(3)	0.1625(5)	0.00286(7)	0.0027(2)	0.0025(5)	0.005(1)
Li13	4*a*	0	0	0	0	0	0	0	0
Zn1	4*a*	-	-	0	-	-	-	0	-

Table S7. Comparison of experimental fractional atomic coordinates for $Li_{16.95}Ge_4$[10] (a = 18.756(2) Å, T = 160 K; space group $F\bar{4}3m$, Z = 20) and computational relaxed ones for $Li_{21}Si_5$[8] ($a_{calc.}$ = 18.55411 Å, $F\bar{4}3m$, Z = 16). Estimated standard deviations are given in parentheses.

Atom	Wyck. pos.	x ($Li_{16.95}Ge_4$)	x ($Li_{21}Si_5$ calc.)	z ($Li_{16.95}Ge_4$)	z ($Li_{21}Si_5$ calc.)
*Tt*1	16*e*	0.15952(5)	0.1605	*x*	*x*
*Tt*2	16*e*	0.91684(5)	0.9149	*x*	*x*
*Tt*3	24*f*	0.32112(7)	0.3219	0	0
*Tt*4	24*g*	0.56965(7)	0.5700	¼	¼
Li1A	16*e*	0.0775	0.0553	*x*	*x*
Li1B	16*e*	0.0587	-	*x*	-
Li2	16*e*	0.3032(6)	0.3027	*x*	*x*
Li3	16*e*	0.4169(9)	0.4189	*x*	*x*
Li4	16*e*	0.5579(6)	0.5572	*x*	*x*
Li5	16*e*	0.6876(7)	0.6862	*x*	*x*
Li6	16*e*	0.8329(7)	0.8301	*x*	0
Li7	24*f*	0.1697(12)	0.1725	0	0
Li8	24*g*	0.0752(12)	0.0747	¼	¼
Li9	48*h*	0.0907(7)	0.0910	0.2660(8)	0.2630
Li10	48*h*	0.0914(7)	0.0905	0.7597(9)	0.7616
Li11	48*h*	0.1540(5)	0.1550	0.5216(9)	0.5203
Li12	48*h*	0.1625(5)	0.1607	0.005(1)	0.0068
Li13	4*a*	0	-	0	-

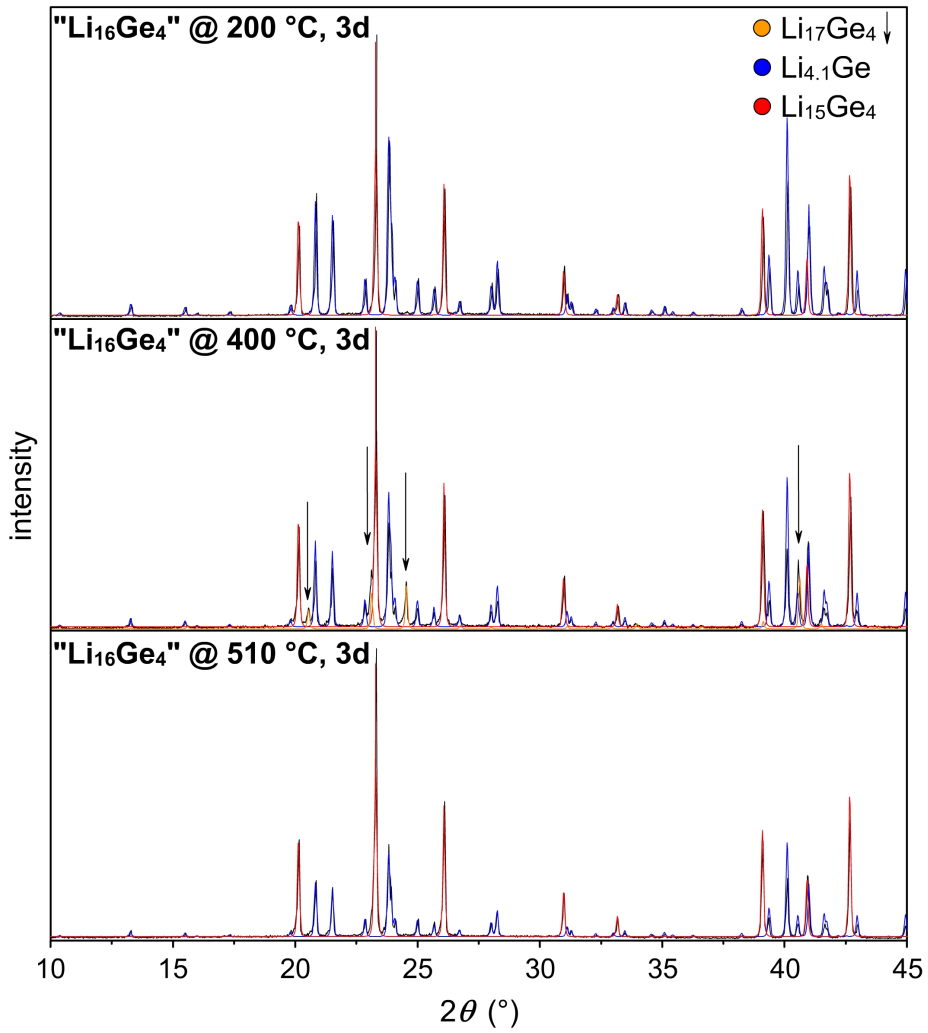

Figure S1. PXRD patterns of "$Li_{16}Ge_4$" samples annealed at 200, 400 and 510 °C in tantalum ampules for three days followed by quenching in water (experimental = black, $Li_{17}Ge_4$ (calc.) = yellow, $Li_{4.10}Ge$ (calc.) = blue, $Li_{15}Ge_4$ (calc.) = red).

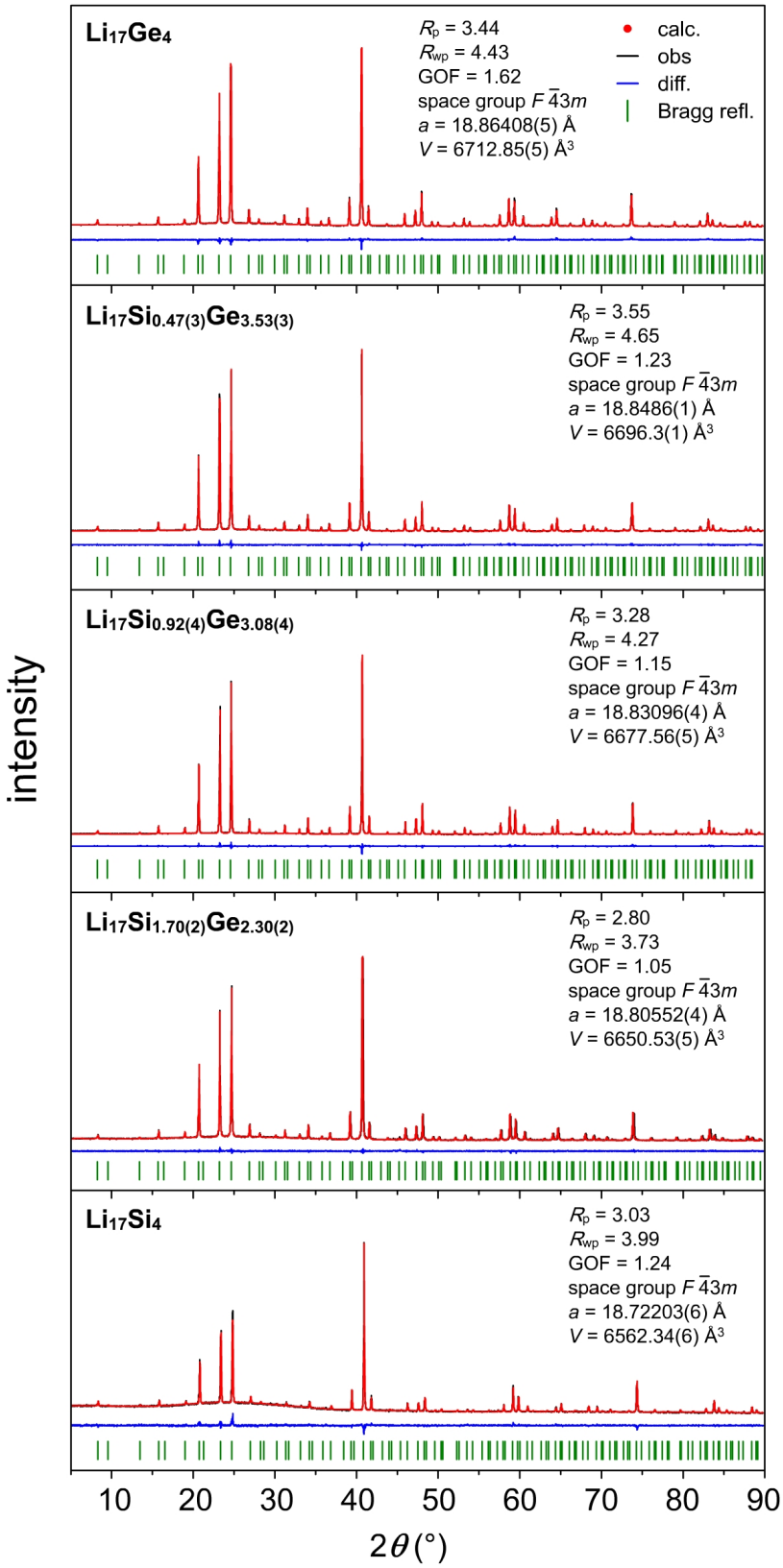

Figure S2. Rietveld[11] fits of the $Li_{17}Si_4$ model to PXRD patterns of ground single crystals of $Li_{17}Si_{4-x}Ge_x$ (x = 0, 2.30(2), 3.08(4), 3.53(3), 4).

REFERENCES

1. CrysalisRED, Version 1.171.33.34d; Oxford Diffraction, UK, 2009.
2. APEX suite of crystallographic software, APEX 2 Version 2008.4, Bruker AXS Inc., Madison, WI, USA, 2008.
3. SAINT, Version 7.56a, Bruker AXS Inc., Madison, WI, USA, 2008.
4. SADABS, Version 2008/1, Bruker AXS Inc., Madison, WI, USA, 2008.
5. G. M. Sheldrick, Shelxs-97 — Program for the Determination of Crystal Structures, University of Göttingen, Göttingen, Germany, 1997.
6. G. M. Sheldrick, Shelxl-97 — Program for Crystal Structure Refinement, University of Göttingen, Göttingen, Germany, 1997.
7. R. Nesper and H. G. von Schnering, *J. Solid State Chem.*, 1987, **70**, 48–57.
8. M. Zeilinger, D. Benson, U. Häussermann and T. F. Fässler, *Chem. Mater.*, 2013, **25**, 1960–1967.
9. L. Lacroix-Orio, M. Tillard and C. Belin, *J. Alloys Compd.*, 2008, **465**, 47–50.
10. G. R. Goward, N. J. Taylor, D. C. S. Souza and L. F. Nazar, *J. Alloys Compd.*, 2001, **329**, 82–91.
11. TOPAS — Rietveld Software, Version 4.0; Bruker AXS Inc., Madison, WI, USA, 2009.

5.6 Allotropism of Silicon: An Experimental Approach toward Amorphous Si and *a-allo*-Si Based on $Li_{15}Si_4$ and Li_3NaSi_6 as well as Theoretical Models for *allo*-Si

Zeilinger, M.; Jantke, L. A.; Scherf, L. M.; Kiefer, F. J.; Konar, S.; Kienle, L.; Karttunen, A. J.; Häussermann, U; Fässler, T. F. *manuscript for publication*.

KEYWORDS

Amorphous silicon, *a*-Si, *allo*-Si, *a-allo*-Si, silicon allotropes, silicon polymorphs, *allo*-Si structure models

ABSTRACT

A versatile chemical synthesis of amorphous silicon (*a*-Si) starting from $Li_{15}Si_4$ powder which is easily accessible through high-energetic ball-milling is presented. Using a custom-built extractor, lithium can be extracted from $Li_{15}Si_4$ through liquid ammonia. After a subsequent aqueous treatment of the intermediate, a mixture of *a*-Si and $LiNH_2$, *a*-Si is retained as a black powder. *a*-Si samples were characterized by powder X-ray diffraction, infrared, Raman, photoluminescence, atomic absorption and energy dispersive X-ray spectroscopy, transmission electron microscopy, selected area electron diffraction as well as differential thermal analysis. Those characterization methods revealed the presence of micro- and nanosized particles, a slight surface oxidation after aqueous treatment, an amorphous-to-crystalline phase transition at around 658 °C and conclusive evidence for the amorphous nature of the samples. Further, we focused on the synthesis of *allo*-Si, a silicon allotrope described in the 1980's which can be obtained through oxidation of the phase Li_3NaSi_6. Previous results from powder X-ray diffraction experiments could not be confirmed and were shown to be ambiguous. Instead, depending on the crystallinity of the precursor, Li_3NaSi_6 undergoes a partial or full amorphization after treatment with protic solvents. The reaction yields amorphous silicon which differs from ordinary *a*-Si regarding the amorphous-to-crystalline transformation temperature ranging from 490 to 570 °C. However, the different phase transition temperatures of *a*-Si and *a-allo*-Si are attributable to the large concentration of *α*-Si crystallites (crystallization nuclei) in *a-allo*-Si samples. Conclusive characteristics that would allow an unambiguous differentiation between *a-allo*-Si and *a*-Si were not found. There are also strong indications that the XRD reflections reported earlier for *allo*-Si (ICSD-41-1111) are identical to those of $NbSi_2$. Therefore the results cast doubts on the existence of the silicon polymorph *allo*-Si. Besides, quantum chemical calculations confirm that upon oxidation Li_3NaSi_6 does not behave analogously to Li_7Ge_{12} which is topotactically converted to *m-allo*-Ge. Furthermore, the previously published **TON** zeolite-type structure (ZSM-22) was found to be a product of a full structural relaxation starting from the Si substructure of Li_3NaSi_6.

1. Introduction

Exploring new allotropes of elements has been a challenging and intriguing field of research ever since. In particular, the variety of properties of a single element that arises from different structures are fascinating, such as the carbon allotropes graphite and diamond, the former a conductive soft material being used as electrode and lubricant and the latter an insulator and one of the hardest known materials. In general, the chemistry of group 14 elements, primarily silicon and germanium, was fueled by the demand for more efficient solar cells, thermoelectric and superconducting materials or high-capacity lithium-ion batteries.

In this field a few crystalline phases, amorphous materials and most notably new allotropes of germanium and silicon have been characterized. In particular, amorphous silicon (*a*-Si) is widely used in thin film transistors and regarded as material for future photovoltaic applications, exploiting its higher optical absorption coefficient for visible light than that of crystalline silicon (*c*-Si).[1,2] In 2005, McMillan et al.[3] reported on a solid state synthesis route for bulk samples of amorphous and nanocrystalline silicon or germanium. A solid state metathesis reaction (SSM) between NaSi and NH_4Cl at 200–300 °C is used to produce *a*-Si beside NaBr, NH_3, and H_2. NaBr is subsequently removed by washing with water. Recently, this method was taken on by Wang et al.[4] to synthesize P-doped amorphous and nanocrystalline silicon. Furthermore, bulk amorphous silicon can also be obtained from crystalline Li–Si phases like $Li_{15}Si_4$ if those are electrochemically delithiated.[5]

Lastly, the discovery of novel allotropic forms of germanium and silicon decisively influenced numerous work in the field of semiconducting materials. Examples of crystalline materials are the clathrate-II-type porous structure Ge-*cF*136,[6] hexagonal Ge (4*H*-Ge),[7,8] and *allo*-Ge/*m*-*allo*-Ge.[7,9] Also mesoporous Ge-based materials have been reported.[10-13] In the case of silicon, the polymorph *allo*-Si was described briefly.[14,15] *allo*-Si/*allo*-Ge have attracted our attention since until lately none of these modifications have been unambiguously and resolutely characterized regarding their structures. The reasons for that can primarily be ascribed to their synthesis. *m*-*allo*-Ge[9] is obtained by mild oxidation of Li_7Ge_{12},[7,16] a phase that consists of two-dimensional polyanionic slabs $^2_\infty[Ge_{12}]^{7-}$ which are separated by Li atoms (Figure 1a). After reaction with protic solvents, interstitial Li is deintercalated and the topology of those layers is retained under interlayer Ge–Ge bond formation. Turning to Si, *allo*-Si can be synthesized analogously from Li_3NaSi_6.[14,15] Similarly to Li_7Ge_{12}, Li_3NaSi_6 possesses polyanionic layers $^2_\infty[Si_6]^{4-}$ which are separated from each other by Li and Na atoms (Figure 1b).

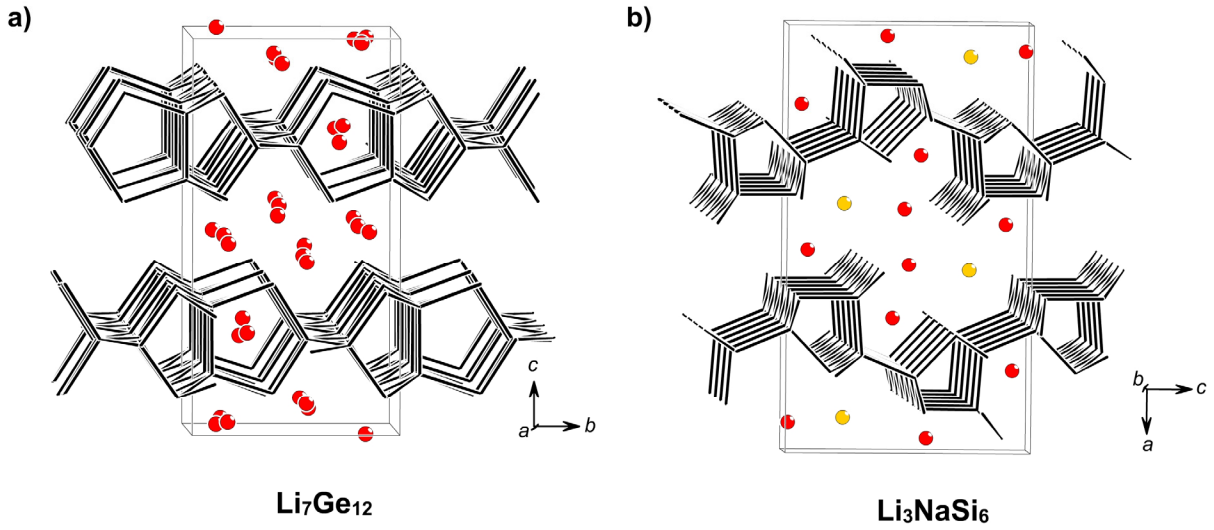

Figure 1. Structures of a) Li_7Ge_{12} and b) Li_3NaSi_6 revealing $^2_\infty[Ge_{12}]^{7-}$ and $^2_\infty[Si_6]^{4-}$ layers (black), respectively, that are separated by Li (red) and Na (yellow) atoms.

In the synthesis of both allotropes, *m*icrocrystalline (*m-allo*-Ge) or poorly crystalline/heavily disordered samples (*allo*-Si) are afforded that do not allow a comprehensive structure determination by single crystal X-ray diffraction.[7,14,15] Yet, just recently the structure model for *m-allo*-Ge could be improved significantly by a combination of selected area electron diffraction (SAED), powder X-ray diffraction (PXRD), quantum chemical calculations and simulated powder X-ray diffraction patterns,[9] whereas the structure of *allo*-Si is still completely unknown.[14,15] Employing theoretical means, structure models for *allo*-Si and several silicon allotropes were predicted.[17-25]

Herein, we present an alternative route for bulk amorphous silicon starting from $Li_{15}Si_4$ which is easily accessible through high-energetic ball-milling. A custom-built apparatus is used to extract Li from $Li_{15}Si_4$ powder with liquid ammonia. *a*-Si is obtained after subsequent aqueous treatment of the *a*-Si/$LiNH_2$ intermediate. The reproduction of the previously reported formation of *allo*-Si by the treatment of Li_3NaSi_6 with protic solvents also leads to an *a*morphous phase which we named accordingly (*a-allo*-Si). However, a careful analysis of its synthesis reveals strong indications that the reported Bragg reflections of *allo*-Si (ICSD 41-1111) originated from $NbSi_2$ which most probably was formed in small amounts during the synthesis of Li_3NaSi_6 in Nb ampules. Although the thermal behavior of *a*-Si considerably differs from that of *a-allo*-Si, conclusive evidence for the existence of *allo*-Si according to reports in literature could not be found. In addition, the difficulties to obtain crystalline samples of *allo*-Si were explained by quantum chemical calculations.

2. Experimental Section

Synthesis. Starting materials were Li rods (99%, Rockwood-Lithium), Na rods (99%, Chempur) and Si powder (99.999%, Sigma Aldrich). All steps for solid state synthesis and preparation of air and moisture sensitive samples were carried out in a glove box (MBraun, Ar-atmosphere, H_2O and O_2 levels < 0.1 ppm). Ta ampules were thoroughly cleaned, heated to 1000 °C under dynamic vacuum ($p < 1\times10^{-3}$ mbar) for at least 2 h and transferred to the glove box. Heating and handling under inert conditions was done using an all-glass Schlenk line supplied with Ar which is dried over P_2O_5, molecular sieve and heated titanium sponge (T = 750 °C).

$Li_{12}Si_7$, NaSi, $Li_{15}Si_4$ and Li_3NaSi_6. The binary precursors $Li_{12}Si_7$ and NaSi were synthesized from stoichiometric mixtures of the elements with a total mass of 2.0 g each. The reactions were carried out in Ta ampules which were encapsulated in silica jackets under vacuum. Sample annealing was carried out in a muffle furnace. In case of $Li_{12}Si_7$, the temperature was raised to 750 °C at 5 K·min^{-1}, followed by one hour dwelling, cooling to 400 °C at a rate of 0.5 K·min^{-1}, dwelling for six hours and subsequent quenching. For NaSi, the temperature was raised stepwise to 600 °C (5 K·min^{-1} to 500 °C, one hour dwelling, 5 K·min^{-1} to 600 °C). After a dwell time of 30 hours a cooling rate of 5 K·min^{-1} was applied. Samples were recovered inside the glove box.

Li_3NaSi_6 was subsequently synthesized from a 1:4:13 molar mixture of $Li_{12}Si_7$, NaSi (Figure S1), and α-Si (cf. Scheme 1) with a total mass of 0.5 g. Reactants were thoroughly homogenized in an agate mortar, pressed to a pellet and sealed in a Ta ampule which was then encapsulated in a silica jacket under vacuum.

$$Li_{12}Si_7 + 4\ NaSi + 13\ Si \longrightarrow 4\ Li_3NaSi_6$$

Scheme 1. Peritectoid reaction of $Li_{12}Si_7$, NaSi and α-Si yielding pure-phase Li_3NaSi_6.

The ampule was annealed in a muffle furnace applying a heating rate of 5 K·min^{-1} to a target temperature of 550 °C, allowing a dwell time of one day. After a slow cooling at 0.075 K·min^{-1} the pure-phase sample is recovered inside the glove box. A sample of Li_3NaSi_6 containing a marginal α-Si impurity was synthesized from a 1:5:26 molar mixture of $Li_{15}Si_4$, Na, and α-Si with a total mass of 2.0 g (Figure S7a). The reactants were homogenized by ball-milling in a stainless steel jar using a RETSCH PM 100 planetary ball mill (duration: 70 min, 250 rpm, ball charge: 3, ball size: 15 mm diameter) and subsequently sealed in a Ta ampule which was encapsulated in a silica jacket under vacuum thereafter. Annealing was carried out in a muffle furnace as follows: 4 K·min^{-1} to 600 °C, seven days dwelling, cooling to room

temperature at a rate of 0.075 $K \cdot min^{-1}$. The synthesis of $Li_{15}Si_4$ bulk material by ball-milling of a stoichiometric mixture of Li and Si using a RETSCH PM 100 planetary ball mill follows the description in ref. 26.

All synthesized samples were ground in agate mortars and analyzed by powder X-ray diffraction. The PXRD patterns in Figure S1, S2 and 3a correspond to pure-phase $Li_{12}Si_7$, NaSi, Li_3NaSi_6, and $Li_{15}Si_4$, respectively. A reaction of Si with the ampule material forming $TaSi_2$ was circumvented by comparatively low reaction temperatures and short reaction times.

***a*-Si.** 0.5 g of $Li_{15}Si_4$ were loaded into a custom-built extractor for liquid ammonia (Figure 2). Using liquid ammonia (WESTFALEN AG; dried over Na), Li was extracted from $Li_{15}Si_4$ under inert conditions at a special high-vacuum glass line which is supplied with purified Ar (see above). The extraction process was stopped after the color of the liquid ammonia solution had turned from deep to light blue after approximately 40 extraction cycles. After evaporating ammonia from the extractor, the solid black product consisting of *a*-Si and $LiNH_2$ (Scheme 2) was recovered in the glove box.

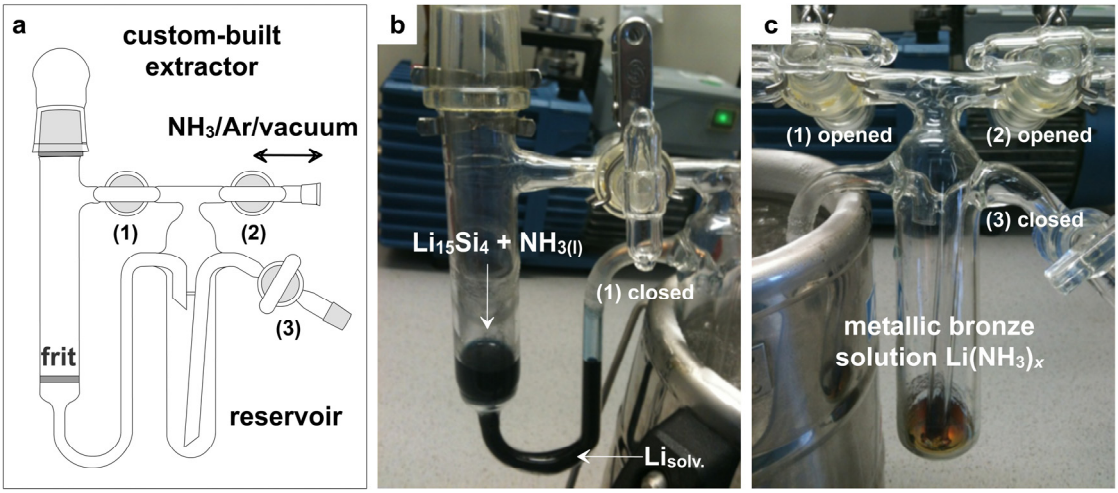

Figure 2. Custom-built apparatus (a) for extracting Li from $Li_{15}Si_4$ with liquid NH_3. $Li_{15}Si_4$ powder is loaded onto the frit inside the glove box. If NH_3 is condensed onto it (sample space is cooled, –78 °C), a deep blue color is observed. Closing valve (1) and cooling the reservoir (b), the extract is transported therein. By opening valve (1) and cooling the sample space, NH_3 can be recondensed onto the solid (c). Thereafter, Li/$LiNH_2$ remains in the reservoir (c). The color is characteristic for a concentrated metallic bronze solution of Li in NH_3 denoted as $Li(NH_3)_x$.[27]

To produce amorphous silicon (*a*-Si), 140 mg of the intermediate (*a*-Si/$LiNH_2$ mixture), were filled into a Schlenk flask. Subsequently, 40 ml of ethanol (dried over Na and distilled) were added and stirred shortly. Afterwards the black suspension (pH > 10) is handled under air and transferred into an Erlenmeyer flask where 200 ml of an 1:1 ethanol-water mixture (V/V) and few milliliters of acetic acid were added to adjust the pH-value (pH ~ 5). After 5 min of

stirring a black solid was separated via centrifugation, washed with 20 ml ethanol three times and finally dried under vacuum for several hours. This procedure yielded 30–40 mg of a black amorphous product.

$$Li_{15}Si_4 \xrightarrow{NH_{3\,(l)}} 15\,(1-x)\,Li_{NH3} + 4\,a\text{-Si} + 15\,x\,LiNH_2 + 7.5\,x\,H_2$$

Scheme 2. Reaction equation for the synthesis of *a*-Si starting from $Li_{15}Si_4$.

The O content of large sample areas was determined as 11.77 ± 1.87 at.% (EDX, cf. Figure S5). Furthermore, traces of Na (< 1 at.%) were detected. The residual Li content in *a*-Si was determined by AAS and amounts to ~1 wt.%, whereas the *a*-Si/$LiNH_2$ intermediate contained 21.9(1) wt.% of Li (48.1 wt.% Li in $Li_{15}Si_4$). C–H–N impurities of *a*-Si samples are marginal (C, H, N < 1.2 wt.%).

***a-allo*-Si (*a*morphous *allo*-Si).** Fully oxidized samples of Li_3NaSi_6 could be obtained by the following procedure: i) ball-milling 400 mg pure-phase Li_3NaSi_6 in a hermetically sealed stainless steel jar (RETSCH PM 100 planetary ball; duration: 8 hours, 300 rpm, ball charge: 3, ball size: 15 mm diameter), ii) reacting 135 mg of ball-milled Li_3NaSi_6 with 30 ml ethanol (Scheme 3) under inert conditions and adding 4 ml concentrated HCl solution subsequently, iii) separating the black solid by centrifugation, iv) washing the product repeatedly (3–4 times) with 30 ml of a 1:1 ethanol-water mixture (V/V) each and drying it under vacuum.

$$Li_3NaSi_6 + 4\,ROH \longrightarrow 6\,a\text{-}allo\text{-Si} + 2\,H_2 + 3\,LiOR + NaOR$$

Scheme 3. Reaction of Li_3NaSi_6 with protic solvents.

Powder X-Ray Diffraction (PXRD). PXRD patterns were recorded on a STOE STADI P diffractometer (Ge(111) monochromator for Cu$K_{\alpha1}$ radiation, λ = 1.54056 Å) equipped with a DECTRIS MYTHEN DCS 1K solid state detector. Samples were ground, sealed inside 0.3 mm glass capillaries and measurements performed in a 2θ range of 5–90° (PSD steps: 0.06–1.00°; time/step: 10–40 s). Rietveld refinements were carried out with the TOPAS 4.0 software.[28]

Differential Thermal Analysis (DTA). Differential thermal analysis was performed with a NETZSCH DSC 404 Pegasus apparatus equipped with a DTA carrier system. Custom-built Nb crucibles were thoroughly cleaned, heated to 1000 °C under dynamic vacuum ($p < 1\times10^{-3}$ mbar) for 2 h and transferred to an Ar-filled glove box. Crucibles were loaded with 20–30 mg of sample. The open end was roughly closed by crimping and then sealed by arc-welding inside the glove box under cooling. A sealed Nb crucible without sample served as

reference. All measurements were performed under an Ar-flow of 60–70 mL·min^{-1} and a heating/cooling rate of 10 K·min^{-1}. Samples were recovered after the measurement by opening the Nb crucibles inside the glove box. Data was handled with the PROTEUS THERMAL ANALYSIS program.[29]

Transmission Electron Microscopy (TEM). Transmission electron microscopy and selected-area electron diffraction (SAED) were performed with a PHILIPS CM30ST microscope (300 kV, LaB_6 cathode, C_s = 1.15 mm) which is equipped with a multiscan CCD camera (GATAN). EDX analysis as part of the TEM examinations were carried out using a NORAN VOYAGER EDX system. A sample of *a*-Si was suspended in *n*-butanol and subsequently coated on a perforated carbon/copper net. All images were evaluated (including Fourier filtering) with the program DIGITAL MICROGRAPH 3.6.1 (GATAN).

Infrared (IR) and Raman Spectroscopy. ATR-FT-IR spectra were recorded on a VARIAN 670 IR FT-IR spectrometer equipped with a PIKE GLADIATR ATR stage. The VARIAN RESOLUTION PRO software was used for data handling.[30] Raman spectra for *a*-Si and *a-allo*-Si were measured using a LABRAM HR 800 spectrometer. The instrument is equipped with an 800 mm focal length spectrograph and an air cooled (–70 °C), back thinned CCD detector. Samples were sealed in 0.7 mm glass capillaries. The capillaries were placed on a glass slide and samples were excited with an air cooled double frequency Nd:YAG laser (532 nm). The laser was focused onto the sample using a 50X super long working distance (WD = 20.5 mm) MITUTOYO objective. The laser power was adjusted by a software controlled filter wheel with 6 ND filters. Spectra were collected with an exposure time of 60 s (10 accumulations) and using a grating of 600 lines/mm. All spectra were calibrated and normalized. The spatial resolution of the instrument is specified as 1 µm in diameter.

Photoluminescence Spectroscopy (PL). PL measurements were performed using a 532 nm CW doubled Nd:YAG laser for photoexcitation. The excitation was in a backscatter microscope configuration focusing through a 100X objective with a 1 µm spot size. The collected energy was energy dispersed through a 0.5 m ACTON spectrometer with an 1800 g·mm^{-1} grating and a back-thinned liquid nitrogen cooled PRINCETON INSTRUMENTS CCD camera.

Elemental Analysis. A JEOL-JSM 7500F scanning electron microscope equipped with an OXFORD X-Max EDX (Energy-Dispersive X-ray Spectroscopy) analyzer with Mn as internal standard was used to determine elements with atomic numbers larger than four. Samples were handled inside an Ar-filled glove box or outside if not air sensitive and fixed on a graphite

platelet which was attached to an aluminum stub. The Li content determination was carried out by atomic absorption spectroscopy using a VARIAN AA280FS device. C–H–N contents were determined by a HEKATECH EURO EA CHNSO-Analyzer.

Computational Details. Quantum chemical calculations with the Perdew-Burke-Ernzerhof hybrid density functional method (DFT-PBE0)[31,32] were performed using the CRYSTAL09 software package.[33] For energetic comparisons, the structures of Conesa[17] were included and labeled as in the original publication. Sp-valence + polarization (SVP) quality basis sets were applied for all elements: The basis set for Si was taken from ref. 20 and for Na and Li the split-valence level basis sets were derived from the molecular def-SVP basis set[34] (see Supporting Information). Both the lattice and the atomic parameters were allowed to relax within the constraints imposed by the space group symmetry for structural optimization. The shrinking factor (SHRINK) used for the generation of a Monkhorst-Pack-type grid of *k*-points in reciprocal space was 4 for lattice sizes larger 10 Å, 8 for lattices smaller or equal 10 Å, but larger 5 Å and 16 for smaller lattice parameters. Tight tolerance factors of 8, 8, 8, 8, and 16 were used for the evaluation of the Coulomb and exchange integrals (TOLINTEG). Default optimization convergence thresholds and an extra-large integration grid (XLGRID) for the density-functional part were applied in all calculations. For the full structural relaxation of the Si substructure of Li_3NaSi_6, the published structure of Li_3NaSi_6[14] was first fully optimized, after which the Si substructure was investigated in further calculations (atomic parameters are in the Supporting Information). As a first step, the initial lattice and atomic parameters of Li_3NaSi_6 without the alkalides were taken to optimize the structure without any symmetry constraints at DFT-PBE[31]/SVP level of theory. At this point the system was metallic and the Fermi surface was smeared with a width of 0.02 a.u.. For the evaluation of the tolerance and exchange integrals (TOLINTEG), tight criteria of 7, 7, 7, 7 and 14 were used and for the density-functional part, a large integration grid (LGRID) was applied. The geometry optimization starting from the Si substructure in Li_3NaSi_6 naturally resulted in large changes in the geometry, and the optimization process had to be carried out carefully and restarted several times. The resulting minimum structure was subsequently optimized at the DFT-PBE0/SVP level of theory and the stricter computational parameters discussed above for all Conesa structures. The space group of the minimum structure was determined to be *Cmcm* (63) with FINDSYM.[35] The structure is identical to Conesa's **SD** structure. The type of stationary point was found to be a minimum for all optimized structures applying frequency calculations.[36,37]

3. Results and Discussion

Synthesis and characterization of the precursors. In accordance with earlier literature reports,[26,38-40] $Li_{15}Si_4$ is obtained from mechanical ball-milling of a stoichiometric mixture of Li and Si. The respective PXRD pattern is depicted in Figure 3a and corresponds to pure-phase $Li_{15}Si_4$. In order to obtain single-phase Li_3NaSi_6, a peritectoid reaction of $Li_{12}Si_7$, NaSi and α-Si was performed at 550 °C just below the decomposition temperature of Li_3NaSi_6 at 600 °C (Figure S2). Li_3NaSi_6 was alternatively synthesized from the elements[14,15] or a mixture of $Li_{15}Si_4$, Na and α-Si yielding α-Si as byproduct, though.

Synthesis and Characterization of *a*-Si. In silicon based lithium-ion batteries (cycling Si against Li), an amorphization of the previously crystalline Si anode is observed when the "Li-inserted" anode (discharged state) is again fully "de-inserted" (charged state).[5,41,42] Crystalline metastable $Li_{15}Si_4$ was found to be present at discharge voltages below 50 mV.[5,41] Thus, in a simplified view the "charged" and "discharged" states correspond to *a*-Si and $Li_{15}Si_4$, respectively. Therefore, we investigated the formation of *a*-Si by chemical delithiation through Li extraction from $Li_{15}Si_4$, a phase consisting of isolated Si atoms, using liquid ammonia as solvent for Li. The extraction procedure was established with a custom-built apparatus shown in Figure 2a. The blue color of liquid ammonia when condensed onto $Li_{15}Si_4$ powder clearly indicates the formation of solvated electrons (Figure 2b). The formation of a metallic bronze solution as shown in Figure 2c typically indicates that Li is extracted.[27] After several extraction cycles solely $LiNH_2$ was identified as crystalline phase in the PXRD pattern of the product (Figure 3b). Additionally, an IR spectrum (Figure S4a) only shows NH stretching and HNH deformation modes[43] at 3259 cm^{-1} and 1560 cm^{-1}/1538 cm^{-1}, respectively. Si–O vibrational modes that typically occur at around 800–1100 cm^{-1} indicating O impurities[4] are not observed. In a further step, $LiNH_2$ is removed by sequential treatment with ethanol and an ethanol/water mixture. Acetic acid is used to adjust to acidity as silicon dissolves under alkaline conditions. Alternatively, a buffered solution could be used to remove $LiNH_2$.

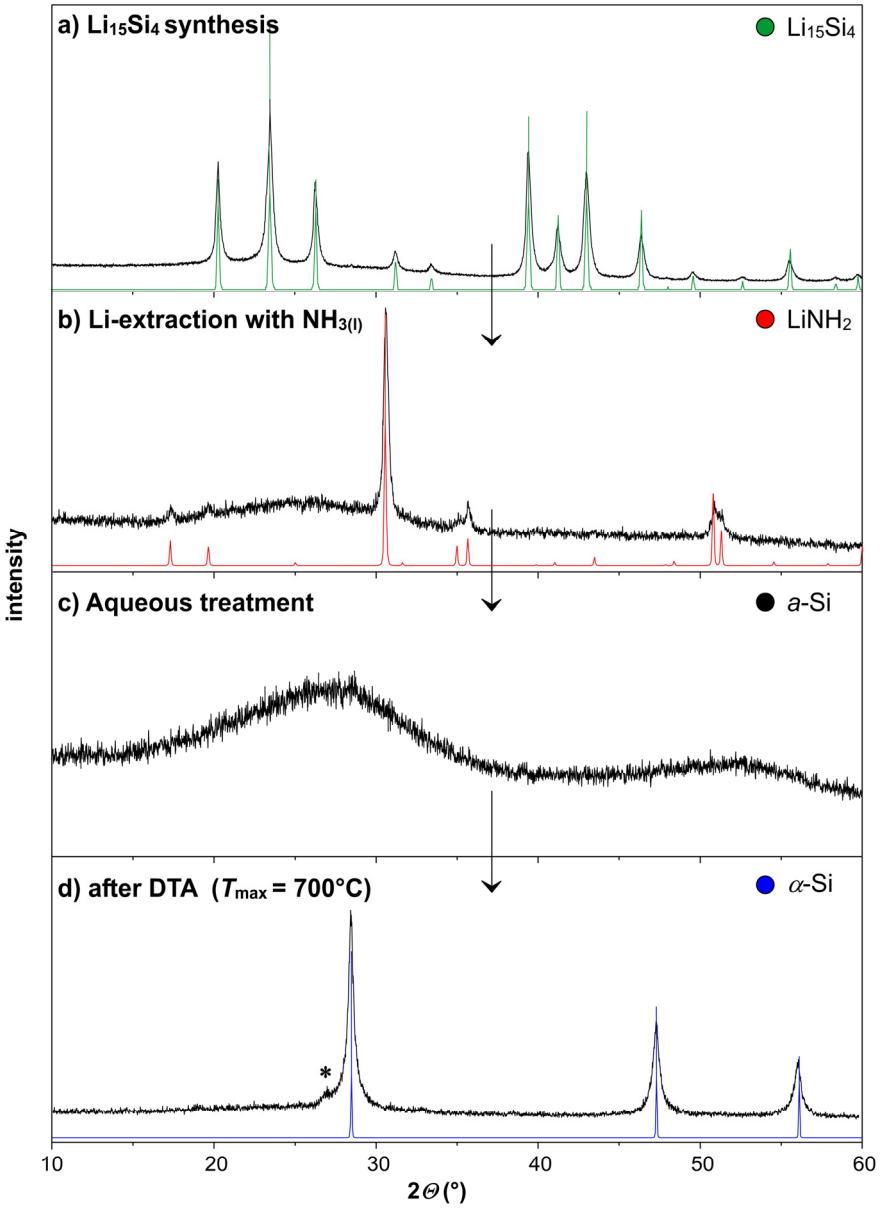

Figure 3. PXRD patterns of a) $Li_{15}Si_4$ bulk material, the sequential products after b) Li-extraction with liquid ammonia, c) subsequent aqueous treatment, and d) differential thermal analysis (calculated patterns for $Li_{15}Si_4$, $LiNH_2$, and α-Si are shown in green, red and blue, respectively; * corresponds to the (111)-reflection of Li_2SiO_3).

As can be seen from the PXRD pattern in Figure 3c, the dried black product after aqueous treatment is fully amorphous. However, IR spectroscopic investigations of several samples clearly reveal Si–O vibrational modes, in particular the Si–O stretching mode at around 1069 cm^{-1} (Figure S4b), indicating a slight partial surface oxidation.[4] This is additionally strengthened by EDX examinations and EDX nanoprobe analysis as part of TEM investigations (Figure 4b,c and S5). Furthermore, TEM images illustrate that *a*-Si samples consist of micro- and nanosized particles (Figure 4a–c). In accordance with X-ray diffraction

experiments, the SAED image (Figure 4d) does not show any diffraction, revealing a fully amorphous character. Concomitantly, the absence of a PL band (Figure S6) and the Raman mode at 466 cm^{-1} (Si–Si stretching mode), which is observed at markedly lower wave numbers than in case of crystalline α-Si (521 cm^{-1}), are characteristic for amorphous silicon.[3]

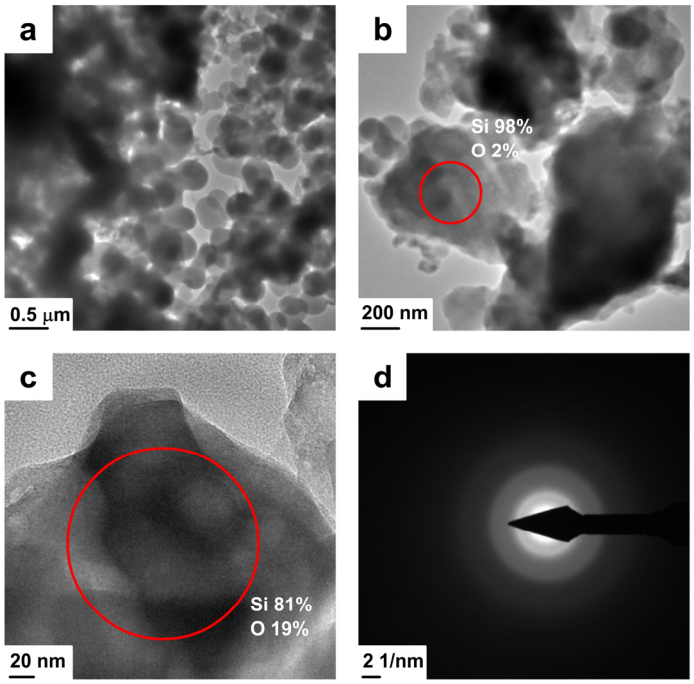

Figure 4. TEM images of *a*-Si (a–c) and results from concomitant EDX nanoprobe investigations (b, c). The SAED (selected area electron diffraction) image (d) clearly reveals a complete amorphous character of the sample.

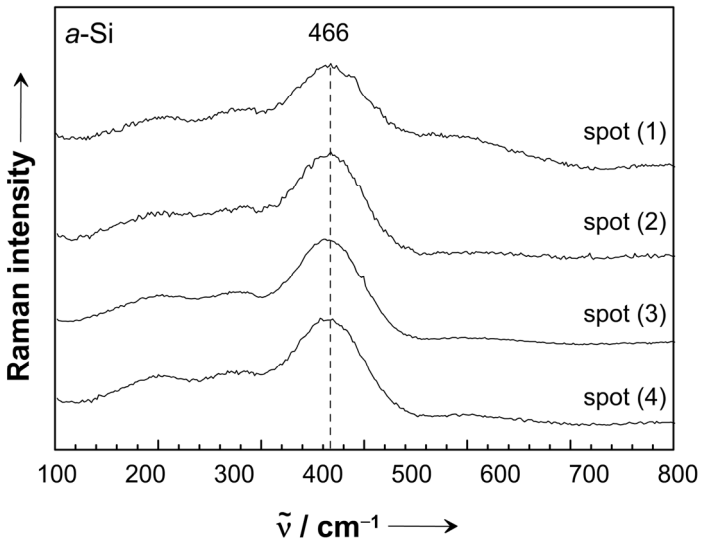

Figure 5. Various Raman spectra of *a*-Si. The Si–Si stretching mode can be recognized as a broad band at 466 cm^{-1}.

Synthesis and Characterization of *a-allo*-Si. The phases Li_7Ge_{12} and Li_3NaSi_6 both reveal polyanionic layers $^2_\infty[Ge_{12}]^{7-}$ and $^2_\infty[Si_6]^{4-}$, respectively, which are separated by Li and Na atoms (Figure 1).[7,14,16] A treatment of these precursors with protic solvents induces a strictly topochemical oxidation reaction in which slabs are connected through interlayer bond formation under retention of their two-dimensional topology. The corresponding products are identified as *m-allo*-Ge and *allo*-Si.[7,9,14,15] Whereas the synthesis of Li_7Ge_{12}, the subsequent oxidation to *m-allo*-Ge and its phase transition to 4*H*-Ge are well established,[8,9,16] the structure of *allo*-Si has only been described sketchily.

Referring to the previously reported synthesis of *allo*-Si, hydrogen is exclusively evolved during the reaction of Li_3NaSi_6 with protic solvents. Silanes were not detected by mass spectroscopy.[14,15] Reacting Li_3NaSi_6 with water, an almost complete conversion (97 %) to *allo*-Si was observed.[14,15] Beside *allo*-Si, α-Si crystallites are formed concomitantly. However, due to heavily disordered products a structure could not be proposed. The poor crystal quality only allowed the determination of cell parameters (orthorhombic, a = 13.29 Å, b = 3.79 Å, c = 12.63 Å).[15] Though, the reflection positions calculated from these parameters decisively differ from the ones reported in the database entry for *allo*-Si (ICSD 41-1111).

We diligently tried to reproduce and closely investigated the reaction of Li_3NaSi_6 with protic solvents in a series of experiments. Generally, consistent with earlier reports,[14,15] we found that the reactivity of Li_3NaSi_6 strongly depends on its crystallinity. For instance, a thoroughly powdered crystalline sample of Li_3NaSi_6 (Figure S7a) was allowed to react with ethanol for 15 days. Thereafter, reflections from Li_3NaSi_6 were still recognizable in the PXRD pattern and the increased background indicates the presence of an amorphous phase (Figure S7b). Additionally, infrared and energy dispersive X-ray spectroscopy revealed a low O-content excluding the formation of significant quantities of SiO_2 (Figure S9). Even after treatment of such samples with concentrated HCl the PXRD pattern did not change considerably. In order to fully oxidize a sample of Li_3NaSi_6, it was ball-milled prior to oxidation to increase the surface area and thus its reactivity (Figures S8a,b). Thereafter, an intense reaction of the ball-milled sample with ethanol was observed. The respective PXRD pattern shows an increased background as well as Bragg reflections of α-Si and Na_8Si_{46} (Figure S8c). The latter phase most probably originates from the initial reactant Li_3NaSi_6 although it is not recognizable in the according PXRD pattern. The formation of α-Si crystallites was also reported in previous work. Note that traces of NaSi in the Li_3NaSi_6 precursor may be oxidized to Na_8Si_{46} with H_2O.[44] Regardless of a slow, fast, partial or full oxidation of Li_3NaSi_6, we never observed the reflections that are reported for *allo*-Si (ICSD-41-1111).[45] Instead, an increased background at 2θ values of ~30° and ~55° is characteristic for the respective PXRD patterns indicating the formation of an amorphous phase. In order to account for the *a*morphous

product being obtained in analogy to *allo*-Ge, it is named *a-allo*-Si (cf. Scheme 3). We note that annealing partially oxidized samples of Li_3NaSi_6 at 300 °C for two weeks did not give rise to any new reflections (Figure S10). The formation of α-Si crystallites which are embedded in an amorphous Si matrix is also strengthened by Raman spectroscopy. The Raman spectra of *a-allo*-Si in Figure 6 show characteristic modes for amorphous and nanocrystalline Si.

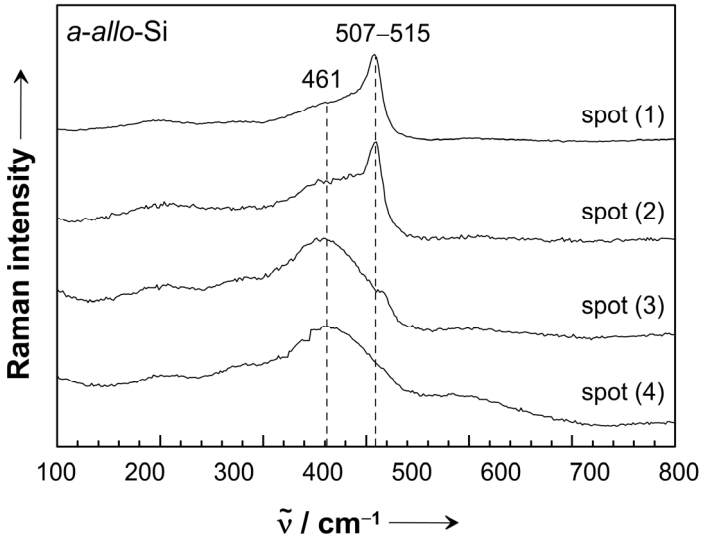

Figure 6. Various Raman spectra of *a-allo*-Si showing the characteristic Si–Si stretching mode for amorphous (*a*-Si:[3] ~450 cm^{-1}) and nanocrystalline Si (*nc*-Si:[3] ~490–507 cm^{-1}).

Analyzing the reflection pattern of *allo*-Si (ICSD 41-1111) more critically, it shows strong analogies to $NbSi_2$ (Figure S11). A possible explanation could be that the reported synthesis of Li_3NaSi_6 was carried out in Nb ampules reaching temperatures of up to 800 °C over a longer period allowing for the formation of $NbSi_2$.[14] Minor portions of $NbSi_2$ may not be recognizable in the diffraction patterns of Li_3NaSi_6 but can dominate the PXRD pattern in an amorphous product.[45] This is a reasonable explanation for the absence of the reported *allo*-Si Bragg reflections in our PXRD patterns and casts doubts on former powder X-ray investigations.

DTA investigations on *a*-Si and *a-allo*-Si. It was shown in the previous section that Li can be removed from $Li_{15}Si_4$ and Li_3NaSi_6 by various methods yielding amorphous Si and a mixture of amorphous Si and α-Si (nano)crystallites, respectively. As yet, it is not clear whether it is justified to identify both products as *a*-Si or if *a-allo*-Si possesses a different amorphous nature. Since *a-allo*-Si is obtained from Li_3NaSi_6 by a strictly topochemical reaction, a resemblance of the local structure of *a-allo*-Si would be reasonable. We investigated the amorphous-to-crystalline phase transition of both materials (*a*-Si/*allo*-Si to α-Si) by differential

thermal analysis since for *allo*-Si a significantly lower transformation temperature was reported and claimed as good "proof that *allo*-Si is in fact a new silicon modification".[14]

Figure 7 shows the first heating traces of thermograms recorded for (i) Li_3NaSi_6, (ii) partially oxidized Li_3NaSi_6 (virtually a mixture of Li_3NaSi_6 and *a-allo*-Si), (iii) *a-allo*-Si, and (iv) *a*-Si. Li_3NaSi_6 decomposes at around 600 °C (effect 2) into $Li_{12}Si_7$, NaSi, and α-Si (Figure S3). For the Li_3NaSi_6/*a-allo*-Si mixture, an additional exothermic effect is observed at 487 °C (effect 1). Comparing the PXRD patterns of both the pure-phase Li_3NaSi_6 sample and the Li_3NaSi_6/*a-allo*-Si mixture after DTA investigations, the latter clearly reveals higher portions of α-Si (Figure S3 and S7c). Additionally, the heating trace of the *a-allo*-Si sample exclusively contains an irreversible exothermic effect that is markedly shifted to higher temperatures (effect 3 at 565 °C). The subsequently recorded PXRD pattern corresponds to α-Si (Figure S8d). Thus, effect (1) and (3) are attributed to the transformation of *a-allo*-Si into α-Si. In case of *a*-Si, the phase transition is found at 658 °C (effect 4) and consistent with previous reports (cf. Figure 3d and 7).[46,47]

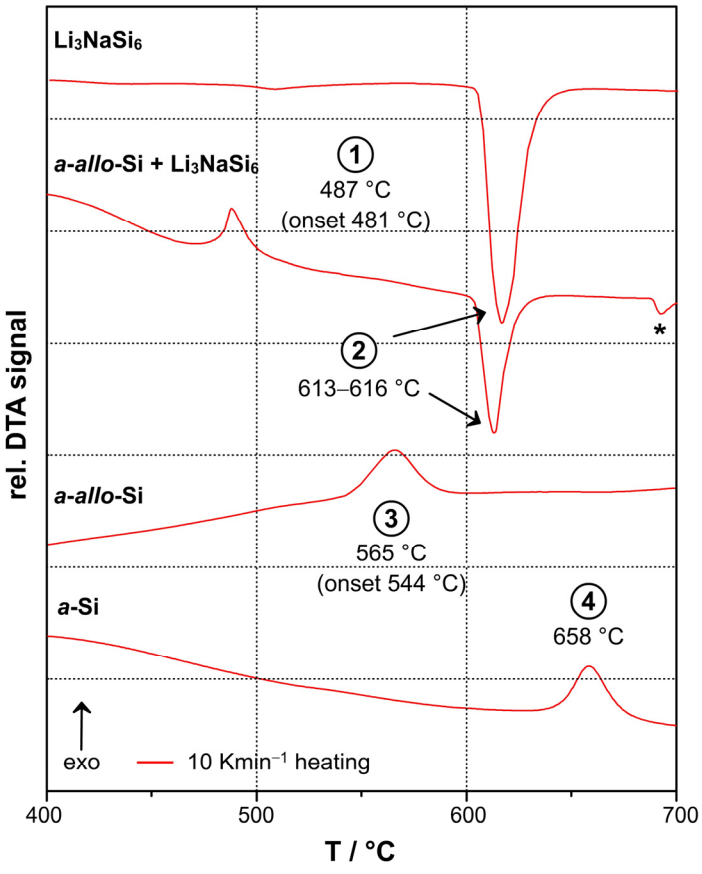

Figure 7. First DTA heating traces of thermograms recorded for Li_3NaSi_6, partially oxidized Li_3NaSi_6 (Li_3NaSi_6/*a-allo*-Si mixture), *a-allo*-Si, and *a*-Si ($T_{max.}$ = 750 °C, ±10 K·min^{-1} heating/cooling rate, heat effects marked with * could not be assigned).

Compared to *a*-Si, *a-allo*-Si samples possess lower amorphous-to-crystalline phase transition temperatures due to a large concentration of *α*-Si (nano)crystallites serving as crystallization nuclei. For *a*-Si, the concentration of such particles is very low and the nucleation has to be induced prior to the transition. Thus, the phase transition temperature of *a*-Si is higher than that of *a-allo*-Si. In case of previous work on *allo*-Si,[14,15] the formation of *α*-Si crystallites was reported as well and the phase transition of *allo*-Si at 527 °C is in line with our findings.[14,15]

Concluding, our experimental results show that a clear differentiation between *a-allo*-Si and *a*-Si is not possible and that the oxidation of Li_3NaSi_6 according to earlier work solely leads to the formation of amorphous products.

Model Structures for *a-allo*-Si derived from Li_3NaSi_6. As shown in the previous chapter, the existence of an allotropic form of silicon obtained from Li_3NaSi_6 according to reports in literature is disputable. Attempts to obtain *m*icrocrystalline samples of *allo*-Si (*m-allo*-Si) failed up to now and its synthesis still remains challenging. Similarly to *m-allo*-Ge, a close resemblance of the *m-allo*-Si structure to the two-dimensional slabs in Li_3NaSi_6 remains reasonable. Yet, the Si substructure of Li_3NaSi_6 significantly differs from the Ge substructure of Li_7Ge_{12}. A calculation of Conesa's structures[17] at the DFT-PBE0/SVP level of theory shows that for Si, most of the allotropic structures derived from a hypothetical Li_7Si_{12} structure (isotypic with Li_7Ge_{12}; "**G**-structures") are favored in total energy over structures derived from Li_3NaSi_6 ("**S**-structures"; Figure 8 and 10, Table S1).

Conesa's **G** structures (Figure 8) are divided into four groups: **GA** are structures in which the tetrel layers are connected to result in 7-membered rings. The tetrel layers are stacked as they appear in the reactant phase Li_7Ge_{12} (opposite orientation by inversion). Group **GB** is also characterized by a stacking of these opposing layers, resulting in 6- and 8-membered rings. Groups **GC** and **GD** represent stacking of layers with the same orientation, **GC** structures are linked to yield 7-membered rings and **GD** contain 6- and 8-membered rings. Therefore, the latter two groups are just hypothetical. For group **G**, the favored structure for Si is **GAa4** (distances: 2.32 Å–2.46 Å, angles: 92.6–126.8°, crystallographic density: 2.220 $g \cdot cm^{-3}$). This is the same result as obtained for the Ge counterpart.[9] The difference in energy per atom to *α*-Si is 8.0 $kJ \cdot (mol \cdot Si)^{-1}$ (optimized structure: distances 2.36 Å, angles 109.4°, crystallographic density: 2.290 $g \cdot cm^{-3}$). The hypothetical structure **GDd1** has the highest total energy of this group (distances: 2.33–2.46 Å, angles: 90.0–137.7°, crystallographic density: 2.098 $g \cdot cm^{-3}$) with a difference of 16.2 $kJ \cdot mol^{-1}$ (Figure 8).

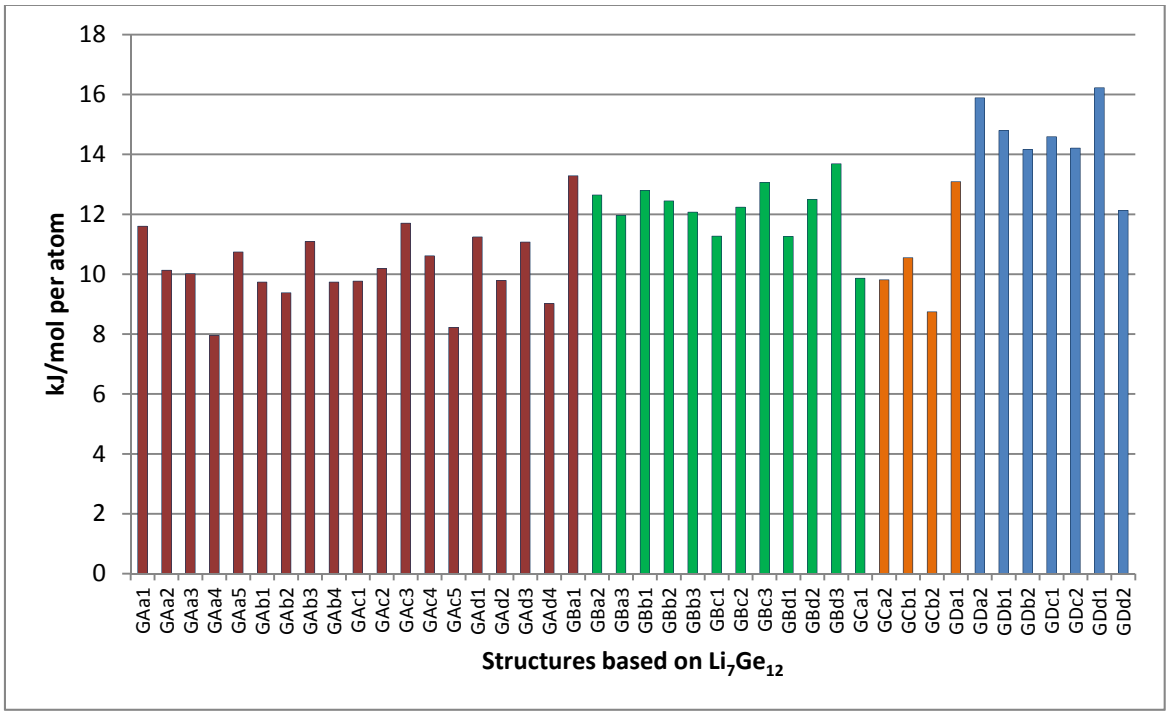

Figure 8. Comparison of the total energies in kJ·(mol·Si)$^{-1}$ in networks optimized on the basis of Conesa's **G**-type structures (derived from the Ge substructure of Li_7Ge_{12}). The single groups **GA** (red), **GB** (green), **GC** (orange), and **GD** (blue) refer to different ways of layer connections.[17]

The two dimensional slabs $^2_\infty[Si_6]^{4-}$ in Li_3NaSi_6 are built of four- (4b), three- (3b), and two-bonded (2b) Si atoms, respectively (cf. Figure 9: 4b = black, 3b = light and dark blue, 2b = red). Based on this structure, Conesa's **S** group is derived which can also be divided into four smaller structure groups. The **SA** group is built by connecting 2b-Si atoms (red) of neighboring layers and bonding them to 3b-Si atoms of their own layers (dark blue). The light blue 3b-Si atoms are bonded to the light blue ones of the neighboring layer. **SB** is a connection of red Si^{2-} atoms (2b) with light blue Si^{-} atoms (3b) of the neighboring layer and dark blue Si^{-} atoms (3b) of their own layer. For structures **SC**, the 2b-Si^{2-} atoms are connected to dark blue 3b-Si^{-} atoms and to the red Si^{2-} of the neighboring layer. The 3b-Si^{-} atoms (light blue) are connected to the same kind of the next layer. For each of these types four structure variations exist. The fourth group **SD** is built by connecting red Si^{2-} atoms (2b) to both Si^{-} atoms (3b) of the next layer. For such a network, only one structure type is possible, the **TON**[48] zeolite-type network (ZSM-22).

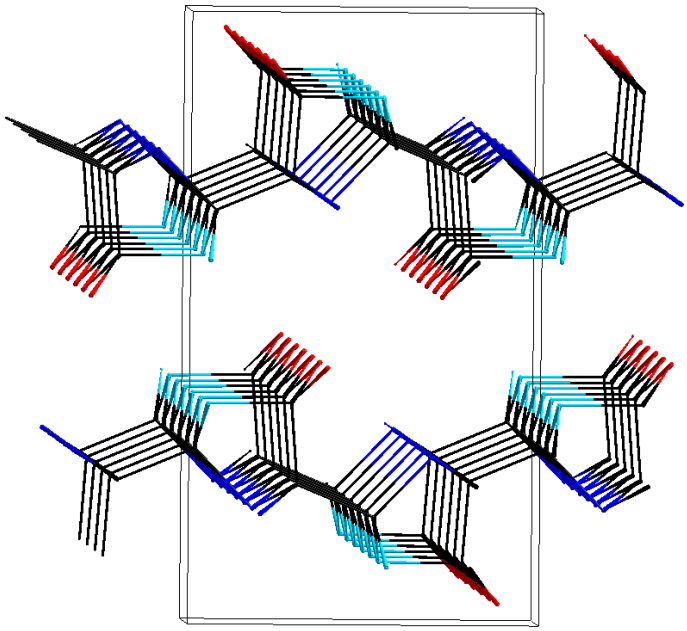

Figure 9. Si substructure in the phase Li_3NaSi_6. The four- (Si^0), three- (Si^-) and two-bonded (Si^{2-}) Si atoms are shown in black, light/dark blue, and red, respectively. For the four different groups of *allo*-Si networks derived from this layered structure, the charged atoms are connected differently.

A comparison of total energies (Figure 10) shows that **SD** is the favored structure with an energy difference to α-Si of 13.7 kJ·(mol·Si)$^{-1}$ (Si–Si distances: 2.34–2.40 Å, angles: 90.7–142.9°, crystallographic density: 2.011 g·cm^{-3}, Figure 11a). Its structure has the lowest density of all **G** and **S** group networks and is equivalent to the zeolite network **TON**.[48] As shown in Figure 11a it contains 10-, 6-, and 5-membered rings which form parallel channels proceeding along the *c*-axis. The diameter of the largest channel ranges from 6.6 to 7.4 Å. In energy, this framework is followed by **SC1** (Figure 11b) with a relative energy of 14.0 kJ·(mol·Si)$^{-1}$. Si–Si distances vary from 2.31 to 2.43 Å and angles range from 92.0 to 128.4°. The crystallographic density of this structure is 2.292 g·cm^{-3} and therefore almost the same as for α-Si (even slightly higher). The **SC** group is the one with the highest densities at around 2.290 g·cm^{-3}, the density of α-Si (all crystallographic densities are listed in Table S1). **SC1** is also a one dimensional channel system bearing 6- and 5-membered rings in *a* direction (Figure 11b). We note that overall the **S** group shows higher relative energies than the **G** group. The total energies per atom of the two most stable phases of the **S** group, **SD** and **SC1**, are 5.7 kJ·(mol·Si)$^{-1}$ and 6.0 kJ·(mol·Si)$^{-1}$ larger than **GAa4**, the most stable structure of the **G** group.

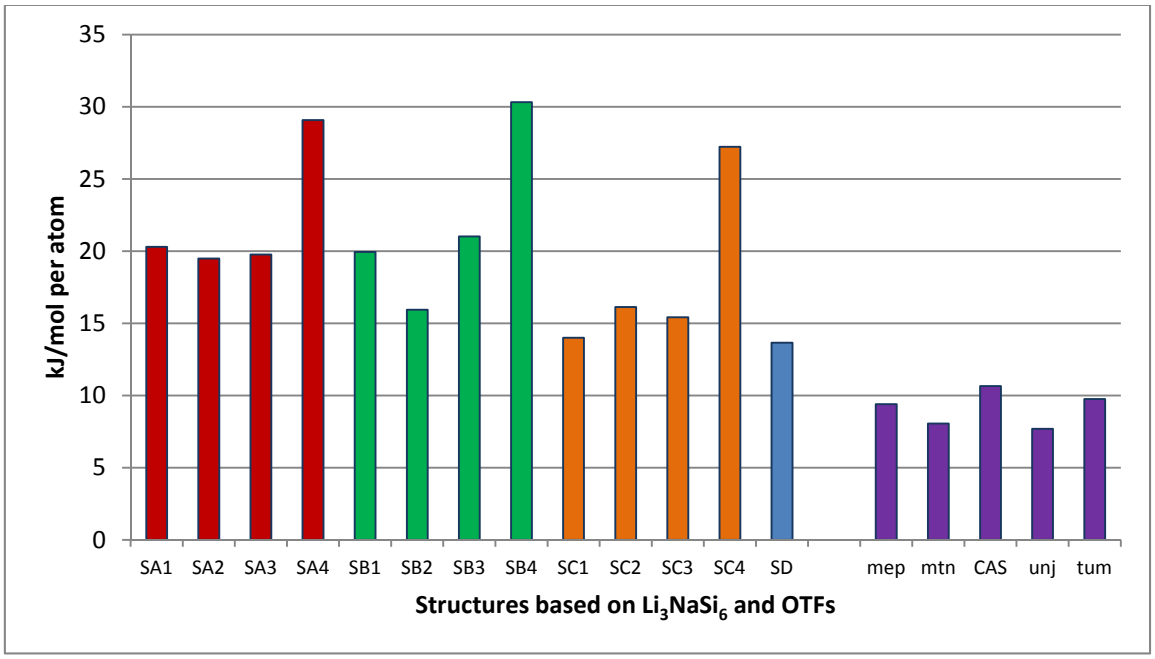

Figure 10. Energies relative to α-Si for Conesa's **S**-type structures (derived from the Si substructure of Li_3NaSi_6). The four different network classes are colored differently; **SA** in red, **SB** in green, **SC** in orange and **SD** in blue. To show the energy difference to well-known open tetrahedral frameworks (OTFs), these are depicted as well (violet). All relative energies are also listed in Table S1.

As Li_3NaSi_6 has a well-ordered and layered Si substructure and is therefore a reasonable reactant phase for the synthesis of *allo*-Si, we also carried out a full structural relaxation of the Si substructure in the optimized structure of Li_3NaSi_6. This resulted in a true local minimum being the **TON** structure, which was also the favored of all "handmade" structures of Conesa,[17] highlighting the key role of this network. Furthermore, the structure with the smallest density is favored in the present structural relaxation without any initial specification of Si–Si bonds. We note that we performed this full structural relaxation in space group *P*1 to avoid any restrictions caused by symmetry. The open tetrahedral frameworks (OTFs) which may also be formed in reactions toward *allo*-Si, have more favorable relative energies than the structures derived from Li_3NaSi_6. The relative energies compared to α-Si range from 7.7 kJ·(mol·Si)$^{-1}$ (**unj**) to 10.7 kJ·(mol·Si)$^{-1}$ (**CAS**). Also, the crystallographic densities are lower and range from 1.979 g/cm^3 (**mtn**) to 2.180 g·cm^{-3} (**tum**) (Table S1).

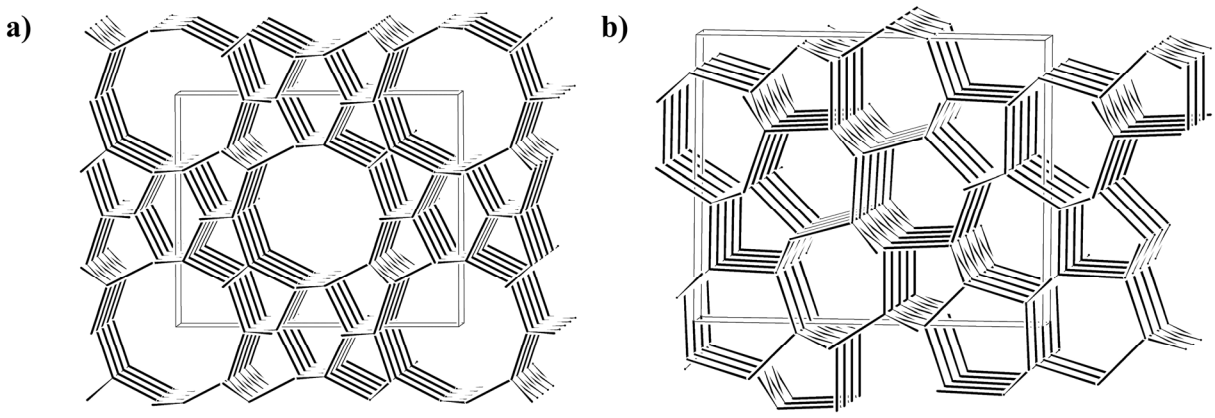

Figure 11. a) The most stable network (**SD**) derived from the Si substructure of Li_3NaSi_6 with view along the *c*-direction emphasizing the one dimensional channel structure built from 10-, 6-, and 5-membered rings; b) Network of the structure **SC1** with view along the *a*-direction. It is built of 6- and 5-membered rings.

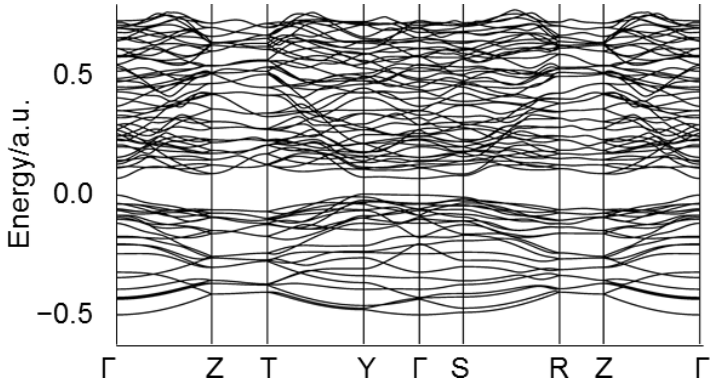

Figure 12. Band structure of **SD** showing an indirect band gap of 1.74 eV and a direct band gap of 1.85 eV, respectively. The band gap in *z*-direction is significantly larger with a value of 3.4 eV. The zero energy level corresponds to the top of the valence bands.

The band gaps of all calculated structures range from 0.73 (**SB4**) to 3.01 eV (**mtn**) (Table S1). The most stable structures, **GAa4**, **SD** and **SC1** possess gaps of 2.23 eV, 1.74 eV, and 1.50 eV, respectively. For both relevant structures derived from Li_3NaSi_6 (**SD** and **SC1**), the bands are flat (Figures 12 and S12). Still, these are no direct band gap materials. **SD** has a narrow gap in the *x* and *y* directions, whereas it is significantly larger in *z* direction. This goes along with the channels in the *z* direction as well, here the gap is 3.4 eV. For the structure **SC4**, there is no band gap at all since it is highly strained (Si–Si bonds: 2.28–2.50 Å, angles: 88.7 to 136.5°).

4. Conclusion

In the course of our investigations on allotropic forms of silicon we focused on the previously reported modification *allo*-Si. Hitherto, its structure is unknown and attempts to obtain crystalline samples from an oxidation of the precursor Li_3NaSi_6 failed. Furthermore, our studies revealed ambiguities regarding the X-ray diffraction pattern reported for *allo*-Si since a strong resemblance to $NbSi_2$ is recognizable. Reactions targeting the synthesis of *allo*-Si solely yielded amorphous products. However, the reported amorphous-to-crystalline transformation temperature of 527 °C is drastically lower than that of ordinary amorphous Si which transforms to α-Si at ~660 °C. In order to clarify this issue, differences between amorphous *allo*-Si (*a-allo*-Si) and amorphous silicon (*a*-Si) were elucidated. The latter was obtained from $Li_{15}Si_4$ by a delithiation process employing liquid ammonia as solvent for Li. Thermal investigations confirmed that *a-allo*-Si recrystallizes at markedly lower temperatures than *a*-Si. However, the lower phase transition temperatures of *a-allo*-Si samples are a consequence of large concentrations of α-Si crystallites that serve as crystallization nuclei. These results call the existence of *allo*-Si into question and maybe other routes could lead to the formation of *allo*-Si. Nevertheless, diverse hypothetical structures for *allo*-Si were approached by quantum chemical investigations on the basis of the Si substructures of Li_3NaSi_6 and a hypothetical phase Li_7Si_{12}. The latter is isotypic with Li_7Ge_{12} which transform into the well characterized Ge polymorph *m-allo*-Ge upon oxidation. Remarkably, structures derived from Li_7Si_{12} are distinctly favored over those obtained from Li_3NaSi_6. On a theoretical level, this is a reasonable explanation for the difficulties to obtain crystalline samples of *allo*-Si. Yet, other phases may also serve as precursors for new Si allotropes since Si network structures conceived of known tetrahedral frameworks were proven to possess considerably more favorable energies relative to α-Si.

Supporting Information. PXRD patterns of $Li_{12}Si_7$, NaSi (Figure S1) and Li_3NaSi_6 (Figure S2), PXRD pattern of Li_3NaSi_6 after DTA investigations (Figure S3), ATR-FT-IR spectra of an *a*-Si/$LiNH_2$ mixture after Li extraction from $Li_{15}Si_4$ and a subsequently synthesized *a*-Si sample (Figure S4), results from EDX investigations of *a*-Si (Figure S5), PL-spectrum of *a*-Si (Figure S6), PXRD patterns of Li_3NaSi_6, the product after partial oxidation with ethanol and subsequent DTA-investigation (Figure S7), PXRD patterns of Li_3NaSi_6 before and after ball-milling, the product after aqueous treatment and subsequent DTA investigation (Figure S8), ATR-FT-IR spectra of partially und fully oxidized Li_3NaSi_6 through aqueous treatment (Figure S9), PXRD pattern of Li_3NaSi_6 after reaction with ethanol and subsequent annealing at 300 °C for two weeks (Figure S10), PXRD pattern of a $NbSi_2$ sample referenced with the database entry for *allo*-Si and $NbSi_2$ (Figure S11), band structure of **SC1** (Figure S12), DFT-PBE0 results in tabular format (Table S1), and basis set listings for Na and Li.

Corresponding Author Note. *E-mail: Thomas.Faessler@lrz.tum.de

Notes. The authors declare no competing financial interest.

Acknowledgement. This work has been funded by the Deutsche Forschungsgemeinschaft project number FA 198/11–1, Academy of Finland (grant 138560/2010), as well as the National Science Foundation through grant DMR-1007557. M.Z., L. A. J. and L. M. S. thank the Fonds der Chemischen Industrie, the Christiane Nüsslein-Volhard Stiftung and the Deutsche Studienstiftung, respectively, for their fellowships. They appreciate the support by the TUM Graduate School. M.Z. thanks F. Kraus for providing the custom-built extractor.

5. REFERENCES

(1) Street, R. A. *Technology and Applications of Amorphous Silicon*; Springer: New York, 2000.

(2) Rech, B.; Wagner, H. *Appl. Phys. A* **1999**, *69*, 155.

(3) McMillan, P. F.; Gryko, J.; Bull, C.; Arledge, R.; Kenyon, A. J.; Cressey, B. A. *J. Solid State Chem.* **2005**, *178*, 937.

(4) Wang, J.; Ganguly, S.; Sen, S.; Browning, N. D.; Kauzlarich, S. M. *Polyhedron* **2013**, *58*, 156.

(5) Obrovac, M. N.; Christensen, L. *Electrochem. Solid-State Lett.* **2004**, *7*, A93.

(6) Guloy, A. M.; Ramlau, R.; Tang, Z.; Schnelle, W.; Baitinger, M.; Grin, Y. *Nature* **2006**, *443*, 320.

(7) Grüttner, A.; Nesper, R.; von Schnering, H. G. *Angew. Chem. Int. Ed.* **1982**, *21*, 912.

(8) Kiefer, F.; Hlukhyy, V.; Karttunen, A. J.; Fässler, T. F.; Gold, C.; Scheidt, E. W.; Scherer, W.; Nylen, J.; Häussermann, U. *J. Mater. Chem.* **2010**, *20*, 1780.

(9) Kiefer, F.; Karttunen, A. J.; Döblinger, M.; Fässler, T. F. *Chem. Mater.* **2011**, *23*, 4578.

(10) Armatas, G. S.; Kanatzidis, M. G. *Science* **2006**, *313*, 817.

(11) Armatas, G. S.; Kanatzidis, M. G. *Nature* **2006**, *441*, 1122.

(12) Sun, D.; Riley, A. E.; Cadby, A. J.; Richman, E. K.; Korlann, S. D.; Tolbert, S. H. *Nature* **2006**, *441*, 1126.

(13) Armatas, G. S.; Kanatzidis, M. G. *Adv. Mater.* **2008**, *20*, 546.

(14) von Schnering, H. G.; Schwarz, M.; Nesper, R. *J. Less-Common Met.* **1988**, *137*, 297.

(15) Schwarz, M. *Dissertation*, Universität Stuttgart: Stuttgart, Germany, 1988.

(16) Kiefer, F.; Fässler, T. F. *Solid State Sci.* **2011**, *13*, 636.

(17) Conesa, J. C. *J. Phys. Chem. B* **2002**, *106*, 3402.

(18) Zwijnenburg, M. A.; Jelfs, K. E.; Bromley, S. T. *Phys. Chem. Chem. Phys.* **2010**, *12*, 8505.

(19) Pickard, C. J.; Needs, R. J. *Phys. Rev. B* **2010**, *81*.

(20) Karttunen, A. J.; Fässler, T. F.; Linnolahti, M.; Pakkanen, T. A. *Inorg. Chem.* **2011**, *50*, 1733.

(21) Wu, F.; Jun, D.; Kan, E.; Li, Z. *Solid State Commun.* **2011**, *151*, 1228.

(22) Zhao, Z.; Tian, F.; Dong, X.; Li, Q.; Wang, Q.; Wang, H.; Zhong, X.; Xu, B.; Yu, D.; He, J.; Wang, H. T.; Ma, Y.; Tian, Y. *J. Am. Chem. Soc.* **2012**, *134*, 12362.

(23) Botti, S.; Flores-Livas, J. A.; Amsler, M.; Goedecker, S.; Marques, M. A. L. *Phys. Rev. B* **2012**, *86*.

(24) Zhao, H.-Y.; Wang, J.; Ma, Q.-M.; Liu, Y. *Phys. Chem. Chem. Phys.* **2013**, *15*, 17619.

(25) Öhrström, L.; O'Keeffe, M. *Z. Kristallogr.* **2013**, *228*, 343.

(26) Zeilinger, M.; Baran, V.; van Wüllen, L.; Häussermann, U.; Fässler, T. F. *Chem. Mater.* **2013**, *25*, 4113.

(27) Zurek, E.; Edwards, P. P.; Hoffmann, R. *Angew. Chem. Int. Ed.* **2009**, *48*, 8198.

(28) *TOPAS - Rietveld Software*, Version 4.0; Bruker AXS Inc.: Madison, WI, USA, **2009**.

(29) *Netzsch Proteus Thermal Analysis*, Version 4.8.2; Netzsch-Gerätebau GmbH: Selb, Germany, **2006**.

(30) *Resolution Pro*, Version 5.1.0.822; Varian Inc.: Santa Clara, CA, USA, **2009**.

(31) Perdew, J. P.; Burke, K.; Ernzerhof, M. *Phys. Rev. Lett.* **1996**, *77*, 3865.

(32) Adamo, C.; Barone, V. *J. Phys. Chem.* **1999**, *110*, 6158.

(33) Dovesi, R.; Orlando, R.; Civalleri, B.; Roetti, C.; Saunders, V. R.; Zicovich-Wilson, C. M. *Z. Kristallogr.* **2005**, *220*, 571.

(34) Schäfer, A.; Horn, H.; Ahlrichs, R. *J. Chem. Phys.* **1992**, *97*, 2571.

(35) Stokes, H. T.; Hatch, D. M. *J. Appl. Cryst.* **2005**, *38*, 237.

(36) Zicovich-Wilson, C. M.; Pascale, F.; Roetti, C.; Saunders, V. R.; Orlando, R.; Dovesi, R. *J. Comput. Chem.* **2004**, *25*, 1873.

(37) Pascale, F.; Zicovich-Wilson, C. M.; Gejo, F. L.; Civalleri, B.; Orlando, R.; Dovesi, R. *J. Comput. Chem.* **2004**, *25*, 888.

(38) Key, B.; Bhattacharyya, R.; Morcrette, M.; Seznec, V.; Tarascon, J. M.; Grey, C. P. *J. Am. Chem. Soc.* **2009**, *131*, 9239.

(39) Hashimoto, Y.; Machida, N.; Shigematsu, T. *Solid State Ionics* **2004**, *175*, 177.

(40) Tamori, R.; Machida, N.; Shigematsu, T. *J. Jpn. Soc. Powder Powder Metall.* **2001**, *48*, 267.

(41) Hatchard, T. D.; Dahn, J. R. *J. Electrochem. Soc.* **2004**, *151*, A838.

(42) Limthongkul, P.; Jang, Y. I.; Dudney, N. J.; Chiang, Y. M. *Acta Mater.* **2003**, *51*, 1103.

(43) Bohger, J. P. O.; Essmann, R. R.; Jacobs, H. *J. Mol. Struct.* **1995**, *348*, 325.

(44) Böhme, B.; Guloy, A.; Tang, Z.; Schnelle, W.; Burkhardt, U.; Baitinger, M.; Grin, Y. *J. Am. Chem. Soc.* **2007**, *129*, 5348.

(45) Kiefer, F. *Dissertation*, Technische Universität München: München, Germany, 2010.

(46) Neiner, D.; Kauzlarich, S. M. *Chem. Mater.* **2010**, *22*, 487.

(47) Shen, T. D.; Koch, C. C.; McCormick, T. L.; Nemanich, R. J.; Huang, J. Y.; Huang, J. G. *J. Mater. Sci.* **1995**, *10*, 139.

(48) Barri, S. A. I.; Smith, G. W.; White, D.; Young, D. *Nature* **1984**, *312*, 533.

SUPPORTING INFORMATION

Zeilinger et al.

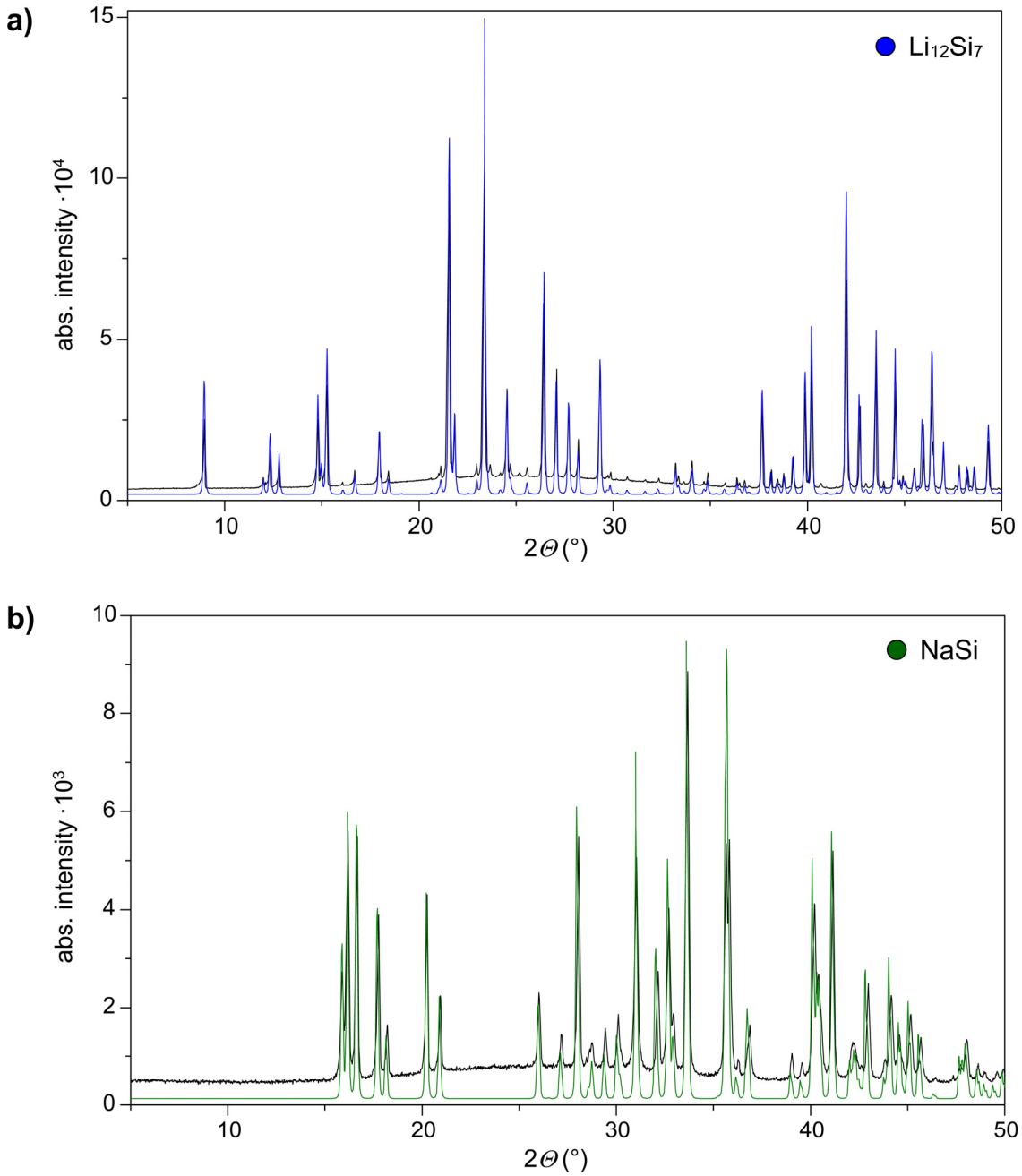

Figure S1. PXRD patterns of $Li_{12}Si_7$ and NaSi referenced with their theoretical patterns ($Li_{12}Si_7$ = blue, NaSi = green).

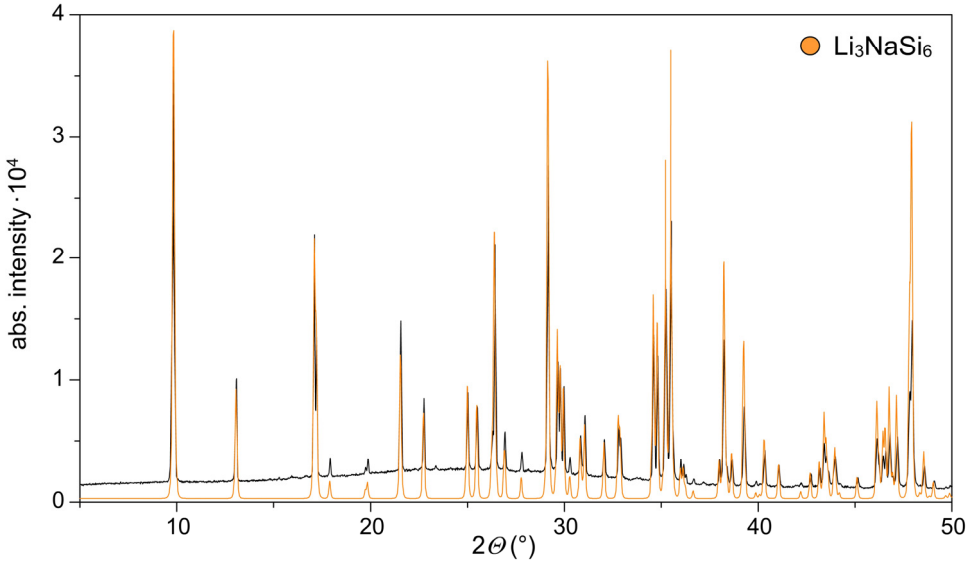

Figure S2. PXRD pattern of Li_3NaSi_6 synthesized from a mixture of $Li_{12}Si_7$, NaSi and α-Si (calculated pattern for Li_3NaSi_6 = orange).

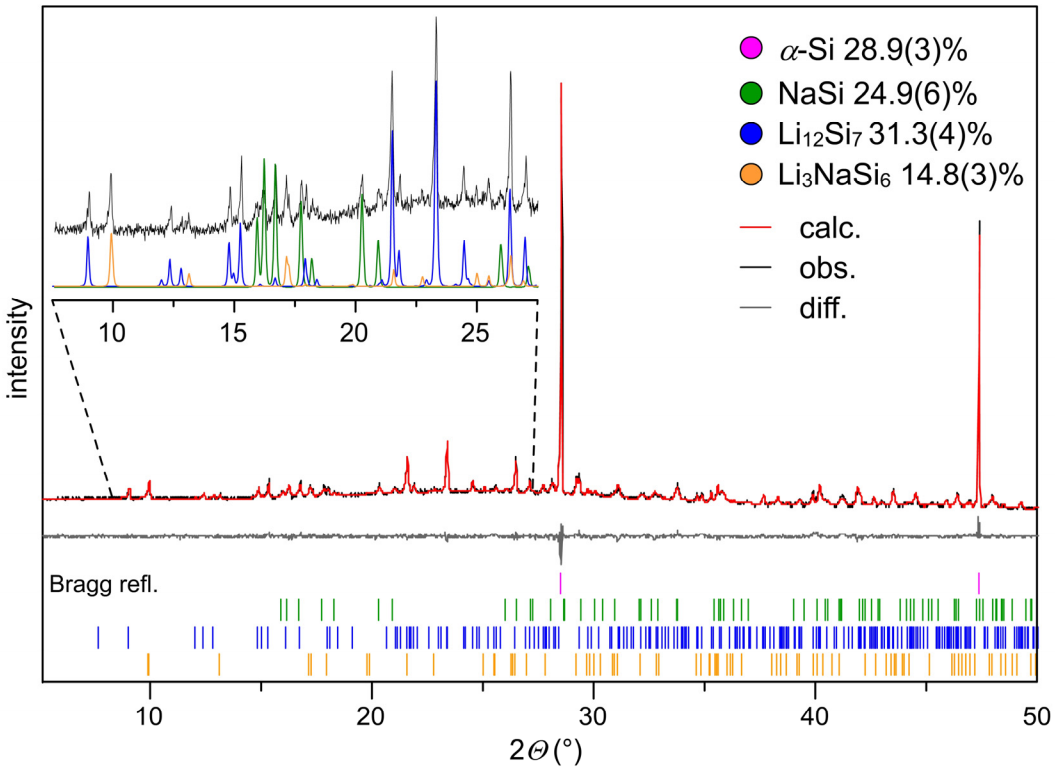

Figure S3. Rietveld fit to the PXRD pattern of Li_3NaSi_6 after DTA investigations ($T_{max.}$ = 700 °C, ±10 $Kmin^{-1}$ heating/cooling rate; α-Si (pink), NaSi (green), $Li_{12}Si_7$ (blue), Li_3NaSi_6 (orange), corresponding weight fractions are given).

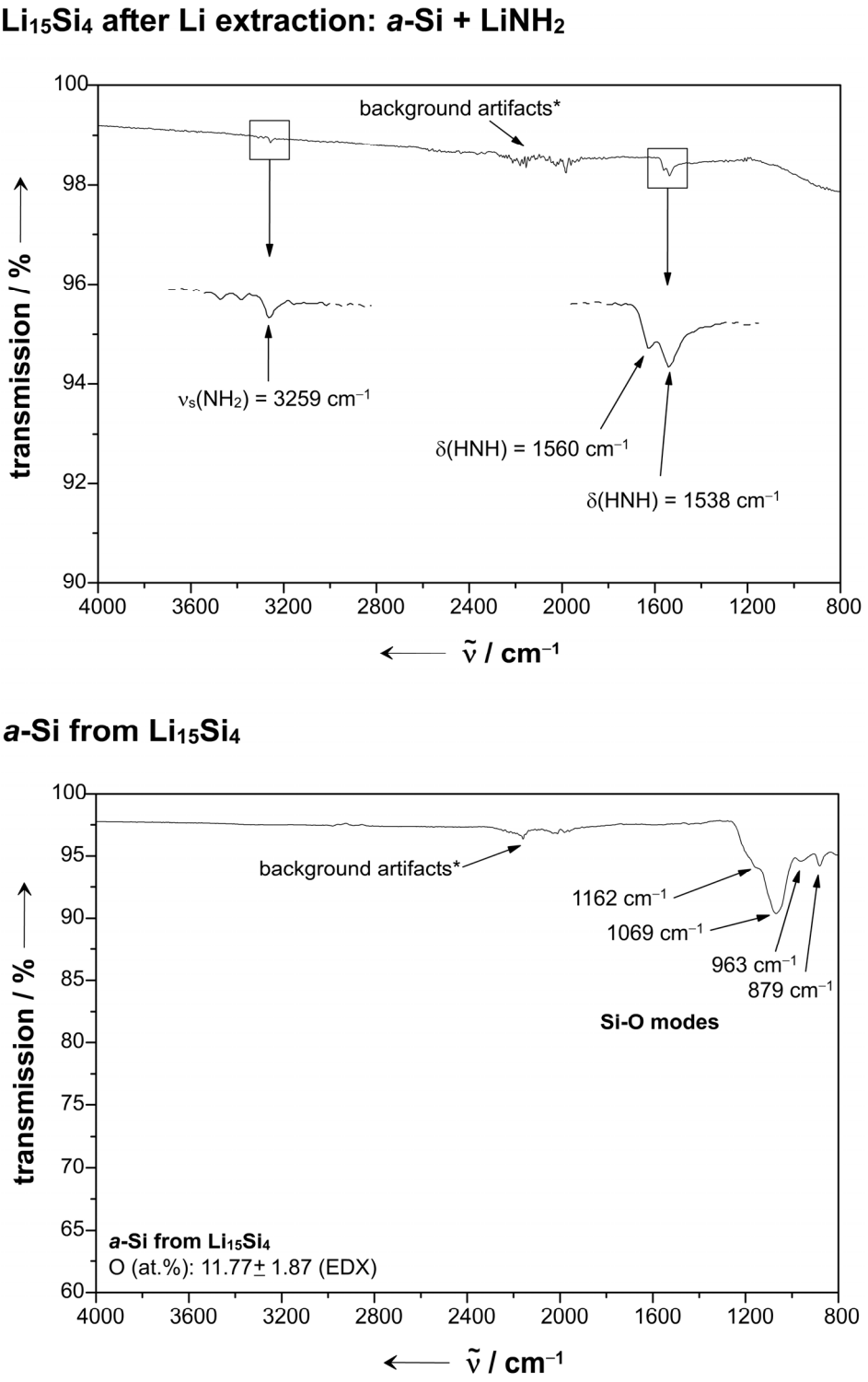

Figure S4. ATR-FT-IR spectra recorded for a) an *a*-Si/$LiNH_2$ mixture after Li extraction from $Li_{15}Si_4$, and b) an *a*-Si sample obtained from aqueous treatment of the *a*-Si/$LiNH_2$ intermediate (*self-absorption of diamond).

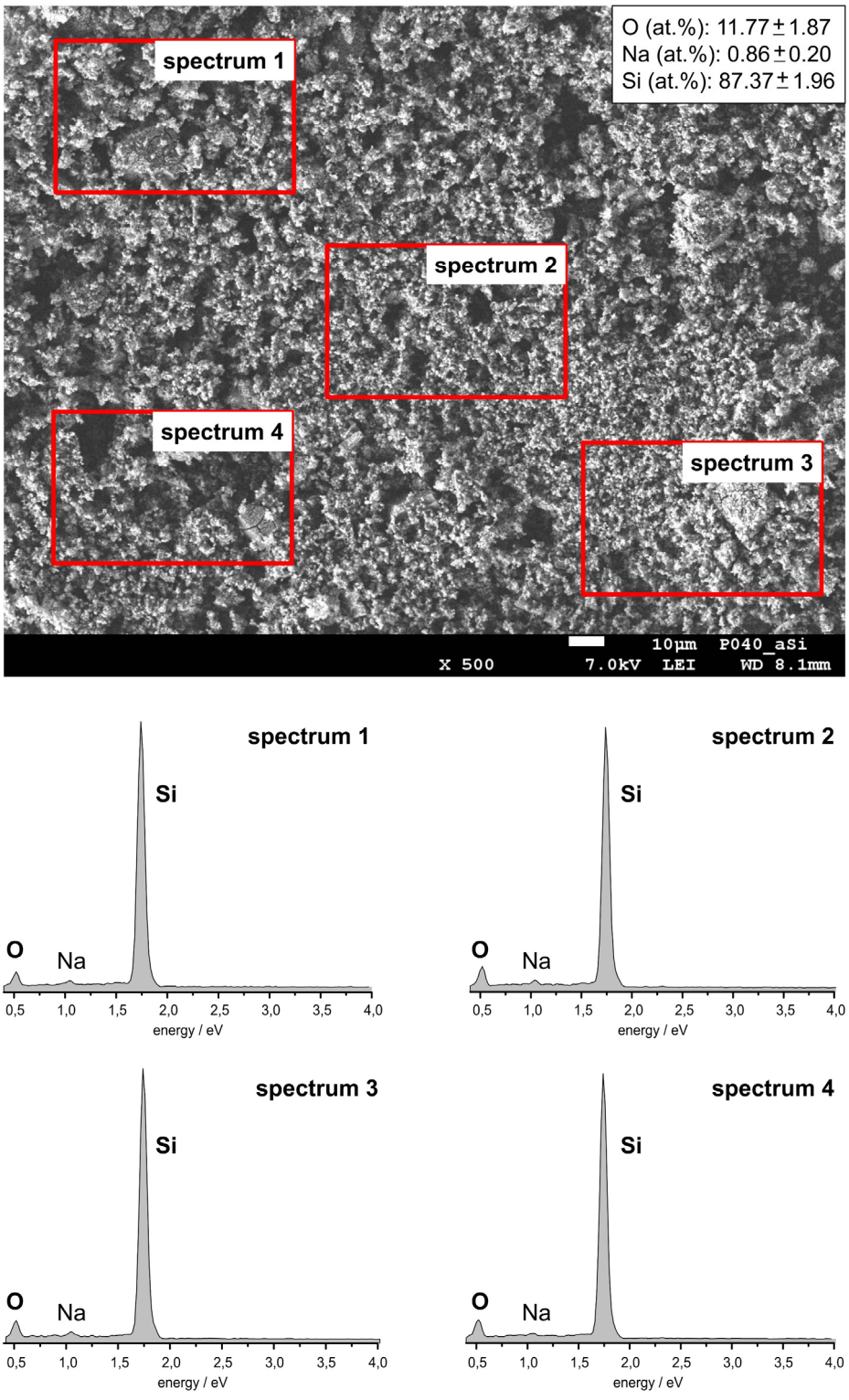

Figure S5. Results from EDX investigations of *a*-Si retained from $Li_{15}Si_4$ (data acquisition: 60 s exposure time at 7.00 kV for each spectrum).

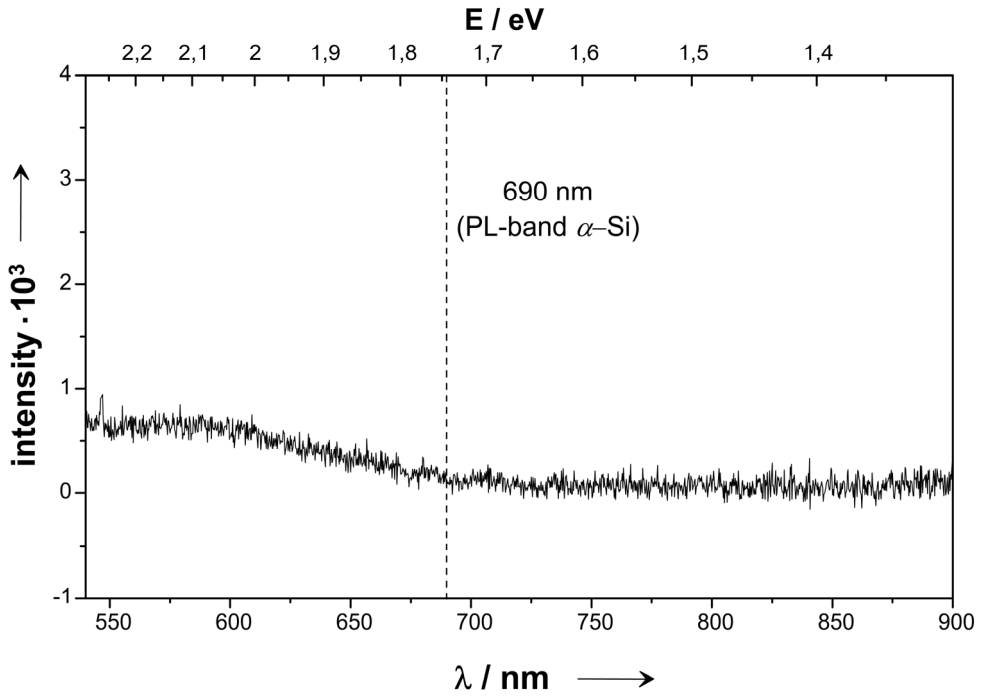

Figure S6. Photoluminescence (PL) spectrum of *a*-Si produced from $Li_{15}Si_4$ through Li-extraction with liquid ammonia and subsequent treatment with ethanol. The PL-band position expected for α-Si is indicated by a dotted line.

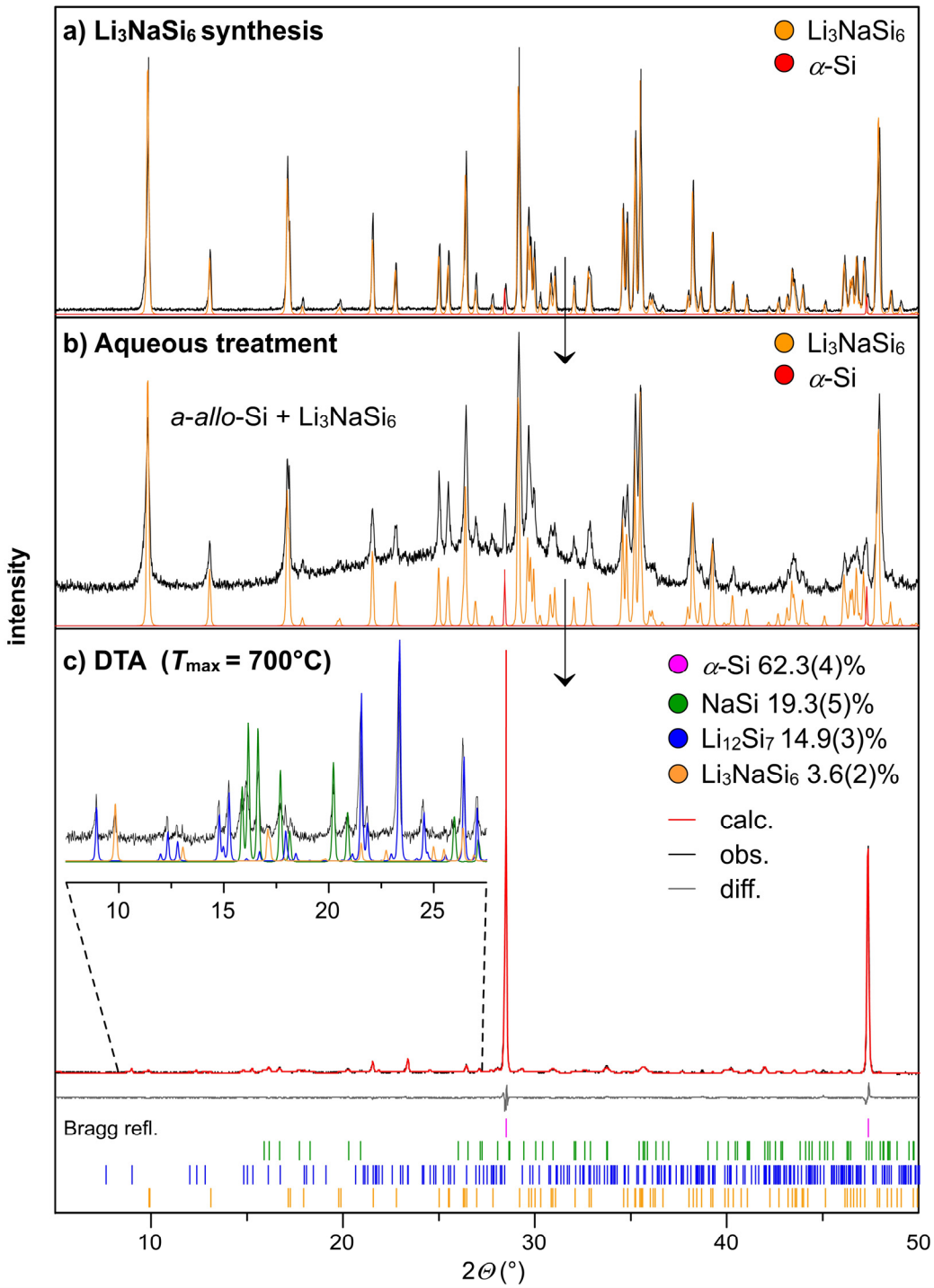

Figure S7. PXRD patterns of a) Li_3NaSi_6 (synthesized from $Li_{15}Si_4$, Na and α-Si), b) the product after partial oxidation with ethanol (15 days reaction time), and c) subsequent DTA-investigation ($T_{max.}$ = 700 °C, ±10 $Kmin^{-1}$ heating/cooling rate; calculated patterns for Li_3NaSi_6, α-Si, NaSi, and $Li_{12}Si_7$ are shown in orange, red/pink, green and blue). For the PXRD pattern shown in (c), a Rietveld fit was applied giving the weight fractions of all components.

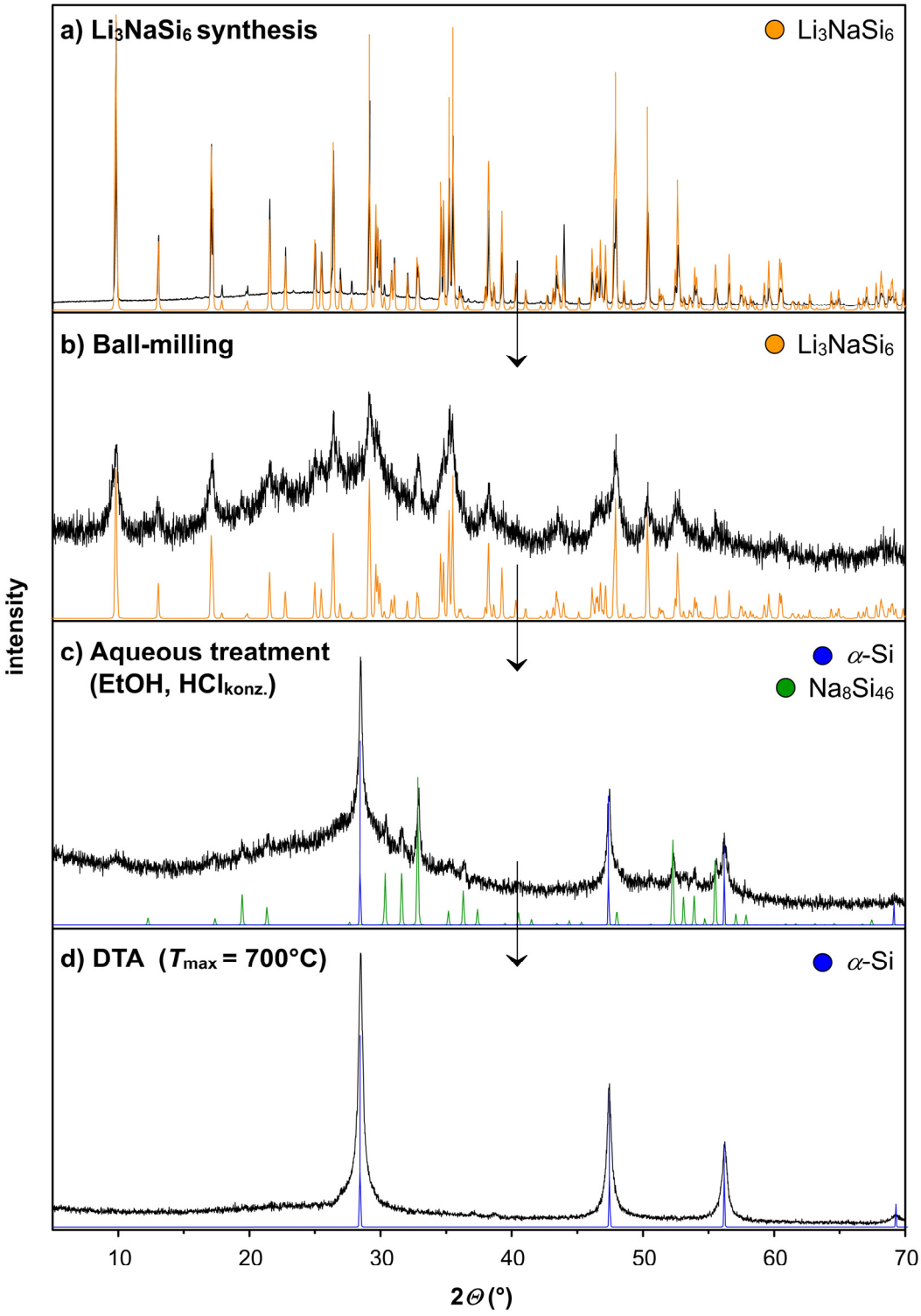

Figure S8. PXRD patterns of Li_3NaSi_6 before (a) and after ball-milling (b), the product after aqueous treatment (c) and subsequent DTA investigation (d; $T_{max.}$ = 700 °C, ±10 Kmin^{-1} heating/cooling rate; calculated patterns for Li_3NaSi_6, α-Si, and Na_8Si_{46} are shown in orange, blue, and green). Note that M_8Si_{46} (M = Na, K) are known to decompose around 600 °C (see ref. 44).

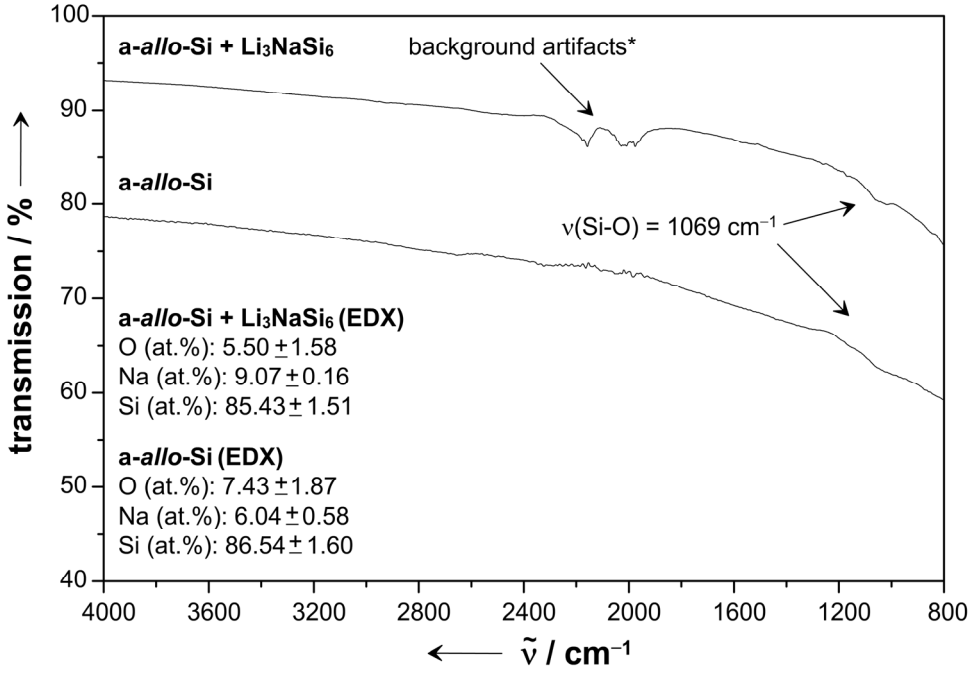

Figure S9. ATR-FT-IR spectra of partially und fully oxidized Li_3NaSi_6 through aqueous treatment (samples correspond to a mixture of Li_3NaSi_6 / *a-allo*-Si, and *a-allo*-Si, respectively). EDX results for both samples are given below. Artifacts labeled with (*) arise from the self-absorption of diamond.

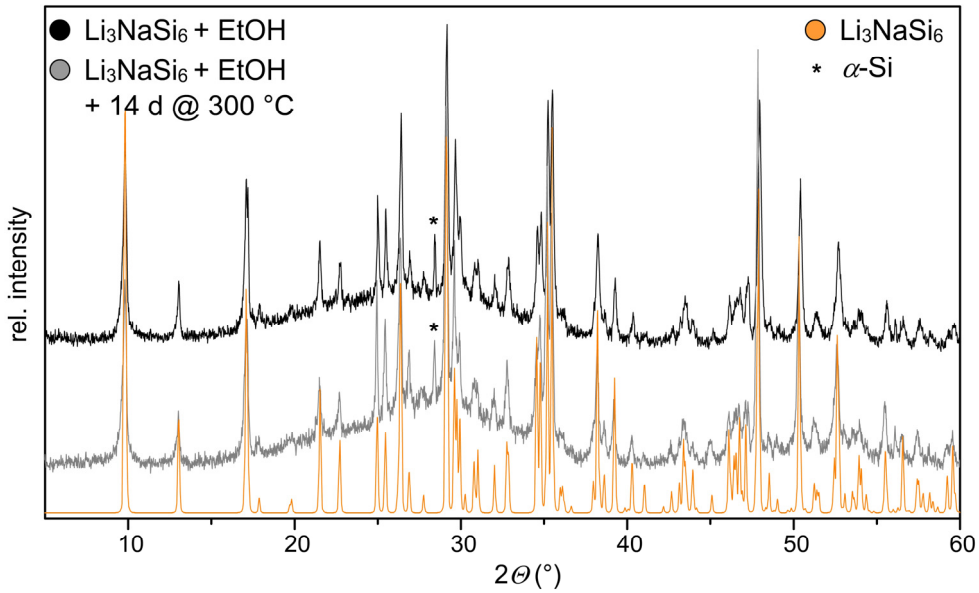

Figure S10. PXRD pattern of Li_3NaSi_6 after reaction with ethanol (15 days) and subsequent annealing at 300 °C for two weeks (calculated pattern for Li_3NaSi_6 = orange).

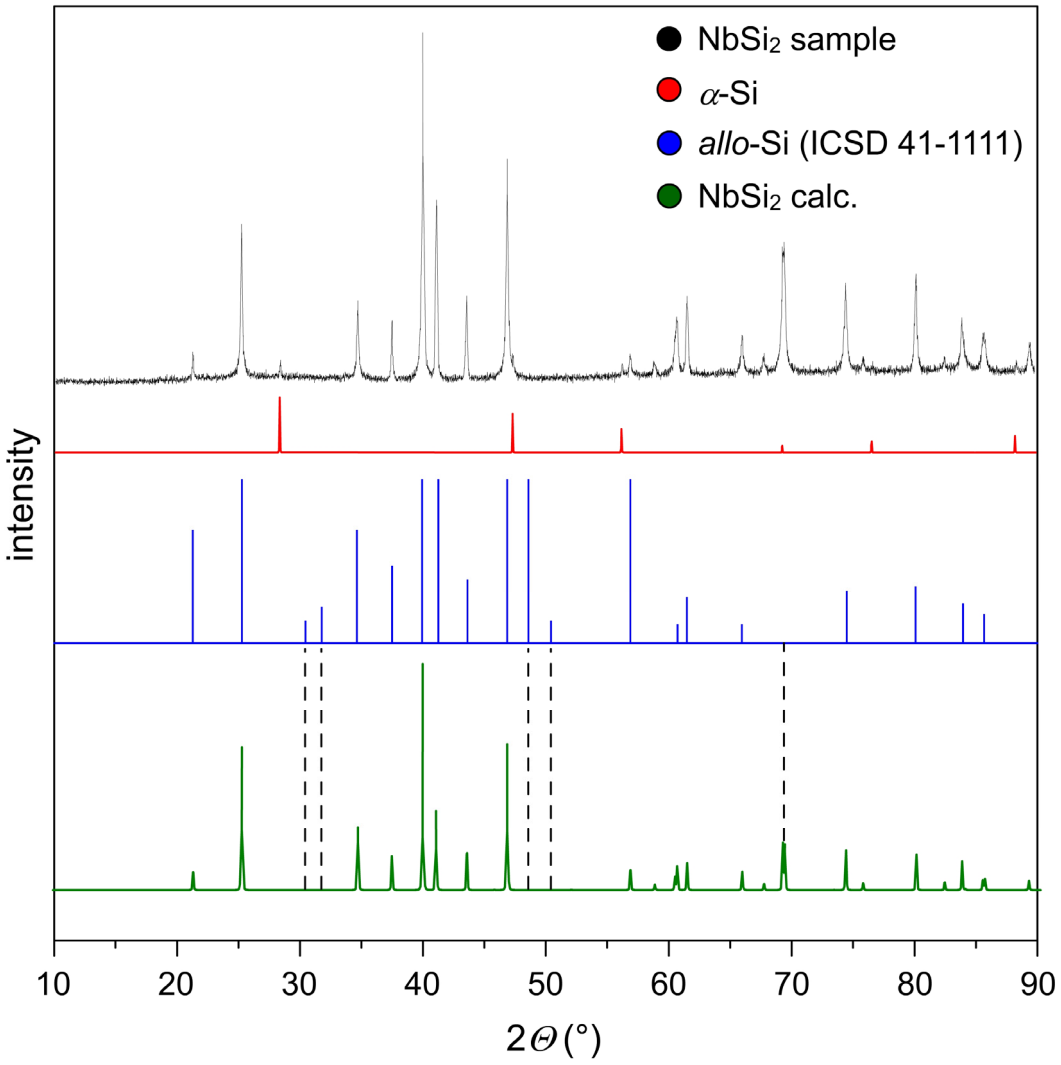

Figure S11. PXRD pattern of a $NbSi_2$ sample referenced with the database entry for α-Si (red), *allo*-Si (ICSD 41-1111, blue), and $NbSi_2$ (green). The Bragg reflection at ~68° which should be observed for $NbSi_2$ is not matched by the *allo*-Si pattern.

Computational Part

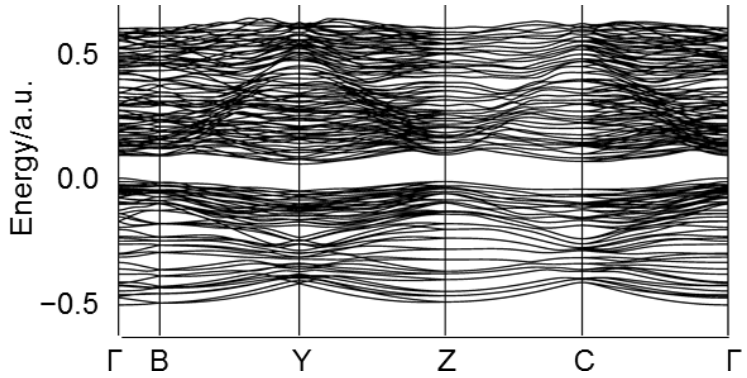

Figure S12. Band structure of **SC1** showing an indirect band gap of 1.50 eV and a direct band gap of 2.47 eV, respectively. The zero energy level corresponds to the top of the valence bands.

Table S1. Comparison of all calculated Si networks

name	ρ/g·cm^{-3}	ΔE/kJ·mol^{-1}	band gap/eV	name	ρ/g·cm^{-3}	ΔE/kJ·mol^{-1}	band gap/eV
GAa1	2.124	11.60	2.30	GCa1	2.158	9.87	2.59
GAa2	2.167	10.13	2.47	GCa2	2.165	9.81	2.60
GAa3	2.190	10.01	2.00	GCb1	2.162	10.55	2.45
GAa4	2.220	7.96	2.23	GCb2	2.154	8.74	2.61
GAa5	2.132	10.74	2.58	GDa1	2.183	13.09	2.03
GAb1	2.171	9.74	2.48	GDa2	2.095	15.89	1.86
GAb2	2.199	9.38	2.08	GDb1	2.104	14.80	2.24
GAb3	2.129	11.09	2.00	GDb2	2.166	14.16	1.55
GAb4	2.171	9.74	2.48	GDc1	2.169	14.59	1.64
GAc1	2.120	9.77	2.45	GDc2	2.093	14.21	2.03
GAc2	2.160	10.19	2.31	GDd1	2.098	16.23	2.13
GAc3	2.129	11.70	2.38	GDd2	2.177	12.13	1.61
GAc4	2.194	10.61	1.92	SA1	2.239	20.30	0.85
GAc5	2.200	8.22	1.78	SA2	2.238	19.49	1.62
GAd1	2.162	11.25	2.22	SA3	2.227	19.77	0.97
GAd2	2.196	9.79	2.04	SA4	2.233	29.07	0.77
GAd3	2.123	11.07	2.43	SB1	2.148	19.95	1.07
GAd4	2.161	9.02	2.22	SB2	2.146	15.94	1.74
GBa1	2.139	13.29	2.22	SB3	2.153	21.02	1.12
GBa2	2.144	12.64	2.56	SB4	2.167	30.32	0.73
GBa3	2.150	11.96	2.80	SC1	2.292	14.00	1.50
GBb1	2.139	12.80	2.33	SC2	2.303	16.13	1.50
GBb2	2.145	12.45	2.62	SC3	2.294	15.42	1.78
GBb3	2.152	12.07	2.69	SC4	2.286	27.23	-
GBc1	2.140	11.27	2.50	SD	2.011	13.66	1.74
GBc2	2.141	12.24	2.61	mep	2.004	9.40	2.78
GBc3	2.143	13.07	2.60	mtn	1.979	8.06	2.83
GBd1	2.140	11.26	2.73	CAS	2.127	10.66	1.84
GBd2	2.140	12.50	2.62	unj/NGS	2.105	7.70	3.01
GBd3	2.140	13.69	2.34	tum	2.180	9.76	2.54

Basis set details for Na and Li

Na: The molecular def-SVP basis set was modified as follows: The exponents of two diffuse outermost s-type functions (0.052 and 0.028) were increased to 0.25 and 0.10 by dividing the third outermost s-exponent of 0.648 by a factor of 2.5. The exponent of a diffuse outermost p-type function (0.052) was increased to 0.10 and the outermost s and p functions were combined into a single sp-type function to increase the efficiency of the CRYSTAL code. A d-type polarization function with an exponent of .265 was added by taking the average of two d-type polarization functions in set def2-TZVP basis set (exponents 0.43 and 0.10; Weigend, F.; Ahlrichs, R. *Phys. Chem. Chem. Phys.* **2005,** *7*, 3297).

Li: The molecular def-SVP basis set was modified as follows: The exponents of two diffuse outermost s-type functions (0.0528 and 0.021) were increased to 0.36 and 0.18 by dividing the third outermost s-exponent of 0.722 by a factor of 2.0. The contracted p-type polarization function with exponents of 0.45 and 0.10 was replaced by a primitive function with an exponent of 0.18 and the outermost s and p functions were combined into a single sp-type function to increase the efficiency of the CRYSTAL code.

Basis sets listed in CRYSTAL09 input format

```
11 6
0 0 5 2.0 1.0
  4098.2003908     -.58535911879E-02
  616.49374031     -.43647161872E-01
  139.96644001     -.19431465884
  39.073441051     -.48685065731
  11.929847205     -.41881705137
0 0 3 2.0 1.0
  20.659966030      .85949689854E-01
  1.9838860978     -.56359144041
  .64836323942     -.51954009048
0 0 1 1.0 1.0
  0.25              1.0000000000
0 1 1 0.0 1.0
  0.10              1.0 1.0
0 2 5 6.0 1.0
  75.401862017     .154353625324E-01
  17.274818978     .997382931840E-01
  5.1842347425     .312095939659
  1.6601211973     .492956748074
  .51232528958     .324203983180
0 3 1 0.0 1.0
  0.265             1.0


3 3
0 0 5 2.0 1.0
  266.27785516      .64920150325E-02
  40.069783447      .47747863215E-01
  9.0559944389      .20268796111
  2.4503009051      .48606574817
  .72209571855      .43626977955
0 0 1 1.0 1.0
  0.36  1.0000000000
0 1 1 0.0 1.0
  0.18  1.0 1.0
```

Structural Parameters

All structural parameters and atomic coordinates are listed in the CRYSTAL09 input format as follows:

```
Space group number
Minimal set of lattice parameters a, b, c, α, β, γ
Number of non-equivalent atoms in the assymetric unit
<atomic number> <fractional x> < fractional y> < fractional z>
```

α-Si

```
227
5.45503610 5.45503610 5.45503610 90.000000 90.000000 90.000000
1
14     1.250000000000E-01  1.250000000000E-01  1.250000000000E-01
```

GAa1

```
51
11.51968402 7.60210801 7.99343475 90.000000
7
14     2.500000000000E-01  0.000000000000E+00  3.336306420909E-01
14     2.500000000000E-01  5.000000000000E-01  3.358211129809E-01
14     2.500000000000E-01  2.554225539019E-01  1.602651561979E-01
14    -9.716186319573E-02  0.000000000000E+00  4.544689545843E-01
14    -9.839815176519E-02  5.000000000000E-01  4.662949034080E-01
14    -1.477049689831E-01 -2.559722310182E-01  3.045386908748E-01
14    -1.003273320247E-01 -3.390758160078E-01  2.995589950820E-02
```

GAa2

```
6
7.95492313 7.53697027 11.44136475 90.030957
22
14    -3.308570690944E-01  1.185735531344E-21  2.512564781479E-01
14    -3.307143575920E-01  5.000000000000E-01  2.115755298555E-01
14    -4.567366428087E-01  1.185735542298E-21 -4.129105831114E-01
14    -4.625037369079E-01  5.000000000000E-01 -4.249541371376E-01
14    -1.545829148461E-01 -2.479291033927E-01  2.290482249716E-01
14     3.074829605624E-01 -2.565855541145E-01  3.338479321754E-01
14     3.266059259271E-02 -3.399192051343E-01  3.806010482918E-01
14    -4.410515326580E-01  1.185735547712E-21 -1.096843392947E-01
14    -4.703027360977E-01 -5.000000000000E-01 -1.189239300664E-01
14     3.037558758881E-01 -2.373519759800E-01  1.291255811344E-01
14     2.774089339692E-02 -1.646773157259E-01  6.966900818622E-02
14     3.350195629936E-01  1.185735522207E-21 -2.575190594118E-01
14     3.377085729811E-01  5.000000000000E-01 -2.734869698881E-01
14     4.486247504013E-01  1.185735550446E-21  3.938362953050E-01
14     4.799100701424E-01  5.000000000000E-01  3.744542745197E-01
14     1.597315330547E-01 -2.568125929163E-01 -2.631744294154E-01
14    -3.022823035631E-01 -2.566097714812E-01 -3.685895714783E-01
14    -2.747480612895E-02 -3.368014325965E-01 -4.169901208292E-01
14     4.832009635135E-01  1.185735553911E-21  8.788461276686E-02
14     4.400596392568E-01  5.000000000000E-01  7.383454354127E-02
14    -2.975098087572E-01 -2.607247673881E-01 -1.630832310750E-01
14    -2.184076426449E-02 -3.338415735472E-01 -1.027557995745E-01
```

GAa3

```
59
11.43732402 7.46648355 7.94834712 90.000000
7
14    -5.000000000000E-01  0.000000000000E+00  3.308634430102E-01
14    -5.000000000000E-01 -5.000000000000E-01  3.336502288773E-01
14    -5.000000000000E-01  2.577688215275E-01  1.527536060586E-01
14     1.537619332775E-01  0.000000000000E+00  4.723801417456E-01
14     1.503059970699E-01 -5.000000000000E-01  4.493102626383E-01
14     1.026528996772E-01  2.387486104244E-01  3.010401792182E-01
14     1.628198749591E-01  1.679123108520E-01  2.572478686383E-02
```

GAa4

```
57
7.88777246 11.34980856 7.48053954 90.000000 90.000000 90.000000
6
14     3.308401228268E-01  2.776393443943E-01 -2.500000000000E-01
14    -1.533866339042E-01 -2.500000000000E-01  0.000000000000E+00
14     4.364442887590E-01 -4.150174140047E-01  2.500000000000E-01
14     4.850386860133E-01 -3.876989632456E-01 -2.500000000000E-01
14     3.014252175481E-01 -3.528420841575E-01 -1.157353482175E-02
14     2.500083519762E-02 -4.131219487405E-01 -8.545510489538E-02
```

GAa5

```
53
7.62005107 7.96949177 11.48081914 90.000000
6
14     0.000000000000E+00 -3.356932538554E-01 -2.623061297915E-01
14    -2.500000000000E-01 -1.614369712208E-01 -2.500000000000E-01
14    -5.000000000000E-01 -4.725965273923E-01  3.991156159656E-01
14     0.000000000000E+00 -4.464592422698E-01  4.055164554202E-01
14    -2.577013312525E-01 -3.043600559211E-01  3.523764677403E-01
14    -3.406789048650E-01 -2.913883652888E-02  3.990176361547E-01
```

GAb1

```
12
22.86874316 7.54679951 7.93493979 90.102551
11
14    -1.340795586098E-01  2.261847200735E-18 -3.350824571481E-01
14    -1.173181927276E-01 -5.000000000000E-01 -3.325580185760E-01
14     2.044925145484E-01 -1.980271610523E-17 -4.373571242234E-01
14     1.979090873799E-01 -5.000000000000E-01 -4.797390345728E-01
14     1.269270793314E-01 -2.514402651751E-01  1.574937861765E-01
14     1.769659845633E-01 -2.620401156207E-01 -3.008356719040E-01
14     2.068503260275E-01 -3.348165171401E-01 -2.434801346658E-02
14     5.130723416901E-02  2.788277178583E-18 -4.753109129268E-01
14     4.711221246905E-02 -5.000000000000E-01 -4.475264412154E-01
14     7.447568108203E-02 -2.425776359688E-01 -3.045438390833E-01
14     5.073871633496E-02 -1.602681902517E-01 -2.932800132083E-02
```

GAb2

```
35
7.47283467 22.82357067 7.92704399 90.000000
13
14     0.000000000000E+00 -5.000000000000E-01  3.257616970615E-01
14     0.000000000000E+00  0.000000000000E+00  3.262657629855E-01
14     2.568936234327E-01  2.059291174921E-17  1.464239341829E-01
14     5.000000000000E-01  1.715509271810E-01  4.343298008063E-01
14     0.000000000000E+00  1.770596331105E-01  4.750966580626E-01
14     2.599894759386E-01  5.145631255370E-02 -3.064804135725E-01
14     3.319811801301E-01  8.193263213140E-02 -3.119199284081E-02
14     0.000000000000E+00  2.592039941030E-01 -3.382203813783E-01
14    -2.500000000000E-01  2.500000000000E-01 -1.596459874479E-01
14     5.000000000000E-01  7.538572616620E-02 -4.781707470387E-01
14     0.000000000000E+00  7.695148912717E-02 -4.544789074685E-01
14    -2.384544153694E-01  1.988119487109E-01  2.953287972102E-01
14    -1.656098527197E-01  1.691267788097E-01  1.931205933211E-02
```

GAb3

```
35
7.61259950 22.99784657 7.97834643 90.000000
13
14    -1.516028706329E-20 -2.425218964616E-01  3.305725291427E-01
14    -2.500000000000E-01  2.500000000000E-01  1.563608910109E-01
14    -1.008594493835E-20  7.557317132660E-02  4.510427608286E-01
14    -5.000000000000E-01  7.682342536707E-02  4.607230444884E-01
14    -2.576816667795E-01  1.989214515800E-01 -3.093137666044E-01
14    -3.407459619346E-01  1.757207847793E-01 -3.429073263372E-02
14    -1.359096035029E-21  1.932253964954E-39 -3.369838293810E-01
14    -1.359096035029E-21 -5.000000000000E-01 -3.415668850266E-01
14    -2.560166859699E-01  0.000000000000E+00 -1.651319748471E-01
14     2.305364761610E-21  1.712516465771E-01 -4.502808117513E-01
14    -5.000000000000E-01  1.767499238514E-01 -4.786851965393E-01
14     2.561861384154E-01  5.124958395992E-02  3.000329287637E-01
```

```
14     3.393132608228E-01  7.507441292378E-02  2.512612790983E-02
```

GAb4

```
12
22.86831111 7.54631619 7.93466666 89.898170
11
14    -1.173162858903E-01 -5.000000000000E-01  3.325862857015E-01
14    -1.340682369037E-01 -4.445273715588E-17  3.350196293937E-01
14     5.131247315794E-02  6.679809623087E-18  4.753211287382E-01
14     4.711229292678E-02  5.000000000000E-01  4.475108632253E-01
14     1.269372204135E-01  2.514813166892E-01 -1.574690417449E-01
14     7.447846296758E-02  2.425718035937E-01  3.045255063905E-01
14     5.073881123783E-02  1.602720064215E-01  2.931140850500E-02
14     2.044776993101E-01 -4.229657275404E-18  4.374281674220E-01
14     1.979154293482E-01  5.000000000000E-01  4.797493713033E-01
14     1.769645890401E-01  2.620275014843E-01  3.008707488997E-01
14     2.068533289797E-01  3.348195006807E-01  2.439487768602E-02
```

GAc1

```
63
7.67033413 15.86240204 11.52902569 90.000000
7
14     5.000000000000E-01 -1.563434594731E-01 -2.500000000000E-01
14     0.000000000000E+00 -1.771758565861E-01 -2.500000000000E-01
14     2.359779368353E-01  8.057260000981E-02  2.500000000000E-01
14     0.000000000000E+00  2.399270933515E-01 -4.005535232688E-01
14     0.000000000000E+00 -2.798383265381E-01 -4.036143125005E-01
14     2.384183851412E-01  1.530644509859E-01 -3.522113430500E-01
14     1.571626211551E-01  1.512684972447E-02 -3.998934582414E-01
```

GAc2

```
8
15.90655125 7.54915599 11.46071405 90.026562
22
14    -1.659747257477E-01  5.000000000000E-01  2.513693253843E-01
14    -1.440924600222E-01 -2.215848872839E-17  2.526062384774E-01
14     2.780364647864E-01  2.938403236946E-17 -4.005944076960E-01
14    -2.169378025776E-01  1.350635576160E-17 -3.964237347542E-01
14    -6.743806173531E-02 -2.662404567391E-01  2.496475513448E-01
14     1.637162728157E-01  2.608298738608E-01  3.547809724436E-01
14     2.643580300174E-02  3.406233847177E-01  4.035929050738E-01
14     2.829344968645E-01  1.351430628542E-17 -9.411202188344E-02
14    -2.198040438826E-01 -1.879973527147E-18 -9.278811523899E-02
14     1.618371771266E-01  2.622754334891E-01  1.496668225228E-01
14     2.419245194127E-02  3.358351965944E-01  8.883102451039E-02
14     1.769428910899E-01  5.000000000000E-01 -2.375644014387E-01
14     1.787753912587E-01  4.434381159996E-18 -2.515440110697E-01
14     2.332153153769E-01 -1.451977931512E-17  4.058267228394E-01
14    -2.490409025385E-01 -5.971255987272E-20  4.036617605200E-01
14     8.975577653030E-02  2.473409679996E-01 -2.426493970969E-01
14    -1.410403662426E-01 -2.548483767646E-01 -3.478276711894E-01
14    -3.661878110983E-03 -3.376996062203E-01 -3.944936761957E-01
14     2.318285953005E-01  1.131335588558E-18  9.765475232969E-02
14    -2.500010567451E-01 -3.112949208385E-17  1.050663445082E-01
14    -1.394054317599E-01 -2.453197188619E-01 -1.428894906207E-01
14    -1.832825148330E-03 -1.679738162261E-01 -8.325326678168E-02
```

GAc3

```
64
7.59110323 16.01372881 11.49003408 90.000000
6
14    -5.000000000000E-01  1.677657393491E-01  2.578999759794E-01
14     2.500000000000E-01  8.065073927843E-02  2.500000000000E-01
14     0.000000000000E+00 -2.721773036127E-01 -3.993640725212E-01
14     0.000000000000E+00  2.314958964385E-01 -4.051875598673E-01
14    -2.456293564192E-01  1.517380201210E-01 -3.524503268273E-01
14    -1.613365185025E-01  1.468844377344E-02 -3.991011230994E-01
```

GAc4

```
64
7.44740202 15.92651865 11.42654329 90.000000
6
14    -5.000000000000E-01 -8.441695590100E-02  2.557604547938E-01
14     2.500000000000E-01 -1.738812231366E-01  2.500000000000E-01
14     5.000000000000E-01 -1.721191595594E-02 -4.018750616111E-01
14     0.000000000000E+00 -2.138430954586E-02 -4.018575237245E-01
14     2.552877887534E-01 -9.955603273772E-02 -3.525282886114E-01
14    -1.692747071907E-01  2.632524699805E-01 -4.121409513935E-01
```

GAc5

```
63
7.51336682 15.76884262 11.40574050 90.000000
7
14     5.000000000000E-01  9.708832510940E-02 -2.500000000000E-01
14     0.000000000000E+00  7.256071752163E-02 -2.500000000000E-01
14     2.307579956379E-01 -1.733670236419E-01  2.500000000000E-01
14     0.000000000000E+00 -2.808080668871E-02 -4.053803751846E-01
14     5.000000000000E-01 -1.057152891076E-02 -3.989557190020E-01
14    -2.616447265754E-01 -9.895900672270E-02 -3.528341428131E-01
14     1.639327882210E-01  2.632184695324E-01 -4.145208531868E-01
```

GAd1

```
12
15.97468510 7.51335364 13.97321350 124.903903
11
14    -4.552396378288E-02 -2.125092300497E-18  2.448146802978E-01
14    -3.648184340956E-02  5.000000000000E-01  2.581030947573E-01
14     7.147830599262E-02 -2.458188264567E-17 -4.025116318239E-01
14    -4.331916184505E-01 -8.366756564251E-18 -4.024229292956E-01
14    -4.822765631250E-02  2.472179353111E-01 -2.532556027169E-01
14    -3.268988144364E-01  2.446115347914E-01 -3.533352657203E-01
14    -2.194706671648E-01  1.684011018444E-01 -4.128590207199E-01
14     2.197924519322E-01 -2.749629249132E-17 -9.573838383623E-02
14    -2.795318362484E-01  3.689755503755E-18 -1.008457734123E-01
14    -2.260714755083E-01 -2.542933587715E-01 -1.483923295199E-01
14    -6.539516701884E-02  3.369232552332E-01 -1.011621571080E-01
```

GAd2

```
42
22.85553701 7.49812251 15.80198454 90.000000
13
14     0.000000000000E+00 -3.139961861997E-17 -1.656096975158E-01
14     0.000000000000E+00  5.000000000000E-01 -1.404125105905E-01
14     0.000000000000E+00 -2.307388899743E-01 -6.460659735280E-02
14    -1.727993131672E-01  6.280917598545E-17  2.795995431036E-01
14    -1.750206326666E-01 -1.570488440399E-17 -2.184555033887E-01
14     5.130618903346E-02  2.381895668954E-01  1.628579597942E-01
14     8.211143254135E-02 -1.639880161808E-01  2.517074188874E-02
14     2.453278174297E-01  2.747577606313E-17  1.765030899008E-01
14    -2.500000000000E-01 -2.500000000000E-01  8.762164822057E-02
14    -7.799477862238E-02 -3.139908759761E-17 -2.669736538520E-01
14    -7.337386297788E-02  3.142209542669E-17  2.522252845071E-01
14     1.987801858812E-01 -2.550038998487E-01 -1.396093839386E-01
14     1.687968074605E-01  3.315155714438E-01 -1.720671287193E-03
```

GAd3

```
42
23.04554151 7.64227689 15.90204450 90.000000
13
14    -2.524490477796E-01 -4.192196157339E-21 -1.638594986435E-01
14    -2.500000000000E-01 -2.500000000000E-01 -7.710665601062E-02
14     7.676093679912E-02 -2.053824811723E-20  2.827384005768E-01
14     7.503590552973E-02 -2.704777918438E-20 -2.348104008724E-01
14    -1.988874547527E-01  2.454596926519E-01  1.561858433279E-01
14    -1.758464716042E-01 -1.607951061293E-01  1.855376846119E-02
14     0.000000000000E+00 -8.736885265302E-21  1.810151920605E-01
14     0.000000000000E+00  5.000000000000E-01  1.607968759359E-01
14     0.000000000000E+00  2.359980648966E-01  8.463109658581E-02
14     1.740093573094E-01 -2.723787462468E-20 -2.697748666672E-01
14     1.732159211573E-01 -1.857177967917E-20  2.365883361796E-01
```

```
14    -5.114230336473E-02 -2.392999289423E-01 -1.486515050672E-01
14    -7.530878851271E-02  1.576218887930E-01 -1.086182929526E-02
```

GAd4

```
12
15.83112051 7.58543777 13.92366345 124.611090
11
14    -2.717676555532E-02 -5.000000000000E-01 -2.453736257825E-01
14    -5.288787944307E-02 -1.191159455779E-18 -2.507569950352E-01
14     2.321001711716E-01  1.770852553607E-17  4.054474907005E-01
14     2.072854819979E-01 -5.000000000000E-01  3.972050402193E-01
14    -4.852044945427E-02  2.331662621515E-01  2.454925014840E-01
14     2.725221988499E-01 -2.606831013570E-01  3.511081845864E-01
14    -6.580750244005E-02  1.586675127916E-01  3.992454030486E-01
14     7.580868458738E-02  6.095918184642E-18  9.475002957414E-02
14     6.191916789540E-02 -5.000000000000E-01  9.967252532011E-02
14     1.720500537468E-01  2.617945136152E-01  1.460189645837E-01
14    -2.206146781438E-01  1.632778918450E-01  8.473735556635E-02
```

GBa1

```
11
7.50768768 11.67031708 7.93400123 90.405423
10
14     1.226052793064E-01 -2.500000000000E-01  4.174032163198E-01
14    -3.727285076445E-01 -2.500000000000E-01  4.170450262641E-01
14    -1.198992235383E-01 -2.500000000000E-01 -4.070511528300E-01
14     3.717879786897E-01 -2.500000000000E-01 -4.075777388064E-01
14     1.207958781465E-01 -9.865440495299E-02  2.246270017454E-01
14    -3.698252989899E-01 -9.999163152596E-02  2.044210418223E-01
14     1.150234054224E-01  1.505544089351E-01 -4.668196506009E-02
14    -3.644115321988E-01  1.473911305826E-01 -5.769283656006E-02
14     3.708022829628E-02  9.490077683004E-02  2.303290224265E-01
14    -2.904640717571E-01  9.564678547020E-02  2.249289927922E-01
```

GBa2

```
3
7.52041460 7.91436660 11.64968695 90.068657
18
14    -1.375502660084E-36 -4.049346519515E-01  0.000000000000E+00
14    -5.000000000000E-01 -4.046822938487E-01  0.000000000000E+00
14    -2.458130347341E-01  4.199737672524E-01 -9.744016624059E-04
14     2.468164585656E-01  2.116775971957E-01  3.463068637762E-01
14    -2.436519471677E-01  2.435198828764E-01  3.531968689049E-01
14     2.387957018350E-01 -4.327476337487E-02  1.082684770004E-01
14    -2.407503410234E-01 -3.676539380398E-02  9.374848236063E-02
14     1.616492655958E-01  2.389148118166E-01  1.543829044454E-01
14    -1.653107384141E-01  2.417595612513E-01  1.553747282788E-01
14    -2.475366755268E-01  4.306100898873E-01 -4.860389664234E-01
14    -1.084202172486E-19 -3.938232100860E-01 -5.000000000000E-01
14    -5.000000000000E-01 -3.951911230093E-01 -5.000000000000E-01
14    -6.440677660826E-03 -2.119190991167E-01  1.516294788356E-01
14    -4.953206388950E-01 -1.917944450558E-01  1.503900746391E-01
14    -9.118783363616E-03  6.010035726075E-02  4.007054889541E-01
14    -4.884728454206E-01  7.091694247485E-02  3.976743197906E-01
14    -9.064680200223E-02 -2.171151511272E-01  3.455730458414E-01
14    -4.136208489557E-01 -2.117735180888E-01  3.462277261175E-01
```

GBa3

```
14
7.89277567 11.62356723 7.53554381 90.390618
8
14     4.181580594609E-01  2.355793770366E-01 -3.767326467415E-01
14    -4.073406444375E-01  2.512544003909E-01 -1.256684624017E-01
14    -1.985806417380E-01 -9.568279485757E-02  3.709550818782E-01
14    -2.312387312652E-01 -1.030312487842E-01 -1.177059286281E-01
14     5.705914946373E-02  1.418408744049E-01  3.620268857579E-01
14     4.961926559686E-02  1.564461870561E-01 -1.170554403365E-01
14    -2.256907886647E-01  9.634386350654E-02  2.828862373657E-01
14    -2.289039891908E-01  9.530539274734E-02 -3.921506324302E-02
```

GBb1

```
13
23.29685296 7.93232395 12.27226127 17.843820
9
14    -5.000000000000E-01 -4.166300973316E-01 -2.500000000000E-01
14    -2.775557561563E-17 -4.201418897328E-01 -2.500000000000E-01
14     2.536764634918E-01  4.067597355660E-01  2.395731501838E-01
14     4.285495638368E-01  2.240156325251E-01  2.398436670755E-01
14    -8.121986844578E-02  2.065596146343E-01  2.642923961663E-01
14     3.066317530315E-01 -5.080406885744E-02  2.281771398459E-01
14    -2.042669784508E-01 -5.627134483975E-02  2.691135561743E-01
14     4.132207164350E-01  2.266293894226E-01  7.533011254131E-02
14    -2.588727919742E-01  2.258888308557E-01  4.247386417974E-01
```

GBb2

```
8
7.52518207 23.28413238 7.90955733 90.456101
18
14     2.522523948323E-01 -1.540743955510E-33 -3.966817952767E-01
14    -2.411002435750E-01 -2.018558256493E-17 -3.939324003501E-01
14    -5.651595889631E-04 -1.971248297356E-19  4.282297182280E-01
14    -4.905049627374E-01  1.540743955510E-33  4.309565749289E-01
14    -3.463844570479E-03 -1.776277673991E-01  2.545279631771E-01
14    -4.907008008834E-01 -1.722680088860E-01  2.186905600036E-01
14    -5.345119360126E-03 -5.002544160141E-02 -2.318660291786E-02
14    -4.848032019303E-01 -5.117763877431E-02 -3.819647503789E-02
14    -8.293483994214E-02 -7.895103555189E-02  2.541070973004E-01
14    -4.077944278726E-01 -7.582100804695E-02  2.449219785851E-01
14     4.685366134633E-03  2.583493687914E-01  4.398690971722E-01
14     2.557869361963E-01 -2.483510148299E-01 -3.857297397794E-01
14     2.484100389903E-01 -7.457998719302E-02 -1.838701488867E-01
14    -2.405890332468E-01 -7.667217507796E-02 -2.016488029204E-01
14     2.412582820949E-01 -1.948728751710E-01  7.866093960621E-02
14    -2.373566988638E-01 -2.043980974883E-01  7.155351586878E-02
14     1.651840158407E-01 -1.717525589894E-01 -2.048583560921E-01
14    -1.580326870526E-01 -1.744135513952E-01 -2.057470748440E-01
```

GBb3

```
13
23.26527697 7.88633680 12.24148553 162.089846
9
14     5.551115123126E-17  4.099262984061E-01  2.500000000000E-01
14     5.000000000000E-01  4.063162094375E-01  2.500000000000E-01
14     2.448492124631E-01 -4.173906536576E-01 -2.431624780413E-01
14    -3.323751319196E-01  2.323476049395E-01  2.300050715683E-01
14     1.731622850653E-01  1.965071481868E-01  2.529741337068E-01
14    -4.571184570254E-01 -4.472675549684E-02  2.358876449565E-01
14     6.504091622742E-02 -6.041255179964E-02  2.782051109943E-01
14     4.900739083163E-01  2.328228542854E-01  7.265644929330E-02
14     1.641433761235E-01  2.234837519548E-01  4.272718225120E-01
```

GBc1

```
11
8.66677409 11.67118177 7.56979337 65.133505
10
14    -1.037761682431E-01  2.500000000000E-01  4.370097383711E-01
14    -5.898026630138E-02  2.500000000000E-01 -9.943158876504E-02
14     8.214886777477E-02  2.500000000000E-01  1.040029666026E-01
14     1.005598330066E-01  2.500000000000E-01 -4.352343411944E-01
14     2.651672478786E-01 -1.009002174400E-01  1.600669824242E-03
14     3.063557744891E-01 -9.869890436694E-02  4.658623544045E-01
14    -4.579035478662E-01  1.503816417396E-01 -1.354291110749E-01
14    -4.359296357174E-01  1.476233518170E-01  3.257997792526E-01
14     2.646445742743E-01  9.385841892323E-02  8.379772978969E-02
14     2.799900387630E-01  9.502296200378E-02  3.954541355577E-01
```

GBc2

```
5
7.53763698 15.81223377 11.65174918 89.650278
18
14     3.117713003799E-17 -3.011839721123E-01  0.000000000000E+00
14    -1.558856501899E-17  2.201417296287E-01  0.000000000000E+00
```

```
14    -2.353744904740E-01 -2.038439945826E-01  2.180138713933E-03
14     2.442709457102E-01 -1.052072287719E-01 -3.539096781139E-01
14    -2.425959397989E-01 -1.089093024260E-01 -3.450620532195E-01
14    -2.354658256189E-01  2.632292176078E-02 -8.969221652541E-02
14     2.371044364583E-01  2.772630470721E-02 -1.122558840512E-01
14     1.613248363817E-01 -1.140107007209E-01 -1.589730976965E-01
14    -1.593324165873E-01 -1.120162105481E-01 -1.511461092341E-01
14    -2.446930352738E-01 -2.091411098347E-01 -4.905479615936E-01
14     6.158268339718E-17 -2.993003862537E-01 -5.000000000000E-01
14    -3.209238430557E-17  2.068229071157E-01 -5.000000000000E-01
14    -4.936208527949E-01  9.759324469761E-02 -1.512791206408E-01
14    -4.654126419475E-03  1.173381149357E-01 -1.496034017994E-01
14    -4.923695332292E-01 -3.028669973814E-02 -3.977416617996E-01
14    -5.197397081012E-03 -2.181742479372E-02 -4.004447650968E-01
14    -4.124984738800E-01  1.105474769731E-01 -3.463268962269E-01
14    -8.734105521930E-02  1.169744691525E-01 -3.448428612807E-01
```

GBc3

```
14
8.77580703 11.62939017 7.51063379 64.804899
8
14     4.184560977152E-01  2.404677882972E-01 -8.226828174646E-02
14    -4.070112863368E-01  2.523194869420E-01  8.063233118433E-02
14    -2.110633201787E-01 -1.035358610872E-01  4.721249627912E-01
14    -2.184170824256E-01 -9.453762790406E-02 -1.353051839225E-02
14     5.430825246051E-02  1.378373710884E-01  3.445419853685E-01
14     5.197246373771E-02  1.601447468772E-01 -1.415848594938E-01
14    -2.278248381097E-01  9.262408335898E-02  4.025762489968E-01
14    -2.240362443623E-01  1.001375909167E-01  7.480160623443E-02
```

GBd1

```
15
23.31004099 15.74882190 12.23354769 161.979260
9
14     0.000000000000E+00 -3.013150886029E-02  2.500000000000E-01
14     5.000000000000E-01 -5.063746250088E-02  2.500000000000E-01
14    -2.650495893375E-01  4.613645737666E-02 -2.786519301401E-01
14    -8.001912986068E-02  1.335898442016E-01 -2.598459105700E-01
14     4.297979936088E-01  1.516205624480E-01 -2.401145287221E-01
14     2.835050500837E-01 -2.244590895330E-01 -2.759092188907E-01
14    -1.821254751307E-01 -2.219766369090E-01 -2.232146328894E-01
14     4.193236477330E-01  1.368206653298E-01 -6.829890445032E-02
14    -2.628949810755E-01  1.362120865220E-01 -4.302386078743E-01
```

GBd2

```
8
7.53251971 23.31904907 8.78935269 64.150537
18
14    -5.033601794929E-02  1.540743955510E-33 -4.046984464523E-01
14     4.403077028279E-01  0.000000000000E+00 -3.647825481466E-01
14     2.933485746542E-01  0.000000000000E+00  4.480451145360E-01
14    -2.282576577972E-01  2.015535775916E-17  4.352037449339E-01
14    -1.257864066929E-01 -1.755959747778E-01  2.417817766605E-01
14     3.777804179741E-01 -1.737732244832E-01  2.541444040719E-01
14     6.318377769970E-04 -5.142275882289E-02 -2.639799568013E-02
14    -4.802400314429E-01 -4.967023899119E-02 -1.251472344700E-02
14     4.594163538815E-01 -7.723772231652E-02  2.644903425468E-01
14    -2.160336378247E-01 -7.797057415409E-02  2.561506671697E-01
14    -2.260753980266E-01  2.529335426284E-01  4.518516864841E-01
14     4.353670661507E-01  2.490653449042E-01 -3.736120733983E-01
14    -1.552833053431E-01 -7.520309279061E-02 -1.986706465436E-01
14     3.388360258104E-01 -7.531918231976E-02 -1.634591217577E-01
14    -2.976852572897E-01 -2.035873142310E-01  8.354009386840E-02
14     2.134485322277E-01 -1.956056008244E-01  8.872767875556E-02
14     4.342952858101E-01 -1.720986534006E-01 -1.932465200971E-01
14    -2.375227838793E-01 -1.734154528433E-01 -1.943045010686E-01
```

GBd3

```
15
7.49563277 15.88947064 12.24114924 107.669141
9
14     5.551115123126E-17 -2.011985516124E-01 -2.500000000000E-01
14     5.000000000000E-01 -2.063539472313E-01 -2.500000000000E-01
14    -2.575543551420E-01  2.086577033066E-01 -2.557410111790E-01
```

```
14     3.327086972727E-01 -1.100301426678E-01  4.025036973140E-01
14    -1.800194064824E-01 -1.040987995372E-01  3.992128521818E-01
14     4.563110202346E-01  2.291609287399E-02 -3.491856508882E-01
14    -5.889764383178E-02  2.900397488350E-02 -3.525960836208E-01
14    -1.620000901152E-01 -1.117557629972E-01 -4.048176451530E-01
14    -4.900715284773E-01 -1.154250115981E-01 -4.033479594156E-01
```

GCa1

```
5
12.11953109 7.97220424 7.53190587 108.780110
9
14     3.351173003643E-22 -3.420864099329E-01 -8.495002510058E-23
14     1.387778780781E-17 -3.388084300156E-01 -5.000000000000E-01
14     1.651133490462E-03 -1.635109540398E-01  2.437808361144E-01
14    -1.546691245689E-01  4.641871118796E-01 -7.166713440931E-02
14     3.497601015777E-01 -5.636497786533E-02  4.143337570341E-01
14     8.831247972003E-02  2.944633804878E-01 -1.942064035719E-01
14     1.164536415398E-01  2.988411242899E-01  3.007484461508E-01
14     1.523638152470E-01  2.431403243509E-02 -8.507486130570E-02
14     1.581335699761E-01  1.968770278711E-02  2.428421456268E-01
```

GCa2

```
5
12.10087582 7.94450060 7.52897198 108.431755
9
14     1.677897628787E-02 -3.450186979728E-01 -2.446906641658E-01
14    -1.670477943808E-52 -1.708605248248E-01 -3.370431415997E-36
14     5.551115123126E-17 -1.657794115091E-01 -5.000000000000E-01
14     3.408406006485E-01 -6.607057332144E-02  1.745187088107E-01
14    -1.461490964442E-01  4.653990827291E-01 -3.308645425737E-01
14     1.043665726588E-01  2.966802219096E-01  6.184291781082E-02
14     9.982838959599E-02  2.870901042167E-01 -4.574772804000E-01
14     1.525156007571E-01  1.667266386960E-02  1.633433492839E-01
14     1.574404322246E-01  1.710216673621E-02  4.901335672851E-01
```

GCb1

```
9
8.82983478 11.45727996 7.51075752 115.183551
8
14    -3.437756783375E-01 -7.681978042536E-03 -4.210688174929E-01
14    -1.671363416680E-01  7.862004057199E-04 -8.287903789743E-02
14     4.486977410626E-01  1.519473356473E-01  4.675460605776E-01
14    -4.808859897596E-02 -3.465884365455E-01 -1.571536125013E-02
14     2.950004578101E-01 -1.142026605491E-01  1.516239995888E-01
14     2.898132005683E-01 -9.051373531018E-02 -3.580392166728E-01
14     1.775695215641E-02 -1.548309523265E-01  9.634636555307E-02
14     2.009226738420E-02 -1.539776431918E-01  4.249860075939E-01
```

GCb2

```
8
8.84543352 11.50786176 7.57899918 116.548640
10
14    -3.464373806147E-01 -5.722986677374E-21 -4.181877523083E-01
14    -3.007644145348E-01 -8.086554703648E-22  8.975248392929E-02
14    -1.390221277931E-01  1.444405574873E-21 -8.679177377935E-02
14    -1.584987445156E-01 -2.610939613677E-21  4.368483996958E-01
14    -1.099655222971E-02 -3.498770490935E-01 -2.101067628104E-02
14     4.494803759442E-01  1.540517487608E-01  4.776381002802E-01
14     3.005937304937E-01 -1.003749271848E-01 -3.463395746437E-01
14     3.247645814207E-01 -1.038654566828E-01  1.419982623181E-01
14     2.943543847441E-02 -1.564258018990E-01 -4.002454849150E-01
14     4.558375962588E-02 -1.561656932603E-01 -7.224130552724E-02
```

GDa1

```
28
7.43782109 5.83111545 7.84977267 90.000000
6
14     2.500000000000E-01  3.400292707726E-02 -3.330294922002E-01
14     1.618016316139E-36  0.000000000000E+00 -1.556087681541E-01
14    -2.500000000000E-01 -3.130777913942E-01  4.466119562843E-01
14     2.500000000000E-01 -2.841970016451E-01  4.773247388183E-01
14    -1.012987358375E-02  1.996923286910E-01  2.972511220710E-01
```

```
14    -8.301039798873E-02  3.233874261032E-01  1.755966055483E-02
```

GDa2

```
25
7.57049563 5.90188979 7.93923492 90.000000 90.000000 90.000000
7
14     3.179993157838E-36  0.000000000000E+00 -3.317755115224E-01
14    -5.000000000000E-01  0.000000000000E+00 -3.314607784709E-01
14    -2.540328419967E-01  0.000000000000E+00 -1.579479917192E-01
14     3.179993157838E-36 -2.979853028507E-01  4.554141035298E-01
14    -5.000000000000E-01 -2.999627393408E-01  4.754017175112E-01
14     2.590927888692E-01  1.986179653488E-01  3.060703246884E-01
14     3.385911708657E-01  2.980604297874E-01  2.746233314896E-02
```

GDb1

```
35
7.59541431 11.78051366 7.89549016 90.000000
6
14     0.000000000000E+00  2.642005531346E-01  3.302794401611E-01
14    -2.500000000000E-01  2.500000000000E-01  1.571668848929E-01
14     0.000000000000E+00 -1.026992514975E-01 -4.850260810050E-01
14     5.000000000000E-01 -9.901998071532E-02 -4.480312177424E-01
14    -2.399029541396E-01  1.508919669789E-01 -3.077034648807E-01
14    -1.593408583616E-01  1.013855755626E-01 -2.834104827259E-02
```

GDb2

```
35
7.43144955 11.69900794 7.89262403 90.000000
7
14    -2.143692597877E-22 -2.919150072659E-23  3.308389861378E-01
14    -2.143692597877E-22 -5.000000000000E-01  3.253973587588E-01
14    -2.425957962051E-01 -5.978546026366E-22  1.498959020619E-01
14     7.387083006208E-22  1.510403570648E-01 -4.752164457752E-01
14     5.000000000000E-01  1.477707544546E-01 -4.594846137887E-01
14     2.402298817750E-01 -9.985686855409E-02 -3.028550744134E-01
14     1.688159009659E-01 -1.615324449463E-01 -2.401643305973E-02
```

GDc1

```
39
5.84848658 7.41715198 15.79905490 90.000000
6
14    -1.638960994073E-02  2.500000000000E-01  1.659092170796E-01
14     8.236518084953E-36  6.530358532011E-21  7.701019242520E-02
14    -3.065101594993E-01 -2.500000000000E-01 -2.341674137868E-01
14    -2.908437149519E-01  2.500000000000E-01 -2.861312484555E-01
14    -1.993882547451E-01 -4.926285748986E-01 -1.492044483476E-01
14    -3.219448837099E-01 -4.197745848825E-01 -9.929987088677E-03
```

GDc2

```
38
5.90505566 7.63274399 15.76074160 90.000000
7
14     0.000000000000E+00 -5.000000000000E-01  1.633551210513E-01
14     0.000000000000E+00  0.000000000000E+00  1.837944206252E-01
14     0.000000000000E+00  2.366205252542E-01  8.788958846703E-02
14    -2.990400303232E-01  0.000000000000E+00  2.859247368472E-01
14    -2.982252297083E-01  0.000000000000E+00 -2.345099525256E-01
14    -1.984835899147E-01 -2.368544151286E-01 -1.452892739785E-01
14    -2.985062921606E-01 -1.578563086331E-01 -5.445297834880E-03
```

GDd1

```
42
7.55498438 11.79093278 15.91157524 90.000000
6
14     0.000000000000E+00 -2.443818206969E-01 -1.644112182880E-01
14     2.500000000000E-01 -2.500000000000E-01 -7.760586014860E-02
14     0.000000000000E+00 -1.012890196698E-01  2.315704157406E-01
14     0.000000000000E+00 -9.985055217040E-02 -2.639652661515E-01
14     2.548567174531E-01  1.508153076484E-01  1.540219825233E-01
14    -3.378965268707E-01  1.013157871508E-01  1.538898190048E-02
```

GDd2

```
42
7.48047459 11.67321414 15.64376015 90.000000
7
14    -5.000000000000E-01 -3.048897875608E-21 -1.614652827886E-01
14     5.410694421563E-22 -5.270635310155E-21 -1.863372786197E-01
14    -2.310807450650E-01  1.005559707372E-17 -8.598569531774E-02
14    -7.183121700806E-21  1.470044077851E-01  2.322037977478E-01
14    -1.996396385265E-21  1.521803269252E-01 -2.858765281339E-01
14    -2.373100507738E-01 -1.001332952628E-01  1.411610666961E-01
14     1.643876186964E-01 -1.632072200375E-01  1.246286507922E-03
```

SA1

```
14
3.79879281 9.41123660 15.15656702 113.199478
6
14    -1.603403382562E-01  5.528069091711E-02  4.241669445307E-01
14    -4.736236411331E-01  3.865406673053E-01  1.974468854905E-01
14    -4.243474896960E-01 -4.475032883607E-01 -4.249135015291E-01
14    -1.937908961109E-01 -4.776811351979E-01  3.384545419622E-01
14    -3.044180218588E-01 -1.997939978661E-01 -3.922820236252E-01
14    -8.382466762014E-02 -2.579346748415E-01  2.778453059092E-01
```

SA2

```
14
3.79869550 14.10610184 11.13781830 123.426255
6
14     3.683449455740E-01 -4.253832417074E-01  4.418030349303E-01
14    -3.178694411755E-01 -1.991886760511E-01  1.112948730396E-01
14     1.628932350954E-01 -4.257430584313E-01  4.859707997928E-02
14    -4.438067354189E-01 -3.397499480721E-01 -2.350288260082E-02
14    -3.828638700633E-01 -3.896355015967E-01  2.988436513015E-01
14     4.150060650640E-01 -2.226741738843E-01  2.564720948725E-01
```

SA3

```
18
9.39598538 14.01473043 3.80171951
6
14     4.453422003931E-01 -4.235405429278E-01 -4.515913973191E-01
14    -1.132457671427E-01  1.991621066607E-01 -3.907613275706E-01
14     5.233821669146E-02 -4.245762023756E-01  1.615104031575E-01
14     2.300920498117E-02  3.391588444943E-01 -3.230827691275E-01
14     3.003727264150E-01 -3.917297080764E-01  6.900940524734E-02
14     2.426061537846E-01  2.770633709954E-01 -1.245392590196E-01
```

SA4

```
34
9.59482095 13.83278547 3.76180196
6
14     5.482681157093E-02 -4.226024838344E-01  3.220324694481E-01
14    -3.876911643296E-01  1.929027382053E-01 -4.706171583443E-01
14     5.243645698824E-02  7.584062907597E-02  4.274258592031E-01
14     4.826576693596E-01  3.363302474130E-01  4.379605688431E-01
14     2.044264521411E-01 -3.909117741787E-01 -1.371627835988E-01
14     2.564035480674E-01  2.787844308194E-01 -4.957889555512E-01
```

SB1

```
14
3.79989848 9.64283210 14.32576473 98.535761
6
14     1.363089844485E-01  1.755289331525E-01 -8.954560585153E-02
14     9.563659279328E-02 -3.524838414482E-01  1.993585768733E-01
14     2.389743664257E-01  3.063741801752E-01 -4.246732848300E-01
14     2.314736557236E-01 -2.785753155109E-01 -1.559763954978E-01
14     3.649211850020E-01 -3.909874256413E-02  1.253878326440E-01
14     3.806449339260E-01  4.974918969217E-01 -2.118023021040E-01
```

SB2

```
14
3.81270689 14.20064425 9.77893864 101.079965
```

```
6
14     1.975074421173E-01 -8.868899509884E-02 -1.723172920195E-01
14    -2.224358671803E-01  1.981412707425E-01  3.537067490716E-01
14    -1.400350365655E-01 -4.244768548383E-01 -3.061776131758E-01
14     3.993656546724E-01 -1.563669289772E-01  2.739332854793E-01
14     2.497672102629E-01  1.277939097620E-01  3.969545377438E-02
14    -3.504554523411E-01 -2.102462068422E-01 -4.979459241721E-01
```

SB3

```
19
14.15329843 3.79872004 9.63300000
6
14     4.110585307345E-01  6.265447812573E-02 -4.259581893984E-01
14     3.017203441350E-01 -1.198521092120E-01  3.972371989129E-01
14    -4.246261052909E-01  1.371703923170E-01 -4.433164968064E-01
14    -1.567885586052E-01  3.424877111639E-01 -2.793794598029E-02
14     1.256814287275E-01  4.231941616351E-01  2.097826819046E-01
14    -2.111356173939E-01  1.419332122004E-01 -2.511695484783E-01
```

SB4

```
33
14.03013049 9.76773911 3.75479302
6
14     4.093518045758E-01  3.236125958836E-01  4.919883079051E-01
14    -3.050015990135E-01 -1.513056278887E-01 -3.199325850540E-01
14     7.471806210964E-02  1.974903254819E-01 -4.300932441695E-01
14     3.416455050974E-01 -2.225622167174E-01 -4.154491128509E-01
14    -3.755166387735E-01 -4.665199285237E-01 -4.749005335711E-01
14     2.885243322777E-01  4.959727502980E-03 -3.434328322596E-01
```

SC1

```
14
3.79536940 10.22995946 12.58083537 95.078688
6
14    -7.473113983735E-02  1.143926747060E-01  6.426269046737E-03
14    -1.779641440326E-01  1.766526967948E-01  1.851927143976E-01
14     4.110011185519E-01  4.392990383896E-01 -7.666270313764E-02
14     1.363890977741E-01 -1.296507582974E-02 -3.183659047397E-01
14     3.991916541821E-01  2.086289046087E-01 -7.482807905567E-02
14     3.179556636571E-01  1.985229197387E-01 -2.636924476369E-01
```

SC2

```
14
3.65875 12.1079 10.43006 108.04197
6
14   -0.00569    0.49341   -0.38837
14    0.13920    0.68374   -0.67654
14    0.88608    0.57690   -0.06232
14    0.41225    0.81688   -0.51684
14    0.58121    0.57399   -0.29048
14    0.53426    0.76413   -0.29998
```

SC3

```
18
10.25118222 12.51361424 3.78814918
6
14     3.843057392786E-01  4.904036133204E-01 -6.448589038786E-02
14     3.192240026298E-01  3.131803413243E-01  1.138044813728E-01
14     6.293182797120E-02 -4.227496518740E-01  3.231941482269E-01
14    -4.851210002322E-01 -1.822605756148E-01  1.873069782155E-01
14     2.914250385330E-01 -4.270923930651E-01  4.189154776264E-01
14     3.052910441773E-01 -2.382031637309E-01  3.735148735192E-01
```

SC4

```
34
10.32789655 12.60145959 3.74789243
6
14    -3.860299534978E-01 -4.869681535342E-01  3.931844219766E-01
14     3.232716076693E-01  3.159150034130E-01  1.036010732916E-01
14    -6.390159720445E-02  4.235233939973E-01  2.432256938691E-02
```

```
14     4.829513370260E-01  1.814991524737E-01  3.269178147935E-02
14    -2.913688680667E-01  4.250805873289E-01 -6.975745673560E-02
14    -3.025462324739E-01  2.384715450045E-01  7.638761060111E-02
```

SD

```
63
10.32789655 12.60145959 3.74789243
6
14    -3.860299534978E-01 -4.869681535342E-01  3.931844219766E-01
14     3.232716076693E-01  3.159150034130E-01  1.036010732916E-01
14    -6.390159720445E-02  4.235233939973E-01  2.432256938691E-02
14     4.829513370260E-01  1.814991524737E-01  3.269178147935E-02
14    -2.913688680667E-01  4.250805873289E-01 -6.975745673560E-02
14    -3.025462324739E-01  2.384715450045E-01  7.638761060111E-02
```

mep

```
223
10.21628464
3
14     0.000000000000E+00  3.080457631353E-01  1.170622392585E-01
14     1.836328729915E-01  1.836328729915E-01  1.836328729915E-01
14     2.500000000000E-01  0.000000000000E+00 -5.000000000000E-01
```

mtn

```
227
14.72399514
3
14    -1.250000000000E-01 -1.250000000000E-01 -1.250000000000E-01
14    -2.169943502463E-01 -2.169943502463E-01 -2.169943502463E-01
14     3.174641942200E-01 -1.825358057800E-01  1.295011757420E-01
```

CAS

```
63
3.83423475 10.74044913 12.72663951
3
14    -3.049695997126E-17  2.570866137000E-01 -5.511620526110E-02
14    -7.624239992815E-18  7.133361706975E-02 -1.573697463423E-01
14    -5.000000000000E-01 -2.898655627853E-02 -9.052835284157E-02
```

NGS

```
178
5.47157777 5.10710666
1
14    -2.322685208250E-01  2.322685208250E-01  4.166666666667E-01
```

tum

```
137
7.45563568 9.20081520
3
14    -1.946318569050E-02  1.946318569050E-02  2.500000000000E-01
14     2.500000000000E-01 -8.703908518123E-02 -4.156697554256E-01
14     2.500000000000E-01  4.142344254555E-01  3.688471736737E-01
```

5.7 $Li_{18}Na_2Ge_{17}$ — a Compound Demonstrating Cation Effects on Cluster Shapes and Crystal Packing in Ternary Zintl Phases

Inorganic Chemistry

Article

pubs.acs.org/IC

$Li_{18}Na_2Ge_{17}$—A Compound Demonstrating Cation Effects on Cluster Shapes and Crystal Packing in Ternary Zintl Phases

Lavinia M. Scherf, Michael Zeilinger, and Thomas F. Fässler*

Department Chemie, Technische Universität München, Lichtenbergstraße 4, 85747 Garching b. München, Germany

Supporting Information

ABSTRACT: The novel ternary Zintl phase $Li_{18}Na_2Ge_{17}$ was synthesized from a stoichiometric melt and characterized crystallographically. It crystallizes in the trigonal space group $P31m$ (No. 157) with a = 17.0905(4) Å, c = 8.0783(2) Å, and V = 2043.43(8) Å^3 (final R indices R1 = 0.0212 and wR2 = 0.0420 for all data). The structure contains three different Zintl anions in a 1:1:1 ratio: isolated anions Ge^{4-}, tetrahedra $[Ge_4]^{4-}$, and truncated, Li-centered tetrahedra $[Li@Ge_{12}]^{11-}$, whose hexagonal faces are capped by four Li cations, resulting in the Friauf polyhedra $[Li@Li_4Ge_{12}]^{7-}$. According to the Zintl–Klemm concept, $Li_{18}Na_2Ge_{17}$ is an electronically balanced Zintl phase, as experimentally verified by its diamagnetism. The compound is structurally related to Li_7RbGe_8, which also contains $[Ge_4]^{4-}$ and $[Li@Li_4Ge_{12}]^{7-}$ in its anionic substructure. However, exchanging the heavier alkali metal cation Rb for Na in the mixed-cation germanides leads to drastic changes in stoichiometry and crystal packing, demonstrating the great effects that cations exert on such Zintl phases through optimized cluster sheathing and space filling.

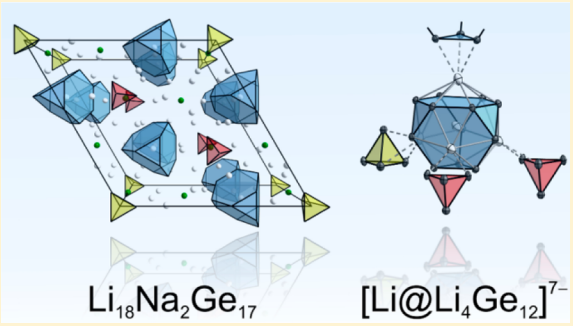

INTRODUCTION

Zintl phases are commonly defined as saltlike intermetallic compounds with highly heteropolar bonds. Formally, they can be described by a complete valence electron transfer from electropositive elements such as alkali or alkaline-earth metals to the more electronegative p-block metals of groups 13–16. Resulting Zintl anions typically behave like elements with the same number of valence electrons N according to the octet (8 − N) rule.[1] Just like the corresponding elements, Zintl anions may take the form of extensive polymeric structures as well as few-atom clusters or isolated atoms. Ge cluster anions range from Br_2-like $[Ge_2]^{6-}$ dumbbells in $BaMg_2Ge_2$[2] and P_4-analogous $[Ge_4]^{4-}$ tetrahedra in A_4Ge_4 (A = Na, K, Rb, Cs)[3] to truncated tetrahedra $[Ge_{12}]^{12-}$ in Li_7RbGe_8.[4] Some examples of such Ge Zintl anions are depicted in Figure 1. Isolated Ge^{4-} anions with noble-gas configurations are frequently observed as well: for example, in compounds E_2Ge (E = Mg, Ca, Sr, Ba).[5] Examples of polymeric germanides are $CaGe_2$ ($^3_\infty[Ge^-]$, As_{gray} structure),[6] CaGe ($^1_\infty[Ge^{2-}]$, polymeric Se structure),[7] Li_7Ge_{12} ($^2_\infty[Ge_{24}^{14-}]$),[8] and clathrate-type compounds Ba_6Ge_{25},[9] A_xGe_{46} (A = K, Rb, Cs, Ba),[10] and A_xGe_{136} (A = Na, K, Rb).[11]

The formation of the novel allotrope *m-allo*-Ge as a microcrystalline bulk material[14] in a topotactic reaction of Li_7Ge_{12} triggered our interest in looking for other allotropes of Ge and Si.[15] In the course of our investigations, we considered Li_3NaSi_6 as a potential precursor because it has a two-dimensional Si substructure similar to that of Li_7Ge_{12} and a topotactic conversion to *allo*-Si has been reported.[16] During our attempts to synthesize a solid solution Li_3NaSi_6/Li_3NaGe_6 as a precursor of a new modification of binary Si–Ge, we serendipitously obtained the new compound $Li_{18}Na_2Ge_{17}$.

A single-crystal X-ray structure determination shows that the novel Zintl phase $Li_{18}Na_2Ge_{17}$ contains the largest known anionic cluster unit, $[Ge_{12}]^{12-}$, which has been observed in only one other compound—the structurally related Li_7RbGe_8.[4] Moreover, $Li_{18}Na_2Ge_{17}$ features three different Ge Zintl anions. Reports of compounds comprised of three or more different Zintl anions are extremely rare. The few examples include $Ba_6Mg_{10.8}Li_{1.2}Si_{12}$ (Si^{4-}, $[Si_2]^{6-}$ dumbbells, bent $[Si_3]^{7.4-}$ chains),[17] $E_{31}Sn_{20}$ (E = Ca, Sr, Yb; Sn^{4-}, $[Sn_2]^{6-}$ dumbbells, linear $[Sn_5]^{12-}$ chains),[18] $Yb_{36}Sn_{23}$ (Sn^{4-}, $[Sn_2]^{6-}$ dumbbells, linear $[Sn_6]^{14-}$ chains)[19] and $Na_{23}K_9Tl_{15.3}$ (Tl^{5-}, linear $[Tl_3]^{7-}$ chains, $[Tl_4]^{8-}$ tetrahedra, trigonal-bipyramidal $[Tl_5]^{7-}$).[20]

Rather complex Zintl phases with various anions of different sizes require an equally complex and efficient coordination by cations. Corbett described the concepts and effects of this cluster "solvation" in detail.[21] In short, surrounding cations stabilize anionic clusters by bridging and separating them. Stable Zintl phases require an optimized balance of specific cluster sheathing and efficient space filling. Interestingly, some Ge Zintl anions (e.g., $[Ge_2]^{6-}$ in $BaMg_2Ge_2$,[2] $[Ge_{12}]^{12-}$ in Li_7RbGe_8[4]) have only been obtained in ternary compounds with mixed cations. Others (e.g., $[Ge_4{-}Na{-}Ge_4]^{7-}$ in A_7NaGe_8 with A = K, Rb)[22] show packing schemes very different from those of their binary analogues. These examples along with extensive studies on mixed cation trielides performed by Dong

Received: October 27, 2013
Published: January 31, 2014

   dx.doi.org/10.1021/ic4027046 | *Inorg. Chem.* 2014, 53, 2096–2101

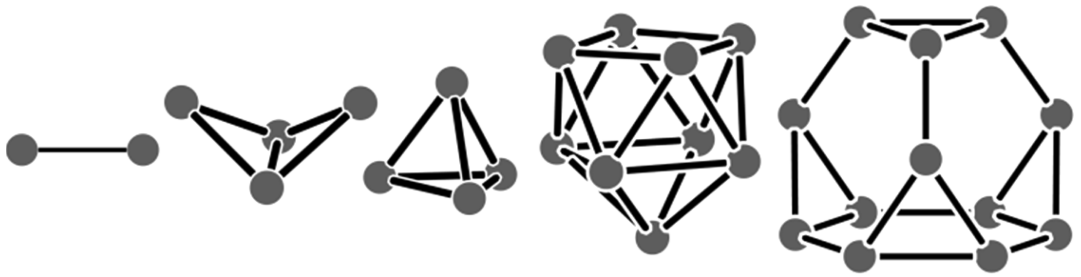

Figure 1. Selected Ge cluster anions from left to right: $[Ge_2]^{6-}$ dumbbell ($BaMg_2Ge_2$),[2] butterfly-shaped $[Ge_4]^{6-}$ (β-Ba_3Ge_4),[12] $[Ge_4]^{4-}$ tetrahedron (A_4Ge_4; A = Na, K, Rb, Cs),[3] monocapped-quadratic-antiprismatic $[Ge_9]^{4-}$ (K_4Ge_9),[13] truncated-tetrahedral $[Ge_{12}]^{12-}$ (Li_7RbGe_8).[4]

and Corbett[20,23] demonstrated that mixing cations of different sizes can be a very useful tool for achieving this balance.[21] Ab initio calculations on the structural differences in NaTl and KTl[24] as well as Li_2AuBi and Na_2AuBi[25] support the frequently observed structure-directing effect of cations in Zintl compounds. The new Zintl phase $Li_{18}Na_2Ge_{17}$ presented here clearly illustrates the influence of cations on cluster shapes and crystal packing in ternary Zintl phases.

EXPERIMENTAL SECTION

Synthesis of $Li_{18}Na_2Ge_{17}$. All steps of synthesis and sample preparation were carried out in an Ar-filled glovebox (MBraun, H_2O level <0.1 ppm, O_2 level <0.1 ppm). $Li_{18}Na_2Ge_{17}$ was prepared from the pure elements (99% Li rods, Rockwood-Lithium; 99% Na rods, Chempur; 99.999% Ge pieces, Chempur) in a tantalum ampule. The sealed ampule containing the stoichiometric reaction mixture with a total mass of 1 g was placed inside a silica reaction container, which was then evacuated and heated to 750 °C for 1 h. The resulting melt was cooled at a rate of 0.5 °C min^{-1} to 300 °C, at which temperature annealing of the reaction product was allowed for 3 h.

Single-Crystal Structure Determination. Crystals of $Li_{18}Na_2Ge_{17}$ were selected in an Ar-filled glovebox and sealed in 0.3 mm glass capillaries. For the best specimen, intensity data were collected at 123 K using a Bruker AXS X-ray diffractometer equipped with a CCD detector (APEX II, κ-CCD), a rotating anode FR591 with Mo Kα radiation (λ = 0.71073 Å), and a MONTEL optic monochromator. Data collection was controlled with the Bruker APEX software package.[26] Integration, data reduction, and absorption correction were performed with the SAINT[27] and SADABS[28] packages. The structure was solved with direct methods (SHELXS-97) and refined with full-matrix least squares on F^2 (SHELXL-97).[29] Details of the single-crystal data collection and refinement are given in Table 1. Further details on the crystal structure investigation may be obtained as Supporting Information (atomic coordinates and isotropic displacement parameters in Table S1, CIF file) and from Fachinformationszentrum Karlsruhe, 76344 Eggenstein-Leopoldshafen, Germany (fax (+49)7247-808-666; e-mail crysdata@fiz-karlsruhe.de; http://www.fiz-karlsruhe.de/request_for_deposited_data.html) on quoting the deposition number CSD-426692.

Powder X-ray Diffraction Analysis. A PXRD pattern of $Li_{18}Na_2Ge_{17}$ was recorded using a Stoe STADI P diffractometer equipped with a Ge(111) monochromator for Cu Kα radiation (λ = 1.54056 Å) and a Dectris MYTHEN DCS 1K solid-state detector. A crystalline sample of a $Li_{18}Na_2Ge_{17}$ synthesis product was ground in an agate mortar and filled into a 0.3 mm glass capillary, which was then sealed. The sample was measured within a 2θ range of 5–89° (PSD steps, 0.075°; time/step, 45 s). The diffraction pattern is shown in Figure S2 in the Supporting Information.

Magnetic Measurements. Using a Quantum Design MPMS 5 XL SQUID magnetometer, the magnetization of 39 mg of a $Li_{18}Na_2Ge_{17}$ synthesis product was measured at applied fields of 5000 and 10000 Oe over the temperature range 2–300 K. The data were corrected for the sample holder and for ion-core diamagnetism using Pascal's constants.[30] The molar susceptibility X_m is negative in the range of $-(1.44–1.55) \times 10^{-3}$ emu mol^{-1} and temperature independent, as expected for a diamagnetic compound. The corresponding graph is shown in Figure S3 in the Supporting Information.

Table 1. Crystallographic Data and Structure Refinement for $Li_{18}Na_2Ge_{17}$

T (K)	123(2)
formula wt	1404.93
cryst size (mm^3)	0.11 × 0.13 × 0.28
cryst color	metallic black
cryst shape	block
space group	$P31m$
unit cell dimens (Å)	
a	17.0905(4)
c	8.0783(2)
Z	3
V ($Å^3$)	2043.43(8)
ρ(calcd) (g cm^{-3})	3.425
μ (mm^{-1})	18.459
F(000)	1860
θ range (deg)	2.38–33.16
index range	$-26 \le h \le 26$
	$-25 \le k \le 23$
	$-12 \le l \le 12$
no. of rflns collected	47691
no. of indep rflns	5466 (R_{int} = 0.0407)
no. of rflns with $I > 2\sigma(I)$	5150 (R_σ = 0.0250)
abs cor	multiscan
no. of data/restraints/params	5466/1/191
goodness of fit on F^2	1.041
final R indices ($I > 2\sigma(I)$)[a,b]	
R1	0.0185
wR2	0.0412
R indices (all data)[a,b]	
R1	0.0212
wR2	0.0420
Flack param	0.01(2)
largest diff peak, hole (e $Å^{-3}$)	0.88, −0.99

[a] $R1 = \sum||F_o| - |F_c||/\sum|F_o|$. [b] $wR2 = [\sum w(F_o^2 - F_c^2)^2/\sum w(F_o^2)^2]^{1/2}$.

RESULTS AND DISCUSSION

Structure of $Li_{18}Na_2Ge_{17}$. $Li_{18}Na_2Ge_{17}$ was serendipitously identified from a reaction intended to yield $Li_3NaSi_3Ge_3$, a derivative of the known Zintl phase Li_3NaSi_6.[16] Subsequently, the air- and moisture-sensitive compound was synthesized directly from the pure elements and characterized crystallographically. $Li_{18}Na_2Ge_{17}$ crystallizes in the trigonal space group $P31m$ (No. 157) with a = 17.0905(4) Å, c = 8.0783(2) Å. and Z

dx.doi.org/10.1021/ic4027046 | Inorg. Chem. 2014, 53, 2096–2101

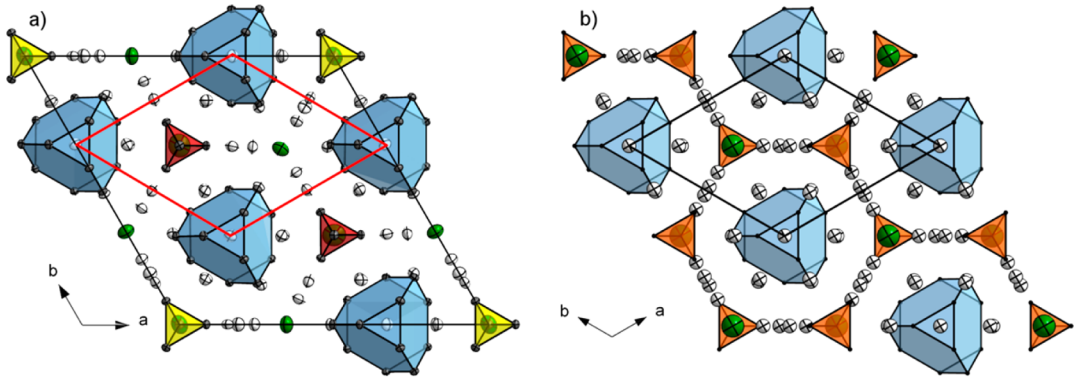

Figure 2. (a) Projection of the structure of $Li_{18}Na_2Ge_{17}$ onto the *ab* plane (Li, white; Na, green; Ge, gray; thermal ellipsoids at 90% probability at 123 K). The anionic Ge clusters are highlighted as colored polyhedra (truncated tetrahedra $[Ge_{12}]^{12-}$, blue; crystallographically different tetrahedra $[Ge_4]^{4-}$ (**A**) red, (**B**) yellow). The hexagonal primitive packing of truncated tetrahedra is indicated by red lines. (b) Projection of the structure of Li_7RbGe_8[4] onto the *ab* plane (Li, white; Rb, green; Ge, gray). The anionic Ge clusters are highlighted as colored polyhedra (truncated tetrahedra $[Ge_{12}]^{12-}$, blue; tetrahedra $[Ge_4]^{4-}$, orange).

= 3. All atoms were refined anisotropically with final reliability factors of R1 = 0.0212 and wR2 = 0.0420 for all data (Table 1).

Interestingly, the structure of $Li_{18}Na_2Ge_{17}$ incorporates three different Zintl anions in a 1:1:1 ratio: truncated Ge tetrahedra $[Ge_{12}]^{12-}$, Ge tetrahedra $[Ge_4]^{4-}$, and isolated Ge anions Ge^{4-} (Figure 2a). Thus, to the best of our knowledge, it is the first germanide containing three different Zintl anions with each of them observing the $(8 - N)$ rule. In addition, the new Zintl phase $Li_{18}Na_2Ge_{17}$ is only the second compound containing the largest known anionic Ge cluster unit, $[Ge_{12}]^{12-}$. Such $[Ge_{12}]^{12-}$ truncated tetrahedra have been reported once before in the related Zintl phase Li_7RbGe_8, in which they occur next to tetrahedral $[Ge_4]^{4-}$.[4] Similar $[Sn_{12}]^{12-}$ clusters are observed in $ENa_{10}Sn_{12}$ (E = Ca, Sr).[31] Larger Ge polyanions have only been isolated via soluble $[Ge_9]^{4-}$, with $[Ge_{45}]^{12-}$ being the largest example of covalently linked Ge atoms.[32]

The shape of the large $[Ge_{12}]^{12-}$ unit, a polyhedron with four triangular and four hexagonal faces, derives from a large tetrahedron with truncated vertices. Four Li atoms cap the hexagonal faces of the truncated tetrahedron and thus constitute the 16-vertex Friauf[33] polyhedron $[Li_4Ge_{12}]^{8-}$. In addition, the Friauf polyhedron is centered by one Li atom (Figure 3). Due to the lower crystal symmetry, Ge−Ge bond lengths (2.4840(5)−2.6948(5) Å) vary in a greater range than in Friauf polyhedra in Li_7RbGe_8 (2.505(2)−2.603(2) Å).[4] However, average Ge−Ge bond lengths are identical (2.567(1) Å for $Li_{18}Na_2Ge_{17}$, 2.569(2) Å for Li_7RbGe_8). Similarly, the average interatomic distances of Ge and capping Li atoms (2.91(1) Å for $Li_{18}Na_2Ge_{17}$, 2.96(2) Å for Li_7RbGe_8) as well as the interatomic distances of centering Li1 to all 16 surrounding atoms (2.99(1) Å for $Li_{18}Na_2Ge_{17}$, 3.02(2) Å for Li_7RbGe_8) fall in the same ranges (Table 2). In addition, the Friauf polyhedron $[Li@Li_4Ge_{12}]^{7-}$ is coordinated by another 30 alkali-metal cations, forming an approximately spherical "solvation" environment (Figure S1 in the Supporting Information).

The four capping Li atoms link the Friauf polyhedron to neighboring Zintl anions (Figure 3). Li2 is coordinated by a triangular face of a neighboring Friauf polyhedron along *c*, whereas Li4 coordinates one edge of crystallographically distinguishable tetrahedra **A** and Li3 coordinates a face of the second tetrahedron type **B**.

Ge tetrahedra **A** and **B** (ratio 2:1) are both located on 3-fold rotation axes (Figure 2a) and differ in their relative orientations

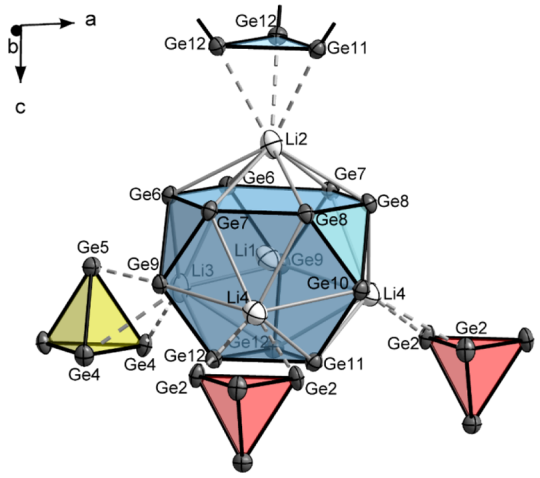

Figure 3. Structure of the Li-centered Friauf polyhedron $[Li@Li_4Ge_{12}]^{7-}$ (Li, white; Ge, gray; truncated tetrahedron $[Ge_{12}]^{12-}$, blue; crystallographically different tetrahedra $[Ge_4]^{4-}$ (**A**) red, (**B**) yellow; thermal ellipsoids at 90% probability at 123 K). Ge−Ge bonds are marked in black, whereas capping Li atoms are connected with gray lines. Interactions of capping Li atoms with edges (**A**) or triangular faces (**B** and $[Li@Li_4Ge_{12}]^{7-}$) of neighboring clusters are shown with broken lines. Relevant interatomic distances are given in Table 2.

as well as their coordination environments (Figure 4a,b). Nevertheless, their Ge−Ge bond lengths of 2.5610(5)−2.5818(6) Å agree well with those in A_4Ge_4 (A = Na, K, Rb, Cs).[3] Tetrahedron **A** has a coordination environment similar to that of $[Ge_4]^{4-}$ tetrahedra in Li_7RbGe_8,[4] containing 12 Li and 2 Na atoms (Figure 4a; Ge−Li distances 2.575(5)−3.114(6) Å, Ge−Na distances 2.980(2)−3.320(2) Å). In contrast, tetrahedron **B** is coordinated by 15 Li and 2 Na atoms (Figure 4b; Ge−Li distances 2.703(7)−3.095(6) Å, Ge−Na distances 3.020(3)−3.335(2) Å). For both tetrahedron types, Li atoms cap trigonal faces or bridge edges or coordinate *exo* at vertices. These coordination modes commonly occur in Zintl cluster sheathing.[21]

The isolated Ge atom Ge1 is coordinated by nine Li atoms and Na1 (Figure 4c) with a Ge−Na distance of 2.877(2) Å. Coordinating Li atoms (Ge−Li distance 2.514(6)−2.903(5) Å) are clearly differentiated from next-nearest neighbors with Ge−Li distances >4.8 Å. All relevant interatomic distances in $Li_{18}Na_2Ge_{17}$ are given in Table 2.

dx.doi.org/10.1021/ic4027046 | Inorg. Chem. 2014, 53, 2096−2101

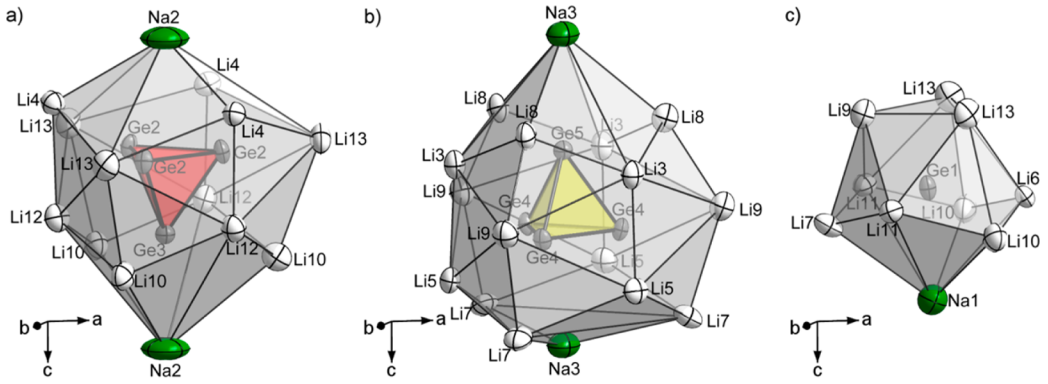

Figure 4. Coordination environments of (a) the Ge tetrahedron **A**, (b) the Ge tetrahedron **B**, (c) and the isolated Ge atom Ge1 (Li, white; Na, green; Ge, gray; thermal ellipsoids at 90% probability at 123 K). Relevant interatomic distances are given in Table 2.

Table 2. Relevant Interatomic Distances in $Li_{18}Na_2Ge_{17}$ ($P31m$, Z = 3, Estimated Standard Deviations in Parentheses)

atom pair			atom pair			atom pair		
		d (Å)			d (Å)			d (Å)
Ge1	Li6	2.514(6)	Ge6	Ge6	2.4883(5)	Ge9	Li8	2.856(4)
	Li11 × 2	2.543(5)		Ge9	2.5980(4)		Li13	2.921(5)
	Li9	2.560(7)		Ge7	2.6596(4)		Li3	2.935(3)
	Li13 × 2	2.643(5)		Li11	2.708(4)		Li4	2.978(4)
	Li7	2.709(7)		Li7	2.740(3)		Li1	3.058(3)
	Na1	2.877(2)		Li8	2.752(3)		Na1	3.161(1)
	Li10 × 2	2.902(5)		Li5	2.836(6)	Ge10	Ge11	2.4840(5)
Ge2	Ge2 × 2	2.5610(5)		Li3	2.906(6)		Ge8 × 2	2.5596(4)
	Ge3	2.5753(4)		Li2	2.974(6)		Li13 × 2	2.826(5)
	Li13	2.575(5)		Li1	2.995(6)		Li4 × 2	2.946(4)
	Li4	2.854(5)	Ge7	Ge8	2.4952(4)		Na1	2.978(2)
	Li4	2.885(5)		Ge9	2.5651(4)		Li1	3.042(6)
	Li12	2.924(5)		Li11	2.618(5)	Ge11	Ge10	2.4839(5)
	Li12	2.932(5)		Ge6	2.6596(4)		Li6	2.585(6)
	Li10	3.114(6)		Li10	2.767(5)		Ge12 × 2	2.5921(4)
	Na2	3.335(2)		Li4	2.882(5)		Li4 × 2	2.871(5)
Ge3	Ge2 × 3	2.5753(4)		Li12	2.951(6)		Li12 × 2	2.903(5)
	Li12 × 3	2.862(5)		Li2	2.980(4)		Li2	2.960(8)
	Li10 × 3	2.975(6)		Li1	2.997(4)		Li1	2.964(7)
	Na2	2.980(2)	Ge8	Ge7	2.4952(4)	Ge12	Ge9	2.5000(4)
Ge4	Ge5	2.5688(6)		Ge10	2.5597(4)		Li11	2.567(5)
	Ge4 × 2	2.5818(6)		Li6	2.659(5)		Ge11	2.5921(4)
	Li9	2.703(7)		Ge8	2.6948(5)		Ge12	2.5992(5)
	Li5 × 2	2.823(6)		Li10	2.768(5)		Li5	2.766(6)
	Li7	2.902(7)		Li4	2.851(5)		Li4	2.857(5)
	Li3 × 2	3.035(6)		Li12	2.912(6)		Li3	2.875(6)
	Li8	3.095(6)		Li2	2.916(6)		Li12	2.942(5)
	Na3	3.320(2)		Li1	2.969(6)		Li1	2.945(7)
Ge5	Ge4 × 3	2.5688(6)	Ge9	Ge12	2.5000(4)		Li2	3.018(7)
	Li8 × 3	2.770(6)		Ge7	2.5651(4)	Li1	Li2	2.94(1)
	Li3 × 3	2.838(6)		Ge6	2.5980(4)		Li3	2.981(9)
	Na3	3.020(3)		Li9	2.855(4)		Li4 × 2	3.009(6)

Electron Count. According to the Zintl–Klemm concept,[1a,34] the truncated Ge tetrahedron may be viewed as a $[Ge_{12}]^{12-}$ anion with one negative charge for every three-connected Ge atom. Adding the four capping Li atoms and Li1 in the center with one positive charge each results in an overall electron count of −7 for $[Li@Li_4Ge_{12}]^{7-}$. $Li_{18}Na_2Ge_{17}$ contains the Friauf polyhedron, tetrahedral $[Ge_4]^{4-}$, and isolated Ge^{4-} in a 1:1:1 ratio. Thus, $(Li^+)_{13}(Na^+)_2[Li@Li_4Ge_{12}]^{7-}[Ge_4]^{4-}(Ge^{4-})$ is an appropriate notation for this novel Zintl phase, in which all Zintl anions obey the $(8 - N)$ rule. A magnetic measurement of $Li_{18}Na_2Ge_{17}$ clearly reveals diamagnetism of the metallic black and brittle compound (Figure S3 in the Supporting Information), which is consistent with a semiconducting Zintl phase.

Cation Effects. The crystal structure of $Li_{18}Na_2Ge_{17}$ is closely related to the structure of Li_7RbGe_8.[4] In both compounds, the Li-centered Friauf polyhedra $[Li@Li_4Ge_{12}]^{7-}$ arrange in a hexagonally primitive fashion, as demonstrated in Figure 2. The resulting voids are filled by $[Ge_4]^{4-}$ tetrahedra and in the case of $Li_{18}Na_2Ge_{17}$ also by isolated Ge anions.

dx.doi.org/10.1021/ic4027046 | Inorg. Chem. 2014, 53, 2096–2101

Alkali-metal cations Li^+ as well as Na^+ and Rb^+, respectively, stabilize the Zintl anions by counterbalancing the negative charge, filling voids and providing cluster sheathing that keeps clusters separated.

Although the heavier alkali-metal content in the two ternary germanides only amounts to 5.41 ($Li_{18}Na_2Ge_{17}$) and 6.25 atom % (Li_7RbGe_8), the exchange of the heavier alkali-metal cation induces a dramatic difference in the crystal structures. A comparison of cell dimensions of the hexagonally primitive framework of Friauf polyhedra in both compounds shows a slight cell contraction upon utilization of Na instead of Rb (Table 3), changing the requirements for effective space filling.

Table 3. Cell Dimensions a', c', and V' of the Hexagonally Primitive Friauf Polyhedron Framework in $Li_{18}Na_2Ge_{17}$ (Room-Temperature Powder Data; $a' = (1/3)^{1/2}a$; $c' = c$; $V' = (1/3)^{1/2}V$) and Li_7RbGe_8 (Room-Temperature Single-Crystal Data;[4] $a' = a$; $c' = (1/2)c$; $V' = (1/2)V$)

	$Li_{18}Na_2Ge_{17}$	Li_7RbGe_8
a' (Å)	9.899(2)	9.8946(7)
c' (Å)	8.100(1)	8.135(2)
V' (Å^3)	679.74(4)	689.74(2)

An isolated Ge^{4-} anion replaces one of the two $[Ge_4]^{4-}$ tetrahedra in each primitive cell. However, the isolated anion, which has the same 4-fold negative charge as the larger $[Ge_4]^{4-}$ tetrahedron, cannot encompass the same number of cations in its coordination environment. Therefore, $[Ge_4]^{4-}$ tetrahedron **B** accommodates three additional Li cations, resulting in decreased overall symmetry and a greater a parameter. The lowered symmetry is accompanied by a slight distortion of the hexagonally primitive Friauf polyhedron framework in $Li_{18}Na_2Ge_{17}$. Whereas the distances of one Friauf polyhedron center to the centers of each of the six neighboring polyhedra in the ab plane are all equal in Li_7RbGe_8 (9.8946(7) Å, room-temperature single-crystal data), these center-to-center distances slightly differ in $Li_{18}Na_2Ge_{17}$ (4 × 9.931(6) Å, 2 × 9.742(6) Å, 123 K single-crystal data).

In addition, the introduction of Na as the heavier alkali-metal cation evokes a drastic change of the crystal packing along the c direction (Figure 5). In Li_7RbGe_8, two $[Ge_4]^{4-}$ tetrahedra are separated by two Rb cations and Friauf polyhedra are staggered due to a 6_3 screw axis. However, in $Li_{18}Na_2Ge_{17}$ a single Na cation alternates with each tetrahedron and isolated Ge anion, respectively. Concomitantly, the length of the c axis is halved (Table 3) because $[Li@Li_4Ge_{12}]^{7-}$ clusters stack in an eclipsed manner in the lower symmetry.

CONCLUSIONS

Mixing cations of different size or even different charge in syntheses of Zintl phases has been shown to be an efficient tool to stabilize rare cluster shapes. The novel compound $Li_{18}Na_2Ge_{17}$ presented here and the related Li_7RbGe_8[4] illustrate this concept well. Although the heavier alkali-metal content only amounts to 5−6 atom % in these compounds, the exchange of Rb by Na introduces a dramatic structural difference. In the case of $Li_{18}Na_2Ge_{17}$ an intriguing structure with three different Zintl anions is obtained. It is therefore easy to imagine that many more novel structures may be stabilized as mixed-cation compounds which are not available in binary systems. Thus, cation ratios must be carefully selected in order to obtain electronically balanced structures with favorable cluster sheathing and efficient space filling. However, owing to the multitude of Zintl anion geometries and countless possible combinations thereof, predicting new ternary Zintl phases remains difficult.

ASSOCIATED CONTENT

Supporting Information

Atomic coordinates and isotropic displacement parameters of $Li_{18}Na_2Ge_{17}$ (Table S1), coordination environment of the Friauf polyhedron $[Li@Li_4Ge_{12}]^{7-}$ in $Li_{18}Na_2Ge_{17}$ (Figure S1), a powder X-ray diffraction pattern of $Li_{18}Na_2Ge_{17}$ (Figure S2), results of magnetic susceptibility measurements (Figure S3), and a CIF file giving crystallographic data. This material is available free of charge via the Internet at http://pubs.acs.org.

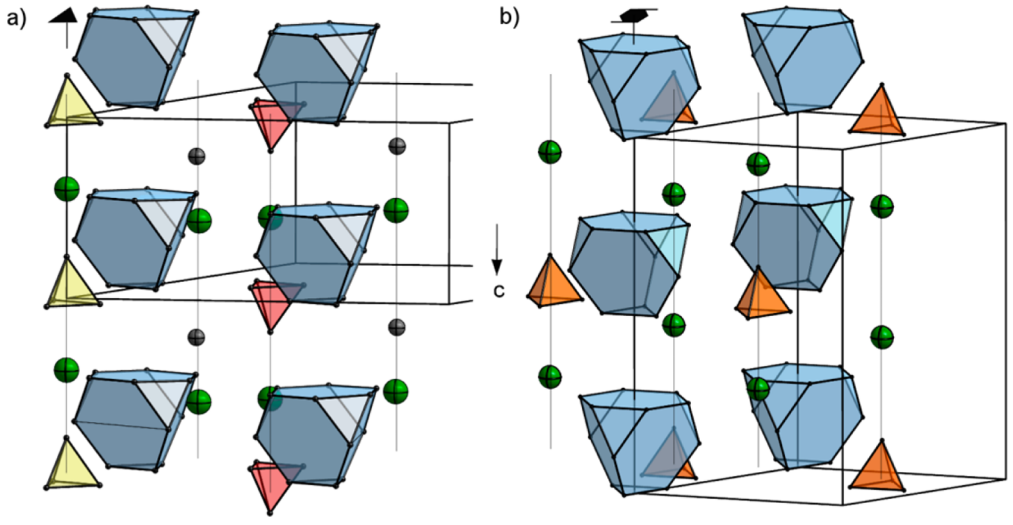

Figure 5. Fragments of the structures of (a) $Li_{18}Na_2Ge_{17}$ (Na, green, Ge, gray; truncated tetrahedra $[Ge_{12}]^{12-}$, blue; crystallographically different tetrahedra $[Ge_4]^{4-}$ (**A**) red, (**B**) yellow) and (b) Li_7RbGe_8[4] (Rb, green; Ge, gray; truncated tetrahedra $[Ge_{12}]^{12-}$, blue; tetrahedra $[Ge_4]^{4-}$, orange), demonstrating the packing of Zintl anions and Na and Rb cations, respectively, along c. The main symmetry elements are indicated by their symbols. Li atoms are omitted for enhanced clarity.

dx.doi.org/10.1021/ic4027046 | Inorg. Chem. 2014, 53, 2096−2101

AUTHOR INFORMATION

Corresponding Author

*E-mail for T.F.F.: thomas.faessler@lrz.tum.de.

Notes

The authors declare no competing financial interest.

ACKNOWLEDGMENTS

The authors thank A. V. Hoffmann for the SQUID measurement and for financial support from the SolTech (Solar Technologies go Hybrid) program of the State of Bavaria. L.M.S. is further grateful to the Studienstiftung des Deutschen Volkes for her fellowship.

REFERENCES

(1) (a) Zintl, E. *Angew. Chem.* **1939**, *52*, 1−6. (b) *Zintl Phases: Principles and Recent Developments*; Fässler, T. F., Ed.; Springer-Verlag: Heidelberg, Germany, 2011; Structure and Bonding Vol. *139*.

(2) (a) Eisenmann, B.; May, N.; Müller, W.; Schäfer, H.; Weiss, A.; Winter, J.; Ziegleder, G. *Z. Naturforsch., B* **1970**, *25*, 1350−1352. (b) Eisenmann, B.; Schäfer, H. *Z. Anorg. Allg. Chem.* **1974**, *403*, 163−172.

(3) (a) Witte, J.; von Schnering, H. G.; Klemm, W. *Z. Anorg. Allg. Chem.* **1964**, *327*, 260−273. (b) Busmann, E. *Z. Anorg. Allg. Chem.* **1961**, *313*, 90−106.

(4) Bobev, S.; Sevov, S. C. *Angew. Chem.* **2001**, *113*, 1555−1558; *Angew. Chem., Int. Ed.* **2001**, *40*, 1507−1510.

(5) (a) Zintl, E.; Kaiser, H. *Z. Anorg. Allg. Chem.* **1933**, *211*, 113−131. (b) Eckerlin, P.; Wölfel, E. *Z. Anorg. Allg. Chem.* **1955**, *280*, 321−331. (c) Eisenmann, B.; Schäfer, H.; Turban, K. *Z. Naturforsch., B* **1975**, *30*, 677−680. (d) Turban, K.; Schäfer, H. *Z. Naturforsch., B* **1973**, *28*, 220−222.

(6) (a) Wallbaum, H. J. *Naturwissenschaften* **1944**, *32*, 76. (b) Tobash, P. H.; Bobev, S. *J. Solid State Chem.* **2007**, *180*, 1575−1581.

(7) Eckerlin, P.; Meyer, H. J.; Wölfel, E. *Z. Anorg. Allg. Chem.* **1955**, *281*, 322−328.

(8) (a) Kiefer, F.; Fässler, T. F. *Solid State Sci.* **2011**, *13*, 636−640. (b) Grüttner, A.; Nesper, R.; von Schnering, H. G. *Angew. Chem.* **1982**, *94*, 933; *Angew. Chem., Int. Ed. Engl.* **1982**, *21*, 912−913.

(9) (a) Fukuoka, H.; Iwai, K.; Yamanaka, S.; Abe, H.; Yoza, K.; Häming, L. *J. Solid State Chem.* **2000**, *151*, 117−121. (b) Kim, S.-J.; Hu, S.; Uher, C.; Hogan, T.; Huang, B.; Corbett, J. D.; Kanatzidis, M. G. *J. Solid State Chem.* **2000**, *153*, 321−329. (c) Carrillo-Cabrera, W.; Curda, J.; von Schnering, H. G.; Paschen, S.; Grin, Y. *Z. Kristallogr.-New Cryst. Struct.* **2000**, *215*, 207−208.

(10) (a) Cros, C.; Pouchard, M.; Hagenmuller, P. *J. Solid State Chem.* **1970**, *2*, 570−581. (b) Liang, Y.; Böhme, B.; Ormeci, A.; Borrmann, H.; Pecher, O.; Haarmann, F.; Schnelle, W.; Baitinger, M.; Grin, Y. *Chem. Eur. J.* **2012**, *18*, 9818−9822. (c) Veremchuk, I.; Wosylus, A.; Böhme, B.; Baitinger, M.; Borrmann, H.; Prots, Y.; Burkhardt, U.; Schwarz, U.; Grin, Y. *Z. Anorg. Allg. Chem.* **2011**, *637*, 1281−1286.

(11) (a) Simon, P.; Tang, Z.; Carrillo-Cabrera, W.; Chiong, K.; Böhme, B.; Baitinger, M.; Lichte, H.; Grin, Y.; Guloy, A. M. *J. Am. Chem. Soc.* **2011**, *133*, 7596−7601. (b) Bobev, S.; Sevov, S. C. *J. Am. Chem. Soc.* **1999**, *121*, 3795−3796.

(12) Zürcher, F.; Nesper, R. *Angew. Chem.* **1998**, *110*, 3451−3454; *Angew. Chem., Int. Ed.* **1998**, *37*, 3314−3318.

(13) Ponou, S.; Fässler, T. F. *Z. Anorg. Allg. Chem.* **2007**, *633*, 393−397.

(14) Kiefer, F.; Karttunen, A. J.; Döblinger, M.; Fässler, T. F. *Chem. Mater.* **2011**, *23*, 4578−4586.

(15) (a) Karttunen, A. J.; Fässler, T. F.; Linnolahti, M.; Pakkanen, T. A. *Inorg. Chem.* **2011**, *50*, 1733−1742. (b) Karttunen, A. J.; Fässler, T. F. *ChemPhysChem* **2013**, *14*, 1807−1817.

(16) von Schnering, H. G.; Schwarz, M.; Nesper, R. *J. Less-Common Met.* **1988**, *137*, 297−310.

(17) Wengert, S.; Nesper, R. *Z. Anorg. Allg. Chem.* **2000**, *626*, 246−252.

(18) Ganguli, A. K.; Guloy, A. M.; Leon-Escamilla, E. A.; Corbett, J. D. *Inorg. Chem.* **1993**, *32*, 4349−4353.

(19) Leon-Escamilla, E. A.; Corbett, J. D. *Inorg. Chem.* **1999**, *38*, 738−743.

(20) Dong, Z.-C.; Corbett, J. D. *Inorg. Chem.* **1996**, *35*, 3107−3112.

(21) Corbett, J. D. *Struct. Bonding (Berlin)* **1997**, *87*, 157−194. (b) Corbett, J. D. *Angew. Chem.* **2000**, *112*, 682−704; *Angew. Chem., Int. Ed.* **2000**, *39*, 670−690.

(22) Llanos, J.; Nesper, R.; von Schnering, H. G. *Angew. Chem.* **1983**, *95*, 1026−1027; *Angew. Chem., Int. Ed. Engl.* **1983**, *22*, 998.

(23) (a) Dong, Z.-C.; Corbett, J. D. *J. Am. Chem. Soc.* **1994**, *116*, 3429−3435. (b) Dong, Z. C.; Corbett, J. D. *J. Am. Chem. Soc.* **1995**, *117*, 6447−6455. (c) Cordier, G.; Müller, V. *Z. Naturforsch., B* **1994**, *49*, 935−938.

(24) Wang, F.; Miller, G. J. *Inorg. Chem.* **2011**, *50*, 7625−7636.

(25) Wang, F.; Miller, G. J. *Eur. J. Inorg. Chem.* **2011**, *2011*, 3989−3998.

(26) *APEX 2: APEX Suite of Crystallographic Software, 2008.4*; Bruker AXS Inc., Madison, WI, USA, 2008.

(27) *SAINT*; Bruker AXS Inc., Madison, WI, USA, 2001.

(28) *SADABS*; Bruker AXS Inc., Madison, WI, USA, 2001.

(29) Sheldrick, G. M. *Acta Crystallogr.* **2008**, *A64*, 112−122.

(30) Bain, G. A.; Berry, J. F. *J. Chem. Educ.* **2008**, *85*, 532−536.

(31) Bobev, S.; Sevov, S. C. *Inorg. Chem.* **2001**, *40*, 5361−5364.

(32) (a) Scharfe, S.; Kraus, F.; Stegmaier, S.; Schier, A.; Fässler, T. F. *Angew. Chem.* **2011**, *123*, 3712−3754; *Angew. Chem., Int. Ed.* **2011**, *50*, 3630−3670. (b) Spiekermann, A.; Hoffmann, S. D.; Fässler, T. F.; Krossing, I.; Preiss, U. *Angew. Chem.* **2007**, *119*, 5404−5407; *Angew. Chem., Int. Ed.* **2007**, *46*, 5310−5313.

(33) Friauf, J. B. *J. Am. Chem. Soc.* **1927**, *49*, 3107−3114.

(34) (a) Klemm, W. *Proc. Chem. Soc.* **1958**, 329−341. (b) Klemm, W.; Busmann, E. *Z. Anorg. Allg. Chem.* **1963**, *319*, 297−311.

SUPPORTING INFORMATION

$Li_{18}Na_2Ge_{17}$ – a Compound Demonstrating Cation Effects on Cluster Shapes and Crystal Packing in Ternary Zintl Phases

*Lavinia M. Scherf, Michael Zeilinger, Thomas F. Fässler**

Table S1. Fractional atomic coordinates and equivalent isotropic atomic displacement parameters for $Li_{18}Na_2Ge_{17}$ ($P31m$, $Z = 3$, $T = 123$ K, estimated standard deviations in parentheses).

atom	Wyckoff position	x	y	z	U_{eq} /Å$^2\cdot10^3$
Ge1	3*c*	0.33940(2)	0	0.20480(5)	9.55(7)
Ge2	6*d*	0.58056(2)	0.24642(1)	0.97870(4)	10.08(5)
Ge3	2*b*	2/3	1/3	0.23971(5)	9.61(9)
Ge4	3*c*	0.08722(2)	0	0.02877(6)	9.46(7)
Ge5	1*a*	0	0	0.76979(8)	9.2(1)
Ge6	6*d*	0.23988(2)	0.15581(2)	0.48856(3)	7.70(5)
Ge7	6*d*	0.41951(2)	0.24371(2)	0.49600(3)	8.40(5)
Ge8	6*d*	0.50333(2)	0.41229(2)	0.49809(3)	8.29(5)
Ge9	6*d*	0.32803(1)	0.15256(2)	0.74800(3)	8.43(5)
Ge10	3*c*	0.49594(2)	0	0.74910(4)	9.31(6)
Ge11	3*c*	0.41729(2)	0.41729(2)	0.99578(4)	8.84(6)
Ge12	6*d*	0.32997(1)	0.24217(2)	0.99415(3)	8.68(5)
Na1	3*c*	0.3462(1)	0	0.5607(2)	26.6(4)
Na2	2*b*	2/3	1/3	0.6086(3)	43.1(7)
Na3	1*a*	0	0	0.3960(3)	28.5(6)
Li1	3*c*	0.3291(3)	0.3291(3)	0.6799(9)	17(2)
Li2	3*c*	0.3333(3)	0.3333(3)	0.316(1)	15(1)
Li3	3*c*	0.1651(4)	0.1651(4)	0.8062(9)	15(1)
Li4	6*d*	0.4944(3)	0.3294(3)	0.8091(7)	16(1)
Li5	3*c*	0.1726(4)	0.1726(4)	0.1776(9)	16(1)
Li6	3*c*	0.4855(3)	0	0.2409(8)	13(1)
Li7	3*c*	0.1897(4)	0	0.3152(8)	19(1)
Li8	3*c*	0.1556(4)	0	0.6740(8)	16(1)
Li9	3*c*	0.2423(4)	0	0.9634(9)	18(1)
Li10	6*d*	0.4987(3)	0.1619(4)	0.3216(7)	18(1)
Li11	6*d*	0.3382(3)	0.1476(3)	0.2332(6)	14.0(9)
Li12	6*d*	0.5013(3)	0.3324(3)	0.1786(7)	17(1)
Li13	6*d*	0.4331(3)	0.0943(3)	0.9449(7)	19(1)

Figures S1 – S3

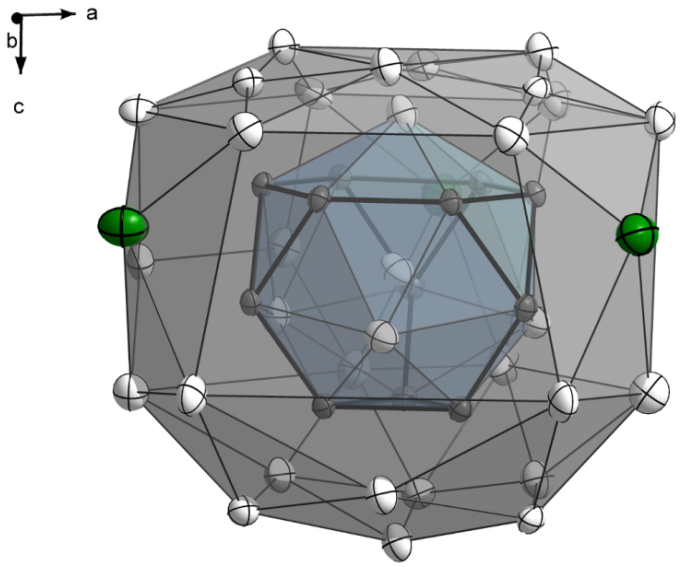

Figure S1. Coordination sphere of the Friauf polyhedron $[Li@Li_4Ge_{12}]^{7-}$ (blue) in $Li_{18}Na_2Ge_{17}$ (Li = white, Na = green, Ge = grey; thermal ellipsoids at 90 % probability at 123 K).

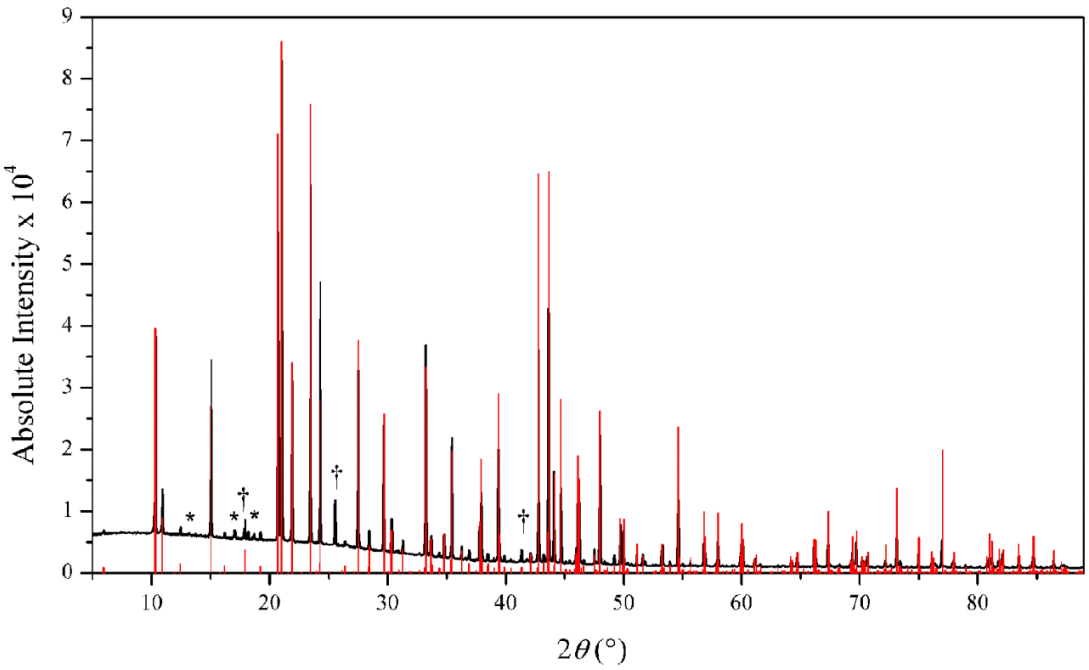

Figure S2. Experimental X-ray powder diffraction pattern of $Li_{18}Na_2Ge_{17}$ (black) referenced with its theoretical powder pattern (red; † = LiGe, * = unknown compound).

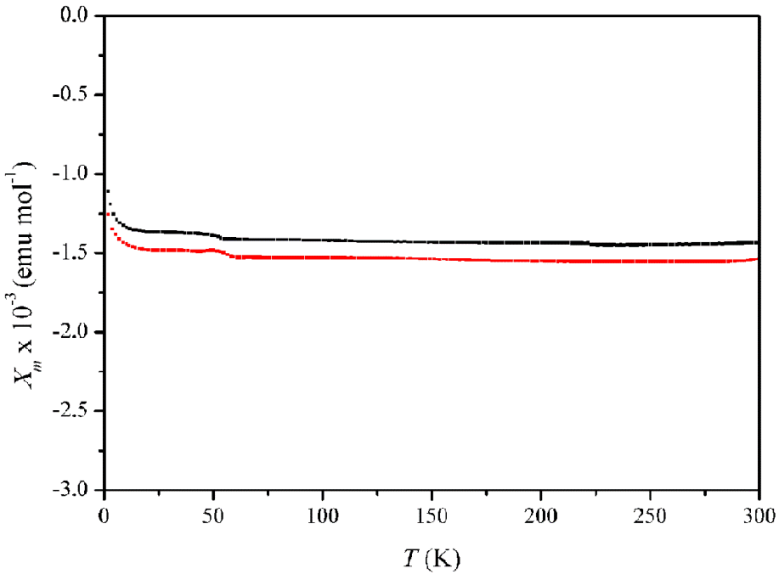

Figure S3. Molar susceptibilities X_m of $Li_{18}Na_2Ge_{17}$ at field intensities H of 5 000 Oe (black) and 10 000 Oe (red) over the temperature range of 2–300 K. The data were corrected for the sample holder and for ion-core diamagnetism using Pascal's constants.[1] Slight deviations from ideal diamagnetic behavior at low temperatures are caused by small sample impurities.

REFERENCES

1. Bain, G. A.; Berry, J. F. *J. Chem. Educ.* **2008,** *85*, 532–536.

5.8 $LiBSi_2$: A Tetrahedral Semiconductor Framework from Boron and Silicon Atoms Bearing Lithium Atoms in the Channels

Zintl Phases

DOI: 10.1002/anie.201301540

$LiBSi_2$: A Tetrahedral Semiconductor Framework from Boron and Silicon Atoms Bearing Lithium Atoms in the Channels**

Michael Zeilinger, Leo van Wüllen, Daryn Benson, Verina F. Kranak, Sumit Konar, Thomas F. Fässler, and Ulrich Häussermann**

Dedicated to Prof. Dr. Dr. h. c. mult. Wolfgang A. Herrmann on the occasion of his 65th birthday

The crystalline open frameworks of zeolites and clathrates are based on three-periodic, four-connected nets with tetrahedral nodes and have long attracted attention for their unique physical properties and great significance to fundamental crystal chemistry.[1] Such open tetrahedral frameworks (OTFs) enclose interstitial volumes in the form of large and separated cages (clathratic frameworks) or channels (zeolitic frameworks). While they most commonly occur with oxide materials, using oxygen to bridge the tetrahedral nodes, intermetallic Zintl phases may realize OTFs where the edges of nets correspond to covalent two-center, two-electron bonds (direct links).[2] Tetrahedral nodes in Zintl-phase OTFs are typically represented by the tetravalent Group 14 element (Tt) atoms Si, Ge, and Sn or mixtures of Tt atoms and trivalent Group 13 element (Tr) atoms (sp^3 hybridized atoms). For the latter systems, the apparent electron deficiency is balanced by electrons of the less electronegative metals situated in cavities in the OTF (guest species), which becomes nominally charged, that is, $(4c\text{-}Tt)_n = (A^+)_m(4c\text{-}Tt)_{n-m}(4c\text{-}Tr^-)_m$ (4c = four-connected, A = alkaline-earth metal) and thus shows a strong analogy to the charge distribution in aluminosilicates.

Among Zintl-phase OTFs the clathrate-I and -II type of structures with the nets **mtn** and **mep**, respectively,[3] are most prominent (Scheme 1). They occur for numerous compositions and have received considerable attention for their thermoelectric and superconducting properties.[4] Guest species in cages (i.e. Na–Cs, Sr, Ba, Eu atoms) play an important role in determining and tuning electric and thermal transport properties.[2a] Other OTFs include zeolitic frameworks such as the chiral net **unj** which is the basis of the structures of $NaInSn_2$, $NaGaSn_2$, and $NaGaSn_5$ as well as *hP*-Na_2ZnSn_5 and *tI*-Na_2ZnSn_5,[5] and **CAS** which describes the topology of the frameworks of $Eu_4Ga_6Si_{16}$ or ASi_6 (A = Ca, Sr, Ba).[6]

Notably, compared with silicates the topological variety of Zintl-phase OTFs is very limited[3a,7] and especially attempts to achieve Zintl-phase OTFs with Li as the guest species have long been unsuccessful,[8] although interesting properties for such materials were predicted.[9] For clathratic frameworks it

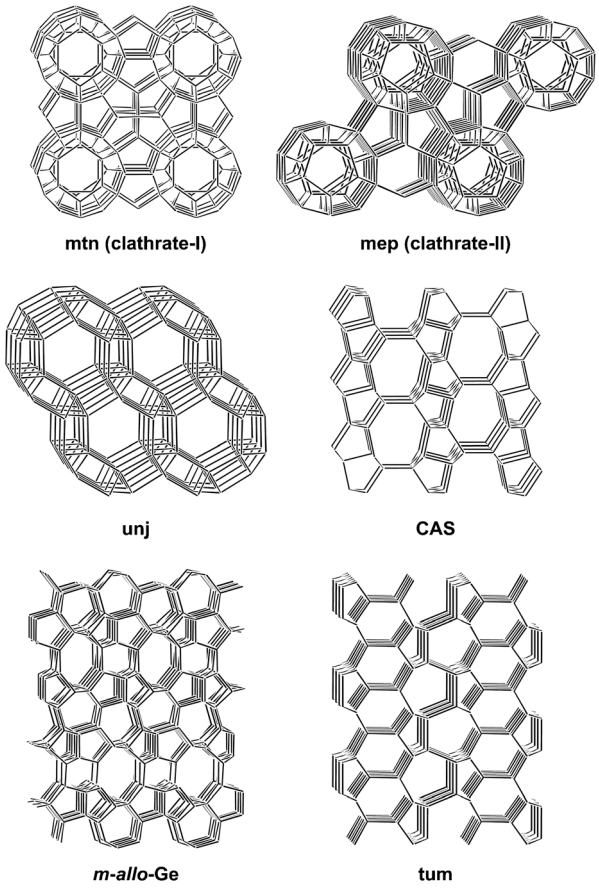

Scheme 1. Open tetrahedral frameworks realized by Zintl phases and Group 14 elements.[3]

[*] M. Zeilinger, Prof. Dr. T. F. Fässler
Department of Chemistry, Technische Universität München, Lichtenbergstrasse 4, 85747 Garching/München (Germany)
E-mail: thomas.faessler@lrz.tum.de
Prof. Dr. L. van Wüllen
Department of Physics, University of Augsburg, Universitätsstrasse 1, 86159 Augsburg (Germany)
D. Benson
Department of Physics, Arizona State University, Tempe, Arizona 85287-1504 (USA)
V. F. Kranak, S. Konar, Prof. Dr. U. Häussermann
Department of Materials and Environmental Chemistry, Stockholm University, SE-10691 Stockholm (Sweden)
E-mail: Ulrich.Haussermann@mmk.su.se

[**] This work was supported by Fonds der Chemischen Industrie, TUM Graduate School, Deutsche Forschungsgemeinschaft FA 198/11-1, the Swedish Research Council under contract number 2010-4827, and the National Science Foundation through grant DMR-1007557.

Supporting information for this article (including further details on the synthesis procedure, the analysis of products, and the computational procedure) is available on the WWW under http://dx.doi.org/10.1002/anie.201301540.

is believed that cages would be too large for Li atoms.[8] The encapsulation of Li atoms (in a stable compound) will probably require the OTF to consist of a large fraction of light elements from the second row, that is, B and C atoms. Thus far, the only known OTF involving a second row element is found in $K_7B_7Si_{39}$,[10] where a comparatively small fraction of the Si atoms in a clathrate-I structure are replaced by B atoms. Although this produced the smallest lattice parameter among Zintl phases with the clathrate-I structure cage, the size remained far too large for Li atoms.

Herein, we report on $LiBSi_2$ displaying a zeolitic framework with a new topology based on a unique strictly ordered distribution of B and Si atoms. This B-Si OTF has mutually orthogonal channels that host Li atoms.

$LiBSi_2$ was obtained as a dark gray, microcrystalline, powder from reaction mixtures LiB:Si = 1:1 that had been pressurized to 10 GPa and heated at 900 °C. $LiBSi_2$ is air and moisture stable, and also inert to strong acids. Its thermal stability exceeds 800 °C. The structure of $LiBSi_2$ depicted in Figure 1 was solved from powder X-ray diffraction data using a parallel tempering algorithm and subsequently finalized by Rietveld refinement.[11]

$LiBSi_2$ crystallizes with the tetragonal space group $P4_2/nmc$ and contains eight formula units in the unit cell

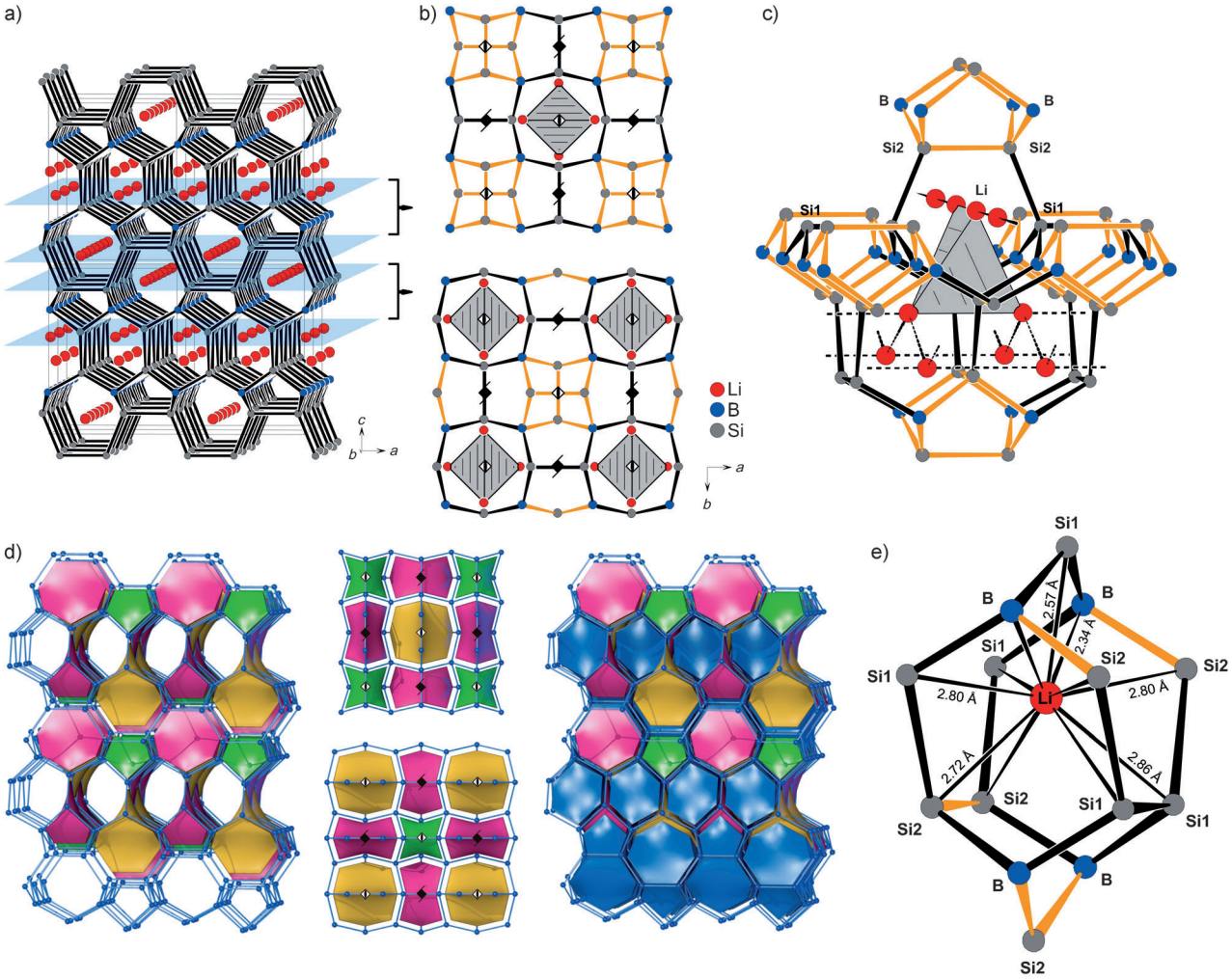

Figure 1. a) Crystal structure of tetragonal $LiBSi_2$ (2×2×2 supercell) viewed approximately along the [100] direction. Atoms are displayed as ellipsoids at a 90% probability (Li red, B blue, Si dark gray). Boundaries of two slab-like building units are marked by light blue planes. b) Two consecutive slab building units projected along the [001] direction. Bonds of the realgar-like $[B_4Si2_4]$ structural unit are drawn in yellow. Elongated tetrahedra produced by the arrangement of Li atoms are highlighted. The position of 4_2 and $\bar{4}$ axes are indicated by their symbol. c) Section of the $LiBSi_2$ structure showing the consequence of connecting slab building units: six- and seven-membered rings are introduced defining orthogonal channels that host the Li atoms. Within seven-ring channels Li atoms are arranged as linear chains, within six-ring channels as zigzag chains. Connecting lines between Li atoms do not indicate interactions, they are only meant to emphasize structural features. d) Natural tiling for the net **tum** formed by B and Si atoms in $LiBSi_2$. There are four different kinds of tiles, three four-faced tiles and one six-faced. (A tile is characterized by a face symbol $[M^m.N^n...]$ indicating that there are m faces that are M-rings, n faces that are N-rings, and so on). Left: Arrangement of 4-faced tiles $[5^4]$ (green), $[7^4]$ (yellow), and $[5^2.7^2]$ (pink) not sharing faces. Middle: Arrangement of four-faced tiles within slab building blocks (Figure 1b). Right: Complete natural tiling of **tum** including also the six-faced "Li tiles" $[5^2.6^2.7^2]$ (blue). Li tiles share common six-ring faces which emphasizes the six-ring channel system (hosting Li zigzag chains) in zeolitic $LiBSi_2$ (seen at the bottom of the figure). e) Coordination environment around Li atoms within a $[5^2.6^2.7^2]$ tile.

(Figure 1a). The B-Si ordered OTF is built from three distinct crystallographic positions—one B site (8*f*) and two Si sites (Si1 and Si2, both on 8*g*)—and thus corresponds to a trinodal net. Li atoms are situated on an *8g* site and occupy channels in the B-Si OTF.

The tetrahedral B-Si framework can be divided into $[B_4Si2_4]$ realgar-like units and Si1-Si1 dumbbells which occur in a 1:2 ratio and are arranged in two-dimensional slabs (Figure 1b). The realgar-like unit represents a cage, which is enclosed by four five-membered rings. Its linkage with the $Si1_2$ dumbbell units creates additional five-membered rings. The slab also contains eight-membered rings, which, however, become part of seven-membered rings upon connecting slabs and thus do not represent strong rings in the three-periodic framework.[12] Finally, a slab hosts mutually perpendicular linear chains of Li atoms at two different heights (corresponding to the thickness of a slab; Figure 1a) running along the *a* and *b* directions. Distances in a linear chain are alternating short (3.36 Å) and long (3.47 Å), and the arrangement of short distances corresponds to elongated Li_4 tetrahedra surrounded by eight-membered rings.

In the three-periodic net, slabs are stacked along the *c* direction, related by the *n* glide perpendicular to *c* (Figure 1b). As a consequence, realgar and Li_4 tetrahedral units are situated alternating on top of each other and $(Si1)_2$ dumbbells are stacked mutually rotated by 90°.[13] The connection of slabs introduces six- and seven-membered rings, which define the channels hosting the Li atoms (Figure 1c, compared to Figure 1a). In channels embraced by seven-membered rings, Li atoms are arranged as the linear chains mentioned above; in channels embraced by six-membered rings, Li atoms form zigzag chains where they are equidistantly separated at 3.66 Å (Figure 1c). This distance corresponds to the separation of Li_4 tetrahedra, or alternatively the distance between parallel linear chains at different heights. Both kinds of channels run along the *a* and *b* directions and are mutually converted by a 90° rotation around the *c* axis.

The outcome of the ordering of B and Si atoms is that B atoms are exclusively bonded to Si atoms with $d_{Si\text{-}B} = 2.05$ and 2.08 Å whereas Si atoms utilize two homoatomic bonds with distances $d_{Si\text{-}Si} = 2.44$, 2.47, and 2.51 Å. Different B–Si and Si–Si bond lengths induce distorted tetrahedral coordination environments ($\sphericalangle$(Si–B–Si) = 91.07°–124.52°; $\sphericalangle$(B–Si–B) = 106.41°, 117.30°; $\sphericalangle$(Si–Si–B) = 100.94°–116.96°; $\sphericalangle$(Si–Si–Si) = 112.33°).

The OTF formed by B and Si atoms in $LiBSi_2$ consists exclusively of five-, six-, and seven-membered rings and represents a not yet described topology for a three-periodic, four-connected net. It has been assigned the symbol **tum** in the TTD topological database.[14] We note that **tum** is also the net of the orthorhombic framework of the recently discovered intermetallic compounds $Na_5M_{2+x}Sn_{10-x}$ ($x \approx 0.5$, M = Zn, Hg) where it is formed by the M and Sn atoms.[15]

The natural tiling associated with **tum** is shown in Figure 1d. A tiling is the filling of space by generalized polyhedra (tiles) that share faces.[16] A tile represents the interior of a cage with typically curved faces that are rings of the net. Thus a tiling carries a net formed by the vertices and edges of tiles. According to a set of rules, natural tilings are unique and provide an unambiguous way to partition space by the net. This in turn enables convenient identification and analysis of the size and location of cavities and channels. For **tum** there are four kinds of tiles: one corresponds to the $[B_4Si2_4]$ realgar-like cage centered at the Wyckoff site 2a and has the face symbol $[5^4]$, indicating that there are four faces that are five-membered rings. Another tile with face symbol $[7^4]$ is located at the center of the Li_4 tetrahedron (position 2b) and a third tile with the face symbol $[5^2.7^2]$ is centered at site 4d, in between two $Si1_2$ dumbbells stacked along the *c* direction. The fourth tile is enclosed by six faces (face symbol $[5^2.6^2.7^2]$) and is centered at a position approximately corresponding to the location of the Li atoms (Figure 1e).

This partitioning appears chemically meaningful; the three four-faced tiles do not share common faces but are tetrahedrally surrounded by Li tiles, which in turn are octahedrally connected to two $[5^2.7^2]$ tiles (through a seven- and a five-membered ring face, respectively), one realgar $[5^4]$ tile, one $[7^4]$ tile, and two other Li tiles (sharing six-sided faces). The face sharing of Li tiles defines the relevant channels (Figure 1f), which, interestingly, are those that are embraced by six-membered rings and host zigzag chains of Li atoms rather than the ones embraced by seven-membered rings that host linear chains. Li atoms in $LiBSi_2$ attain a clearly defined coordination by two B and nine Si atoms (Figure 1e). Distances range from 2.34 Å (Li-B) to 2.86 Å (Li-Si1) and are well separated from the next nearest neighbor distances starting off at 3.34 Å (Li-B). However, the tile (cage) associated with Li is larger (14 vertices) and Li is positioned quite off-centered in its tile.

The structure was further confirmed by the Raman spectrum of $LiBSi_2$ (Figure 2). The rather complex structure gives rise to 31 Raman-active modes,[17] of which about 20 are observed. Excitation with a green laser ($\lambda = 532$ nm) yields better resolved high-frequency modes, whereas red-laser excitation ($\lambda = 785$ nm) results in better resolved low-frequency modes. The assignment of bands was assisted by first-principles zone center phonon calculations. The modes with lowest and highest wave number were calculated at 168 and 683 cm^{-1}, respectively, which is in good agreement with the span of wave numbers of the observed spectrum. The bands in the wave number region 600–700 cm^{-1} correspond to B-Si vibrations (modes 14–19; Figure 2) and are detached from the bulk of modes between 150 and 470 cm^{-1}. The latter range of wave numbers is typical for Si-Si stretching and bending vibrations in silicide clathrates,[18] however, for $LiBSi_2$ we find that bands from Si-Si and Li-Si vibrations appear at similar wave numbers. In fact, mode 13 at around 467 cm^{-1} corresponds to a Li-Si vibration, whereas the first Si-Si stretching mode (12) is at around 430 cm^{-1}. This indicates a strong interaction between Li and the host OTF. Also, the optical mode with the lowest wave number involves displacement contributions from all atoms and is not, as perhaps expected, dominated by Li atoms.

The electronic structure of $LiBSi_2$ has been calculated and the density of states (DOS) is shown in Figure 3. $LiBSi_2$ is a semiconductor with a band gap of 1.1 eV. Because DFT-calculated band gaps are known to be underestimated, the

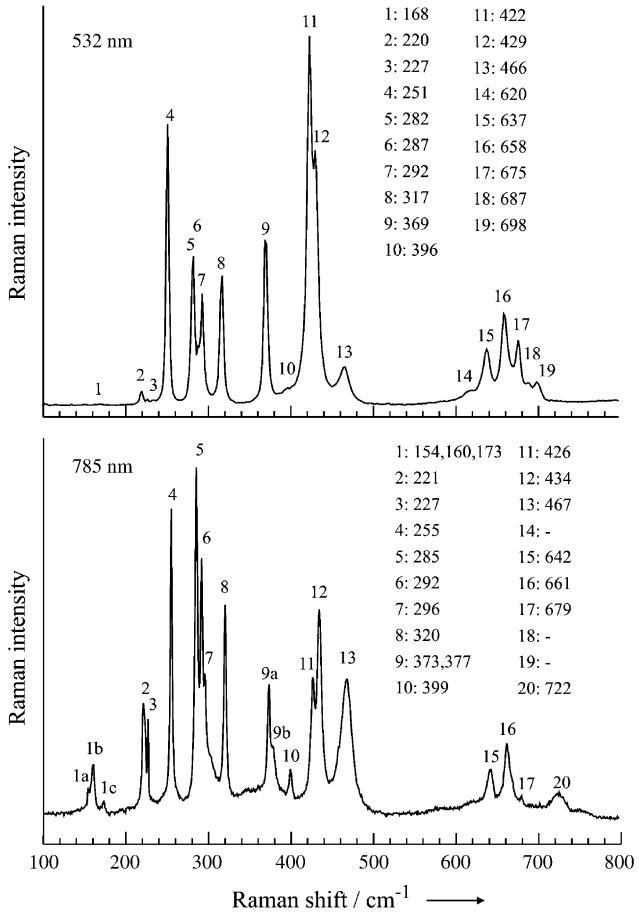

Figure 2. Raman spectrum of $LiBSi_2$ recorded with excitation wavelengths 532 and 785 nm. Values listed are wavenumbers (cm^{-1}) of the labeled bands (1–20). The origin of band 20 in the lower spectrum is not known.

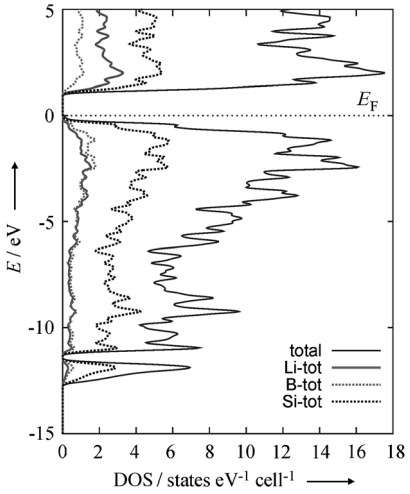

Figure 3. Electronic density of states for $LiBSi_2$ and the site projected contributions from Li, B, and Si atoms. The Fermi level (E_F) is set at 0 eV at the top of the valence band (dotted line).

experimental band gap may approach 2 eV. The occurrence of a band gap is in agreement with an electron precise B-Si OTF where Li acts as an electron donor, as expected for a Zintl phase. However, the site-projected DOS reveals that the Li and B states contribute almost equally and homogenously to the valence band throughout its range of dispersion. Such an intimate admixture of states from the less electronegative—electron-donating—component to the occupied valence band is not typical of a Zintl phase and is also indicative of strong Li-OTF interactions. Preliminary ^{7}Li- and ^{11}B-MAS-NMR investigations (chemical shift of ^{7}Li: −0.35 ppm) reveal the diamagnetic character. Further details on the NMR-spectroscopic investigations are given in the Supporting Information.

Apart from its new topology, the B-Si net in $LiBSi_2$ is also chemically unique: it represents the first example where B and Si atoms form an ordered common framework structure with boron exclusively engaged in heteronuclear B-Si contacts. Typically frameworks of borosilicides are characterized by either segregated B and Si structural entities or separated B_{12} icosahedra and Si_4 rhomboid rings as in β-SiB_3[19] or the occurrence of B/Si disorder as manifested in mixed occupied positions as, for example, in α-SiB_3, $Na_8B_{74.5}Si_{17.5}$,[20] and the earlier mentioned $K_7B_7Si_{39}$.[10] Since the **tum** net exclusively consists of four-connected nodes it additionally enlarges the number of models for novel tetrel allotropes, such as the recently predicted Si allotrope[21] or the experimentally established *m-allo*-Ge.[22]

In conclusion, we have shown that high-pressure reactions between LiB and Si afford $LiBSi_2$ with a novel intermetallic B-Si OTF dubbed **tum**. Unique to this compound is the encapsulation of small-sized Li as the guest species and the topology of the OTF, based on a strictly ordered distribution of B and Si atoms. Owing to the low density and its open framework structure, doped $LiBSi_2$ may be the basis for useful electrode materials.[9c] Also, **tum** may be an interesting model for a low-density allotrope of Group 14 elements. The search for such allotropes has recently become a very active field of research.[7,21] $LiBSi_2$ is predicted to be a semiconductor with a band gap exceeding 1 eV. Vibrational properties and the calculated electronic structure indicate that the Li guest species interacts strongly with the OTF host. The physical properties, the detailed formation conditions of $LiBSi_2$, as well as an analysis of the NMR-spectroscopic investigations will be presented in a forthcoming paper.

Experimental Section

In a typical synthesis a mixture of LiB and Si (80–100 mg, molar ratio 1:1) were sealed in a salt capsule. The capsules were compressed in a multi-anvil device[23] to a pressure of 10 GPa and subsequently heated to 900 °C at a rate of 5 °C min^{-1}. After equilibrating samples at their target temperature for one hour, the temperature was quenched and the pressure released at a rate of approximately 0.5 GPa per hour. The preparation of salt capsules and their recovery after high-pressure, high-temperature treatment was performed in an Ar-filled glove box. Thereafter, the product was treated with half concentrated HCl and washed several times with water and ethanol followed by drying in air. A synthesis run typically yielded 40–50 mg product. Products were analyzed by powder X-ray diffraction (PXRD), Raman, and ^{7}Li- and ^{11}B-MAS NMR spectroscopy.

Samples were ground, loaded into 0.3 mm capillaries, and measured on a STOE STADI P diffractometer (Ge-(111) monochromator for CuK_α radition, $\lambda = 1.54056$ Å) equipped with a linear position-sensitive detector (PSD). Tetragonal unit cell: $a =$ 6.83225(3) Å, $c = 8.83924(6)$ Å and space group $P4_2/nmc$. Further

details on the crystal structure may be obtained from the Fachinformationszentrum Karlsruhe, 76344 Eggenstein-Leopoldshafen, Germany (fax: (+49) 7247-808-666; e-mail: crysdata@fiz-karlsruhe.de), by quoting the depository number CSD-425643 ($LiBSi_2$).

Raman spectra were recorded on powder samples placed on a glass slide using a LabRAM HR 800 spectrometer with a back-thinned CCD detector and lasers at 532 and 785 nm as excitation sources. ^{7}Li- and ^{11}B-MAS (magic angle spinning) NMR spectra (Supporting Information, Figures S3,S4) were collected on a Varian VNMRs 500 spectrometer, operating at 160.37 MHz and 194.24 MHz for ^{11}B and ^{7}Li, respectively. MAS was performed at spinning speeds of 15–40 kHz with a Varian 1.6 mm triple resonance T^3-MAS probe. Theoretical calculations were performed in the framework of the frozen core all-electron projected augmented wave (PAW) method, as implemented in the program VASP.[24]

Received: February 22, 2013
Published online: April 22, 2013

Keywords: open tetrahedral frameworks · silicon · zeolites · Zintl phases

[1] a) J. V. Smith, *Chem. Rev.* **1988**, *88*, 149; b) M. O'Keeffe, B. G. Hyde, *Crystal Structures 1: Patterns and Symmetry*, Monograph, Mineralogical Assoc. of America, Washington DC, **1996**; c) O. Delgado Friedrichs, A. W. M. Dress, D. H. Huson, J. Klinowski, A. L. Mackay, *Nature* **1999**, *400*, 644.

[2] a) "Zintl Clathrates": A. V. Shevelkov, K. Kovnir in *Zintl Phases: Principles and Recent Developments*, *Vol. 139* (Eds.: D. M. P. Mingos, T. F. Fässler), Springer, Heidelberg **2011**, p. 97; b) "Structural Relationships Between Intermetallic Clathrates, Porous Tectosilicates and Clathrate Hydrates": D. Santamaria-Perez, F. Libeau in *Inorganic 3D Structures: The Extended Zintl-Klemm Concept*, *Vol. 138* (Eds.: D. M. P. Mingos, A. Vegas), Springer, Heidelberg **2011**, p. 1.

[3] Symbols for nets follow either the zeolite code according to ref. [3a] or the RCSR identifiers according to ref. [3b]; a) C. Baerlocher, W. M. Meier, D. H. Olson, *Atlas of Zeolite Framework Types*, 6th rev. ed., Elsevier, Amsterdam, **2007**. Data available online at http://www.iza-structure.org/databases/; b) M. O'Keeffe, M. A. Peskov, S. J. Ramsden, O. M. Yaghi, *Acc. Chem. Res.* **2008**, *41*, 1782.

[4] a) M. Beekman, G. S. Nolas, *J. Mater. Chem.* **2008**, *18*, 842; b) G. S. Nolas, J. L. Cohn, G. A. Slack, S. B. Schujman, *Appl. Phys. Lett.* **1998**, *73*, 178; c) S. Yamanaka, *Dalton Trans.* **2010**, *39*, 1901.

[5] a) W. Blase, G. Cordier, R. Kniep, R. Schmidt, *Z. Naturforsch. B* **1989**, *44*, 505; b) J. T. Vaughey, J. D. Corbett, *J. Am. Chem. Soc.* **1996**, *118*, 12098; c) W. Blase, G. Cordier, *Z. Naturforsch. B* **1988**, *43*, 1017; d) S. Stegmeier, S.-J. Kim, A. Henze, T. F. Fässler, unplublished results.

[6] a) J. D. Bryan, G. D. Stucky, *Chem. Mater.* **2001**, *13*, 253; b) W. Carrillo-Cabrera, S. Paschen, Y. Grin, *J. Alloys Compd.* **2002**, *333*, 4; c) A. Wosylus, Y. Prots, U. Burkhardt, W. Schnelle, U. Schwarz, *Sci. Technol. Adv. Mater.* **2007**, *8*, 383; d) A. Wosylus, Y. Prots, U. Burkhardt, W. Schnelle, U. Schwarz, Y. Grin, *Z. Naturforsch. B* **2006**, *61*, 1485; e) S. Yamanaka, S. Maekawa, *Z. Naturforsch. B* **2006**, *61*, 1493.

[7] a) M. M. J. Treacy, I. Rivin, E. Balkovsky, K. H. Randall, M. D. Foster, *Microporous Mesoporous Mater.* **2004**, *74*, 121; b) A. J. Karttunen, T. F. Fässler, M. Linnolahti, T. A. Pakkanen, *Inorg. Chem.* **2011**, *50*, 1733.

[8] Li replaces small amounts of Ge in the clathrate-I host structure. See: Y. Liang, B. Bohme, A. Ormeci, H. Borrmann, O. Pecher, F. Haarmann, W. Schnelle, M. Baitinger, Y. Grin, *Chem. Eur. J.* **2012**, *18*, 9818.

[9] a) A. Ker, E. Todorov, R. Rousseau, K. Uehara, F. X. Lannuzel, J. S. Tse, *Chem. Eur. J.* **2002**, *8*, 2787; b) N. Rey, A. Munoz, P. Rodriguez-Hernandez, A. San Miguel, *J. Phys. Condens. Matter* **2008**, *20*, 215218; c) A recent report gives evidence that Li can be inserted electrochemically into Si clathrate-II and may have potential as a novel electrode material for lithium-ion batteries, see: T. Langer, S. Dupke, H. Trill, S. Passerini, H. Eckert, R. Pöttgen, M. Winter, *J. Electrochem. Soc.* **2012**, *159*, A1318.

[10] W. Jung, J. Lorincz, R. Ramlau, H. Borrmann, Y. Prots, F. Haarmann, W. Schnelle, U. Burkhardt, M. Baitinger, Y. Grin, *Angew. Chem.* **2007**, *119*, 6846; *Angew. Chem. Int. Ed.* **2007**, *46*, 6725.

[11] a) F.O.X., Free Objects for Crystallography V 1.9.7.0, http://objcryst.sourceforge.net, **2011**; b) R. Černý, V. Favre-Nicolin, *Powder Diffr.* **2005**, *20*, 359; c) V. Favre-Nicolin, R. Cerny, *J. Appl. Crystallogr.* **2002**, *35*, 734; d) TOPAS 4.0—Rietveld Software, Bruker AXS, Madison (Wisconsin, USA), **2009**.

[12] Strong rings are defined as rings that are not the sum of any number of smaller cycles, see: O. Delgado-Friedrichs, M. O'Keeffe, *J. Solid State Chem.* **2005**, *178*, 2480.

[13] Realgar and Li_4 tetrahedral units have $-4m2$ symmetry. Note that the 4_2 screw axis runs through the centers of gravity of the $(Si1)_2$ units.

[14] a) V. A. Blatov, D. M. Proserpio, *Acta Crystallogr. Sect. A* **2009**, *65*, 202; b) V. A. Blatov, *IUCr CompComm. Newsletter* **2006**, *7*, 4; c) TOPOS Topological Databases and Topolgical Types Observed, http://www.topos.ssu.samara.ru.

[15] S. Ponou, S. J. Kim, T. F. Fässler, *J. Am. Chem. Soc.* **2009**, *131*, 10246.

[16] a) V. A. Blatov, O. Delgado-Friedrichs, M. O'Keeffe, D. M. Proserpio, *Acta Crystallogr. Sect. A* **2007**, *63*, 418; b) O. Delgado-Friedrichs, M. O'Keeffe, O. M. Yaghi, *Phys. Chem. Chem. Phys.* **2007**, *9*, 1035; c) V. A. Blatov, M. O'Keeffe, D. M. Proserpio, *CrystEngComm* **2010**, *12*, 44.

[17] E. Kroumova, C. Capillas, S. Ivantchev, H. Wondratschek, *Phase Transitions* **2003**, *76*, 155.

[18] a) G. S. Nolas, C. A. Kendziora, J. Gryko, J. Dong, C. W. Myles, A. Poddar, O. F. Sankey, *J. Appl. Phys.* **2002**, *92*, 7225; b) D. Machon, P. Toulemonde, P. F. McMillan, M. Amboage, A. Munoz, P. Rodriguez-Hernandez, A. San Miguel, *Phys. Rev. B* **2009**, *79*, 184101.

[19] J. R. Salvador, D. Bilc, S. D. Mahanti, M. G. Kanatzidis, *Angew. Chem.* **2003**, *115*, 1973; *Angew. Chem. Int. Ed.* **2003**, *42*, 1929.

[20] a) B. Magnusson, C. Brosset, *Acta Chem. Scand.* **1962**, *16*, 449; b) H. F. Rizzo, L. R. Bidwell, *J. Am. Ceram. Soc.* **1960**, *43*, 550; c) H. Morito, B. Eck, R. Dronskowski, H. Yamane, *Dalton Trans.* **2010**, *39*, 10197.

[21] a) M. A. Zwijnenburg, K. E. Jelfs, S. T. Bromley, *Phys. Chem. Chem. Phys.* **2010**, *12*, 8505; b) C. J. Pickard, R. J. Needs, *Phys. Rev. B* **2010**, *81*, 014106.

[22] a) A. Grüttner, R. Nesper, H. G. von Schnering, *Angew. Chem.* **1982**, *94*, 933; *Angew. Chem. Int. Ed. Engl.* **1982**, *21*, 912; b) F. Kiefer, A. J. Karttunen, M. Döblinger, T. F. Fässler, *Chem. Mater.* **2011**, *23*, 4578.

[23] E. Stoyanov, U. Häussermann, K. Leinenweber, *High Pressure Res.* **2010**, *30*, 175.

[24] a) P. E. Blöchl, *Phys. Rev. B* **1994**, *50*, 17953; b) G. Kresse, D. Joubert, *Phys. Rev. B* **1999**, *59*, 1758; c) G. Kresse, J. Hafner, *Phys. Rev. B* **1993**, *48*, 13115; d) G. Kresse, J. Furthmüller, *Comput. Mater. Sci.* **1996**, *6*, 15.

Angewandte Chemie
Eine Zeitschrift der Gesellschaft Deutscher Chemiker

Supporting Information

69451 Weinheim, Germany

$LiBSi_2$: A Tetrahedral Semiconductor Framework from Boron and Silicon Atoms Bearing Lithium Atoms in the Channels**

Michael Zeilinger, Leo van Wüllen, Daryn Benson, Verina F. Kranak, Sumit Konar, Thomas F. Fässler, and Ulrich Häussermann**

anie_201301540_sm_miscellaneous_information.pdf

Supporting Information

Synthesis. Starting materials were rods of Li (99 %, Rockwood-Lithium), boron chunks (99.95 %, ChemPur) and silicon powder (99.999%, Sigma-Aldrich). All steps for synthesis and sample preparation were carried out in a glove box (MBraun, Ar-atmosphere, H_2O and O_2 levels < 0.1 ppm). Stainless steel ampoules were thoroughly cleaned, heated to 700 °C under dynamic vacuum ($p < 1 \cdot 10^{-3}$ mbar) for at least 1 h and transferred to the glove box. Heating and handling under inert conditions was done by using an all-glass Schlenk line supplied with Ar, which is dried over phosphorous pentoxide, molecular sieve and heated titanium sponge ($T = 750$ °C).

LiB: Lithium and boron were filled into a stainless steel ampoule with a molar ratio of 1:1 and a total mass of 0.5 g. The ampoule was sealed by arc-welding inside the glove box and then encapsulated in a silica jacket under vacuum. After annealing at 470 °C in a muffle oven for three days pure LiB is obtained (Figure S1). For further synthesis steps LiB was ground inside an agate mortar.

$LiBSi_2$: High pressure syntheses were performed in a 6-8 Walker-type multi-anvil high pressure device using an 18/12 assembly developed by Stoyanov et al..[1] Mixtures of powdered LiB and Si with a molar ratio of 1:1 and a total amount between 80 and 100 mg were compacted and placed inside a NaCl capsule (inner diameter: 4 mm, outer diameter: 8 mm, length: 8 mm; prepared from NaCl dried under vacuum at 250-300 °C). Subsequently, capsules were sealed and transferred outside the glove box. To prepare the high pressure cell assembly NaCl sample capsules were positioned in a graphite furnace which in turn was placed together with a Zircon thermal insulating sleeve (0.57 mm wall thickness, 7.77 mm OD, 10.80 mm length) in a magnesia octahedron with 18 mm edge length. Samples were pressurized at a rate of about 0.5 GPa/h with 25 mm tungsten carbide cubes truncated to 12 mm edge length. After reaching the target pressure of 10 GPa the samples were heated. Deviations from the target pressure are estimated as +/– 0.3 GPa. The temperature was measured close to the sample using a thermocouple type C (W5%Re – W26%Re wire) in an Al_2O_3 sleeve. The samples were heated to 900 °C within 3 h. After applying a dwelling time of 1 h samples were quenched by turning off the power to the furnace (quench rate ~50 °C/min and at approximately constant pressure). Afterwards, the pressure was released at a rate of approximately 0.5 GPa/h and the samples were recovered in the glove box. Thereafter, the product was treated with diluted HCl and washed several times with water and ethanol followed by drying in air. The product was obtained as a fine, grey colored, powder. According to powder X-Ray diffraction it corresponds to crystalline $LiBSi_2$ and a minor amount of an unidentified crystalline impurity (Figure 2, reflections at 2θ ~21° and ~28°). Solid state NMR investigations (see below) revealed the presence of an amorphous byproduct next to crystalline $LiBSi_2$, which most likely is associated with the excess of LiB employed in the high pressure synthesis.

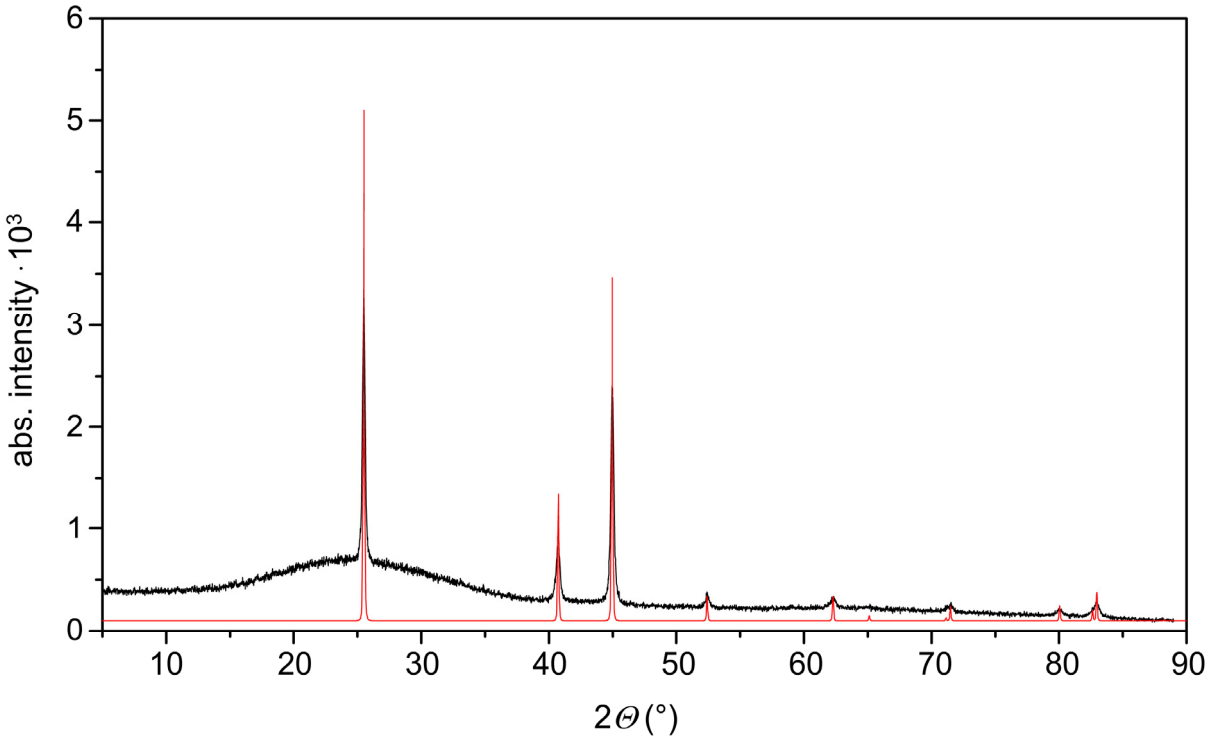

Figure S1. Experimental X-ray powder diffraction pattern of LiB (black) referenced with its theoretical powder pattern (red).

Powder X-ray diffraction. X-ray powder diffraction patterns were recorded on a STOE STADI P diffractometer (Ge-(111) monochromator for CuK_α radiation, $\lambda = 1.54056$ Å) equipped with a linear PSD. Samples were ground in an agate mortar, sealed in 0.3 mm glass capillaries and measured within a 2θ range of 5-90° using two measurement runs, each with a PSD step width of 0.05° and an exposure time of 40 sec per step.

Structure determination. The structure of $LiBSi_2$ was determined *ab initio* from X-ray powder diffraction data by using the parallel tempering algorithm implemented in the software FOX.[2] The X-ray diffraction pattern could be indexed with a tetragonal cell $a = 6.83225(3)$ Å, $c = 8.83924(6)$ Å and the space group $P4_2/nmc$ was assigned after Le Bail profile fitting. As the main idea of the FOX program is to approach structure solutions by starting with "structural building blocks" several structure motifs having B-B bonds could be excluded because Raman spectroscopy clearly showed the absence of those. Consequently, the idea of a tetrahedral B-Si network arose and resulted in a successful structure solution with acceptable reliability factors ($R_{wp} = 0.067$, GOF = 1.24). The final structure is provided by Rietveld refinement which was done with the program TOPAS 4.0.[3] The results of the refinement are presented in Figure S2 and Tables 1-3. Further data may be obtained from Fachinformationszentrum Karlsruhe, D-76344 Eggenstein-Leopoldshafen, Germany (fax: (+49)7247-808-666; e-mail: crysdata@fiz-karlsruhe.de) on quoting the depository numbers CSD-425643 ($LiBSi_2$).

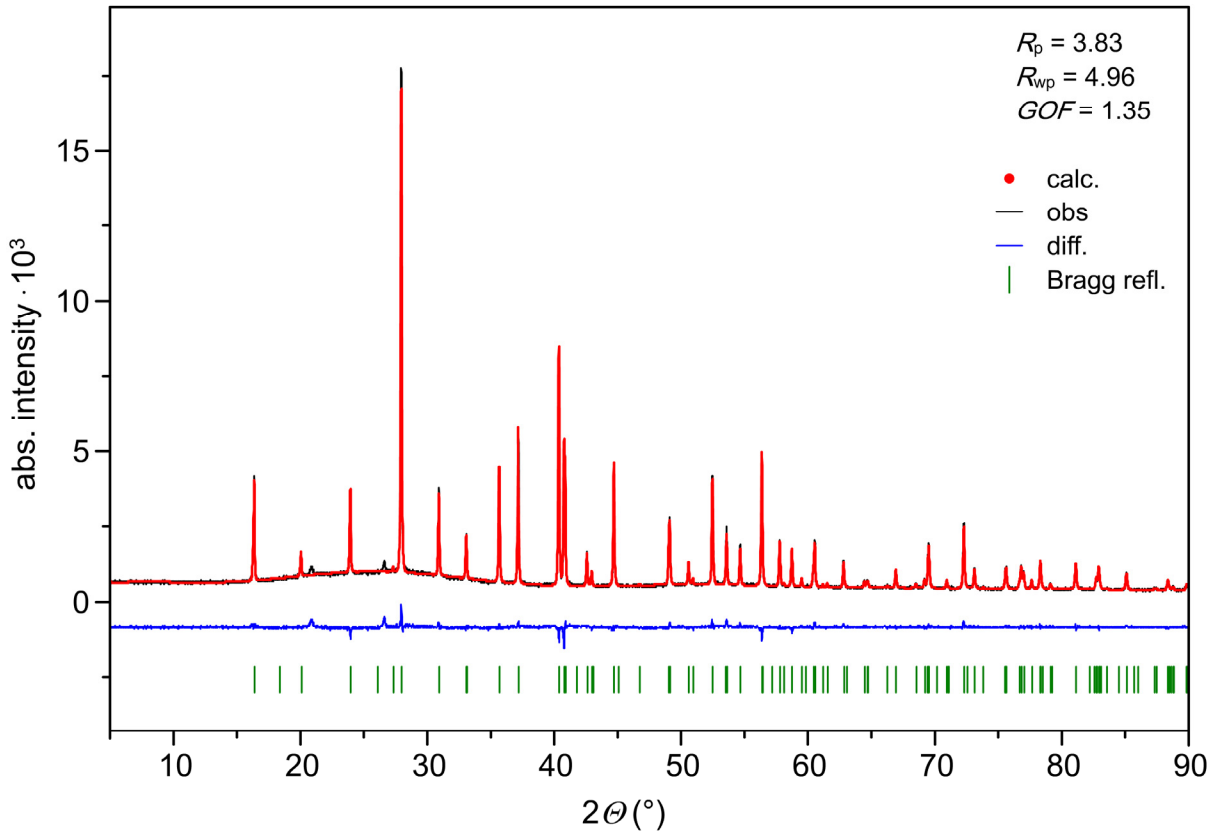

Figure S2. Experimental X-ray powder diffraction pattern of $LiBSi_2$ (black) referenced with the theoretical powder pattern based on Rietveld refinement (red). The difference plot is shown in blue.

Table 1. Crystallographic data of $LiBSi_2$ from Rietveld refinement ($P4_2/nmc$, $Z = 8$, origin at –1 (choice 2); estimated standard deviations in parentheses)

empirical formula	$LiBSi_2$
formula weight ($g \cdot mol^{-1}$)	73.92
space group	$P4_2/nmc$
unit cell dimension	a = 6.83225(3) Å, c = 8.83924(6) Å, V = 412.612(5) Å^3
Z	8
ρ (calc.) (g/cm^3)	2.38
μ (mm^{-1})	11.60
R_p / R_{wp} / GOF	3.83 / 4.96 / 1.35

Table 2. Fractional atomic coordinates, isotropic equivalent atomic displacement parameters and side occupancy factors for $LiBSi_2$ ($P4_2/nmc$, $Z = 8$, origin at –1 (choice 2); estimated standard deviations in parentheses).

Atom	Wyckoff position	*x*	*y*	*z*	*s.o.f.*	U_{iso} ($Å^2 \cdot 10^3$)
Li	8*g*	1/4	0.5042(9)	0.0784(5)	1	12(2)
B	8*f*	0.5095(3)	0.4905(3)	1/4	1	6(1)
Si1	8*g*	1/4	0.0690(1)	0.3632(1)	1	5.4(4)
Si2	8*g*	1/4	0.5665(1)	0.6181(1)	1	5.8(4)

Table 3. Interatomic distances in $LiBSi_2$ ($P4_2/nmc$, $Z = 8$, origin at –1 (choice 2); estimated standard deviations in parentheses).

Atom pair			*d*(Å)	Atom pair			*d*(Å)
Li-	B	2x	2.335(3)	Si1-	B1	2x	2.076(2)
	Si1		2.567(4)		Si2		2.436(1)
	Si2	2x	2.722(5)		Si1		2.474(1)
	Si2	2x	2.796(4)		Li		2.567(4)
	Si1	2x	2.799(4)		Li	2x	2.799(5)
	Si1	2x	2.857(5)		Li	2x	2.857(4)
B-	Si2	2x	2.052(2)	Si2-	B	2x	2.052(2)
	Si1	2x	2.076(2)		Si1		2.436(1)
	Li1	2x	2.335(5)		Si2		2.507(1)
					Li	2x	2.722(4)
					Li	2x	2.796(5)

Raman spectroscopy. Raman spectra were collected using a LabRAM HR 800 spectrometer. The instrument is equipped with an 800 mm focal length spectrograph and an air cooled (–70°C), back thinned CCD detector (pixel size 26x26 microns). The fine powdered sample was placed on a glass slide and the laser was focused onto the sample using a 50X super long working distance (WD=20.5 mm) Mitutoyo objective with a numerical aperture of 0.42 and depth of focus of 1.6 mm. The sample was excited using an air cooled double frequency Nd:YAG laser (532 nm, 5.6 mW) and an air cooled intra cavity regulated laser diode with point source (785 nm, 0.88 mW). The spectrum was collected with an exposure time of 60 sec, accumulation number of 10 and grating of 600 lines/mm.

Differential Scanning Calorimetry. Differential scanning calorimetry (DSC) measurements were performed with a NETZSCH DSC 404 Pegasus apparatus under an Ar gas flow of ~60 ml/min. About 5 mg of powder sample $LiBSi_2$ were sealed in a niobium crucible by arc-welding in an Ar-filled glove box. An empty niobium crucible served as reference. The scanning range was from room temperature to 800 °C with a heating/cooling rate of 10 K/min. The sample was recovered after the measurement and investigated by PXRD. Handling of DSC data was done with the program Proteus Thermal Analysis.[4] From the DSC trace and PXRD pattern of the recovered sample it could be concluded that $LiBSi_2$ does not decompose in the investigated temperature range.

Solid State Nuclear Magnetic Resonance (NMR) Spectroscopy. The ^{7}Li- and ^{11}B-MAS (magic angle spinning) NMR spectra (Figure S3 and S4) were collected on a Varian VNMRs 500 spectrometer operating at 160.37 MHz and 194.24 MHz for ^{11}B and ^{7}Li, respectively. MAS was performed at spinning speeds of 15 - 40 kHz employing a Varian 1.6 mm triple resonance T^{3}-MAS probe. $LiBSi_2$ appears as the only crystalline product beside an amorphous byproduct.

The ^{7}Li MAS NMR spectrum exhibits a signal at 0.95 ppm, accompanied by a set of spinning sidebands. From the positions of the outermost spinning sidebands a quadrupolar coupling constant C_Q = 0.18 MHz is estimated. At longer relaxation delays (up to 2h), a second contribution at -0.35 ppm adds to the signal.

In the ^{11}B-MAS NMR spectrum, a broad NMR signal appears centered around -0.5 ppm, with spinning sidebands covering a range of ± 0.8 MHz. In addition to this, a second contribution is found at -30.8 ppm, which exhibits a rather long relaxation time and but a small number of spinning sidebands. The quadrupolar coupling constants for these two components are estimated to C_Q= 1.6 MHz for the signal at -0.5 ppm and C_Q = 0.3 MHz for the narrow signal at -30.8 ppm. We tentatively assign the two signals with the long relaxation times (^{7}Li: -0.35 ppm; ^{11}B: -30.8 ppm) to $LiBSi_2$.

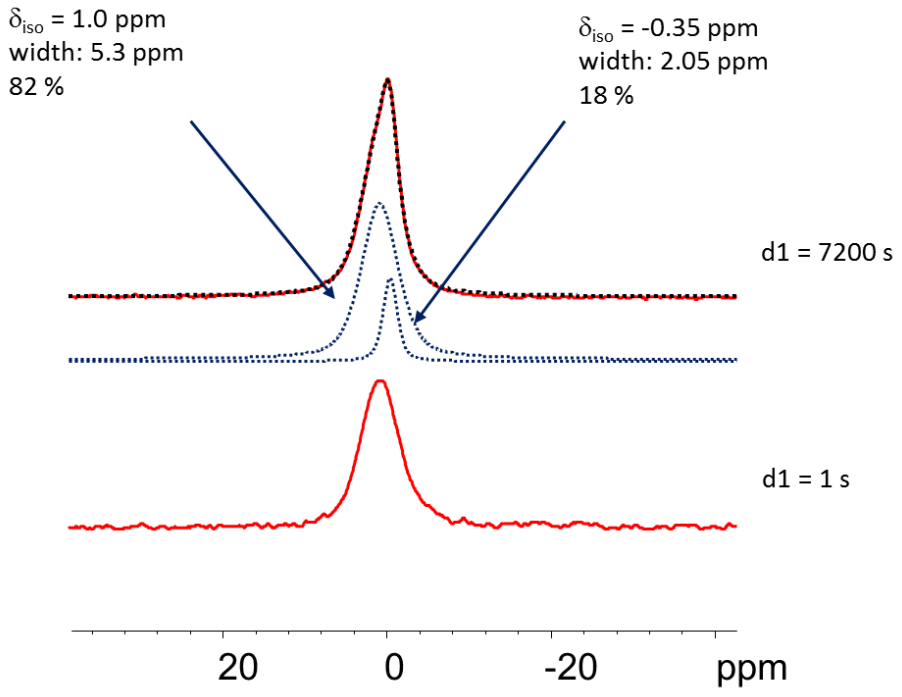

Figure S3: ^{7}Li-MAS NMR spectrum of $LiBSi_2$. Exp. details: ν_{RF} = 113.6 kHz; ν_{MAS} = 15 kHz; relaxation delay: 3600 s.

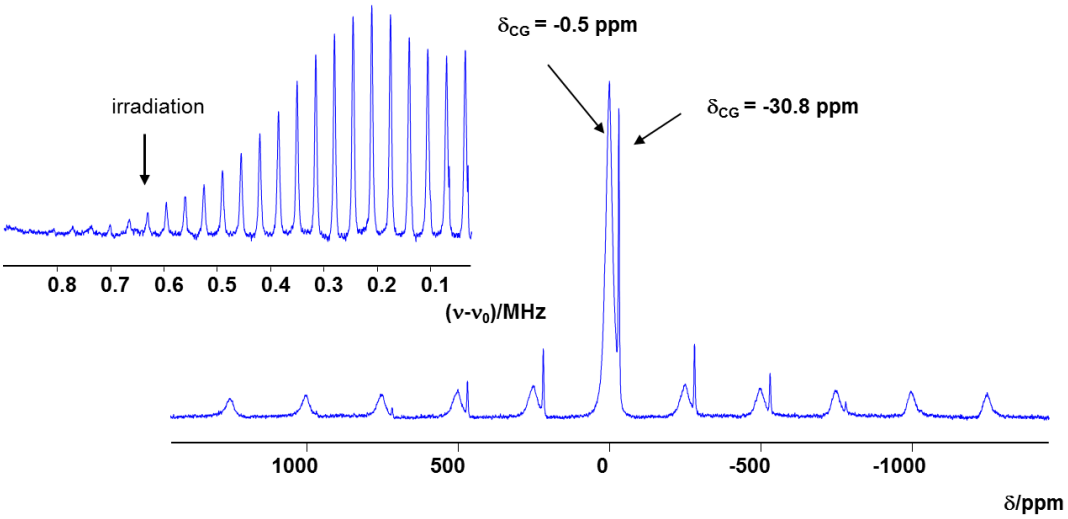

Figure S4: ^{11}B MAS NMR spectrum of $LiBSi_2$. Exp. details: ν_{RF} = 68.5 kHz; ν_{MAS} = 35 kHz; relaxation delay: 8000 s. Insert: sideband pattern for the broad component, from which a quadrupolar coupling constant C_Q = 1.6 MHz can be estimated (for I = 3/2, C_Q is identical to the overall width of the spectrum).

Computational details. Theoretical calculations of the electronic structure were performed using the first principles all-electron projected augmented wave (PAW) method[5] as implemented by the Vienna Ab Initio Simulation Package (VASP[6]). Exchange-correlation effects were treated within the generalized gradient approximation (GGA[7]) using the Perdew-Burke-Ernzerhof (PBE[8]) parameterization. The $LiBSi_2$ structure was relaxed with respect to volume, lattice parameters, and atom positions and using experimental parameters as starting values. Forces were converged to better than 1×10^{-3} eV/Å. The equilibrium volume was obtained by fitting to a third order Birch-Murnaghan equation of state.[9] The integration over the Brillion Zone (BZ) was done on a grid of special k-points with size 11×11×11 (6×6×6 for the equation of state) determined according to the Monkhorst-Pack scheme[10] and using the tetrahedron method with Blöchl correction.[11] The energy cutoff was set to 500 eV. Zone-centered phonon calculations were performed using VASP's density functional perturbation theory (DFPT) approach. The decomposition of the density of state (DOS) into atomic contributions is based on spheres with radii Li = 1.5 Å, Si = 1.25 Å, B = 0.8 Å, exceeding slightly the covalent radii of B and Si, and the ionic radius of Li (extrapolated to a coordination number 11). The structure parameters after relaxation and equations of states (EOS) parameters are specified in Tables S4 and S5. Note that the agreement with the experimental structure parameters is excellent (cf. Tables 1 and 2).

Table S4. Computationally relaxed structure parameters for $LiBSi_2$. Space group $P4_2/nmc$, a = 6.8328 Å, c = 8.8524 Å

Atom	Wyckoff position	*x*	*y*	*z*
Li	8*g*	1/4	0.5037	0.0766
B	8*f*	0.5080	0.4920	1/4
Si1	8*g*	1/4	0.0691	0.3637
Si2	8*g*	1/4	0.5663	0.6206

Table S5. Computed equation of states parameters:

	E_0 (eV/fu)	V_0 (Å^3/fu)	B_0 (GPa)	B_0'
Li_2BSi_2	-20.0308	51.702	103.7	4.1

References for Supporting Information

[1] E. Stoyanov, U. Häussermann, K. Leinenweber, *High Pressure Res.* **2010**, *30*, 175.
[2] a) F.O.X., Free Objects for Crystallography V 1.9.7.0, http://objcryst.sourceforge.net, **2011**; b) R. Cerny, V. Favre-Nicolin, *Powder Diffr.* **2005**, *20*, 359; c) V. Favre-Nicolin, R. Cerny, *J. Appl. Crystallogr.* **2002**, *35*, 734.
[3] TOPAS 4.0 - Rietveld Software, Bruker AXS, Madison (Wisconsin, USA), **2009**.
[4] Netzsch, Proteus Thermal Analysis V4.8.2, Netzsch-Gerätebau GmbH, Selb, Germany, **2006**.
[5] a) P. E. Blöchl, *Phys. Rev. B* **1994**, *50*, 17953; b) G. Kresse, D. Joubert, *Phys. Rev. B* **1999**, *59*, 1758.
[6] a) G. Kresse, J. Hafner, *Phys. Rev. B* **1993**, *48*, 13115; b) G. Kresse, J. Furthmüller, *Comp. Mater. Sci.* **1996**, *6*, 15.
[7] a) Y. Wang, J. P. Perdew, *Phys. Rev. B* **1991**, *44*, 13298; b) J. P. Perdew, J. A. Chevary, S. H. Vosko, K. A. Jackson, M. R. Pederson, D. J. Singh, C. Fiolhais, *Phys. Rev. B* **1992**, *46*, 6671.
[8] J. P. Perdew, K. Burke, M. Ernzerhof, *Phys. Rev. Lett.* **1996**, *77*, 3865.
[9] F. Birch, *Phys. Rev.* **1947**, *71*, 809.
[10] H. J. Monkhorst, J. D. Pack, *Phys. Rev. B* **1976**, *13*, 5188.
[11] P. E. Blöchl, O. Jepsen, O. K. Andersen, *Phys. Rev. B* **1994**, *49*, 16223.